BEILSTEIN JOURNAL OF NANOTECHNOLOGY

Ten years of the helium ion microscope

Edited by Gregor Hlawacek and Annalena Wolff

Imprint

Beilstein Journal of Nanotechnology
www.bjnano.org
ISSN 2190-4286
Email: journals-support@beilstein-institut.de

The *Beilstein Journal of Nanotechnology* is published by the Beilstein-Institut zur Förderung der Chemischen Wissenschaften.

Beilstein-Institut zur Förderung der Chemischen Wissenschaften
Trakehner Straße 7–9
60487 Frankfurt am Main
Germany
www.beilstein-institut.de

BEILSTEIN JOURNAL OF NANOTECHNOLOGY

3D superconducting hollow nanowires with tailored diameters grown by focused He$^+$ beam direct writing

Rosa Córdoba[*1], Alfonso Ibarra[2], Dominique Mailly[3], Isabel Guillamón[4], Hermann Suderow[4] and José María De Teresa[*2,5,6]

Full Research Paper

Open Access

Address:
[1]Instituto de Ciencia Molecular, Universitat de València, Catedrático José Beltrán 2, 46980 Paterna, Spain, [2]Laboratorio de Microscopías Avanzadas (LMA)-Instituto de Nanociencia de Aragón (INA), Universidad de Zaragoza, E-50018 Zaragoza, Spain Departamento de Física de la Materia Condensada, Universidad de Zaragoza, E-50009 Zaragoza, Spain, [3]Centre de Nanosciences et de Nanotechnologies, CNRS, Univ Paris Sud, Université Paris Saclay, 91120 Palaiseau, France, [4]Laboratorio de Bajas Temperaturas y Altos Campos Magnéticos, Departamento de Física de la Materia Condensada, Instituto de Ciencia de Materiales Nicolás Cabrera, Condensed Matter Physics Center (IFIMAC), Universidad Autónoma de Madrid, 28049, Madrid, Spain, [5]Instituto de Nanociencia y de Materiales de Aragón (INMA), Universidad de Zaragoza-CSIC, E-50009 Zaragoza, Spain and [6]Departamento de Física de la Materia Condensada, Universidad de Zaragoza, E-50009 Zaragoza, Spain

Email:
Rosa Córdoba[*] - rosa.cordoba.castillo@gmail.com;
José María De Teresa[*] - deteresa@unizar.es

* Corresponding author

Keywords:
electron tomography; focused ion beam induced deposition (FIBID); helium ion microscope; magneto-transport measurements; nano-superconductors; tungsten carbide (WC)

Beilstein J. Nanotechnol. **2020,** *11,* 1198–1206.
doi:10.3762/bjnano.11.104

Received: 06 May 2020
Accepted: 14 July 2020
Published: 11 August 2020

This article is part of the thematic issue "Ten years of the helium ion microscope".

Guest Editors: G. Hlawacek and A. Wolff

Abstract

Currently, the patterning of innovative three-dimensional (3D) nano-objects is required for the development of future advanced electronic components. Helium ion microscopy in combination with a precursor gas can be used for direct writing of three-dimensional nanostructures with a precise control of their geometry, and a significantly higher aspect ratio than other additive manufacturing technologies. We report here on the deposition of 3D hollow tungsten carbide nanowires with tailored diameters by tuning two key growth parameters, namely current and dose of the ion beam. Our results show the control of geometry in 3D hollow nanowires, with outer and inner diameters ranging from 36 to 142 nm and from 5 to 28 nm, respectively; and lengths from 0.5 to 8.9 µm. Transmission electron microscopy experiments indicate that the nanowires have a microstructure of large grains with a crystalline structure compatible with the face-centered cubic WC_{1-x} phase. In addition, 3D electron tomographic reconstructions show that the hollow center of the nanowires is present along the whole nanowire length. Moreover, these nanowires become superconducting at

6.8 K and show high values of critical magnetic field and critical current density. Consequently, these 3D nano-objects could be implemented as components in the next generation of electronics, such as nano-antennas and sensors, based on 3D superconducting architectures.

Introduction

Superconductors are dissipationless carriers of electric current and provide macroscopic, and thus robust, quantum coherence. This allows for a wide range of applications, particularly at the nanometer-scale, where they can be easily integrated in circuits and used as ultrasensitive sensors of magnetic fields, temperature and as key elements for quantum computation. The behavior of nanosized superconductors as one-dimensional quantum oscillators [1], Josephson junction arrays [2], electronic transport devices [3-7], very small-scale devices [8,9], micrometer-scale coolers [10], or thermal and spin sensors [11,12] has been studied in detail.

Nowadays, research on manufacturing highly energy-efficient three-dimensional (3D) structures [13] is critical for the development of future electronics. However, when approaching the nanometer-scale, the number of works on real 3D nano-superconductors [14-19] decreases dramatically, mostly due to the complex fabrication and characterization. A technique successfully utilized for fabricating 3D nano-objects is direct writing by a focused beam of positively charged particles, the so-called focused-ion-beam induced deposition (FIBID) [20]. A very promising development of FIBID is based on Ga^+ ions. Functional 3D nanomaterials have been grown by Ga^+ FIBID in the last decade [21-26]. In particular, Ga^+ FIBID in combination with $W(CO)_6$ as precursor material yielded 3D superconducting W-based wires with a critical temperature (T_c) below 5 K and a critical magnetic field ($\mu_0 H_{c2}(0)$) up to 9.5 T [14-16]. Alternatively, in combination with $Nb(NMe_2)_3(N\text{-}t\text{-}Bu)$, Ga^+ FIBID yielded NbC wires with a broadened T_c range from 4 to 11 K [18]. One significant limitation is that 3D elements below 100 nm in diameter cannot be obtained with Ga^+ FIBID, mainly due to the relatively large Ga^+ beam diameter (approx. 5 nm) and a high proximity effect generated by Ga^+ ion scattering.

Regarding a higher spatial resolution, the helium ion microscope (HIM) [27], based on a gas field-ionization source, has emerged as a tool for direct writing of complex 3D nano-objects taking advantage of its small beam diameter (approx. 0.3 nm) and low proximity effect [28]. When precursor molecules from the gas phase are adsorbed on a substrate surface, He^+ FIB dissociates them into non-volatile and volatile products. The non-volatile products attach to the surface, resulting in a deposit, whereas the volatile products ones are pumped out of the process chamber. Normally, the final deposit is a mixture of carbon, metallic elements and oxygen. As clearly described using analytical modelling [29] and Monte-Carlo simulations [30], the vertical growth of 3D nano-objects by He^+ FIBID is mainly caused by secondary electrons of the first order produced from the primary ion beam, whereas the lateral growth is induced by secondary electrons of the second order generated from scattered ions. Thus, the direct contribution of the primary He^+ ion beam and the scattered He^+ ions is almost negligible for the growth of these 3D nano-objects. Nevertheless, it is worth mentioning that its resolution, volume per dose and throughput are very sensitive to the selected growth conditions such as ion beam energy, ion beam current, precursor flux, surface interactions with the beam, and precursor molecules [29,30]. Hence, the He^+ FIBID technique is highly recommended for direct writing of 3D nano-objects with high resolution and aspect ratio [17,19,31-35]. A successful example of tailored 3D nano-objects grown by He^+ FIBID has been reported by Kohama and co-workers [35]. The authors deposited W-based pillars with diameters down to approx. 40 nm and aspect ratios of approx. 50. The microstructure of the grown material consisted of fcc WC_{1-x} and $W_2(C,O)$ grains. Moreover, when the He^+ beam was well focused the authors observed columnar voids created at the center of the pillars with a diameter ranging from 1 to 15 nm, showing the path to build complex 3D nano-objects beyond standard nanowires (NWs). Recent breakthroughs in the growth of 3D WC superconducting nano-objects with extremely large aspect ratios using He^+ FIBID have been reported by some of the authors, such as hollow NW-like nanotubes as small as 32 nm in diameter [17] and nanohelices with controllable geometries, including the smallest and most densely packed nanohelix to date with a diameter of 100 nm [19].

In this work, we present the direct writing of 3D WC crystalline superconducting hollow NWs with tailored diameters grown using a HIM. The hollow NW geometry is successfully controlled by tuning the ion beam current and dose from 0.65 to 7 pA and from 0.1 to 0.4 nC, respectively, resulting in NWs with outer diameters from 36 to 142 nm and with inner diameters from 5 to 28 nm, and total length from 0.5 to 8.9 μm (aspect ratio ≈ 196). These values are significantly better than those reported in previous works [17,35]. The NWs microstructure consists of large grains of fcc WC_{1-x}, in good agreement

with [17,35]. In addition, the NWs are hollow along the whole NW length, which could make them nonconventional nanopipettes, as demonstrated in 3D reconstructions of electron tomography experiments. Finally, these 3D hollow NWs exhibit superconductivity below 6.8 K (T_c), as well as high upper critical magnetic fields $\mu_0 H_{c2} \approx 14.7$ T, and large critical current densities $J_c \approx 0.15$ MA/cm^2.

Results and Discussion

Growth of 3D hollow nanowires by He$^+$ FIBID

We use a HIM in combination with a $W(CO)_6$ precursor to grow individual, out-of-plane WC NWs in a single step, controlling inner and outer diameter and total length. The precursor gas is delivered to the process chamber and adsorbed onto the substrate surface, while the He$^+$ FIB spot remains fixed during the deposition favoring continuous vertical growth along [17].

Dimensional control for nanowires

We investigated the dimensional control for these NWs by optimizing in the deposition the following parameters: the ion beam current and ion dose. SEM images of typical NWs grown with ion beam currents ranging from 0.54 to 6.47 pA and doses from 0.1 to 1.4 nC are depicted in Figure 1a–d.

Varying these parameters enables us to fabricate 3D NWs with diameters ranging from 45 to 125 nm, lengths ranging from 0.5 to 8.9 µm, and with aspect ratios up to 198. Further details regarding the growth conditions are described in the Experimental section. We found a linear dependence of the NW volume (determined as $\pi \times$ (outer diameter/2 – inner diameter/2)$^2 \times$ height) as a function of the ion dose for the mentioned ion beam currents (Figure 1e). Moreover, we noted that the NW volume rapidly decreases as a function of the ion beam current for the same dose (Figure 2). When using high currents several effects can play a role in this dependence such as precursor depletion, local heating, which decreases the precursor molecule sticking coefficient, and low precursor diffusion from the substrate to the top of the pillar [36,37]. This shows the need for future systematic experiments varying the dwell time in pulsed growth or varying the flux of precursor gas.

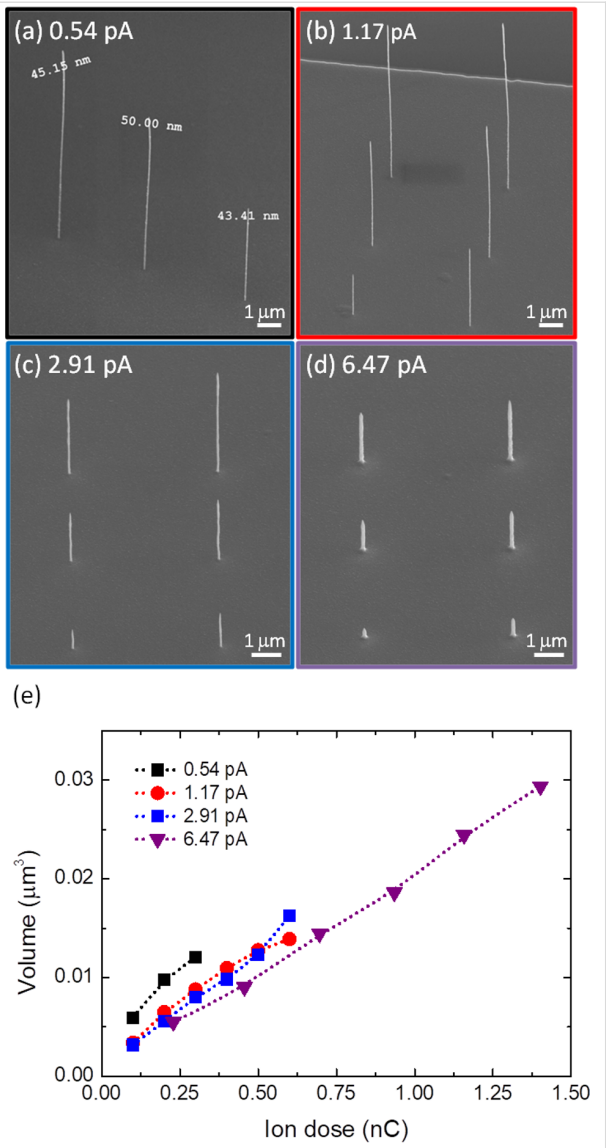

Figure 1: (a–d) SEM images of hollow NWs grown by He$^+$ FIBID; (a) ion beam current: 0.54 pA, dose: 0.1–0.3 nC from right to left; (b) ion beam current: 1.17 pA, dose: 0.1–0.6 nC from left to right and upwards; (c) ion beam current: 2.91 pA, dose: 0.1–0.6 nC from left to right and upwards; (d) ion beam current: 6.47 pA, dose: 0.229, 0.456, 0.696, 0.935, 1.158, and 1.402 nC from left to right and upwards. (e) NW volume in (a) as a function of the ion beam dose.

(High-resolution) scanning transmission electron microscopy

Dependence of NW inner diameter on the ion beam current

To investigate the dependence of the NW inner diameter on the ion beam current, scanning transmission electron microscopy (STEM) experiments were performed. We found that inner diameter of the hollow NWs changes from 5 to 28 nm, whereas the outer diameter changes from 36 to 143 nm upon increasing the ion beam current from 1.3 to 7 pA. STEM images of these hollow NWs are shown in Figure 3a. The observed non-uniform shape of the cavity in the central nanowire could be explained by several reasons, such as He$^+$ FIB instability or irregular substrate surface. We find a linear dependence of the inner diameter on the ion beam current (Figure 3b), which indicates that the ion beam forms the cavity due to a milling effect. Thus via tuning the ion beam current and dose we have full control to tailor the diameters of the hollow 3D NWs. The specific deposition parameters and NW diameters are listed in Table 1.

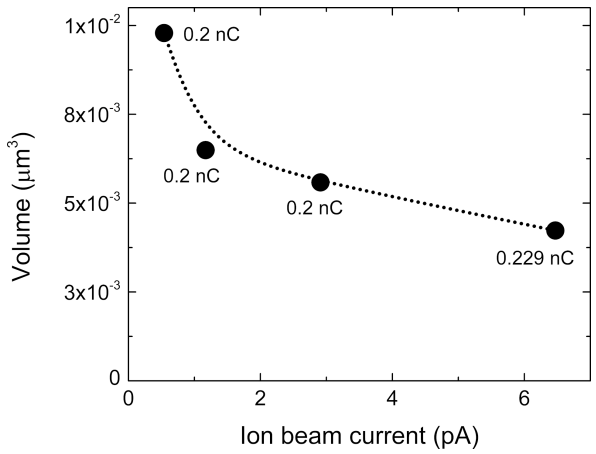

Figure 2: NW volume for a specific dose, as a function of the ion beam current.

Table 1: Growth parameters and diameters of hollow WC NWs.

hollow nanowire type	1	2	3
ion beam current (pA)	1.3	2.3	7.0
outer diameter (nm)	36	71	142
inner diameter (nm)	5	9	28

Electron tomography

In order to further examine the NW diameters along their length, electron tomography experiments on two specific NWs were carried out. Figure 4 shows the tomographic reconstruction of hollow WC NWs grown at (a) 7 pA and (b) 2 pA. One can see from the images that the cavities are present up to the tip of the NW. On the left panel of Figure 4a, a STEM image of the NW with outer and inner diameter of 142 and 28 nm, respectively, is shown. On the right panel, a snapshot of the colored 3D tomographic reconstruction is depicted. Figure 4b shows a STEM image of the NW with outer and inner diameter of 77 and 8 nm, respectively, on the left panel, and a snapshot of the colored 3D tomographic reconstruction is displayed on the right panel. Three movies of the tomographic reconstruction for each hollow NW are added in Supporting Information File 1–7, including a transversal (x–y) and a longitudinal (y–z) section, and a colored three-dimensional reconstruction.

Microstructure

Concerning the microstructure of the NWs, high-resolution scanning transmission electron microscopy (HRSTEM) images have been acquired sequentially and processed to extract the crystallographic structure (Figure 5). We indexed the spots indicated in the fast Fourier transform (Figure 5b) of the image in Figure 5a with the planes (−11−1), (−200) and (−1−11), and the

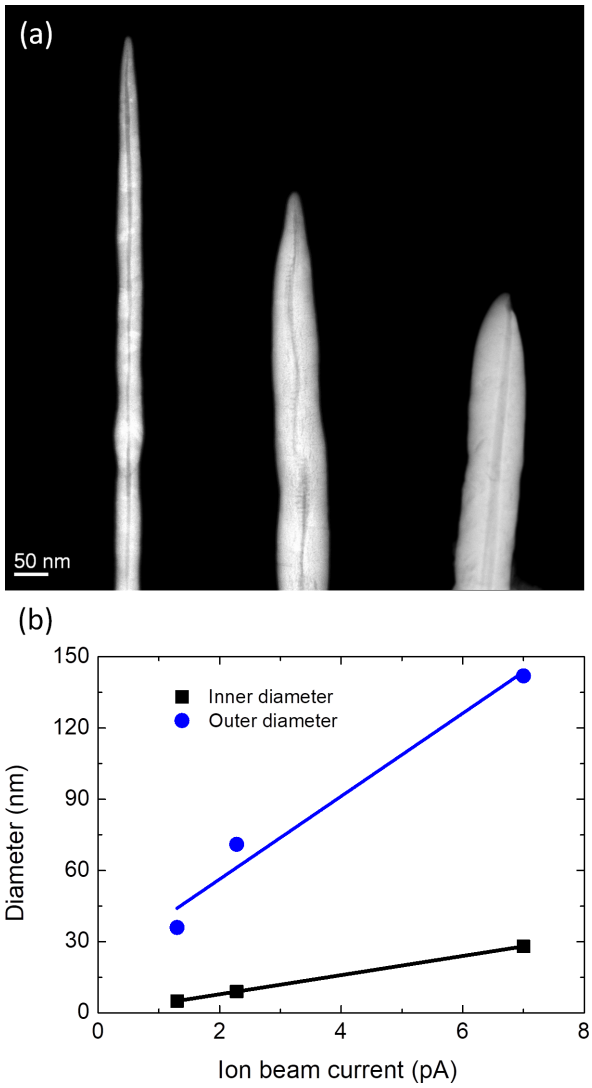

Figure 3: (a) STEM images of hollow NWs grown at 1.3, 2.3, and 7 pA, from left to right. (b) NW diameter in (a) as a function of the ion beam current.

[011] zone axis of the WC_{1-x} fcc structure, with a lattice parameter of a = 0.4272 nm. A lower magnification STEM image of the NW grown at 1.3 pA is depicted in Figure 5c. These results are in good agreement with the previous work reported by some of the authors [17].

Magneto-electrical-transport study

To determine the critical superconducting parameters in NWs grown at 0.65, 1.3, and 2.18 pA (Figure 6 and Table 2), a magneto-electrical transport study using the typical four-point-probe configuration has been performed. Following the procedure described in [17], first 3D NWs were placed flat on the SiO_2 layer of a Si/SiO_2 substrate by means of a nano-manipulator. Then, four Pt FIBID contacts were grown to connect the NWs to pre-patterned Ti pads. Finally, we made

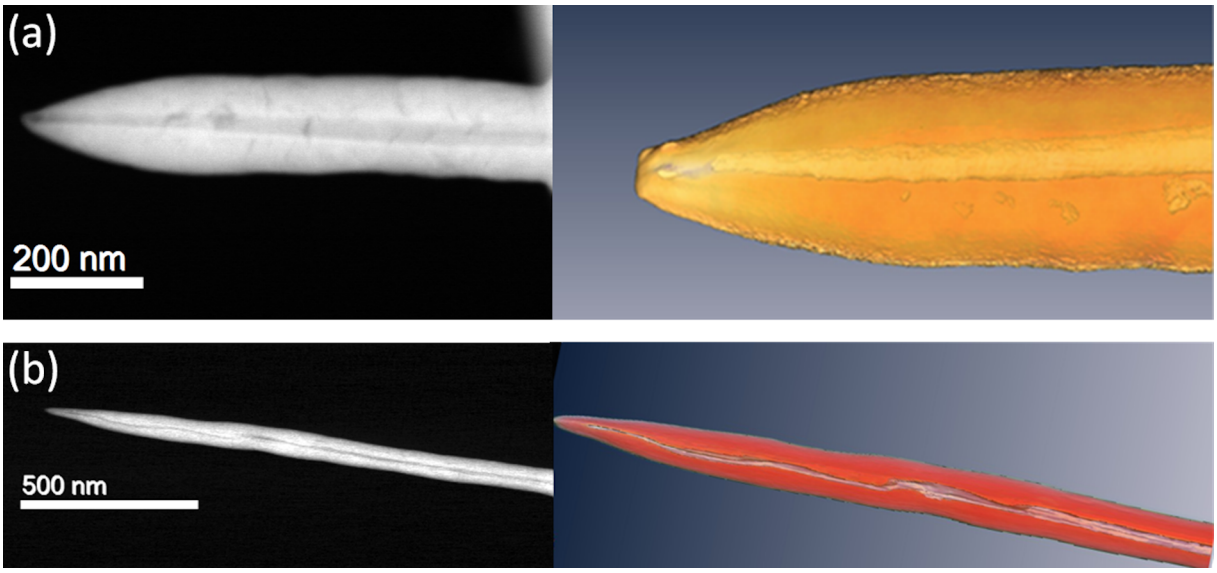

Figure 4: (a) Tomography of a hollow WC NW grown at 7 pA, with an outer diameter of 142 nm and an inner diameter of 28 nm; left panel: STEM image, right panel: snapshot of the 3D tomographic reconstruction. (b) Tomography of a hollow WC NW grown at 2 pA, with an outer diameter of 77 nm and inner diameter of 8 nm; left panel: STEM image, right panel: snapshot of the 3D tomographic reconstruction.

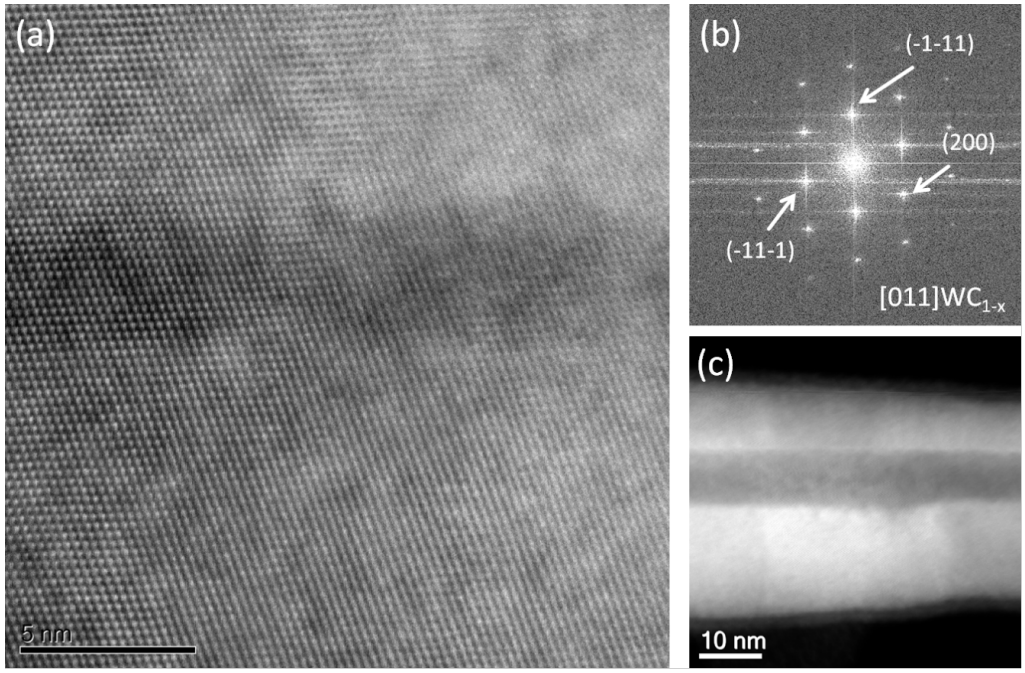

Figure 5: (a) HRSTEM image of a typical hollow WC NW grown at 1.3 pA. (b) Fast Fourier transform of the image in (a), showing the crystalline nature of the material and indexed as the [011] zone axis of the fcc WC_{1-x} structure. (c) Lower magnification STEM image of the WC NW in (a).

four-point-probe electrical measurements at low temperature (down to 0.5 K) and under a magnetic field perpendicular to the substrate plane (up to 9 T).

The NWs change from the normal to the superconducting state at T_c ($0.5R_N$) values between 5.45 and 6.78 K (Figure 6a and Table 2). No clear trend was visible in T_c values for NWs grown using different currents, although the identified T_c range is in good agreement with the previously reported results [17]. Also, it is up to 1.5 times higher than that of Ga^+ FIBID nanostructures of similar dimensions [9]. The inset of Figure 6a shows the measured resistance as a function of the temperature in the full temperature range investigated for a NW grown at 0.65 pA. The value of $\mu_0 H_{c2}$ as a function of the temperature

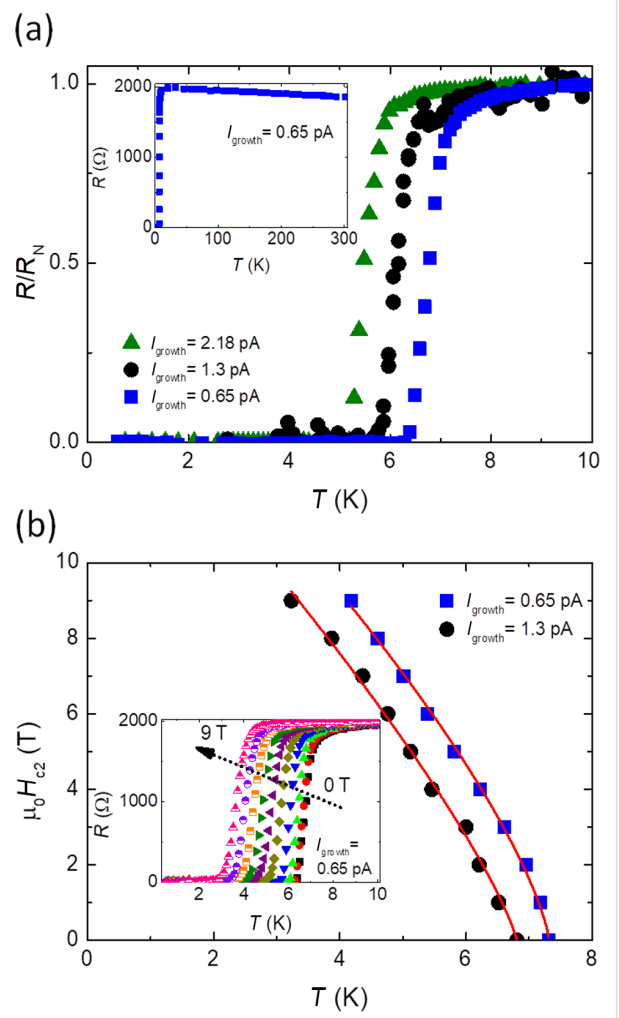

Figure 6: (a) Normalized resistance as a function of the temperature of hollow NWs grown using ion beam currents indicated in the legend. R_N is the resistance for the normal state at T = 10 K. The inset shows the resistance as function of the temperature (full range) for a NW grown at 0.65 pA, I_{bias} = 100 nA. (b) Upper critical magnetic field ($\mu_0 H_{c2}$) as a function of the temperature of NWs grown using ion beam currents indicated in the legend. Data is fitted to a power-law equation. The inset shows the resistance as a function of the temperature for a NW grown at 0.65 pA under perpendicular magnetic fields from 0 to 9 T.

for NWs grown at 0.65 and 1.3 pA is depicted in Figure 6b. The values of $\mu_0 H_{c2}$ ($0.9R_N$) are extracted from the resistance-vs-temperature curves under perpendicular magnetic field (inset of Figure 6b). By fitting $\mu_0 H_{c2}(T)$ to a power-law equation $\mu_0 H_{c2}(T) \propto (1 - T/T_c)^n$, $\mu_0 H_{c2}(0\ \text{K})$ is estimated to be approx. 14.5 T for the different NWs. The coherence length, ξ, at 0 K is around 4.77 nm and the estimated magnetic field penetration depth, λ, [38,39] ranges from 720 to 874 nm. Additionally, J_c (0.6 K, 0 T) is approx. 0.15 MA/cm^2.

Summarizing, the estimated superconducting parameters (T_c, $\mu_0 H_{c2}$, J_c, ξ, λ) for these NWs (Table 2) are mostly compatible with those reported for He$^+$ FIBID out-of-plane WC nanotubes

Table 2: Superconducting parameters of NWs estimated from experimental magneto-transport measurements.

hollow nanowire type	1	2	3
ion beam current (pA)	0.65	1.30	2.18
outer diameter (nm)	36	41	72
R_N (Ω)	1959	2101	430
T_c (K)	6.78	6.16	5.45
$\mu_0 H_{c2}$ (0 K) (T)	14.66	14.48	—
J_c (0 T) (MA/cm^2)	0.083 (0.6 K)	0.151 (0.6 K)	0.026 (1 K)
ξ (0 K) (nm)	4.74	4.77	—
λ (0 K) (nm)	839	720	874

[17], nanohelices [19], and in-plane NWs used in hybrid microwave resonators [40]. They are potential building blocks for highly packed 3D nano-resonators, superconducting logic gates [41], quantum switches [42], and single-photon detectors [43-45].

Conclusion

We report a direct writing methodology to create 3D superconducting hollow NWs with tailored diameters using $W(CO)_6$ precursor with a highly focused He$^+$ beam. The resulting 3D hollow NWs have inner and outer diameters from 5 to 28 nm and from 36 to 142 nm, respectively, and aspect ratios above 196, which is unachievable by other additive manufacturing methods. The electron tomography study proved that the center hole is present along the whole length of the NWs.

As expected, the microstructure corresponds to the fcc WC_{1-x} phase. By studying their magnetotransport properties, we found $T_c \approx 6.8$ K, as well as $\mu_0 H_{c2} \approx 14.7$ T and $J_c \approx 0.15$ MA/cm^2. The presented methodology yields an advanced bottom-up approach for the fabrication of innovative 3D nano-architectures, in which nano-superconductivity may provide an advantage, for future electronic components, particularly for sensors, energy-storage components, and quantum computing.

Experimental

Growth of 3D hollow WC nanowires

He$^+$ FIBID hollow WC NWs have been fabricated in a ZEISS ORION NanoFab instrument equipped with a helium ion beam column and a single-needle gas injection system (GIS) through which $W(CO)_6$ gas is delivered to the process chamber.

The NWs were deposited on top of the pre-patterned Ti pads (150 nm in thickness) to prevent charge effects on the insulator

layer (250 nm thick of SiO_2) thermally grown on a silicon wafer [23]. These chips were fabricated following a routine recipe for UV optical lithography using a lift-off method. For the electron tomography and (HR)STEM experiments, NWs were directly grown on Cu TEM grids. Typical deposition conditions used for the He^+ FIBID process were as follows; precursor material: tungsten hexacarbonyl, $W(CO)_6$; $T_{precursor}$ = 55 °C; $GIS_{needle\ diameter} \approx 500$ µm; $GIS_z \approx 500$ µm; $GIS_{x,y} \approx 60$ µm; $P_{base} \approx 3 \times 10^{-7}$ mbar; $P_{process} \approx 4 \times 10^{-6}$ mbar; acceleration voltage = 30 kV; pattern shape: spot mode; ion beam current range of 0.54 to 6.47 pA and dose range of 0.1 to 1.4 nC.

Microstructure and tomography at the nanometer-scale

Scanning transmission electron microscopy (STEM) imaging and EDS were carried out in a probe-corrected FEI Titan 60–300 operated at 300 kV and equipped with a high-brightness X-FEG and a CETCOR C_s corrector for the condenser system to provide sub-angstrom probe size.

STEM high-angle annular dark-field (HAADF) tomography was performed using a Thermo Fisher Tecnai field-emission gun operated at 300 kV. The angular range for the tilt series was ±70° with pictures taken every 1°. Image alignment and 3D reconstruction was carried out with FEI tomography acquisition software Inspect 3D after the acquisition of 140 images. The movies of the tomographic reconstruction for each hollow NW were performed using Amira 3D software.

Magneto-electrical transport study

The magneto-electrical transport measurements on the NWs were carried out using a "Physical Property Measurement System" (PPMS), from Quantum Design equipped with a helium-3 refrigerator insert.

Supporting Information

Movies of 3D tomographic reconstruction.

Supporting Information File 1

Electron tomography_3D reconstruction_hollow NW grown at 2 pA and 0.6 nC.
[https://www.beilstein-journals.org/bjnano/content/supplementary/2190-4286-11-104-S1.wmv]

Supporting Information File 2

Electron tomography_3D longitudinal_hollow NW grown at 2 pA and 0.6 nC.
[https://www.beilstein-journals.org/bjnano/content/supplementary/2190-4286-11-104-S2.wmv]

Supporting Information File 3

Electron tomography_longitudinal section_hollow NW grown at 2 pA and 0.6 nC.
[https://www.beilstein-journals.org/bjnano/content/supplementary/2190-4286-11-104-S3.wmv]

Supporting Information File 4

Electron tomography_transversal section_hollow NW grown at 2 pA and 0.6 nC.
[https://www.beilstein-journals.org/bjnano/content/supplementary/2190-4286-11-104-S4.wmv]

Supporting Information File 5

Electron tomography_3D reconstruction_hollow NW grown at 7 pA and 1.009 nC.
[https://www.beilstein-journals.org/bjnano/content/supplementary/2190-4286-11-104-S5.wmv]

Supporting Information File 6

Electron tomography_3D longitudinal_hollow NW grown at 7 pA and 1.009 nC.
[https://www.beilstein-journals.org/bjnano/content/supplementary/2190-4286-11-104-S6.wmv]

Supporting Information File 7

Electron tomography_transversal section_hollow NW grown at 7 pA and 1.009 nC.
[https://www.beilstein-journals.org/bjnano/content/supplementary/2190-4286-11-104-S7.wmv]

Acknowledgements

The authors highly acknowledge Rubén Valero for the UV lithography process. The microscopy works have been conducted in the “Laboratorio de Microscopías Avanzadas” at “Instituto de Nanociencia de Aragón - Universidad de Zaragoza”. The authors acknowledge the LMA-INA for offering access to their instruments and expertise. The authors would like to acknowledge the use of Servicio General de Apoyo a la Investigación-SAI, Universidad de Zaragoza, particularly the Servicio de Medidas Físicas.

Funding

This work was supported by the financial support from Spanish Ministry of Economy and Competitiveness through the projects MAT2017-82970-C2-2-R, PIE201760E027, including FEDER funding, FIS2017-84330-R, CEX2018-000805-M, EU ERC (Grant Agreement No. 679080), from the EU-H2020 research and innovation programme under grant agreement No 654360 NFFA-Europe, and Nanocohybri COST CA-16218, from

regional Gobierno de Aragón (grants E13_20R and E28-20R) with European Social Fund (Construyendo Europa desde Aragón) and Comunidad de Madrid through project NANOMAGCOST-CM (Grant No. (S2018/NMT-4321)). The project that gave rise to these results received the support of a fellowship from "la Caixa" Foundation (ID 100010434). The fellowship code is LCF/BQ/PR19/11700008. The French RENATECH network (French national nanofabrication platform).

ORCID® iDs

Rosa Córdoba - https://orcid.org/0000-0002-6180-8113
Alfonso Ibarra - https://orcid.org/0000-0002-4599-3013
Hermann Suderow - https://orcid.org/0000-0002-5902-1880
José María De Teresa - https://orcid.org/0000-0001-9566-0738

References

1. Giordano, N. *Phys. Rev. Lett.* **1988,** *61,* 2137–2140. doi:10.1103/physrevlett.61.2137
2. Fazio, R. *Phys. Rep.* **2001,** *355,* 235–334. doi:10.1016/s0370-1573(01)00022-9
3. Guillamón, I.; Suderow, H.; Fernández-Pacheco, A.; Sesé, J.; Córdoba, R.; De Teresa, J. M.; Ibarra, M. R.; Vieira, S. *Nat. Phys.* **2009,** *5,* 651–655. doi:10.1038/nphys1368
4. Guillamón, I.; Suderow, H.; Vieira, S.; Fernández-Pacheco, A.; Sesé, J.; Córdoba, R.; De Teresa, J. M.; Ibarra, M. R. *New J. Phys.* **2008,** *10,* 093005. doi:10.1088/1367-2630/10/9/093005
5. Guillamón, I.; Córdoba, R.; Sesé, J.; De Teresa, J. M.; Ibarra, M. R.; Vieira, S.; Suderow, H. *Nat. Phys.* **2014,** *10,* 851–856. doi:10.1038/nphys3132
6. Guillamón, I.; Suderow, H.; Vieira, S.; Sesé, J.; Córdoba, R.; De Teresa, J. M.; Ibarra, M. R. *Phys. Rev. Lett.* **2011,** *106,* 077001. doi:10.1103/physrevlett.106.077001
7. Córdoba, R.; Orús, P.; Jelić, Ž. L.; Sesé, J.; Ibarra, M. R.; Guillamón, I.; Vieira, S.; Palacios, J. J.; Suderow, H.; Milosević, M. V.; De Teresa, J. M. *Sci. Rep.* **2019,** *9,* 12386. doi:10.1038/s41598-019-48887-7
8. Tonomura, A.; Kasai, H.; Kamimura, O.; Matsuda, T.; Harada, K.; Nakayama, Y.; Shimoyama, J.; Kishio, K.; Hanaguri, T.; Kitazawa, K.; Sasase, M.; Okayasu, S. *Nature* **2001,** *412,* 620–622. doi:10.1038/35088021
9. Córdoba, R.; Baturina, T. I.; Sesé, J.; Yu Mironov, A.; De Teresa, J. M.; Ibarra, M. R.; Nasimov, D. A.; Gutakovskii, A. K.; Latyshev, A. V.; Guillamón, I.; Suderow, H.; Vieira, S.; Baklanov, M. R.; Palacios, J. J.; Vinokur, V. M. *Nat. Commun.* **2013,** *4,* 1437. doi:10.1038/ncomms2437
10. Muhonen, J. T.; Meschke, M.; Pekola, J. P. *Rep. Prog. Phys.* **2012,** *75,* 046501. doi:10.1088/0034-4885/75/4/046501
11. Anahory, Y.; Naren, H. R.; Lachman, E. O.; Buhbut Sinai, S.; Uri, A.; Embon, L.; Yaakobi, E.; Myasoedov, Y.; Huber, M. E.; Klajn, R.; Zeldov, E. *Nanoscale* **2020,** *12,* 3174–3182. doi:10.1039/c9nr08578e
12. Marguerite, A.; Birkbeck, J.; Aharon-Steinberg, A.; Halbertal, D.; Bagani, K.; Marcus, I.; Myasoedov, Y.; Geim, A. K.; Perello, D. J.; Zeldov, E. *Nature* **2019,** *575,* 628–633. doi:10.1038/s41586-019-1704-3
13. Shulaker, M. M.; Hills, G.; Park, R. S.; Howe, R. T.; Saraswat, K.; Wong, H.-S. P.; Mitra, S. *Nature* **2017,** *547,* 74–78. doi:10.1038/nature22994
14. Li, W.; Gu, C.; Warburton, P. A. *J. Nanosci. Nanotechnol.* **2010,** *10,* 7436–7438. doi:10.1166/jnn.2010.2850
15. Romans, E. J.; Osley, E. J.; Young, L.; Warburton, P. A.; Li, W. *Appl. Phys. Lett.* **2010,** *97,* 222506. doi:10.1063/1.3521262
16. Li, W.; Fenton, J. C.; Cui, A.; Wang, H.; Wang, Y.; Gu, C.; McComb, D. W.; Warburton, P. A. *Nanotechnology* **2012,** *23,* 105301. doi:10.1088/0957-4484/23/10/105301
17. Córdoba, R.; Ibarra, A.; Mailly, D.; De Teresa, J. M. *Nano Lett.* **2018,** *18,* 1379–1386. doi:10.1021/acs.nanolett.7b05103
18. Porrati, F.; Barth, S.; Sachser, R.; Dobrovolskiy, O. V.; Seybert, A.; Frangakis, A. S.; Huth, M. *ACS Nano* **2019,** *13,* 6287–6296. doi:10.1021/acsnano.9b00059
19. Córdoba, R.; Mailly, D.; Rezaev, R. O.; Smirnova, E. I.; Schmidt, O. G.; Fomin, V. M.; Zeitler, U.; Guillamón, I.; Suderow, H.; De Teresa, J. M. *Nano Lett.* **2019,** *19,* 8597–8604. doi:10.1021/acs.nanolett.9b03153
20. Utke, I.; Hoffmann, P.; Melngailis, J. *J. Vac. Sci. Technol., B: Microelectron. Nanometer Struct.–Process., Meas., Phenom.* **2008,** *26,* 1197. doi:10.1116/1.2955728
21. Matsui, S.; Kaito, T.; Fujita, J.; Komuro, M.; Kanda, K.; Haruyama, Y. Three-Dimensional Nanostructure Fabrication by Focused-Ion-Beam Chemical Vapor Deposition. In *papers from 44th international conference on electron, ion, and photon beam technology and nanofabrication,* Rancho Mirage, California, (USA); AVS, 2000; pp 3181–3184.
22. Morita, T.; Kometani, R.; Watanabe, K.; Kanda, K.; Haruyama, Y.; Hoshino, T.; Kondo, K.; Kaito, T.; Ichihashi, T.; Fujita, J.; Ishida, M.; Ochiai, Y.; Tajima, T.; Matsui, S. *J. Vac. Sci. Technol., B: Microelectron. Nanometer Struct.–Process., Meas., Phenom.* **2003,** *21,* 2737. doi:10.1116/1.1630329
23. Esposito, M.; Tasco, V.; Todisco, F.; Benedetti, A.; Sanvitto, D.; Passaseo, A. *Adv. Opt. Mater.* **2014,** *2,* 154–161. doi:10.1002/adom.201300323
24. Esposito, M.; Tasco, V.; Cuscunà, M.; Todisco, F.; Benedetti, A.; Tarantini, I.; De Giorgi, M.; Sanvitto, D.; Passaseo, A. *ACS Photonics* **2015,** *2,* 105–114. doi:10.1021/ph500318p
25. Fujii, T.; Iwasaki, K.; Munekane, M.; Takeuchi, T.; Hasuda, M.; Asahata, T.; Kiyohara, M.; Kogure, T.; Kijima, Y.; Kaito, T. *J. Micromech. Microeng.* **2005,** *15,* S286–S291. doi:10.1088/0960-1317/15/10/s06
26. Nakai, Y.; Kang, Y.; Okada, M.; Haruyama, Y.; Kanda, K.; Ichihashi, T.; Matsui, S. *Jpn. J. Appl. Phys.* **2010,** *49,* 06GH07. doi:10.1143/jjap.49.06gh07
27. Scipioni, L.; Stern, L. A.; Notte, J.; Sijbrandij, S.; Griffin, B. *Adv. Mater. Processes* **2008,** *166,* 27.
28. Maas, D.; van Veldhoven, E.; Chen, P.; Sidorkin, V.; Salemink, H.; van der Drift, E.; Alkemade, P. Nanofabrication with a Helium Ion Microscope. In *Metrology, Inspection, and Process Control for Microlithography XXIV,* Raymond, C. J., Ed.; Proc. SPIE 7638, 2010; 763814 . doi:10.1117/12.862438
29. Alkemade, P. F. A.; Chen, P.; van Veldhoven, E.; Maas, D. *J. Vac. Sci. Technol., B: Nanotechnol. Microelectron.: Mater., Process., Meas., Phenom.* **2010,** *28,* C6F22–C6F25. doi:10.1116/1.3517536
30. Smith, D. A.; Joy, D. C.; Rack, P. D. *Nanotechnology* **2010,** *21,* 175302. doi:10.1088/0957-4484/21/17/175302
31. Chen, P.; van Veldhoven, E.; Sanford, C. A.; Salemink, H. W. M.; Maas, D. J.; Smith, D. A.; Rack, P. D.; Alkemade, P. F. A. *Nanotechnology* **2010,** *21,* 455302. doi:10.1088/0957-4484/21/45/455302
32. Alkemade, P. F. A.; Miro, H. *Appl. Phys. A: Mater. Sci. Process.* **2014,** *117,* 1727–1747. doi:10.1007/s00339-014-8763-y

33. Chen, P.; Salemink, H. W. M.; Alkemade, P. F. A. *J. Vac. Sci. Technol., B: Microelectron. Nanometer Struct.–Process., Meas., Phenom.* **2009,** *27,* 1838. doi:10.1116/1.3155825
34. Sanford, C. A.; Stern, L.; Barriss, L.; Farkas, L.; DiManna, M.; Mello, R.; Maas, D. J.; Alkemade, P. F. A. *J. Vac. Sci. Technol., B: Microelectron. Nanometer Struct.–Process., Meas., Phenom.* **2009,** *27,* 2660–2667. doi:10.1116/1.3237095
35. Kohama, K.; Iijima, T.; Hayashida, M.; Ogawa, S. *J. Vac. Sci. Technol., B: Nanotechnol. Microelectron.: Mater., Process., Meas., Phenom.* **2013,** *31,* 031802. doi:10.1116/1.4800983
36. Mutunga, E.; Winkler, R.; Sattelkow, J.; Rack, P. D.; Plank, H.; Fowlkes, J. D. *ACS Nano* **2019,** *13,* 5198–5213. doi:10.1021/acsnano.8b09341
37. Winkler, R.; Lewis, B. B.; Fowlkes, J. D.; Rack, P. D.; Plank, H. *ACS Appl. Nano Mater.* **2018,** *1,* 1014–1027. doi:10.1021/acsanm.8b00158
38. Gor'kov, L. P. *Sov. Phys. JETP* **1960,** *37,* 1407–1416.
39. Kes, P. H.; Tsuei, C. C. *Phys. Rev. B* **1983,** *28,* 5126–5139. doi:10.1103/physrevb.28.5126
40. Basset, J.; Watfa, D.; Aiello, G.; Féchant, M.; Morvan, A.; Estève, J.; Gabelli, J.; Aprili, M.; Weil, R.; Kasumov, A.; Bouchiat, H.; Deblock, R. *Appl. Phys. Lett.* **2019,** *114,* 102601. doi:10.1063/1.5080925
41. Puig, T.; Rosseel, E.; Baert, M.; Van Bael, M. J.; Moshchalkov, V. V.; Bruynseraede, Y. *Appl. Phys. Lett.* **1997,** *70,* 3155–3157. doi:10.1063/1.119118
42. Chiorescu, I.; Nakamura, Y.; Harmans, C. J. P. M.; Mooij, J. E. *Science* **2003,** *299,* 1869–1871. doi:10.1126/science.1081045
43. Kadin, A. M.; Leung, M.; Smith, A. D. *Phys. Rev. Lett.* **1990,** *65,* 3193–3196. doi:10.1103/physrevlett.65.3193
44. Dauler, E. A.; Kerman, A. J.; Rosenberg, D.; Pan, S.; Grein, M. E.; Molnar, R. J.; Correa, R. E.; Bawendi, M. G.; Berggren, K. K.; Moores, J. D.; Boroson, D. M. Superconducting nanowire single photon detectors. In *IEEE Photonic Society 24th Annual Meeting,* Arlington, VA, USA , Oct 9–13, 2011; IEEE, 2011; pp 350–351. doi:10.1109/pho.2011.6110571
45. Natarajan, C. M.; Tanner, M. G.; Hadfield, R. H. *Supercond. Sci. Technol.* **2012,** *25,* 063001. doi:10.1088/0953-2048/25/6/063001

License and Terms

BEILSTEIN JOURNAL OF NANOTECHNOLOGY

An atomic force microscope integrated with a helium ion microscope for correlative nanoscale characterization

Santiago H. Andany[1], Gregor Hlawacek[2], Stefan Hummel[3], Charlène Brillard[1], Mustafa Kangül[1] and Georg E. Fantner[*1]

Full Research Paper

Open Access

Address:
[1]Laboratory for Bio- and Nano-Instrumentation, Swiss Federal Institute of Technology Lausanne (EPFL), Lausanne CH-1015, Switzerland, [2]Institute of Ion Beam Physics and Materials Research, Helmholtz-Zentrum Dresden-Rossendorf, Dresden 01328, Germany and [3]GETec Microscopy GmbH, Vienna 1220, Austria

Email:
Georg E. Fantner[*] - georg.fantner@epfl.ch

* Corresponding author

Keywords:
atomic force microscopy (AFM); combined setup; correlative microscopy; helium ion microscopy (HIM); self-sensing cantilevers

Beilstein J. Nanotechnol. **2020,** *11,* 1272–1279.
https://doi.org/10.3762/bjnano.11.111

Received: 01 April 2020
Accepted: 30 July 2020
Published: 26 August 2020

This article is part of the thematic issue "Ten years of the helium ion microscope".

Associate Editor: T. Glatzel

Abstract

In this work, we report on the integration of an atomic force microscope (AFM) into a helium ion microscope (HIM). The HIM is a powerful instrument, capable of imaging and machining of nanoscale structures with sub-nanometer resolution, while the AFM is a well-established versatile tool for multiparametric nanoscale characterization. Combining the two techniques opens the way for unprecedented in situ correlative analysis at the nanoscale. Nanomachining and analysis can be performed without contamination of the sample and environmental changes between processing steps. The practicality of the resulting tool lies in the complementarity of the two techniques. The AFM offers not only true 3D topography maps, something the HIM can only provide in an indirect way, but also allows for nanomechanical property mapping, as well as for electrical and magnetic characterization of the sample after focused ion beam materials modification with the HIM. The experimental setup is described and evaluated through a series of correlative experiments, demonstrating the feasibility of the integration.

Introduction

Shortly after the invention of the atomic force microscope (AFM) in 1986 [1], efforts were made towards combining this scanning probe microscopy technique with electron beam and ion beam techniques for correlative nanoscale characterization and nanoscale fabrication. The motivation was driven by the new opportunity to investigate and transform features in situ with complementary techniques, thus revealing maximum information without breaking the vacuum. The scanning electron microscope (SEM) was first combined with scanning tunneling microscopy (STM) [2,3], allowing for the visual observation at the tip–sample interaction point with the SEM. Later, Ermakov et al. [4] successfully integrated an AFM into an SEM for the

first time, enabling correlative imaging on electrically insulating samples. In this first attempt, the readout of cantilever deflection was achieved using the electron beam itself. Shortly after, better performing combined setups were described utilizing more conventional self-sensing [5] and optical [6] techniques for the readout of cantilever deflection. Since then, more advanced and versatile combined instruments have been proposed for a broad spectrum of applications in nanoscale characterization and nanoscale fabrication inside SEM and focused ion beam (FIB) setups [7-11].

Given the extent of the interest sparked by SEM/FIB-AFM systems, it is reasonable to assume that the most recent ion beam microscope, the helium ion microscope (HIM), would be a serious contender for the use in combined setups in conjunction with AFM. Introduced by Ward et al. [12], the imaging capability of the HIM surpasses that of the SEM in terms of lateral resolution, depth of field, surface sensitivity, and ability to image electrically insulating samples [13]. Furthermore, nanoscale structuration with noble gas ions can yield sub-10 nm structures without unwanted metal ion implantation, a sizeable advantage over traditional gallium-ion FIBs. The resulting combined AFM–HIM instrument would, therefore, profit from the sub-nanometer lateral resolution of the HIM and the atomic resolution in the vertical axis of the AFM, proving particularly powerful for high-resolution correlative characterization of non-conductive samples.

With the integrated electron flood gun (FG) of the HIM providing charge neutralization, uncoated polymers and biological samples can be imaged with high resolution while the AFM would bring complementary information such as laterally resolved mechanical properties. These multiparametric measurements have previously been difficult to obtain as sample preparation of such samples for SEM or TEM are often incompatible with the needs of high-resolution AFM measurements.

AFM is also useful in assisting helium ion beam lithography. Many resists, including poly(methyl methacrylate) (PMMA), have higher sensitivities to helium ion irradiation than to electron irradiation in terms of charge per area [14]. Patterning resolution down to 4 nm has been demonstrated on HSQ resist [15], surpassing electron beam lithography, which greatly suffers from the proximity effect. In a combined AFM–HIM setup, the AFM could be used, in situ, in between exposures to assess the shrinkage, stiffness change or sputtering of the resist. More applications such as conductive AFM, piezo-force microscopy or magnetic force microscopy are within reach of the presented technology and would make AFM–HIM appealing to the microelectronics and materials research community.

Instrumentation

Spatial constraints inside SEMs and ion microscopes often dictate the feasibility of the integration of the AFM. Compact AFM setups have to fit around the host microscope as not to hinder excessively its capabilities. The reported AFM integration is depicted in Figure 1. The prototype tip-scanning AFM scan head is designed explicitly for correlative analysis inside electron and ion-beam microscopes. Unlike sample scanning

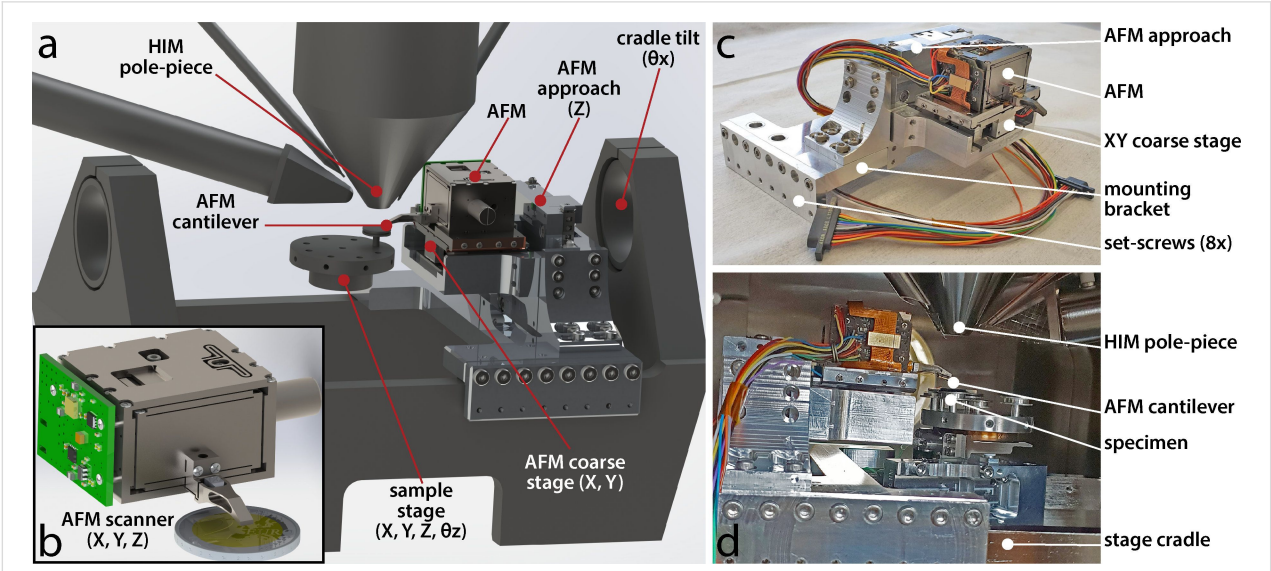

Figure 1: AFM assembly and integration inside a Zeiss ORION NanoFab helium ion microscope. a) Simplified CAD rendering of the AFM assembly mounted onto the HIM cradle and b) detailed view of the AFM scan head with a 2 EUR coin for scale. c) Annotated photograph of the AFM assembly and d) after being mounted inside the chamber of the HIM.

solutions [9,16], where the sample is raster-scanned relative to a stationary cantilever, a tip-scanning configuration [10,17] requires no alteration of the sample stage and has the advantage of having the sample stationary within the field of view of the HIM during AFM imaging. The scanner is a flexure design with serial kinematics [18] and the cantilever is mounted at the end of a low-profile protruding *z*-flexure, which fits seamlessly between the pole piece and the sample. The assembly is made from grade-5 titanium (Ti-6Al-4V) and the three axes of motion are actuated by stack-piezo actuators, offering an achievable scan range of 30 × 30 × 12 µm.

The reported AFM uses a self-sensing readout for measuring cantilever deflection [19]. Although optical beam deflection (OBD) techniques are traditionally preferred for their lower noise, they require bulky components and precise optical alignment. Prohibitively large instruments with optical readout are difficult to integrate into electron or ion microscopes and re-alignment of the optics is very impractical, as it requires the user to vent the chamber. Using self-sensing readout addresses these concerns [5,10,17] and also significantly improves the usability of the correlative instrument for users outside of the AFM community. The reported AFM uses silicon cantilever probes with boron-doped 1 kΩ sensing elements, connected in a Wheatstone bridge configuration with aluminum tracks [20,21] and with single crystal diamond (SCD) tips that are commercially available (SCL-SensorTech Fabrication GMBH, Vienna, Austria). The SCD tips (tip radius below 15 nm, height 12–16 µm), which are glued to the cantilevers, offer high aspect ratio and excellent resistance to wear [22]. Because tip wear is the main cause of cantilever failure, and because cantilever exchange in the HIM requires the user to vent the chamber, wear resistance is critically important.

To maneuver the AFM relative to the sample and the ion beam, the AFM is mounted onto a coarse stage consisting of a custom-built *XY* stick–slip positioner, which in turn is attached to a vertical approach mechanism built around a linear, stick–slip piezo actuator (Picomotor^{TM} 8301-UHV, Newport Corporation, CA, USA). The AFM assembly tilts together with the sample stage. The three orthogonal translational degrees of freedom of the sample are decoupled from the AFM coarse positioning stage, as shown in Figure 1a. The integration of the AFM into the HIM requires no alteration of the HIM microscope stage. The AFM assembly is positioned onto the HIM cradle and secured with set screws pressing firmly on the sides of the cradle. Electrical connections necessary for AFM operation are cabled through a CF40 flange. After opening the microscope door, the AFM head can be removed seamlessly from the chamber for cantilever exchange thanks to a spring-loaded kinematic mount.

Operating the AFM inside the HIM chamber has drawbacks regarding resolution and noise performance. Ideally, the mechanical loop between the cantilever probe and the sample needs to be compact and stiff for optimal AFM performance. The mechanical loop for the reported tip-scanning AFM includes the AFM scan head, coarse stage and stationary sample stage. However, after integration with the HIM, stiffness is degraded through the incorporation of the HIM cradle, the four-axis sample stage, and the mounting bracket to the mechanical loop. This reduces rigidity and makes the AFM more susceptible to vibrations present inside of the HIM chamber.

The AFM and motorized coarse stages are controlled with a custom-made AFM software [23], a standalone FPGA (USB-7856R OEM, National Instruments, Austin TX, USA), a high-voltage piezo amplifier (Techproject, Vienna, Austria) and a stick–slip controller (8742-4 PicomotorTM drive, Newport Corporation). The AFM can operate in contact mode and in an off-resonance mode based on force–distance curves [24]. In this off-resonance mode, which we refer to as off-resonance tapping (ORT), the cantilever is moved sinusoidally up and down the sample using the *z*-piezo of the scanner, causing intermittent contact between the cantilever and the sample [25]. The maximum interaction force is computed and used as feedback by the controller, providing fine force control, reducing shear forces and thus preserving the tip and the sample [26,27]. Operating in ORT mode instead of amplitude-modulation AFM (AM-AFM) is particularly advantageous in vacuum, where the Q-factor of the cantilever is about one order of magnitude higher than in air. Indeed, AM-AFM imaging bandwidth is inversely proportional to the Q-factor [28] and is therefore very slow in vacuum [29]. In ORT, the tapping rate is a least one order of magnitude below the first resonance of the cantilever and hence the enhancement of the Q-factor in vacuum is less detrimental to the achievable scan speed.

Results

The system has been experimentally tested on a variety of sample surfaces in contact and off-resonance imaging modes, demonstrating the feasibility of the integration through a series of three experiments. Correlative AFM and HIM imaging is demonstrated in Figure 2 by imaging silicon nanopillars [30]. The HIM offers a large field of view, which allows for the cantilever to be navigated onto the region of interest (Figure 2b,c) to perform AFM topography imaging (Figure 2d).

PMMA has traditionally been used as a positive resist in electron beam lithography. Helium ion beam lithography has emerged as a powerful technique to achieve even smaller feature size thanks to higher resist sensitivity, reduced proximity effect and small spot size [15]. Upon ion beam exposure, chain

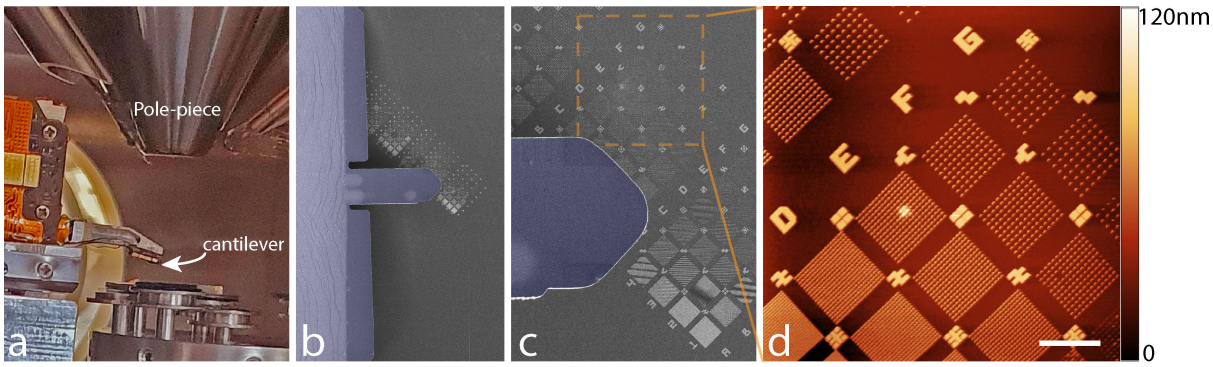

Figure 2: Correlative imaging in process on silicon pillars. a) Optical image showing how the AFM cantilever is positioned at the end of a low-profile, overhanging structure, which fits between the pole piece and the sample. b, c) The cantilever (colorized in purple on the HIM images) can be navigated by making use of the large FOV image provided by the HIM. d) AFM height image of Si nanopillars taken in off-resonance tapping mode. Scale bar 5 µm.

scission occurs leaving the exposed region soluble in a suitable developer. Very high ion doses also break short side chains that later cross-link, allowing PMMA to be also used as a negative resist [31]. Chain scission leads to volume loss through the release of gas molecules, and this leads to the shrinkage of exposed PMMA [32], which can be easily quantified using AFM. In a second experiment, we tested the effect on a PMMA thin film exposed to different doses under the focused He ion beam. Figure 3a and Figure 3b show two AFM topography images of PMMA exposed to a dose of 1×10^{13} cm^{-2} and 3×10^{13} cm^{-2} 30 keV He ions, respectively, as well as the corresponding height profiles of the irradiated PMMA surface.

Focused ion beam damage and implantation can hinder the imaging and nanoscale fabrication capabilities of the HIM [33] and studying these local defects created at the micro- and nanoscale can provide valuable information towards understanding these limitations. For example, a focused helium ion beam can locally destroy the crystalline structure of silicon and lead to the growth of amorphous silicon bubbles at the surface [34]. Furthermore, focused helium ion beam exposure inside a HIM can be used as a way of locally replicating the harsh radiation conditions found in nuclear fission and fusion reactors, to study the response of structural materials used in the reactors [35]. We characterized the defects caused by He ion exposure in a correlative AFM–HIM experiment. Amorphous silicon bubbles are created on a crystalline silicon substrate through point exposition with the HIM at 25 kV and 14 pA using doses between 4.2×10^8 and 4.2×10^9 He ions (Figure 3). He ions penetrate deep into the silicon and lead to the formation of microscale and nanoscale bubbles, which coalesce and ultimately result in the formation of a large silicon bubble in the amorphized silicon.

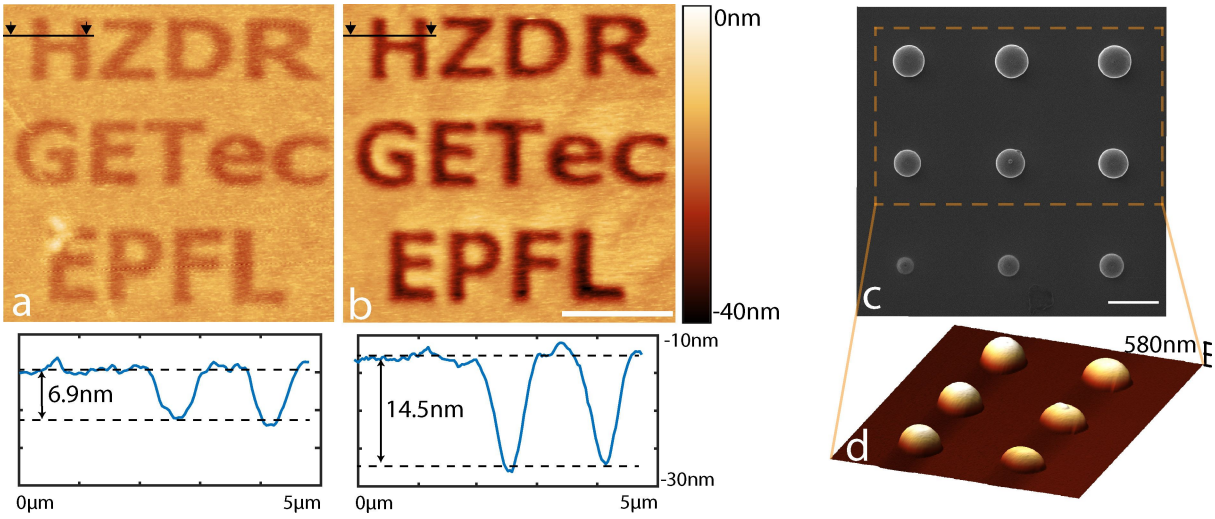

Figure 3: AFM height images of poly(methyl methacrylate) after exposure to a) 1×10^{13} and b) 3×10^{13} He ion cm^{-2}. The images were taken in contact mode, scale bar 4 µm. c) Silicon bubbles imaged with HIM (scale bar 1 µm) and d) AFM (off-resonance tapping mode).

The resulting 3 × 3 bubble grid is imaged with HIM (Figure 3c) and AFM (Figure 3d) to reveal the height and volume of the features.

Discussion

For the successful integration of two different microscopy techniques, they should be both complementary and compatible. The techniques should, on the one hand, be sufficiently different so that the combination creates real added value. On the other hand, the application space of the techniques should have sufficient overlap so that a meaningful correlation can be established in space and time. One requirement for compatibility is that the AFM can operate in an ultra-high vacuum (UHV) environment, a prerequisite for the HIM. This requirement puts additional restrictions on the AFM. In our AFM design, we accounted for this already in the mechanical design (avoidance of trapped air pockets, no lubricants, UHV-compatible motors) as well as in the assembly by using, wherever possible, Kapton flex-PCBs or scarcely outgassing Teflon-coated wires. It is also critical that the AFM, the coarse stage, and the mounting elements are thoroughly cleaned before assembly and that assembly and storage are carried out in a clean environment. Disassembly and thorough cleaning of all the components prior to integration into the HIM was inadequately performed, which resulted in an inferior chamber vacuum pressure of 6.12×10^{-7} mbar after overnight pumping, although normal HIM operation remained possible for our experiments. We strongly believe that if cleaning and storing recommendations are followed, the system vacuum would drastically improve, reaching more than adequate vacuum levels. It should also be noted that our AFM system is not compatible with baking the system at high temperatures above 100 °C since this would result in irreversible damage to the piezo actuators.

Another requirement for compatibility is that the two techniques can use samples prepared in the same way. For AFM and HIM, this is particularly advantageous since both can image non-conductive samples at very high resolution without charging. This is essential for correlative mechanical property and HIM surface imaging, and it is a clear advantage of AFM–HIM compared to AFM–SEM, where a conductive coating is often necessary for high-resolution SEM imaging.

The other aspect necessary for a useful integration of two techniques is that they are sufficiently complementary to each other to warrant the additional effort. While both AFM and HIM can yield images with very high resolution, the two techniques do have very different strengths. The HIM, for example, has a very good lateral resolution and a large depth of field, which makes it well suited for imaging high aspect ratio structures. The *Z*-resolution of the method, however, is less accurate, since the height of objects has to be reconstructed from two tilted images. AFM, on the other hand, has its highest resolution in the *Z*-direction, and profiles or volumes can be accurately extracted (see Figure 3d). The depth of field is, however, limited and the maximum slope of the sample that can be faithfully measured is dictated by the aspect ratio of the tip [36]. The true strength of the integrated setup is the combination of sample modification by the He ion beam and the multiparametric characterization of sample properties using AFM. In Figure 3, we showed a basic application where we characterized the effect of ion-beam radiation on the topography of the photoresist PMMA. Many more examples can be envisioned. The He ion beam is known to change the mechanical [37], electrical [38], and magnetic properties of materials [39]. AFM can be used to measure mechanical properties using contact resonance [40,41] or off-resonance tapping techniques [24] with very high resolution. Magnetic properties of nanostructures can be measured using magnetic force microscopy (MFM) [42], and a host of AFM techniques are available to measure electrical properties of samples (e.g., conductive AFM (cAFM) [43], scanning capacitance microscopy (SCM) [44], and spreading resistance microscopy (SSRM) [45]). While the implementation of these different imaging modes will require some additional modifications to our existing instrument, the path towards achieving such a truly multi-physics characterization and manipulation tool by combining advanced AFM with HIM can clearly be envisioned.

One aspect where HIM and AFM are, however, not well matched is in the image acquisition time. The relatively long time required for an AFM image (several minutes) has been a severe disadvantage when combining it with other electron or ion-beam microscopes. The same limitation exists for the combination of AFM and HIM. While much progress has been made towards increasing the imaging speed of AFM [46-50], most of this progress has been limited to imaging in liquid, due to the inherent bandwidth limitation of cantilevers when using them in dynamic mode in vacuum. Recent signs of progress in cantilever materials have shown the potential to increase the imaging speed of AFM also in ambient air or vacuum [51-53]. These approaches could also be implemented for the combined AFM–HIM instrument, thereby holding promise for interactive use of AFM and HIM at similar size- and time-scales.

Conclusion

We have demonstrated the integration of an atomic force microscope into a helium ion microscope. Correlative measurements of AFM topography with He ion imaging and modification demonstrate the feasibility of this integration. The complementarity of the two methods in terms of vertical and lateral resolution, nanoscale machining, and measurement of physical prop-

erties of the sample will allow for a multi-physics investigation in many areas of materials science and technology, such as energy materials, magnetic nanostructures, and (bio-)composites.

Experimental

All AFM measurements were taken using silicon piezo-resistive self-sensing cantilevers (PRS-L100-F400-SCD-PCB SCL-SensorTech Fabrication GMBH, Vienna, Austria) with a spring constant of ca. 100 N/m, and a footprint of 110 × 48 µm. Imaging gains on the custom-made controller were adjusted as high as possible before significant oscillations were seen. AFM images were processed in the software Gwyddion [54]. Pixels were squared to account for X–Y pixel size mismatch when necessary, the background was flattened and a conservative de-noising filter was applied. Finally, hysteresis correction was performed in MATLAB using closed-loop sensor data obtained prior to imaging on the AFM scan head.

For Figure 2, the AFM image shown was recorded at 300 mHz line rate at a resolution of 1024 pixels and 512 lines and over a scan range of 30 × 30 µm. The imaging mode used was off-resonance tapping (ORT) at a tapping rate of 2 kHz and a tapping amplitude of 600 nm. For Figure 3a and Figure 3b, the images were taken in contact mode at 500 mHz line rate and 1 Hz line rate respectively. Additionally, to the processing described in detail above, the two images were cropped and rotated to obtain the final images (the original images are 17.8 × 17.8 µm and 16.6 × 16.6 µm, respectively, and each is 512 × 512 pixels). An additional 2-dimensional FFT filtering was applied to correct for the main mechanical vibrations in the two original images. The AFM image in Figure 3d is obtained in ORT at 2 kHz tapping rate, 600 nm amplitude and 200 mHz line rate. The scan range is 9.7 × 7.3 µm and the image size is 512 × 386 pixels.

Acknowledgements

The authors acknowledge the support of Jeff Markakis for the mechanical design of the AFM scanner and Christian Schwalb for conceptual discussions.

Funding

This work was funded by the Swiss National Science Foundation (the Swiss National Science Foundation through grant 200021_182562), the European Union Eurostars Program (Eurostars E!8213), the H2020 IONS4SET project (H2020 Grant number: 688072), the Ion Beam Center of the Helmholtz Zentrum Dresden Rossendorf through GATE proposal 19001761 and the Austrian Research Promotion Agency FFG in the frame of the “Beyond Europe” initiative (Project AIM, No. 11056459).

ORCID® iDs

Gregor Hlawacek - https://orcid.org/0000-0001-7192-716X
Stefan Hummel - https://orcid.org/0000-0002-4426-3609
Georg E. Fantner - https://orcid.org/0000-0001-5889-3022

Preprint

A non-peer-reviewed version of this article has been previously published as a preprint: https://arxiv.org/abs/2004.00536

References

1. Binnig, G.; Quate, C. F.; Gerber, C. *Phys. Rev. Lett.* **1986,** *56,* 930–933. doi:10.1103/physrevlett.56.930
2. Vázquez, L.; Bartolomé, A.; García, R.; Buendía, A.; Baró, A. M. *Rev. Sci. Instrum.* **1988,** *59,* 1286–1289. doi:10.1063/1.1139710
3. Ehrichs, E. E.; Smith, W. F.; de Lozanne, A. L. *J. Vac. Sci. Technol., B: Microelectron. Nanometer Struct.–Process., Meas., Phenom.* **1991,** *9,* 1380–1383. doi:10.1116/1.585201
4. Ermakov, A. V.; Garfunkel, E. L. *Rev. Sci. Instrum.* **1994,** *65,* 2853–2854. doi:10.1063/1.1144627
5. Stahl, U.; Yuan, C. W.; de Lozanne, A. L.; Tortonese, M. *Appl. Phys. Lett.* **1994,** *65,* 2878–2880. doi:10.1063/1.113030
6. Troyon, M.; Lei, H. N.; Wang, Z.; Shang, G. *Microsc., Microanal., Microstruct.* **1997,** *8,* 393–402. doi:10.1051/mmm:1997130
7. Fukushima, K.; Saya, D.; Kawakatsu, H. *Jpn. J. Appl. Phys., Part 1* **2000,** *39,* 3747–3749. doi:10.1143/jjap.39.3747
8. Mick, U.; Eichhorn, V.; Wortmann, T.; Diederichs, C.; Fatikow, S. Combined nanorobotic AFM/SEM system as novel toolbox for automated hybrid analysis and manipulation of nanoscale objects. In *Proceedings of the 2010 IEEE International Conference on Robotics and Automation,* 2010; pp 4088–4093. doi:10.1109/robot.2010.5509414
9. Angelov, T.; Ahmad, A.; Guliyev, E.; Reum, A.; Atanasov, I.; Ivanov, T.; Ishchuk, V.; Kaestner, M.; Krivoshapkina, Y.; Lenk, S.; Lenk, C.; Rangelow, I. W.; Holz, M.; Nikolov, N. *J. Vac. Sci. Technol., B: Nanotechnol. Microelectron.: Mater., Process., Meas., Phenom.* **2016,** *34,* 06KB01. doi:10.1116/1.4964290
10. Kreith, J.; Strunz, T.; Fantner, E. J.; Fantner, G. E.; Cordill, M. J. *Rev. Sci. Instrum.* **2017,** *88,* 053704. doi:10.1063/1.4983317
11. Rangelow, I. W.; Kaestner, M.; Ivanov, T.; Ahmad, A.; Lenk, S.; Lenk, C.; Guliyev, E.; Reum, A.; Hofmann, M.; Reuter, C.; Holz, M. *J. Vac. Sci. Technol., B: Nanotechnol. Microelectron.: Mater., Process., Meas., Phenom.* **2018,** *36,* 06J102. doi:10.1116/1.5048524
12. Ward, B. W.; Notte, J. A.; Economou, N. P. *J. Vac. Sci. Technol., B: Microelectron. Nanometer Struct.–Process., Meas., Phenom.* **2006,** *24,* 2871–2874. doi:10.1116/1.2357967
13. Hlawacek, G.; Veligura, V.; van Gastel, R.; Poelsema, B. *J. Vac. Sci. Technol., B: Nanotechnol. Microelectron.: Mater., Process., Meas., Phenom.* **2014,** *32,* 020801. doi:10.1116/1.4863676
14. Komuro, M.; Atoda, N.; Kawakatsu, H. *J. Electrochem. Soc.* **1979,** *126,* 483–490. doi:10.1149/1.2129067
15. Kalhor, N.; Alkemade, P. F. A. Resist assisted patterning. In *NanoScience and Technology;* Hlawacek, G.; Gölzhäuser, A., Eds.; Springer: Cham, Switzerland, 2016; pp 395–414. doi:10.1007/978-3-319-41990-9_16
16. Uruma, T.; Tsunemitsu, C.; Terao, K.; Nakazawa, K.; Satoh, N.; Yamamoto, H.; Iwata, F. *AIP Adv.* **2019,** *9,* 115011. doi:10.1063/1.5125163

17. Yang, C.; Winkler, R.; Dukic, M.; Zhao, J.; Plank, H.; Fantner, G. E. *ACS Appl. Mater. Interfaces* **2017,** *9,* 24456–24461. doi:10.1021/acsami.7b07762
18. Leang, K. K.; Fleming, A. J. *Asian J. Control* **2009,** *11,* 144–153. doi:10.1002/asjc.90
19. Tortonese, M.; Barrett, R. C.; Quate, C. F. *Appl. Phys. Lett.* **1993,** *62,* 834–836. doi:10.1063/1.108593
20. Fantner, G. E.; Burns, D. J.; Belcher, A. M.; Rangelow, I. W.; Youcef-Toumi, K. *J. Dyn. Syst., Meas., Control* **2009,** *131,* 061104. doi:10.1115/1.4000378
21. Fantner, G. E.; Schumann, W.; Barbero, R. J.; Deutschinger, A.; Todorov, V.; Gray, D. S.; Belcher, A. M.; Rangelow, I. W.; Youcef-Toumi, K. *Nanotechnology* **2009,** *20,* 434003. doi:10.1088/0957-4484/20/43/434003
22. Obraztsov, A. N.; Kopylov, P. G.; Loginov, B. A.; Dolganov, M. A.; Ismagilov, R. R.; Savenko, N. V. *Rev. Sci. Instrum.* **2010,** *81,* 013703. doi:10.1063/1.3280182
23. Nievergelt, A. P.; Brillard, C.; Eskandarian, H. A.; McKinney, J. D.; Fantner, G. E. *Int. J. Mol. Sci.* **2018,** *19,* 2984. doi:10.3390/ijms19102984
24. Rosa-Zeiser, A.; Weilandt, E.; Hild, S.; Marti, O. *Meas. Sci. Technol.* **1997,** *8,* 1333–1338. doi:10.1088/0957-0233/8/11/020
25. Nievergelt, A. P.; Erickson, B. W.; Hosseini, N.; Adams, J. D.; Fantner, G. E. *Sci. Rep.* **2015,** *5,* 11987. doi:10.1038/srep11987
26. de Pablo, P. J.; Colchero, J.; Gómez-Herrero, J.; Baró, A. M. *Appl. Phys. Lett.* **1998,** *73,* 3300–3302. doi:10.1063/1.122751
27. Alsteens, D.; Dupres, V.; Yunus, S.; Latgé, J.-P.; Heinisch, J. J.; Dufrêne, Y. F. *Langmuir* **2012,** *28,* 16738–16744. doi:10.1021/la303891j
28. Mertz, J.; Marti, O.; Mlynek, J. *Appl. Phys. Lett.* **1993,** *62,* 2344–2346. doi:10.1063/1.109413
29. Jaafar, M.; Martínez-Martín, D.; Cuenca, M.; Melcher, J.; Raman, A.; Gómez-Herrero, J. *Beilstein J. Nanotechnol.* **2012,** *3,* 336–344. doi:10.3762/bjnano.3.38
30. Xu, X.; Prüfer, T.; Wolf, D.; Engelmann, H.-J.; Bischoff, L.; Hübner, R.; Heinig, K.-H.; Möller, W.; Facsko, S.; von Borany, J.; Hlawacek, G. *Beilstein J. Nanotechnol.* **2018,** *9,* 2883–2892. doi:10.3762/bjnano.9.267
31. Calcagno, L.; Compagnini, G.; Foti, G. *Nucl. Instrum. Methods Phys. Res., Sect. B* **1992,** *65,* IN7–422. doi:10.1016/0168-583x(92)95077-5
32. Kallweit, R.; Baur, M.; Eichinger, P.; Strack, H. *Nucl. Instrum. Methods Phys. Res., Sect. B* **1991,** *59–60,* 1288–1291. doi:10.1016/0168-583x(91)95813-s
33. Wang, Y.; Boden, S. A.; Bagnall, D. M.; Rutt, H. N.; de Groot, C. H. *Nanotechnology* **2012,** *23,* 395302. doi:10.1088/0957-4484/23/39/395302
34. Livengood, R.; Tan, S.; Greenzweig, Y.; Notte, J.; McVey, S. *J. Vac. Sci. Technol., B: Microelectron. Nanometer Struct.–Process., Meas., Phenom.* **2009,** *27,* 3244–3249. doi:10.1116/1.3237101
35. Guo, Q.; Landau, P.; Hosemann, P.; Wang, Y.; Greer, J. R. *Small* **2013,** *9,* 691–696. doi:10.1002/smll.201201614
36. Akamine, S.; Barrett, R. C.; Quate, C. F. *Appl. Phys. Lett.* **1990,** *57,* 316–318. doi:10.1063/1.103677
37. Bergner, F.; Hlawacek, G.; Heintze, C. *J. Nucl. Mater.* **2018,** *505,* 267–275. doi:10.1016/j.jnucmat.2017.07.054
38. Fox, D. S.; Zhou, Y.; Maguire, P.; O'Neill, A.; Ó'Coileáin, C.; Gatensby, R.; Glushenkov, A. M.; Tao, T.; Duesberg, G. S.; Shvets, I. V.; Abid, M.; Abid, M.; Wu, H.-C.; Chen, Y.; Coleman, J. N.; Donegan, J. F.; Zhang, H. *Nano Lett.* **2015,** *15,* 5307–5313. doi:10.1021/acs.nanolett.5b01673
39. Franken, J. H.; Hoeijmakers, M.; Lavrijsen, R.; Kohlhepp, J. T.; Swagten, H. J. M.; Koopmans, B.; van Veldhoven, E.; Maas, D. J. *J. Appl. Phys.* **2011,** *109,* 07D504. doi:10.1063/1.3549589
40. Rabe, U.; Arnold, W. *Appl. Phys. Lett.* **1994,** *64,* 1493–1495. doi:10.1063/1.111869
41. Yamanaka, K.; Nakano, S. *Jpn. J. Appl. Phys., Part 1* **1996,** *35,* 3787–3792. doi:10.1143/jjap.35.3787
42. Martin, Y.; Wickramasinghe, H. K. *Appl. Phys. Lett.* **1987,** *50,* 1455–1457. doi:10.1063/1.97800
43. Murrell, M. P.; Welland, M. E.; O'Shea, S. J.; Wong, T. M. H.; Barnes, J. R.; McKinnon, A. W.; Heyns, M.; Verhaverbeke, S. *Appl. Phys. Lett.* **1993,** *62,* 786–788. doi:10.1063/1.108579
44. Matey, J. R.; Blanc, J. *J. Appl. Phys.* **1985,** *57,* 1437–1444. doi:10.1063/1.334506
45. Eyben, P.; Vandervorst, W.; Alvarez, D.; Xu, M.; Fouchier, M. Probing semiconductor technology and devices with scanning spreading resistance microscopy. *Scanning Probe Microscopy;* Springer: New York, NY, USA, 2007; Vol. 2, pp 31–87. doi:10.1007/978-0-387-28668-6_3
46. Kodera, N.; Yamamoto, D.; Ishikawa, R.; Ando, T. *Nature* **2010,** *468,* 72–76. doi:10.1038/nature09450
47. Fantner, G. E.; Schitter, G.; Kindt, J. H.; Ivanov, T.; Ivanova, K.; Patel, R.; Holten-Andersen, N.; Adams, J.; Thurner, P. J.; Rangelow, I. W.; Hansma, P. K. *Ultramicroscopy* **2006,** *106,* 881–887. doi:10.1016/j.ultramic.2006.01.015
48. Hansma, P. K.; Schitter, G.; Fantner, G. E.; Prater, C. *Science* **2006,** *314,* 601–602. doi:10.1126/science.1133497
49. Ando, T.; Kodera, N.; Takai, E.; Maruyama, D.; Saito, K.; Toda, A. *Proc. Natl. Acad. Sci. U. S. A.* **2001,** *98,* 12468–12472. doi:10.1073/pnas.211400898
50. Humphris, A. D. L.; Miles, M. J.; Hobbs, J. K. *Appl. Phys. Lett.* **2005,** *86,* 034106. doi:10.1063/1.1855407
51. Adams, J. D.; Erickson, B. W.; Grossenbacher, J.; Brugger, J.; Nievergelt, A.; Fantner, G. E. *Nat. Nanotechnol.* **2016,** *11,* 147–151. doi:10.1038/nnano.2015.254
52. Alsharif, N.; Burkatovsky, A.; Lissandrello, C.; Jones, K. M.; White, A. E.; Brown, K. A. *Small* **2018,** *14,* 1800162. doi:10.1002/smll.201800162
53. Hosseini, N.; Neuenschwander, M.; Peric, O.; Andany, S. H.; Adams, J. D.; Fantner, G. E. *Beilstein J. Nanotechnol.* **2019,** *10,* 2357–2363. doi:10.3762/bjnano.10.226
54. Nečas, D.; Klapetek, P. *Cent. Eur. J. Phys.* **2012,** *10,* 181–188. doi:10.2478/s11534-011-0096-2

BEILSTEIN JOURNAL OF NANOTECHNOLOGY

Effect of localized helium ion irradiation on the performance of synthetic monolayer MoS_2 field-effect transistors

Jakub Jadwiszczak[1], Pierce Maguire[1], Conor P. Cullen[2], Georg S. Duesberg[2,3] and Hongzhou Zhang[*1]

Full Research Paper

Open Access

Address:
[1]School of Physics, Trinity College Dublin, Dublin 2, Ireland, [2]School of Chemistry, Trinity College Dublin, Dublin 2, Ireland and [3]State Institute of Physics, EIT 2, Faculty of Electrical Engineering and Information Technology, Universität der Bundeswehr München, Werner-Heisenberg-Weg 39, 85577 Neubiberg, Germany

Email:
Hongzhou Zhang[*] - hozhang@tcd.ie

* Corresponding author

Keywords:
2D materials; contacts; defect engineering; helium ion microscope; ion beam doping; vacancies; two-dimensional materials

Beilstein J. Nanotechnol. **2020,** *11,* 1329–1335.
https://doi.org/10.3762/bjnano.11.117

Received: 06 May 2020
Accepted: 19 August 2020
Published: 04 September 2020

This article is part of the thematic issue "Ten years of the helium ion microscope".

Guest Editors: G. Hlawacek and A. Wolff

Abstract

Helium ion irradiation is a known method of tuning the electrical conductivity and charge carrier mobility of novel two-dimensional semiconductors. Here, we report a systematic study of the electrical performance of chemically synthesized monolayer molybdenum disulfide (MoS_2) field-effect transistors irradiated with a focused helium ion beam as a function of increasing areal irradiation coverage. We determine an optimal coverage range of approx. 10%, which allows for the improvement of both the carrier mobility in the transistor channel and the electrical conductance of the MoS_2, due to doping with ion beam-created sulfur vacancies. Larger areal irradiations introduce a higher concentration of scattering centers, hampering the electrical performance of the device. In addition, we find that irradiating the electrode–channel interface has a deleterious impact on charge transport when contrasted with irradiations confined only to the transistor channel.

Introduction

Layered two-dimensional (2D) semiconductors have come to the fore in recent years as promising candidates for the implementation of flexible, transparent, and low-power electronics. In particular, transition metal dichalcogenides (TMDs), such as molybdenum disulfide (MoS_2), have demonstrated impressive on/off ratios (approx. 10^7) in field-effect transistors (FETs), while maintaining carrier mobilities that may be adequate for commercial applications [1,2]. At the same time, advances in chemical vapor deposition (CVD) techniques have allowed for the reliable millimeter-scale synthesis of well-performing monolayer TMD films [3-5], leading to viable large-scale integration of on-chip TMD FETs. With device miniaturization, it

becomes key to understand the impact of defects such as chalcogen vacancies on the electrical transport properties of FETs based on 2D semiconductors. This is particularly crucial for device applications in radiation-rich environments (e.g., space satellite technologies), since defects can be introduced by ionizing particle irradiation while the devices are in continuous operation.

Recently, noble gas ion beam irradiation has opened the field to the exploration of nanometer-scale structural modifications of TMD devices [6-8]. The localized formation of defects by focused ion beam irradiation has been shown to induce unusual electronic properties in monolayer TMDs, such as pseudo-metallic phase transitions in MoS_2 and WSe_2 [9,10], resistive switching in MoS_2 [11], as well as enhanced out-of-plane charge transfer in 2D graphene/WSe_2 heterostructures [12]. Energetic light ions are known to preferentially sputter chalcogen atoms from TMDs while retaining an adequate micrometer-scale structural integrity for irradiation doses up to approx. 10^{16} ions cm^{-2} [13-17], as well as good electrical conductivity for up to approx. 10^{18} ions cm^{-2} [9,10,18]. Sulfur vacancies (SVs) and the formation of a dislocation–divacancy complex can lead to significant n-doping in MoS_2 [19], which shifts the threshold voltage (V_{th}) of the FET to higher negative gate biases [20,21]. These complex states may also improve the carrier mobility across a given gate bias range by forming stable impurity bands near the conduction band [22]. Some theoretical studies suggest, however, that individual SVs ought to act as electron acceptors in MoS_2 [23,24]. As the spread of a typical focused He^+ ion probe is several nanometers, the formation of other defects in the irradiated 2D crystal lattice is also expected [25,26], which may bring about the often-observed negative shifts of the MoS_2 FET threshold voltage after ion irradiation. Such n-type doping behavior achieved by selective ion sputtering in thin film transistors has also been observed in He^+-irradiated InGaZnO devices [27]. This irradiation-induced carrier activation depends not only on the fluence of the ion beam, but also on the absolute number of defects that can be introduced. Therefore, the creation of defects in TMD FETs may serve to improve charge transport and tune the device performance [10,20,28], while the effective donor concentration and the introduced scattering potentials need to be tailored accordingly [29,30]. Thus far, these studies have focused either on spatially confined defect generation, or full-channel modifications in TMD FETs. A research space exists for exploring the intermediate regime between these two extrema by finely controlling the area over which defects are seeded. For practical devices, it is also important to consider the effect of particle irradiation on the deposited metal–semiconductor contact interface. Recent work has shown that irradiation-induced heating of the electrode area can reverse majority carrier polarity in $MoTe_2$ [31], while pre-treatment with a broad-beam argon ion source can decrease the contact resistance of Ni-MoS_2 two-fold [32]. In this paper, we investigate the effect of the defect population on the performance of MoS_2 FETs via varying the area of ion irradiation in the FET channel. We also examine the performance of devices upon irradiation of one of the electrical contact interfaces.

Experimental

Monolayer MoS_2 samples were synthesized using a CVD microreactor method, described in detail in [33], directly on 285 nm SiO_2/Si substrates, which also served as the back-gate in the FET configuration. MoS_2 flakes were contacted with electrodes using standard electron beam lithography on polymethyl methacrylate (PMMA) resist, followed by lift-off in acetone and metal deposition by evaporation (5 nm Ti and 35 nm Au). Electrical testing was carried out using a dual-channel source–measure unit connected to tungsten micromanipulator probes (Imina miBot) in the vacuum chamber of a customized Zeiss EVO scanning electron microscope (SEM). Prior to testing, the devices were outgassed at a pressure of approx. 10^{-5} mbar for 12 h to minimize surface adsorbates. Helium ion irradiations were carried out at a beam energy of 30 keV and He gas pressure of 2×10^{-6} Torr, using a Zeiss Nanofab microscope. The fabricated MoS_2 FETs were placed in the helium ion microscope chamber (after initial electrical testing to confirm functionality) and were irradiated with the stage tilt angle set to 0°. At this angle of incidence, the helium ion beam ought to produce sulfur vacancies chiefly in the bottom sulfuric layer of the SiO_2-supported MoS_2 flake [34]. The average recorded beam current throughout the irradiations was 37.5 ± 0.4 pA, and the probe size was determined at approx. 7 nm [9]. The areal ion dose delivered to each sample was maintained at approx. 10^{17} ions cm^{-2}, with a step size of 1 nm and a dwell time of 4.3 µs throughout the duration of a unidirectional probe scan. Post-irradiation SEM imaging was carried out in a Zeiss Supra microscope using the in-lens detector at a low beam energy of less than 5 keV to ensure a strong surface sensitivity. Figure 1a shows a sketch of the experimental geometry. A SEM micrograph of a typical irradiated device is also presented in Figure 1b. The marked distances W and L denote the width of the irradiated region and the length of the FET channel, respectively. L was kept constant at 5 µm in this work, while W was varied to obtain a designated irradiation-to-channel ratio, $I_R = W/L$. Following the irradiation and electrical testing, these dimensions were re-measured in the SEM to obtain accurate I_R values in case of beam drift throughout the procedure.

Results and Discussion

As shown in Figure 1c, the localized irradiation (dose = 10^{17} ions cm^{-2}, I_R = 7%) causes a notably higher electrical

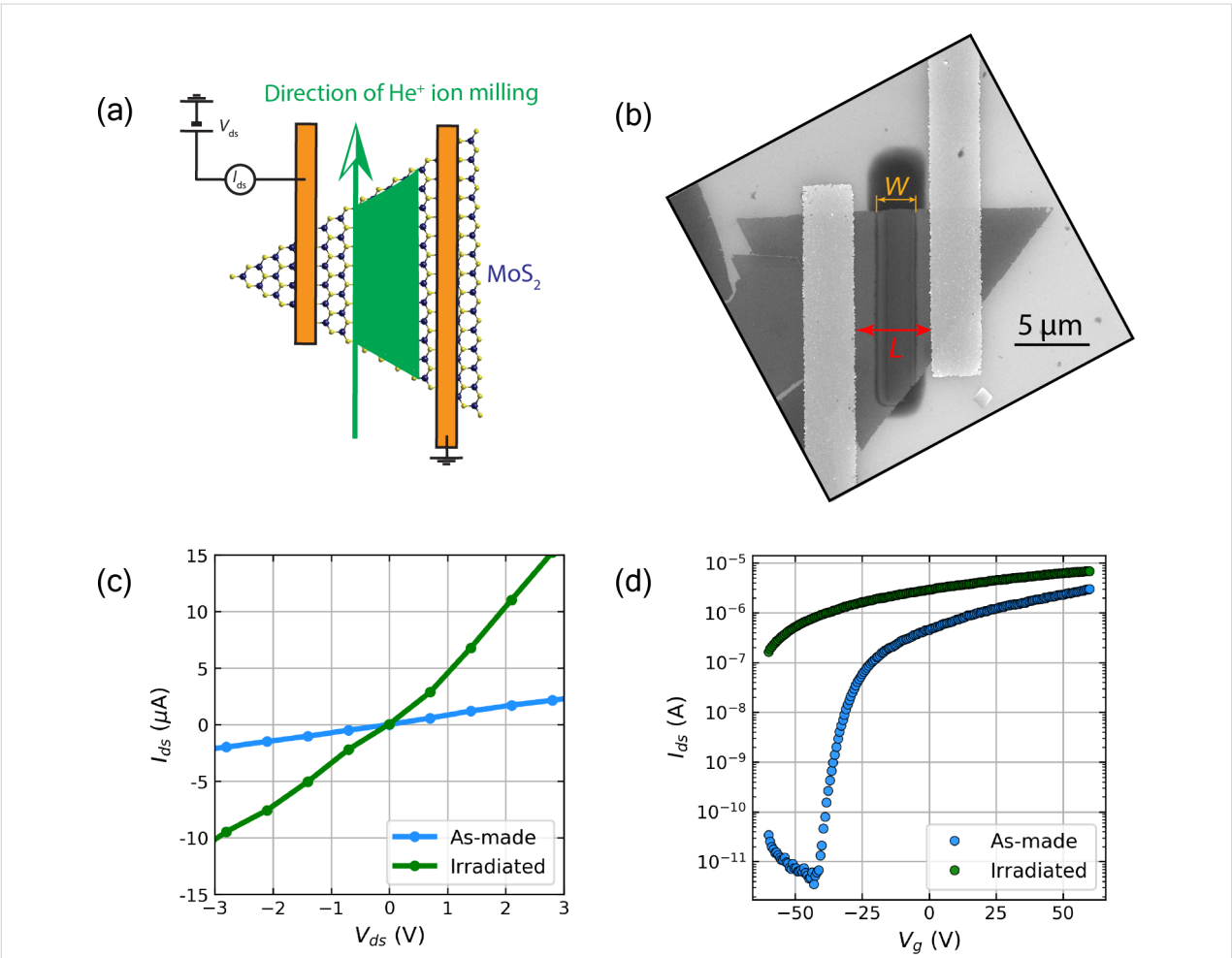

Figure 1: Experimental design and basic electrical characteristics. (a) Sketch demonstrating the irradiation strategy on contacted CVD-grown monolayer MoS_2 devices. The green area marks the designed irradiation area. (b) SEM image of an irradiated device. *W* marks the width of the exposed region, while *L* is the length of the FET channel. *L* is 5 µm in the image. (c) *I*–*V* curve of a device after irradiation (corresponding to I_R = 7%). (d) Transfer curve of the same device demonstrating reduced gate tunability and a higher electrical conductance after He+ ion irradiation.

conduction to emerge in the monolayer MoS_2 device. The output current (I_{ds}) increases approx. fivefold for the same drain–source bias (V_{ds}) when compared with the non-irradiated device. After the helium ion beam exposure, the transfer characteristics, Figure 1d, reveal a clearly reduced electrostatic response to the applied gate field. The FET channel cannot be effectively turned off in the tested bias range, with significant drain currents persisting even at V_g = −60 V. This leads to a sharp increase in the subthreshold swing and a large shift of V_{th} towards negative gate bias values (Δ> 10 V), thus deepening the depletion-mode n-type channel functionality. This observed near-degenerate doping behavior is typical of an increased concentration of sulfur vacancies in defect-rich MoS_2 [9,20,21]. We note here, that a recent high-energy irradiation study has also called for attention to charge traps generated in the underlying oxide, as the source of donor states in the FET channel [35]. Further studies on flakes decoupled from the substrate need to be performed to clarify the exact origin of the threshold voltage shift in TMDs irradiated at moderate beam energies.

The effects of increasing I_R are evident from changes to the recorded output and transfer characteristics in Figure 2a,b. The data are organized into three groups, marked blue, green, and red, corresponding to small (2–18%), medium (28–41%) and large (48–76%) I_R values, respectively. The I_{ds}–V_{ds} curves, taken at V_g = 0 V, demonstrate an increase in the channel conductance between the I_R = 2% and I_R = 7% irradiations, followed by a continuing drop when I_R > 18%. For small values of I_R (blue curves in Figure 2b), the FET experiences a large V_{th} shift (Δ > 10 V) to negative gate biases, a lowered on/off ratio (approx. 10^2), and an increased conductance relative to the untreated device. As I_R is increased into the green (28–41%) and red (48–76%) groups, the device conductance drops

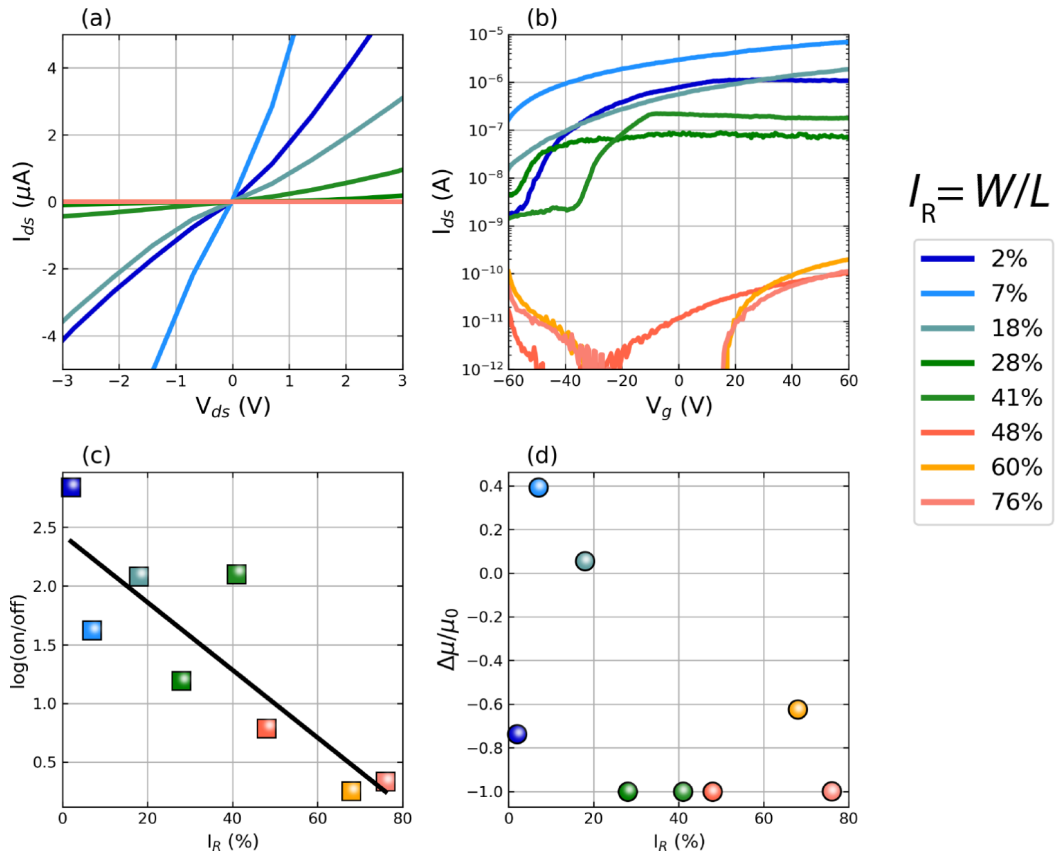

Figure 2: Effects of changing the irradiated area on the performance of monolayer MoS_2 FETs. Note that all the plots share the same color legend on the right. (a) *I*–*V* and (b) gate sweeps of different devices with varying I_R. (c) Semi-log plot of the extracted electron branch on/off ratios corresponding to each gate curve in (b). The black line is a linear fit to the semi-log data. (d) Changes in the field-effect mobility, μ, relative to as-made device mobilities, μ_0, extracted from transfer curves in (b).

heavily, accompanied by positive-bias V_{th} shifts, while the on/off ratio is also seen to decrease roughly exponentially. This is demonstrated in Figure 2c, which tracks the log-transformed on/off ratio as a function of I_R with a good linear correlation ($R = -0.85$) from the semi-logarithmic fit. This suggests that an optimal ion irradiation strategy for improving the channel conductance, i.e., when the areal channel exposure is close to 10%, needs to be a balance between introducing significant n-dopant densities and suppressing the unwanted crystal structure amorphization which results from high irradiation doses. At high I_R values (red group), we observe the emergence of a weak ambipolar response in our transfer curves. At these ratios, the device starts to enter a regime where more than half of the channel has been treated with the ion beam. Thus, we expect a dominant contribution of oxygen-containing atmospheric adsorbates (known p-type dopants in MoS_2) in saturating the vacancy sites created by the ion beam, allowing for residual hole conduction in the newly formed effective medium channel [36-38]. However, the role of other impurities such as hydrogen and carbon from adventitious surface hydrocarbons in the observed p-doping ought to also be considered in future studies. For a given delivered dose, the ion beam provides a high concentration of effective adsorption sites for atmospheric p-dopants (or adventitious hydrocarbons) within the area defined by the spread of the Gaussian probe extension. The probe has spatially trailing lower-dose tails, the damage of which extends to more than 10 nm and may induce additional n-doping with no complementary adsorbant saturation, i.e., by creating unsaturated SVs in the bottom sulfuric layer [34,39]. A larger irradiation area will thus provide more effective p-doping sites while stifling the n-doping response as the probe tails begin to extend past the FET channel. In addition, low-dose trail areas will be irradiated repeatedly by adjacent line scans, increasing the effective delivered dose and shifting that region to a more acceptor-rich area. This leads to the observed ambipolar gate response for large I_R values. The formation of these back-to-back heterojunctions may result in unconventional charge transport phenomena if the dose of the irradiation is varied across several orders of magnitude [9], which we leave for future studies.

Figure 2d charts the effect of I_R on the change in the carrier field-effect mobility, μ, of the irradiated device relative to its as-fabricated mobility, μ_0. Extracted from the linear region of the transfer curve, μ is seen to improve by up to 40% in two out of three devices in the blue region. For the green and red regions of I_R, μ is always seen to worsen as the area of the irradiated channel is increased. μ is expected to drop heavily as the rate of electron scattering rises with the increased defective channel area. The improved mobility at $I_R \approx 10\%$ indicates the screening of scattering centers by the increased carrier concentrations induced by SV doping, which leads to the increased conductance observed in Figure 2a. We note that our measurements were performed in a two-probe geometry. Thus, the absolute values of μ extracted here (approx. 1 $cm^2\ V^{-1}\ s^{-1}$) are limited by the contact resistance between the gold and the MoS_2 [40].

We now consider the effect of irradiating the metal–semiconductor interface. We treated two FETs within each I_R regime. For one of the devices in each pair a single electrode interface was also irradiated. SEM images in Figure 3a show the irradiated channel areas colored in green and the non-irradiated MoS_2 channel areas in red, on example devices in the high I_R regime. In all three I_R regimes, allowing one of the electrode–MoS_2 interfaces to be damaged by the helium ion beam leads to a drop in the device conductance, as evident in Figure 3b for the representative case of medium I_R values. Moreover, the conductance of the device where the electrode–MoS_2 interface was treated with the ion beam is lower than the conductance of the as-fabricated non-irradiated device. The transfer curves in Figure 3c indicate that as the device approaches the strong inversion regime, the electrode–channel interface damage (green curve) inhibits high drain currents in the FET, in contrast to the case of no electrode damage (purple curve).

We simulated the atomic vacancy yield per each delivered ion as a function of target penetration depth on the 35 nm-Au/5 nm-Ti/0.7 nm-MoS_2/285 nm-SiO_2 stack [41]. As evident from Figure 3d, the sulfur sputtering yield at the Ti–MoS_2 interface is very close to that of unencapsulated MoS_2 [15], indicating notable damage to the interface at this delivered dose. It may be expected that an increase in the Schottky barrier height will occur if the normally pinned Fermi level [42] is now a function of the physical state of the beam-altered metal–semiconductor interface. Ion beam pre-treatment of the contact region before metal deposition increases the concentration of dangling bonds available for molecular hybridization when the contact metal is deposited [32]. As we are treating an already hybridized interface, we suspect that the formation of point defects therein, such as migrated interstitials and antisite defects, will serve to trap carriers at the interface and will reduce the crowded injection current at the contact [43]. This

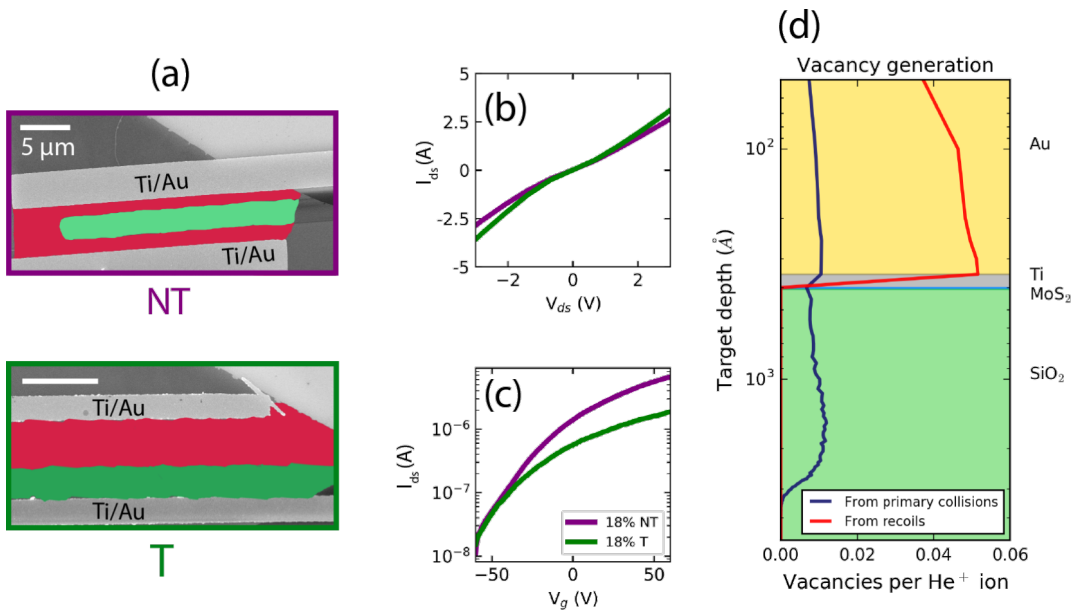

Figure 3: (a) Example SEM images of electrode non-touching (NT) and touching (T) devices with a similar I_R. The colored green area is the channel region damaged by the He^+ ion beam, while the red area is the non-irradiated MoS_2 channel. Scale bars are both 5 μm. (b) Output and (c) transfer curves of devices with I_R = 18% from the NT and T categories, highlighting the deleterious effect of electrode irradiation on the current injection. (d) Simulation of the S vacancy yield generated as the He^+ ion beam penetrates the device at the contact stack, indicating damage to the metal–semiconductor interface.

may be empirically confirmed with a combination of low-temperature electrical characterization and capacitance measurements [44,45] in future work.

Conclusion

In summary, we have studied the effects of varying the irradiated channel area of helium ion-treated monolayer MoS_2 FETs. Introducing a small number of defects into the material (approx. 10% of irradiated-to-pristine channel area) can serve to improve the charge carrier mobility and the electrical conductance. We found that irradiating the electrode–MoS_2 interface was deleterious to the performance of the FET, with a conductance drop noticed for each of the areal irradiation regimes. Our work demonstrates that by tuning the helium ion irradiation strategy, and localizing the exposure to specific sites, the electronic characteristics of on-dielectric MoS_2 FETs can be well-controlled in the monolayer limit. Post-metallization irradiations need to be finely controlled to ensure that the hybridized metal–semiconductor interface is not disturbed, otherwise the drive current in ion beam-treated 2D FETs will be limited for certain applications.

Acknowledgements

We acknowledge D. Keane for helpful discussions and D. Daly for assistance with the helium ion microscope.

Funding

The following sources of funding are acknowledged: the Leverhulme Trust International Networks Grant (PicoFIB), Science Foundation Ireland (12/TIDA/I2433) and the Irish Research Council (GOIPG/2014/972).

ORCID® iDs

Jakub Jadwiszczak - https://orcid.org/0000-0002-9518-9402
Pierce Maguire - https://orcid.org/0000-0002-5117-4233

References

1. Jariwala, D.; Sangwan, V. K.; Late, D. J.; Johns, J. E.; Dravid, V. P.; Marks, T. J.; Lauhon, L. J.; Hersam, M. C. *Appl. Phys. Lett.* **2013,** *102,* 173107. doi:10.1063/1.4803920
2. Baugher, B. W. H.; Churchill, H. O. H.; Yang, Y.; Jarillo-Herrero, P. *Nano Lett.* **2013,** *13,* 4212–4216. doi:10.1021/nl401916s
3. O'Brien, M.; McEvoy, N.; Motta, C.; Zheng, J.-Y.; Berner, N. C.; Kotakoski, J.; Elibol, K.; Pennycook, T. J.; Meyer, J. C.; Yim, C.; Abid, M.; Hallam, T.; Donegan, J. F.; Sanvito, S.; Duesberg, G. S. *2D Mater.* **2016,** *3,* 021004. doi:10.1088/2053-1583/3/2/021004
4. Bergeron, H.; Sangwan, V. K.; McMorrow, J. J.; Campbell, G. P.; Balla, I.; Liu, X.; Bedzyk, M. J.; Marks, T. J.; Hersam, M. C. *Appl. Phys. Lett.* **2017,** *110,* 053101. doi:10.1063/1.4975064
5. Smithe, K. K. H.; Suryavanshi, S. V.; Muñoz Rojo, M.; Tedjarati, A. D.; Pop, E. *ACS Nano* **2017,** *11,* 8456–8463. doi:10.1021/acsnano.7b04100
6. Iberi, V.; Ievlev, A. V.; Vlassiouk, I.; Jesse, S.; Kalinin, S. V.; Joy, D. C.; Rondinone, A. J.; Belianinov, A.; Ovchinnikova, O. S. *Nanotechnology* **2016,** *27,* 125302. doi:10.1088/0957-4484/27/12/125302
7. Klein, J.; Kuc, A.; Nolinder, A.; Altzschner, M.; Wierzbowski, J.; Sigger, F.; Kreupl, F.; Finley, J. J.; Wurstbauer, U.; Holleitner, A. W.; Kaniber, M. *2D Mater.* **2017,** *5,* 011007. doi:10.1088/2053-1583/aa9642
8. Stanford, M. G.; Lewis, B. B.; Mahady, K.; Fowlkes, J. D.; Rack, P. D. *J. Vac. Sci. Technol., B: Nanotechnol. Microelectron.: Mater., Process., Meas., Phenom.* **2017,** *35,* 030802. doi:10.1116/1.4981016
9. Fox, D. S.; Zhou, Y.; Maguire, P.; O'Neill, A.; Ó'Coileáin, C.; Gatensby, R.; Glushenkov, A. M.; Tao, T.; Duesberg, G. S.; Shvets, I. V.; Abid, M.; Abid, M.; Wu, H.-C.; Chen, Y.; Coleman, J. N.; Donegan, J. F.; Zhang, H. *Nano Lett.* **2015,** *15,* 5307–5313. doi:10.1021/acs.nanolett.5b01673
10. Stanford, M. G.; Pudasaini, P. R.; Gallmeier, E. T.; Cross, N.; Liang, L.; Oyedele, A.; Duscher, G.; Mahjouri-Samani, M.; Wang, K.; Xiao, K.; Geohegan, D. B.; Belianinov, A.; Sumpter, B. G.; Rack, P. D. *Adv. Funct. Mater.* **2017,** *27,* 1702829. doi:10.1002/adfm.201702829
11. Jadwiszczak, J.; Keane, D.; Maguire, P.; Cullen, C. P.; Zhou, Y.; Song, H.; Downing, C.; Fox, D.; McEvoy, N.; Zhu, R.; Xu, J.; Duesberg, G. S.; Liao, Z.-M.; Boland, J. J.; Zhang, H. *ACS Nano* **2019,** *13,* 14262–14273. doi:10.1021/acsnano.9b07421
12. Liu, Y.; Gao, Z.; Tan, Y.; Chen, F. *ACS Nano* **2018,** *12,* 10529–10536. doi:10.1021/acsnano.8b06503
13. Ma, Q.; Odenthal, P. M.; Mann, J.; Le, D.; Wang, C. S.; Zhu, Y.; Chen, T.; Sun, D.; Yamaguchi, K.; Tran, T.; Wurch, M.; McKinley, J. L.; Wyrick, J.; Magnone, K.; Heinz, T. F.; Rahman, T. S.; Kawakami, R.; Bartels, L. *J. Phys.: Condens. Matter* **2013,** *25,* 252201. doi:10.1088/0953-8984/25/25/252201
14. Li, Z.; Chen, F. *Appl. Phys. Rev.* **2017,** *4,* 011103. doi:10.1063/1.4977087
15. Maguire, P.; Fox, D. S.; Zhou, Y.; Wang, Q.; O'Brien, M.; Jadwiszczak, J.; Cullen, C. P.; McManus, J.; Bateman, S.; McEvoy, N.; Duesberg, G. S.; Zhang, H. *Phys. Rev. B* **2018,** *98,* 134109. doi:10.1103/physrevb.98.134109
16. Maguire, P.; Downing, C.; Jadwiszczak, J.; O'Brien, M.; Keane, D.; McManus, J. B.; Duesberg, G. S.; Nicolosi, V.; McEvoy, N.; Zhang, H. *J. Appl. Phys.* **2019,** *125,* 064305. doi:10.1063/1.5086366
17. Stanford, M. G.; Pudasaini, P. R.; Cross, N.; Mahady, K.; Hoffman, A. N.; Mandrus, D. G.; Duscher, G.; Chisholm, M. F.; Rack, P. D. *Small Methods* **2017,** *1,* 1600060. doi:10.1002/smtd.201600060
18. Stanford, M. G.; Pudasaini, P. R.; Belianinov, A.; Cross, N.; Noh, J. H.; Koehler, M. R.; Mandrus, D. G.; Duscher, G.; Rondinone, A. J.; Ivanov, I. N.; Ward, T. Z.; Rack, P. D. *Sci. Rep.* **2016,** *6,* 27276. doi:10.1038/srep27276
19. Yu, Z. G.; Zhang, Y.-W.; Yakobson, B. I. *Nano Lett.* **2015,** *15,* 6855–6861. doi:10.1021/acs.nanolett.5b02769
20. Jadwiszczak, J.; O'Callaghan, C.; Zhou, Y.; Fox, D. S.; Weitz, E.; Keane, D.; Cullen, C. P.; O'Reilly, I.; Downing, C.; Shmeliov, A.; Maguire, P.; Gough, J. J.; McGuinness, C.; Ferreira, M. S.; Bradley, A. L.; Boland, J. J.; Duesberg, G. S.; Nicolosi, V.; Zhang, H. *Sci. Adv.* **2018,** *4,* eaao5031. doi:10.1126/sciadv.aao5031
21. Bertolazzi, S.; Bonacchi, S.; Nan, G.; Pershin, A.; Beljonne, D.; Samorì, P. *Adv. Mater. (Weinheim, Ger.)* **2017,** *29,* 1606760. doi:10.1002/adma.201606760
22. Sangwan, V. K.; Hersam, M. C. *Annu. Rev. Phys. Chem.* **2018,** *69,* 299–325. doi:10.1146/annurev-physchem-050317-021353

23. Shang, M.-H.; Hou, H.; Zheng, J.; Yang, Z.; Zhang, J.; Wei, S.; Duan, X.; Yang, W. *J. Phys. Chem. Lett.* **2018,** *9,* 6032–6037. doi:10.1021/acs.jpclett.8b02591
24. Komsa, H.-P.; Krasheninnikov, A. V. *Phys. Rev. B* **2015,** *91,* 125304. doi:10.1103/physrevb.91.125304
25. Buchheim, J.; Wyss, R. M.; Shorubalko, I.; Park, H. G. *Nanoscale* **2016,** *8,* 8345–8354. doi:10.1039/c6nr00154h
26. Yoon, K.; Rahnamoun, A.; Swett, J. L.; Iberi, V.; Cullen, D. A.; Vlassiouk, I. V.; Belianinov, A.; Jesse, S.; Sang, X.; Ovchinnikova, O. S.; Rondinone, A. J.; Unocic, R. R.; van Duin, A. C. T. *ACS Nano* **2016,** *10,* 8376–8384. doi:10.1021/acsnano.6b03036
27. Stanford, M. G.; Noh, J. H.; Mahady, K.; Ievlev, A. V.; Maksymovych, P.; Ovchinnikova, O. S.; Rack, P. D. *ACS Appl. Mater. Interfaces* **2017,** *9,* 35125–35132. doi:10.1021/acsami.7b10449
28. Lin, Z.; McCreary, A.; Briggs, N.; Subramanian, S.; Zhang, K.; Sun, Y.; Li, X.; Borys, N. J.; Yuan, H.; Fullerton-Shirey, S. K.; Chernikov, A.; Zhao, H.; McDonnell, S.; Lindenberg, A. M.; Xiao, K.; LeRoy, B. J.; Drndić, M.; Hwang, J. C. M.; Park, J.; Chhowalla, M.; Schaak, R. E.; Javey, A.; Hersam, M. C.; Robinson, J.; Terrones, M. *2D Mater.* **2016,** *3,* 042001. doi:10.1088/2053-1583/3/4/042001
29. Kaasbjerg, K.; Martiny, J. H. J.; Low, T.; Jauho, A.-P. *Phys. Rev. B* **2017,** *96,* 241411. doi:10.1103/physrevb.96.241411
30. Li, S.-L.; Tsukagoshi, K.; Orgiu, E.; Samorì, P. *Chem. Soc. Rev.* **2016,** *45,* 118–151. doi:10.1039/c5cs00517e
31. Seo, S.-Y.; Park, J.; Park, J.; Song, K.; Cha, S.; Sim, S.; Choi, S.-Y.; Yeom, H. W.; Choi, H.; Jo, M.-H. *Nat. Electron.* **2018,** *1,* 512–517. doi:10.1038/s41928-018-0129-6
32. Cheng, Z.; Cardenas, J. A.; McGuire, F.; Najmaei, S.; Franklin, A. D. *IEEE Electron Device Lett.* **2016,** *37,* 1234–1237. doi:10.1109/led.2016.2591552
33. O'Brien, M.; McEvoy, N.; Hallam, T.; Kim, H.-Y.; Berner, N. C.; Hanlon, D.; Lee, K.; Coleman, J. N.; Duesberg, G. S. *Sci. Rep.* **2014,** *4,* 7374. doi:10.1038/srep07374
34. Ghorbani-Asl, M.; Kretschmer, S.; Spearot, D. E.; Krasheninnikov, A. V. *2D Mater.* **2017,** *4,* 025078. doi:10.1088/2053-1583/aa6b17
35. Arnold, A. J.; Shi, T.; Jovanovic, I.; Das, S. *ACS Appl. Mater. Interfaces* **2019,** *11,* 8391–8399. doi:10.1021/acsami.8b18659
36. Pudasaini, P. R.; Oyedele, A.; Zhang, C.; Stanford, M. G.; Cross, N.; Wong, A. T.; Hoffman, A. N.; Xiao, K.; Duscher, G.; Mandrus, D. G.; Ward, T. Z.; Rack, P. D. *Nano Res.* **2018,** *11,* 722–730. doi:10.1007/s12274-017-1681-5
37. Dhall, R.; Li, Z.; Kosmowska, E.; Cronin, S. B. *J. Appl. Phys.* **2016,** *120,* 195702. doi:10.1063/1.4967398
38. Yoo, G.; Hong, S.; Heo, J.; Kim, S. *Appl. Phys. Lett.* **2017,** *110,* 053112. doi:10.1063/1.4975626
39. Kretschmer, S.; Maslov, M.; Ghaderzadeh, S.; Ghorbani-Asl, M.; Hlawacek, G.; Krasheninnikov, A. V. *ACS Appl. Mater. Interfaces* **2018,** *10,* 30827–30836. doi:10.1021/acsami.8b08471
40. Choi, H. H.; Cho, K.; Frisbie, C. D.; Sirringhaus, H.; Podzorov, V. *Nat. Mater.* **2018,** *17,* 2–7. doi:10.1038/nmat5035
41. Ziegler, J. F.; Ziegler, M. D.; Biersack, J. P. *Nucl. Instrum. Methods Phys. Res., Sect. B* **2010,** *268,* 1818–1823. doi:10.1016/j.nimb.2010.02.091
42. Kim, C.; Moon, I.; Lee, D.; Choi, M. S.; Ahmed, F.; Nam, S.; Cho, Y.; Shin, H.-J.; Park, S.; Yoo, W. J. *ACS Nano* **2017,** *11,* 1588–1596. doi:10.1021/acsnano.6b07159
43. Arutchelvan, G.; Lockhart de la Rosa, C. J.; Matagne, P.; Sutar, S.; Radu, I.; Huyghebaert, C.; De Gendt, S.; Heyns, M. *Nanoscale* **2017,** *9,* 10869–10879. doi:10.1039/c7nr02487h
44. Moon, B. H.; Han, G. H.; Kim, H.; Choi, H.; Bae, J. J.; Kim, J.; Jin, Y.; Jeong, H. Y.; Joo, M.-K.; Lee, Y. H.; Lim, S. C. *ACS Appl. Mater. Interfaces* **2017,** *9,* 11240–11246. doi:10.1021/acsami.6b16692
45. Kim, H.-J.; Kim, D.-H.; Jeong, C.-Y.; Lee, J.-H.; Kwon, H.-I. *IEEE Electron Device Lett.* **2017,** *38,* 481–484. doi:10.1109/led.2017.2673854

License and Terms

BEILSTEIN JOURNAL OF NANOTECHNOLOGY

Helium ion microscope – secondary ion mass spectrometry for geological materials

Matthew R. Ball[*1], Richard J. M. Taylor[2], Joshua F. Einsle[3], Fouzia Khanom[4], Christelle Guillermier[4] and Richard J. Harrison[1]

Full Research Paper

Open Access

Address:
[1]Department of Earth Sciences, University of Cambridge, UK, [2]Carl Zeiss Microscopy Ltd, Cambourne, Cambridgeshire, UK, [3]School of Geographical and Earth Sciences, University of Glasgow, UK and [4]Carl Zeiss SMT Inc., Peabody, MA, USA

Email:
Matthew R. Ball[*] - mb977@cam.ac.uk

* Corresponding author

Keywords:
geoscience; helium ion microscopy (HIM); lithium; secondary ion mass spectrometry (SIMS)

Beilstein J. Nanotechnol. **2020,** *11,* 1504–1515.
https://doi.org/10.3762/bjnano.11.133

Received: 29 June 2020
Accepted: 09 September 2020
Published: 02 October 2020

This article is part of the thematic issue "Ten years of the helium ion microscope".

Guest Editors: G. Hlawacek and A. Wolff

Abstract

The helium ion microscope (HIM) is a focussed ion beam instrument with unprecedented spatial resolution for secondary electron imaging but has traditionally lacked microanalytical capabilities. With the addition of the secondary ion mass spectrometry (SIMS) attachment, the capabilities of the instrument have expanded to microanalysis of isotopes from Li up to hundreds of atomic mass units, effectively opening up the analysis of all natural and geological systems. However, the instrument has thus far been underutilised by the geosciences community, due in no small part to a lack of a thorough understanding of the quantitative capabilities of the instrument. Li represents an ideal element for an exploration of the instrument as a tool for geological samples, due to its importance for economic geology and a green economy, and the difficult nature of observing Li with traditional microanalytical techniques. Also Li represents a “best-case” scenario for isotopic measurements. Here we present details of sample preparation, instrument sensitivity, theoretical, and measured detection limits for both elemental and isotopic analysis as well as practicalities for geological sample analyses of Li alongside a discussion of potential geological use cases of the HIM–SIMS instrument.

Introduction

The helium ion microscope (HIM) is a focussed ion beam (FIB) instrument, which uses a gas field ion source (GFIS) to create highly focussed beams of noble gas ions, utilising the same working principle as the field ion microscope (FIM). This was originally used to form a primary helium beam [1], but the principle of the GFIS has since been extended to the heavier noble gas neon [2] and may be applicable for even heavier noble gases such as argon. Whilst the HIM was shown to achieve exceptional imaging resolution using secondary electrons generated by the primary ion beam [3-6], it lacked microanalytical

capabilities. There were several suggestions for the possibility of microanalysis on the HIM, the most common of these being Rutherford backscattered ion imaging (RBI) and secondary ion mass spectrometry (SIMS) [7-9]. However, the variation of RBI intensity with changing surface chemistry, specifically the atomic number, Z, reaches a plateau at relatively low Z values of around 50 [7], limiting its use to lighter elements only. SIMS, however, opens the entire range of mass numbers, from a few atomic mass units up to several hundred atomic mass units, whilst also leaving open the possibility of in situ isotopic measurements. This combined HIM–SIMS instrument has intriguing possibilities for geological materials as, unlike previous SIMS techniques limited by the probe size of the primary beam, the small beam size theoretically allows for chemical mapping at high sensitivity with the spatial resolution controlled only by beam–sample interactions [9]. The possibility of isotopic measurements at such a high spatial resolution, around 10 nm, is of particular importance in the planetary sciences, where variations are extreme in both their magnitude and their nanometre-scale size [10,11]. Additionally, planetary materials pose a particular challenge to traditional microanalysis techniques, since they are often rare or one-of-a-kind samples, limiting them to non-destructive analysis, or analysis that preserves as much of the sample as possible. They also typically contain very small components, which record the signals of different stellar processes [10,12], resulting in extreme heterogeneity of data across nanometre-scale distances. Ion imaging in cosmochemistry is typically performed with the NanoSIMS instrument, which can reach spatial resolutions of 50–100 nm for Cs^+ with a beam current below 1 pA and 200–400 nm for O^- with a beam current below 10 pA [13]. However, the scale of some inclusions within some planetary materials can be of the order of hundreds of nanometres, making detailed imaging of such inclusions with the NanoSIMS unfeasible. The HIM–SIMS however, with spatial resolutions of less than 10 nm, represents an ideal tool for such imaging, allowing for detailed nanometre-scale chemical imaging over large areas.

Whilst many geological materials could benefit from the analytical capabilities of the HIM–SIMS, they also present challenges for the device. In particular, the insulating nature of silicates, which make up most geological materials on Earth, requires additional sample preparation, which, if performed incorrectly, can have a negative impact on both qualitative and quantitative use of the instrument. Here, we demonstrate the instrumental sensitivity, capability, and repeatability of the HIM–SIMS using Li as a test element. The choice of Li is particularly relevant for geoscience applications as it represents a key geological resource for green energy storage, a challenge to the commonly used scanning electron microscope (SEM)-based microanalysis methods, which rely on energy/wavelength dispersive X-ray spectroscopy, as well as a best-case scenario for isotope measurements, since it has one of the largest relative mass differences between isotopes of any element. Alongside this, the practicalities of sample preparation and a discussion of further potential use cases of the HIM–SIMS for geological materials are also provided.

Results and Discussion

Methods

All analyses were performed using an ORION NanoFab HIM with an attached V500 double focussing magnetic sector mass spectrometer [14]. The gas field ion source (GFIS) of the ORION instrument produces a highly focussed single ion stream of He^+ or Ne^+, with a very small probe size (0.5 nm for He^+ and less than 3 nm for Ne^+). Primary ion currents of 1–10 pA were applied to the samples with acceleration voltages between 10,000 and 20,000 keV. Positive secondary ions of Li^+ were extracted by the application of a 500 V extraction voltage applied to the sample surface along an extraction system mounted directly above the sample, which subtends a large solid angle at the sample for a high collection efficiency. Ions were then measured by electron multiplier detectors set to fixed positions at m/z 6, m/z 7, and an arbitrary value of m/z for which no secondary ions were expected, for the measurement of a "background count rate", with a fixed, low magnetic field of around 100 mT. The primary beam was rastered over the sample to simultaneously map ion counts on each detector with a typical dwell time per pixel of 4 ms, leading to an average mapping time of 20 min.

Sample preparation

Sample mounting

Unlike many traditional SIMS instruments, the HIM–SIMS has fewer constraints on sample mount size, as the sample holder is unmodified from the holder of the HIM, allowing for larger mounts, with space for multiple thin sections alongside standards. Whilst a large sample holder allows for multiple samples at a time, with fewer concerns on mount size, care must be taken to maintain a constant height across the mounts, as the extractor sits at a constant height above the holder for a given focus, which can lead to potential collisions with other samples if the heights and, therefore, focal distance is not constant.

Sample coating

Due to size constraints within the chamber, it is currently not possible to have both an electron flood gun and SIMS attachment on the same device. This is a problem for geological samples, as the vast majority of them are insulators. To counteract this insulating behaviour and prevent the buildup of charge on the sample surface, samples must be coated with an electrically conducting material before they are introduced to the instru-

ment. Traditional SIMS instruments apply a thin metallic coating, typically gold, using a sputter coater. Here we employ a similar technique, coating samples with either gold or platinum, or, in the case of analysis of platinum-group elements [15], carbon. This coating is removed by the action of the primary beam in the region of interest prior to analysis, allowing for the removal of charge at the edges, but exposure of the sample surface within the analytical area. Figure 1 shows a mass spectrum taken on a natural zircon grain from NW Scotland, UK, mounted in epoxy resin with a carbon coating. Count rates before rastering with the primary beam are shown in red, whilst count rates from the same sample area are shown in blue, after rastering with the neon beam to remove the carbon coating. The count rate increases dramatically after the removal of the carbon coating. For some mass/charge values, which were not present in the original mass spectrum, such as the ZrO^+ fragment at *m*/*z* 106 and the ZrO_2^+ fragment at *m*/*z* 122, signals became measurable significantly above the background noise. Figure 2 shows the same zircon sample as Figure 1, immediately after the first mass spectrum in Figure 2b and immediately before the second mass spectrum in Figure 2c. The dramatic increase in signal is again demonstrated here, with almost no signal from the $^{90}Zr^+$ in Figure 2b, in contrast to the same mass-filtered image in Figure 2c. This demonstrates how important the removal of the conductive coating is for analysis of unknown material. While the coating is necessary for conductivity across the sample surface, it can dampen the signal to a point where some elements fall below the background noise level.

However, the primary beam is not designed for the rapid removal of material and if the applied coating is thicker than 5–10 nm, its removal can take an unreasonable amount of time. The increase in signal shown in Figure 1 and Figure 2 comes after 240 min of rastering with the primary neon beam, which corresponds to almost 300 min of instrument use, an unfeasible time for a single image. One solution is to pre-raster the areas of interest with a gallium beam before the sample is taken to this instrument, but this leads to the implantation of gallium ions and can lead to potential damage to the sample if an incorrect dose is used. Instead, care should be taken to apply thin (5–10 nm) coating layers to the sample, to maximise analysis time on the instrument.

Sample polishing

Figure 2 also demonstrates another issue with sample preparation, that is, polishing. Polishing is critical for the extraction of quantitative information using the SIMS method, since surface relief distorts the extraction field, enhancing extraction of secondary ions at topographic highs relative to lows, distorting the distribution of counts from the true distribution within the sample. The intensity variation is further modified by variations in

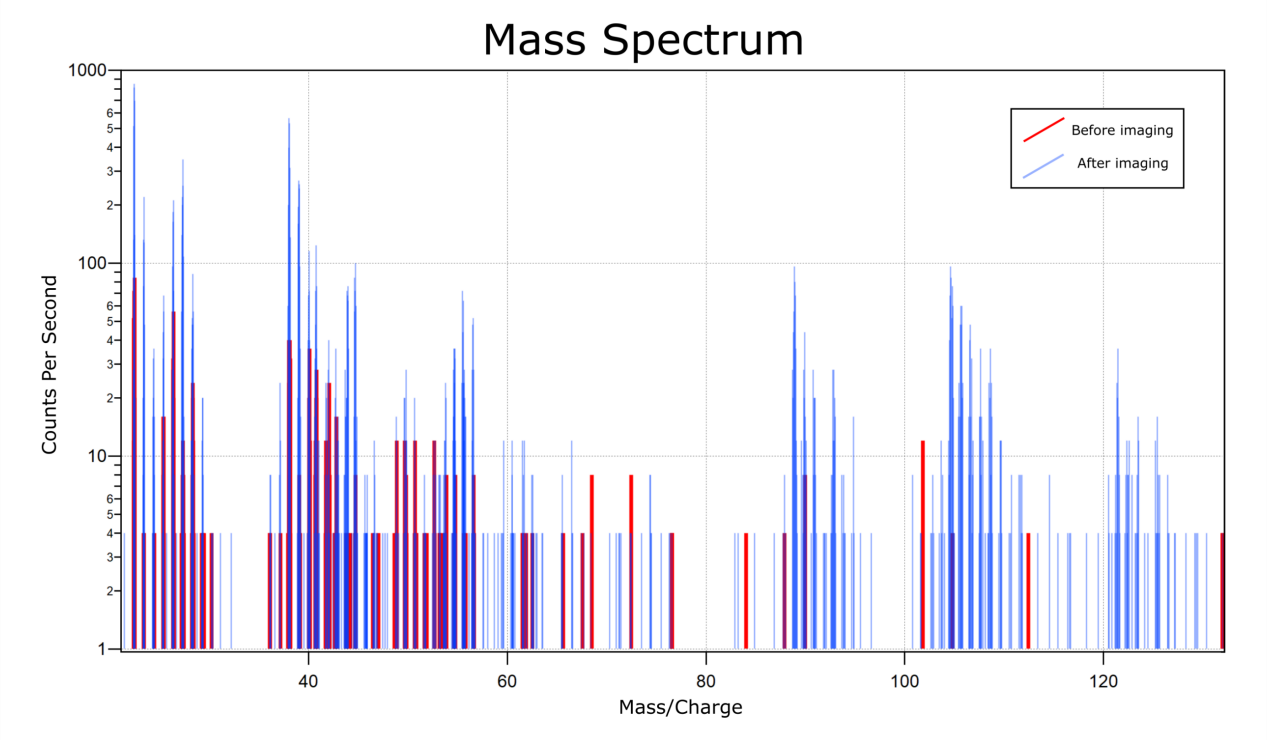

Figure 1: Mass spectra of a natural zircon sample before rastering with the primary beam (red) and after rastering with the primary beam for 240 min (blue). Count rates increase dramatically after the sample coating has been removed.

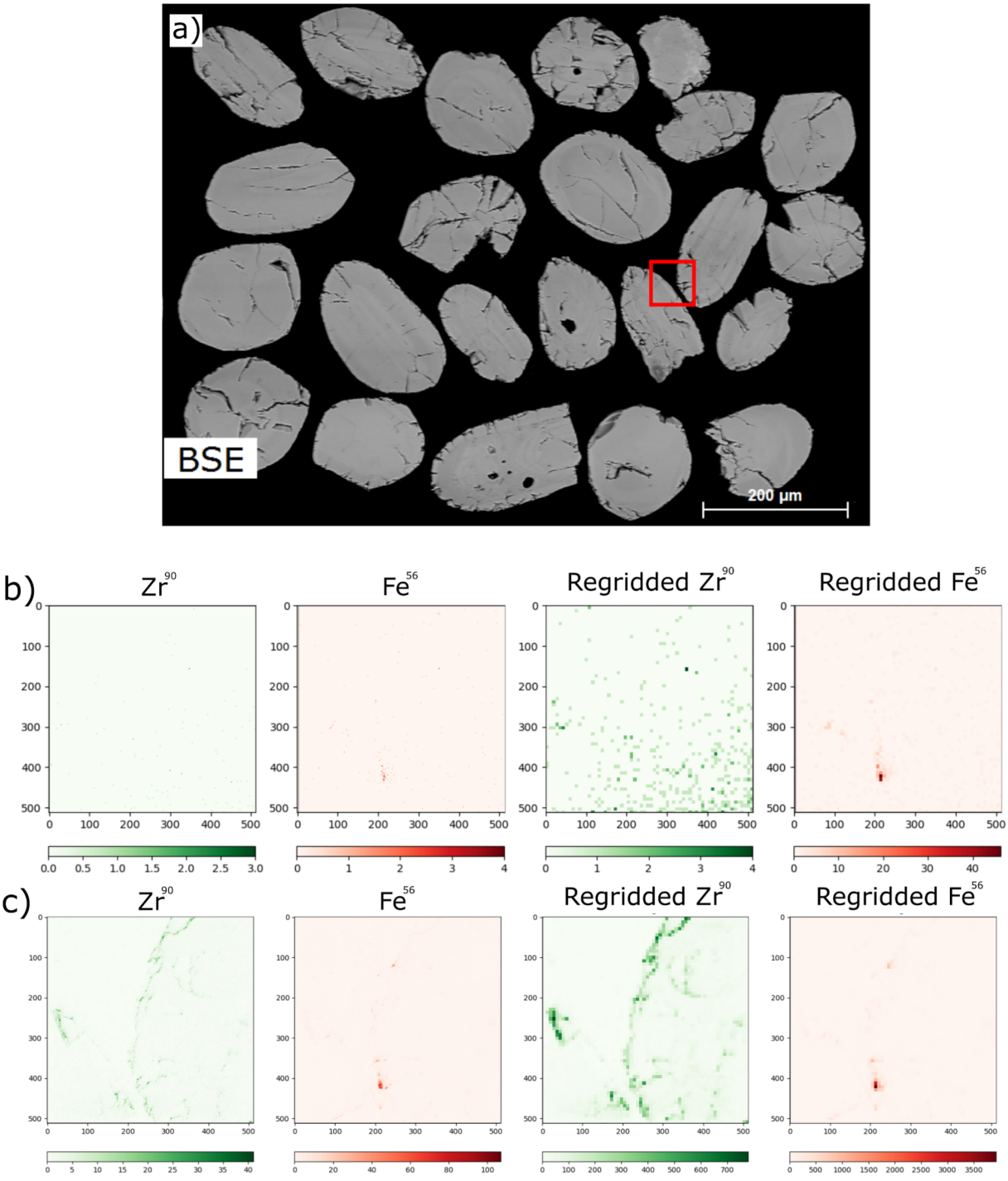

Figure 2: a) Backscattered electron (BSE) map of the sample, SIMS location outlined in red; b) raw and processed ^{90}Zr and ^{56}Fe mass images after 20 min of rastered beam exposure on the sample; c) raw and processed ^{90}Zr and ^{56}Fe mass images after 240 min of rastered beam exposure on the sample. Initial maps were 512 × 512 pixels, covering a field of view of 70 µm. The scales show the absolute number of ions detected.

the sputter yield at areas with a grazing incidence angle. This can be seen in Figure 2. Most of the signal comes from the edges of the zircon grains, where the zircon is raised relative to the epoxy. The formation of relief is a balancing act for SIMS analysis. During HIM–SIMS all the typical effects are exaggerated, therefore requiring an exceptional polish as well as minimal relief. However, whilst techniques exist to reduce relief to a minimum, for example, lapping films, they may not yield a

polish smooth as lapping cloths do. As a result, it is almost impossible to satisfy both requirements. The recommendation should be to minimize relief as much as possible using appropriate preparation techniques for the sample before a final polish (here we ended with a 0.25 µm polish). However, even after minimising the effect of relief, samples should be analysed away from the sample edge in order to obtain quantitative data.

Quantification

Concentration calibration

Quantification of concentrations using SIMS data is typically performed using one of two approaches. These are the useful yield approach [9] and the relative sensitivity factor approach [16], both of which rely on the effective use of appropriate standards. The useful yield approach depends on the calculation of the useful yield of an element, defined as the ratio of detected ions of species x to the number of sputtered atoms of x, in a matrix-matched reference sample. The concentration of x, C_x, can then be calculated using Equation 1, and depends on the secondary ion current, I_x, the calculated useful yield UY_x, the primary ion beam current, I_p and the sputtering yield, Y, which is typically measured after the analysis:

$$C_x = \frac{I_x}{UY_x \cdot I_p \cdot Y}. \quad (1)$$

The sputtering yield depends on the nature of the atoms as well as the matrix in which they are bound. This yield can be predicted semi-empirically for a primary Ne beam [17]. Figure 3 shows how the calculated yield of different atoms varies for a silicate glass matrix with two different densities, 2.2 and 3.3 g·cm^{-3}, that is, respectively, low-density and high-density silica glass. Different matrix materials can also affect the ionization probability of the sputtered material. Thus, it is necessary to properly match the matrix of the samples and standards, since small changes in the matrix can have a large effect on the constants involved in calculating the concentration of an element.

The relative sensitivity factor approach relies on the measurement of both the target element, x, as well as a known matrix element, m. The concentration of the element x, C_x, can then be calculated using the secondary ion current of species x, I_x, the secondary ion current of the matrix element m, I_m, and the relative sensitivity of the two elements, which is calculated using a matrix-matched standard under the same beam conditions. This approach can be simplified by relating the concentration of an element within a standard to the secondary ion current for that element from the standard and applying this correction to the secondary ion current measured on a sample under identical beam conditions. This simplified approach does not account for variations in measurement conditions, which are accounted for

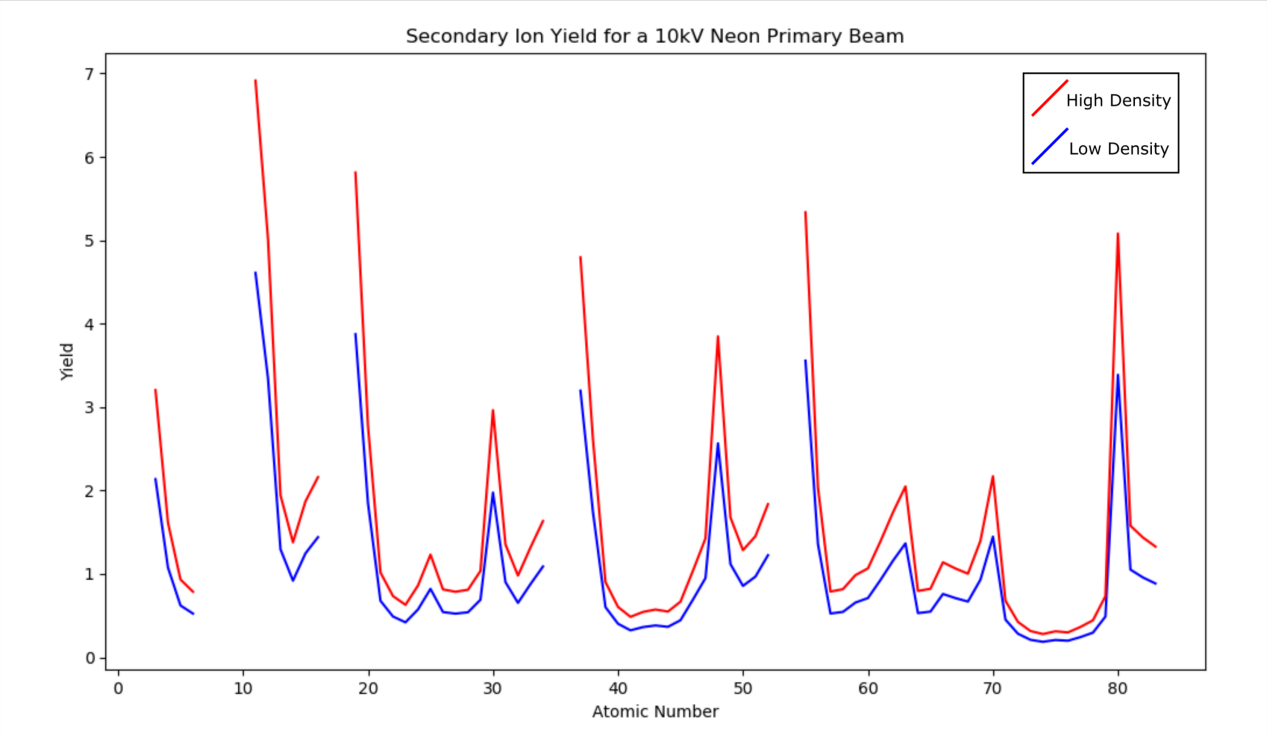

Figure 3: The calculated sputtering yield as a function of the atomic number for a 10 kV primary Ne beam impacting a silicate glass matrix for a low-density glass (2.2 g·cm^{-3}, blue) and a high-density glass (3.3 g·cm^{-3}, red), calculation after [17].

in a "true" relative sensitivity factor approach by the secondary ion current of a matrix element, I_m, as shown in Equation 2:

$$C_x = \frac{I_x}{I_m} \cdot \mathrm{RSF}_x. \quad (2)$$

Both of these methods rely on calibration to a known standard and using standards on the HIM–SIMS comes with many of the same necessities as on a traditional SIMS instrument, such as matrix-matching samples and standards. However, an additional problem when using standards on the HIM–SIMS is the homogeneity of the standard material. Whilst an electron microprobe standard should be homogeneous on a length scale of several micrometres, this same standard is required to maintain this homogeneity at a nanometre length scale in order to be used accurately with the HIM–SIMS instrument. It is extremely difficult to manufacture a standard material for all elements that is homogeneous at the nanometre scale. Platinum group elements, for example, commonly form micrometre-scale nuggets [18,19].

Isotopic calibration

Isotopic quantification also relies on the use of matrix-matched standards that are homogeneous on the nanometre length scale. Measured isotopic variations are typically expressed in delta notation. An example calculation for Li isotopes is shown in Equation 3. This accounts for the small variations in raw isotopic ratios typically seen in geological materials.

$$\delta^7\mathrm{Li} = \left\{ \frac{\left(\left[\frac{^7\mathrm{Li}}{^6\mathrm{Li}} \right]_{\mathrm{sample}} - \left[\frac{^7\mathrm{Li}}{^6\mathrm{Li}} \right]_{\mathrm{standard}} \right)}{\left[\frac{^7\mathrm{Li}}{^6\mathrm{Li}} \right]_{\mathrm{standard}}} \times 1000 \right\} \quad (3)$$

Data processing

Due to the small size of the primary ion beam interaction of less than 10 nm [9,20], combined with typical primary ion beam currents in the range of 10–100 pA, a very small volume of material is removed during each interaction between beam and sample surface. Whilst this makes the instrument extremely surface sensitive, it can also result in very low count rates for low concentrations and/or low-yield elements. However, even in such cases, appropriate data processing techniques can extract data with meaningful counting statistics for elemental and isotopic analysis, although this processing does have consequences, for example, it can reduce the lateral resolution significantly.

One method for increasing count rates is to regrid data, effectively reducing pixel number and image resolution whilst increasing pixel size and counts per pixel. Figure 5 shows ^{7}Li and ^{6}Li maps taken from a thin section containing the economic Li-bearing mineral Spodumene ($LiAlSi_2O_6$) as raw and regridded data, with different regridding sizes, taken across a region of alteration. The raw maps in Figure 5a can be used to define the altered region from the unaltered regions. Within the unaltered region are pixels with zero counts for either isotope of Li. Since we can assume variations in Li concentration are not occurring on a wavelength similar to the pixel size (14.6 nm), these must be measurement error. The regridded maps act to remove these anomalous pixels. The inverse relationship between counts per pixel and resolution can be clearly seen. However, in some respects regridding the data in this manner reduces the advantages of the extreme spatial resolution offered by HIM–SIMS. Another method is to sum counts over individual regions of the data, maintaining the lateral resolution of the data, but increasing the count rates under the assumption that different regions have roughly homogenous concentrations of an element or isotope ratios. In the case of the data shown in Figure 6, the regions can be separated into Li-bearing Spodumene and Li-free regions of altered Spodumene, which intrude from the edges of the grain, as shown in Figure 4. These Li-bearing regions can be further separated on the basis of connectivity. The ^{7}Li and ^{6}Li data can then be used together to calculate the variability of isotopic ratios across the region of alteration, as shown in Figure 6, where the shape and outline of the regions can be seen in comparison to the regridded data with lower spatial resolution.

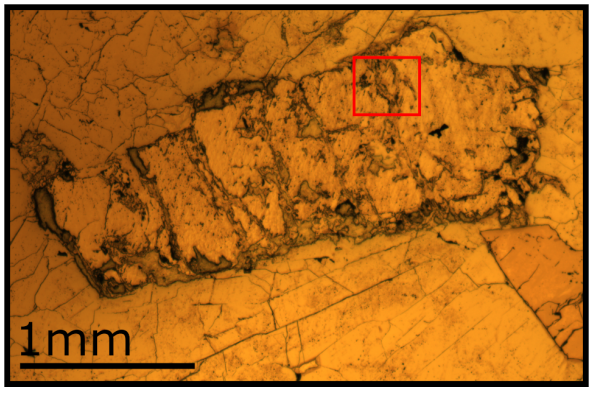

Figure 4: Reflected-light micrograph of the analysed Spodumene grain. The grain has relatively unaltered regions, separated by altered regions which intrude from the edge of the grain. Figure 5 was taken from within the region shown in red, across one such zone of alteration.

Irregular regridding can also be used to create effective line profiles along features that are at least as wide as the field of

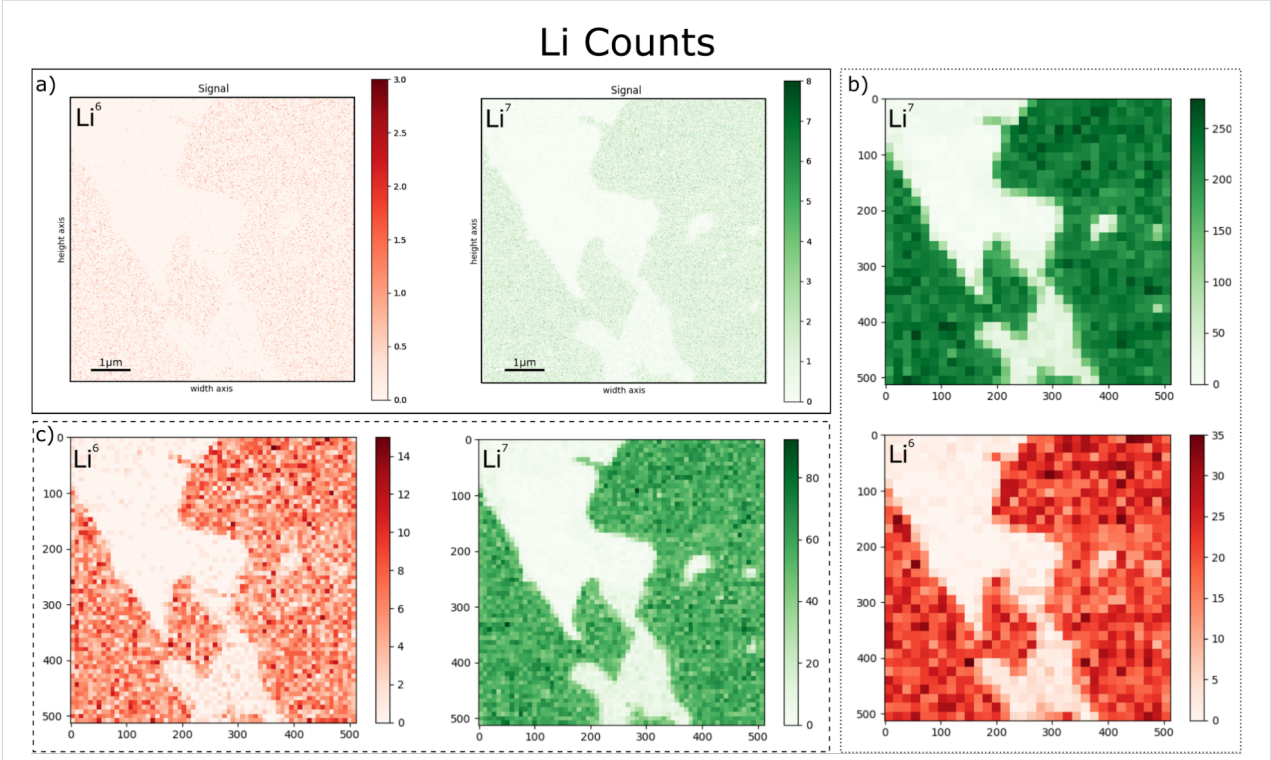

Figure 5: a) Raw (solid line), b) 32 × 32 regridded (dotted line) and c) 64 × 64 regridded (dashed line) maps of ^{6}Li (red) and ^{7}Li (green) from a Spodumene grain, see Figure 4.

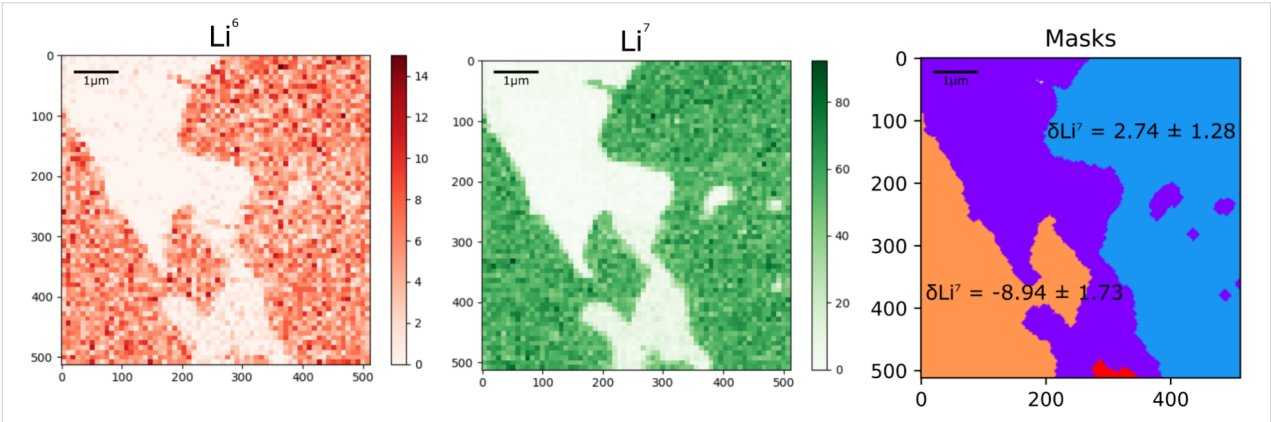

Figure 6: The relative δ^{7}Li ratios for regions within the same grain of Spodumene as in Figure 4 and Figure 5. Four connected regions with roughly similar counts have been identified, the purple region, an altered region, shows no Li, whilst the red region contains too few pixels to calculate a δ^{7}Li value with a reasonable error. Values are not calibrated to an external standard, but instead to the average ratio across all measurements of the grain, which should lead to values of zero for isotopically homogenous material.

view of one HIM–SIMS map. This data can then be regridded to sum along an axis perpendicular to the beam rastering direction, which should negate any effects of variable beam conditions. This is particularly useful for isotopic analysis, as it generates data with significantly better internal error/counting statistics [21], whilst still summing data from a width that is much smaller than a traditional SIMS instrument line profile.

Another method to increase counts is to image the same area sequentially. This method has been used for 3D imaging of extremely thin materials. However, for most geological samples the thickness of any layer of interest is much greater than the approx. 10 nm of removed material per map. In this way multiple maps may be summed, on the assumption that the region of interest is thicker than the total removed material [15]. This method is effective only when the surrounding area

remains able to compensate the charge and the electric field is not so distorted as to prevent the removal of the generated secondary ions.

Geological applications

Light elements

Some of the most important elements in the geosciences have low atomic numbers. Lithium, for example, is critical to a low-carbon energy landscape through electric vehicles and battery materials [22,23]. The global carbon cycle is likewise critical for the continued evolution of surface conditions on Earth, both in the geological record [24,25] and for the future [26]. Oxygen is a critical element as it is both one of the main constituents of the most common geological materials, silicates, and one of the best understood isotopic systems [12,27]. However, mapping the distribution of these elements by traditional methods, typically using SEM–EDS techniques, is extremely difficult, as the characteristic X-rays produced by these elements have such low energies that they are prone to re-absorption within the sample as well as being difficult to separate from other peaks in the produced spectra. This makes quantification almost impossible. The HIM–SIMS, in contrast, has its highest mass resolving power at low masses (around 400 $M/\Delta M$) with a low magnetic field applied within the mass spectrometer, making it an ideal tool for mapping these elements.

Lithium mapping

Figure 7 shows a comparison of the SEM–EDS signal obtained from a sample of Li-bearing mica and the HIM–SIMS signal from a subregion of the same sample. Both isotopes of Li can

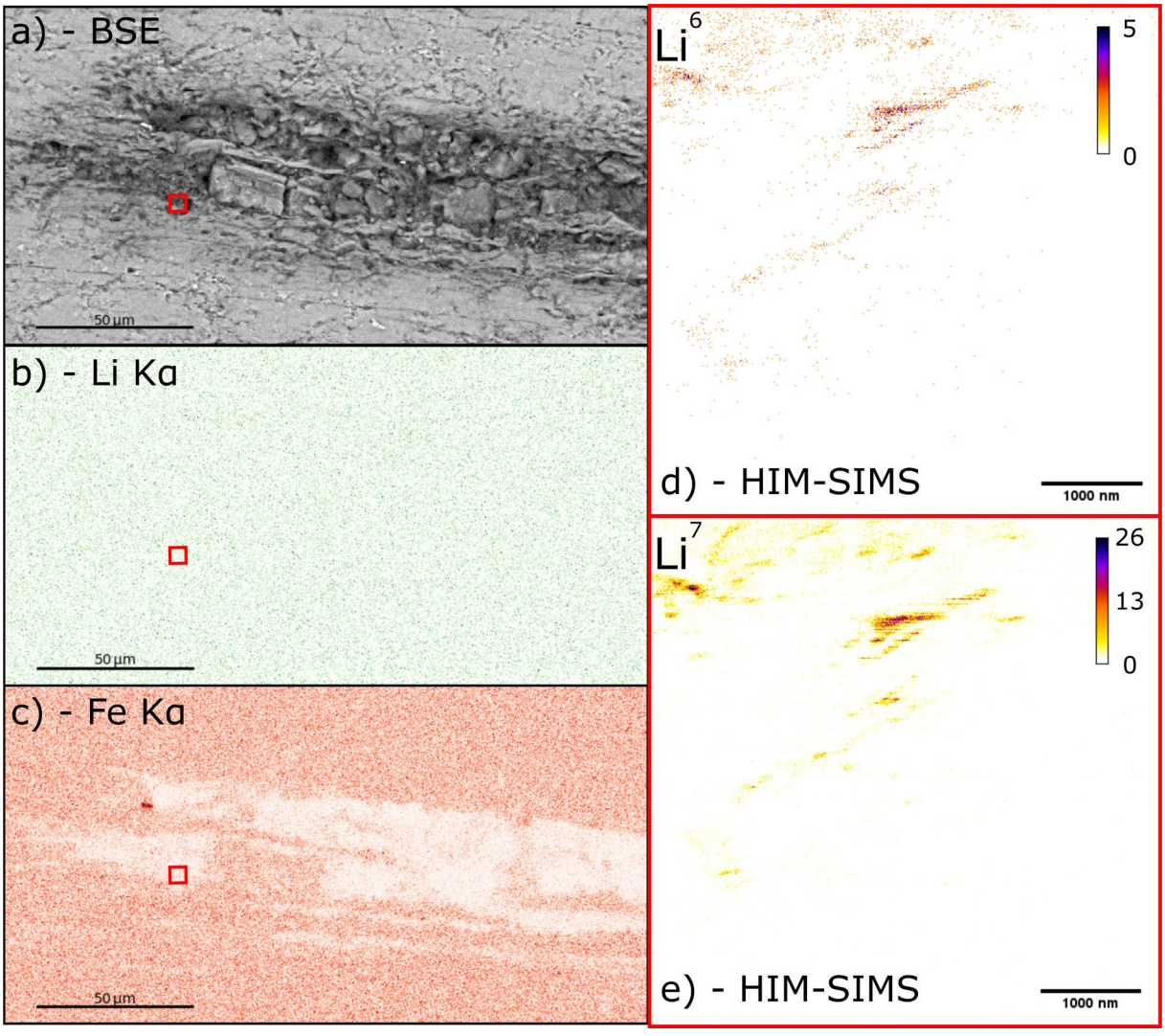

Figure 7: a) Backscatter electron image of the region of interest. The red square shows the region mapped using HIM–SIMS; b) Li EDS map of the region shown in a); c) Fe EDS map of the region shown in a); d) ^{6}Li map of the region within the red square in a) using HIM–SIMS; e) ^{7}Li map of the region within the red square in a) using HIM–SIMS.

be clearly seen in HIM–SIMS where no Li signal can be detected above background noise in the SEM–EDS data. The Fe signal is also shown, which should be inversely proportional to the Li signal as Fe and Li substitute in the crystal lattice within a solid solution. The Li signal appears to be stronger along mica sheets perpendicular to the *c*-axis of the crystal structure. However, this may be the result of surface topography similar to that observed in the zircon samples, as a result of polishing picking out the *c*-axis of the crystal structure, instead of a geological effect, such as greisenization.

The sensitivity toward Li has also been investigated in NIST glass standards. The NIST 612 standard has a known total Li concentration of 40 µg/g [28], which corresponds to concentrations of 37 µg/g for ^{7}Li and 3 µg/g for ^{6}Li. With one detector positioned at a fractional mass/charge ratio, which does not correspond to any elemental mass/charge ratio or half mass/charge ratio, the background count rate can be measured alongside the target mass/charge values. Figure 8 shows the count rates of ^{6}Li and ^{7}Li for NIST 612 glass relative to this background count rate, showing an experimentally derived instrumental sensitivity greater than 3 µg/g for Li.

Lithium isotopes

Lithium isotopes can be used as a tracer of important geological processes [29], responding readily to fractionation due to the large percentage mass difference between the two isotopes, ^{6}Li and ^{7}Li. Using the Li isotope system within a single sample of unaltered spodumene, the internal error due to counting statistics [21] and the external standard error over multiple measurements has been investigated. Figure 9 shows the δ^{7}Li values measured on a spodumene sample, calculated relative to the average ratio across all measurements, rather than relative to a standard as in Equation 3. Due to this, accurate measurements would always sit within the error of a δ^{7}Li value of 0. All measurements were taken over an area between 10 and 30 µm, except for the fourth point, which was over a 200 nm area. For the latter measurement with a 128 × 128 pixel map, the pixel size (1.5 nm) is smaller than the interaction volume of the beam, reducing the count rate significantly. The first measured pixel sputters material from a region effecting many more pixels, reducing any signal from these pixels when the beam does "measure" these points. Whilst this does drastically increase the internal error of this measurement, the data is still within the error of 0. The external error (ca. ±48‰) also appears to be negatively affected by this 200 nm data point, but is not significantly lower without this point included, remaining higher than the terrestrial range of variation [30].

Lithium isotope line profiles have also been measured, taking sequential maps perpendicular to deformed cleavage planes found in a sample of Li-rich biotite mica. These deformed cleavage planes are shown perpendicular to the *c*-axis of the biotite in Figure 10a. Again, δ^{7}Li values are calculated relative to the average across all measurements, showing variation from the average values, rather than true isotopic variation. Figure 10b shows the isotopic variations across the sample, calculated using the asymmetric regridding method outlined

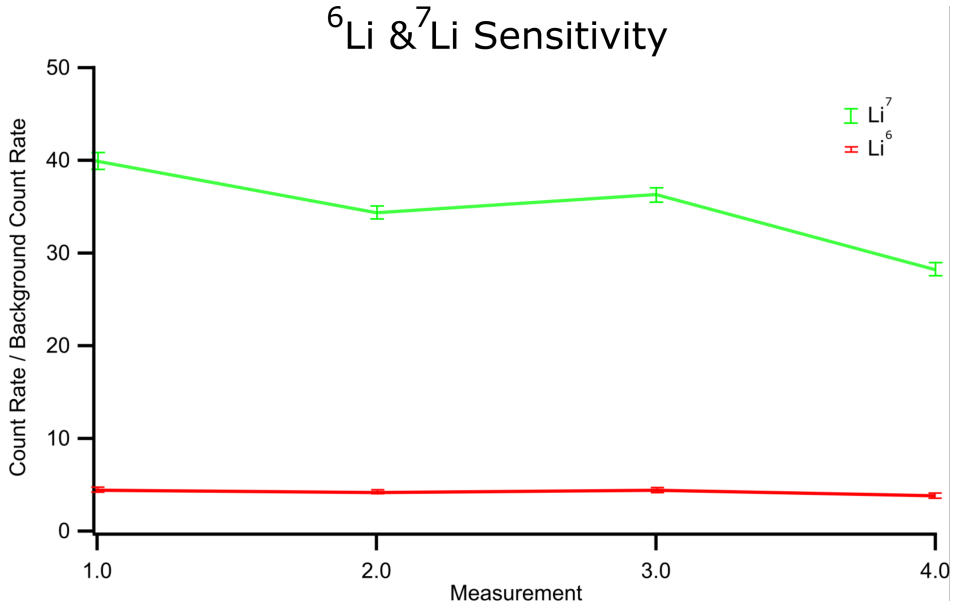

Figure 8: Count rates relative to background count rates for ^{6}Li (red, 3 µg/g) and ^{7}Li (green, 37 µg/g) for the NIST 612 glass standard. Background counts were collected simultaneously on a detector positioned over a fractional mass/charge ratio with no real counts.

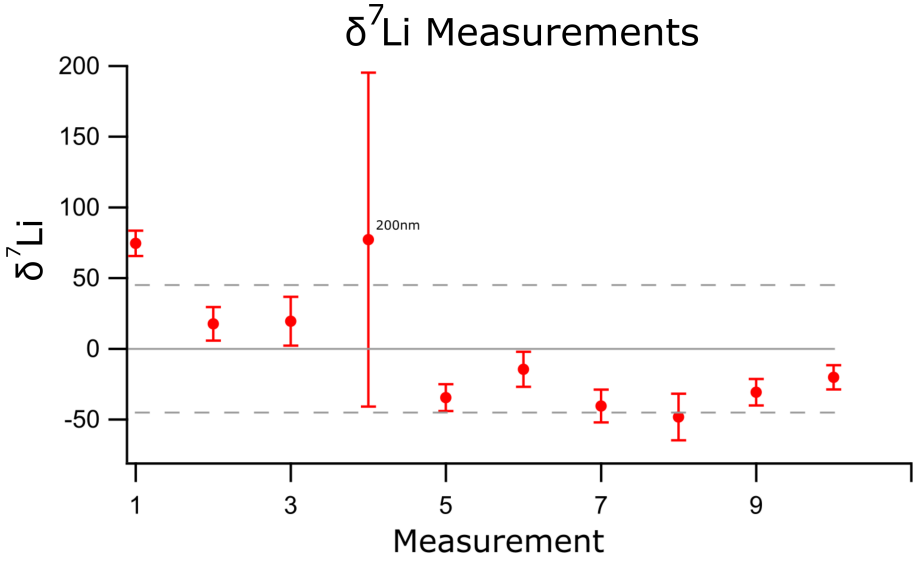

Figure 9: The relative δ^7Li ratios for regions within the same grain of Spodumene. Values are not calibrated to an external standard, but instead to the average ratio across all measurements, which should lead to values of zero for isotopically homogeneous material. The internal statistical counting error is shown in red for each point with the external error across all measurements in grey.

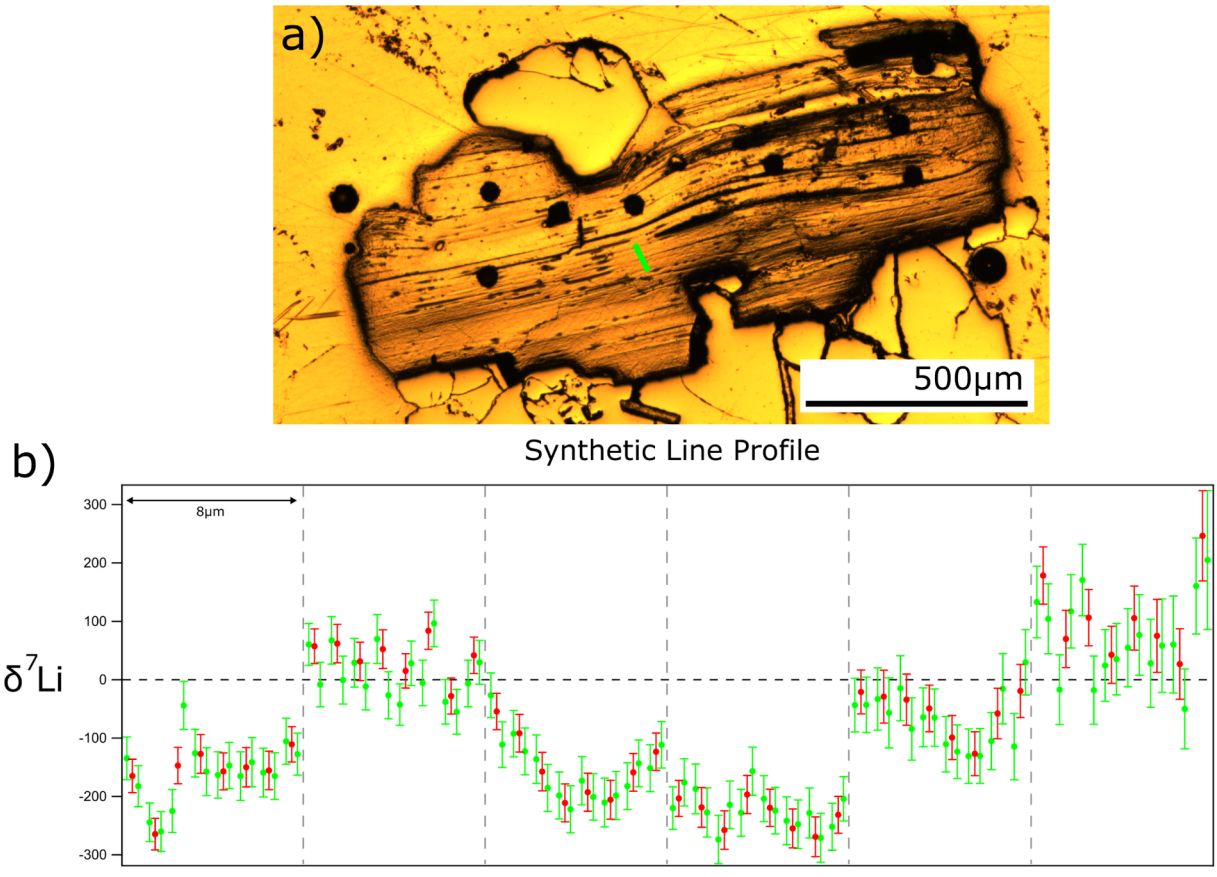

Figure 10: a) Examples of deformed cleavage planes in a Li-rich biotite mica shown parallel to the *c*-axis and b) δ^7Li values for vertical strips taken perpendicular to the scanning direction of the beam, along the green line in a). Each vertical grey line represents two microns of space left between each image, whilst red values are calculated using 1/8th width strips of the original maps and green values are calculated using 1/16th strips. Values are normalised to the average ratio across all measurements of the sample, rather than to an external standard.

above. The effect of calculating values for strips of different widths can be seen, larger variations are smoothed out by summing over strips with larger widths. This demonstrates the effect of increased count rate, with smaller internal error for each point, for all points except two. The values calculated for wider strips lie within the error of the values for two strips of half width. The external error of both datasets is approximately constant at ca. ±127‰, which is too low to explain the entire variation through instrument effects alone, leaving true geological variation as a possible cause.

Conclusion

The helium ion microscope provides an imaging tool with extreme spatial resolution using secondary electron imaging. With the addition of secondary ion mass spectrometry capabilities at the highest resolution, the HIM–SIMS is now set to fill a critical length-scale gap in the field of microanalysis, with resolutions second only to the atom probe, but with field of views of the order of micrometres, allowing for high resolution over a relatively large sample area. The HIM–SIMS is therefore a useful tool for a wide range of geological applications. The critical capability of sensitivity to light elements makes it an important tool for economic geology focused on a low-carbon future [19]. The experimentally measured sensitivity on the ppm level for Li is more than enough for the analysis of a wide range of economically important Li-bearing minerals. The spatial resolution over an area of micrometres yields exciting prospects in the field of planetary materials, where micrometre-sized or smaller inclusions hold important information about both the early solar system and the nature of extrasolar conditions [10].

Acknowledgements

We would like to thank the British Geological Society, Cornish Lithium and Ben Ellis for samples and ZEISS for instrument access.

Funding

The research leading to these results has received funding from Carl Zeiss CASE award RG92740.

ORCID® iDs

Matthew R. Ball - https://orcid.org/0000-0003-3058-7968
Richard J. M. Taylor - https://orcid.org/0000-0003-3013-9372
Joshua F. Einsle - https://orcid.org/0000-0001-8263-8531

References

1. Scipioni, L.; Sanford, C. A.; Notte, J.; Thompson, B.; McVey, S. *J. Vac. Sci. Technol., B: Microelectron. Nanometer Struct.–Process., Meas., Phenom.* **2009,** *27,* 3250. doi:10.1116/1.3258634
2. Rahman, F. H. M.; McVey, S.; Farkas, L.; Notte, J. A.; Tan, S.; Livengood, R. H. *Scanning* **2012,** *34,* 129–134. doi:10.1002/sca.20268
3. Notte, J. A.; Farkas, L.; Hill, R.; Ward, B. An Introduction to Helium Ion Microscopy and its Nanotechnology Applications. *Technical Proceedings of the 1006 NSTI Nanotechnology Conference and Trade Show;* 2006; Vol. 1, pp 737–740.
4. Vladár, A. E.; Postek, M. T.; Ming, B. *Microsc. Today* **2009,** *17* (2), 6–13. doi:10.1017/s1551929500054420
5. Joens, M. S.; Huynh, C.; Kasuboski, J. M.; Ferranti, D.; Sigal, Y. J.; Zeitvogel, F.; Obst, M.; Burkhardt, C. J.; Curran, K. P.; Chalasani, S. H.; Stern, L. A.; Goetze, B.; Fitzpatrick, J. A. J. *Sci. Rep.* **2013,** *3,* 3514. doi:10.1038/srep03514
6. Petrov, Y. V.; Vyvenko, O. F. Secondary Electron Generation in the Helium Ion Microscope: Basics and Imaging. In *Helium Ion Microscopy;* Hlawacek, G.; Golzhauser, A., Eds.; Nanoscience and Technology; Springer International Publishing: Cham, Switzerland, 2016; pp 119–146. doi:10.1007/978-3-319-41990-9_5
7. Joy, D. C.; Griffin, B. J. *Microsc. Microanal.* **2011,** *17,* 643–649. doi:10.1017/s1431927611000596
8. Wirtz, T.; Vanhove, N.; Pillatsch, L.; Dowsett, D.; Sijbrandij, S.; Notte, J. *Appl. Phys. Lett.* **2012,** *101,* 041601. doi:10.1063/1.4739240
9. Wirtz, T.; Philipp, P.; Audinot, J.-N.; Dowsett, D.; Eswara, S. *Nanotechnology* **2015,** *26,* 434001. doi:10.1088/0957-4484/26/43/434001
10. Lodders, K.; Amari, S. *Chem. Erde* **2005,** *65,* 93–166. doi:10.1016/j.chemer.2005.01.001
11. Hoppe, P.; Leitner, J.; Gröner, E.; Marhas, K. K.; Meyer, B. S.; Amari, S. *Astrophys. J.* **2010,** *719,* 1370–1384. doi:10.1088/0004-637x/719/2/1370
12. Yurimoto, H.; Krot, A. N.; Choi, B.-G.; Aleon, J.; Kunihiro, T.; Brearley, A. J. *Rev. Mineral. Geochem.* **2008,** *68,* 141–186. doi:10.2138/rmg.2008.68.8
13. Hoppe, P.; Cohen, S.; Meibom, A. *Geostand. Geoanal. Res.* **2013,** *37,* 111–154. doi:10.1111/j.1751-908x.2013.00239.x
14. Dowsett, D.; Wirtz, T. *Anal. Chem. (Washington, DC, U. S.)* **2017,** *89,* 8957–8965. doi:10.1021/acs.analchem.7b01481
15. Ball, M. R.; Taylor, R. J. M.; Einsle, J. F.; Audinot, J.-N.; Harrison, R. J. *Microsc. Microanal.* **2019,** *25,* 890–891. doi:10.1017/s143192761900518x
16. Benninghoven, A.; Rudenauer, F. G.; Werner, H. W. *Secondary Ion Mass Spectrometry: Basic Concepts, Instrumental Aspects, Applications and Trends;* Wiley: NY., 1987.
17. Seah, M. P. *Nucl. Instrum. Methods Phys. Res., Sect. B* **2005,** *229,* 348–358. doi:10.1016/j.nimb.2004.12.129
18. Koeberl, C.; Reimold, W. U.; McDonald, I.; Rosing, M. Search for petrographic and geochemical evidence for the late heavy bombardment on earth in early archean rocks from Isua, Greenland. In *Impacts and the Early Earth;* Gilmour, I.; Koeberl, C., Eds.; Lecture Notes in Earth Sciences; Springer-Verlag: Berlin, Germany, 2000; pp 73–97. doi:10.1007/bfb0027757
19. Goderis, S.; Paquay, F.; Claeys, P. Projectile Identification in Terrestrial Impact Structures and Ejecta Material. In *Impact Cratering;* Osinski, G. R.; Pierazzo, E., Eds.; John Wiley & Sons, Ltd,: Chichester, United Kingdom, 2012; pp 223–239. doi:10.1002/9781118447307.ch15
20. Pillatsch, L.; Vanhove, N.; Dowsett, D.; Sijbrandij, S.; Notte, J.; Wirtz, T. *Appl. Surf. Sci.* **2013,** *282,* 908–913. doi:10.1016/j.apsusc.2013.06.088
21. Fitzsimons, I. C. W.; Harte, B.; Clark, R. M. *Mineral. Mag.* **2000,** *64,* 59–83. doi:10.1180/002646100549139
22. Grosjean, C.; Miranda, P. H.; Perrin, M.; Poggi, P. *Renewable Sustainable Energy Rev.* **2012,** *16,* 1735–1744. doi:10.1016/j.rser.2011.11.023

23. Martin, G.; Rentsch, L.; Höck, M.; Bertau, M. *Energy Storage Mater.* **2017,** *6,* 171–179. doi:10.1016/j.ensm.2016.11.004
24. Glikson, A. *Energy Procedia* **2018,** *146,* 3–11. doi:10.1016/j.egypro.2018.07.002
25. Wong, K.; Mason, E.; Brune, S.; East, M.; Edmonds, M.; Zahirovic, S. *Front. Earth Sci.* **2019,** *7,* 263. doi:10.3389/feart.2019.00263
26. Barker, S.; Higgins, J. A.; Elderfield, H. *Philos. Trans. R. Soc., A* **2003,** *361,* 1977–1999. doi:10.1098/rsta.2003.1238
27. Pearson, P. N. *Paleontol. Soc. Pap.* **2012,** *18,* 1–38. doi:10.1017/s1089332600002539
28. Jochum, K. P.; Weis, U.; Stoll, B.; Kuzmin, D.; Yang, Q.; Raczek, I.; Jacob, D. E.; Stracke, A.; Birbaum, K.; Frick, D. A.; Günther, D.; Enzweiler, J. *Geostand. Geoanal. Res.* **2011,** *35,* 397–429. doi:10.1111/j.1751-908x.2011.00120.x
29. Liu, S.; Li, Y.; Liu, J.; Ju, Y.; Liu, J.; Yang, Z.; Shi, Y. *Geochim. Cosmochim. Acta* **2018,** *235,* 360–375. doi:10.1016/j.gca.2018.05.029
30. Elliott, T.; Jeffcoate, A.; Bouman, C. *Earth Planet. Sci. Lett.* **2004,** *220,* 231–245. doi:10.1016/s0012-821x(04)00096-2

License and Terms

BEILSTEIN JOURNAL OF NANOTECHNOLOGY

Out-of-plane surface patterning by subsurface processing of polymer substrates with focused ion beams

Serguei Chiriaev*[1], Luciana Tavares[1], Vadzim Adashkevich[2], Arkadiusz J. Goszczak[1] and Horst-Günter Rubahn[1]

Full Research Paper

Open Access

Address:
[1]NanoSYD, Mads Clausen Institute, University of Southern Denmark, Alsion 2, Sønderborg, 6400, Denmark and [2]Centre for Industrial Electronics, Department of mechanical and electronic engineering, University of Southern Denmark, Alsion 2, Sønderborg, 6400, Denmark

Email:
Serguei Chiriaev* - schi@mci.sdu.dk

* Corresponding author

Keywords:
direct patterning; focused helium ion beam; out-of-plane nanopatterning; polymers; thin films

Beilstein J. Nanotechnol. **2020,** *11,* 1693–1703.
https://doi.org/10.3762/bjnano.11.151

Received: 30 June 2020
Accepted: 23 October 2020
Published: 06 November 2020

This article is part of the thematic issue "Ten years of the helium ion microscope".

Guest Editors: G. Hlawacek and A. Wolff

Abstract

This work explores a new technique for the out-of-plane patterning of metal thin films prefabricated on the surface of a polymer substrate. This technique is based on an ion-beam-induced material modification in the bulk of the polymer. Effects of subsurface and surface processes on the surface morphology have been studied for three polymer materials: poly(methyl methacrylate), polycarbonate, and polydimethylsiloxane, by using focused ion beam irradiation with He^+, Ne^+, and Ga^+. Thin films of a $Pt_{60}Pd_{40}$ alloy and of pristine Au were used to compare the patterning of thin films with different microstructures. We show that the height of $Pt_{60}Pd_{40}$ thin films deposited onto poly(methyl methacrylate) and polycarbonate substrates can be patterned by He^+ ion beams with ultrahigh precision (nanometers) while preserving in-plane features, at the nanoscale, of the pre-deposited films. Ion irradiation of the Au-coated samples results in delamination, bulging, and perforation of the Au film, which is attributed to the accumulation of gases from radiolysis at the film–substrate interface. The irradiation with Ne^+ and Ga^+ ions destroys the films and roughens the surface due to dominating sputtering processes. A very different behavior, resulting in the formation of complex, multiscale 3D patterns, is observed for polydimethylsiloxane samples. The roles of the metal film structure, elastic properties of the polymer substrate, and irradiation-induced mechanical strain in the patterning process are elaborated and discussed.

Introduction

Micro- and nanofabrication with focused ion beams (FIBs) is currently a subject of strong interest within diverse fields of materials science and technology [1]. In recent years, the capabilities of FIBs have been substantially enhanced leading to a broad range of applications by the implementation of light ion beams (He^+ and Ne^+) emitted by a gas field ion source (GFIS). This

has enabled direct, maskless surface patterning with a superior lateral resolution and depth control [2,3]. The portfolio of the currently used FIB-based and FIB-assisted surface patterning techniques includes a number of different methods, such as ion-beam sputtering of surface layers (ion-beam milling), ion-beam-assisted chemical etching and ion-beam-assisted chemical vapor deposition [1-3]. All these methods are based on processes that either add or remove atoms on the surface or in the subsurface atomic layers.

The ion beams deposit their energy and, therefore, affect the structure and properties of materials over the entire depth of their penetration path in a target. In our recent work [4], we demonstrated that, in addition to the direct surface patterning by the abovementioned techniques, the radiation damage generated by He^+ FIB in the bulk of poly(methyl methacrylate) (PMMA) substrates can be used for well-controlled and nanometer-precise patterning of the height of metal thin films and nanostructures prefabricated on the surface of these substrates. This technique is based on subsurface chemical decomposition, structural reconstruction, and, as a result of these processes, volume shrinkage of the PMMA polymer under ion irradiation [5-7]. The most important physical and chemical phenomena behind this material modification include scission and cross-linking of polymer chains, which can occur simultaneously, as well as the formation of volatile molecules and their desorption from the polymer bulk [7]. In fact, the method utilizes ion energy losses to manipulate the surface morphology by means of radiation damage generated in the substrate bulk and minimizes the surface damage resulting from sputtering. This leaves the thin films and the prefabricated thin-film nanostructures on the PMMA surface essentially intact and provides a new route to their out-of-plane patterning, which is interesting for a range of thin film applications.

In the current work, we extend our study to the effects of the ion mass by irradiating PMMA substrates with He^+, Ne^+, and Ga^+ ions, and to the role of pathways for volatile radiolysis products to leave the irradiated material. We also investigate the possibility to pattern the surface of other polymer substrates, such as polycarbonate (PC) and polydimethylsiloxane (PDMS), by subsurface processing with He^+ ions. The choice of materials for this work has been directed by their diverse applications in micro- and nanotechnology and by the high susceptibility of their structure to ion irradiation [5]. Another important aspect is that the chosen materials are different in their chemical structure, chemical composition, and mechanical properties. This is the basis of a comparative study of the role of material-related factors in the FIB-induced surface patterning. PMMA and PC polymers are especially interesting for many reasons: PMMA is widely used as a positive resist for X-ray, deep UV [8], electron and ion-beam lithography [9]. Structural transformation and volume shrinkage of PMMA under ion irradiation have been reported in several publications [6,7,9-13]. PC is the second most sold thermoplastic polymer. It is extensively used in microtechnology due to its excellent optical, mechanical, and chemical properties [14]. Compared to PMMA, it has a much higher mechanical toughness, thermal resistance, chemical stability, and as PMMA, it is widely used in optical applications. A range of publications show that, owing to its radiation susceptibility, PC can be used as a positive or negative resist for electron beam lithography [15,16]. It has also been demonstrated that it acts as a type of ion-beam resist in the fabrication of micro- and nanopore membranes and templates for nanowires by chemical etching of through-holes along ion tracks produced by high-energy ions [17,18].

In contrast to PMMA and PC polymers, PDMS is a mineral-organic polymer (its structure includes both carbon and silicon atoms). It is an elastomer and its elasticity can be tuned within a very broad range by changing the degree and the type of polymerization and by post-curing treatments [19,20]. The high and easily tunable elasticity, combined with high transparency, biocompatibility, and low cost, enable the broad use of PDMS for the fabrication of microfluidic, microelectromechanical, and microoptical devices [20]. The effects of ion irradiation on chemical and physical properties and on the surface morphology of PDMS have been extensively investigated [21-24]. It has been shown that the ion beam irradiation can result in a significant compacting and, under certain conditions, in swelling of the irradiated PDMS areas [25]. In addition, a stiff “skin” layer produced by ion irradiation on the PDMS surface leads to the formation of ordered wrinkle-like micropatterns [23,24].

In this work, we have employed thin films of a $Pt_{60}Pd_{40}$ alloy and of pristine Au. The primary reason for this choice was the difference in their microstructures, specifically in the availability of structural defects capable of providing the release of gases from radiolysis. As it has been shown before [4], the as-deposited 15 nm $Pt_{60}Pd_{40}$ thin films contain arrays of nanoscale cracks. In contrast, our studies have not revealed any cracks or other discontinuities in the as-deposited Au thin films. To study the effects of the ion mass, ultrathin (5 nm thick) $Pt_{60}Pd_{40}$ films were used in order to minimize energy losses of Ne^+ and Ga^+ ions in these films. In all other cases, such as patterned $Pt_{60}Pd_{40}$ films on PC and PDMS substrates and patterned Au films on PMMA substrates, 15 nm metal thin films were used to facilitate the comparison with previously published results [4], in which 15 nm $Pt_{60}Pd_{40}$ films were patterned. Also, for the same reason of a more direct comparison, 200 nm thick PMMA substrates were used in this work to study possible effects of changing ion masses.

Results and Discussion

Irradiation of PMMA

Figure 1 shows an example of an atomic force microscopy (AFM) image and the corresponding depth profile for a surface region of the $Pt_{60}Pd_{40}$/PMMA sample irradiated with He^+ FIB at a fluence of 1.0×10^{16} cm^{-2}. It is evident that the irradiation homogeneously lowers the entire irradiated surface to a depth of approx. 80 nm. For convenience, we define the value of the surface depression as a reduction in the surface height (or as a change in the surface depth), for which the baseline values correspond to the non-irradiated area. Patterns of similar shape have been observed for the entire fluence range of the irradiation with He^+ ions, and also for the irradiation with Ne^+ and Ga^+ ions.

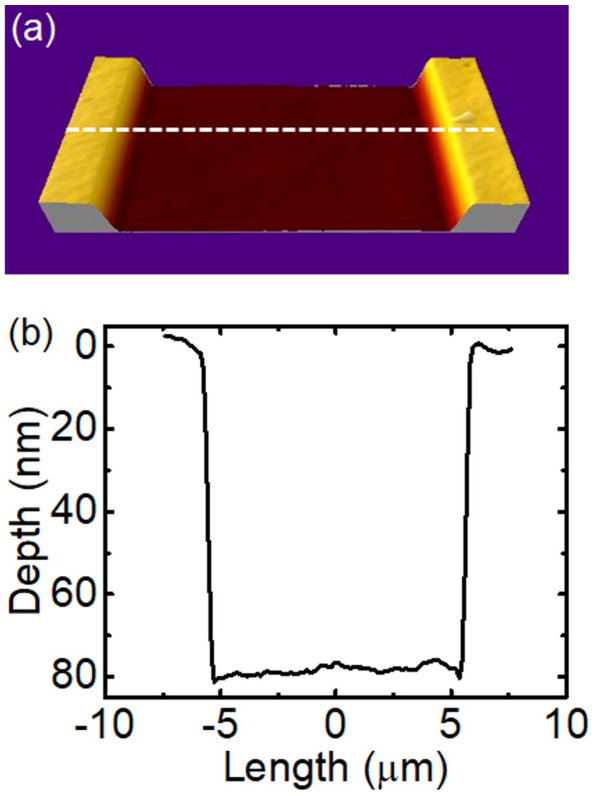

Figure 1: (a) AFM image and (b) the corresponding depth profile of a fragment of the surface depression produced in a 5 nm $Pt_{60}Pd_{40}$/200 nm PMMA sample by irradiation with He^+ FIB at an energy of 25 keV and with a fluence of 1.0×10^{16} cm^{-2}. The dashed line in (a) indicates the place of the depth profile.

Figure 2 summarizes the surface depthening as a function of the irradiation fluence for He^+, Ne^+, and Ga^+ ions. All curves demonstrate a very steep increase in depth with increasing fluence in the low-fluence range, followed by a saturation when the fluence increases. The influence of the ion type on the surface depthening is evident from the comparison of these plots: Both the depth-change rate at low-fluence values and the depth saturation level increase with an increase in the ion mass. From a linear regression of the dependence in Figure 2, in the low-fluence range (up to a fluence of 5.0×10^{14} cm^{-2}), the surface depression rates are estimated as 0.9, 1.5, and 1.7 nm per 1.0×10^{13} cm^{-2} of irradiation fluence for He^+, Ne^+, and Ga^+ ions, respectively.

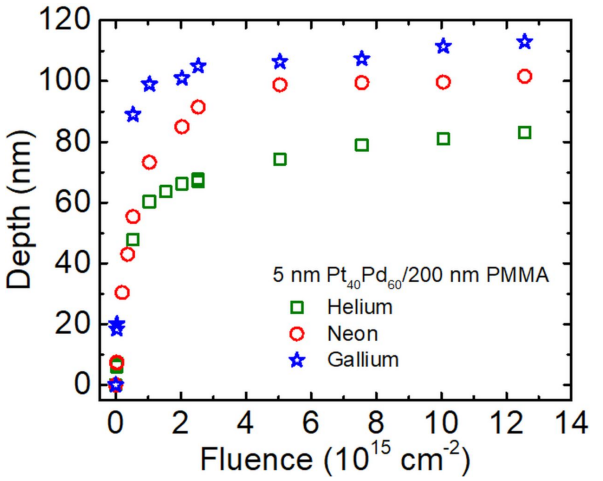

Figure 2: Fluence dependence on the irradiation-induced surface depthening for a 5 nm $Pt_{60}Pd_{40}$/200 nm PMMA sample, irradiated with 25 keV He^+, Ne^+, and Ga^+ FIBs.

Figure 3 compares the surface morphology of 5 nm $Pt_{60}Pd_{40}$/200 nm PMMA samples in the case of a high-fluence irradiation with He^+ and Ga^+ ions. The metal film withstood the irradiation with He^+ ions but it was removed by the irradiation with Ga^+ ions. Besides, the Ga^+-irradiated area is significanly rougher and characterized by erosions and spot-like elevations. For an irradiation fluence of 2.0×10^{15} cm^{-2}, the values of the root-mean-square (RMS) roughness, measured with AFM in the irradiated areas, were approx. 0.7 and 4.4 nm for irradiation with He^+ and Ga^+ ions, respectively. The RMS roughness value of the pristine sample was approx. 0.6 nm. The irradiation with Ne^+ ions also significantly roughens the surface and sputters away the metal film. The RMS roughness was approx. 3.1 nm after the irradiation with Ne^+ FIB at a fluence of 2.0×10^{15} cm^{-2}.

The sputtering efficiency of Ga^+ and Ne^+ ions is substantially higher than that of He^+ ions [3] due to the significantly higher mass values of Ne^+ and Ga^+ ions (20 and 70 amu, respectively) when compared to He^+ ions (4 amu). Thus, these results confirm that ions with intermediate and high mass values cannot be used in the scope of our nanopatterning technique since they destroy the pristine surface morphology and sputter away the pre-deposited films.

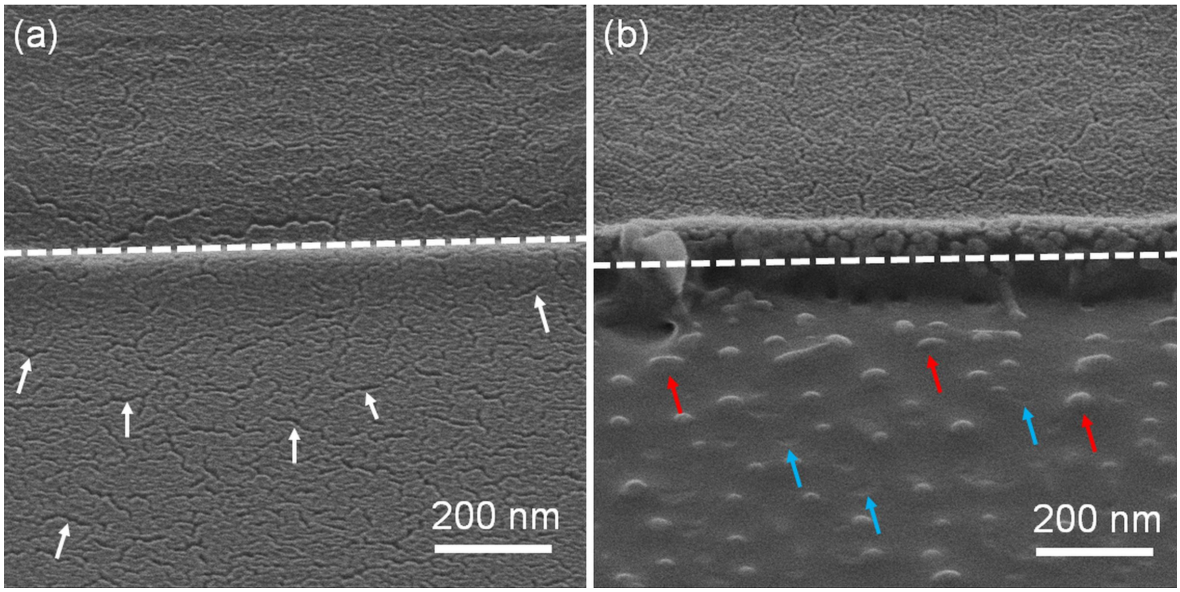

Figure 3: Helium ion microscopy (HIM) images of a 5 nm $Pt_{60}Pd_{40}$/200 nm PMMA sample irradiated at a fluence of 1.2×10^{16} cm^{-2} with He^+ (a) and Ga^+ FIB (b). In (a) and (b), dashed lines indicate the border between the irradiated (lower parts) and non-irradiated regions (upper parts). White arrows in (a) indicate some nanoscale cracks. In (b), red and blue arrows indicate local surface elevations and erosions, respectively. Both images are taken at a 54° tilt angle of the sample stage.

The observed increase in the surface descending rates and in the saturation level upon irradiation with Ne^+ and Ga^+ ions (Figure 2) indicate that, in those cases, both surface sputtering and subsurface volume shrinkage contribute to the changes in depth across the sample. According to our previous study [4], the reduction in surface height of the metal-coated PMMA surface is controlled by two major parameters. The first parameter is the irradiation fluence of He^+ ions, which determines the total amount of radiation energy dissipated by the ions over their entire path in the sample. The second parameter is the thickness of the polymer layer, which determines the fraction of the total energy that is specifically dissipated in the polymer layer. An additional and important aspect is that polymer materials cannot shrink infinitely with an increase in the irradiation fluence and, at a certain fluence, the material capacity to shrink decreases, which explains the saturation effect in the case of irradiation with He^+ ions. In the case of PMMA, the high irradiation fluence results in the formation of a compact carbon-rich material that can no longer shrink [13]. Taking this into consideration, we assume that a combination of several factors is responsible for the reduction in the surface height upon irradiation with Ne^+ and Ga^+ ions in comparison to the irradiation with He^+ ions. The first factor is that heavier ions deposit a larger fraction of energy in the PMMA layer. This is depicted by the energy loss profiles simulated with the "Stopping and Range of Ions in Matter (SRIM)" software, as shown in Figure S1 (Supporting Information File 1). In the case of He^+ ion irradiation, a significant fraction of the total ion energy is lost in the silicon substrate below the PMMA layer (Figure S1a and Figure S1b, Supporting Information File 1), meaning that this fraction is wasted with regard to defect generation inside the PMMA layer. In contrast, Ne^+ and Ga^+ ions lose their energy entirely in the PMMA layer; therefore, the total ion energy is utilized for generating the defects in this layer (Figure S1c–f, Supporting Information File 1). The second important factor includes the simultaneous contribution of ion sputtering and compacting processes near the surface. These events are significantly more pronounced when the irradiation is performed with ions with intermediate and high mass values, due to the higher density of the ion energy deposited near the surface in nuclear collisions.

The saturation effect in the case of irradiation with Ne^+ and Ga^+ ions shows that in the high-fluence range not only the material shrinking mechanism becomes inactive, but also the material sputtering becomes markedly slow. The estimated value of the surface depression rate in the saturation region of Ga^+ ion irradiation is approx. 0.12 nm per 1.0×10^{13} cm^{-2} fluence. This value is approx. 14 times lower than the estimated surface depression rate for the irradiation with Ga^+ ions in the low-fluence range. This value is also approx. eight times lower than the estimated surface depression rate in the low-fluence range of the irradiation with He^+ ions in which only the shrinking mechanism occurs. These results are consistent with previously published results [13], which show that the formation of a highly carbonized layer on the PMMA surface significantly retards the sputtering process.

Figure 4 shows the results for PMMA samples coated with a 15 nm thick Au film and irradiated with 25 keV/He^+ FIB. In contrast with previously published results for samples coated with 15 nm $Pt_{60}Pd_{40}$ films [4], the results shown in this work demonstrate that for samples coated with 5 nm $Pt_{60}Pd_{40}$ films, extensive delamination and bulging of the Au film from the substrate surface are observed in the irradiated cells and in the regions surrounding the cells. This is seen as changes in the color contrast of the cells in rows 1 and 2 in Figure 4a and confirmed by AFM imaging in Figure 4b. These effects are attributed to the accumulation of gases from radiolysis at the Au film/PMMA interface and to the pressure that becomes, at a certain fluence and at certain places, sufficiently high to delaminate and bulge the film. At higher fluence values (corresponding to the cells in row 3, Figure 4a), the bulges are almost inexistent, which can be explained by the appearance of holes in the irradiated regions (e.g., cells A3 and B3 in Figure 4a). This induces gas release and deflation of the bulges. These results demonstrate the importance of pathways for desorption of gases resulting from radiolysis. Moreover, our study shows that Au thin films (in our case, 15 nm thick) form very strong barriers for the permeation of gases and can withstand high degrees of stretching required for the observed bulging. Another remarkable result is the bulging outside the irradiated areas (Figure 4b), which is considered a result of bulge nucleation at the boundary between irradiated and non-irradiated regions, followed by an in-plane bulge propagation inside and outside the irradiated regions.

The results show that continuous films of low permeability cannot be patterned with the technique described here. In order to apply the technique, a gas-leakage path, for instance, in the form of an array of microholes, needs to be prefabricated in the films before irradiation. As an alternative to a continuous film, an array of discrete film features can also be pre-deposited onto the substrate.

Irradiation of PC

The results obtained for the irradiation with He^+ FIB on 15 nm $Pt_{60}Pd_{40}$/PC samples appear to be similar to those obtained for the 15 nm $Pt_{60}Pd_{40}$/PMMA samples. AFM images and the corresponding depth profiles (Figure 5a) show that, within the entire fluence range, He^+ FIB irradiation uniformly lowers the surface. High-magnification HIM images (Figure 5b) demonstrate the preservation of the metal film and the presence of cracks in the irradiated and non-irradiated areas of this film.

The dependence of the surface depression depth on the irradiation fluence for the 15 nm $Pt_{60}Pd_{40}$/PC sample is shown in Figure 6 (red circles) and compared to the fluence dependence for a 15 nm $Pt_{60}Pd_{40}$/770 nm PMMA sample (blue squares) obtained in our previous work [4]. In the latter, the 770 nm thick PMMA layer corresponds to a PMMA bulk substrate since the entire path of He^+ ions is located within this layer (see Figure S2, in the supplementary material of [4]). The curves in Figure 6 have similar shapes. However, the depth-change rate and the absolute values as a function of the fluence are signifi-

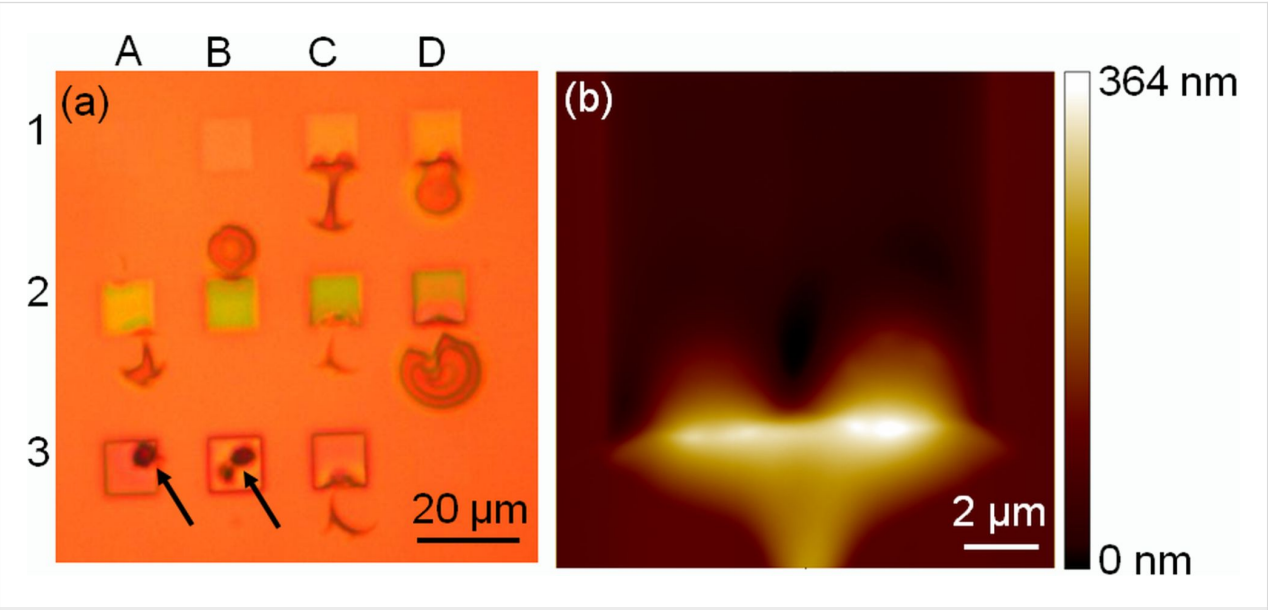

Figure 4: (a) Optical micrograph of an array of squares produced with He^+/25 keV FIB in a 15 nm Au/200 nm PMMA sample. The irradiation fluence increases in the following raster scan order: A1 (3.3×10^{13} cm^{-2}), B1 (2.0×10^{14} cm^{-2}), C1 (3.7×10^{14} cm^{-2}), D1 (5.3×10^{14} cm^{-2}), A2 (1.0×10^{15} cm^{-2}), B2 (2.0×10^{15} cm^{-2}), C2 (2.5×10^{15} cm^{-2}), D2 (5.1×10^{15} cm^{-2}), A3 (7.6×10^{15} cm^{-2}), B3 (1.0×10^{16} cm^{-2}), C3 (1.3×10^{16} cm^{-2}), and D3 (3.3×10^{13} cm^{-2}). The lowest fluence (3.3×10^{13} cm^{-2}) was irradiated in cells A1 and D3 to control the reproducibility of the obtained results. Black arrows indicate the holes in the Au film in the irradiated regions. (b) AFM image of the C1 square.

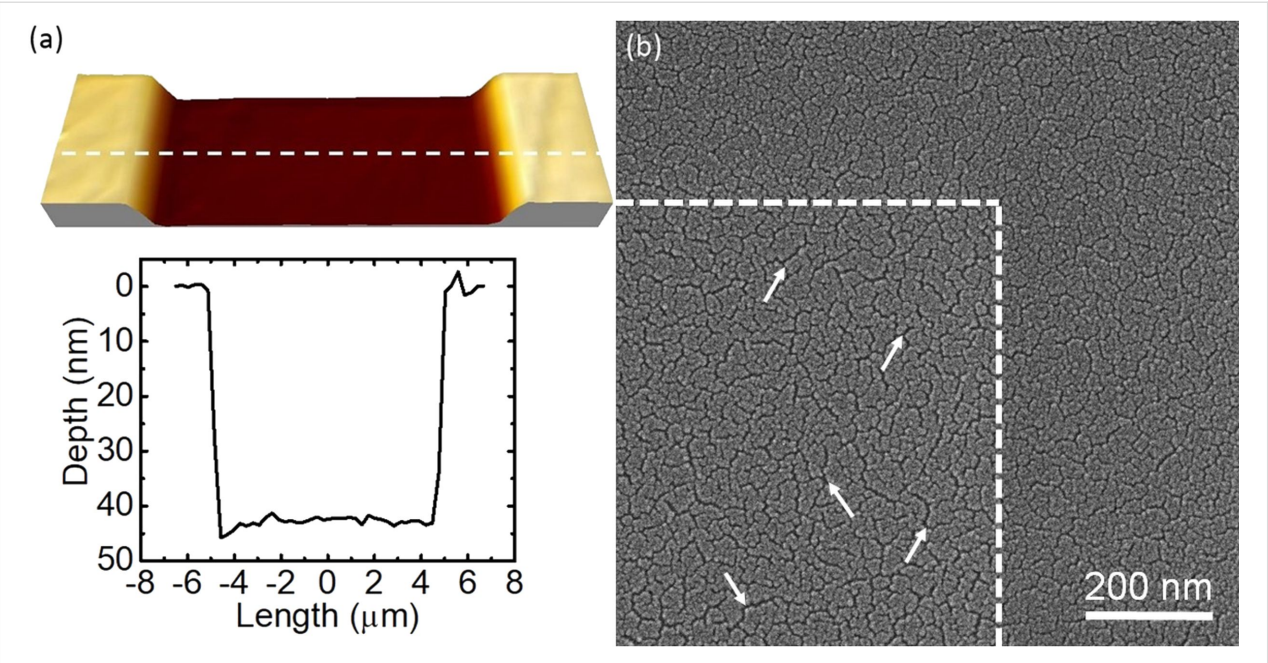

Figure 5: (a) AFM image and the corresponding depth profile of a part of the surface depression produced in a 15 nm $Pt_{60}Pd_{40}$/PC sample by irradiation with He^+ FIB at an energy of 25 keV with a fluence of 2.0×10^{15} cm^{-2}. The dashed line indicates the place of the depth profile. (b) HIM image of a part of the same depression, demonstrating the persistence of the metal film. White arrows indicate some nanoscale cracks in the $Pt_{60}Pd_{40}$ film in the irradiated region. Dashed lines indicate the border between irradiated and non-irradiated regions.

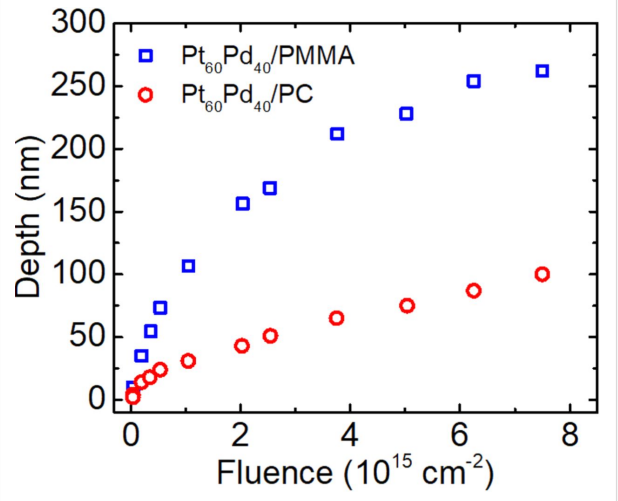

Figure 6: Fluence dependence of the irradiation-induced depth for the $Pt_{60}Pd_{40}$/PC sample (red circles). For comparison, the fluence dependence for a 15 nm $Pt_{60}Pd_{40}$/770 nm PMMA sample (blue squares) measured in our previous study [4] is also presented. The samples were irradiated with a 25 keV He^+ FIB within a fluence range from 4.0×10^{13} to 7.5×10^{15} cm^{-2}.

cantly lower in the case of PC substrates. As a result, the total depth change observed in the PC substrate at the highest dose (7.5×10^{15} cm^{-2}) is approx. 2.5 times smaller than that in the case of the PMMA substrate. This difference can result from a combination of several factors related to the polymer structure and composition, as well from the structural response of these materials to irradiation. This requires a more extended study; however, within the scope of this article, we can conclude that the PC material is applicable for the suggested patterning scheme similarly to PMMA. Higher rates and values of the surface height reduction can be achieved by increasing the ion energy. These results are consistent with previous reports on chain scission, cross-linking, and material compacting under the exposure to different types of electromagnetic and corpuscular radiation [26,27].

Irradiation of PDMS

In terms of surface morphology and its dependence on the irradiation fluence, the results obtained for PDMS samples appear to be significantly different from the results obtained for PMMA and PC samples. Figure 7 shows examples of He^+ ion irradiation of 15 nm $Pt_{60}Pd_{40}$/PDMS samples using square and circular patterns. Here, the irradiation of the PDMS samples with He^+ FIB results in the formation of complex surface patterns. The patterns are composed of surface depressions in the irradiated areas and surface ripples surrounding the irradiated areas. The surface depressions have concave shapes, which are characterized by maximum surface depths at the geometrical centers of the irradiated squares (Figure 7a) and circles (Figure 7b). Some additional features (rectangular elevations at the left-hand sides of circles B2 and B3 in Figure 7b) are artifacts generated by scanning these areas with the He^+ ion probe beam for imaging just after the irradiation.

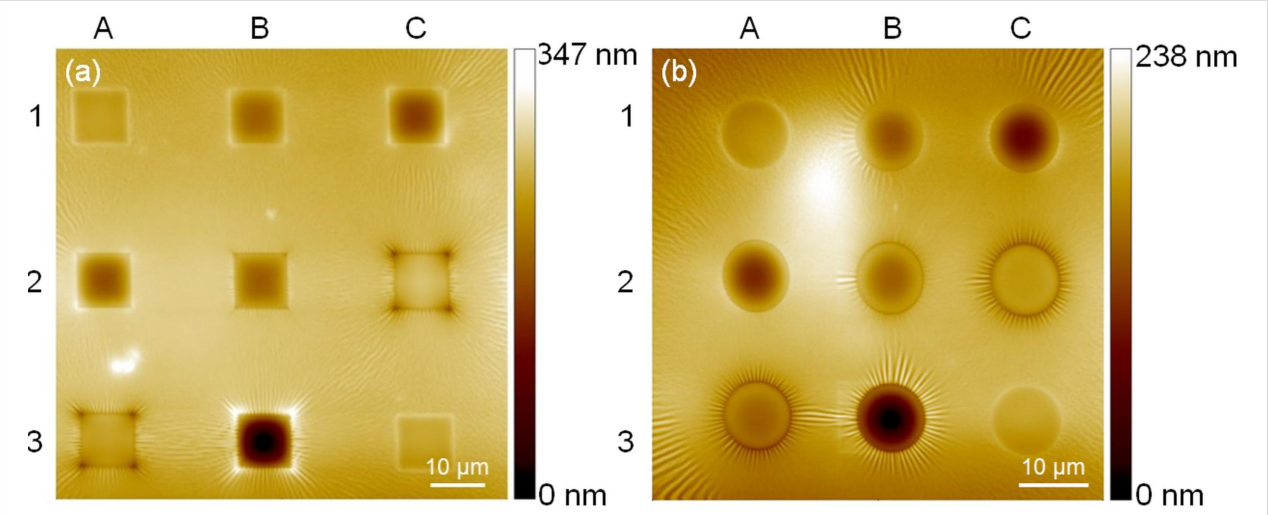

Figure 7: HIM images of square (a) and circular (b) arrays produced in 15 nm $Pt_{60}Pd_{40}$/PDMS samples by irradiation with different fluence values of 25 keV-He^+ ions. In both images, the irradiation fluence increases in the following raster scan order: A1 (3.7×10^{13} cm^{-2}), B1 (2.0×10^{14} cm^{-2}), C1 (3.7×10^{14} cm^{-2}), A2 (5.3×10^{14} cm^{-2}), B2 (1.0×10^{15} cm^{-2}), C2 (2.0×10^{15} cm^{-2}), A3 (2.5×10^{15} cm^{-2}), B3 (5.0×10^{15} cm^{-2}), C3 (3.7×10^{13} cm^{-2}). The lowest fluence was irradiated in two cells (A1 and C3) to control the reproducibility of the obtained results.

The dependence of the maximum surface sinking depth on the ion fluence was measured in both arrays and is presented in Figure 8. In contrast to the fluence dependence for PMMA and PC samples, the graphs for PDMS samples include a region with a negative slope within an intermediate fluence range (from 3.7×10^{14} cm^{-2} to 2.0×10^{15} cm^{-2}). This means that, at low- and high-fluence values the irradiated material volume pulls the surface down, whereas in the intermediate fluence range it pushes the surface back to the baseline position. In other words, with an increase in the irradiation dose, the PDMS material first shrinks, then swells, and then shrinks again.

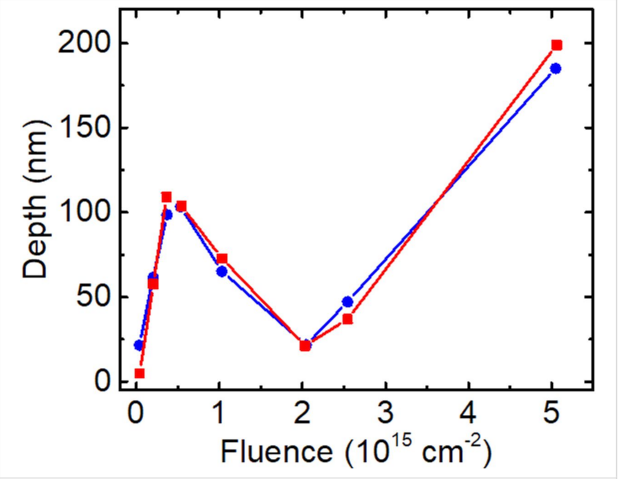

Figure 8: Fluence dependence of the irradiation-induced depth for a 15 nm $Pt_{60}Pd_{40}$/PDMS sample irradiated with a 25 keV He^+ FIB within a fluence range from 3.7×10^{13} to 5.0×10^{15} cm^{-2}. The depth is determined as the maximum depth within each irradiated area. Red squares and blue circles correspond to measurements performed in the irradiated areas of Figure 7a and Figure 7b, respectively.

The concave shapes of the surface inside of the irradiated PDMS regions can, to a large extent, be attributed to the elasticity of this material. A very low Young's modulus for the Sylgard-184 PDMS material, ranging from 1.32 to 2.97 MPa [28], provides a long-range strain relaxation when compared to a short-range strain relaxation in non-elastic polymers, such as PMMA and PC. Therefore, instead of directly projecting the initially flat surface to another depth position, the irradiation-induced strain warps the pristine surface. The existence of long-range strain fields, sufficient for a significant deformation in the surface of our PDMS samples, is identified by the observation of ripple patterns around the irradiated areas. Other features associated with the strain fields in highly elastic materials are the sharp surface elevations or depressions at the corners of the irradiated squares in Figure 7b. Considering continuum mechanics, these features are places where mechanical stress can concentrate, resulting in the enhancement of local deformations.

In numerous previous studies, the occurrence of ripples (also referred to in the literature as "wrinkles") on the irradiated PDMS surface has also been reported. This is attributed to the formation of a silica-like, stiff skin layer that buckles to release the accumulated strain energy [29]. Remarkably, we did not observe any rippling in the irradiated areas within the entire fluence range. The only ripple patterns we observed were those generated by the stress field outside the irradiated regions, where there is no skin or any other structural or compositional material modification. One of the likely reasons for the absence of rippling inside of the irradiated areas in our PDMS samples is that the density of the total energy lost by He^+ ions in the

samples is not large enough to build up a sufficiently high stress to trigger rippling. This result is also interesting with regard to potential applications, because it opens up for a possibility of changing the surface curvature at the microscale while preserving the surface morphology at the nanoscale.

An even more remarkable result is the transition from shrinkage to expansion and then from expansion to shrinkage, as a function of the irradiation fluence (Figure 8). To explain this non-trivial surface kinetics, we assume that the structural transformations in the irradiated PDMS material depend on the mechanical strain induced in the irradiated polymer volume by the compacting process. In this case, the strain accumulates with the irradiation fluence and, at a certain fluence value, it reaches a threshold level above which changes in the structural reconstruction processes are observed. This leads to the transition from a compacting to an expanding phase. We emphasize that such a transition is favorable from a thermodynamic point of view because the volume expansion provides relaxation of the tensile strain specifically at the compacted regions. Therefore, it results in the reduction of the strain energy accumulated in the system. The energy minimization provides a thermodynamic force for the strain relaxation. In addition to this, the ion irradiation is needed to break atomic bonds and to lower the energy barrier for material expansion and relaxation. This entirely phenomenological model is consistent with the conclusions drawn in a previous study [25], in which swelling was observed in PDMS samples irradiated with a 2 MeV proton beam. In that the case, the irradiated surface was fabricated by cutting a piece of the PDMS polymer from a bulk sample. In contrast, the irradiation of a pristine PDMS surface of this sample resulted in material compacting. The authors explained that this difference was due to mechanical stress in the cut surface.

Other important aspects of the transformation of the PDMS sample induced by ion irradiation include irreversible changes in the material structure and in the elastic properties with an increase in the irradiation dose [21-25]. These factors can contribute significantly to set the threshold dose for the first strain-driven transition and can be responsible for the occurrence of the second transition followed by material shrinkage in the high-dose range. We also do not exclude that a certain accumulation of gases from radiolysis inside the irradiated volume occurs in our samples, and to some degree it can contribute to shape the dependence between depth and fluence presented in Figure 8. Further structural studies are required to complement the contribution of the radiation effects on the material parameters.

We emphasize that the suggested method for controlling the out-of-plane position of the surface features can be interesting for the fabrication of a range of microoptical and microfluidic devices and microelectromechanical systems (MEMS). Possible applications of the method for microoptical devices are discussed in detail in our previous work [4]. They include tuning the thickness of the dielectric layer in the metal–insulator–metal (MIM) structures used in linearly variable bandpass filters (LVBFs) [30-33]. The capabilities of PDMS substrates to induce multiscale surface curving are also very interesting regarding the manufacturing of photonic structures and microlens arrays. Nanometer-thick gaps and cavities with prefabricated nanostructures can be implemented in different schemes for nanoparticle control and separation in microfluidic systems [34], and as components of actuators or switches in MEMS [35,36].

Considering the future technological potential of the suggested method it is important to comprehend its limitations and advantages, especially in comparison to the direct 3D patterning with FIB milling. First of all, we noticed that the method is limited to the fabrication of low-aspect-ratio pattern features and does not impose a challenge to the area of high-aspect-ratio and high-lateral-precision 3D structures, in which FIB milling is a well-established technique for a broad range of materials. This limitation results from a combination of the limited capacity of the polymer substrates to shrink and a relatively large lateral straggle of He^+ ions scattered in the bulk of the polymer materials. For instance, in the case of patterning with He^+ ions (Figure 2), the maximum depth of a surface depression achieved in the high-fluence range is approx. 250 nm, while the projected lateral straggle of He^+ ions is approx. 120 nm, as calculated with the SRIM code. The lateral straggle value gives a rough estimate of the smallest lateral size of the interaction volume involved in the shrinking process. Therefore, it estimates the smallest possible lateral size of the surface depression and the lateral precision achievable in this example. In addition, this method is only applicable to systems containing materials that shrink or swell under ion irradiation.

The most promising feature of the subsurface processing is its capability to pattern the out-of-plane position of objects (thin films and nanostructures [4]) prefabricated on the surface by other techniques, which can also include FIB milling. Thus, the subsurface processing can be exploited either as an editing tool or as one of the patterning steps in combination with different patterning processes for the fabrication of devices containing complex hierarchical structures composed of both nano- and micropatterns. Owing to the very small ion-induced sputtering impact, in the case of irradiation with He^+ ions, the method is unsusceptible to a range of drawbacks associated with FIB milling, including redeposition of sputtered material, preferential milling, and edge effects [1,37]. Other harmful effects re-

sulting from the interaction between ions and materials, such as structural damage and chemical modification that affect functional properties of the near-surface layers, are substantially reduced in comparison to FIB milling. Another advantage of the subsurface processing is that the local heating is negligible in comparison to ion milling with heavy ions [38,39]. This is due to the fact that the energy loss of He^+ ions in the patterning approach is spread over larger stopping distances than that in the case of milling with heavy ions.

One of the major advantages of FIB milling with heavy ions, which is often cited in the literature, is its high patterning speed. However, the results of this work (Figure 2) show that in the case of milling PMMA polymers this advantage is no longer observed in comparison to the fluence rates achieved with He^+ ions because of the substantial retardation of the milling process in the high-fluence range.

Conclusion

In summary, the role of the subsurface and surface processes in the modification of the surface morphology of thin metal films was studied for three types of polymer substrates (PMMA, PC, and PDMS) by exposing these materials to He^+, Ne^+, and Ga^+ FIBs in a Zeiss Orion NanoFab Helium Ion Microscope. We demonstrated the out-of-plane film patterning by the He^+ FIB for all three polymer substrates coated with thin $Pt_{60}Pd_{40}$ films. The ion-induced material modifications in the bulk of the underlying polymer substrates generate film patterning while sustaining the essential film features. The irradiation of the Au-coated samples results in delamination of the Au thin film followed by its bulging and perforation, which points to the important role of available pathways for the desorption of gases resulting from radiolysis. The irradiation with Ne^+ or Ga^+ ion beams destroys the films and roughens the surface due to the prevalence of a sputtering process induced by ions with a high mass. In contrast to the flat surface depression observed in the case of PMMA and PC substrates, complex, multiscale surface patterns, and a transition from polymer compacting to polymer swelling were observed in $Pt_{60}Pd_{40}$-coated PDMS samples irradiated with He^+ ions. The formation of complex surface shapes in this case is attributed to the inherent elasticity of the PDMS material. The transition from polymer compacting to polymer swelling is explained by the irradiation-induced mechanical strain accumulation followed by the relaxation of this strain at a certain critical value.

Experimental

Materials and samples

The PMMA and PDMS substrates used in this study were deposited onto the surface of blank silicon wafers. The deposition of PMMA was performed by spin coating in an RRT Lanz EBS 11 spin coater, in the same manner described in [4]. After the deposition, the samples were annealed at 200 °C for 90 s to remove solvent residuals. The PDMS polymer used was a two-component Dow Sylgard™ 184 silicone elastomer with a hardness value of 43 in the Durometer Shore scale. After mixing the components, the elastomer was deposited onto the surface of the silicon wafer, degassed in vacuum, and cured for 48 h at room temperature, which resulted in the formation of an approx. 0.8 mm thick PDMS layer. For the preparation of PDMS samples we intentionally avoided any spin coating, in order to fabricate a uniform layer that is free from any spinning-induced structural anisotropy [40]. The PC samples were 10×10 mm^2 square pieces cut from 1.5 mm thick wafers of an optical-grade PC polymer manufactured by microfluidic ChipShop GmbH.

Thin metal films of either a $Pt_{60}Pd_{40}$ alloy or of Au were deposited onto the surface of the polymer substrates to study the patterning of these films by in-bulk processes. An important argument for using metal films is that these films prevent surface charging. The use of charge compensation by irradiation with electron beams can generate additional radiation damage in polymer materials. The $Pt_{60}Pd_{40}$ alloy films were deposited by DC sputtering as described in [4], in a Cressington 208HR sputter apparatus. The Au films were deposited with an e-beam in a Cryofox Explorer 600 physical vapor deposition system. We have been using very thin metal films (5 and 15 nm thick) to minimize the ion path length in these films and potential sputtering effects.

FIB irradiation and sample characterization

The irradiation of the samples with He^+, Ne^+, and Ga^+ ions was done in a Zeiss Orion NanoFab Helium Ion Microscope at a landing energy of 25 keV and with different fluence values ranging from 1.0×10^{13} cm^{-2} to 2.0×10^{16} cm^{-2}. The beam current was kept at a value of approx. 1.7 pA for all irradiation experiments with He^+ and Ne^+ ions, and at approx. 2.0 pA for irradiation experiments with Ga^+ ions. All irradiation experiments were performed in a single raster scanning mode with multiple passes and a beam dwell time of 2 µs. Arrays of 10×10 µm^2 squares irradiated with different doses were used for measuring the dependence of the surface height on the irradiation dose, as previously described [4]. The distance between the square edges was kept at either 10 or 15 µm to avoid possible interactions between the irradiated areas, such as the overlaps originating from transverse ion straggle.

The samples were characterized with AFM and HIM. The measurements of the surface height were performed with a Veeco Dimension 3100 AFM instrument in the tapping mode. High-resolution imaging with a He^+ ion-beam probe was performed using a very small beam current (below 0.1 pA) to minimize

imaging artifacts from radiation damage generated by the probe beam.

Supporting Information

SRIM simulations of collision and ionization in 5 nm $Pt_{60}Pd_{40}$/200 nm PMMA samples irradiated with He^+, Ne^+, and Ga^+ FIBs.

Supporting Information File 1

SRIM simulations.
[https://www.beilstein-journals.org/bjnano/content/supplementary/2190-4286-11-151-S1.pdf]

Funding

Partfunding from Interreg Deutschland-Danmark within the European Regional Development Fund (ERDF) via the CELLTOM project is gratefully acknowledged.

ORCID® iDs

Serguei Chiriaev - https://orcid.org/0000-0001-8274-9864
Luciana Tavares - https://orcid.org/0000-0002-1432-524X
Arkadiusz J. Goszczak - https://orcid.org/0000-0002-1731-4781
Horst-Günter Rubahn - https://orcid.org/0000-0002-3606-5653

Preprint

A non-peer-reviewed version of this article has been previously published as a preprint: https://doi.org/10.3762/bxiv.2020.78.v1

References

1. Yao, N., Ed. *Focused Ion Beam Systems;* Cambridge University Press: Cambridge, United Kingdom, 2007. doi:10.1017/cbo9780511600302
2. Joy, D. C. *Helium Ion Microscopy - Principles and Applications,* 1st ed.; Springer: New York, U.S.A., 2013. doi:10.1007/978-1-4614-8660-2
3. Shorubalko, I.; Pillatsch, L.; Utke, I. Direct–Write Milling and Deposition with Noble Gases. In *Helium Ion Microscopy;* Hlawacek, G.; Gölzhäuser, A., Eds.; Springer International Publishing: Cham, Switzerland, 2016; pp 355–393. doi:10.1007/978-3-319-41990-9_15
4. Tavares, L.; Chiriaev, S.; Adashkevich, V.; Taboryski, R.; Rubahn, H.-G. *Nanotechnology* **2020,** *31,* 145303. doi:10.1088/1361-6528/ab6679
5. Kondyurin, A.; Bilek, M. *Ion Beam Treatment of Polymers - Application aspects from medicine to space,* 2nd ed.; Elsevier: Amsterdam, N.L., 2014. doi:10.1016/c2012-0-06085-1
6. Zhang, L.; Thomas, J. P.; Guan, X.; Heinig, N. F.; Leung, K. T. *Nanotechnology* **2020,** *31,* 325301. doi:10.1088/1361-6528/ab8d69
7. Thomaz, R. S.; Papaléo, R. M. Ion Beam Modification of Poly(methyl methacrylate) (PMMA). In *Radiation Effects in Polymeric Materials;* Kumar, V.; Chaudhary, B.; Sharma, V.; Verma, K., Eds.; Springer International Publishing: Cham: Switzerland, 2019; pp 113–139. doi:10.1007/978-3-030-05770-1_4
8. Haiducu, M.; Rahbar, M.; Foulds, I. G.; Johnstone, R. W.; Sameoto, D.; Parameswaran, M. *J. Micromech. Microeng.* **2008,** *18,* 115029. doi:10.1088/0960-1317/18/11/115029
9. Valiev, K. A. *The Physics of Submicron Lithography,* 1st ed.; Springer US: New York, U.S.A., 1992. doi:10.1007/978-1-4615-3318-4_1
10. Licciardello, A.; Fragalà, M. E.; Foti, G.; Compagnini, G.; Puglisi, O. *Nucl. Instrum. Methods Phys. Res., Sect. B* **1996,** *116,* 168–172. doi:10.1016/0168-583x(96)00029-8
11. Schrempel, F.; Kim, Y.-S.; Witthuhn, W. *Appl. Surf. Sci.* **2002,** *189,* 102–112. doi:10.1016/s0169-4332(02)00009-0
12. Torrisi, L. *Radiat. Eff. Defects Solids* **1998,** *145,* 285–296. doi:10.1080/10420159808223996
13. Koval, Y. *J. Vac. Sci. Technol., B: Microelectron. Nanometer Struct.–Process., Meas., Phenom.* **2004,** *22,* 843–851. doi:10.1116/1.1689306
14. Olabisi, O.; Adewale, K., Eds. *Handbook of Thermoplastics,* 2nd ed.; CRC Press: Boca Raton, FL, U.S.A., 2016. doi:10.1201/b19190
15. Abbas, A. S.; Yavuz, M.; Cui, B. *Microelectron. Eng.* **2014,** *113,* 140–142. doi:10.1016/j.mee.2013.08.006
16. Zheng, N.; Min, H.; Jiang, Y.; Cheng, X. *J. Vac. Sci. Technol., B: Nanotechnol. Microelectron.: Mater., Process., Meas., Phenom.* **2018,** *36,* 021603. doi:10.1116/1.5012028
17. Apel, P. *Radiat. Meas.* **2001,** *34,* 559–566. doi:10.1016/s1350-4487(01)00228-1
18. Toimil Molares, M. E.; Brötz, J.; Buschmann, V.; Dobrev, D.; Neumann, R.; Scholz, R.; Schuchert, I. U.; Trautmann, C.; Vetter, J. *Nucl. Instrum. Methods Phys. Res., Sect. B* **2001,** *185,* 192–197. doi:10.1016/s0168-583x(01)00755-8
19. Mark, J. E., Ed. *Physical Properties of polymers handbook,* 2nd ed.; Springer-Verlag: New York: U.S.A., 2007. doi:10.1007/978-0-387-69002-5
20. Tiwari, A.; Soucek, M. D., Eds. *Concise Encyclopedia of High Performance Silicones;* John Wiley & Sons, Inc.: Hoboken, NJ, U.S.A., 2014. doi:10.1002/9781118938478
21. Huszank, R. Irradiation Induced Chemical and Physical Effects in Silicones. In *Concise Encyclopedia of High Performance Silicones;* Tiwari, A.; Soucek, M. D., Eds.; John Wiley & Sons, Inc.: Hoboken, NJ, U.S.A., 2014; pp 75–84. doi:10.1002/9781118938478.ch6
22. Huszank, R.; Bonyár, A.; Kámán, J.; Furu, E. *Polym. Degrad. Stab.* **2018,** *152,* 253–258. doi:10.1016/j.polymdegradstab.2018.05.004
23. Moon, M.-W.; Lee, S. H.; Sun, J.-Y.; Oh, K. H.; Vaziri, A.; Hutchinson, J. W. *Proc. Natl. Acad. Sci. U. S. A.* **2007,** *104,* 1130–1133. doi:10.1073/pnas.0610654104
24. Lee, S.; Yang, J.; Jung, S.; Kim, D.-G.; Byeon, E. *Appl. Sci. Convergence Technol.* **2018,** *27,* 130–134. doi:10.5757/asct.2018.27.6.130
25. Szilasi, S. Z.; Huszank, R.; Csik, A.; Cserháti, C.; Rajta, I. *Nucl. Instrum. Methods Phys. Res., Sect. B* **2009,** *267,* 2296–2298. doi:10.1016/j.nimb.2009.03.038
26. Hareesh, K.; Sanjeev, G. Effects of Radiations on the Properties of Polycarbonate. In *Radiation Effects in Polymeric Materials;* Kumar, V.; Chaudhary, B.; Sharma, V.; Verma, K., Eds.; Springer Series on Polymer and Composite Materials; Springer International Publishing: Cham, Switzerland, 2019; pp 293–318. doi:10.1007/978-3-030-05770-1_9
27. Thorat, A. B.; Sonawane, A.; Jadhav, A.; Dhole, S. D.; Dahiwale, S. S. *AIP Conf. Proc.* **2019,** *2115,* 030328. doi:10.1063/1.5113167
28. Johnston, I. D.; McCluskey, D. K.; Tan, C. K. L.; Tracey, M. C. *J. Micromech. Microeng.* **2014,** *24,* 035017. doi:10.1088/0960-1317/24/3/035017

29. Winton, B. R.; Ionescu, M.; Dou, S. X.; Wexler, D.; Alvarez, G. A. *Acta Mater.* **2010,** *58,* 1861–1867. doi:10.1016/j.actamat.2009.11.029
30. Emadi, A.; Wu, H.; De Graaf, G.; Hedsten, K.; Enoksson, P.; Correia, J. H.; Wolffenbuttel, R. F. *Procedia Eng.* **2010,** *5,* 416–419. doi:10.1016/j.proeng.2010.09.135
31. Williams, C.; Rughoobur, G.; Flewitt, A. J.; Wilkinson, T. D. *Appl. Opt.* **2016,** *55,* 9237–9241. doi:10.1364/ao.55.009237
32. Li, Z.; Butun, S.; Aydin, K. *ACS Photonics* **2015,** *2,* 183–188. doi:10.1021/ph500410u
33. Grushina, A. *Adv. Opt. Technol.* **2019,** *8,* 163–169. doi:10.1515/aot-2019-0024
34. Salafi, T.; Zeming, K. K.; Zhang, Y. *Lab Chip* **2017,** *17,* 11–33. doi:10.1039/c6lc01045h
35. Sugiyama, S.; Amaya, S.; Viet Dao, D. *Adv. Nat. Sci.: Nanosci. Nanotechnol.* **2012,** *3,* 015009. doi:10.1088/2043-6262/3/1/015009
36. Wang, K.; Ouyang, G.; Chen, X.; Jakobsen, H. *Polym. Rev. (Philadelphia, PA, U. S.)* **2017,** *57,* 369–396. doi:10.1080/15583724.2016.1268156
37. Utke, I.; Moshkalev, S.; Russell, P., Eds. *Nanofabrication using focused ion and electron beams;* Oxford University Press: New York, U.S.A., 2012.
38. Kim, S.; Jeong Park, M.; Balsara, N. P.; Liu, G.; Minor, A. M. *Ultramicroscopy* **2011,** *111,* 191–199. doi:10.1016/j.ultramic.2010.11.027
39. Schmied, R.; Chernev, B.; Trimmel, G.; Plank, H. *RSC Adv.* **2012,** *2,* 6932–6938. doi:10.1039/c2ra21025h
40. Liu, M.; Sun, J.; Sun, Y.; Christopher Bock, C.; Chen, Q. *J. Micromech. Microeng.* **2009,** *19,* 035028. doi:10.1088/0960-1317/19/3/035028

License and Terms

BEILSTEIN JOURNAL OF NANOTECHNOLOGY

Imaging and milling resolution of light ion beams from helium ion microscopy and FIBs driven by liquid metal alloy ion sources

Nico Klingner[*1], Gregor Hlawacek[1], Paul Mazarov[*2], Wolfgang Pilz[1,2], Fabian Meyer[2] and Lothar Bischoff[*1]

Full Research Paper

Open Access

Address:
[1]Helmholtz-Zentrum Dresden-Rossendorf, Institute of Ion Beam Physics and Materials Research, Bautzner Landstrasse 400, 01328 Dresden, Germany and [2]Raith GmbH, Konrad-Adenauer-Allee 8, 44263 Dortmund, Germany

Email:
Nico Klingner[*] - n.klingner@hzdr.de; Paul Mazarov[*] - Paul.Mazarov@raith.de; Lothar Bischoff[*] - l.bischoff@hzdr.de

* Corresponding author

Keywords:
focused ion beam; gas field ion source; liquid metal alloy ion source; resolution

Beilstein J. Nanotechnol. **2020,** *11,* 1742–1749.
https://doi.org/10.3762/bjnano.11.156

Received: 31 July 2020
Accepted: 28 October 2020
Published: 18 November 2020

This article is part of the thematic issue "Ten years of the helium ion microscope".

Associate Editor: A. Gölzhäuser

Abstract

While the application of focused ion beam (FIB) techniques has become a well-established technique in research and development for patterning and prototyping on the nanometer scale, there is still a large underused potential with respect to the usage of ion species other than gallium. Light ions in the range of m = 1–28 u (hydrogen to silicon) are of increasing interest due to the available high beam resolution in the nanometer range and their special chemical and physical behavior in the substrate. In this work, helium and neon ion beams from a helium ion microscope are compared with ion beams such as lithium, beryllium, boron, and silicon, obtained from a mass-separated FIB using a liquid metal alloy ion source (LMAIS) with respect to the imaging and milling resolution, as well as the current stability. Simulations were carried out to investigate whether the experimentally smallest ion-milled trenches are limited by the size of the collision cascade. While He^+ offers, experimentally and in simulations, the smallest minimum trench width, light ion species such as Li^+ or Be^+ from a LMAIS offer higher milling rates and ion currents while outperforming the milling resolution of Ne^+ from a gas field ion source. The comparison allows one to select the best possible ion species for the specific demands in terms of resolution, beam current, and volume to be drilled.

Introduction

In modern nanotechnology, focused ion beam (FIB) techniques are well-established for nanoscale structuring, local surface modification, doping, prototyping, as well as for ion beam analysis. One of the main components of such a FIB system is the ion source providing the needed ion species [1]. Currently, the majority of such instruments use a gallium liquid metal ion

source (Ga-LMIS), but the demand in research as well as in the industry for other ion species is increasing permanently. Today, nearly half of the elements of the periodic table are demonstrated to be usable in FIB applications [2]. In particular, light elements in the mass range of m = 1–28 u (hydrogen to silicon) and energies between a few and 80 kiloelectronvolts are of special interest. The combination of this energy range with the particular mass range allows one to reach single-digit nanometer and even sub-nanometer resolution. This mass range is of interest due to the interaction of the ions with the near-surface region and, among other use cases, the application of these ions for indirect or resist-aided lithography [3]. The introduction of the helium ion microscope (HIM) [4], working with a gas field ion source (GFIS), about ten years ago solved a lot of problems in this field. However, besides the excellent resolution of the beam, there are also some disadvantages such as small available currents in the low-picoampere range, low number of sputtered ions per incident ion (sputter yield) during structuring, or the formation of helium bubbles in the substrate when using high fluences [5]. In addition to many imaging applications, HIM has been used to create and study new device concepts, including the fabrication of nanometer-sized ferromagnets [6], the controlled tuning of memristive properties of 2D materials [7], the fabrication of graphene nanomeshes [8], the formation of single Si nanocrystals embedded in SiO_2 for single-electron transistors [9], the spatially resolved engineering of the thermal conductivity in individual Si nanowires [10], as well as the creation of nano-Josephson superconducting tunnel junctions in high-temperature superconductors [11].

Although HIM is highly suitable for imaging and nanometer-scale patterning, there is a need of focused ion beams other than helium or neon with comparable properties. Alternative developments were made using laser-cooled magneto-optical trap ion sources (MOTISs) [12] or classical FIBs equipped with mass separation and liquid metal alloy ion sources working with suitable alloys containing light elements [2].

In the past, mostly heavier ions have been used in liquid metal alloy ion sources (LMAISs). A number of applications have been shown, including using mass-separated FIBs from a $Co_{36}Nd_{64}$ LMAIS to implant Co into Si at elevated temperatures, leading to metallic $CoSi_2$ nanostructures down to 20 nm [13]. Ge nanowires could be grown by molecular beam epitaxy, via a vapor–liquid–solid process, on a Si substrate after formation of a regular seed array using a mass-separated FIB for Au implantation from a $Au_{82}Si_{18}$ LMAIS [14].

In this work, the performance of light ion beams from LMAISs will be compared with that of helium and neon ions delivered by the GFIS of a HIM. In Figure 1, a comparison of the performance with respect to the achievable spot size as a function of the beam current for light-ion FIBs and some commercially available FIBs with heavier primary ions is shown. The best values from the literature are evaluated to compare the beam profiles of different ion and source types. Deterioration of the spot size due to vibrations or thermal drift are not explicitly considered in this work, since they are not a fundamental limitation but rather depend on the tool and the setup.

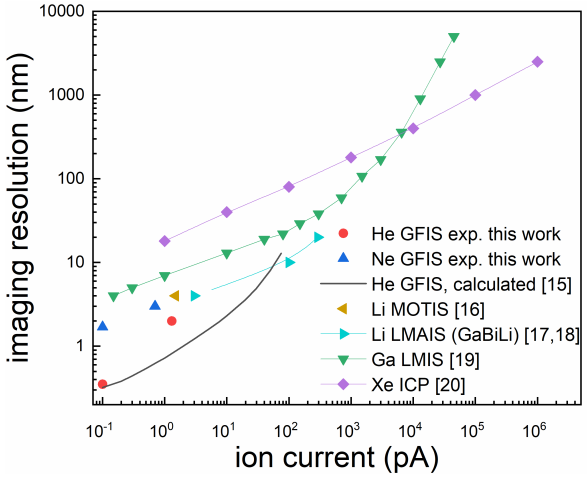

Figure 1: Comparison of the spot size (imaging resolution) as a function of the ion beam current for different relevant FIB systems determined theoretically [15] (r50) and from experiments using a 20% to 80% rise of intensity for He, Li [16-18], Ne, and Ga [19]. The beam size criterion for Xe [20] is unknown.

Experimental

Depending on the application, a FIB column can be operated in different modes. High currents can be obtained in a crossover mode (large-diameter apertures) delivering a weaker resolution [2]. Better resolution requires lower currents (in crossover mode) or a parallel or divergent beam to avoid beam broadening caused by Coulomb interaction. The beam spot size d can be described in the following form [2]:

$$d = \sqrt{\left(Md_{\mathrm{q}}\right)^2 + d_{\mathrm{S}}^2 + d_{\mathrm{C}}^2}. \quad (1)$$

Here, d_{q} is the virtual source size, which is of utmost importance for the achievable resolution of the FIB. For a LMAIS, it depends on the ion mass and typically has values in the range of 20 to 50 nm [21]. For a GFIS used in a HIM, this value is, under optimal conditions, about 100 times smaller, comparable to the size of a single atom. M denotes the magnification of the column [22]. The quantities d_{S} and d_{C} are defined as the spherical and axial chromatic aberrations, respectively, given as:

$$d_S = \frac{1}{2} C_S \alpha^3, \quad d_C = C_C \frac{\Delta E}{E} \alpha. \tag{2}$$

$$\frac{m}{\Delta m} = \frac{E_x}{2U_{acc}} \frac{l}{d} \left(\frac{1}{2} l + D \right). \tag{3}$$

Here, C_S and C_C are the spherical and chromatic aberration coefficients of the ion optical column, respectively [22]. The quantity α is the acceptance half-angle on the sample and can be determined by $\alpha^2 = I^*(\pi M^2(dI/d\Omega))^{-1}$, where I is the ion current and $dI/d\Omega$ is the angular intensity [22]. The energy spread ΔE of the ion source is a second key parameter for the final resolution concerning the chromatic aberration. While this value varies for different LMAISs, it is less than 1 eV for a GFIS [23,24]. E denotes the primary ion energy. For our special case of interest, that is, light ions and small ion beam currents, the spherical aberration can be neglected and diffraction phenomena, important for electron beams, have no impact [25].

In the following, the discussion will focus on the usage of GFISs and LMAISs in FIBs. GFISs are operated with highly purified helium or neon. No additional mass separation is required in the column. In a LMAIS, in contrast, the source material is a complex alloy delivering several ion species simultaneously in a process of field evaporation. This initially provides a beam containing ions with different masses and charge states, whose fractions depend on the composition of the alloy and the ionization probability. To overcome this problem, an ExB mass filter is introduced in the ion optical column, described in more detail in [2]. In principle, an ExB filter acts as a velocity filter and splits the beam according to the mass-to-charge ratio of its constituents. The mass resolution $m/\Delta m$ of an ExB filter can be written in the following form [26]:

Here, U_{acc} is the acceleration voltage of the ion beam and E_x is the electric field strength of the filter perpendicular to the optical axis of the ion column. l is the filter length, D is the distance between the filter and the separation aperture at the exit of the filter, and d is the diameter of this aperture.

As an example for a LMAIS mass spectrum, we show results obtained with a $Ga_{33}Bi_{57}Li_{10}$ source [17] in Figure 2. The used FIB system is equipped with a retarding field analyzer and is described elsewhere [27]. This setup allows one to determine the energy spread of all ion species that can be extracted from the LMAIS. This is important to determine the chromatic aberration, which strongly influences the achievable resolution of the FIB. The current was measured using a secondary electron multiplier and is therefore given in arbitrary units. For the light isotope $^6Li^+$ at 1 µA emission current a ΔE of 3 eV could be determined [17], which is in a good agreement with the $\Delta E \sim m^{1/3}$ dependence for single-charged monomers [2].

In the noble gas irradiation experiments described here, a GFIS in a helium ion microscope ORION NanoFab (Carl Zeiss) [5,28] was used. For irradiation with light metal ions, a LMAIS installed in a FIB/SEM VELION system (Raith) [2,18,29] was used. All milling experiments were performed on a 100 nm thin gold film on glass. For measuring the trench width milled into the gold layer, either the same primary ion beam microscope or a scanning electron microscope have been used to image the

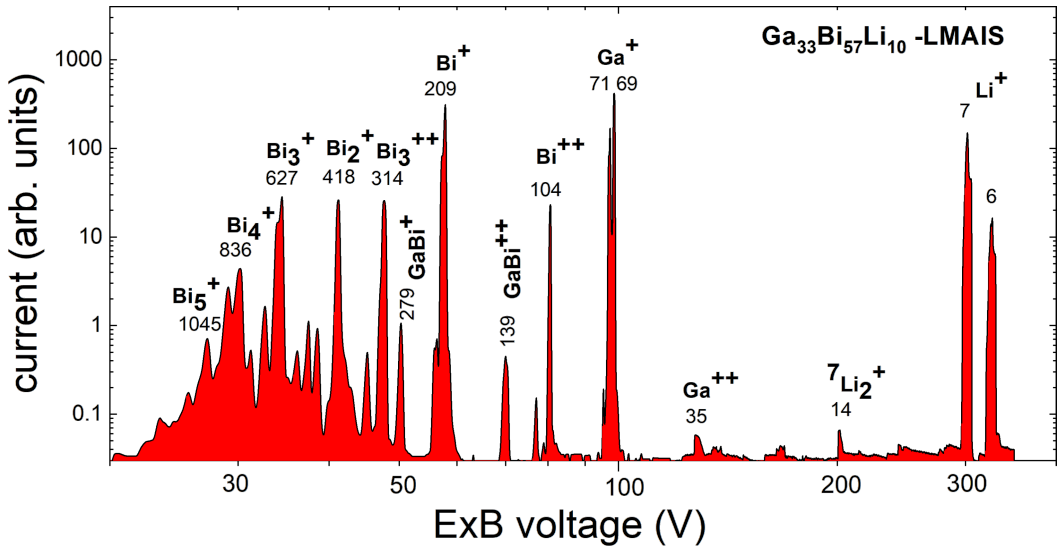

Figure 2: Mass spectrum of a $Ga_{33}Bi_{57}Li_{10}$ LMAIS at an acceleration potential of 10 kV scanned by the ExB voltage using a constant magnetic field. The numbers below the ion label specify the total ion mass m in u.

sputtered trenches. The investigated sources are listed in Table 1. Details of fabrication and operation principle are given in the corresponding references.

Results and Discussion

Resolution values obtained with different light ion species on a Au film are summarized in Table 2. The sputter yields Y_{theo} for normal incidence based on the work of Yamamura et al. [34] are also given in Table 2. They are in a good agreement with the experimentally determined data from literature (volume-loss method), for example, for 30 keV helium in gold $Y_{exp} = 0.13$ and for 35 keV lithium in gold $Y_{exp} = 0.4$ [17]. Single-pixel lines have been milled with different fluence values using small ion currents to get the best possible resolution. The imaging resolution was determined by sweeping the beam over a sharp border in a one-line scan and examining the slope in 80/20 intensity mode. For determining the imaging resolution in HIM, few pixel wide line profiles are made across selected edges in previously recorded images with an appropriate pixel size and are evaluated according to the same 80/20 criterion.

Representative images used to obtain the results in Table 2 are shown in Figure 3. They should be exemplary for demonstrating the imaging and milling resolution of the different ion

Table 1: Light ion species, source type, source temperature for GFIS and LMAIS, source material, emitter tip material, and corresponding references. For the LMAIS, the listed temperatures are the melting points of the eutectic alloy. The actually used temperatures are a little higher.

Light ion species	Source type	$T_{operation}$ (K)	Material	Emitter	Ref.
He^+, Ne^+	GFIS	80	He, Ne gas	W	[4,5]
Li^+	LMAIS	495	$Ga_{35}Bi_{60}Li_5$	W	[18]
Be^+, Be^{++}	LMAIS	640	$Au_{70}Si_{15}Be_{15}$	W	[30]
B^+, B^{++}	LMAIS	920	$Co_{31}Nd_{64}B_5$	Ta, W	[31]
C^+	LMAIS	933	$C_{20}Al_{10}Ce_{70}$	Ta	[32]
Si^+, Si^{++}	LMAIS	638	$Au_{82}Si_{18}$	W	[33]

Table 2: Irradiation parameters for several available ions, calculated sputter yields Y_{theo} [34] of Au, imaging resolution (80/20 criterion), the smallest achieved milling trench width and typical ion beam currents as well as their stability logged over several hours. Literature values are indicated by their reference, data from this work is marked by an asterisk.

Source	Ion	Y_{theo} [33] on Au	Imaging resolution	Trench width	Ion beam current stability
GFIS					
	30 keV $^4He^+$	0.12	(0.38 ± 0.08) nm [5]	5 nm [5]	(0.54 ± 0.01) pA 1.9% over 1 h *
	25 keV $^{20}Ne^+$	5.4	2.85 nm [35]	12 nm *	(0.64 ± 0.04) pA 6.3% over 1 h *
LMAIS					
CoNdB	35 keV $^{11}B^+$	1.74	(19 ± 2) nm *	no data	(19.2 ± 0.4) pA 2.1% over 2.5h [31]
GaBiLi	35 keV $^7Li^+$	0.5	(2.9 ± 0.5) nm *	6 nm *	(2.89 ± 0.08) pA 2.8% over 16 h *
	35 keV $^{209}Bi^+$	27	11 nm *	50 nm [36]	(228 ± 1.6) pA 0.7% over 10 h *
Ga	35 keV 70Ga+	18	2 nm [37]	8.4 nm [38]	(19 ± 0.2) pA 1.1% over 67 h *
AuGeSi	70 keV $^{74}Ge^{++}$	21	10 nm *	20 nm *	(14 ± 0.5) pA 3.6% over 15 h *
AuSi	70 keV $^{197}Au^{++}$	35	10–15 nm [30]	19 nm [38]	(7 ± 0.2) pA 2.9% over 25 h [30]
	70 keV $^{28}Si^{++}$	8.42	6–10 nm [30]	13 nm [38]	(12 ± 0.4) pA 3.3% over 15 h *
AuSiBe	70 keV 9Be++	0.84	3–4 nm [30]	7 nm [38]	(6.2 ± 0.1) pA 1.6% over 10 h *

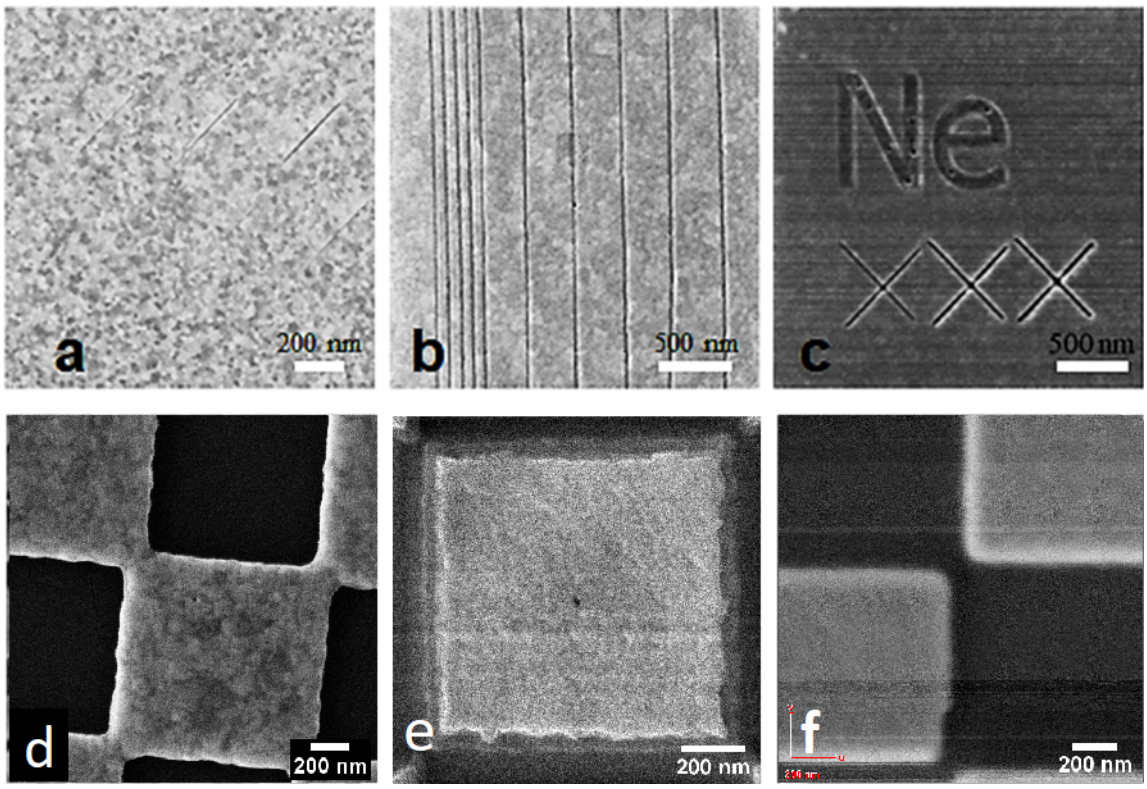

Figure 3: Examples using different ions: a) 30 keV He^+, field of view (FOV): 1.5 × 1.5 µm^2, trench width: 4 nm, b) 40 keV Li^+, FOV: 2.5 × 2.5 µm^2, trench width: 6 nm, c) 25 keV Ne^+, FOV: 2.5 × 2.5 µm^2, trench width: 12 nm, d) 70 keV Be^{++}, FOV: 1.9 × 1.9 µm^2, best imaging res: (4.0 ± 0.5) nm, e) 35 keV Li^+, FOV: 1.2 × 1.2 µm^2, best imaging res: (2.9 ± 0.5) nm, f) 35 keV B^+, FOV: 1.6 × 1.6 µm^2, best imaging res: (19 ± 2) nm.

beams. Figure 3 also shows the best imaging resolution for lithium and boron published so far. Examples for the other ion species can be found in the references listed in Table 2.

The resolution results for the different ion species listed in Table 2 are plotted in Figure 4. The minimum milling width in dependence of the ion mass, determined from sputtered features (lines, holes), follows a weak linear increase in the double-logarithmic plot. In the case of the imaging resolution the behavior is not so clear. There is a strong variation of the results, due to different beam profiles and ion optical columns, but the imaging resolution is always better than the corresponding milling resolution. The relative difference between the resolution in the two different modes is more pronounced for the GFIS compared to the LMAIS, that is, from 5 nm (milling) to 0.4 nm (imaging) for helium (13 fold) but only from 6 nm (milling) to 4 nm (imaging) for lithium (1.5 fold).

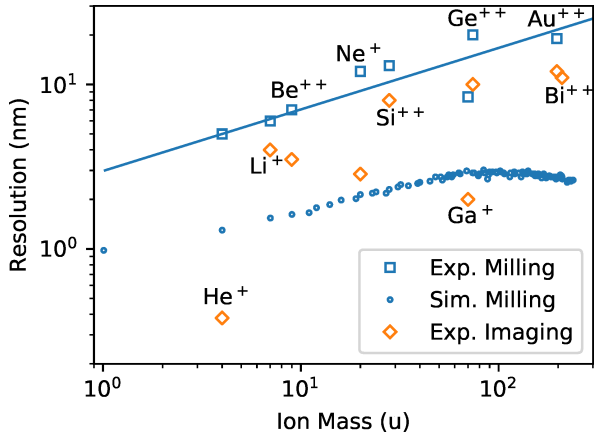

Figure 4: Summary of the imaging resolution (80/20), experimentally achieved trench width, and simulated minimum milling width (FWHM) for FIBs working with different ion species and technologies depending on the ion mass. The line serves as a guide to the eye.

The simulated minimum milling width of a 30 keV point-like ion beam in Figure 4 has been obtained using SRIM [39]. The "monolayer collision steps/surface sputtering" mode has been used to simulate the size of the collision cascade and the origin of sputtered particles. From 2.5 × 10^5 ion impacts, for light elements such as hydrogen, down to 5000 ion impacts, for uranium, have been simulated (1 × 10^6 in total for all elements). The emission position of the sputtered particles (8.5 × 10^6 in total for all elements) has been evaluated in terms of the distance to the impinging ion. To account for the milling of a line

we calculated the projected distance instead of evaluating the radial distance of the emission site from the beam center. The resulting Gaussian-like sputtering profiles have been normalized and analyzed for the full width of the profile at half height or corresponding trench depth (FWHM). The normalized expected trench profiles from a point-like beam in a gold substrate have been plotted for selected ion species in Figure 5. The beam profiles however, are not Gaussian and the edge profiles cannot be described by simple error functions due to the enhanced secondary electron yield on the sample edges. While the imaging resolution was measured using the 80/20 criteria, this is not suitable for trenches. To compare the image resolution with the trench width, for Gaussian profiles, the reader would have to multiply the 20/80 resolution value by a factor of 1.39.

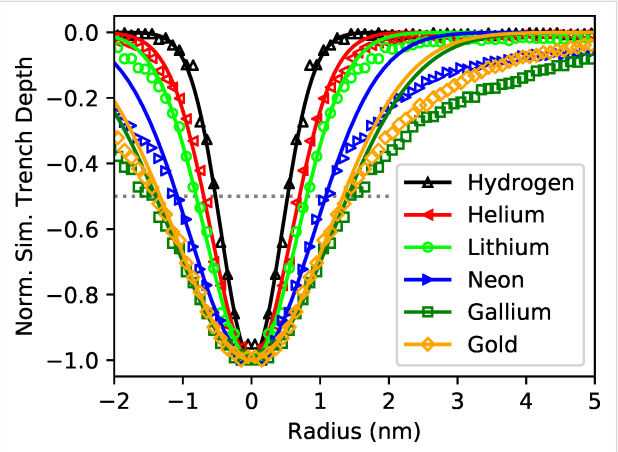

Figure 5: SRIM simulation [39] of the sputter profile from a 30 keV point-like beam in a gold substrate as a function of the ion mass. The dotted line denotes 50% trench depth and corresponds to the minimum milling width of a point-like ion beam.

The simulated minimum milling widths are clearly smaller than the experimentally achieved results for all ion species. The main limiting factor for most of them is the spot profile of the ion beam itself. The two exceptions are helium and gallium for which the spot size should be smaller than the simulated minimum milling width. For 30 keV helium in gold, a spot size of 0.38 nm [5] is smaller than the simulated minimum milling of 1.3 nm and much smaller than the smallest achieved trenches of 5 nm [5]. An explanation could be the neglected ion beam stability, mechanical vibrations, drift, or electromagnetic fields during realistic long-term milling processes for light ions due to the small sputter yield (0.12 for 30 keV He in Au [34]). Additionally, large fluences, necessary for deep milling, often cannot be applied when using light ions since the implantation will lead to bubble formation in the target material [40,41]. Gallium in gold has a larger sputter yield of 18 [34] and much higher beam currents are available. Both significantly reduce the milling time and, consequently, the influence of mechanical or electronic drifts. In addition, gas bubble formation will not take place when Ga ions are used.

To discuss the deviation between the simulated minimum milling width and the achieved trench widths in more detail, the experimental sputter beam profiles have been analyzed further. For HIM, the profiles of the helium beam were measured by examining sputtered lines [42] as well as pores [43] in membranes. Gallium is used and optimized for industrial and scientific applications and sputtering beam profiles were measured by TEM [44,45]. The additional influence of the required ExB filter for multi-element or multi-isotope LMAISs is a further factor of uncertainty that, in general, will worsen the achievable spatial resolution.

Literature data for He and Ga are compiled in Figure 6. Normalized half profiles (ion beam radius) for helium beams averaged for different substrates (taken from [42,43]) and for 40 keV Ga beams on a crystalline Si sample from different studies [44,45]

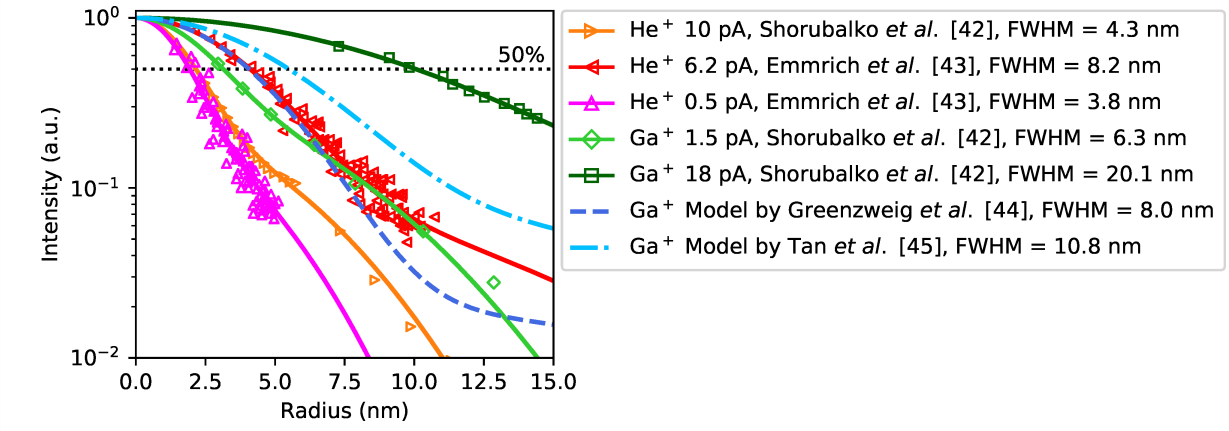

Figure 6: Comparison of the normalized ion beam profiles (normalized half profiles = beam radius) obtained from 1/fluence-dependent milled structures of a helium beam (HIM) on different targets [42,43] and a Ga-LMIS driven FIB [44,45].

are plotted and fitted by a double Gaussian for comparison in Figure 6. The near-axis resolution of the He beam from a GFIS is smaller than that of the LMIS-driven Ga FIB but the beam tails lead to a comparable behavior along the profile with increasing fluences and, correspondingly, higher milling rates.

The beam tails visible in the sputtering profiles are not visible in the 20/80 imaging resolution tests. This is one contribution leading to larger trenches than expected from the image resolution. Another explanation why the spot size is always smaller than the measured trench width could be the different sample types used for the measurements. While ultimate imaging resolutions are typically measured as an edge contrast on thin free-standing membranes, trenches are typically milled in a metal layer of a few nanometers thickness. Milling membranes removes their support from one side and dangling bonds can lead to morphological changes making milling tests difficult to interpret. In metal layers of a few nanometers thickness, sputter redeposition can take place, which is not taken into account in our static SRIM simulation. As mentioned above the milling of trenches also takes much longer than recording line profiles for capturing SE images, leading to an increased susceptibility for mechanical and electromechanical disturbances.

Conclusion

In this article, the performance of light ion beams from LMAIS FIBs in terms of imaging resolution and minimum milling width were compared with those of helium and neon beams provided by a GFIS-driven HIM system. According to our simulations and experiments, the imaging and milling resolution of all systems is determined by the ion beam profile and the stability of the ion beam and the instrument itself. While GFIS-driven noble gas beams still deliver the best lateral resolution, LMAISs allow for a wider application spectrum due to the vast number of different ion species and charge states available. Especially for very light ions, such as Li, LMAIS FIBs provide nearly the same milling resolution. Improvement is possible in both cases as GFIS technology can be extended to other gases [46-48]. Resolution improvements should be obtainable for both technologies using better optics and optimized platforms.

Acknowledgements

Parts of this research were carried out at the Ion Beam Center (IBC) at the Helmholtz-Zentrum Dresden-Rossendorf e.V., a member of the Helmholtz Association.

Funding

The authors would like to thank the German Federal Ministry of Economics BMWi for financial support under grant no. ZF4330902DF7.

ORCID® iDs

Nico Klingner - https://orcid.org/0000-0001-9539-5874
Gregor Hlawacek - https://orcid.org/0000-0001-7192-716X
Paul Mazarov - https://orcid.org/0000-0003-4401-8352
Lothar Bischoff - https://orcid.org/0000-0003-3968-7498

References

1. Gierak, J. *Semicond. Sci. Technol.* **2009,** *24,* 043001. doi:10.1088/0268-1242/24/4/043001
2. Bischoff, L.; Mazarov, P.; Bruchhaus, L.; Gierak, J. *Appl. Phys. Rev.* **2016,** *3,* 021101. doi:10.1063/1.4947095
3. Bruchhaus, L.; Mazarov, P.; Bischoff, L.; Gierak, J.; Wieck, A. D.; Hövel, H. *Appl. Phys. Rev.* **2017,** *4,* 011302. doi:10.1063/1.4972262
4. Stanforg, M. G.; Lewis, B. B.; Mahady, K.; Fowlkes, J. D.; Rack, P. D. *J. Vac. Sci. Technol., B: Microelectron. Nanometer Struct.–Process., M eas., Phenom.* **2007,** *35,* 030802. doi:10.1116/1.4981016
5. Hlawacek, G.; Gölzhäuser, A., Eds. *Helium Ion Microscopy;* Springer: Cham, Switzerland, 2016. doi:10.1007/978-3-319-41990-9
6. Nord, M.; Semisalova, A.; Kákay, A.; Hlawacek, G.; MacLaren, I.; Liersch, V.; Volkov, O. M.; Makarov, D.; Paterson, G. W.; Potzger, K.; Lindner, J.; Fassbender, J.; McGrouther, D.; Bali, R. *Small* **2019,** *15,* 1904738. doi:10.1002/smll.201904738
7. Jadwiszczak, J.; Keane, D.; Maguire, P.; Cullen, C. P.; Zhou, Y.; Song, H.; Downing, C.; Fox, D.; McEvoy, N.; Zhu, R.; Xu, J.; Duesberg, G. S.; Liao, Z.-M.; Boland, J. J.; Zhang, H. *ACS Nano* **2019,** *13,* 14262–14273. doi:10.1021/acsnano.9b07421
8. Schmidt, M. E.; Iwasaki, T.; Muruganathan, M.; Haque, M.; Van Ngoc, H.; Ogawa, S.; Mizuta, H. *ACS Appl. Mater. Interfaces* **2018,** *10,* 10362–10368. doi:10.1021/acsami.8b00427
9. Xu, X.; Prüfer, T.; Wolf, D.; Engelmann, H.-J.; Bischoff, L.; Hübner, R.; Heinig, K.-H.; Möller, W.; Facsko, S.; von Borany, J.; Hlawacek, G. *Beilstein J. Nanotechnol.* **2018,** *9,* 2883–2892. doi:10.3762/bjnano.9.267
10. Zhao, Y.; Liu, D.; Chen, J.; Zhu, L.; Belianinov, A.; Ovchinnikova, O. S.; Unocic, R. R.; Burch, M. J.; Kim, S.; Hao, H.; Pickard, D. S.; Li, B.; Thong, J. T. L. *Nat. Commun.* **2017,** *8,* 15919. doi:10.1038/ncomms15919
11. Cybart, S. A.; Cho, E. Y.; Wong, T. J.; Wehlin, B. H.; Ma, M. K.; Huynh, C.; Dynes, R. C. *Nat. Nanotechnol.* **2015,** *10,* 598–602. doi:10.1038/nnano.2015.76
12. McClelland, J. J.; Steele, A. V.; Knuffman, B.; Twedt, K. A.; Schwarzkopf, A.; Wilson, T. M. *Appl. Phys. Rev.* **2016,** *3,* 011302. doi:10.1063/1.4944491
13. Akhmadaliev, C.; Bischoff, L.; Schmidt, B. *Mater. Sci. Eng., C* **2006,** *26,* 818–821. doi:10.1016/j.msec.2005.09.026
14. Marcus, I. C.; Berbezier, I.; Ronda, A.; Alonso, M. I.; Garriga, M.; Goñi, A. R.; Gomes, E.; Favre, L.; Delobbe, A.; Sudraud, P. *Cryst. Growth Des.* **2011,** *11,* 3190–3197. doi:10.1021/cg200433r
15. Calculated r50 probe size He GFIS beam: 30 kV, 6 mm working distance, Ray Hill, 2020, private communication.
16. Gardner, J. R.; McGehee, W. R.; McClelland, J. J. *J. Appl. Phys.* **2019,** *125,* 074904. doi:10.1063/1.5085068
17. Pilz, W.; Klingner, N.; Bischoff, L.; Mazarov, P.; Bauerdick, S. *J. Vac. Sci. Technol., B: Nanotechnol. Microelectron.: Mater., Process., Meas., Phenom.* **2019,** *37,* 021802. doi:10.1116/1.5086271

18. Mazarov, P.; Pilz, W.; Meyer, F.; Richter, T.; Bruchhaus, L.; Jede, R.; Yu, Y.; Sanabia, J. E.; Bischoff, L.; Hlawacek, G.; Gierak, J. AVS 66th International Symposium & Exhibition, Colorado, USA, Oct 26–30, 2019; online AVS technical library, 2019.
19. *Zeiss SmartSEM,* V05.03NV for NVision40; 2008.
20. Bassim, N.; Scott, K.; Giannuzzi, L. A. *MRS Bull.* **2014,** *39,* 317–325. doi:10.1557/mrs.2014.52
21. Schwind, G. A.; Swanson, L. W. *J. Vac. Sci. Technol., B: Microelectron. Nanometer Struct.–Process., Meas., Phenom.* **2007,** *25,* 2586–2592. doi:10.1116/1.2781520
22. Prewett, P. D.; Mair, G. L. R. *Focused ion beams from liquid metal ion sources;* Research Studies Press: Taunton Somerset, 1991; Vol. 1.
23. Hlawacek, G.; Veligura, V.; van Gastel, R.; Poelsema, B. *J. Vac. Sci. Technol., B: Nanotechnol. Microelectron.: Mater., Process., Meas., Phenom.* **2014,** *32,* 020801. doi:10.1116/1.4863676
24. Ernst, N.; Bozdech, G.; Schmidt, H.; Schmidt, W. A.; Larkins, G. L. *Appl. Surf. Sci.* **1993,** *67,* 111–117. doi:10.1016/0169-4332(93)90301-q
25. Hagen, C. W.; Kruit, P. *J. Vac. Sci. Technol., B: Microelectron. Nanometer Struct.–Process., Meas., Phenom.* **2009,** *27,* 2654–2659. doi:10.1116/1.3237132
26. Melngailis, J. *J. Vac. Sci. Technol., B: Microelectron. Process. Phenom.* **1987,** *5,* 469–595. doi:10.1116/1.583937
27. Bischoff, L.; Teichert, J.; Hausmann, S.; Ganetsos, T.; Mair, G. L. R. *Nucl. Instrum. Methods Phys. Res., Sect. B* **2000,** *161–163,* 1128–1131. doi:10.1016/s0168-583x(99)00859-9
28. ORION NanoFab product website, Carl Zeiss Microscopy GmbH. https://www.zeiss.de/mikroskopie/produkte/multi-ionenstrahl/orion-nanofab-fuer-materialien.html.
29. VELION product website, Raith GmbH. https://www.raith.com/products/velion.html?mobile=0.
30. Bauerdick, S.; Bruchhaus, L.; Mazarov, P.; Nadzeyka, A.; Jede, R.; Fridmann, J.; Sanabia, J. E.; Gila, B.; Appleton, B. R. *J. Vac. Sci. Technol., B: Nanotechnol. Microelectron.: Mater., Process., Meas., Phenom.* **2013,** *31,* 06F404. doi:10.1116/1.4824327
31. Bischoff, L.; Klingner, N.; Mazarov, P.; Pilz, W.; Meyer, F. *J. Vac. Sci. Technol., B: Nanotechnol. Microelectron.: Mater., Process., Meas., Phenom.* **2020,** *38,* 042801. doi:10.1116/6.0000073
32. Mazarov, P.; Wieck, A. D.; Bischoff, L.; Pilz, W. *J. Vac. Sci. Technol., B: Microelectron. Nanometer Struct.–Process., Meas., Phenom.* **2009,** *27,* L47–L49. doi:10.1116/1.3253471
33. Mair, G. L. R.; Bischoff, L.; Londos, C. A.; Ganetsos, T.; Akhmadaliev, C.; Aidinis, C. J. *Appl. Phys. A: Mater. Sci. Process.* **2005,** *81,* 385–388. doi:10.1007/s00339-004-2563-8
34. Yamamura, Y.; Tawara, H. *At. Data Nucl. Data Tables* **1996,** *62,* 149–253. doi:10.1006/adnd.1996.0005
35. Livengood, R. H.; Tan, S.; Hallstein, R.; Notte, J.; McVey, S.; Faridur Rahman, F. H. M. *Nucl. Instrum. Methods Phys. Res., Sect. A* **2011,** *645,* 136–140. doi:10.1016/j.nima.2010.12.220
36. Mazarov, P.; Bruchhaus, L.; Nadzeyka, A.; Richter, T.; Jede, R.; Yu, Y.; Sanabia, J. E.; Bischoff, L.; Pilz, W.; Klingner, N.; Hlawacek, G., conference talk, MRS Fall Meeting 2019, Boston, USA.
37. Chroma ExB product website, Orsay Physics. http://www.orsayphysics.com/fib.
38. Multi species ion sources, whitepaper Raith GmbH. https://www.raith.com/technology/column-technologies/multi-species-ion-sources/.
39. Biersack, J. P.; Haggmark, L. G. *Nucl. Instrum. Methods* **1980,** *174,* 257–269. doi:10.1016/0029-554x(80)90440-1
40. Wang, Z.-J.; Allen, F. I.; Shan, Z.-W.; Hosemann, P. *Acta Mater.* **2016,** *121,* 78–84. doi:10.1016/j.actamat.2016.08.085
41. Veligura, V.; Hlawacek, G.; Berkelaar, R. P.; van Gastel, R.; Zandvliet, H. J. W.; Poelsema, B. *Beilstein J. Nanotechnol.* **2013,** *4,* 453–460. doi:10.3762/bjnano.4.53
42. Shorubalko, I.; Choi, K.; Stiefel, M.; Park, H. G. *Beilstein J. Nanotechnol.* **2017,** *8,* 682–687. doi:10.3762/bjnano.8.73
43. Emmrich, D.; Beyer, A.; Nadzeyka, A.; Bauerdick, S.; Meyer, J. C.; Kotakoski, J.; Gölzhäuser, A. *Appl. Phys. Lett.* **2016,** *108,* 163103. doi:10.1063/1.4947277
44. Greenzweig, Y.; Drezner, Y.; Tan, S.; Livengood, R. H.; Raveh, A. *Microelectron. Eng.* **2016,** *155,* 19–24. doi:10.1016/j.mee.2016.01.016
45. Tan, S.; Livengood, R.; Greenzweig, Y.; Drezner, Y.; Shima, D. *J. Vac. Sci. Technol., B: Nanotechnol. Microelectron.: Mater., Process., Meas., Phenom.* **2012,** *30,* 06F606. doi:10.1116/1.4766882
46. Lai, W.-C.; Lin, C.-Y.; Chang, W.-T.; Li, P.-C.; Fu, T.-Y.; Chang, C.-S.; Tsong, T. T.; Hwang, I.-S. *Nanotechnology* **2017,** *28,* 255301. doi:10.1088/1361-6528/aa6ed3
47. Shichi, H.; Matsubara, S.; Hashizume, T. *Jpn. J. Appl. Phys.* **2017,** *56,* 06GC01. doi:10.7567/jjap.56.06gc01
48. Aramaki, F.; Kozakai, T.; Matsuda, O.; Yasaka, A.; Yoshikawa, S.; Kanno, K.; Miyashita, H.; Hayashi, N. *Proc. SPIE* **2014,** *9235,* 92350F. doi:10.1117/12.2069435

License and Terms

BEILSTEIN JOURNAL OF NANOTECHNOLOGY

Scanning transmission imaging in the helium ion microscope using a microchannel plate with a delay line detector

Eduardo Serralta*[1,2], Nico Klingner[1], Olivier De Castro[3], Michael Mousley[3], Santhana Eswara[3], Serge Duarte Pinto[4], Tom Wirtz[3] and Gregor Hlawacek[1]

Full Research Paper

Open Access

Address:
[1]Institute of Ion Beam Physics and Materials Research, Helmholtz-Zentrum Dresden-Rossendorf, Bautzner Landstr. 400, 01328 Dresden, Germany, [2]Technische Universität Dresden, Dresden 01069, Germany, [3]Advanced Instrumentation for Nano-Analytics (AINA), MRT Department, Luxembourg Institute of Science and Technology, 41, rue du Brill, L-4422, Belvaux, Luxembourg and [4]Photonis Netherlands B.V., Dwazziewegen 2, 9301 ZR Roden, Netherlands

Email:
Eduardo Serralta* - e.serralta@hzdr.de

* Corresponding author

Keywords:
bright-field; channeling; dark-field; delay line detector; helium ion microscopy; scanning transmission ion microscopy

Beilstein J. Nanotechnol. **2020,** *11,* 1854–1864.
https://doi.org/10.3762/bjnano.11.167

Received: 08 September 2020
Accepted: 13 November 2020
Published: 11 December 2020

This article is part of the thematic issue "Ten years of the helium ion microscope".

Associate Editor: A. Gölzhäuser

Abstract

A detection system based on a microchannel plate with a delay line readout structure has been developed to perform scanning transmission ion microscopy (STIM) in the helium ion microscope (HIM). This system is an improvement over other existing approaches since it combines the information of the scanning beam position on the sample with the position (scattering angle) and time of the transmission events. Various imaging modes, such as bright field and dark field or the direct image of the transmitted signal, can be created by post-processing the collected STIM data. Furthermore, the detector has high spatial and temporal resolution, is sensitive to both ions and neutral particles over a wide energy range, and shows robustness against ion beam-induced damage. A special in-vacuum movable support gives the possibility of moving the detector vertically, placing the detector closer to the sample for the detection of high-angle scattering events, or moving it down to increase the angular resolution and distance for time-of-flight measurements. With this new system, we show composition-dependent contrast for amorphous materials and the contrast difference between small-angle and high-angle scattering signals. We also detect channeling-related contrast on polycrystalline silicon, thallium chloride nanocrystals, and single-crystalline silicon by comparing the signal transmitted at different directions for the same data set.

Introduction

The helium ion microscope (HIM) is an instrument that has already proven its value for high-resolution imaging, compositional analysis, nanofabrication, and materials modification [1,2]. It generates a focused helium (or neon) ion beam with sub-nanometer spot size and rasters it across the sample. The beam can be used for both imaging and modification of sam-

ples at the nanometer scale. The standard and most widely used imaging mode in the HIM is using an Everhart–Thornley detector (ET) [3] for collecting secondary electrons (SEs) emitted from the top surface of the sample, which carry mainly topographic information [4].

Other detectors and signals have been used to expand the capabilities of the HIM. Imaging with back-scattered particles [5,6] can add compositional information and reveal buried structures [7]. Ionoluminescence has been studied by detecting the light emitted from the sample during ion bombardment [8-10]. Moreover, compositional analyses using secondary ion mass spectrometry (SIMS) can be performed in the HIM with a lateral resolution of the order of 10 nm [11-14].

Transmission-mode imaging can further improve the capabilities of the HIM since it depends on different contrast mechanisms and gives information on sub-surface features as well. There are several ways of using the transmitted signal to form an image. In thin samples, the helium bean also generates SEs that can leave the sample from the bottom surface. This type of SEs was already used as an imaging signal [15]. More commonly, transmission imaging signals depend on the particles that pass through the sample and on how they are scattered. In bright-field (BF) mode, the image is produced by mapping the part of the beam that has suffered very little, or no, deflection. In dark-field (DF) mode, the deflected part of the beam is used to generate the signal for the image. In annular dark-field (ADF) mode, the beam transmitted at a particular polar angle region is integrated over a complete annulus. Alternatively, the image can be formed using the beam deflected in a polar and azimuthal angular sector.

For amorphous materials under perpendicular incidence, the transmitted beam is expected to be scattered symmetrically around the axis of incidence. The average polar angle of scattering depends on both the material and the thickness of the sample. Different materials and thickness combinations create distinct polar-angle distributions of scattering, producing a contrast similar to the mass-thickness contrast in transmission electron microscopy. In BF mode, the areas of the sample with little or no scattering appear with high intensity in the image, and regions of the sample that scatter more than the collection angle of the detector will appear with low intensity. In a complementary manner, in ADF mode, the areas of the sample that scatter to the considered angular interval will appear bright in the image, and the areas of the sample with little scattering will appear dark. BF imaging has the advantage of having higher count rates for the same beam current in thin samples. On the other hand, by adjusting the collection angles to fit the maximum of this distribution for a given material and thickness, ADF imaging can enhance the contrast of certain compositional features of the sample.

Crystalline materials can also give rise to additional contrast mechanisms. In crystalline materials, the stopping force depends on the orientation of the crystal [16]. Along some orientations, the target atoms are aligned in rows or planes, thereby creating easier directions for the penetration of the projectile atom. If the projectile atom reaches the crystal at an angle smaller than the critical angle for such an axial or planar channeling direction, the projectile will be steered along this direction and will experience a reduced probability of undergoing large-angle scattering. Hence, it will have a smaller energy loss per distance compared to random directions. This phenomenon is called the channeling effect and has been described for megaelectronvolt ions in detail in [17]. When compared to a random orientation, the channeling directions also have reduced secondary electron [18], back-scattering and sputter yields. Conversely, the ions have increased range and transmission probability in these directions. Channeling contrast in the HIM was demonstrated using SE imaging [18,19] and using the back-scattering signal [20]. The channeling effect in the HIM has also been studied using Monte Carlo [21] and molecular dynamics [22] simulations.

Measuring the energy of the transmitted particles is a novel technique that adds an information channel to the previously discussed transmission imaging modes. It will provide information on the phenomena occurring during the projectile–target interaction and can increase the signal-to-noise ratio [23]. Since most likely a considerable fraction of the transmitted particles at this energy range is neutral [24,25], magnetic or electrostatic spectrometers cannot be used. Therefore, ion energy-loss spectrometry and energy-resolved imaging require an energy-sensitive detector or a detection system in which time-of-flight (ToF) measurements can be implemented.

Likewise, the use of the transmission signal in the HIM for visualizing diffraction patterns is, in theory, possible but has not been reported yet. Diffraction patterns yield additional information on the crystal lattice and orientation. However, this application demands a detector with high spatial resolution taking into consideration the energy range and typical space restrictions in the HIM.

In the past, several attempts to utilize the transmission signal in the HIM have been made. One approach is converting the transmitted particles into SEs by positioning a material with high SE yield below the sample and using the ET detector to collect the SEs coming from this material. This method has been used in BF mode for assessing the thickness of milled materials in the

microscope [26,27] and has also been implemented for ADF imaging [15,28]. Mass-thickness contrast and thickness-fringes contrast have been shown in transmission mode in the HIM using this approach with a combined bright- and dark-field conversion detector [29]. Another approach using an annular microchannel plate detector was used for investigating gold–silica core–shell nanoparticles in ADF mode [30]. These approaches require a physical aperture to restrict the acceptance angle when performed in BF, and a physical change of the distance between the sample and the annular detector to adjust the acceptance angle interval when performed in DF. Most recently, a position-sensitive detector consisting of a silicon diode array has also been adopted for use in the HIM [31]. Later the same group also studied channeling effects on single-crystalline silicon with this detector [32].

In this work, we present a new system for comprehensive scanning transmission ion microscopy (STIM) analyses that gives more flexibility to the user than the earlier approaches. We adopted a microchannel plate (MCP) and a delay line readout structure as a position-sensitive detector to be used in the HIM. A special in-vacuum detector support allows one to mechanically control the acceptance angle during analysis. The resulting system has high spatial resolution and can be positioned to detect polar angles of deflection from 0 to 19°, with an angular resolution always better than 0.0033°. The selection of the transmission imaging mode and further tuning of acceptance angles can be done in post-processing. Additionally, ToF-resolved recording of the transmission events can be integrated into this system. Here, we use this system to study the mass-thickness-dependent contrast in amorphous materials and demonstrate transmission-channeling contrast using polycrystalline silicon, thallium chloride samples and beam steering in single-crystalline silicon.

Experimental

The new STIM detector comprises a stack of two MCPs and a resistive anode layer with a delay line readout structure behind it, as represented in Figure 1c. The combination of MCPs with a delay line readout structure as a position-sensitive detector was first implemented for the detection of 1–15 keV electrons [33]. Since then, it has been used in many other applications such as in astrophysics [34], transmission electron microscopy [35], and hard X-ray photoelectron spectroscopy [36].

The working principle of the detector can be summarized as follows: At the front side of the MCP, SEs are produced by the impact of the impinging energetic particles (He ions and atoms). These SEs are drawn into the microchannels due to the applied bias. The number of SEs is multiplied by numerous collisions along the way within the channels creating an electron cloud. The electron cloud hits the resistive anode layer in front of the delay lines and, by capacitive coupling, induces signals on the delay line meanders. These signals are collected at the endpoints of each delay line and passed through separate constant-fraction discriminators. Finally, with a time-to-digital converter, the position of the cascade is computed by comparing the time of arrival of the pulses at the ends of each delay line. This can be performed with picosecond accuracy and thus makes the detector ideally suited for future ToF applications.

In the present form of the detector, we use two MCPs, each with a 50 mm by 50 mm square active area, stacked and rotated by 90° to each other with a gap of 100 µm between them. The first MCP has a magnesium oxide coating to increase the SE yield [37]. The MCP pores have a diameter of 25 µm and a center-to-center spacing of 32 µm. The bias angle of the pores is 16°. The combination of delay line readout performance and MCP characteristics results in a spatial resolution of 47.2 µm in the

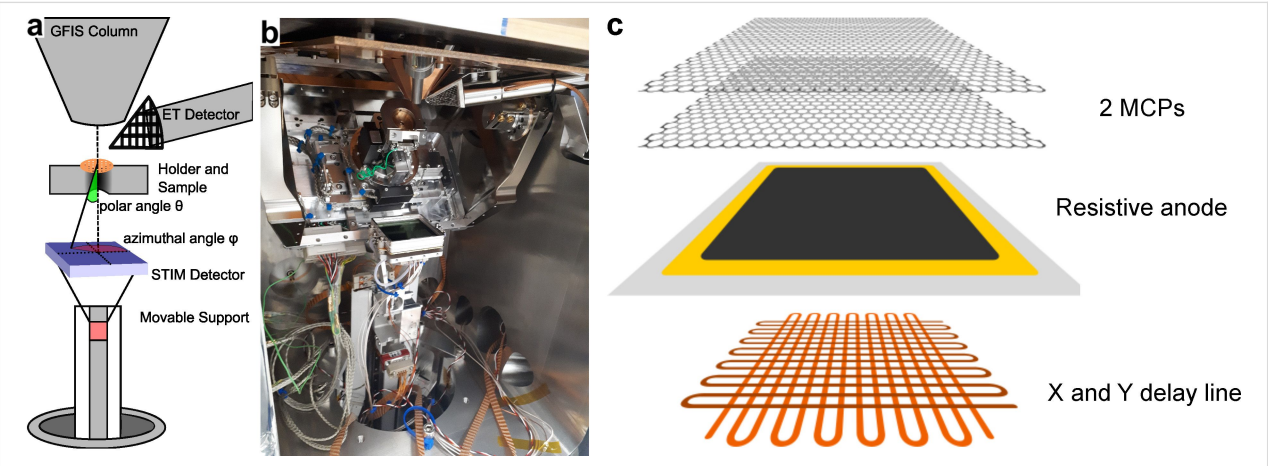

Figure 1: (a) Schematic representation of the STIM experiment. (b) Picture of the inner part of the chamber. (c) Schematic representation of the STIM detector.

x-direction and 58.1 µm in the y-direction. Effectively, the detector has approximately 4 megapixels over its entire area. The MCP front is biased to a potential of approximately −2 kV, while the MCP back is kept at approximately −400 V, relative to the anode, which is at ground potential. With this bias scheme, in the working instrument (detectors and gauges powered up, column isolation valve closed) at a sample chamber pressure of 2×10^{-7} mbar, we measured a dark-count rate of 80 cps. The delay line readout has a specified maximum count rate of 5 Mcps for randomly distributed events.

However, in practice, the count rate is limited by the non-random nature of the transmitted particles. In thin light samples, most of the transmitted particles will hit the center of the detector. The pores of the MCP have an individual recharging time of the order of 0.5 ms, estimated considering the MCP pores as parallel capacitors and resistors. This results in the fact that a single channel can only correctly detect count rates lower than 2 kcps or currents smaller than 0.3 fA. In addition to that, given that the position on the detector is calculated based on the time difference between the signals, when dealing with multiple simultaneous events, there might be multiple solutions for the combinations of position and time. Therefore, when trying to compute events that are too close in time and position, the delay line structure algorithm might produce imaging artifacts with shapes reflecting these multiple solutions for multi-hit events.

For each detected event, the STIM data consists of the position on the detector, the position of the beam on the sample, and a time reference to an internal or external signal (used in ToF mode). The beam position on the sample is controlled by an external scan generator, which also provides the beam position to the detection hardware. The acquisition of the STIM data and the external scan generator are controlled by a LabView interface based on an earlier implementation used for ToF-SIMS in the HIM [14]. The program allows for the generation of sample images in which the gray value, or color, of each pixel is assigned based upon the strength of the signal striking the transmission detector or selected sub-regions thereof. In any case, we store a comprehensive data set containing the 2D location where the beam is rastered over the sample, together with the 2D location where the transmitted helium strikes the detector, and the ToF information. Therefore, the user can generate BF, ADF, or other DF images through post-processing the transmission data at will at any time.

The experiments were conducted using the npSCOPE prototype, which is a high-vacuum instrument based on the gas field ion source (GFIS) column technology. This instrument combines the helium ion microscopy techniques with SIMS using a magnetic sector spectrometer, STIM with this new detector, and cryo-microscopy capabilities in a single instrument and will be described in detail elsewhere. In comparison to a commercial HIM, this microscope has a larger vacuum chamber that allows for the installation of the STIM detector and its movable support. A schematic representation of the measuring geometry is displayed in Figure 1a together with an overview image of the STIM detector, the stage without the sidewall, the adapted sample holder, cryo-shields, and ion optical column (Figure 1b).

An in-vacuum movable linear support is used to control the detector distance to the sample. This means that the distance can be chosen to give the best compromise between maximum collection angle for high-angle scattering events, and angular resolution with longer distance (and time-of-flight) for higher energy resolution. The support consists of a vertically mounted movable rail, on which a carriage supporting the detector can travel up and down. The rail is mounted on a flange attached around the pumping hole of the chamber. The motion is driven by piezo motors (Nanomotion HR-8), and controlled by a motion controller (Nanomotion XCDX) using a closed feedback loop with optically encoded linear rails (Schneeberger Miniscale Plus). This construction is compatible with the high-vacuum requirements, is self-locking, requires no mechanical feedthroughs nor lubricants, and provides high accuracy regarding the position of the detector (down to 100 nm). In the npSCOPE prototype, the distance between the detector and the sample can be adjusted from 101 to 496 mm, with the closest position being limited by the current stage. In the highest vertical position, the detection of 13.9° polar deflection angles is possible for any azimuthal angle, or up to 19° in selected azimuthal angles corresponding to the corners of the square detector.

The sample is currently mounted in a way similar to the one presented in [31]. A sample holder with an extension arm with a hole is used to mount the sample. Since the extension arm is attached at 45°, the stage has to be tilted so that the sample can be aligned with the column axis. In order to allow the transmitted particles to reach the detector, we removed the sidewall of the cradle of the current stage. With a new dedicated stage design (currently under construction), the detector can reach a minimum distance to the sample of 50 mm, achieving maximum polar angles of 25° for any azimuthal angle, or up to 33° in the corners of the square detector. The detector support is designed in a way that it can be adapted and installed into the commercially available Orion NanoFab chamber, with a reduced travel range.

The images presented in this work in transmission mode, unless stated differently, were taken while operating the microscope at

30 kV acceleration voltage, with a 10 µm aperture, in spot control 6 (crossover position of −247 mm) and gun gas pressure of 5×10^{-7} mbar. These conditions provide an estimated beam current of 50 fA. For the STIM images, a single scan with pixel dwell time of 110 µs was used. In the SE imaging mode, we used the line average mode with ten scans and a pixel dwell time of 10 µs. The research data used in this publication is available in an open access repository [38].

Results and Discussion

Mass-thickness contrast

Bright-field and dark-field contrast

In Figure 2, we show images of a carbon film under lacey carbon using the SE imaging mode (Figure 2a), BF STIM (Figure 2b), and ADF STIM (Figure 2c). The data for Figure 2b and Figure 2c was acquired in a single acquisition after Figure 2a, and the two images were generated selecting from the data two appropriate angular sectors of the detector.

The areas of the sample where the carbon film has the lacey carbon on top show different gray levels compared to the areas where there is only a homogeneous film. In general, since the average polar angle of scattering increases with the thickness, correctly adjusting the cut-off angle for the BF image can effectively suppress the signal from thicker areas of the sample in the final image. In contrast, in ADF thin areas of the sample are suppressed, while thicker regions appear bright if an appropriate minimum angle is chosen.

Here, we show two STIM images with different contrast using the same data set. During post-processing, the discrimination between ADF and BF has been done by choosing different minimum and maximum scattering angles for each image in order to maximize the contrast for each of them individually. Scattering angles between 0° and 3° have been used for BF while only scattered particles with scattering angles between 8 and 13.9° have been used for the corresponding ADF. The contrast due to the difference in thickness of the material can be noticed in these images.

Quantitative analysis

Figure 3a is a bright-field image of a multilayer sample used to study STIM contrast using combinations of light and heavy elements. In the BF image (Figure 3a BF angles: 0 to 4.5°), we can clearly differentiate all four regions based on their gray levels. For this image we used 30 kV acceleration voltage, with a 5 µm aperture, in spot control 5, a gun gas pressure of 1.3×10^{-6} mbar, and 300 µs pixel dwell time.

The sample comprises a 20 nm thick silicon nitride membrane used as a support layer. A 20 nm thick layer of silicon dioxide was deposited on one half, visible on the upper left half of the area in Figure 3a. Then, in the next step, a gold layer of 20 nm was deposited on the lower left half of the sample, creating four distinct areas on the window. The different material stacks are indicated in the STIM image. In Figure 3b, we show simulations of the exit angular distribution of 30 keV He for the different stacks of materials that are present in the sample, using TRIDYN [39] in static mode. The graph presented in Figure 3b shows the corresponding transmission angular distribution for the region used in Figure 3a. The expected contrast between different areas of the sample for the detection range of 0 to 4.5° is calculated from these distributions. In Table 1, a comparison between the contrast calculated in the simulations and the contrast obtained from Figure 3a is given.

For this sample, the simulated and experimental contrast match qualitatively. A quantitative analysis shows relevant differences in the intensity levels of the regions. The relative intensity level of the area with the layer of silicon dioxide on top of the

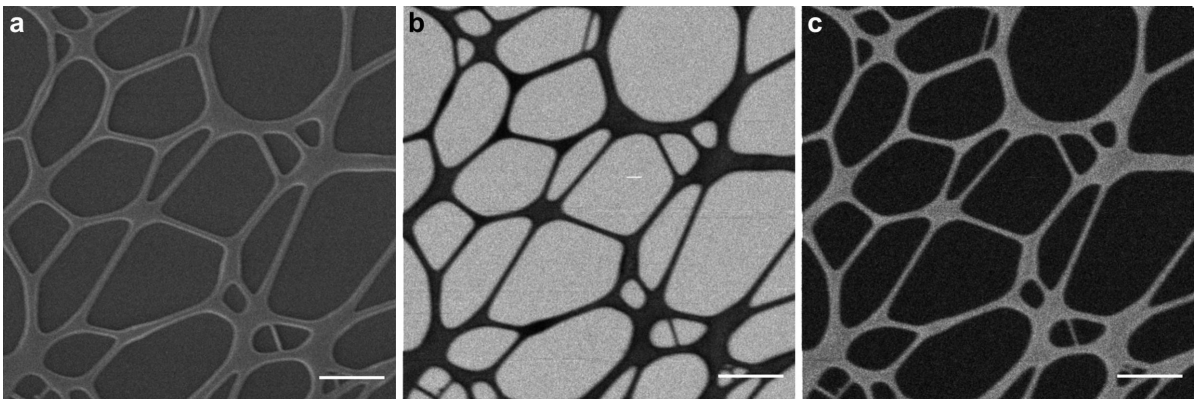

Figure 2: Micrographs of lacey carbon on carbon film. (a) Secondary electron imaging mode, (b) bright-field STIM image, with collection angle from 0 to 3°, and (c) annular dark-field STIM image, with collection angle from 8 to 13.9°. The scale bars are 1 µm.

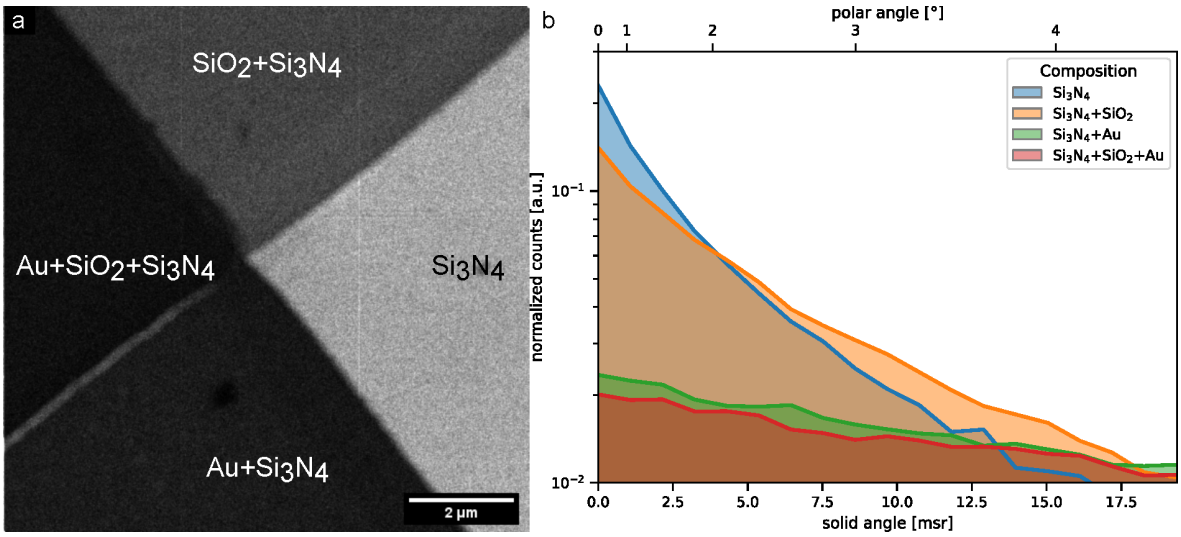

Figure 3: Bright-field image showing contrast due to the dependence of the exit angle on the material and the thickness of the layer. (a) Bright-field STIM image with collection angle from 0 to 4.5° of a silicon nitride membrane with silicon dioxide deposited on the upper left half and gold deposited on the lower left half. (b) TRIDYN simulation of the angular distribution of the transmitted beam.

Table 1: Bright-field STIM contrast comparison: Intensity of the transmitted signal from 0 to 4.5°.

Material	Si_3N_4	$SiO_2 + Si_3N_4$	$Au + Si_3N_4$	$Au + SiO_2 + Si_3N_4$
Average counts per pixel	45.73	19.03	7.42	4.78
Experimental signal normalized	1	0.42	0.16	0.10
Simulated signal normalized	1	0.67	0.12	0.11

silicon nitride differs considerably in experiment and simulation. The signal in the area on which only gold is deposited is stronger than expected while the signal on the area on which only silicon dioxide is deposited is weaker. A further study on the thickness of each layer using different techniques has not been performed, although deviations of the layer thickness could be responsible for the observed mismatch.

Beam steering and channeling

Polycrystalline silicon

A 15 nm thick nanoporous polycrystalline silicon membrane (available from Electron Microscopy Sciences, item number: 76042–79) has been investigated using STIM. In Figure 4b–f we present several STIM images, which were generated by a single data acquisition process. Figure 4a corresponds to the same field of view in the SE imaging mode. In the SE image (Figure 4a), one can note that the bigger pores are completely black, since they are totally open and no signal comes from these areas. The smaller pores are possibly partially filled with carbon and yield some SE signal.

The bigger pores appear dark in dark-field mode (Figure 4c–e) because there is no scattering. Counterintuitively, the same pores appear dark in bright-field mode (Figure 4b) as well. This behavior can be explained by the intensity of the full primary beam exceeding the local rate capability of the detector. At a distance of 151 mm behind the sample, the beam diameter has only widened to 53 µm and quickly saturates the MCP pores with diameters of 25 µm, for a beam with 0.35 mrad convergence. The high local current density temporarily discharges the irradiated pores preventing the creation of further electron cascades above the discriminator value, resulting in dark pixels. Grains that are thinner than the others, and smaller pores partially filled with residual carbon, appear brighter than the average in BF and darker in DF as expected. This contrast is due to the reduced scattering that the ions undergo when passing through such an area. Figure 4c–e shows dark-field images created using the same polar angle but different azimuthal directions on the detector (different from annular dark-field images where all azimuthal angles are considered).

The regions indicated by the arrows show contrast variations in different azimuthal directions of detection, with the same polar angle. The size and shape of these regions are comparable to the size and shape of the grains of the sample. This contrast change

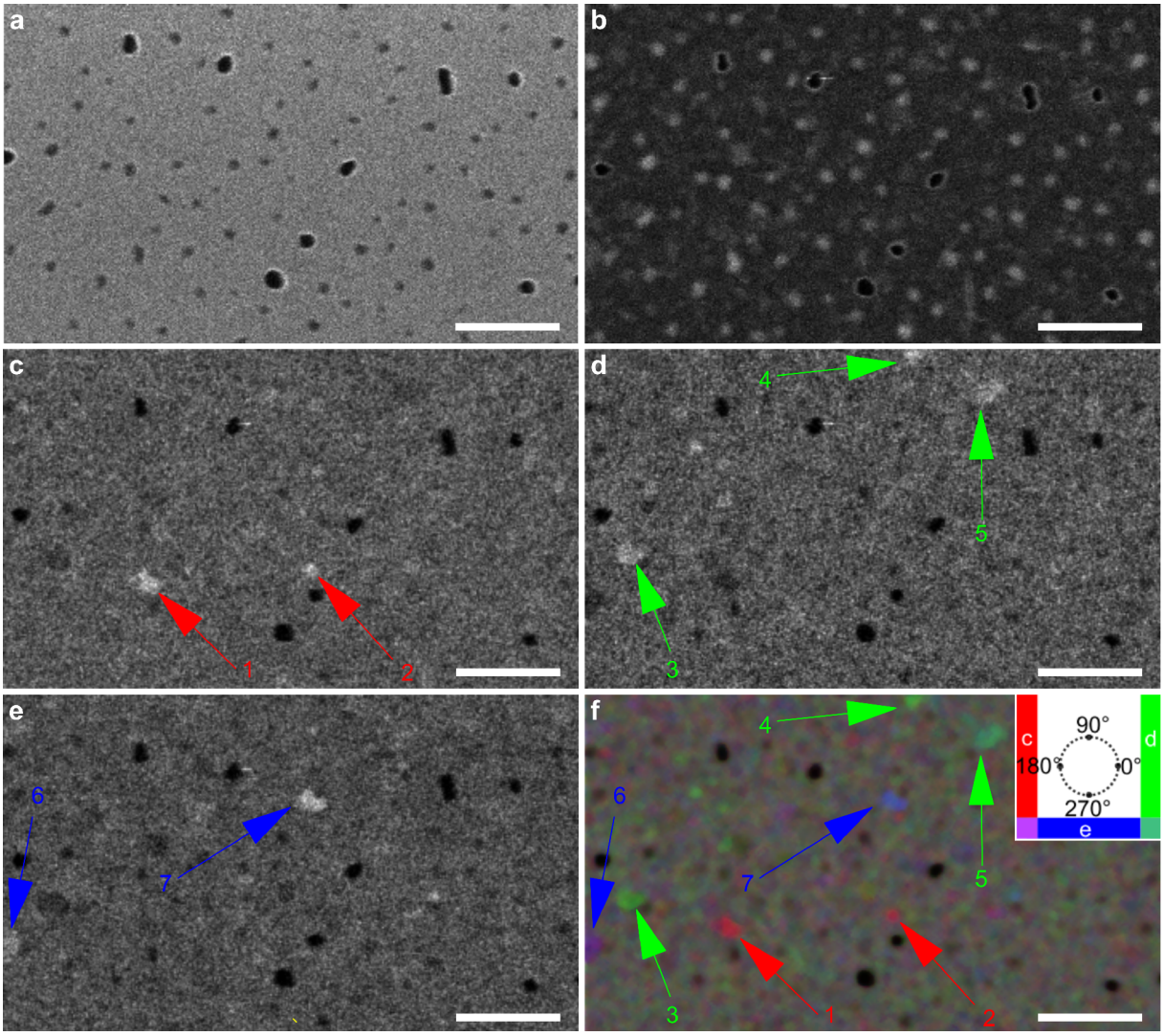

Figure 4: Helium ion microscopy images of the nanoporous polycrystalline silicon membrane. (a) SE image. (b) BF STIM image with polar angle θ < 3° and ϕ from 0 to 360°. Post-processed DF images with polar angle θ > 6° and azimuthal angle ϕ from (c) 135 to 225°, (d) 315 to 45°, (e) 225 to 315°. (f) Composite colored image using (c), (d), and (e) as RGB color channels. The inset shows the color mapping used in Figure 6f for the areas on the detector. The scale bars are 250 nm. The pixel dwell time used in the STIM data acquisition was 200 µs.

can be explained by channeling and blocking effects. For a random orientation or an amorphous material the polar angle of the scattering would depend only on the mass-thickness product of the traversed material and no azimuthal pattern is expected. However, for crystalline materials, depending on the crystal orientation with respect to the beam, the ions can be channeled along a low-index crystal axis or plane and, as a result, are steered into a particular direction. In a STIM image composed of the intensity in this particular polar and azimuthal direction, the grain will appear brighter than the average (e.g., grain 3 in Figure 4d). Conversely, the same grain will show a lower intensity than a randomly oriented grain for other non-channeling directions, since the beam is not being scattered into random directions as much as it would be the case for a randomly oriented grains (grain 3 in Figure 4c and Figure 4d). Figure 4f is an RGB image created using the three different DF directions as color channels. Using appropriate azimuthal angles for the channels, this composite image shows the grains that are steering the beam to directions between two directions used for individual channels presented in Figure 4c–e. For instance, grain 5 appears as cyan (overlap between d and e) and grain 6 appears purple (overlap between c and e).

The exit-angle distribution depends on the channeling occurring in the crystalline grains the beam traverses. The best contrast for the grains is obtained at angles larger than the largest critical angle for silicon. Therefore, we can infer that the ions are not following the same channel from the beginning to

the end. Since this effect would steer the beam to the angle between the crystal axis and the beam, having an upper limit equal to the maximum critical angle for channeling. In silicon, this value would be 3.51°, for the ⟨110⟩ directions, calculated using an adaptation of [40]. This is also the direction where the minimum backscattering yield (maximum transmission) is expected. Instead, the ions enter the crystal and, after some deviation due to random scattering, they reach directions in which they are channeled. Holeňák et al. [23] showed the blocking pattern of 50 keV helium through a 200 nm single-crystalline silicon foil at a pseudo-random orientation. In their report, some high-intensity spots were present at angles higher than twice the channeling critical angle.

Thallium chloride

A transmission electron microscopy (TEM) grid coated with evaporated thallium chloride (available on https://scienceservices.de/ with product code: Sku:E80045) was also analyzed using STIM. This sample has several small crystallites randomly oriented and it is used as a diffraction standard for TEM. Here, we perform a analysis similar to that carried out with the polycrystalline sample.

The SE image presented in Figure 5a and the BF STIM image (Figure 5b) show crystallites with different sizes. Additionally, the BF image (Figure 5b) gives information on the size of the crystallite along the beam axis according to their intensity level. The DF images Figure 5c and Figure 5d were obtained using the same polar angle, but with opposite azimuthal directions.

A comparison between the size of the structures in the SE image (Figure 5a) and the BF image (Figure 5b) shows larger structures in the SE image. Considering that a thin film of a light material would show in the SE signal but would not increase significantly the scattering and, hence, would not appear in the BF STIM mode, we assume that there is a film of approximately 10 nm over the crystallites. As expected, most of the smaller crystallites that show as dark in BF are bright in DF. Some larger crystallites are dark both in bright-field and dark-field images because of their larger thickness, which causes the beam to be scattered to angles higher than the maximum angle covered by the detector. A fraction of the ions might be stopped since the thickness of some crystallites is comparable to the projected ion range of helium under the experimental conditions (estimated as 170 nm using SRIM [41]). There are, how-

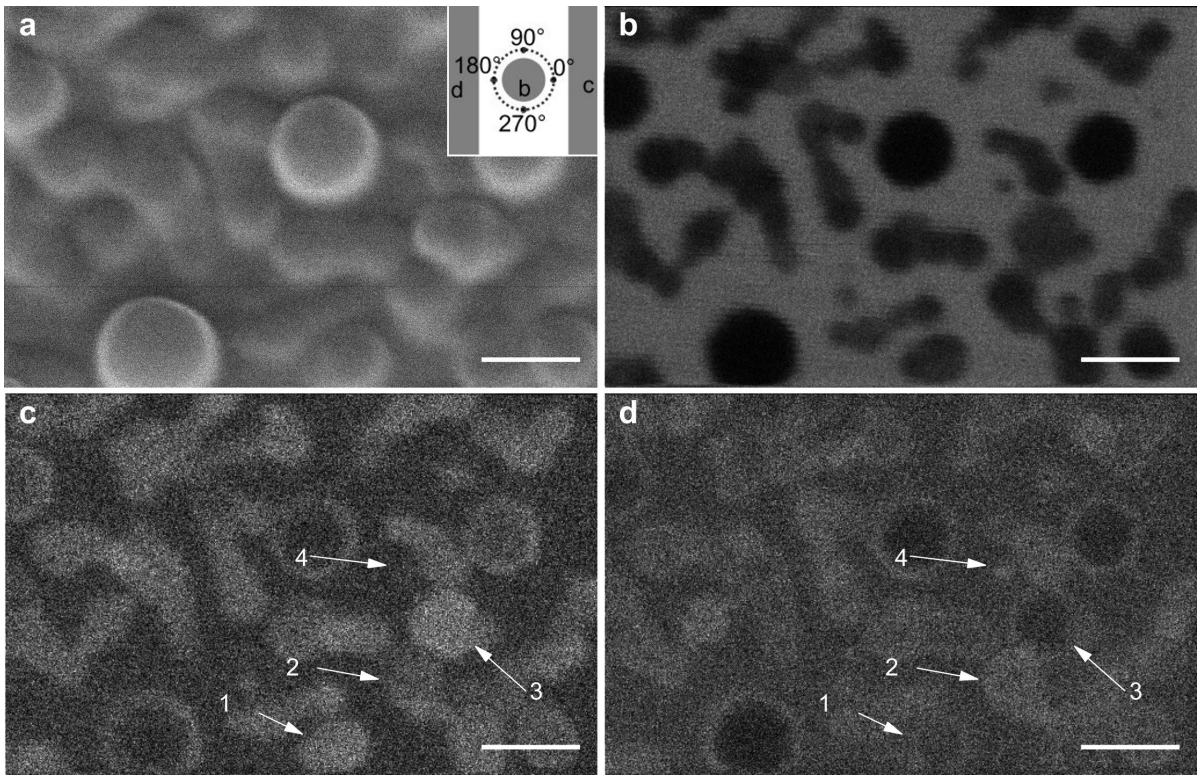

Figure 5: Thallium chloride evaporated on a TEM grid. (a) Secondary electron image. Inset of (a) shows the regions of the detector used to generate the following STIM images. (b) BF STIM image with acceptance angle of 0 to 4°. (c) DF STIM using the signal from the region on the right. (d) DF STIM using the signal from the region on the left. The scale bars are 100 nm.

ever, crystallites marked by arrows that show different intensity levels for different azimuthal directions. Crystallites 1 and 3 appear brighter in Figure 5c than in Figure 5d, while crystallites 2 and 4 behave in the opposite way. This difference would not occur in amorphous samples and can be explained with preferential scattering along low-index directions. Since the crystallites are randomly oriented, the axis in which the transmission of ions is enhanced points in different directions creating this variation of contrast for different azimuthal angles.

Single-crystalline silicon

In Figure 6a–e, we show STIM using different sections of the detector and the image of the transmission signal (Figure 6). The sample was a 35 nm thick, ⟨100⟩-oriented silicon membrane window (available on http://TEMwindows.com, product code: US100-C35Q33). From Figure 6a, one can see that the membrane has wrinkles, which create different angles of incidence between the sample and the incoming beam. The images shown in Figure 6b–e are DF STIM images created using the same polar angles but different azimuthal angles. One can notice that the same areas of the sample show different contrast at different DF directions. This means that different areas of the sample scatter the beam in different preferential directions, depending on the local inclination of the film. Since the membrane is oriented in the ⟨100⟩ direction, we assume that channeling will predominantly occur along the same direction. The critical angle for 30 keV helium ions along this direction is 1.16°, calculated using an adaptation of [40]. Therefore, areas that are bright in dark-field images (Figure 6b–e) can be interpreted as areas in which this channeling direction points towards the corresponding dark-field region on the detector due to the local inclination of the film. If, for the given experiment, we assume that channeling will occur along the ⟨100⟩ direction close by, we can obtain the local tilt angle from the measured polar angles. The images presented in Figure 6 highlight the areas with a local tilt angle of 3.8°.

Conclusion

In this work, we presented the development of a detection system for STIM that adds new functionalities to instruments

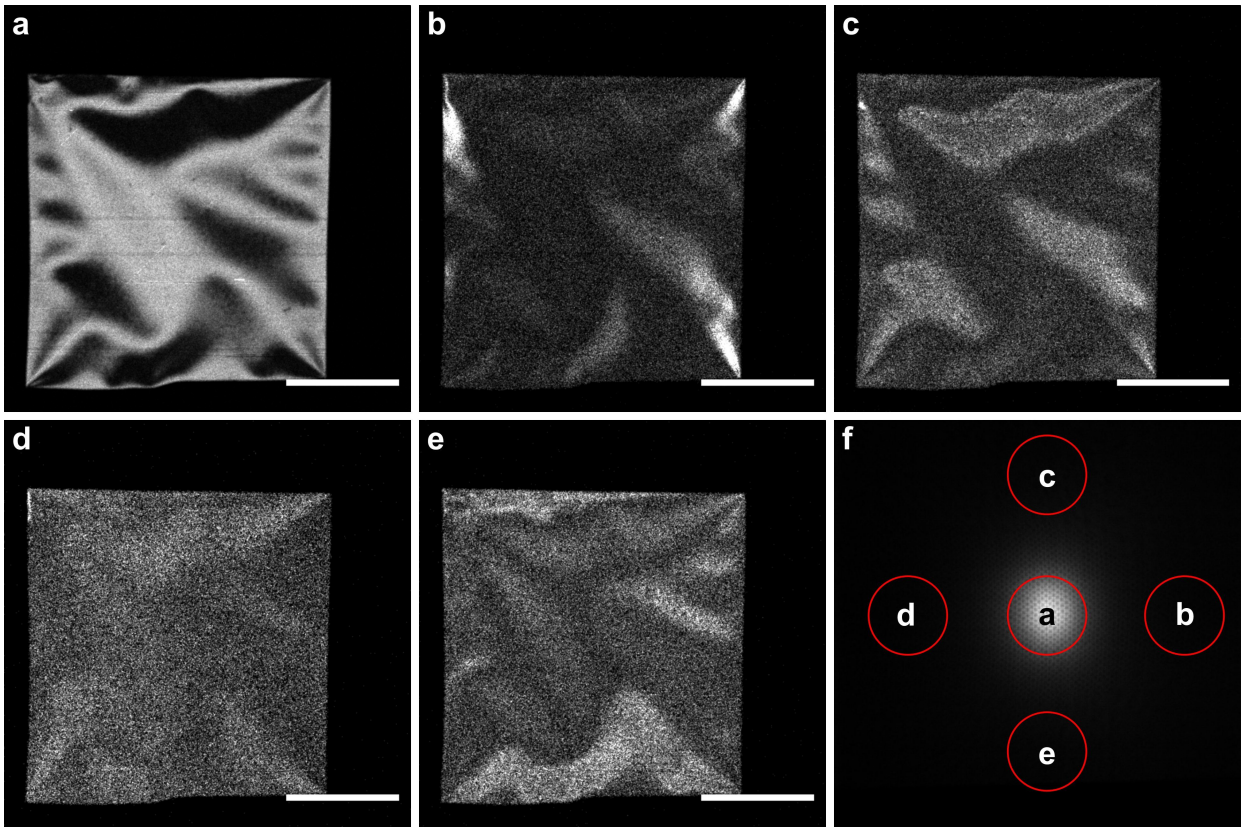

Figure 6: STIM images of a single-crystalline silicon ⟨100⟩ membrane in (a) bright-field with θ ≤ 1.09°, and in dark-field centered at the polar scattering angle θ = 3.8°, with azimuthal angle center ϕ = 0° in (b), ϕ = 90° in (c), ϕ = 180° in (d), and ϕ = 270° in (e). (f) Overall distribution of all counts on the detector. The areas on the detector for the corresponding STIM image are marked in red. The scale bars are 50 μm for (a–e). In (f), the distance from the center of the image to edge corresponds to a 5.58° deflection in the polar angle.

based on the GFIS ion column, such as the helium ion microscope or other light ion beam methods with high lateral resolution. The system is based on the combination of MCPs and a delay line detector mounted on a movable support so that the experiment geometry can be optimized. The used imaging detector is capable of a random count rate of up to 5 Mcps and has a spatial resolution of approximately 50 µm. This detector has not shown performance degradation due to energetic particle damage even when exposed to the primary beam directly. Advantages of this detector over earlier approaches are its flexibility and numerous supported imaging modes. These include bright-field, annular dark-field, and dark-field for channeling applications. In the future the detector will also provide time-of-flight support for these modes with a temporal resolution of 200 ps (or 29 eV energy for our current setup using SE detection for the start signal). In addition, the concept provides the possibility for post-processing the recorded data into BF and DF according to the operator's needs.

Using this detection system, we show applications of STIM for amorphous, polycrystalline, and single-crystalline materials. For amorphous samples, we show the contrast change for low and high scattering angles using BF and ADF detection. We also demonstrate the qualitative match of the contrast in bright-field mode with predictions from binary collision approximation calculations using a test sample. In the case of polycrystalline silicon, we can see channeling-related contrast in DF. Employing DF and post-processing, we see a contrast dependence on the orientation of thallium chloride nanocrystals. Finally, beam steering effects were shown to occur for a single-crystalline silicon sample.

Acknowledgements

We acknowledge Stefan Findeisen from the HZDR's mechanical engineering department and Rachid Barrahma from LIST for the mechanical designs of several parts. We thank Olivier Bouton from LIST for the technical support, and Ciarán Fowley from HZDR for sample preparation. We also thank Pasqual Bernhard and Andreas Oelsner from Surface Concept GmbH for insightful discussions on MCPs and delay line detectors. Parts of this research were carried out at the Ion Beam Center (IBC) at the Helmholtz-Zentrum Dresden-Rossendorf e.V., a member of the Helmholtz Association.

Funding

This work has been supported by the H2020 Project npSCOPE under grant number 720964 and by the Luxembourg National Research Fund (FNR) through project STHIM (C16/MS/11354626). ES also received financial support from the PicoFIB network.

ORCID® iDs

Eduardo Serralta - https://orcid.org/0000-0001-6254-022X
Nico Klingner - https://orcid.org/0000-0001-9539-5874
Olivier De Castro - https://orcid.org/0000-0001-9968-6695
Michael Mousley - https://orcid.org/0000-0002-0968-4846
Santhana Eswara - https://orcid.org/0000-0003-4151-2304
Serge Duarte Pinto - https://orcid.org/0000-0001-5205-5554
Tom Wirtz - https://orcid.org/0000-0002-7912-5193
Gregor Hlawacek - https://orcid.org/0000-0001-7192-716X

Preprint

A non-peer-reviewed version of this article has been previously published as a preprint: https://doi.org/10.3762/bxiv.2020.101.v1

References

1. Hlawacek, G.; Veligura, V.; van Gastel, R.; Poelsema, B. *J. Vac. Sci. Technol., B: Nanotechnol. Microelectron.: Mater., Process., Meas., Phenom.* **2014,** *32,* 20801. doi:10.1116/1.4863676
2. Hlawacek, G.; Gölzhäuser, A., Eds. *Helium Ion Microscopy;* NanoScience and Technology; Springer International Publishing: Cham, Switzerland, 2016. doi:10.1007/978-3-319-41990-9
3. Everhart, T. E.; Thornley, R. F. M. *J. Sci. Instrum.* **1960,** *37,* 246–248. doi:10.1088/0950-7671/37/7/307
4. Petrov, Y. V.; Vyvenko, O. F. Secondary Electron Generation in the Helium Ion Microscope: Basics and Imaging. In *Helium Ion Microscopy;* Hlawacek, G.; Gölzhäuser, A., Eds.; NanoScience and Technology; Springer International Publishing: Switzerland, 2016; pp 119–146. doi:10.1007/978-3-319-41990-9_5
5. van Gastel, R.; Hlawacek, G.; Dutta, S.; Poelsema, B. *Nucl. Instrum. Methods Phys. Res., Sect. B* **2015,** *344,* 44–49. doi:10.1016/j.nimb.2014.11.073
6. Klingner, N.; Heller, R.; Hlawacek, G.; von Borany, J.; Notte, J.; Huang, J.; Facsko, S. *Ultramicroscopy* **2016,** *162,* 91–97. doi:10.1016/j.ultramic.2015.12.005
7. van Gastel, R.; Hlawacek, G.; Zandvliet, H. J. W.; Poelsema, B. *Microelectron. Reliab.* **2012,** *52,* 2104–2109. doi:10.1016/j.microrel.2012.06.130
8. Veligura, V.; Hlawacek, G.; van Gastel, R.; Zandvliet, H. J. W.; Poelsema, B. *J. Phys.: Condens. Matter* **2014,** *26,* 165401. doi:10.1088/0953-8984/26/16/165401
9. Boden, S. A.; Franklin, T. M. W.; Scipioni, L.; Bagnall, D. M.; Rutt, H. N. *Microsc. Microanal.* **2012,** *18,* 1253–1262. doi:10.1017/s1431927612013463
10. Ogawa, S.; Iijima, T.; Awata, S.; Sugie, R.; Kawasaki, N.; Otsuka, Y. *Microsc. Microanal.* **2012,** *18,* 814–815. doi:10.1017/s1431927612005922
11. Wirtz, T.; Vanhove, N.; Pillatsch, L.; Dowsett, D.; Sijbrandij, S.; Notte, J. *Appl. Phys. Lett.* **2012,** *101,* 041601. doi:10.1063/1.4739240
12. Dowsett, D.; Wirtz, T. *Anal. Chem. (Washington, DC, U. S.)* **2017,** *89,* 8957–8965. doi:10.1021/acs.analchem.7b01481
13. Wirtz, T.; De Castro, O.; Audinot, J.-N.; Philipp, P. *Annu. Rev. Anal. Chem.* **2019,** *12,* 523–543. doi:10.1146/annurev-anchem-061318-115457
14. Klingner, N.; Heller, R.; Hlawacek, G.; Facsko, S.; von Borany, J. *Ultramicroscopy* **2019,** *198,* 10–17. doi:10.1016/j.ultramic.2018.12.014
15. Scipioni, L.; Sanford, C. A.; Notte, J.; Thompson, B.; McVey, S. *J. Vac. Sci. Technol., B: Microelectron. Nanometer Struct.–Process., Meas., Phenom.* **2009,** *27,* 3250–3255. doi:10.1116/1.3258634

16. Lindhard, J. *Phys. Lett.* **1964,** *12,* 126–128. doi:10.1016/0031-9163(64)91133-3
17. Gemmell, D. S. *Rev. Mod. Phys.* **1974,** *46,* 129–227. doi:10.1103/revmodphys.46.129
18. Hlawacek, G.; Veligura, V.; van Gastel, R.; Poelsema, B. Channeling and Backscatter Imaging. In *Helium Ion Microscopy;* Hlawacek, G.; Gölzhäuser, A., Eds.; NanoScience and Technology; Springer International Publishing: Switzerland, 2016; pp 205–224. doi:10.1007/978-3-319-41990-9_9
19. Veligura, V.; Hlawacek, G.; van Gastel, R.; Zandvliet, H. J. W.; Poelsema, B. *Beilstein J. Nanotechnol.* **2012,** *3,* 501–506. doi:10.3762/bjnano.3.57
20. Hijazi, H.; Li, M.; Barbacci, D.; Schultz, A.; Thorpe, R.; Gustafsson, T.; Feldman, L. C. *Nucl. Instrum. Methods Phys. Res., Sect. B* **2019,** *456,* 92–96. doi:10.1016/j.nimb.2019.07.002
21. Ohya, K. *AIP Adv.* **2018,** *8,* 015120. doi:10.1063/1.5018126
22. Ghaderzadeh, S.; Ghorbani-Asl, M.; Kretschmer, S.; Hlawacek, G.; Krasheninnikov, A. V. *Nanotechnology* **2019,** *31,* 035302. doi:10.1088/1361-6528/ab4847
23. Holeňák, R.; Lohmann, S.; Primetzhofer, D. *Ultramicroscopy* **2020,** *217,* 113051. doi:10.1016/j.ultramic.2020.113051
24. Dissanaike, G. A. *Philos. Mag. (1798-1977)* **1953,** *44,* 1051–1063. doi:10.1080/14786441008520363
25. Lohmann, S.; Primetzhofer, D. *Phys. Rev. Lett.* **2020,** *124,* 096601. doi:10.1103/physrevlett.124.096601
26. Scipioni, L.; Ferranti, D. C.; Smentkowski, V. S.; Potyrailo, R. A. *J. Vac. Sci. Technol., B: Nanotechnol. Microelectron.: Mater., Process., Meas., Phenom.* **2010,** *28,* C6P. doi:10.1116/1.3517514
27. Hall, A. R. *Microsc. Microanal.* **2013,** *19,* 740–744. doi:10.1017/s1431927613000500
28. Emmrich, D. A. Mikroskopie und Modifikation von Nanostrukturen mit Helium-Ionen. Ph.D. Thesis, Universität Bielefeld, 2019.
29. Notte, J., IV; Hill, R.; McVey, S. M.; Ramachandra, R.; Griffin, B.; Joy, D. *Microsc. Microanal.* **2010,** *16,* 599–603. doi:10.1017/s1431927610093682
30. Woehl, T. J.; White, R. M.; Keller, R. R. *Microsc. Microanal.* **2016,** *22,* 544–550. doi:10.1017/s1431927616000775
31. Kavanagh, K. L.; Herrmann, C.; Notte, J. A. *J. Vac. Sci. Technol., B: Nanotechnol. Microelectron.: Mater., Process., Meas., Phenom.* **2017,** *35,* 06G902. doi:10.1116/1.4991898
32. Wang, J.; Huang, S. H. Y.; Herrmann, C.; Scott, S. A.; Schiettekatte, F.; Kavanagh, K. L. *J. Vac. Sci. Technol., B: Nanotechnol. Microelectron.: Mater., Process., Meas., Phenom.* **2018,** *36,* 021203. doi:10.1116/1.5020667
33. Keller, H.; Klingelhöfer, G.; Kankeleit, E. *Nucl. Instrum. Methods Phys. Res., Sect. A* **1987,** *258,* 221–224. doi:10.1016/0168-9002(87)90059-3
34. Mende, S. B.; Heetderks, H.; Frey, H. U.; Stock, J. M.; Lampton, M.; Geller, S. P.; Abiad, R.; Siegmund, O. H. W.; Habraken, S.; Renotte, E.; Jamar, C.; Rochus, P.; Gerard, J.-C.; Sigler, R.; Lauche, H. *Space Sci. Rev.* **2000,** *91,* 287–318. doi:10.1023/a:1005292301251
35. Müller-Caspary, K.; Oelsner, A.; Potapov, P. *Appl. Phys. Lett.* **2015,** *107,* 072110. doi:10.1063/1.4927837
36. Beni, A.; Ott, N.; Pawelkiewicz, M.; Wardé, M.; Young, K.; Bauer, B.; Rajput, P.; Detlefs, B.; Zegenhagen, J.; McGrath, R.; Barthés-Labrousse, M.-G.; Jeurgens, L. P. H.; Schmutz, P. *Electrochem. Commun.* **2014,** *46,* 13–17. doi:10.1016/j.elecom.2014.05.024
37. Uhm, H. S.; Choi, E. H.; Cho, G. S. *Appl. Phys. Lett.* **2009,** *94,* 031501. doi:10.1063/1.3073983
38. Serralta, E.; Klingner, N.; De Castro, O.; Mousley, M.; Eswara, S.; Duarte Pinto, S.; Wirtz, T.; Hlawacek, G. Data for: Scanning transmission imaging in the helium ion microscope using a microchannel plate with a delay line detector. 2000; https://doi.org/10.14278/rodare.516. doi:10.14278/rodare.516
39. Möller, W.; Eckstein, W. *Nucl. Instrum. Methods Phys. Res., Sect. B* **1984,** *2,* 814–818. doi:10.1016/0168-583x(84)90321-5
40. Doyle, B. L. *Nucl. Instrum. Methods Phys. Res., Sect. B* **2016,** *371,* 63–68. doi:10.1016/j.nimb.2015.08.047
41. Ziegler, J. F.; Ziegler, M. D.; Biersack, J. P. *Nucl. Instrum. Methods Phys. Res., Sect. B* **2010,** *268,* 1818–1823. doi:10.1016/j.nimb.2010.02.091

License and Terms

BEILSTEIN JOURNAL OF NANOTECHNOLOGY

Bio-imaging with the helium-ion microscope: A review

Matthias Schmidt*[1], James M. Byrne[2] and Ilari J. Maasilta[3]

Review

Open Access

Address:
[1]Helmholtz-Centre for Environmental Research GmbH - UFZ, Permoserstraße 15, 04318 Leipzig, Germany, [2]School of Earth Sciences, University of Bristol, Wills Memorial Building, Queens Road, Bristol BS8 1RJ, United Kingdom and [3]Nanoscience Center, Department of Physics, University of Jyväskylä, P.O. Box 35, FI-40014 Jyväskylä, Finland

Email:
Matthias Schmidt* - matthias.schmidt@ufz.de

* Corresponding author

Keywords:
bio-imaging; flood gun; helium-ion microscopy; high resolution; HIM; HIM-SIMS; ionofluorescense

Beilstein J. Nanotechnol. **2021,** *12,* 1–23.
https://doi.org/10.3762/bjnano.12.1

Received: 10 July 2020
Accepted: 26 November 2020
Published: 04 January 2021

This article is part of the thematic issue "Ten years of the helium ion microscope".

Guest Editors: G. Hlawacek and A. Wolff

Abstract

Scanning helium-ion microscopy (HIM) is an imaging technique with sub-nanometre resolution and is a powerful tool to resolve some of the tiniest structures in biology. In many aspects, the HIM resembles a field-emission scanning electron microscope (FE-SEM), but the use of helium ions rather than electrons provides several advantages, including higher surface sensitivity, larger depth of field, and a straightforward charge-compensating electron flood gun, which enables imaging of non-conductive samples, rendering HIM a promising high-resolution imaging technique for biological samples. Starting with studies focused on medical research, the last decade has seen some particularly spectacular high-resolution images in studies focused on plants, microbiology, virology, and geomicrobiology. However, HIM is not just an imaging technique. The ability to use the instrument for milling biological objects as small as viruses offers unique opportunities which are not possible with more conventional focused ion beams, such as gallium. Several pioneering technical developments, such as methods to couple secondary ion mass spectrometry (SIMS) or ionoluminescence with the HIM, also offer the possibility for new and exciting research on biological materials. In this review, we present a comprehensive overview of almost all currently published literature which has demonstrated the application of HIM for imaging of biological specimens. We also discuss some technical features of this unique type of instrument and highlight some of the new advances which will likely become more widely used in the years to come.

Review

Introduction

Since its commercialisation in 2006 [1-5], the helium-ion microscope (HIM) has become a well-established tool for nanoscale imaging and nanoscale fabrication in physics and materials science. It is attractive for those applications as it combines high-resolution imaging of insulating samples with nanoscale milling capabilities in one instrument. The milling efficiency can also be increased by the use of heavier ion species, such as Ne or Ga, where Ne is available for the standard He column,

whereas Ga requires an additional column. In contrast to its success in materials science, HIM is much less frequently used for imaging biological specimens. To date, 13 years after the first HIMs were commissioned, only about 70 papers (we are aware of 72) have been published which include HIM bio-imaging data for medical, geomicrobiological, or life sciences. Figure 1 provides an overview of some key applications of HIM in bio-imaging together with an indication for the growth in the volume of literature which has been published in related fields. This steady growth of publications gives an indication for the increasing demand for HIM in biological applications and the opportunity for further developments. On the one hand, it is as flexible and straightforward to use as a scanning electron microscope (SEM) but with a five times larger depth of field [1] and a lateral resolution of about 0.5 nm [4] (demonstrated record: 0.24 nm [5]), which is between high-end field-emission SEMs (FE-SEM) and transmission electron microscopes (TEM). On the other hand, HIM is less demanding in terms of sample preparation compared to both SEM and TEM. In particular, the advantage of HIM is that opaque and non-conductive specimens, which possess a relatively strong topography, can be imaged. This is possible owing to the combination of a large depth of focus and the possibility of charge compensation [6], by pointing an electron beam emitted from a flood gun, onto the area of analysis.

The first HIM micrographs of biological specimens were published between 2007 and 2010 [2,5,7], but did not immediately trigger a wave of follow-up studies. At that time, most of the typical applications for SEMs did not demand a "better" SEM. If they did, the issues appeared to be solvable by the emerging technique of ultralow-voltage SEM [8]. Furthermore, HIM was not yet ready, and, in fact, is still not ready, for studying the finest details of the ultrastructure of cells or to resolve protein structures, which is state of the art in modern transmission electron microscopy. Another obstacle which had to be overcome was the absence of in situ chemical nanoscale analytical tools for the HIM, which were unavailable due to a lack of X-rays created under a 30 kV He^+ beam due to conservation of momentum. This is in stark contrast to SEM in which X-ray detection methods, such as energy dispersive X-ray spectoscopy (EDX), are more or less available as standard.

The turning point for bio-imaging with HIM in the field of medicine came in 2011 when Bazou et al. used the HIM to study tumor cells [9,10] and Arey et al. studied the interaction of nanoparticles with alveolar epithelial cells [11]. In the following two years, reports on HIM imaging of the nanostructures on butterfly scales by Boden et al. [12], fruit flies by Boseman et al. [13], and pine leaves by Kim [14] marked the entrance of HIM into general biology. Soon afterwards, two more milestones were reached. Firstly, Rice et al. [15] successfully imaged 15 nm gold labels on cell-surface proteins in rat kidneys, which demonstrated that HIM is compatible with the powerful technique of immunogold labelling. Secondly, Joens et al. introduced the ion-beam milling capabilities of the HIM to biological applications when they opened up the mouth cavity of a nematode [6]. In the same paper, Joens et al. furthermore

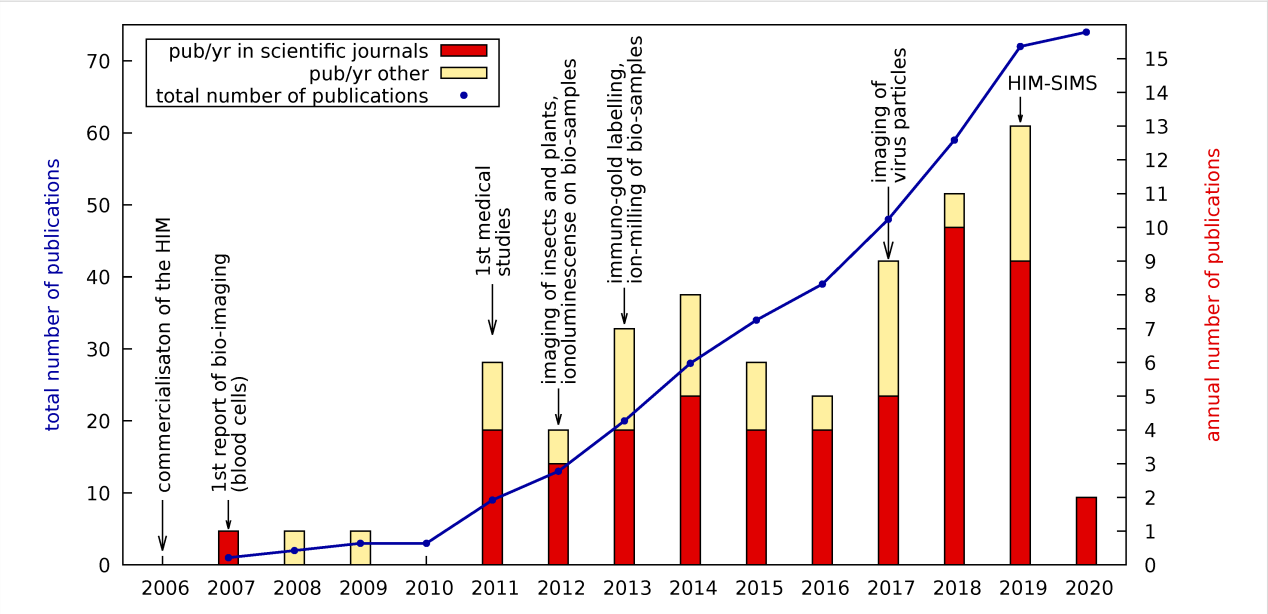

Figure 1: Annual (bars) and accumulated (blue line) numbers of publications on bio-imaging using the helium-ion microscope since its commercialisation. Some important milestones are also indicated. Red bars refer to annual publications in peer-reviewed scientific journals, yellow bars list other publications, such as white papers, Ph.D. theses, and extended conference abstracts.

demonstrated on mitotic HeLa cells that HIM is ready for ultrastructure research in cell biology. Research on the ultrastructure of cells with the HIM was subsequently continued by Schürmann et al., who presented HIM micrographs of cell-membrane nanodomains in mammalian cells [16].

HIM entered the field of virology in 2017 when Leppänen et al. used the technique to image T4 bacteriophages infecting *Escherichia coli* bacteria for the first time [17]. Images of a phage-infected bacterium in a sample from the environment was then presented by Sharma et al. in the following year [18]. The possibility to image the attachment of bacterial parasites to the outer membranes of bacteria at high resolution in, at least compared to TEM, a relatively natural state makes HIM a very powerful tool for the investigation of living antibiotics. The work on the life cycle of the bacterial predator *Bdellovibrio bacteriovorus* by Said et al. [19] and a study on the pH-responsive encapsulation of bacteriophages for phage therapy by Vinner et al. [20] are first examples.

Since the early days of HIM, attempts have been made to add nanoscale analytics to the HIM. Already in 2007, Notte et al. stated in their article "An Introduction to the Helium Ion Microscope" [3]: "We have observed that there is photon production from certain materials as the helium beam enters the sample. As with the standard cathodoluminescense effect, we expect that these photons may reveal information about the materials." With regard to the potential of using the HIM for secondary ion mass spectroscopy (SIMS) they wrote: "[If] a heavier gas in addition to or in place of helium [would be used] the resulting beam [c]ould then be used to generate enough secondary ions to permit SIMS analysis." Both ideas were quickly proven to be correct in the following years. Ionoluminescense in the HIM (IL-HIM) was used by Veligura et al. to investigate NaCl and semiconductor materials [21-23]. Franklin first investigated the suitability of IL-HIM for studying biological specimens tagged with fluorescent markers [24]. Another application in bio-imaging was published in 2018 by Sato et al., who used the ionoluminescense generated by the He ion beam to detect ZnO nanoparticles which were incubated with COS7 cells [25]. Today HIM-SIMS is possible via two different approaches. The first, a sector-field mass-spectrometer SIMS, was developed by Dowsett, Wirtz, et al. [26-29], and commercialised by Carl Zeiss Microscopy [30]. The second approach, developed by Klingner, Hlawacek et al., integrated a spectrometer for Rutherford backscattering analysis with time-of-flight (ToF) SIMS for the HIM [31-35]. The first biological application of HIM-SIMS was published by Lovric et al., who investigated *E.coli* bacteria exposed to TiO_2 nanoparticles using the sector-field SIMS spectrometer [36]. In this review article, we build upon previous articles by Kim [37] and Gölzhäuser and Hlawacek [38] to present an overview on past discoveries and recent developments reported for bio-imaging using HIM for biological, medical, plant, animal, microbiology, virology, and geomicrobiology studies. We briefly discuss the imaging, detection, and analytical technologies which make the HIM so powerful and explain why these technologies have been so beneficial to biological applications. We have highlighted, to the best of our knowledge, most publications which include HIM bio-imaging and have separated these articles into specific categories to provide the reader with a quick and concise overview of their particular field, or fields, of interest. We also briefly touch upon some of the most commonly applied preparation methods which are applicable to both electron and ion microscopy. Overall, this review has been written to inspire new and exciting studies using this powerful imaging technique based on helium ions. We expect that the next decade will see some remarkable discoveries, especially as the combination of high-resolution imaging with nanoscale analytics becomes more widespread.

Resolution and contrast mechanisms in the HIM

The key to high-resolution imaging with a scanning microscope is a high-brilliance source of small size. In the HIM this is realised by the atomic level (or gas field) ion source, which, in essence, is a single tungsten atom at which the gas atoms are ionised [1,39]. The column optics projects an image of that atom onto the sample, which commonly is referred to as "beam spot". The achievable lateral resolution in the HIM is naturally determined by the size of the beam spot, which has a minimum threshold of 0.25 nm [1]. In reality, achieving such a small spot size is extremely challenging and is affected by the ion landing energy as well as instrument parameters, such as the choice of aperture and source de-magnification, which both affect the quality of focus and beam shape [40]. However, the lateral and depth resolution of the measurement also depends on the type of detector which is used for the analysis. This can be understood from the interactions of the impinging ions with matter in the sample (Figure 2). Ion collisions with a nucleus in the sample result in (back-)scattering of the primary ion, displacement of atoms in the sample, sputtering of material and generation of phonons (heat). However, incoming ions also undergo many interactions with electrons in the sample, leading to the generation of secondary electrons, photons, and heat.

With the exception of heat generation, every possible ion–solid interaction can, in principle, be used for imaging or nanoscale analysis in the HIM given a suitable detector. We provide a brief overview of the main detectors which are applicable for HIM, though most of them are not commonly available at the moment.

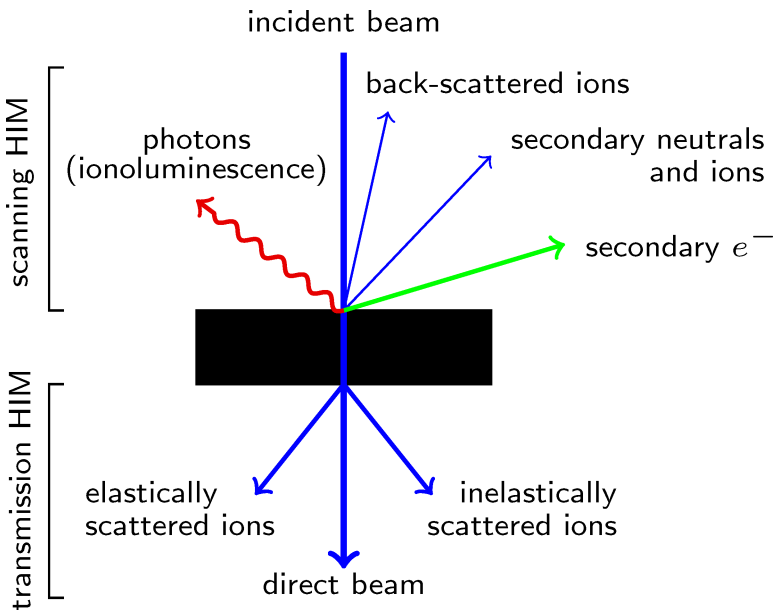

Figure 2: When the ion beam of the HIM interacts with the sample, primary ions and secondary particles escape the sample and can be detected. The figure schematically depicts particles which are, in principle, detectable in the scanning HIM and, in the case of a sufficiently thin sample, in the transmission HIM.

Secondary electron imaging

The high secondary electron yield in a HIM, which is significantly higher than that for low-energy electrons in an SEM [41], makes the detection of secondary electrons favourable for imaging. To date, the majority of HIM studies have employed secondary electron imaging using an Everhart–Thornley (ET)-type electron detector [5,42,43]. This is mainly because the ET detector is the standard detector for the HIM, but also because secondary electron imaging provides the highest resolution currently available with a demonstrated lateral resolution of 0.24 nm [5].

Such a high resolution is possible because of the relatively small amount of energy which is transferred from the helium ion to the secondary electron. Employing the formula for a central elastic collision, a 25 keV helium ion transfers as little as 13.7 eV to the secondary electron. In SEM, the acceleration voltage of the electron beam needs to be lowered to yield low-energy secondary electrons. This increases surface sensitivity since only secondary electrons produced directly under the surface will be able to overcome the work function of the sample and reach the detector. In HIM, the emitted secondary electrons already have low energy, which results in a strong edge and topography contrast. Furthermore, the low energies of the secondary electrons in a HIM produce excellent contrast due to changes in the work functions of the materials. An interesting contrast mechanism occurs when HIM is used to study insulating or poorly conducting materials such as most biological specimens. Here, differences in local conductivity result in the accumulation of positive charges under the ion beam, which hampers the emission of secondary electrons and results in a blackening of the charged areas in the micrograph.

Charge compensation

One of the most frequently cited advantages of using HIM compared to SEM for bio-imaging is the possibility to image typically non-conductive biological specimens without the prior coating with a thin layer of metal to make their surfaces conductive. This is possible due to the development of the charge-compensating electron flood gun, which is one of the flagship features of HIMs [5,43]. The technique is straightforward to use: After having scanned one line, the ion beam is blanked and electrons from the flood gun are directed into the field of view. Then, a new line is scanned followed by another electron flooding. This is particularly useful for biological specimens, which are typically insulators or poor conductors, as it enables imaging at high resolution without depositing a thin conductive layer (e.g., Au, Pt, or C) onto the surface in order to avoid charging. Charge compensation can even be considered to be necessary for conductive metals, because the high surface sensitivity of the HIM would only reveal the metal layer and not the fine detail of the surface ultrastructure without the use of the flood gun. From a practical perspective, charge compensation can be challenging as the total amount of charges required for compensation depends linearly on the number of charges implanted per line scanned. In other words, the settings of the

flood gun have to be adjusted whenever the number of pixels per line, dwell time, or beam current are changed. Figure 3 illustrates how the variation of the dwell time of the ion beam on a pixel influences the brightness of the image if the flooding parameters are kept constant. Similar results can be obtained when the flood time is varied at a constant dwell time.

Secondary ion mass spectrometry (SIMS)

A major disadvantage of using standard HIM rather than SEM is the lack of analytical detectors for elemental quantification, such as EDX. This is because 30 keV helium ions cannot transfer enough energy to the bound inner-shell electrons of the sample to excite them out of the core states and to enable fluorescent X-ray de-excitation (this would require energies of several kiloelectronvolts). However, recent analytical developments of the HIM have focused on the detection of secondary ions which are sputtered when the primary ion beam of the HIM is scanned across the sample material. The ionised fraction of this material can be extracted by electrostatic extractor optics and passed through a mass spectrometer in order to obtain chemical and isotopic information about the sample. At present, there are two different types of HIM-SIMS available. On the one hand, there is a sector-field SIMS developed by Dowsett, Wirtz et al. [26-30], in which up to four ions can be analysed simultaneously. On the other hand, there is a time-of-flight spectrometer developed by Klingner, Hlawacek et al. [31,33,35]. Both spectrometers have a mass resolution of about 400. So far, HIM-SIMS remains in the development stage with few commercial systems available. However, they are potential game changers for the investigation of biological samples at high spatial resolution in combination with chemical characterisation. A first biological application was presented by Lovric et al. when they investigated *E.coli* which were exposed to TiO_2 nanoparticles with the sector-field spectrometer [36]. The authors report on secondary ion maps of CN^- from the biomass as well as of Ti^+ from the nanoparticles. So far, the mass resolution achieved does not allow for using HIM-SIMS to characterise isotopically labelled samples, which requires a ten to

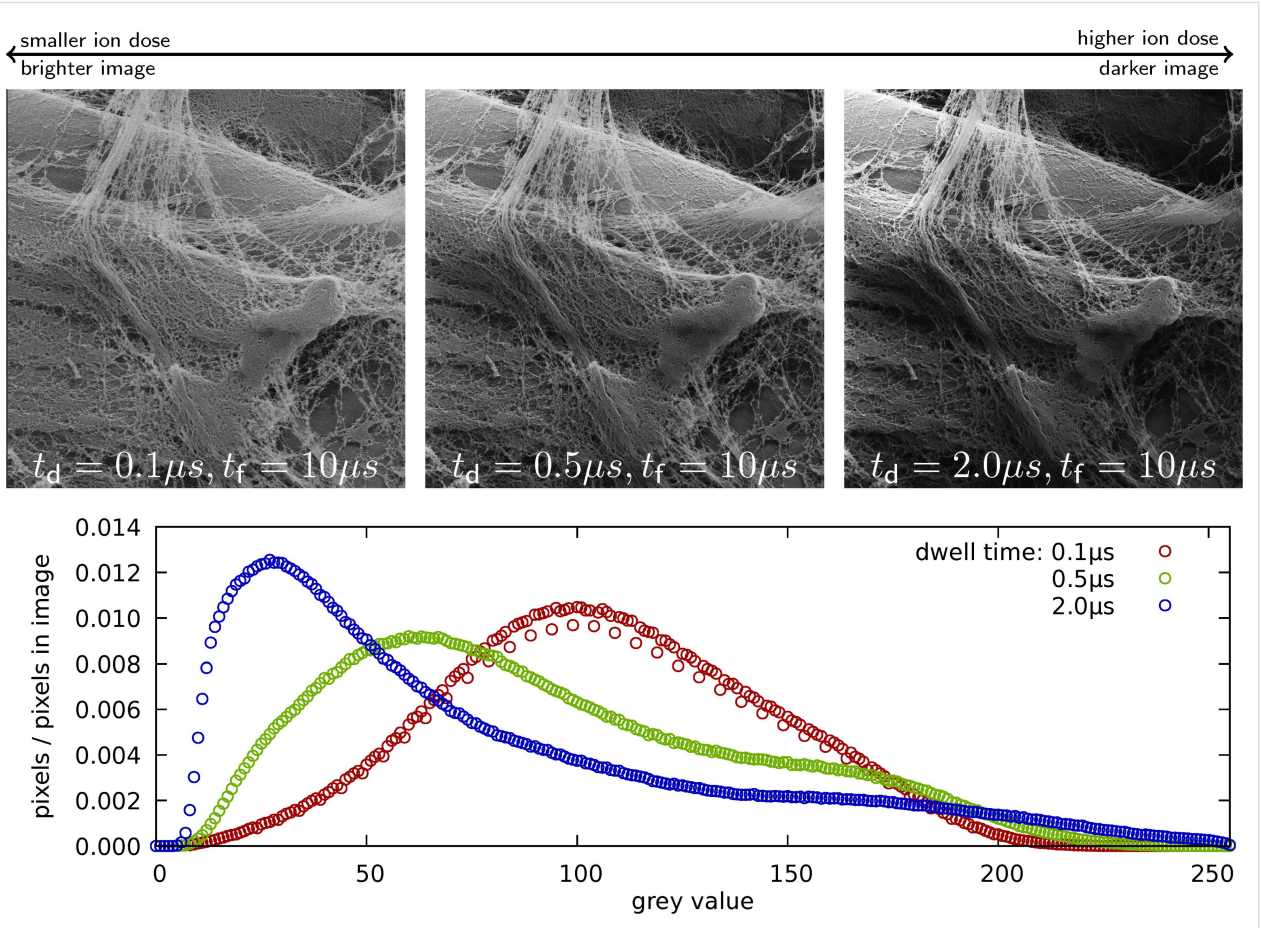

Figure 3: Charge compensation in the HIM using the flood gun. An uncoated maize root was imaged with different dwell times, t_d = {0.1,0.5,20} µs, while flood time, t_f = 10 µs, image size, 2048 × 2048 pixels, and brightness/contrast settings of the Everhart–Thornley detector were kept constant. The histograms clearly show a shift towards lower pixel intensities with increasing dwell time. No flooding at all (not shown here) resulted in a black image. The field of view is 20 µm. Unpublished data, sample provided by Yalda Davoudpour.

twenty times higher resolution. To illustrate this, consider a ^{13}C-labelled sample. In order to distinguish, for instance, the ion $^{12}CH^+$ of mass 13.007 u from $^{13}C^+$ of mass 13.003 u a mass resolution of more than about 4000 is needed. If in future HIM-SIMS systems the mass resolutions were improved by about one order of magnitude, HIM-SIMS could enable the localisation of specific bacteria which have metabolised labelled substrates within a microbial community. This type of application is already possible using NanoSIMS instruments. However, such instruments lack the spatial resolving power of the HIM [44]. An interesting and well-characterised geomicrobiological test system for HIM-SIMS spectrometers would be magnetosomes synthesised by magnetotactic bacteria, which are Fe_3O_4 nanocrystals of about 50 nm length [45]. HIM-SIMS also appears to be a promising tool to study intracellular deposits of certain chemical elements. An example are phosphate granules in algal biofilms, which were previously investigated using multiple microscopes in a correlative study [46]. Another, certainly more challenging, example would be the identification of iron–sulfur clusters in microbes [47] or mitochondria [48] by HIM-SIMS. Nevertheless, the current mass resolution of the spectrometers allows for several interesting applications in biology, which comprise biomineralisation, microbial corrosion, and interactions between nanoparticles and cells or tissues.

Alternative detectors

Rutherford back-scattering (RBS) of high-energy (typically in the range of 1 to 5 MeV) ions is a well-known (micro)analytical technique for the investigation of the elemental composition of a sample. Recently, Klingner, Heller, and Hlawacek demonstrated a time-of-flight RBS spectrometer for the HIM [32,34,49]. We are not aware of any currently published biological application of RBS in the HIM. However, from scattering kinetics it follows that RBS is most sensitive to heavy elements in a light matrix. For bio-imaging this implies that RBS could be a promising technique to study systems containing organic and inorganic matter, for example, the interactions of nanoparticles and cells, immunogold-labelled cells or tissues, and biomineralisation processes, such as the formation of bones or tooth enamel.

In SEM, cathodoluminescence refers to the emission of photons of characteristic wavelengths from a material under electron bombardment. Ionoluminescence (IL) describes the equivalent phenomenon in HIM when free electrons in the sample are excited by the bombardment of the sample by helium ions and emit photons in the range from near-IR to near-UV [3,21-23]. IL spectra as well as the temporal decay of IL after excitation contain information about the emitting material. IL emitted under megaelectronvolt proton or alpha-particle irradiation has proven to be a powerful tool for the investigation of medical and biological samples [50]. In the context of bio-imaging with the HIM, IL-HIM holds promise to detect fluorescent biomarkers with better resolution than that achievable even with the most advanced super-resolution optical microscopy techniques, for instance, stimulated emission depletion microscopy [51]. In particular, it may allow for correlating fluorescence microscopy with HIM. Few bio-imaging studies have focused on the detection of IL. To the best of our knowledge, the only work on IL-HIM bio-imaging was done by Franklin and is published in his Ph.D. thesis [24]. He investigated the IL of fluorescent dyes and applied this to study an Alexa Fluor 488-tagged mouse incisor. However, he found that “the area of interest was becoming increasingly bleached under the beam. It was discovered that only one [IL-HIM] image was achievable before bleaching the sample at a 20 μm field of view.” In order to overcome the ionobleaching of biomarkers, Franklin also tested nanoscale diamonds doped with the fluorescent nitrogen-vacancy defect as well as rare earth metal-based nanoparticles regarding bleaching under the ion beam. Although they are believed to be photostable under electron irradiation, the IL of the nanoscale diamonds decreased significantly under the ion beam even at doses lower than 10^{14} ions·cm^{-2}. However, lanthanide-doped nanoparticles proved to be relatively stable against the ion irradiation and seem to be promising materials for biomarkers to be used with the HIM. Later, Mi developed a particle-accelerator-based setup with high-energy protons and alpha particles to excite IL in biological specimens [52]. In this Ph.D. thesis, Alexa Fluor 514-labelled HeLa cells were imaged with 2 MeV protons. Furthermore, optimisation protocols for the design of luminescent lanthanide-doped nanoparticles with a quantum yield of up to 0.673 were presented. In the aforementioned work by Sato et al., HIM imaging was used to study COS7 kidney fibroblast cells [25]. In one of the experiments described in the paper, the cells were incubated with ZnO nanoparticles whose fluorescense was detected by IL-HIM. In general, it can be concluded that IL-HIM is particularly promising for biological applications if ionobleaching of fluorescent bio-markers can be overcome. The few studies available so far suggest to develop bio-markers on the basis of rare earth metal-doped nanoparticles.

The portfolio of possible contrast mechanisms in HIM is not complete without the detection of transmitted ions. Whilst accelerator-based transmission ion-microscopy using protons or alpha particles has been used to investigate biological specimens since the 1980s [53], none of the few (scanning) transmission helium-ion microscopy (THIM) studies using 10 to 40 kV helium ions have imaged biological specimens [5,54-56]. It can be speculated that this is mainly due to a lack of a detector for transmitted ions in the latest-generation HIM (Zeiss Orion NanoFab) [43], although it was a standard detector in the first-

generation HIM (Zeiss Orion Plus) [5]. However, THIM is desirable as it would extend the range of applications to thin sections, similar to the transmission option in SEMs. In combination with the well-established heavy-metal staining techniques used in transmission electron microscopy (TEM), this would allow for ultrastructural research comparable to standard TEM. SRIM [57] simulations show that up to 400 nm thick sections of epoxy resins could be penetrated by 30 kV helium ions (unpublished work by M. Schmidt). Even more importantly, THIM is highly complementary to secondary electron imaging in the HIM. It provides insight into an object whereas the latter only images its surface. If a segmented detector with a central segment and ring segments was used, it would be even possible to distinguish between absorption contrast (bright-field imaging) and scatter-contrast (dark-field imaging). Compared to other imaging modes in the HIM, it can be anticipated that THIM will be the best choice for imaging cell organelles, bacterial nanoparticles, or bacteriophages inside infected bacterial cells.

This section would be incomplete without mentioning two interesting new developments. Firstly, Mouseley et al. have developed a full-field THIM, which is not based on a Zeiss Orion instrument, and which holds promise to conduct exciting THIM experiments also on biological samples [58]. Secondly, within the npSCOPE H2020 project an "instrument [is being developed] that couples the extraordinarily high resolution of the […] helium-ion microscope with sensors for composition (a mass spectrometer) and 3D visualization (transmitted ion detector) in order to more fully characterise individual nanoparticles and their interaction with their environment (tissue, cells, etc.) […]" [59].

Sample preparation

Sample preparation is critical to the success of imaging any biological material at high resolution using electron and ion microscopy techniques. Depending on the sample under investigation, biological samples prepared for HIM might include structures such as bacterial cells, biofilms, exopolymeric substances (EPS), or minerals. The high vacuum applied in HIM means that any liquid remaining in a sample is subject to surface tension, which can lead to damage of the specimen during imaging. To overcome this issue, researchers typically focus on removing any liquid water from a sample whilst, at the same time, maintaining the cellular integrity. This is usually achieved by chemical fixation, followed by dehydration and then drying. For non-conductive samples, as is typical of biological materials, established protocols for SEM also involve methods to overcome charging effects, which are, however, not absolutely necessary for HIM owing to the charge compensation.

Fixation

Fixation is often applied as the first step during sample preparation to prevent or limit alterations to biological materials during sample drying. Chemical fixatives such as glutaraldehyde, formaldehyde, or a combination of the two (Karnovsky's solution) cross-link proteins and lipids to physically stabilise samples [60]. Glutaraldehyde (2–2.5%) fixation is usually performed at cold temperature (4 °C) to avoid the formation of artifacts and is well suited for samples containing a high density of cells, such as biofilms. The length of the fixation time should be varied depending on the sample. Before fixation, specimens are also sometimes treated with additional chemicals, such as 1% tannic acid (TA), and/or osmium-fixed to promote membrane integrity [61]. After fixation, water is removed from samples via dehydration in ethanol or methanol with increasing concentrations, for example, 30%, 75%, 95%, and 100% for 10 min each [60,62]. Samples can be stored in about 70% ethanol prior to drying.

Drying

The next stage in sample preparation of biological samples focuses on drying to avoid damages to fragile cell surfaces, internal structures, EPS, biofilms, or mineral associations. In the following, a brief overview over different routinely applied drying methods is given. (I) Freeze drying: Samples are frozen (e.g., using a plunge or high-pressure freezer) and then dried under vacuum. Uryu et al. suggested a pathway which includes plunge freezing for instantaneous immobilization followed by freeze drying in a cold nitrogen gas and finally critical point drying [63]. This method (termed $FDGN_2$) resulted in unprecedented structural detail during imaging with SEM but yielded various artifacts during imaging with HIM [64]. (II) Critical point drying (CPD): The basic principle of CPD is to substitute ethanol in the dehydration preparation stage with a supercritical fluid, such as carbon dioxide (CO_2). The temperature and pressure around the sample are raised to the critical point, 31 °C and 7.4 MPa (1073 psi), at which point CO_2 becomes supercritical. The pressure is then lowered at constant temperature returning the CO_2 to a gaseous state. Through this process the sample is dried without ever crossing the liquid–gaseous boundary and, thus, avoiding surface tension, which is so damaging to the sample. The operating procedures for CPD vary depending on the sample or instrument, with some being automated and others manually operated. Rice et al. used methanol during the dehydration stage, purged the samples with cold liquid CO_2, and raised temperature and pressure to, respectively, 42 °C and 1200 psi for equilibration for more than 4 min [15]. The pressure was then reduced (<100 psi/min) at constant temperature (32 °C) until the samples were dried. The samples were stored under desiccant at room temperature, and the authors noted no obvious changes to the samples after one week of storage. This

protocol was repeated by Paunescu et al. to preserve the morphology of rat and mouse epididymal tissue [65]. (III) Hexamethyldisilazane (HMDS): Low-tension media, such as HMDS, can be added after the final stage of ethanol dehydration. This method is most often used as an alternative to CPD due to the ease and rapidity of application. However, its carcinogenic properties mean that careful handling is necessary. Several studies have applied HMDS treatment for HIM [17,60,64,66]. (IV) Air drying: During air drying, the liquid–gaseous boundary is crossed, leading to strong surface tension, which acts on the sample and causes damage to the structure, leading to agglomeration and collapse. Consequently, air drying should only be used as a last resort [60]. (V) Resin embedding: Samples can be embedded within a resin, such as epoxy, which infiltrates biological material and is later polymerised without affecting the cellular structure. For example, Bidlack et al. investigated tooth enamel, which contains both mineral and organic phases, in a three-dimensional configuration [67]. They found the best preparation method was to first fix the sample chemically and then perform a gradual ethanol substitution with LR White acrylic resin. Samples were then polymerized at 60 °C for 24 h and allowed to cool. The blocks were then polished at room temperature to expose the area of interest within the tooth enamel.

As biological samples are electrical insulators, charging effects typically affect the imaging quality in conventional SEM. Various approaches are used to remove the charge, including coating with electrically conductive materials, such as carbon, platinum, or gold. Coating the samples can, however, result in minute changes to surface features which are only visible at very high resolution. One of the main advantages of HIM is the ability to neutralise charge by implementation of an electron flood gun. This flood gun eliminates the need for coating biological samples with conductive materials to obtain high-resolution information. In fact, this is often cited as one of the main benefits of using HIM and has been reported in a number of publications focusing on biological samples [11,62,65].

Ionic liquid preparation

An alternative approach to the fixation, dehydration, drying, and even coating stages outlined above is to apply ionic liquids during sample preparation. Ionic liquids are organic salts with low melting points which are fluid at room temperature. They are persistent as liquids under the high-vacuum conditions of a typical electron microscope and exhibit conductive properties. This means that samples can be immersed in an ionic liquid, for 10–600 s, blotted, loaded onto a sample holder, and then imaged [68]. Compared to other preparation techniques, the preparation time using ionic liquids is extremely short and the morphology is reasonably well maintained. However, the surface is less well preserved. Figure 4 shows a *Pseudomonas putida* biofilm imaged using HIM [69]. One image shows the biofilm prepared using ethanol dehydration followed by HMDS

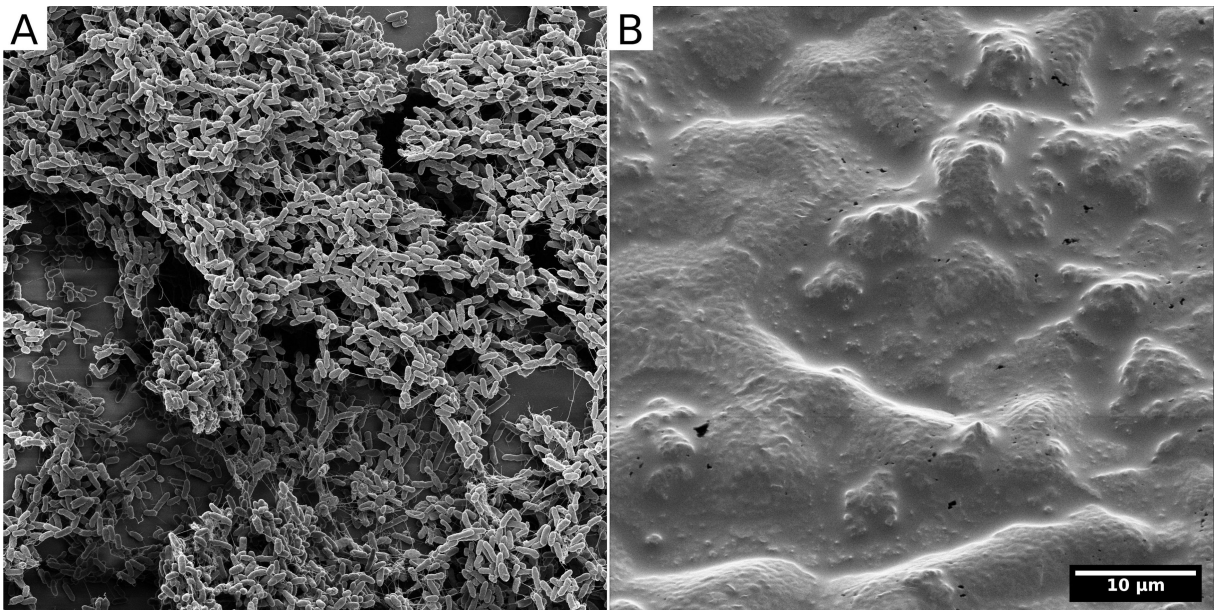

Figure 4: HIM of two *Pseudomonas putida* biofilms grown on polyvinylchloride coverslips in parallel under exactly the same conditions. Both films were chemically fixed with 2% glutaraldehyde for 2 h at room temperature. Subsequently (A) was dehydrated in a graded ethanol series and dried with hexamethyldisilazane. In contrast, (B) was not dried but the water was substituted with the ionic liquid 1-butyl-3-methylimidazolium tetrafluoroborate according to the protocol published by Golding et al. [69]. Unpublished data, sample provided by Nedal Said.

drying (Figure 4A). The other image shows the biofilm prepared with an ionic liquid (Figure 4B). Though the HMDS-prepared sample clearly shows a high density of individual bacteria, the ionic liquid treatment appears to have maintained the EPS and is perhaps a better representation of the true biofilm. Nevertheless, this study suggests that multiple preparation treatments should be applied to best image a sample.

HIM in medical research

Besides the example micrograph of a white blood cell published by Ward et al. in 2007 [2], the usage of HIM for medical studies did not begin until around 2011 when Arey et al. reported on the interaction of alveolar epithelial cells with silica nanoparticles with HIM at the Microscopy and Microanalytics Conference 2011 [11]. In their abstract, they suggested that Rutherford back-scattering imaging in the HIM enables the distinction of nanoparticles from cell surface structures at nanometre resolution. In a different study published in the same year, Bazou et al. employed HIM to image human colon cancer cells (Caco2) [9]. The glutaraldehyde-fixed and freeze-dried cells were imaged by both HIM and SEM to enable the direct comparison between the two instruments. HIM analysis of gold-coated and uncoated samples showed that coating, as required for SEM, introduces artefacts such as a granular structure on the cell surfaces and a partial closing of pores, thus highlighting one of the benefits of HIM. Bazou et al. also studied tumour cell-induced platelet aggregation by fluorescence microscopy and HIM. In this study, HIM provided high-resolution insight into the complex network of interactions of platelets with cancer cells [10].

In 2012, Berg-Foels et al. used transmission electron microscopy, SEM, and HIM to image rabbit cartilage samples [70]. The long depth of field provided by HIM renders the technique particularly powerful for imaging the three-dimensional articular cartilage collagen networks at a resolution of down to 0.81 nm (Figure 5).

Another application benefiting from the large depth of field and the possibility to work without coating the sample with metal is the use of HIM for the investigation of the development of mammalian tooth enamel [67,71]. Tooth enamel consists of hydroxyapatite crystals, which form needle-shaped nanocrystals of several micrometres length with a diameter below 100 nm. HIM revealed insight into the complex interactions between the enamel-forming cells, matrix proteins, and the mineral phase [71]. Bidlack et al. visualised the amelogenin proteins involved in tooth enamel development in a study combining SEM and HIM for three-dimensional imaging [67].

In 2013, Rice et al. presented the, to the best of our knowledge, first images of immunogold labels detected by HIM [15]. For this study, the authors used the proximal tubule marker gp330/megalin and wheat germ agglutinin to label surface glycoproteins of the proximal tubule in mouse kidneys. Conjugation

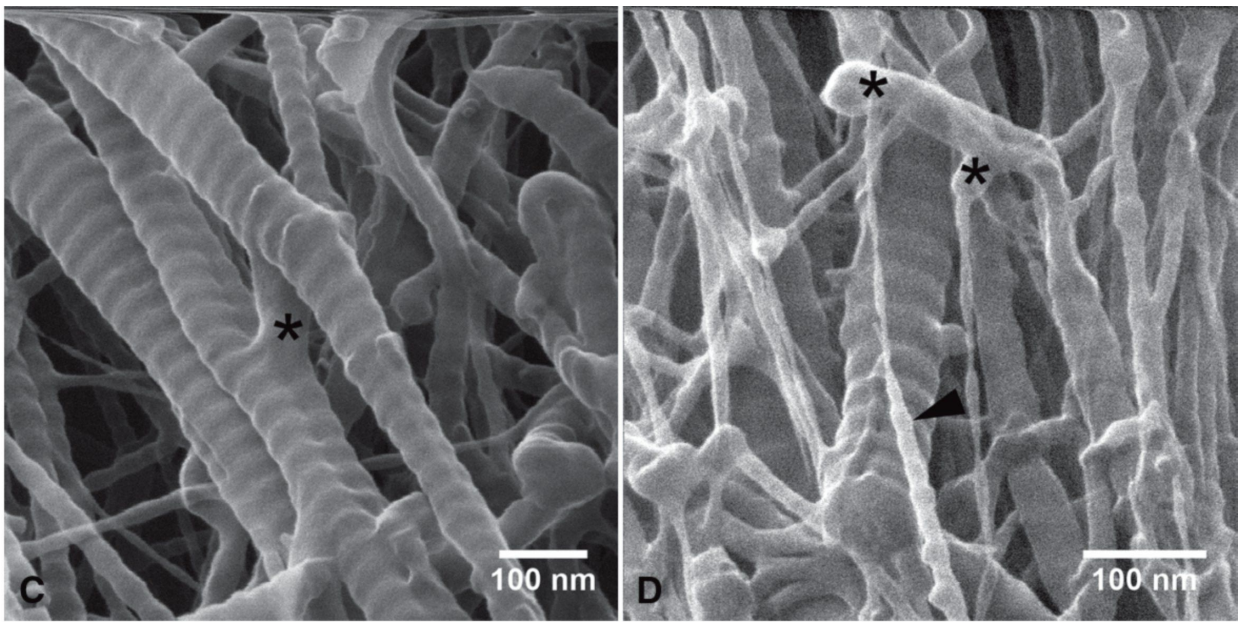

Figure 5: Rabbit cartilage collagen imaged by HIM. High resolution and depth of field reveal nanoscopic network features such as nanofibrils and their connections (asterisks). Dwell time and resolution are, respectively, 2 µs, 0.90 nm (left) and 0.5 µs, 0.81 nm (right). Reproduced from [70]. Copyright ©2012 The Authors Journal of Microscopy; ©2012 Royal Microscopical Society. Used with permission from Vanden Berg-Foels et al., Helium ion microscopy for high-resolution visualization of the articular cartilage collagen network, Journal of Microscopy, John Wiley and Sons.

to 26 nm colloidal gold allowed the authors to visualise the label with the HIM (Figure 6). Soon afterwards, a number of publications on HIM imaging of kidneys were published. Paunescu et al. focused on the microstructures of the kidney glomerulus as well as on the brush border microvilli of the proximal convoluted tubules [72]. On the latter they found "micropits on the microvillar surface as well as thin filaments joining adjacent microvilli" at high magnification. Tsuji et al. investigated the alteration of endothelium and podocytes during progressing glumerulopathy in Col4a3 (Alport syndrome) mice [73]. HIM was used to visualise the podocyte and endothelial interface, which, in contrast to previously published transmission electron micrographs of sections, provided pseudo-3D data. The authors pointed out that using conventional SEM it was not possible to determine whether the glomerular basement membrane defect affects the endothelial structure. However, they stated "HIM allows the endothelial surface to be directly and clearly visualised."

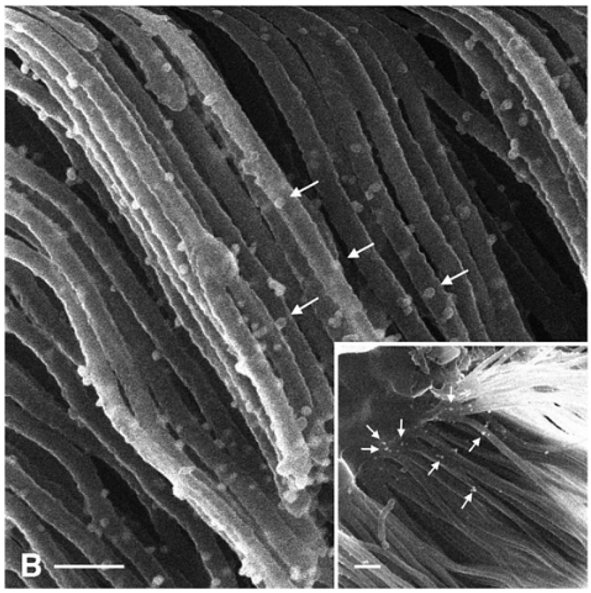

Figure 6: Helium-ion micrograph showing an immunogold-labelled (arrows) proximal tubule in a mouse kidney. Scale bar is 200 nm. Reproduced from [15]. Copyright ©2013 Rice et al., distributed under the terms and conditions of the Creative Commons Attribution License CC BY 4.0., https://creativecommons.org/licenses/by/4.0/.

Using HIM, Schürmann et al. impressively showed how closely ultrastructural details of cell membranes visualised by HIM are linked to sample preparation [16]. In the study, lipid nanodomains in mammalian cells were investigated. HIM was used to image osmium tetroxide-fixed, uncoated, and critical-point-dried human neurons and mouse hippocampal neurons. The achieved lateral resolution of 1.5 nm allowed for visualising pits in the ultrastructure of the cell membranes. Based on that finding the authors hypothesised "that the pit-like domains are a direct visualization of the shape of membrane nanodomains, including lipid rafts and caveolae." It was concluded that the pits result from the sample preparation since "the cell fixation with OsO_4 cross-links the lipid bilayer outside the nanodomains while the lipid bilayer inside the nanodomains is removed by the required subsequent rinsing with ethanol for the cell drying process." In turn, the pits in the HIM image reveal "the shape of the nanodomains as missing lipid bilayers."

In 2018, HIM was used to study peptide nanostructures for the first time. Herrera et al. studied the initial stages of the oligomerisation of the 33-mer peptide gliadin [74]. The HIM data helped the authors to "show a plausible pathway of 33-mer peptide protofilaments formation" via the contact of square-like oligomers and the formation of protofilaments by "longitutinal association of matured rod-like oligomers."

Imaging animals and plants

HIM imaging of small animals and plants has been around since the early years of helium ion microscopy, when pollen samples [7,8] and pine leaves [14] were imaged. The first in-depth and notable HIM imaging demonstration of small animals was done in 2012 by Boden et al. [12], when the intricate micro- and nanostructures responsible for the structural colouration of the wings of two different butterfly species, *Papilio ulysses* (Blue Mountain Butterfly) and *Parides sesostris* (Emerald-patched Cattleheart), were imaged to a level of detail not obtained previously with SEM. The study took advantage of the strengths of HIM producing images with a large depth of field and a high level of surface detail (Figure 7). The work also directly demonstrated the superiority of HIM at high magnifications over environmental SEM, the older technology for high-resolution microscopy of uncoated insulating samples. In addition, the large depth of field of the HIM was exploited in an innovative way by creating stereo pairs of images.

Fairly soon after applying HIM on butterflies, HIM was also used for ultrastructural analysis of both wild-type and genetically modified fruit flies, *Drosphila melanogaster*, by Boseman et al. [13]. Many different areas were imaged such as the eye, the wing and body surfaces, the sensory bristles, and the legs, with observations of nanoscale features. In addition, the pupal case and some larval tissues were also investigated.

In 2013, Joens et al. [6] published a groundbreaking study regarding biological HIM imaging of a whole variety of biological samples, including plants, bacteria, cancer cells, and a nematode worm, *Pristionchus pacificus*. The imaging of that worm will be discussed later in the section "Nanofabrication" regarding its innovative use of the combination of milling and

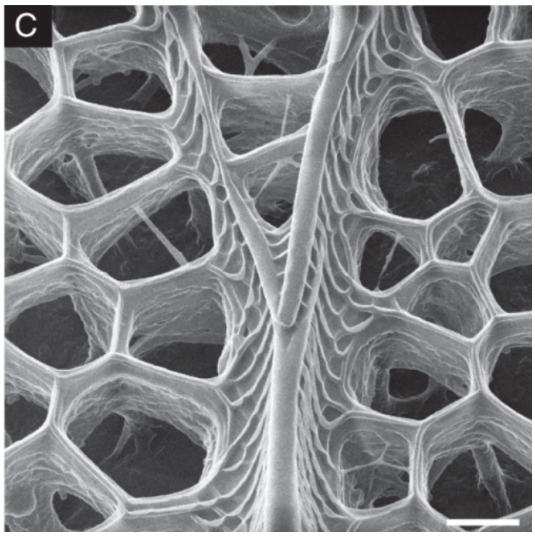

Figure 7: HIM image of a *Papilio ulysses* butterfly black ground scale. Scale bar is 400 nm. Adapted from [12]. Copyright 2011 ©Wiley Periodicals, Inc. Used with permission from Boden et al., Helium ion microscopy of Lepidoptera scales, Scanning, John Wiley and Sons.

imaging. Plant imaging was done on the model species *Arabidopsis thaliana*. The HIM images of the uncoated cuticle samples showed fine textures and minute ridges not discernible in the low-voltage field-emission SEM images of the same samples. *Arabidopsis* samples were also HIM-imaged by Curtin et al. [75]. Their study examined how the surface texture of genetically different samples varied after acid treatment to see the potential for enzymatic biofuel production.

HIM imaging was once again used in studies of insect wings and their nanostructures by Bandara et al. [76,77]. In this case, a nanopillar texture on the wing of a dragonfly *Orthetrum villosovittatum* was studied. In addition to imaging the wing alone, samples were prepared with *E. coli* bacteria on them, to study the bactericidal properties of the nanostructure. Along similar lines, the nanostructures on the wings of three different species of *Cicada* were imaged using HIM in [78].

Microbiology

HIM imaging has already been used to study numerous microorganisms including bacteria [6,18,19,60,79,80], bacteriophages [17,18,81], yeast [82], protozoa [83-85], and microalgae [46]. The highly resolved and contrast-rich views of the tiniest creatures that were obtained in these studies are discussed in the following.

Virus particles/bacteriophages

Bacteriophages are viruses that use bacteria as hosts, often causing lysis of the bacterial cell at the stage where new virus particles are released from the cell. For this reason, they have long been considered as possible treatments for bacterial infections. In particular, because they are host-specific and, therefore, do not exhibit some of the side effects of the more broadly affecting chemical antibiotics, which can lead to evolution of strains with broad antibiotic resistance.

Microscopy of bacteriophages has a long history, going all the way back to 1940, as one of the very first imaging applications of the newly invented electron microscopes (for a review see [81]). Ever since, TEM has been the mainstay of phage microscopy, but the complexities of TEM and SEM sample fabrication (lamellae preparation and conductive coatings) have hindered the studies of phage–bacterium interactions in their natural microbial environments.

HIM imaging of phages and phage–bacterium interactions were performed for the first time in 2017 in [17] for bacterial colonies of *E. coli* on an agar substrate. Different stages of the phage life cycle were imaged by looking at different regions of the viral plaques caused by the initial T4 phage infection seeded at the centre of the plaque. Figure 8 shows some examples of the detail obtained in this study. In particular, the changes in the appearance of the phage during active infection (contraction of the tail and spread-out of the tail fibres) were imaged.

Only a few works followed after this initial demonstration of the HIM capabilities for bacteriophage studies, although there is clearly a potential to image many more types of phage–bacterium systems. One more recent example was in a study by Sharma et al. [18] in which environmental sediment samples were imaged using HIM with findings of viruses attached to bacteria.

For bacteriophage imaging, the strength of HIM lies not just in the resolution, which is higher than that of SEM, but in the possibility to study the phage–host interaction, with a sufficiently high resolution to see nanometre-scale details of the phage particles (Figure 8).

Predatory bacteria

Similar to bacteriophages, predatory bacteria are bacterial parasites. In contrast to bacteriophages, predatory bacteria have a metabolism and undergo cell division for reproduction. However, compared to other bacteria, metabolism and reproduction are very uncommon and require preying on other gram-negative bacteria [86]. Therefore, following the philosophy of “the enemy of my enemy is my friend”, bacterial predators are promising candidates for “living anti-biotics” [87]. While bacteriophages are very host-specific, *Bdellovibriones* can be considered as broad-spectrum antibiotics, as they can potentially infect all gram-negative bacteria. Considering the 2017 priority list of

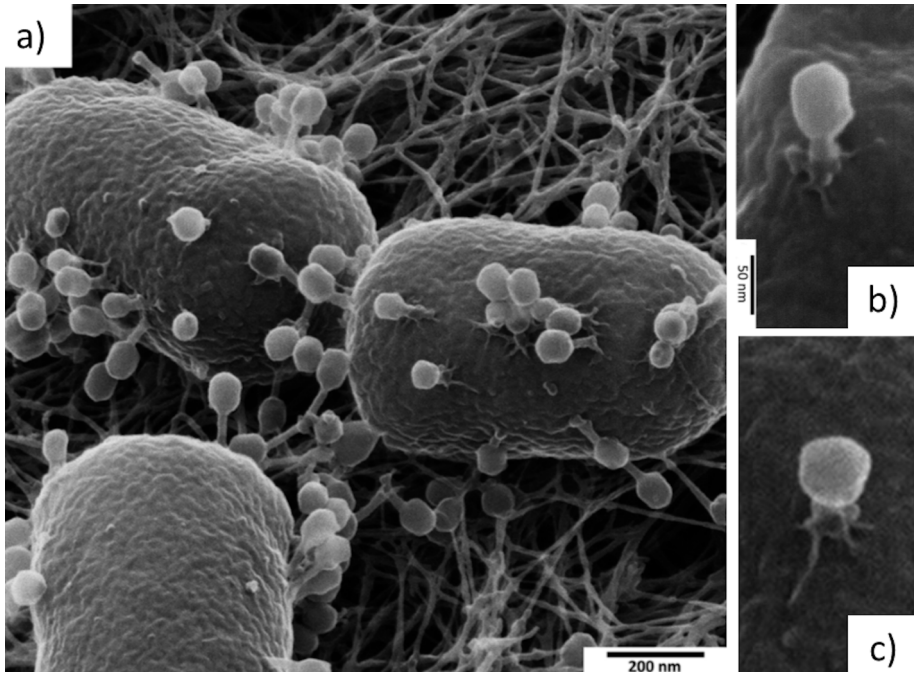

Figure 8: Helium-ion micrographs of the T4 bacteriophage infecting *Escherichia coli*. (a) Three bacteria with ongoing infection. (b) A higher-resolution image of a single T4 bacteriophage attached on the cell surface. The tail is contracted and the tail fibers are spread out, indicating a genome injection in progress. The icosahedral shape of the head is also apparent. (c) Another individual phage with even more contracted tail. Adapted from [17]. Copyright ©2017 WILEY-VCH Verlag GmbH & Co. KGaA, Weinheim. Used with permission from Leppänen et al., Imaging bacterial colonies and phage-bacterium interaction at sub-nanometre resolution using helium-ion microscopy, Advanced Biosystems, John Wiley and Sons.

antibiotic-resistant bacteria published by the World Health Organisation, the targeted use of *Bdellovibrio* would be a strong means to fight the three highest-priority strains, which are all gram-negative [88].

Said et al. investigated the life cycle of the bacterial predator *Bdellovibrio bacteriovorous* HD100 with the HIM [19]. At time $t = 0$ they combined cultures of *Bdellovibrio* and prey, for example, *Escherichia coli*, and stopped the experiment by chemical fixation at specific points during incubation. This allowed for the study of the attachment of the predator to its prey, followed by penetration of the membrane, and the entering into the cytoplasm. After that, the prey cell is transformed into a bdelloplast, in which the predator elongates and divides. In a final step, the bdelloplast lyses and the *Bdellovibrio* offspring is released and ready to attack another cell. A HIM micrograph of the attachment of a *Bdellovibrio* to *E. coli* is shown in Figure 9. Again, it is not merely its high resolution but rather surface sensitivity and charge compensation that make HIM an excellent tool to study interactions of bacterial predators with their prey.

Eukaryotic parasites

Unicellular parasitic eukaryots have also been imaged using HIM. In 2015, de Souza and Attias investigated *Toxoplasma gongii*, an obligate intracellular parasite which causes the disease toxoplasmosis [83]. Extracellular *Toxoplasma gongii* are found to be "teardrop-shaped" with an apical conoid. Rhesus monkey kidney cells were infected with *Toxoplasma gongii*. After dry-cleaving, parasitophorous vacuole in the cells were exposed and the intracellular parasite was imaged. The helium-ion micrographs revealed an intravacular network of tubules formed by *Toxoplasma gongii* (Figure 10).

In the same year, Gadelha et al. investigated *Giardia intestinalis*, a flagelled parasite causing the diarrheal disease giardias, with ultrahigh-resolution SEM and HIM [84]. Of particular interest to the authors was the cytoskeleton of *Giardia intestinalis* for which HIM enabled the visualisation of "a lattice-like array material that covered the microtubular sheets of the funis." A review article on protozoa imaging by de Souza and Attias nicely placed HIM imaging in the context of high-resolution SEM, environmental SEM, cryo-SEM, the usage of cytochemistry, and 3D reconstruction with focused ion beam SEM and TEM [85].

Biofilms

The large depth of field, the efficient charge compensation and the strong edge contrast make HIM an excellent tool for the visualisation of the structural organisation of biofilms. To date,

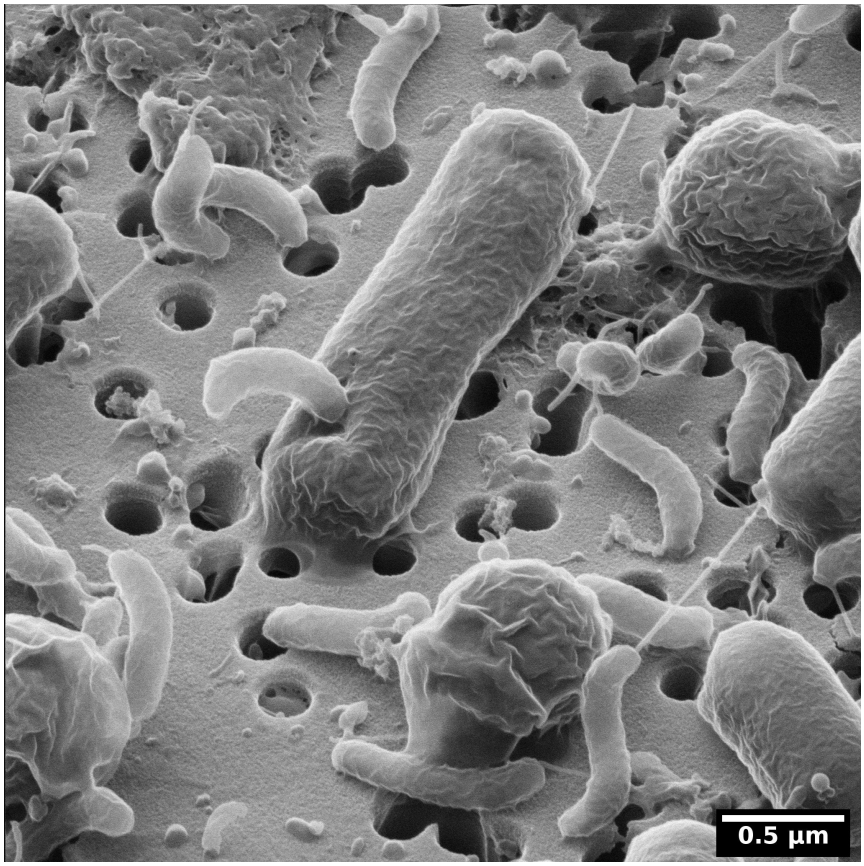

Figure 9: Helium-ion micrograph of the predatory bacterium *Bdellovibrio bacteriovorus* infecting *Escherichia coli*. The sample was prepared by M. Krüger and N. Said as preliminary work for the study published in [19].

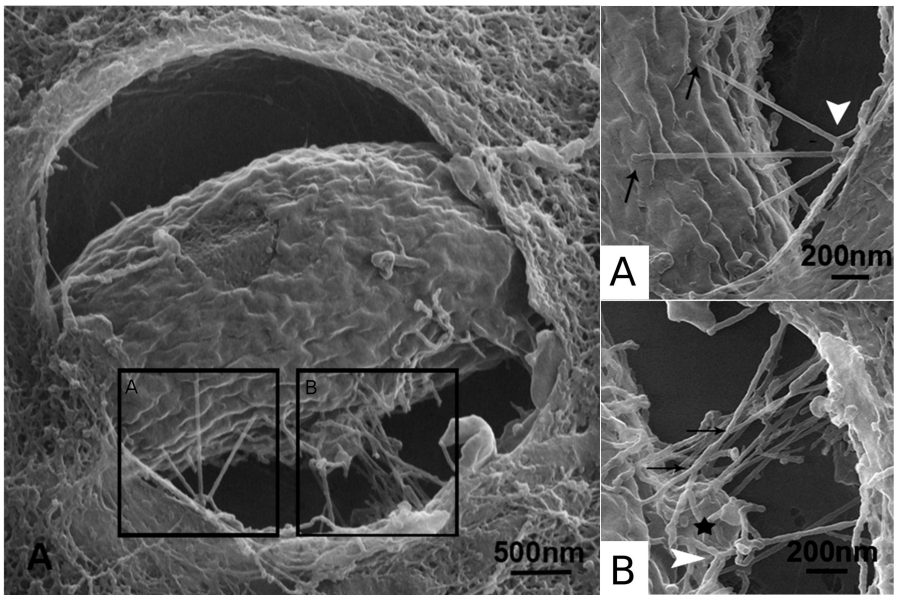

Figure 10: HIM of *Toxoplasma gongii* inside a vacuole of an infected Rhesus monkey kidney epithelial cell. The close-ups (A) and (B) show the intravacuolar network of tubules formed by the parasite soon after invasion. White arrows point at bifurcating tubules, black arrows point at crossing tubules that do not fuse. Adapted from [83], Journal of Structural Biology, Vol. 191(1), by de Souza et al., “New views of the Toxoplasma gondii parasitophorous vacuole as revealed by Helium Ion Microscopy (HIM)”, pages 76–85, Copyright (2015), with permission from Elsevier.

the great potential of HIM for the analysis of biofilms has not been fully exploited yet and only few publications exist. To our knowledge, the earliest publication in this direction is the extended abstract of LeTourneau et al. on rhizobacterial biofilms in the proceedings of Microscopy and Microanalytics 2015 [89]. On wheat roots, they grew a phenazine-1-carboxylic acid (PCA)-producing fluorescent pseudomonad strain and an isogenic mutant impaired in the synthesis of PCA. The formation of the rhizobacterial biofilm on the root under dryland and irrigation conditions was studied by fluorescent microscopy and SEM on a larger scale. HIM was used to visualise the nanostructure of the bacterial colonies; however, no micrographs with sub-20 nm resolution are shown. The second publication is an extended abstract by Belianinov et al. on the investigation of the biofilm structure of *Geobacter sulfurreducens* by HIM [79]. The helium-ion micrograph of the bacterium shown in this abstract displays the importance of an appropriate preparation of the sample. The preparation method used by the authors – chemical fixation in 4% formaldehyde, rinsing in buffer, dehydration with ethanol, and air-drying – did not suffice to maintain the ultrastructure of the cell membrane as well as the fine layer of EPS, which HIM can, in principle, visualise.

In the context of the microscopic analysis of bacterial and archaeal viruses of the Himalayan hot springs at Manikaran, Sharma et al. [18] imaged microbial mats with the HIM (Figure 11). The variety of microbes embedded in EPS shows the complexity of natural biofilms. Preparing these samples for HIM is difficult because each fixation, rinsing, dehydration, and drying step is a trade-off between preservation of the cell morphology, avoiding precipitates on the sample and maintaining the filigreed EPS. Therefore, Sharma et al. used a protocol both simple and effective: The sample was kept in the medium (water from the hot springs at Manikaran) to which gently and slowly ethanol was added. Once a concentration of about 70% ethanol was reached, the sample was kept in the fridge overnight in order to use the gentle fixation effect ethanol provides [90]. Subsequently, the ethanol/medium mixture was pipetted off and the sample was treated with a graded ethanol series to finish the dehydration. After critical point drying the sample was ready for HIM analysis.

Moreno-Osorio et al. [46] investigated biofilms formed by *Chlorella* microalgae of which an example is shown in Figure 12. In this study, the biofilm was fixed in 4% paraform-

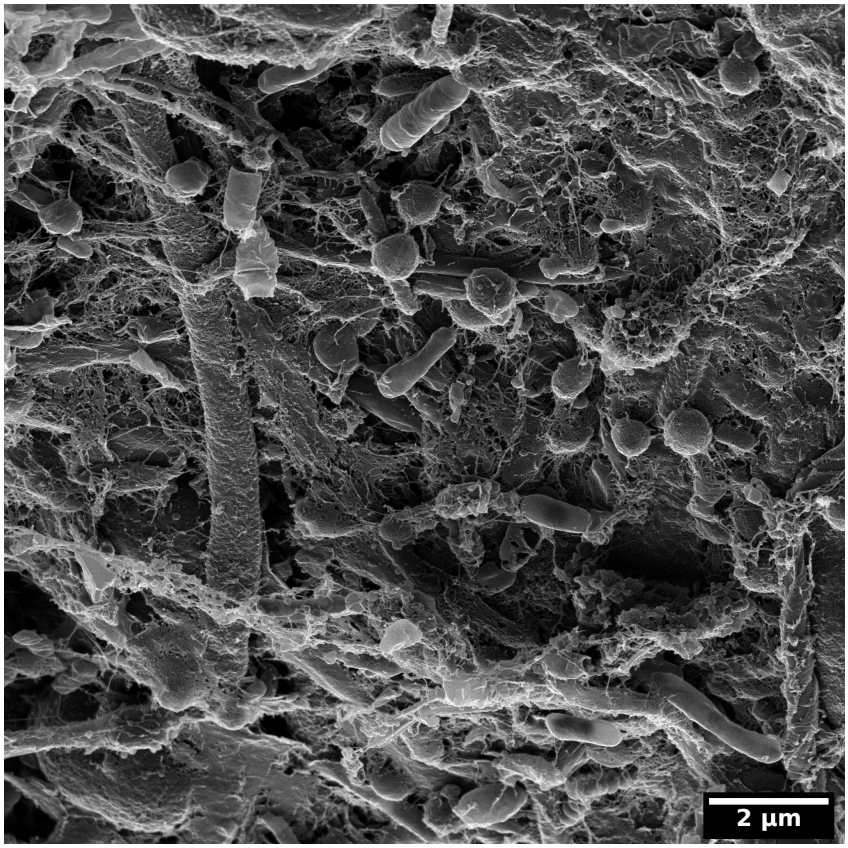

Figure 11: Microbial mat collected at the Himalayan hot springs at Manikaran imaged with the HIM. Unpublished data from the study of A. Sharma et al. [18].

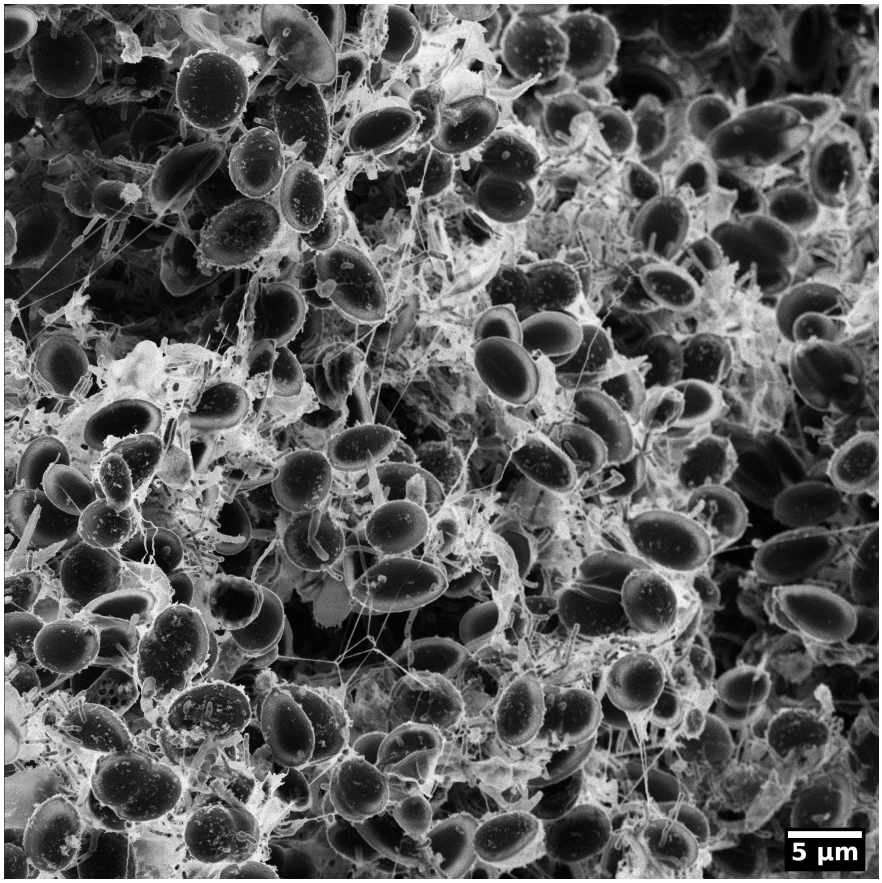

Figure 12: A biofilm of *Chlorella* microalgae imaged using HIM. Charge compensation allowed for imaging the biofilm without any metallisation. The exopolymeric polymeric substances between the algal cells are visualised with high contrast owing to the high surface sensitivity of the HIM. The sample was prepared by J. H. Moreno-Osorio within the study published in [46].

aldehyde dissolved in sodium cacodylate buffer for 2 h at room temperature, followed by rinsing in buffer to remove precipitates. Subsequently, the sample was dehydrated in a graded ethanol series and critical point dried. This approach results in an excellent preservation of the algal cells, however, at the cost of a partial shrinkage of the EPS. The micrograph was recorded using secondary electron imaging. The high surface sensitivity and the strongly pronounced edges in this imaging mode render the thin EPS between the algal cells bright white. Furthermore, it is remarkable that despite the strong topography of more than 20 µm in the field of view, almost the entire image is well focused owing to the large depth of field of the HIM.

Geomicrobiology

Microbe–mineral interactions are fundamental to many processes taking place in the environment such as rock weathering, nutrient release, toxic metal(loid) mobilization, and greenhouse gas formation [91]. However, the combination of soft biological material with hard minerals brings unique challenges to imaging these interactions at nanoscale resolution. Traditionally, scanning electron or transmission electron microscopy techniques have been applied to great effect to study many aspects of microbe–mineral interactions, such as the formation of intra- or extracellular mineral precipitates, or intracellular organelles associated with energy gain or electron transfer [92]. However, over recent years, the number of articles related to geomicrobiology and containing HIM data has increased. This is due to several factors such as the ability to image without first coating a sample with conductive materials (e.g., Pt, Au, or C). Such coatings have been shown to cause artefacts which can be misinterpreted as being from the material under investigation [6]. Furthermore, helium ions have a smaller interaction volume with a sample than electrons. This means that HIM can be used to provide better material contrast and depth of focus compared to SEM. Consequently, HIM is considered as a viable alternative to SEM for studying processes in geomicrobiology, with a steadily increasing number of published articles reflecting this fact.

One area which has seen increasing use of HIM is the investigation of redox interactions between iron-metabolizing bacteria with ferrous (Fe(II)) and ferric (Fe(III)) iron. The ubiquity and availability of iron on Earth has led to the evolution of Fe(II)-oxidizing and Fe(III)-reducing bacteria, which use Fe(II) and Fe(III) as electron source and sink, respectively. Three types of Fe(II)-oxidizing bacteria are thought to exist under neutrophilic conditions in the environment including phototrophs, microaerophiles and nitrate-reducers [93]. Phototrophic Fe(II) oxidizers use light as energy and Fe(II) as an electron source for growth. They are thought to have been partially responsible for the deposition of banded iron formations during the Archean. Laufer et al. [66] isolated a halotolerant anoxygenic phototrophic Fe(II)-oxidizing green sulfur bacterium from a marine sediment and used HIM to show the surface of the cells to be smooth and free of iron minerals. This lack of cell-surface encrustation is considered to be an important identifier. Byrne et al. [80] used HIM to investigate the formation of organic–metal fibres, known as twisted stalks, by microaerophilic Fe(II)-oxidizing bacteria. These stalks consist of organic material as well as nanometre- and micrometre-sized iron minerals which are loosely bound to the bacterial cells (Figure 13). It is thought that these appendages help to eliminate Fe(III) waste produced during Fe(II) oxidation and provide a surface for the sorption of nutrients as well as heavy metals. In the study, Byrne et al. took advantage of the flood gun to analyse the development of twisted stalks over time without coating the samples with a conductive material. They observed the precipitation of lepidocrocite plates, which appeared to grow and become denser over time. Regarding nitrate reducers, Joens et al. [6] published the earliest article using HIM to investigate microbe–mineral interactions. The authors compared the performance of both SEM and HIM for studying the nitrate reducer *Acidovorax sp.* BoFeN1. The authors noted the ability of HIM to greatly reduce charging artefacts associated with field-emission SEM. The same organism was also investigated by Zeitvogel et al. [60]. They investigated the effect of preparation approaches on sample preservation and how this affects the quality of the HIM micrographs (see section “Sample preparation”). Nordhoff et al. [94] applied HIM to investigate microbe–mineral associations for culture KS, which is another nitrate-reducing Fe(II) oxidizer and is in fact the only widely accepted bacterium which is able

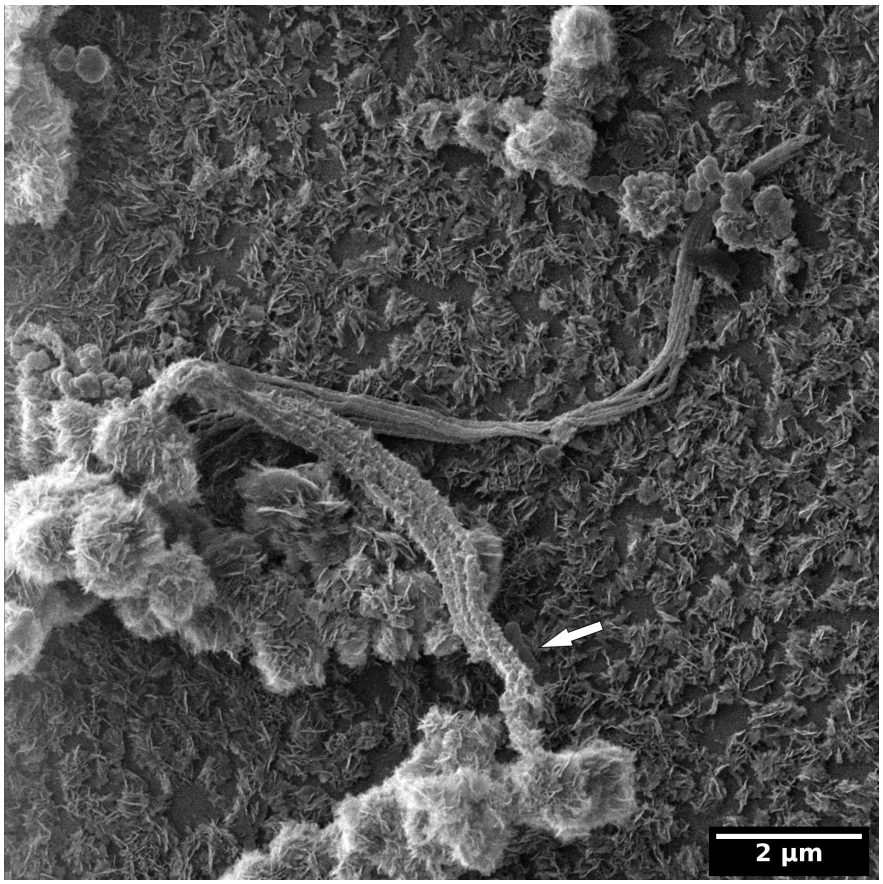

Figure 13: Helium-ion micrograph of a twisted stalk produced by a microaerophilic Fe(II)-oxidizing bacterium (unpublished). The white arrow indicates a single bacterium.

to enzymatically couple nitrate reduction with Fe(II) oxidation. To date, there are not many studies which have applied HIM to study microbial Fe(III) reduction. The study by Belianov et al. [79], who imaged a biofilm of the Fe(III)-reducing bacterium *Geobacter sulfurreducens*, is the only published example, to the best of our knowledge.

Apart from iron geomicrobology, a study by [95] used HIM to characterise the colonization of mineral substrates by the soil mineral-weathering microorganism *Pinus resinosa*, which is widespread in North American pine forests. Through correlative approaches with TEM, SEM, HIM, and X-ray tomography, they were able to gain insight into microbially driven weathering processes under nutrient-rich conditions. Mineral weathering was also assessed by [96] and [97], who developed methods to analyse biological and geochemical drivers of weathering in natural settings. HIM was used to image sub-nanometre mineral–organic interactions, whereas SEM (EDX) was used for elemental quantification. They preferred the superior imaging capabilities of the HIM to image minerals weathered in soil mesh bags filled with granular granite, basalt, and quartz (53–250 µm), which were deployed in the field for one year. They were able to identify grain microtopography and nanocrystal edges characteristic of quartz, lamella structures and smooth surfaces of biotite in the granite, and vesicles of basalt embedded with amorphous glass. The HIM also revealed a fungal hyphae network in all samples with nanoscale imaging suggesting accelerated weathering along the mineral surface due to biological interactions. Moreover, HIM is being applied for soil-based studies. Biochar, a carbon-rich material formed by the pyrolysis of biomass is under fervent research because of its ability to improve soil quality and improve agricultural productivity. Rasa et al. [98] used HIM to investigate the relationship between internal porosity and pore size distribution of biochar. HIM indicated that cell-wall structures in biochar do not contain visible nanoscale pores and suggest that the water storage and flow within willow biochar takes place in cylindrical capillaries. LeTourneau et al. [99] used SEM, HIM, and NanoSIMS to show that phenazine-1-carboxylic acid, produced by rhizobacteria in unirrigated wheat fields, and soil moisture promotes biofilm formation at root surfaces.

With the exception of Joens et al., all other geomicrobiology-related studies using HIM have been published in the past three years. Most recently, HIM was used to great effect, such as for studying vesicular structures budding off an ethane-degrading anaerobe (*Candidatus Argoarchaeum ethanivorans*) [100]. Overall, it is thus clear that HIM is an extremely powerful technique and is likely to be used increasingly in the field, especially, if analytical capabilities soon become more widespread.

Nanofabrication

Ion microscopy has the added benefit over electron microscopy that the same instrument has the capability not only to image, but to also mill away parts of the sample material. The change between the two functionalities depends on the ion current and ion species. With sufficiently high currents, even He ions can mill materials. In recent years, another ion species also became available as an option in the commercial instruments, namely neon. As Ne is much heavier than He, it has a stronger milling capability, with the trade-off of reduced resolution. Initially, He-ion milling with HIM was used in non-biological applications such as the direct fabrication of graphene nanostructures and sub-5 nm size nanopores in suspended membranes. We will not review these applications in detail here, as they have been discussed in earlier reviews [101,102].

It is worth mentioning that some of the known nanopore applications are linked to biology, as nanopore membranes could be used for advanced DNA sequencing technologies or the filtration and detection of biomolecules. In contrast, much less work has been done regarding the milling of biological samples, which will be reviewed below.

One of the first practical examples of using the combined imaging and milling capabilities of a HIM in a biological study was demonstrated in the seminal work by Joens et al. [6], in which Ne-ion milling was used. They first imaged the mouth of a predatory nematode *Pristionchus pacificus* with HIM (Figure 14a) showing a membraneous sheath structure covering the internal mouth cavity. After that, the sheath structure was removed by milling, exposing the internal tooth structure, Figure 14b.

Combining HIM imaging and He- and Ne-ion milling for microbiological samples has also been initiated. In the HIM-imaging study of bacteriophage–bacteria interactions by Leppänen et al. [17], cross-sectional He-ion milling of a *E. coli* cell was demonstrated (Figure 15a). Controllable cuts were made, but the resulting exposed surface was smooth and did not show any detail. In particular, no internal cavity or structure was found. However, the image does also show a cut bacteriophage attached on the surface of the bacterium, with a hollow head. For another species, *Flavobacterium* sp. 183 on Si substrates, some indications of cross-sectional details were also reported. No clear explanations for the differences of imaging detail between the two cases were offered, but one should at least note the very different substrates (porous dried agar vs solid Si), which could affect heat dissipation, for example. In the same study, a larger trench with 13 µm × 5 µm area and several micrometres deep was also milled into an agar substrate with Ne ions, exposing a subsurface bacterial colony.

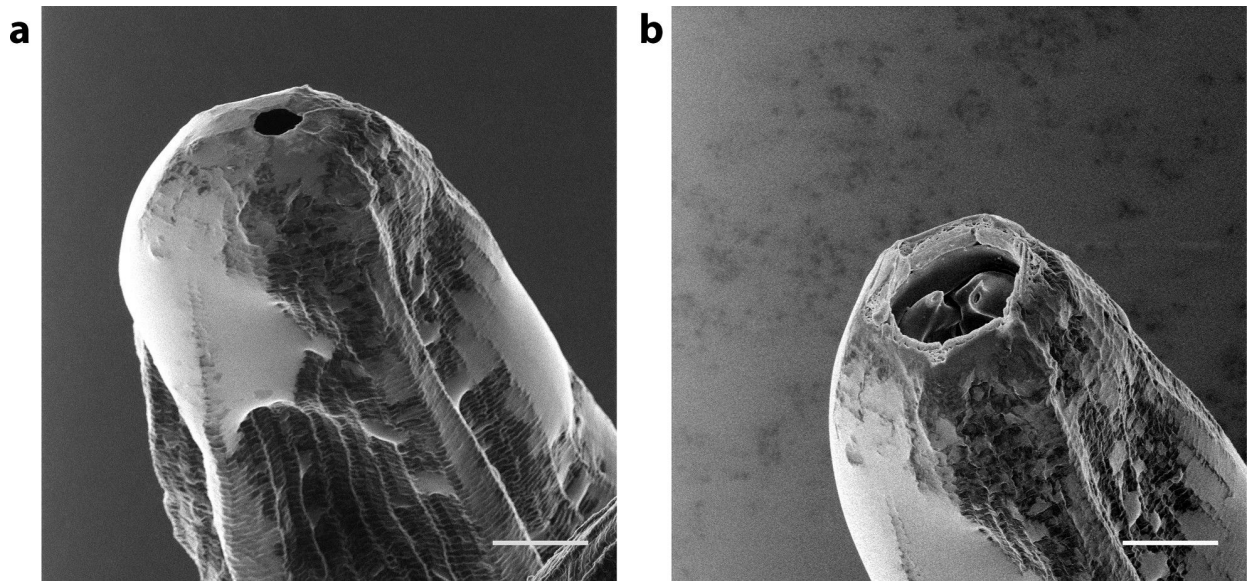

Figure 14: Helium-ion micrographs of the predatory nematode *Pristionchus pacificus* before (a) and after (b) the removal of the membraneous sheath covering the internal tooth structure by Ne-ion milling. Scale bar 5 µm. Adapted from [6], Joens et al., "Helium Ion Microscopy (HIM) for the imaging of biological samples at sub-nanometer resolution." Licensed under a Creative Commons Attribution-NonCommercial-NoDerivs 3.0 Unported License, http://creativecommons.org/licenses/by-nc-nd/3.0/. Copyright © 2013, with permission from Springer Nature. This figure must not be reproduced or adapted without permission from Springer Nature.

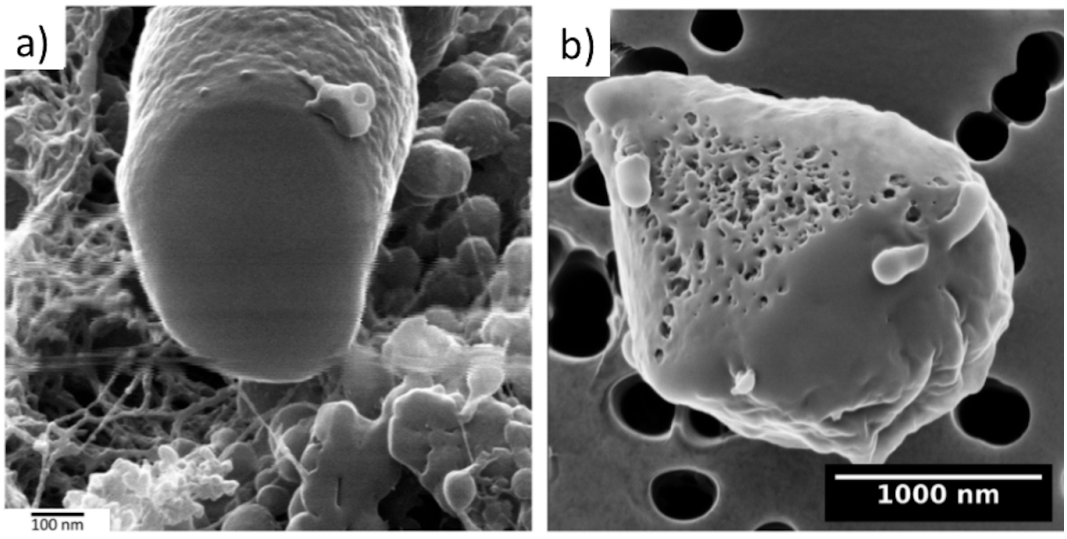

Figure 15: Helium-ion micrographs of sectioned microbiological samples. (a) He-ion-milled cross section of a *E. coli* with a half-cut bacteriophage on top of it. (b) Ne-ion-milled cross section of a *Bdellovibrio-E. coli* bdelloblast with visible internal structure and *Bdellovibrio* progeny penetrating the membrane. Figure 15a adapted from [17], Copyright © 2017 WILEY-VCH Verlag GmbH & Co. KGaA, Weinheim. Used with permission from Leppänen et al., Imaging bacterial colonies and phage-bacterium interaction at sub-nanometer resolution using helium-ion microscopy, Advanced Biosystems, John Wiley and Sons; Figure 15b adapted from [19], Copyright © 2018 WILEY-VCH Verlag GmbH & Co. KGaA, Weinheim. Used with permission from Said et al., Have an Ion on It: The Life-Cycle of Bdellovibrio bacteriovorus Viewed by Helium-Ion Microscopy, Advanced Biosystems, John Wiley and Sons.

In an another HIM-imaging study on a microbiological sample by Said et al. [19], Ne-ion milling was used to make a cross section of a *Bdellovibrio-E. coli* bdelloblast shortly after lysis (Figure 15b). A porous internal structure was revealed, with *Bdellovibrio* progeny penetrating the membrane. It is possible that the use of a Ne ion beam with its stronger cutting efficiency helped to reveal the internal structure better than in the milling study of Leppänen et al. [17].

In a recent study on the microencapsulation of bacteriophages with a membrane emulsification process, the internal structure of the microcapsules was also studied with a combination of Ne-ion cross sectioning and HIM imaging [20,103]. It was shown that the method of sample drying (either freeze drying or critical point drying) had a strong influence on the observed internal structure. However, it was not stated which preparation method represented the true structure.

Very recently, Ne-ion milling in HIM was also used to make very precise cuts of a *E. coli* bacterium on a nanopillared dragonfly wing [104], at the exact location where the bacterial cell is attached to the wing (Figure 16). The following HIM imaging revealed intricate sharp structures at the interface between the bacterium and the nanopillared wing surface. Clear deformations of the bacterial cell were visible, without any evidence of piercing of the cell membrane by the nanopillars.

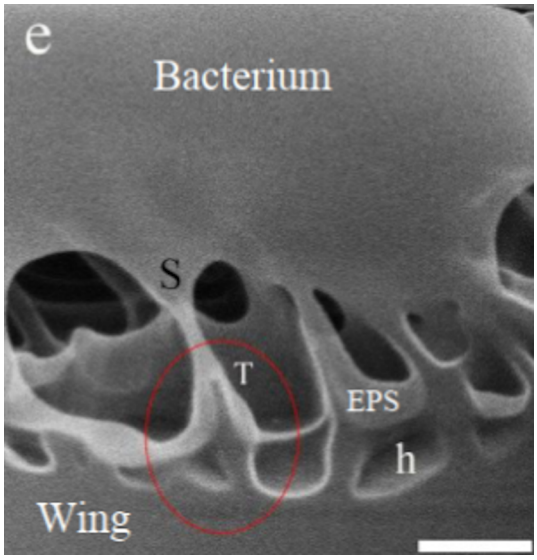

Figure 16: Helium-ion micrograph of a Ne-ion-milled section of a *E. coli*–nanopillared dragonfly wing interface. A partly deformed and stretched membrane is marked as "S", and the tip of a nanopillar as "T". Scale bar 200 nm. Adapted with permission from [104]. Copyright 2020 American Chemical Society.

All the above examples demonstrate that HIM milling combined with in situ HIM imaging is a promising novel avenue for the microscopy of subsurface structures and, sometimes, for cross sections. Internal porous structures are revealed particularly well. The strength of the technique is that the milling can be done in a point-and-shoot mode at a precisely determined location, in best cases at sub-nanometre resolution, without the typical and restricting resin-embedding and metal-coating techniques often used with focused gallium ion beam milling of biological samples in more common focused ion beam instruments.

HIM in correlative approaches

The triad of imaging, nanofabrication, and nanoanalytics puts HIM amongst the most versatile microanalytical tools available at present. However, HIM alone cannot solve every problem in microscopy. In subcellular chemical imaging, for instance, correlative workflows combining high-resolution electron microscopy and nanoanalytics (e.g., X-ray spectroscopy and SIMS) are currently being established [105]. It can be expected that HIM imaging, HIM-SIMS, and IL-HIM will soon become part of such workflows because HIM will be one means to push the limits of nanoanalytics to the (sub-)10 nm range. Early work in this direction was published by Chen et al., who imaged human liver cells correlatively by HIM and fast (1.2 MeV) helium ions [106]. This correlative microscopy approach connected surface-sensitive HIM with He-ion energy loss data which represents the mass distribution in the cell. Furthermore, the authors speculate that ion-induced fluorescence will allow for fluorescence microscopy at the nanometre scale. Sanders et al. reported a correlative study on the interaction of rat cortical neural progenitor cells with gold nanoparticles at the Microscopy and Microanalytics Meeting 2014 [107]. They used HIM alongside with optical and fluorescense microscopy, electron microscopy, and electron-microscopic tomography techniques to locate cells and nanoparticles. Fluorescent markers were used to identify neurons and astrocytes, which subsequently were found and imaged at high resolution. The correlative studies by Sato et al. [25] and Moreno-Osorio et al. [46] have already been discussed in previous sections. Recently, LeTourneau et al. published a correlative study on rhizobacterial colonies on wheat roots where stable isotope labelling in combination with NanoSIMS, electron microscopy, and HIM, was used to study the carbon and nitrogen cycles [99]. The influence of phenazine-1-carboxylic acid and soil moisture on the biofilm formation by rhizobacteria was investigated. In the workflow of analyses, as can be expected, HIM was used to obtain structural information at high resolution. However, in future correlative workflows with HIM-SIMS or IL-HIM the role of HIM may change towards its nanoanalytical capabilities.

Conclusion

The past decade of bio-imaging using HIM has seen the evolution of studies from those initially focused on the technological advantages of the instrument to more recent publications which use the HIM as part of a suite of tools to answer their research questions. This gradual change in the application of HIM provides an extremely positive indication that HIM has shifted from being highly specialised to being more widely applied and

used to reveal information which could not have been previously obtained with more conventional techniques. The current generation of HIMs has remarkable capabilities in terms of spatial resolution, very large depth of field, and the ability to image non-conductive samples without the application of conductive coatings. These technical capabilities place the imaging performance of HIM well above the most technologically advanced SEMs. This is particularly evident for the ability to interrogate non-conductive samples, as is the case for most biological materials, without first sputter coating with a heavy metal, such as platinum or gold. This is possible thanks to the presence of the flood gun, which is, in effect, a charge-compensating device. It floods the imaging area with electrons to remove excess charge from a sample and to prevent localised build-up beneath the incident ion beam. Furthermore, the low energy transfer between helium ions and secondary electrons means that only the very near surface of a sample is imaged, similar to using an SEM with low acceleration voltage. In this way, HIM has been able to image the surface of biological materials as close to the native state as possible, without defects and artefacts which are evident when imaging a coated sample at high resolution or with low-voltage electrons.

On top of its remarkable imaging capabilities the ion beam of the HIM is one of the most precise tools for nanoscale fabrication. It has been already used for milling delicate objects such as bacteriophages [17], bdelloplasts [19], and bacteria on natural nanotextured surfaces [104]. However, the full potential of HIM nanoscale fabrication for biological applications has certainly not yet been exploited. The potential future applications comprise, for instance, the sectioning of bacterial nanowires, which are produced by iron(III)-reducing bacteria as conductive appendages for electron transfer [108], to study their internal structure. Alternatively, nanoscale fabrication could be used to better understand biomineralization by bacteria in the environment. Milling experiments could also provide insight into the development and release of extracellular vesicles or viruses from cell membranes. In addition to microbiological applications, in general, subsurface imaging of any biological sample at a precisely defined location could become another application area, in particular, if porous features are to be expected.

Despite its power as an imaging device, the ability to obtain analytical information with HIM is still not widespread. However, an increasing number of instruments are being equipped with mass spectrometry (SIMS) detectors, which combine the high resolution provided by helium ions with elemental or isotope-selective quantification. This technology will remove one of the key differences between HIM and SEM. Other detectors, such as RBS and ionoluminescence, will further improve the capabilities of HIM to image and analyse biological samples. Advancements in the detection of transmitted helium ions with specifically designed ion detectors which are being developed as part of the npScope project mean that bio-imaging using HIM is likely to improve still further. Another important advancement that is anticipated to emerge in HIM instruments over the next few years is the ability to image samples at cryogenic temperature. This development would complement cryo-TEM and cryo-SEM, which are already established for studying hydrated and biological materials. Essentially, samples are rapidly frozen to cryogenic temperatures. This effectively fixes the samples without the requirement to use chemicals (e.g., glutaraldehyde), which can induce side reactions. The main technical requirement is a cryogenic sample stage to be mounted within the instrument, which can maintain the specimen temperature below −120 °C [109]. To the best of our knowledge, there is currently no HIM equipped with such a stage. However, the ability to combine cryogenic imaging of biological samples with the high-resolution and milling capabilities (see section “Nanofabrication”) would likely be of broad interest to the imaging community.

In this review paper, we have highlighted just some of the exciting developments which have been made with HIM in studies ranging from medical research to microbiology, plants, small animals, and geomicrobiology. From imaging white blood cells [2] to providing pseudo-3D micrographs of cartilage at unparalleled resolution [70], or from images of the nanopillar texture on the wings of a butterfly [12] to the precipitation of iron oxide minerals onto organic templates created by iron(II)-oxidizing bacteria [80], HIM bio-imaging offers enormous potential and we hope to see its adoption continuing to spread.

Acknowledgements

The authors wish to thank Yalda Davoudpour for providing the maize root sample shown in Figure 3 and Nedal Said for the preparation of the bacterial biofilms displayed in Figure 4. Furthermore, the authors thank Markus Krüger for providing the sample of *Bdellovibrio* infecting *E. coli* shown in Figure 9. For the biofilm samples displayed in Figure 11 and Figure 12 the authors are grateful to Anukriti Sharma and Jairo-Hernan Osorio-Moreno. The authors thank Chiththaka Chaturanga Devapriya Bandara Imihami Mudiyanselage for critically reading and commenting the manuscript. We are thankful for the use of the helium-ion microscope at the Centre for Chemical Microscopy (ProVIS) at UFZ Leipzig, which is supported by European Regional Development Funds (EFRE-Europe funds Saxony) and the Helmholtz Association, and for the use of the helium-ion microscope at University of Jyväskylä, which is funded by the Academy of Finland within the FIRI2014 programme.

ORCID® iDs

Matthias Schmidt - https://orcid.org/0000-0002-0161-8326
James M. Byrne - https://orcid.org/0000-0002-4399-7336
Ilari J. Maasilta - https://orcid.org/0000-0001-8566-1569

References

1. Ward, B. W.; Notte, J. A.; Economou, N. P. *J. Vac. Sci. Technol., B: Microelectron. Nanometer Struct.–Process., Meas., Phenom.* **2006,** *24,* 2871–2874. doi:10.1116/1.2357967
2. Ward, B.; Notte, J. A.; Economou, N. P. *Photonics Spectra* **2007,** *41,* 68–70.
3. Notte, J.; Ward, B.; Economou, N.; Hill, R.; Percival, R.; Farkas, L.; McVey, S. *AIP Conf. Proc.* **2007,** *931,* 489–496. doi:10.1063/1.2799423
4. Scipioni, L.; Stern, L. A.; Notte, J.; Sijbrandij, S.; Griffin, B. *Adv. Mater. Processes* **2008,** *166,* 27–30. Product code: ZAMP16606P27.
5. Carl Zeiss Microscopy, White paper: Zeiss Orion Plus (2008), (not available online anymore).
6. Joens, M. S.; Huynh, C.; Kasuboski, J. M.; Ferranti, D.; Sigal, Y. J.; Zeitvogel, F.; Obst, M.; Burkhardt, C. J.; Curran, K. P.; Chalasani, S. H.; Stern, L. A.; Goetze, B.; Fitzpatrick, J. A. J. *Sci. Rep.* **2013,** *3,* No. 3514. doi:10.1038/srep03514
7. Bell, D. C.; Erdman, N.; Jepson, M. A.; Rodenburg, C.; Inkson, B. J. *Microsc. Microanal.* **2009,** *15,* 652–653. doi:10.1017/s1431927609097025
8. Bell, D. *Microsc. Microanal.* **2011,** *17,* 660–661. doi:10.1017/s143192761100417x
9. Bazou, D.; Behan, G.; Reid, C.; Boland, J. J.; Zhang, H. Z. J. *J. Microsc. (Oxford, U. K.)* **2011,** *242,* 290–294. doi:10.1111/j.1365-2818.2010.03467.x
10. Bazou, D.; Santos-Martinez, M. J.; Medina, C.; Radomski, M. W. *Br. J. Pharmacol.* **2011,** *162,* 1577–1589. doi:10.1111/j.1476-5381.2010.01182.x
11. Arey, B.; Shutthanandan, V.; Orr, G. *Microsc. Microanal.* **2011,** *17,* 926–927. doi:10.1017/s1431927611005502
12. Boden, S. A.; Asadollahbaik, A.; Rutt, H. N.; Bagnall, D. M. *Scanning* **2012,** *34,* 107–120. doi:10.1002/sca.20267
13. Boseman, A.; Nowlin, K.; Ashraf, S.; Yang, J.; LaJeunesse, D. *Micron* **2013,** *51,* 26–35. doi:10.1016/j.micron.2013.06.005
14. Kim, K.-W. *Appl. Microsc.* **2012,** *42,* 147–150. doi:10.9729/am.2012.42.3.147
15. Rice, W. L.; Van Hoek, A. N.; PÇunescu, T. G.; Huynh, C.; Goetze, B.; Singh, B.; Scipioni, L.; Stern, L. A.; Brown, D. *PLoS One* **2013,** *8,* e57051. doi:10.1371/journal.pone.0057051
16. Schürmann, M.; Frese, N.; Beyer, A.; Heimann, P.; Widera, D.; Mönkemöller, V.; Huser, T.; Kaltschmidt, B.; Kaltschmidt, C.; Gölzhäuser, A. *Small* **2015,** *11,* 5781–5789. doi:10.1002/smll.201501540
17. Leppänen, M.; Sundberg, L.-R.; Laanto, E.; de Freitas Almeida, G. M.; Papponen, P.; Maasilta, I. J. *Adv. Biosyst.* **2017,** *1,* 1700070. doi:10.1002/adbi.201700070
18. Sharma, A.; Schmidt, M.; Kiesel, B.; Mahato, N. K.; Cralle, L.; Singh, Y.; Richnow, H. H.; Gilbert, J. A.; Arnold, W.; Lal, R. *Front. Microbiol.* **2018,** *9,* 3095. doi:10.3389/fmicb.2018.03095
19. Said, N.; Chatzinotas, A.; Schmidt, M. *Adv. Biosyst.* **2019,** *3,* 1800250. doi:10.1002/adbi.201800250
20. Vinner, G. K.; Rezaie-Yazdi, Z.; Leppanen, M.; Stapley, A. G. F.; Leaper, M. C.; Malik, D. J. *Pharmaceuticals* **2019,** *12,* 43. doi:10.3390/ph12010043
21. Veligura, V.; Hlawacek, G.; van Gastel, R.; Zandvliet, H. J. W.; Poelsema, B. *J. Phys.: Condens. Matter* **2014,** *26,* 165401. doi:10.1088/0953-8984/26/16/165401
22. Veligura, V.; Hlawacek, G.; Jahn, U.; van Gastel, R.; Zandvliet, H. J. W.; Poelsema, B. *J. Appl. Phys.* **2014,** *115,* No. 183502. doi:10.1063/1.4875480
23. Veligura, V.; Hlawacek, G.; van Gastel, R.; Zandvliet, H. J. W.; Poelsema, B. *J. Lumin.* **2015,** *157,* 321–326. doi:10.1016/j.jlumin.2014.09.016
24. Franklin, T. M. W. Scanning Ionoluminescence Microscopy with a Helium Ion Microscope. Ph.D. Thesis, University of Southampton, 2012.
25. Sato, C.; Sato, M.; Ogawa, S. *Int. J. Mol. Med.* **2018,** *42,* 309–321. doi:10.3892/ijmm.2018.3604
26. Dowsett, D.; Wirtz, T.; Vanhove, N.; Pillatsch, L.; Sijbrandij, S.; Notte, J. *J. Vac. Sci. Technol., B: Nanotechnol. Microelectron.: Mater., Process., Meas., Phenom.* **2012,** *30,* 06F602. doi:10.1116/1.4754309
27. Wirtz, T.; Vanhove, N.; Pillatsch, L.; Dowsett, D.; Sijbrandij, S.; Notte, J. *Appl. Phys. Lett.* **2012,** *101,* 041601. doi:10.1063/1.4739240
28. Wirtz, T.; Dowsett, D.; Philipp, P. SIMS on the Helium Ion Microscope: A Powerful Tool for High-Resolution High-Sensitivity Nano-Analytics. In *Helium Ion Microscopy;* Hlawacek, G.; Gölzhäuser, A., Eds.; Springer International Publishing: Cham, Switzerland, 2016; pp 297–323. doi:10.1007/978-3-319-41990-9_13
29. Dowsett, D.; Wirtz, T. *Anal. Chem. (Washington, DC, U. S.)* **2017,** *89,* 8957–8965. doi:10.1021/acs.analchem.7b01481
30. Eyhusen, S. Carl Zeiss Microscopy White paper: Multi-Modal Characterization with Secondary Ion Mass Spectrometry on ZEISS ORION NanoFab. https://pages.zeiss.com/rs/896-XMS-794/images/ZEISS_White-Paper_SIMS-Orion-NanoFab.pdf.
31. Klingner, N.; Heller, R.; Hlawacek, G.; Facsko, S.; von Borany, J.; Wilhelm, R. A. Patentschrift Ionenmikroskopievorrichtung. 102016112328.5, 2016.
32. Klingner, N. Ionenstrahlanalytik im Helium-Ionen-Mikroskop. Ph.D. Thesis, Universität Dresden, 2016.
33. Klingner, N.; Heller, R.; Hlawacek, G.; von Borany, J.; Notte, J.; Huang, J.; Facsko, S. *Ultramicroscopy* **2016,** *162,* 91–97. doi:10.1016/j.ultramic.2015.12.005
34. Heller, R.; Klingner, N.; Hlawacek, G. Backscattering Spectrometry in the Helium Ion Microscope: Imaging Elemental Compositions on the nm Scale. In *Helium Ion Microscopy;* Hlawacek, G.; Gölzhäuser, A., Eds.; Springer International Publishing: Cham, Switzerland, 2016; pp 265–295. doi:10.1007/978-3-319-41990-9_12
35. Klingner, N.; Heller, R.; Hlawacek, G.; Facsko, S.; von Borany, J. *Ultramicroscopy* **2019,** *198,* 10–17. doi:10.1016/j.ultramic.2018.12.014
36. Lovric, J.; Audinot, J.-N.; Wirtz, T. *Microsc. Microanal.* **2019,** *25* (Suppl. 2), 1026–1027. doi:10.1017/s1431927619005865
37. Kim, K. W. *Appl. Microsc.* **2013,** *43,* 9–13. doi:10.9729/am.2013.43.1.9
38. Gölzhäuser, A.; Hlawacek, G. HIM of Biological Samples. In *Helium Ion Microscopy;* Hlawacek, G.; Gölzhäuser, A., Eds.; Springer International Publishing: Cham, Switzerland, 2016; pp 173–185. doi:10.1007/978-3-319-41990-9_7

39. Ward, B. The ALIS Story. In *Helium Ion Microscopy;* Hlawacek, G.; Gölzhäuser, A., Eds.; Springer International Publishing: Switzerland, 2016; Vol. 1, pp 500–517.
40. Leppänen, M. Infection under the ion beam : focused ion beams and antibacterial properties of biomaterials. Ph.D. Thesis, University of Jyväskylä, 2020.
41. Inai, K.; Ohya, K.; Ishitani, T. *J. Electron Microsc.* **2007,** *56,* 163–169. doi:10.1093/jmicro/dfm024
42. Everhart, T. E.; Thornley, R. F. M. *J. Sci. Instrum.* **1960,** *37,* 246–248. doi:10.1088/0950-7671/37/7/307
43. Carl Zeiss Microscopy White Paper (2016): Zeiss ORION NanoFab. https://www.zeiss.com/microscopy/int/products/multiple-ion-beam/orion-nanofab-for-materials.html.
44. Tominski, C.; Lösekann-Behrens, T.; Ruecker, A.; Hagemann, N.; Kleindienst, S.; Mueller, C. W.; Höschen, C.; Kögel-Knabner, I.; Kappler, A.; Behrens, S. *Appl. Environ. Microbiol.* **2018,** *84,* e02166-17. doi:10.1128/aem.02166-17
45. Meldrum, F. C.; Mann, S.; Heywood, B. R.; Frankel, R. B.; Bazylinski, D. A. *Proc. R. Soc. London, Ser. B* **1993,** *251,* 237–242. doi:10.1098/rspb.1993.0035
46. Moreno-Osorio, J. H.; Benettoni, P.; Schmidt, M.; Stryhanyuk, H.; Schmitt-Jansen, M.; Pinto, G.; Pollio, A.; Frunzo, L.; Lens, P. N. L.; Richnow, H. H.; Esposito, G.; Musat, N. *FEMS Microbiol. Ecol.* **2019,** *95,* fiz029. doi:10.1093/femsec/fiz029
47. Imlay, J. A. *Mol. Microbiol.* **2006,** *59,* 1073–1082. doi:10.1111/j.1365-2958.2006.05028.x
48. Rouault, T. A.; Tong, W.-H. *Nat. Rev. Mol. Cell Biol.* **2005,** *6,* 345–351. doi:10.1038/nrm1620
49. Klingner, N.; Hlawacek, G.; Heller, R.; von Borany, J.; Facsko, S. Nanometer Scale Time of Flight Back Scattering Spectrometry in the Helium Ion Microscope. In *European Microscopy Congress 2016: Proceedings,* American Cancer Society, 2016; pp 955–956.
50. Pallon, J.; Yang, C.; Utui, R. J.; Elfman, M.; Malmqvist, K. G.; Kristiansson, P.; Sjöland, K. A. *Nucl. Instrum. Methods Phys. Res., Sect. B* **1997,** *130,* 199–203. doi:10.1016/s0168-583x(97)00182-1
51. Hell, S. W.; Wichmann, J. *Opt. Lett.* **1994,** *19,* 780–782. doi:10.1364/ol.19.000780
52. Mi, Z. Development and biological applications of high-resolution ion beam induced fluorescense microscopy. Ph.D. Thesis, National University of Singapore, 2015.
53. Breese, M. B. H.; Landsberg, J. P.; King, P. J. C.; Grime, G. W.; Watt, F. *Nucl. Instrum. Methods Phys. Res., Sect. B* **1992,** *64,* 505–511. doi:10.1016/0168-583x(92)95524-u
54. Marshall, M. M.; Yang, J.; Hall, A. R. *Scanning* **2012,** *34,* 101–106. doi:10.1002/sca.21003
55. Hall, A. R. *Microsc. Microanal.* **2013,** *19,* 740–744. doi:10.1017/s1431927613000500
56. Woehl, T. J.; White, R. M.; Keller, R. R. *Microsc. Microanal.* **2016,** *22,* 544–550. doi:10.1017/s1431927616000775
57. Ziegler, J. F. SRIM 2013 - The Stopping and Range of Ions in Matter. https://www.srim.org (accessed July 7, 2020).
58. Mousley, M.; Eswara, S.; De Castro, O.; Bouton, O.; Klingner, N.; Koch, C. T.; Hlawacek, G.; Wirtz, T. *Beilstein J. Nanotechnol.* **2019,** *10,* 1648–1657. doi:10.3762/bjnano.10.160
59. npSCOPE. https://www.npscope.eu (accessed July 7, 2020).
60. Zeitvogel, F.; Burkhardt, C. J.; Schroeppel, B.; Schmid, G.; Ingino, P.; Obst, M. *Geomicrobiol. J.* **2017,** *34,* 317–327. doi:10.1080/01490451.2016.1189467
61. Loftus, A. F.; Joens, M. S.; Dunn, S. E.; Adams, M. W.; Huynh, C.; Goetze, B.; Fitzpatrick, J. A. J. *Microsc. Microanal.* **2015,** *21* (Suppl. 3), 511–512. doi:10.1017/s1431927615003359
62. Goetze, B.; Huynh, C.; Stern, L.; Wu, H.; Ferranti, D.; Ananth, M. *Microsc. Microanal.* **2013,** *19* (Suppl. 2), 908–909. doi:10.1017/s1431927613006533
63. Uryu, K.; Soplop, N.; Acehan, D.; Winer, B. Y.; Fischetti, V. A.; Sheahan, T.; Rice, C. M.; Hsu, M.; Robbiani, M.; Santulli, G.; Totary-Jain, H.; Goetze, B.; Catanese, M.-T. *Microsc. Microanal.* **2016,** *22* (Suppl. 3), 1142–1143. doi:10.1017/s1431927616006553
64. Uryu, K.; Rice, C. M.; Catanese, M. T.; Santulli, G.; Totary-Jain, H.; Huynh, C.; Goetze, B. *Microsc. Microanal.* **2017,** *23* (Suppl. 1), 1370–1371. doi:10.1017/s1431927617007516
65. P unescu, T. G.; Shum, W. W. C.; Huynh, C.; Lechner, L.; Goetze, B.; Brown, D.; Breton, S. *Mol. Hum. Reprod.* **2014,** *20,* 929–937. doi:10.1093/molehr/gau052
66. Laufer, K.; Niemeyer, A.; Nikeleit, V.; Halama, M.; Byrne, J. M.; Kappler, A. *FEMS Microbiol. Ecol.* **2017,** *93,* fix054. doi:10.1093/femsec/fix054
67. Bidlack, F. B.; Huynh, C.; Marshman, J.; Goetze, B. *Front. Physiol.* **2014,** *5,* 395. doi:10.3389/fphys.2014.00395
68. Tsuda, T.; Nemoto, N.; Kawakami, K.; Mochizuki, E.; Kishida, S.; Tajiri, T.; Kushibiki, T.; Kuwabata, S. *ChemBioChem* **2011,** *12,* 2547–2550. doi:10.1002/cbic.201100476
69. Golding, C. G.; Lamboo, L. L.; Beniac, D. R.; Booth, T. F. *Sci. Rep.* **2016,** *6,* 26516. doi:10.1038/srep26516
70. Vanden Berg-Foels, W. S.; Scipioni, L.; Huynh, C.; Wen, X. J. *J. Microsc. (Oxford, U. K.)* **2012,** *246,* 168–176. doi:10.1111/j.1365-2818.2012.03606.x
71. Huyuan, C.; Marshman, J.; Dobeck, J.; Goetze, B.; Bidlack, F. B. *Microsc. Microanal.* **2013,** *19* (Suppl. 2), 1640–1641. doi:10.1017/s1431927613010192
72. Paunescu, T. G.; Breton, S.; Brown, D. *Physiol. News* **2014,** 32–35. doi:10.36866/pn.95.32
73. Tsuji, K.; Păunescu, T. G.; Suleiman, H.; Xie, D.; Mamuya, F. A.; Miner, J. H.; Lu, H. A. J. *Sci. Rep.* **2017,** *7,* 8321. doi:10.1038/s41598-017-08304-3
74. Herrera, M. G.; Pizzuto, M.; Lonez, C.; Rott, K.; Hütten, A.; Sewald, N.; Ruysschaert, J.-M.; Dodero, V. I. *Nanomedicine (N. Y., NY, U. S.)* **2018,** *14,* 1417–1427. doi:10.1016/j.nano.2018.04.014
75. Curtin, A. E.; Chiaramonti, A. N.; Sanders, A. W.; Ciesielski, P. N.; Chapple, C.; Mosier, N.; Donohoe, B. S. *Microsc. Microanal.* **2014,** *20* (Suppl. 3), 1338–1339. doi:10.1017/s1431927614008423
76. Bandara, C. D.; Singh, S.; Afara, I. O.; Wolff, A.; Tesfamichael, T.; Ostrikov, K.; Oloyede, A. *ACS Appl. Mater. Interfaces* **2017,** *9,* 6746–6760. doi:10.1021/acsami.6b13666
77. Bandara, C. C. D. I. M. Characterisation of the bactericidal efficiancy of natural nanotopography using dragonfly. Ph.D. Thesis, Queensland University of Technology, 2017.
78. Shahali, H.; Hasan, J.; Mathews, A.; Wang, H.; Yan, C.; Tesfamichael, T.; Yarlagadda, P. K. D. V. *J. Mater. Chem. B* **2019,** *7,* 1300–1310. doi:10.1039/c8tb03295e
79. Belianinov, A.; Halsted, M. C.; Burch, M. J.; Songkil, K.; Retterer, S. T. *Microsc. Microanal.* **2017,** *23* (Suppl. 1), 1152–1153. doi:10.1017/s1431927617006420
80. Byrne, J. M.; Schmidt, M.; Gauger, T.; Bryce, C.; Kappler, A. *Environ. Sci. Technol. Lett.* **2018,** *5,* 209–213. doi:10.1021/acs.estlett.8b00077

81. Almeida, G. M. F.; Leppänen, M.; Maasilta, I. J.; Sundberg, L.-R. *Res. Microbiol.* **2018,** *169,* 488–494. doi:10.1016/j.resmic.2018.05.006
82. Prasad, K.; Recek, N.; Zhou, R.; Zhou, R.; Aramesh, M.; Wolff, A.; Speight, R. E.; Mozetič, M.; Bazaka, K.; Ostrikov, K. *Sustainable Mater. Technol.* **2019,** *22,* e00123. doi:10.1016/j.susmat.2019.e00123
83. de Souza, W.; Attias, M. *J. Struct. Biol.* **2015,** *191,* 76–85. doi:10.1016/j.jsb.2015.05.003
84. Gadelha, A. P. R.; Benchimol, M.; de Souza, W. *J. Struct. Biol.* **2015,** *190,* 271–278. doi:10.1016/j.jsb.2015.04.017
85. de Souza, W.; Attias, M. *Exp. Parasitol.* **2018,** *190,* 10–33. doi:10.1016/j.exppara.2018.04.018
86. Starr, M. P.; Seidler, R. J. *Annu. Rev. Microbiol.* **1971,** *25,* 649–678. doi:10.1146/annurev.mi.25.100171.003245
87. Sockett, R. E. *Annu. Rev. Microbiol.* **2009,** *63,* 523–539. doi:10.1146/annurev.micro.091208.073346
88. WHO priority pathogens list for Research and Development of new antibiotics. https://www.who.int/news-room/detail/27-02-2017-who-publishes-list-of-bacteria-for-which-new-antibiotics-are-urgently-needed (accessed June 25, 2020).
89. LeTourneau, M. K.; Marshall, M. M.; Thomashow, L. S.; Harsh, J. B. *Microsc. Microanal.* **2015,** *21* (Suppl. 3), 711–712. doi:10.1017/s1431927615004353
90. Kniggendorf, A.-K.; Gaul, T. W.; Meinhardt-Wollweber, M. *Microsc. Res. Tech.* **2011,** *74,* 177–183. doi:10.1002/jemt.20889
91. Samuels, T.; Bryce, C.; Landenmark, H.; Marie-Loudon, C.; Nicholson, N.; Stevens, A. H.; Cockell, C. Microbial Weathering of Minerals and Rocks in Natural Environments. *Biogeochemical Cycles;* Geophysical Monograph Series; Wiley, 2020; pp 59–79. doi:10.1002/9781119413332.ch3
92. Bryce, C.; Franz-Wachtel, M.; Nalpas, N. C.; Miot, J.; Benzerara, K.; Byrne, J. M.; Kleindienst, S.; Macek, B.; Kappler, A. *Appl. Environ. Microbiol.* **2018,** *84,* e01166–18. doi:10.1128/aem.01166-18
93. Melton, E. D.; Swanner, E. D.; Behrens, S.; Schmidt, C.; Kappler, A. *Nat. Rev. Microbiol.* **2014,** *12,* 797–808. doi:10.1038/nrmicro3347
94. Nordhoff, M.; Tominski, C.; Halama, M.; Byrne, J. M.; Obst, M.; Kleindienst, S.; Behrens, S.; Kappler, A. *Appl. Environ. Microbiol.* **2017,** *83,* e00752–17. doi:10.1128/aem.00752-17
95. Dohnalkova, A.; Arey, B.; Varga, T.; Miller, M.; Kovarik, L. *Microsc. Microanal.* **2017,** *23* (Suppl. 1), 2172–2173. doi:10.1017/s1431927617011527
96. Lybrand, R. A.; Austin, J. C.; Fedenko, J.; Gallery, R. E.; Rooney, E.; Schroeder, P. A.; Zaharescu, D. G.; Qafoku, O. *Sci. Rep.* **2019,** *9,* 5377. doi:10.1038/s41598-019-41357-0
97. Qafoku, O.; Lybrand, R. A.; Shutthanandan, V.; Gallery, R. E.; Austin, J. C.; Schroeder, P. A.; Fedenko, J.; Rooney, E.; Zaharescu, D. G. *Microsc. Microanal.* **2019,** *25* (Suppl. 2), 2436–2437. doi:10.1017/s1431927619012911
98. Rasa, K.; Heikkinen, J.; Hannula, M.; Arstila, K.; Kulju, S.; Hyväluoma, J. *Biomass Bioenergy* **2018,** *119,* 346–353. doi:10.1016/j.biombioe.2018.10.004
99. LeTourneau, M. K.; Marshall, M. J.; Cliff, J. B.; Bonsall, R. F.; Dohnalkova, A. C.; Mavrodi, D. V.; Devi, S. I.; Mavrodi, O. V.; Harsh, J. B.; Weller, D. M.; Thomashow, L. S. *Environ. Microbiol.* **2018,** *20,* 2178–2194. doi:10.1111/1462-2920.14244
100. Chen, S.-C.; Musat, N.; Lechtenfeld, O. J.; Paschke, H.; Schmidt, M.; Said, N.; Popp, D.; Calabrese, F.; Stryhanyuk, H.; Jaekel, U.; Zhu, Y.-G.; Joye, S. B.; Richnow, H.-H.; Widdel, F.; Musat, F. *Nature* **2019,** *568,* 108–111. doi:10.1038/s41586-019-1063-0
101. Hill, R.; Notte, J. A.; Scipioni, L. Scanning Helium Ion Microscopy. *Advances in Imaging and Electron Physics;* Elsevier: Amsterdam, Netherlands, 2012; pp 65–148. doi:10.1016/b978-0-12-394396-5.00002-6
102. Shorubalko, I.; Pillatsch, L.; Utke, I. Direct–Write Milling and Deposition with Noble Gases. In *Helium Ion Microscopy;* Hlawacek, G.; Gölzhäuser, A., Eds.; Springer International Publishing: Cham, Switzerland, 2016; pp 355–393. doi:10.1007/978-3-319-41990-9_15
103. Vinner, G. K.; Richards, K.; Leppänen, M.; Sagona, A. P.; Malik, D. J. *Pharmaceutics* **2019,** *11,* 475. doi:10.3390/pharmaceutics11090475
104. Bandara, C. D.; Ballerin, G.; Leppänen, M.; Tesfamichael, T.; Ostrikov, K. K.; Whitchurch, C. B. *ACS Biomater. Sci. Eng.* **2020,** *6,* 3925–3932. doi:10.1021/acsbiomaterials.9b01973
105. Decelle, J.; Veronesi, G.; Gallet, B.; Stryhanyuk, H.; Benettoni, P.; Schmidt, M.; Tucoulou, R.; Passarelli, M.; Bohic, S.; Clode, P.; Musat, N. *Trends Cell Biol.* **2020,** *30,* 173–188. doi:10.1016/j.tcb.2019.12.007
106. Chen, X.; Udalagama, C. N. B.; Chen, C.-B.; Bettiol, A. A.; Pickard, D. S.; Venkatesan, T.; Watt, F. *Biophys. J.* **2011,** *101,* 1788–1793. doi:10.1016/j.bpj.2011.08.028
107. Sanders, A. W.; Jeerage, K. M.; Schwartz, C. L.; Curtin, A. E.; Chiaramonti, A. N. *Microsc. Microanal.* **2014,** *20* (Suppl. 3), 976–977. doi:10.1017/s1431927614006606
108. Reguera, G.; McCarthy, K. D.; Mehta, T.; Nicoll, J. S.; Tuominen, M. T.; Lovley, D. R. *Nature* **2005,** *435,* 1098–1101. doi:10.1038/nature03661
109. Stokes, D. J.; Mugnier, J.-Y.; Clarke, C. J. *J. Microsc. (Oxford, U. K.)* **2004,** *213,* 198–204. doi:10.1111/j.1365-2818.2004.01282.x

License and Terms

BEILSTEIN JOURNAL OF NANOTECHNOLOGY

Imaging of SARS-CoV-2 infected Vero E6 cells by helium ion microscopy

Natalie Frese[1], Patrick Schmerer[2], Martin Wortmann[3], Matthias Schürmann[4], Matthias König[2], Michael Westphal[1], Friedemann Weber[2], Holger Sudhoff[4] and Armin Gölzhäuser[*1]

Full Research Paper

Open Access

Address:
[1]Physics of Supramolecular Systems and Surfaces, Faculty of Physics, Bielefeld University, Bielefeld, Germany, [2]Institute of Virology, Faculty of Veterinary Medicine, Justus-Liebig-University Giessen, Germany, [3]Faculty of Engineering and Mathematics, Bielefeld University of Applied Sciences, Bielefeld, Germany and [4]University Clinic for Otolaryngology, Head and Neck Surgery, Medical Faculty OWL at Bielefeld University, Germany

Email:
Armin Gölzhäuser[*] - ag@uni-bielefeld.de

* Corresponding author

Keywords:
bioimaging; cell membrane; charge compensation; helium ion microscopy; SARS-CoV-2; Vero E6 cells

Beilstein J. Nanotechnol. **2021,** *12,* 172–179.
https://doi.org/10.3762/bjnano.12.13

Received: 02 December 2020
Accepted: 28 January 2021
Published: 02 February 2021

This article is part of the thematic issue "Ten years of the helium ion microscope".

Guest Editors: G. Hlawacek and A. Wolff

Abstract

Helium ion microscopy (HIM) offers the opportunity to obtain direct views of biological samples such as cellular structures, virus particles, and microbial interactions. Imaging with the HIM combines sub-nanometer resolution, large depth of field, and high surface sensitivity. Due to its charge compensation capability, the HIM can image insulating biological samples without additional conductive coatings. Here, we present an exploratory HIM study of SARS-CoV-2 infected Vero E6 cells, in which several areas of interaction between cells and virus particles, as well as among virus particles, were imaged. The HIM pictures show the three-dimensional appearance of SARS-CoV-2 and the surface of Vero E6 cells at a multiplicity of infection of approximately 1 with great morphological detail. The absence of a conductive coating allows for a distinction between virus particles bound to the cell membrane and virus particles lying on top of the membrane. After prolonged imaging, it was found that ion-induced deposition of hydrocarbons from the vacuum renders the sample sufficiently conductive to allow for imaging even without charge compensation. The presented images demonstrate the potential of the HIM in bioimaging, especially for the imaging of interactions between viruses and their host organisms.

Introduction

The last decade of helium ion microscopy (HIM) was characterized by a rapid exploration of its sub-nanometer imaging and ion-beam nanofabrication capabilities in materials science and engineering [1]. Although HIM soon proved to be a promising tool in the life sciences, the examination of biological samples by HIM proceeded at a much slower pace. In recent years, it has

been used in the field of cell biology for imaging various human and animal cells. These include cartilage [2], cancer [3], liver [4], kidney [5] and stem cells [6], as well as fibrin fibers [7]. To visualize viruses and their host organisms, HIM has so far been applied to image T4 phage-infected *E. coli* bacteria [8], various phases of the life cycle of the bacterial predator *Bdellovibrio bacteriovorus* [9] and the vesicular structure of ethane-oxidizing archaea [10]. A comprehensive review on the subject of bioimaging with HIM has recently been published by Schmidt and co-workers [11].

In this work, we use HIM to investigate Vero E6 cells infected with the novel severe acute respiratory syndrome coronavirus 2 (SARS-CoV-2). Several members of the family *Coronaviridae* have been described in the human population and usually cause mild respiratory disease. SARS-CoV-2 demonstrated a worldwide spread causing a significant global public health emergency [12,13]. As of January 18th, 2021, more than 95 million cases worldwide have been confirmed with the infection and over two million infected patients have died [14]. African green monkey kidney Vero E6 cells have been reported to support SARS-CoV-2 replication in culture, while many more cell lines have been reported to be refractory to SARS-CoV-2 infection [15]. Both scanning electron microscopy (SEM) and transmission electron microscopy (TEM) have been used to image SARS-CoV-2 [16-20]. While TEM achieves unsurpassed resolution and can visualize macromolecular structures such as spike glycoproteins or transmembrane proteins [21], SEM provides topographic images of infected cells and virus particles distributed on their surface, albeit only after the samples have been coated with a conductive layer. In contrast, the HIM delivers a topographic image of the uncoated surface morphology of cells and virus particles, allowing one to identify and investigate sites at which a cell interacts with the virus. While its principle of operation is very similar to SEM, HIM utilizes a beam of positively charged helium ions (He^+) instead of negatively charged electrons to excite and detect secondary electrons from the sample surface. Due to the high brightness and low energy spread of its atomically sharp gas field ion source, the smallest attainable focused spot size is about 0.3 nm [22]. With its significantly smaller convergence angle compared to SEM, HIM achieves a much larger depth of field, which is particularly useful for imaging three-dimensional structures [22]. Due to their higher mass, He^+ ions penetrate deeper into the sample and do not spread as wide as electrons, resulting in a smaller escape volume of the secondary electrons and a higher surface resolution of the HIM, compared to the SEM [23]. A further benefit of HIM is its charge compensation capability during secondary electron detection. SEM imaging of biological specimen usually necessitates a thin conductive coating to prevent negative charge accumulation from the impinging electrons. Such coatings, albeit only a few nanometers thick, can significantly alter and conceal fine details of biological nanostructures [2], which is noticeable in SEM images of virus particles [19,24]. Since in the HIM positive charge accumulates on insulating samples, a low-energy electron flood gun can be used for charge compensation, which irradiates the sample with a diffuse beam of electrons. This eliminates the need for a conductive coating, and allows for a direct view on nanoscale structures [6,25]. Here, we demonstrate the benefits of high-resolution HIM by imaging SARS-CoV-2 interacting with Vero E6 cells without any conductive coating. The presented images allow for the identification of SARS-CoV-2 virus particles, their interaction with the cell membrane and a distinction between virus particles bound to the cell surface from those lying on it.

Experimental

Vero E6 cells were cultivated in Dulbecco's modified Eagle's medium (Thermo Fisher Scientific) supplemented with 10% fetal bovine serum (Capricorn Scientific) in a 5% CO_2 atmosphere at 37 °C. SARS-CoV-2 (strain SARS-CoV-2 /München-1.2/2020/984, p.2) [26] was grown on Vero E6 cells and titrated as described [27]. Infection experiments were done under biosafety level 3 conditions with enhanced respiratory personal protection equipment.

For HIM, cells were seeded onto coverslips placed in 24-well plates. The coverslips were previously sputter coated with 30 nm of gold to improve charge neutralization during HIM imaging. After 24 h, nearly confluent monolayers were infected with SARS-CoV-2 at a multiplicity of infection (MOI) of approximately 1 or mock-infected using cell culture medium. Following an incubation period of 18 h in a cell culture incubator (37 °C), cells were washed with 0.1 M sodium cacodylate (NaCac, pH 7.4) and fixed in 2% (v/v) glutaraldehyde, 2% (w/v) paraformaldehyde in NaCac buffer at room temperature for 30 min. After fixation at room temperature, the samples were transferred to the normal laboratory area and then fixed at 4 °C with fresh fixatives. The coverslips were subsequently washed and dehydrated in a graded series of ethanol (50%, 70%, 95%, 99.5% (2×)), transferred to water-free acetone and critical point dried in carbon dioxide.

HIM was performed with an Orion Plus microscope (Carl Zeiss) at an acceleration voltage of about 36 kV and a working distance of 20 mm. The spot control was set to 6 to obtain a beam current of 0.2 to 0.4 pA. To avoid charging effects during secondary electron detection, an electron flood gun was used after each line scan, if not stated otherwise, with a flood energy of 540 eV, flood time of 10 µs and a focus of 107 V. It should be mentioned that the flood gun parameters have to be opti-

mized for each magnification level. All HIM images were recorded with 1024 × 1024 pixels. Before imaging, each sample was stored in the vacuum chamber of the microscope at 3.3×10^{-7} mbar for at least 24 h to remove most volatile organic contaminants.

Results and Discussion

A comparison between a native and an infected Vero E6 cell at multiple magnification levels is shown in Figure 1. Figure 1a shows a sequence of four HIM images of native Vero E6 cells (mock-infected). Figure 1b displays a sequence of HIM images of Vero E6 cells after they have been exposed to SARS-CoV-2 at a multiplicity of infection of approximately 1 (MOI 1) and an incubation time of 18 h. The surface of the infected cells is covered by a number of micrometer-sized vesicles and segments of cell membranes, which is a first indication that apoptosis occurred during viral replication. Regularly shaped particles below 100 nm diameter on the cell membrane shown in Figure 1b$_4$ were only abundant on the cells of the MOI 1 sample and were therefore identified as SARS-CoV-2 virus particles. This is in accordance with a study of Bojkova et al. [28], which demonstrated the presence of newly synthesized viral particles of SARS-CoV-2 even 10 h after initial infection. The cell membrane of the infected cell is covered with the virus particles, which are predominantly spherically shaped. Holes in the cell membrane, illustrated in Figure 1b$_4$ and Figure S1 of Supporting Information File 1, have previously been observed in uncoated mammalian cells and indicate lipid nanodomains or caveolea [6]. Figure 1c shows an evaluation of the virus particle size in five arbitrarily chosen regions on the MOI 1 sample resulting in an average diameter of the virus particles of 75 ± 13 nm, noting that this value has been obtained from viruses after fixation and critical point drying.

As He^+ ions can penetrate several hundred nanometers into the sample [29], the outer rim of the cells appears brighter because the ions pass through the cells and generate additional secondary electrons at the back of the cells and in the gold-coated specimen slide [30]. The edges appear brightest where the cells bend upwards from the substrate. The edge resolution in two

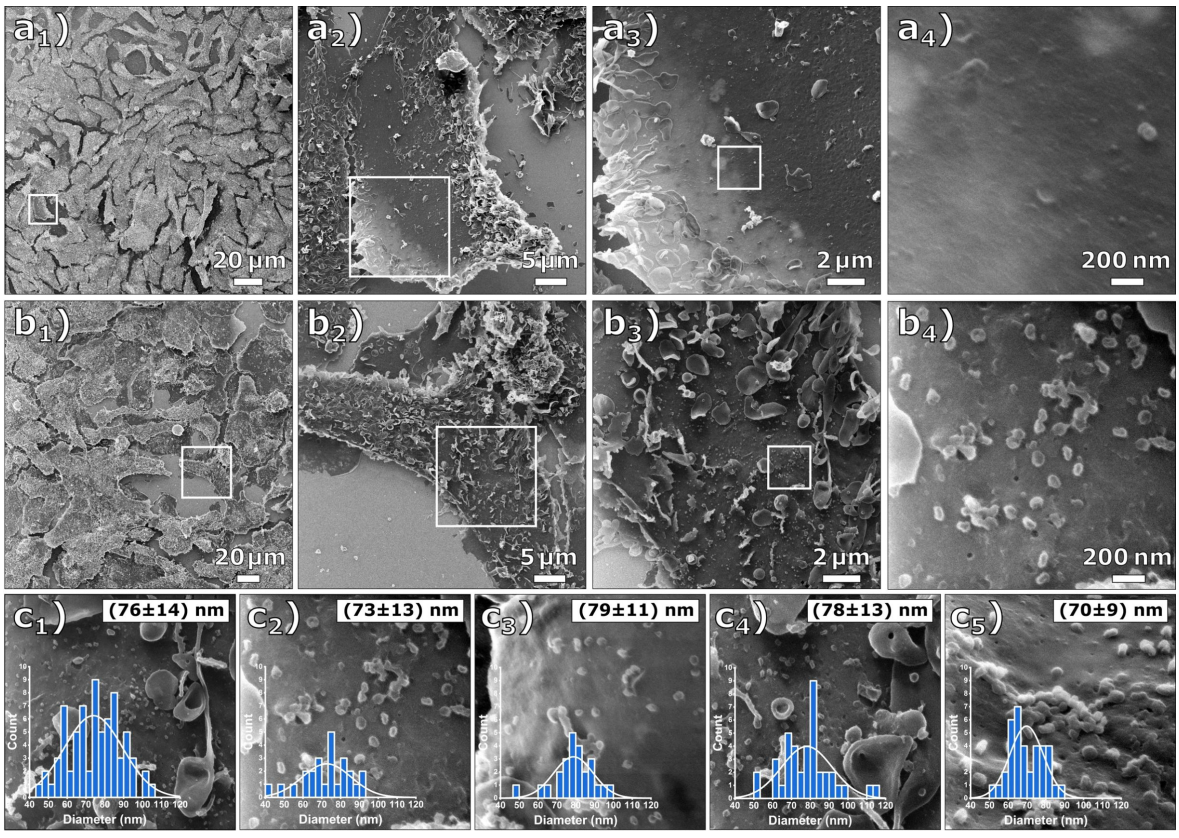

Figure 1: Comparative HIM images of Vero E6 cells that were mock-infected and infected at MOI 1. ($a_{1–4}$) Mock-infected cells at different magnifications (FOV 200 µm, 45 µm, 15 µm, and 1.7 µm) and ($b_{1–4}$) cells infected at MOI 1 at different magnifications (FOV 250 µm, 45 µm, 15 µm, and 1.7 µm). The cell membrane is covered with the virus particles. ($c_{1–5}$) Determined virus particle diameter distributions. The inserted histograms show the respective image evaluation with normal distribution, mean value, and standard deviation. The average diameter of all evaluated images is 75 ± 13 nm.

highly magnified images, shown in Figure S2 of Supporting Information File 1, has been determined by plotting the corresponding gray-scale values over the edges of two holes, resulting in values of 1.3 and 2.1 nm. The edge resolution of the images is determined by an interplay between the size of the focused He^+ beam and the widening of the beam within the sample material. The obtained values are typical for biological materials [6-8,11].

An effect frequently occurring during HIM imaging with charge compensation can be observed in the sequence of HIM images shown in Figure 2a$_{1–3}$, where a location on a MOI 1-infected Vero E6 sample was first imaged at a field of view (FOV) of 23 µm (Figure 2a$_1$), followed by two higher magnification images with a FOV of 4.5 µm and a FOV of 1 µm (Figure 2a$_2$). Figure 2a$_3$ shows the same region as Figure 2a$_1$, but the parts that were previously imaged at high magnification (FOV of 4.5 µm) with a dose of 1.4×10^{16} ions/cm^2 appear noticeably brighter. This is caused by He^+ beam-induced carbonaceous deposits resulting in a thin conductive coating. In addition to the improved conductivity of the specimen, the deposited layer may contribute to the electron density of the surface, thus increasing

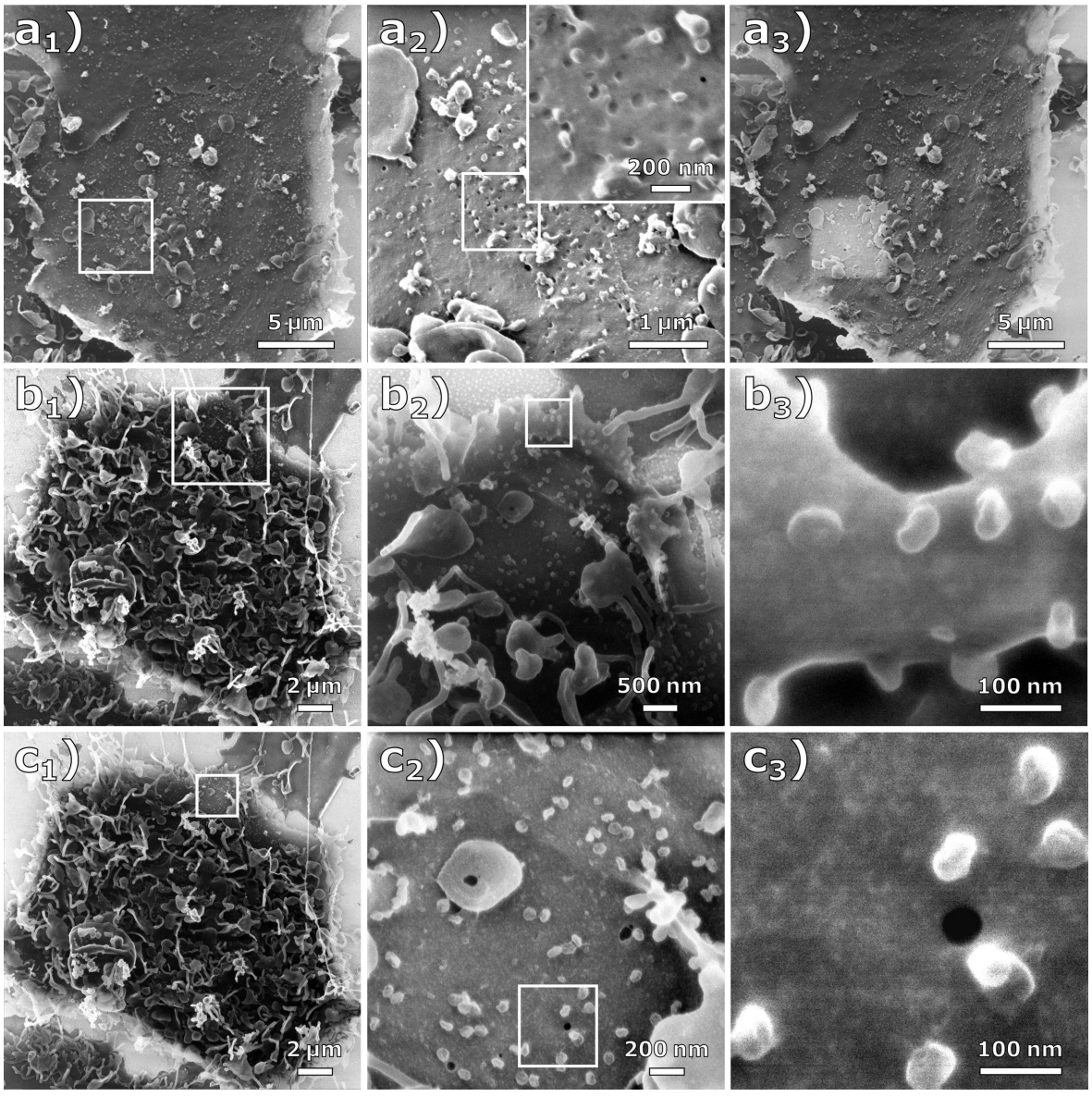

Figure 2: Effect of carbon deposition during HIM imaging. (a$_1$) HIM image (FOV 20 µm) of a cell infected at MOI 1 with charge compensation. (a$_2$) HIM images at high magnification (FOV 4.5 µm and 1 µm) with charge compensation. (a$_3$) The same image section as (a$_1$) after imaging the regions in (a$_2$). Due to increased conductivity, this region appears significantly brighter than the rest of the image. (b$_{1–3}$) HIM images of a cell infected at MOI 1 at different magnifications (FOV 20 µm, 5 µm, and 450 nm) with charge compensation. (c$_{1–3}$) HIM images of the same cell (FOV 20 µm, 2 µm, and 450 nm) after imaging the magnified sections in (b). (c$_1$) and (c$_2$) were imaged with and (c$_3$) was imaged without charge compensation.

secondary electron yield. This effect, commonly referred to as electron- and/or ion beam-induced deposition, is commonly observed in charged-particle microscopes. In electron microscopes, deposition rates of up to 3 Å/s at high current densities have been reported. As the deposition rate quickly reaches an equilibrium with rising current density, it can be assumed that the limiting factor is the density of residual hydrocarbons in the vacuum [31]. In the HIM, residual gas as well as the specimen itself are considered the main contributors of hydrocarbons [32,33]. Due to the much larger mass of He^+ ions compared to electrons, their sputter rate is typically much higher. Since organic compounds are ablated from the sample surface, hydrocarbon deposition is likely to be more pronounced when imaging biological samples in HIM. A schematic illustration of this effect can be seen in Figure S3 of Supporting Information File 1.

Figure $2b_{1–3}$ shows an infected Vero E6 cell at different magnification levels. Figure $2b_3$ depicts the highest magnification (FOV 450 nm) of the cell seen in Figure $2b_1$, showing the virus particles on top of the cell membrane in a side view. Note that after the zoom-out in Figure $2c_1$, the previously imaged regions appear again brighter. After imaging Figure $2c_2$ with a dose of 1.9×10^{17} ions/cm^2, the flood gun was turned off, which allowed imaging of Figure $2c_3$ without any external charge compensation. From the quality of this image, it can be inferred that the deposited carbon layer rendered the sample sufficiently conductive. However, small structures are still visible on the membrane surface, which may originate from surface topography or material contrast. The deposited carbon film is presumably thinner than typical conductive metal or carbon coatings for SEM imaging, and it does not show any surface masking and clustering as seen on the gold substrate in the upper left of Figure $2b_2$. The energy of the incident hydrocarbons is much lower compared to the energy of sputter-deposited metals. However, it is possible that this unintended, but sometimes useful, carbon deposition can be reduced by HIM imaging in ultra-high vacuum [34-36].

The cell structures shown in the HIM images of Figure 3a are sharply resolved over tens of micrometers, which demonstrates the high depth of field of HIM compared to SEM [37]. In image $3a_3$, at the surface of the cell, a cluster of virus particles seems to be bound to the cell membrane (arrow). We suggest that this

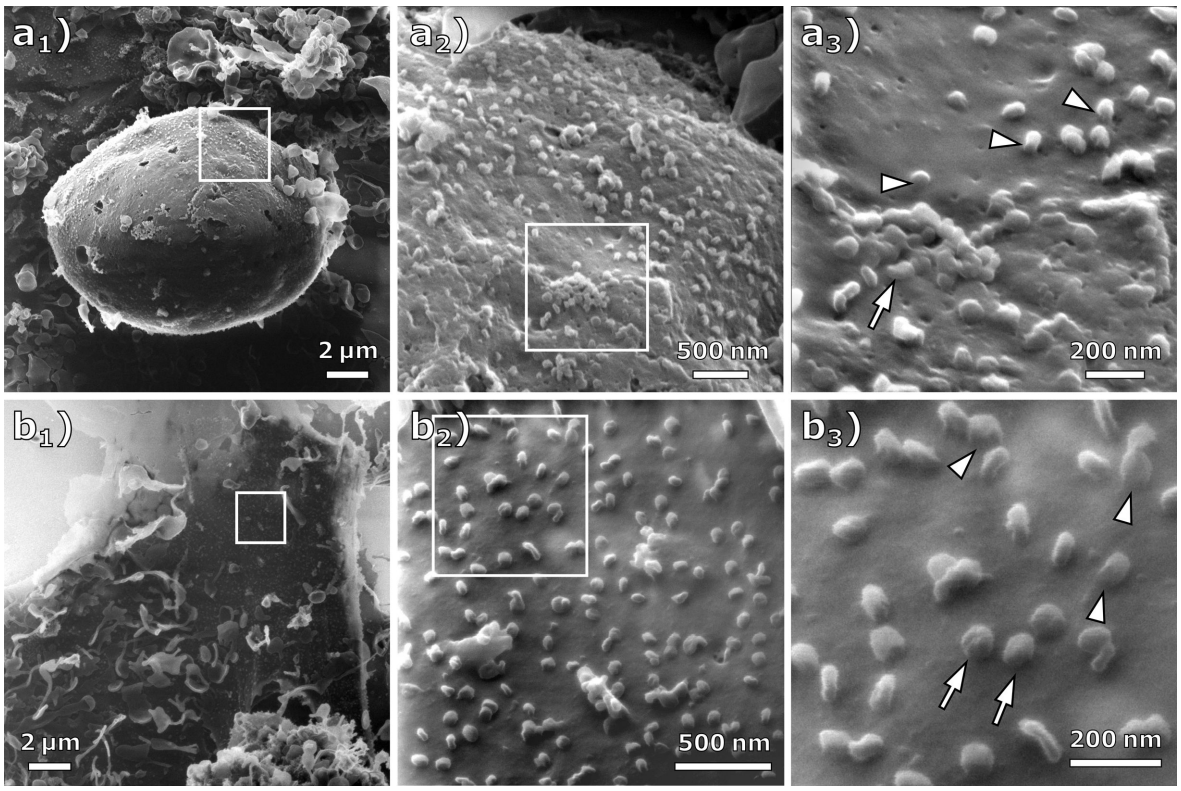

Figure 3: HIM images of cells infected at MOI 1 imaged with charge compensation. ($a_{1–3}$) Different magnifications of an infected cell (FOV 17 µm, 3.5 µm, and 1.3 µm). At the high magnification in (a_3), clusters of virus particles (arrow) and junctions (arrowheads) between the virus particle and the cell membrane become visible. ($b_{1–3}$) Different magnifications of an infected cell (FOV 18 µm, 2 µm, and 850 nm). While some of the virus particles appear to be bound to the cell membrane (arrowheads), others seem to just lie on top of it (arrow).

resembles the particle clustering by host defense protein BST-2 as it was observed for human coronavirus229E and quantified in HeLa cells by Wang and co-workers [38]. However, the metal coating applied by Wang et al. is clearly visible at high resolution in the SEM images as a rough layer on the cell membrane that hides the true topography [25,39]. In contrast, the HIM images presented here not only allow for the quantification of particles and clusters, but also enable an unveiled view on the interaction of virus particles with the cell membrane. The presented particle cluster seems to have a coalesced appearance, which might be caused by the virus–virus and virus–membrane interactions mediated through agglutinating BST-2 [40,41]. Some viral particles appear to be connected to the cell membrane by a continuous junction (arrowheads). Figure 3b shows another cell on the MOI 1 sample at different magnification levels. At the highest magnification shown in Figure $3b_3$ (FOV 850 nm), these junctions can also be observed (arrowheads). We assume that this resembles the tubulating cell membrane, which is stabilized by BST-2 to prevent viral scission. This alternative BST-2 interaction was already described for HIV-infected cells via immuno-TEM [42] but has not yet been observed for SARS-CoV-2. Aside from this observation, the HIM images allow for the distinction between viruses bound to the membrane and virus particles lying on top of the membrane (Figure 3b, arrows). Compared to a SEM study in which all visible virus particles on a cell membrane were quantified [38], HIM images could provide additional information about bound and unbound particles, resulting in more accurate data by counting only the bound particles. The presented images demonstrate that the HIM is well suited for the imaging of virus–membrane and virus–virus interactions, for example, when the virus particles are bound to the cell membrane or/and have a coalesced appearance.

It is known that the spike glycoproteins can be visualized by TEM. As the HIM images depicted the virus particles without conductive coating, it is an interesting question, whether or not the spike glycoproteins could, in principle, be resolved in HIM images. Inspecting the highest magnification images, Figure $2b_3$ and Figure $2c_3$, we do not see unequivocal evidence of structures indicating the spike glycoproteins. However, it is conceivable that a dedicated sample preparation could preserve their structure for imaging in HIM.

Conclusion

In this study, HIM images of Vero E6 cells without infection and infected with SARS-CoV-2 are presented. On infected cells, the ultrastructure of the cell–virus interaction, as well as interaction among virus particles, is shown. The absence of a previously applied conductive coating allows for the distinction between virus particles bound to the cell membrane and virus particles lying on top of the cell membrane. The images unveil the three-dimensional appearance of SARS-COV-2 and the surface of Vero E6 cells at MOI 1 with an edge resolution of up to 1.3 nm. Additionally, it is shown that ion-induced deposition renders the sample surface sufficiently conductive to be imaged without charge compensation. The presented images demonstrate the potential of the HIM in bioimaging, especially for the imaging of interactions between viruses and their host organisms. HIM thus represents a versatile complement to conventional methods in the life sciences.

Supporting Information

Supporting Information File 1

Additional experimental data.
[https://www.beilstein-journals.org/bjnano/content/supplementary/2190-4286-12-13-S1.pdf]

Acknowledgements

The authors thank André Beyer and Daniel Emmrich for valuable discussions.

Funding

F.W. is funded by the LOEWE Centre for Novel Drug Targets against Poverty-Related and Neglected Tropical Infectious Diseases (DRUID), which is part of the excellence initiative of the Hessen State Ministry of Higher Education, Research and the Arts (HMWK), the RAPID consortium of the Federal Ministry of Education and Research (BMBF, grant number 01KI1723E), and the European Union's Horizon 2020 research and innovation program under grant agreement No 101003666 (OPENCORONA). This work was further conducted within the framework of the COST Action CA19140 (FIT4NANO).

ORCID® iDs

Martin Wortmann - https://orcid.org/0000-0002-5101-4643
Matthias König - https://orcid.org/0000-0001-5877-6643
Friedemann Weber - https://orcid.org/0000-0001-9737-337X
Holger Sudhoff - https://orcid.org/0000-0002-9274-5645
Armin Gölzhäuser - https://orcid.org/0000-0002-0838-9028

Preprint

A non-peer-reviewed version of this article has been previously published as a preprint: https://doi.org/10.3762/bxiv.2020.136.v1

References

1. Hlawacek, G.; Gölzhäuser, A., Eds. *Helium Ion Microscopy;* NanoScience and Technology; Springer International Publishing: Cham, Switzerland, 2016. doi:10.1007/978-3-319-41990-9

2. Vanden Berg-Foels, W. S.; Scipioni, L.; Huynh, C.; Wen, X. *J. Microsc. (Oxford, U. K.)* **2012,** *246,* 168–176. doi:10.1111/j.1365-2818.2012.03606.x
3. BAZOU, D.; BEHAN, G.; REID, C.; BOLAND, J. J.; ZHANG, H. Z. *J. Microsc. (Oxford, U. K.)* **2011,** *242,* 290–294. doi:10.1111/j.1365-2818.2010.03467.x
4. Chen, X.; Udalagama, C. N. B.; Chen, C.-B.; Bettiol, A. A.; Pickard, D. S.; Venkatesan, T.; Watt, F. *Biophys. J.* **2011,** *101,* 1788–1793. doi:10.1016/j.bpj.2011.08.028
5. Rice, W. L.; Van Hoek, A. N.; Păunescu, T. G.; Huynh, C.; Goetze, B.; Singh, B.; Scipioni, L.; Stern, L. A.; Brown, D. *PLoS One* **2013,** *8,* e57051. doi:10.1371/journal.pone.0057051
6. Schürmann, M.; Frese, N.; Beyer, A.; Heimann, P.; Widera, D.; Mönkemöller, V.; Huser, T.; Kaltschmidt, B.; Kaltschmidt, C.; Gölzhäuser, A. *Small* **2015,** *11,* 5781–5789. doi:10.1002/smll.201501540
7. Greiner, J. F. W.; Hauser, S.; Widera, D.; Müller, J.; Qunneis, F.; Zander, C.; Martin, I.; Mallah, J.; Schuetzmann, D.; Prante, C.; Schwarze, H.; Prohaska, W.; Beyer, A.; Rott, K.; Hütten, A.; Gölzhäuser, A.; Sudhoff, H.; Kaltschmidt, C.; Kaltschmidt, B. *Eur. Cells Mater.* **2011,** *22,* 403–419. doi:10.22203/ecm.v022a30
8. Leppänen, M.; Sundberg, L.-R.; Laanto, E.; de Freitas Almeida, G. M.; Papponen, P.; Maasilta, I. J. *Adv. Biosyst.* **2017,** *1,* 1700070. doi:10.1002/adbi.201700070
9. Said, N.; Chatzinotas, A.; Schmidt, M. *Adv. Biosyst.* **2019,** *3,* 1800250. doi:10.1002/adbi.201800250
10. Chen, S.-C.; Musat, N.; Lechtenfeld, O. J.; Paschke, H.; Schmidt, M.; Said, N.; Popp, D.; Calabrese, F.; Stryhanyuk, H.; Jaekel, U.; Zhu, Y.-G.; Joye, S. B.; Richnow, H.-H.; Widdel, F.; Musat, F. *Nature* **2019,** *568,* 108–111. doi:10.1038/s41586-019-1063-0
11. Schmidt, M.; Byrne, J. M.; Maasilta, I. J. *Beilstein J. Nanotechnol.* **2021,** *12,* 1–23. doi:10.3762/bjnano.12.1
12. Corman, V. M.; Lienau, J.; Witzenrath, M. *Internist* **2019,** *60,* 1136–1145. doi:10.1007/s00108-019-00671-5
13. Wu, F.; Zhao, S.; Yu, B.; Chen, Y.-M.; Wang, W.; Song, Z.-G.; Hu, Y.; Tao, Z.-W.; Tian, J.-H.; Pei, Y.-Y.; Yuan, M.-L.; Zhang, Y.-L.; Dai, F.-H.; Liu, Y.; Wang, Q.-M.; Zheng, J.-J.; Xu, L.; Holmes, E. C.; Zhang, Y.-Z. *Nature* **2020,** *579,* 265–269. doi:10.1038/s41586-020-2008-3
14. Coronavirus COVID-19 Dashboard, Johns Hopkins University. https://gisanddata.maps.arcgis.com/apps/opsdashboard/index.html#/bda7594740fd40299423467b48e9ecf6 (accessed Jan 18, 2021).
15. Takayama, K. *Trends Pharmacol. Sci.* **2020,** *41,* 513–517. doi:10.1016/j.tips.2020.05.005
16. Zhu, N.; Zhang, D.; Wang, W.; Li, X.; Yang, B.; Song, J.; Zhao, X.; Huang, B.; Shi, W.; Lu, R.; Niu, P.; Zhan, F.; Ma, X.; Wang, D.; Xu, W.; Wu, G.; Gao, G. F.; Tan, W. *N. Engl. J. Med.* **2020,** *382,* 727–733. doi:10.1056/nejmoa2001017
17. Algarroba, G. N.; Rekawek, P.; Vahanian, S. A.; Khullar, P.; Palaia, T.; Peltier, M. R.; Chavez, M. R.; Vintzileos, A. M. *Am. J. Obstet. Gynecol.* **2020,** *223,* 275–278. doi:10.1016/j.ajog.2020.05.023
18. Harcourt, J.; Tamin, A.; Lu, X.; Kamili, S.; Sakthivel, S. K.; Murray, J.; Queen, K.; Tao, Y.; Paden, C. R.; Zhang, J.; Li, Y.; Uehara, A.; Wang, H.; Goldsmith, C.; Bullock, H. A.; Wang, L.; Whitaker, B.; Lynch, B.; Gautam, R.; Schindewolf, C.; Lokugamage, K. G.; Scharton, D.; Plante, J. A.; Mirchandani, D.; Widen, S. G.; Narayanan, K.; Makino, S.; Ksiazek, T. G.; Plante, K. S.; Weaver, S. C.; Lindstrom, S.; Tong, S.; Menachery, V. D.; Thornburg, N. J. *Emerging Infect. Dis.* **2020,** *26,* 1266–1273. doi:10.3201/eid2606.200516
19. Bouhaddou, M.; Memon, D.; Meyer, B.; White, K. M.; Rezelj, V. V.; Correa Marrero, M.; Polacco, B. J.; Melnyk, J. E.; Ulferts, S.; Kaake, R. M.; Batra, J.; Richards, A. L.; Stevenson, E.; Gordon, D. E.; Rojc, A.; Obernier, K.; Fabius, J. M.; Soucheray, M.; Miorin, L.; Moreno, E.; Koh, C.; Tran, Q. D.; Hardy, A.; Robinot, R.; Vallet, T.; Nilsson-Payant, B. E.; Hernandez-Armenta, C.; Dunham, A.; Weigang, S.; Knerr, J.; Modak, M.; Quintero, D.; Zhou, Y.; Dugourd, A.; Valdeolivas, A.; Patil, T.; Li, Q.; Hüttenhain, R.; Cakir, M.; Muralidharan, M.; Kim, M.; Jang, G.; Tutuncuoglu, B.; Hiatt, J.; Guo, J. Z.; Xu, J.; Bouhaddou, S.; Mathy, C. J. P.; Gaulton, A.; Manners, E. J.; Félix, E.; Shi, Y.; Goff, M.; Lim, J. K.; McBride, T.; O'Neal, M. C.; Cai, Y.; Chang, J. C. J.; Broadhurst, D. J.; Klippsten, S.; De wit, E.; Leach, A. R.; Kortemme, T.; Shoichet, B.; Ott, M.; Saez-Rodriguez, J.; tenOever, B. R.; Mullins, R. D.; Fischer, E. R.; Kochs, G.; Grosse, R.; García-Sastre, A.; Vignuzzi, M.; Johnson, J. R.; Shokat, K. M.; Swaney, D. L.; Beltrao, P.; Krogan, N. J. *Cell* **2020,** *182,* 685–712.e19. doi:10.1016/j.cell.2020.06.034
20. Prasad, S.; Potdar, V.; Cherian, S.; Abraham, P.; Basu, A.; ICMR-NIV NIC Team. *Indian J. Med. Res.* **2020,** *151,* 241–243. doi:10.4103/ijmr.ijmr_577_20
21. Wolff, G.; Limpens, R. W. A. L.; Zevenhoven-Dobbe, J. C.; Laugks, U.; Zheng, S.; de Jong, A. W. M.; Koning, R. I.; Agard, D. A.; Grünewald, K.; Koster, A. J.; Snijder, E. J.; Bárcena, M. *Science* **2020,** *369,* 1395–1398. doi:10.1126/science.abd3629
22. Ward, B. W.; Notte, J. A.; Economou, N. P. *J. Vac. Sci. Technol., B: Microelectron. Nanometer Struct.–Process., Meas., Phenom.* **2006,** *24,* 2871. doi:10.1116/1.2357967
23. Hlawacek, G.; Veligura, V.; van Gastel, R.; Poelsema, B. *J. Vac. Sci. Technol., B: Nanotechnol. Microelectron.: Mater., Process., Meas., Phenom.* **2014,** *32,* 020801. doi:10.1116/1.4863676
24. "New Images of Novel Coronavirus SARS-CoV-2 Now Available", NIAID Media Team, Feb 17, 2020, USA. https://www.niaid.nih.gov/news-events/novel-coronavirus-sarscov2-images (accessed Dec 1, 2020).
25. Joens, M. S.; Huynh, C.; Kasuboski, J. M.; Ferranti, D.; Sigal, Y. J.; Zeitvogel, F.; Obst, M.; Burkhardt, C. J.; Curran, K. P.; Chalasani, S. H.; Stern, L. A.; Goetze, B.; Fitzpatrick, J. A. J. *Sci. Rep.* **2013,** *3,* 3514. doi:10.1038/srep03514
26. Rothe, C.; Schunk, M.; Sothmann, P.; Bretzel, G.; Froeschl, G.; Wallrauch, C.; Zimmer, T.; Thiel, V.; Janke, C.; Guggemos, W.; Seilmaier, M.; Drosten, C.; Vollmar, P.; Zwirglmaier, K.; Zange, S.; Wölfel, R.; Hoelscher, M. *N. Engl. J. Med.* **2020,** *382,* 970–971. doi:10.1056/nejmc2001468
27. Felgenhauer, U.; Schoen, A.; Gad, H. H.; Hartmann, R.; Schaubmar, A. R.; Failing, K.; Drosten, C.; Weber, F. *J. Biol. Chem.* **2020,** *295,* 13958–13964. doi:10.1074/jbc.ac120.013788
28. Bojkova, D.; Klann, K.; Koch, B.; Widera, M.; Krause, D.; Ciesek, S.; Cinatl, J.; Münch, C. *Nature* **2020,** *583,* 469–472. doi:10.1038/s41586-020-2332-7
29. Cohen-Tanugi, D.; Yao, N. *J. Appl. Phys.* **2008,** *104,* 063504. doi:10.1063/1.2976299
30. Bell, D. C. *Microsc. Microanal.* **2009,** *15,* 147–153. doi:10.1017/s1431927609090138
31. Ennos, A. E. *Br. J. Appl. Phys.* **1953,** *4,* 101–106. doi:10.1088/0508-3443/4/4/302
32. Isaacson, M. *Ultramicroscopy* **1979,** *4,* 193–199. doi:10.1016/s0304-3991(79)90193-1
33. Hren, J. J. *Ultramicroscopy* **1978,** *3,* 375–380. doi:10.1016/s0304-3991(78)80057-6

34. van Gastel, R.; Barriss, L.; Sanford, C.; Hlawacek, G.; Scipioni, L.; Merkle, A. P.; Voci, D.; Fenner, C.; Zandvliet, H. J. W.; Poelsema, B. *Microsc. Microanal.* **2011,** *17* (Suppl. 2), 928–929. doi:10.1017/s1431927611005514
35. Hlawacek, G.; Veligura, V.; Lorbek, S.; Mocking, T. F.; George, A.; van Gastel, R.; Zandvliet, H. J. W.; Poelsema, B. *Beilstein J. Nanotechnol.* **2012,** *3,* 507–512. doi:10.3762/bjnano.3.58
36. Veligura, V.; Hlawacek, G.; van Gastel, R.; Zandvliet, H. J. W.; Poelsema, B. *Beilstein J. Nanotechnol.* **2012,** *3,* 501–506. doi:10.3762/bjnano.3.57
37. Wirtz, T.; De Castro, O.; Audinot, J.-N.; Philipp, P. *Annu. Rev. Anal. Chem.* **2019,** *12,* 523–543. doi:10.1146/annurev-anchem-061318-115457
38. Wang, S.-M.; Huang, K.-J.; Wang, C.-T. *Virology* **2014,** *449,* 287–296. doi:10.1016/j.virol.2013.11.030
39. Caldas, L. A.; Carneiro, F. A.; Higa, L. M.; Monteiro, F. L.; da Silva, G. P.; da Costa, L. J.; Durigon, E. L.; Tanuri, A.; de Souza, W. *Sci. Rep.* **2020,** *10,* 16099. doi:10.1038/s41598-020-73162-5
40. Mahauad-Fernandez, W. D.; Okeoma, C. M. *Immun., Inflammation Dis.* **2016,** *4,* 4–23. doi:10.1002/iid3.92
41. Berry, K. N.; Kober, D. L.; Su, A.; Brett, T. J. *BioEssays* **2018,** *40,* 1800086. doi:10.1002/bies.201800086
42. Hammonds, J.; Wang, J.-J.; Yi, H.; Spearman, P. *PLoS Pathog.* **2010,** *6,* e1000749. doi:10.1371/journal.ppat.1000749

License and Terms

BEILSTEIN JOURNAL OF NANOTECHNOLOGY

Scanning transmission helium ion microscopy on carbon nanomembranes

Daniel Emmrich*[1], Annalena Wolff[2], Nikolaus Meyerbröker[3], Jörg K. N. Lindner[4], André Beyer[1] and Armin Gölzhäuser[1]

Full Research Paper

Open Access

Address:
[1]Physics of Supramolecular Systems and Surfaces, Bielefeld University, 33615 Bielefeld, Germany, [2]Central Analytical Research Facility, Institute for Future Environments, Queensland University of Technology, 2 George St, Brisbane 4000, QLD, Australia, [3]CNM Technologies, Bielefeld, Germany and [4]Department of Physics, Paderborn University, Paderborn, Germany

Email:
Daniel Emmrich* - demmrich@physik.uni-bielefeld.de

* Corresponding author

Keywords:
carbon nanomembranes; dark field; helium ion microscopy (HIM); scanning transmission ion microscopy (STIM); SRIM simulations

Beilstein J. Nanotechnol. **2021,** *12,* 222–231.
https://doi.org/10.3762/bjnano.12.18

Received: 21 September 2020
Accepted: 12 February 2021
Published: 26 February 2021

This article is part of the thematic issue "Ten years of the helium ion microscope".

Associate Editor: P. Leiderer

Abstract

A dark-field scanning transmission ion microscopy detector was designed for the helium ion microscope. The detection principle is based on a secondary electron conversion holder with an exchangeable aperture strip allowing its acceptance angle to be tuned from 3 to 98 mrad. The contrast mechanism and performance were investigated using freestanding nanometer-thin carbon membranes. The results demonstrate that the detector can be optimized either for most efficient signal collection or for maximum image contrast. The designed setup allows for the imaging of thin low-density materials that otherwise provide little signal or contrast and for a clear end-point detection in the fabrication of nanopores. In addition, the detector is able to determine the thickness of membranes with sub-nanometer precision by quantitatively evaluating the image signal and comparing the results with Monte Carlo simulations. The thickness determined by the dark-field transmission detector is compared to X-ray photoelectron spectroscopy and energy-filtered transmission electron microscopy measurements.

Introduction

Throughout the past decade, the helium ion microscope (HIM) has emerged as a versatile instrument that is used to drive research across multiple disciplines. While it can be operated like a scanning electron microscope (SEM) for imaging applications, it offers a higher resolution at a larger depth of field than SEMs [1]. A major advantage of the technology besides its surface-sensitive imaging capability is the ability to record charge-compensated images on insulating samples such as biological specimen or polymers without requiring a conductive coating layer [2-4].

In addition, the ability to record images with high signal-to-noise ratio while using low beam currents (the HIM creates up to five times more secondary electrons (SE) than an SEM [5]) is advantageous when working with beam-sensitive samples. An overview of the imaging as well as recently added analytical capabilities using secondary ion mass spectroscopy can be found in a recent review [6].

Beyond imaging, the HIM has been established as a key nanofabrication tool for milling [7-9], defect engineering [10,11], and resist-based lithography [12,13], overcoming the resolution limitations of other FIB techniques [14,15].

Both bulk samples as well as thin membranes have been structured using the HIM. On membranes, the sputter yield is significantly increased because sputtering occurs not only in backward but also in forward direction [16,17]. To observe and control the milling process, the ion transmission signal is preferred over the SE signal because it is related to the membrane thickness. The detection of the transmission signal can be achieved in different ways. In a SE conversion plate holder, the sample is placed above a polished metal plate that is turned towards the SE detector of the microscope. Transmitted ions release SE from the plate while apertures on the polished metal plate filter bright-field and dark-field signal, similar to scanning transmission electron microscopy (STEM). In this way, it is possible to check qualitatively the milling progress on membranes or even to determine quantitatively the thickness of a sample. Notte et al. used thickness fringes on MgO crystals for thickness determination [18], Hall measured the thickness of a silicon nitride membrane down to 5 nm using the bright-field signal [19]. A different detection method is the use of a microchannel plate (MCP). Woehl et al. were able to resolve the core–shell structure of silica-coated gold nanoparticles with an annular detector in the dark field [20]. Kavanagh et al. used a silicon diode array as a pixelated sensor for transmission imaging to observe ion beam scattering with a static beam and as an end-point detection for pore milling into graphite sheets [21].

This work presents the design and capabilities of a dark-field scanning transmission ion microscopy (STIM) holder. The holder design is based on the concept of a SE conversion holder. The holder can easily be implemented into any existing HIM. It is mounted on the sample stage without modifications to the microscope.

Carbon nanomembranes (CNMs) serve as test samples. These membranes are made from aromatic molecules, typically from self-assembled monolayers. Upon electron irradiation, cross-linking of the molecules is induced. A mechanically stable membrane is formed, which can be transferred onto any other substrate, such as TEM grids [22,23]. Since CNMs originate from a molecular thin film, they can be as thin as 1 nm. The conductivity of such membranes is low, which poses a challenge to SE imaging with charged-particle microscopes such as SEM or HIM [24].

This work demonstrates that the holder is easily optimized for such difficult samples. It is possible to image a sample area and vary the acceptance angles from 3 to 98 mrad under constant microscope conditions. Thus, it is possible to study the behavior of the STIM signal at different acceptance angles.

Results and Discussion

STIM detector design

The designed dark-field STIM detector (Figure 1a) is based, in principle, on a SE conversion holder. It is mounted as a specimen holder onto the microscope stage at which the beam is scanned over the sample. Multiple samples can be mounted at a distance above a brass plate. On this conversion plate, ions release SE, which are detected by the Everhart–Thornley detector (ETD). Ions that are transmitted through a thin specimen (e.g., a membrane), undergo elastic and inelastic scattering processes, which lead to deflection of the ion trajectories. Depending on the resulting scattering angle, the transmitted ions hit different points on the conversion plate below the sample. This plate has holes centered underneath each specimen position. The holes act as Faraday cups. Ions that are deflected by a low angle will pass the hole and do not create a signal on the conversion plate. Ions that are deflected by large angles will hit the conversion plate and create a signal that can be detected with the ETD. Therefore, the brightness of a pixel in the final image is determined by the degree of scattering. Additionally, the brightness is determined by the acceptance angle α of the STIM holder. This angle is defined by the size of the hole on the conversion plate. It is the minimum deflection angle for ions to create a transmission signal and can be calculated using

$$\tan\alpha = r/h, \tag{1}$$

with α as the acceptance angle, h as the operational height of the holder (i.e., the distance between a thin membrane and the conversion plate) and r as the radius of the hole (Figure 1a). An increasing acceptance angle results in an overall darker image as more and more scattered ions are excluded from the STIM signal.

The dark-field STIM holder (Figure 1b) allows one to load up to five samples at one time. Each sample is mounted 15.3 mm above the conversion plate. Different conversion plates with

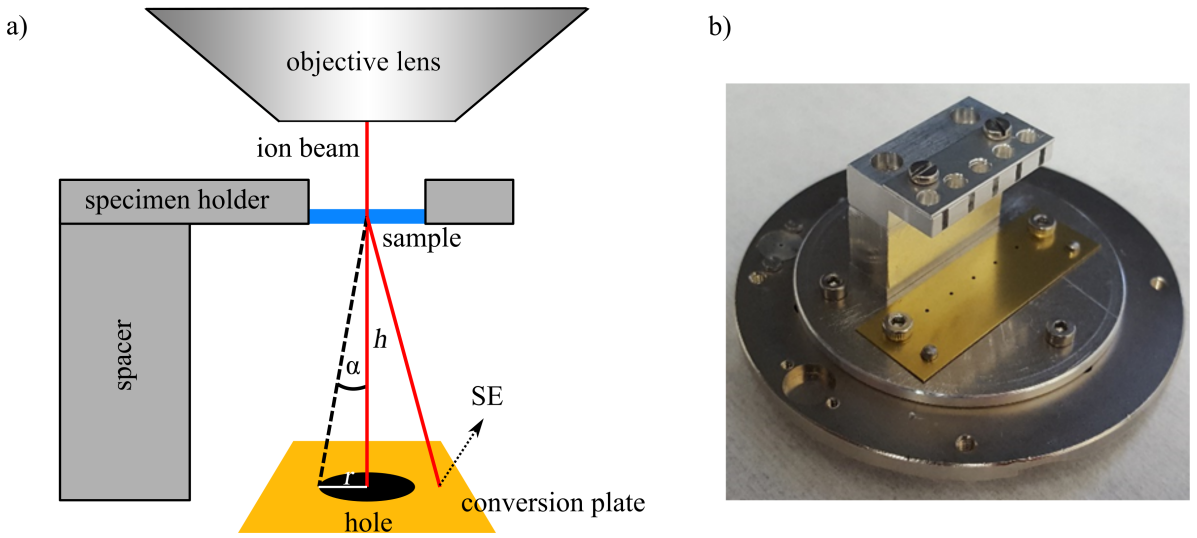

Figure 1: (a) Operating principle of the STIM dark-field detector. Thin foils or membranes are placed in the top part of the detector, which is mounted above the conversion plate at a specific height *h*. The height can be adjusted by an exchangeable spacer block. The metal conversion plate has differently sized holes directly underneath the mounted sample. Ion trajectories are altered during the ion–solid interaction and exit the thin foils or membranes at the bottom at different angles. The acceptance angle α depends on the height *h* and the radius of the hole *r*. Transmitted ions either enter the hole or they hit the metal conversion plate, which produces SE that can be detected with the ETD. (b) Photo of the detector for the HIM showing slots for five samples.

hole diameters from 100 µm to 3 mm lead to acceptance angles between 3 and 98 mrad. Two centering pins ensure that all aperture strips are always mounted at the identical position on the holder. The total size of the holder is limited by the dimensions of the load lock valve as well as by the gap between holder in the specimen chamber and objective lens.

The required hole sizes depend on the deflection angles, which are determined by beam energy, sample thickness, and sample material. The angles can be predicted using Monte Carlo simulations, which yield information about the relevant range of hole diameters by employing Equation 1.

For quantitative analysis of the STIM signal, a proper alignment of the sample is crucial. A beam shift needs to be avoided to ensure a perpendicular beam on the sample and the imaging area must be centered above the hole in the conversion plate.

In order to measure the pure STIM signal, SE emitted directly from the sample need to be blocked. Ideally, the resulting signal consists exclusively of SE released by transmitted ions. Three measures were taken to filter out direct SE. Firstly, CNMs have a low conductivity, which leads to charging and reduces the SE emission from the sample surface [25]. In addition, the holder is set to a positive voltage of 180 V that pulls the SE away from the detector. Furthermore, the samples are placed in 2.5 mm deep boreholes for signal shadowing, while the holder is in close proximity to the objective lens.

To visualize the SE contribution that is overlaying the STIM signal in later experiments, a CNM with a thickness of about 2 nm was imaged (Figure 2). This amorphous and insulating membrane is placed on a conductive Quantifoil TEM support grid. The sample was first imaged in a configuration that excludes all transmitted ions from the detection chain and leads to a SE signal only originating from the sample (Figure 2a). For this configuration, the aperture strip is removed, exposing a large hole in the base plate, and the spacer block (see Figure 1) is removed to mount the specimen holder directly over the hole. In Figure 2b the same sample area was imaged with the holder in STIM configuration as depicted in Figure 1, that is, spacer block and aperture strip were installed. In both configurations a stage bias of 180 V was applied. While the free-standing CNM shows nearly no signal in the SE configuration, the STIM signal reveals details about ruptures and folds in the membrane. The conducting Quantifoil support is visible in both configurations, with an average grey level of 23 in SE and 117 in STIM, suggesting a significant amount of direct SE in STIM configuration in this region. STIM analysis will only be conducted on areas of freestanding CNM. Intensity profiles across a feature (a rupture and a fold) show that the portion of direct SE from the CNM is negligible for the STIM analysis (Figure 2c).

Monte Carlo simulations and signal/contrast modelling

In order to understand the physics behind the STIM signal, the program Stopping and Range of Ions in Matter (SRIM) was

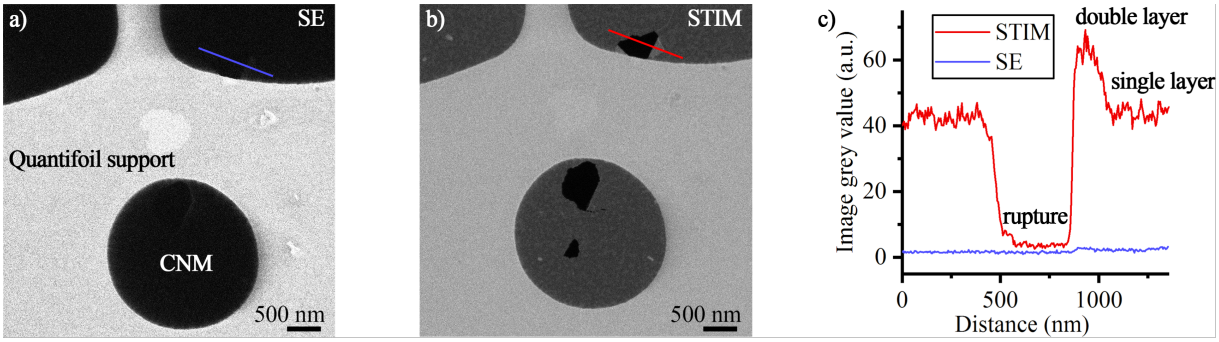

Figure 2: Comparison of HIM detection schemes. (a) SE and (b) dark-field STIM signal at an acceptance angle of 13 mrad show the strength of STIM on the CNM. Both images were recorded with the same ETD settings, but contrast was adjusted individually for publication. Line profiles from each raw signal (c) prove that in STIM configuration, the SE contribution originating directly from the sample is negligible. In the STIM analysis of CNM, the signal difference between rupture and double layer is one grey level in SE, compared to 57 grey levels in STIM, while there is no difference between single and double layer in SE configuration.

used for Monte Carlo simulations [26]. When simulating thin membranes, it is important to use the monolayer collisions calculation type. Otherwise inaccurate results could be obtained as the collisions will be averaged over the mean free path. The simulation was run with 50,000 ions at energies of either 15 or 30 keV. The CNM was approximated as a carbon layer with a thickness between 0.3 and 13 nm. From the SRIM output file of all transmitted ions, an angular distribution was generated (see Figure 3a). The simulation results, obtained for different values of the CNM thickness show that the mean value of the scattering angle is reduced for thinner membranes. This is intuitive as the ions undergo fewer collision while traversing through the sample, leading to less accumulated deflection.

The following data treatment is intended to explain the STIM signal for CNMs of different thickness. Since the detector only converts ions that are scattered beyond the acceptance angle α, it is important to consider the cumulative sum of all ions beyond the angle α. An example of this data processing is shown in Figure 3. From a scattering distribution (Figure 3a) the ions are summed up to a theoretical STIM signal (Figure 3b). This was done for sample thicknesses of 1.5 nm (corresponding to a single-layer CNM) and 3 nm (a double-layer CNM). In the extreme case of an acceptance angle of 0 mrad (i.e., a plain metal sheet as conversion plate), all transmitted ions create a signal that can be subsequently detected. At larger acceptance angles the overall intensity decreases (Figure 3b). The signal decreases faster for a thinner membrane than for a thicker membrane towards larger angles. This makes sense, as thinner membranes lead to smaller deflection angles. Thus, the transmitted ions hit the hole, rather than creating a signal on the metal conversion plate. The difference (blue area in Figure 3b) between both signals, however, does not stay constant throughout the range of the acceptance angle. The plot in Figure 3c shows the difference in STIM signal between 3 nm thin and 1.5 nm thin CNMs for different acceptance angles.

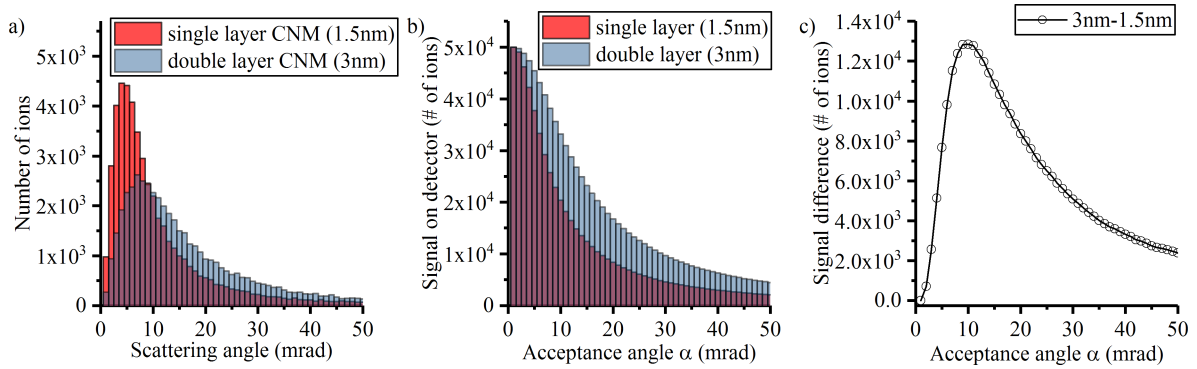

Figure 3: (a) SRIM scattering distribution of 30 keV He ions for single- and double-layer membranes, assuming a membrane thickness of 1.5 nm per layer. (b) Predicted detector signal for the dark-field STIM detector with indicated acceptance angle. (c) Signal difference between the double-layer and the single-layer membrane as a function of the detector acceptance angle.

While the difference in the signal is low at small and large angles, the simulation results show that it reaches a maximum at an acceptance angle of 10 mrad.

Depending on the acceptance angle of the detector, maximum brightness or maximum contrast between different thicknesses are adjustable. The simulation results suggest that smaller acceptance angles are ideal for applications where brightness is important, such as end-point detection for, for example, nanopores. Especially on extremely thin membranes such as CNMs, milling processes are very fast and need a clearly defined signal change when the membrane is milled through. With acceptance angle and ETD settings tuned correctly, an abrupt signal change from bright to dark could easily trigger a stop command. If thickness variations, such as folds, or contaminations are of interest, larger acceptance angles serve better, at the cost of losing overall image brightness.

Experimental evaluation of signal and contrast using the HIM

Figure 4 shows a series of HIM images of CNMs using the dark-field STIM detector configured with a range of difference acceptance angles. For each image, a different conversion plate with a hole size corresponding to the acceptance angle is installed on the holder. The two sets of images were taken of membranes of different thicknesses. For each set, microscope and ETD settings were optimized and conditions were kept constant for all images within the set.

Figure 4a shows a freestanding membrane that was intentionally ruptured by a high-flux helium ion beam prior to imaging. The image shows the rupture, the membrane, and a folded layer of the CNM. At small acceptance angles, the membrane yields a high-intensity signal, while the overall intensity drops when increasing the acceptance angle. This is in agreement with the SRIM simulations. At low and at high acceptance angles, single layer and double layer are hard to distinguish. Maximum contrast, that is, maximum signal difference between the single layer and the double layer, is achieved at an acceptance angle of 11 mrad.

Figure 4b shows a thicker membrane. The images show a single layer and a double layer of the membrane spanning over a hole in the Quantifoil support. Overall intensity and contrast between the different layers are similar to those of the thin membrane, but shifted to larger acceptance angles. Single layer and double layer are hard to distinguish at an acceptance angle of 13 mrad. This angle yielded almost the maximum contrast for the thin CNM. The maximum contrast for the thick CNM is reached at an acceptance angle of about 52 mrad.

Thickness measurements using dark-field STIM and Monte Carlo simulations

As shown in Figure 4, the maximum contrast between single- and double-layer membrane shifts towards larger angles for a thicker membrane. Quantifying this effect allows for the determination of the membrane thickness by comparing the measured grey levels to SRIM simulations as demonstrated in the following.

In Figure 3c the existence of a maximum signal difference between a single- and a double-layer membrane was predicted. In this case, the thickness of the membrane was assumed to be 1.5 nm resulting in a maximum at an acceptance angle of 10 mrad. To determine the membrane thicknesses of both imaged samples in Figure 4, many curves of the signal difference, as in Figure 3c, were simulated for different membrane thicknesses. The acceptance angle of the maximum was extracted from each signal difference graph and plotted as a function of the membrane thickness. The result is shown in

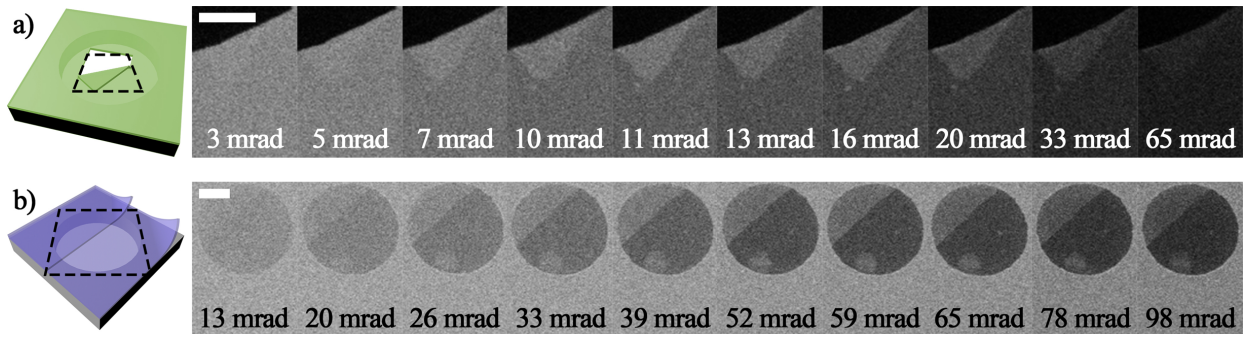

Figure 4: Dark-field STIM images of (a) a thin and (b) a thick membrane. The membrane in (a) shows a rupture (black area) and a folded CNM. The example in (b) shows a CNM spanning over a hole in the Quantifoil support. Both are showing the signal intensity of single- and double-layer membranes. For the thicker membrane in (b), the signal of maximum contrast between one layer and two layers is shifted towards larger acceptance angles. Scale bars are 400 nm.

Figure 5. Each point in the graph is based on two simulations with the thickness corresponding to a single- and a double-layer membrane. The simulations were run using kinetic ion energies of 30 and 15 keV. This plot serves as a reference chart for thickness determination of the examined samples.

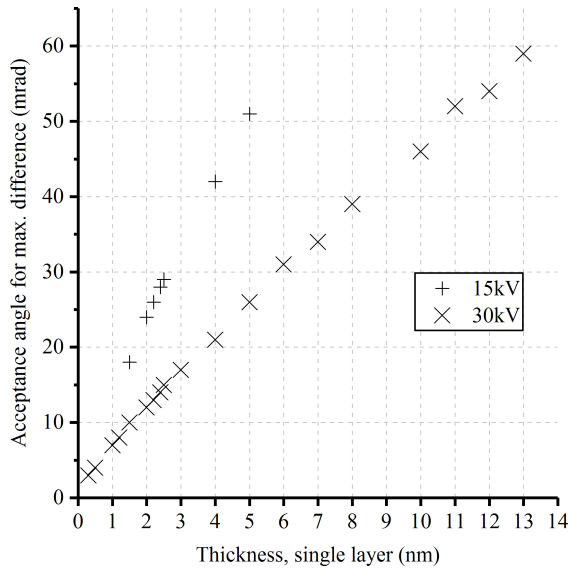

Figure 5: Acceptance angle at which the maximum signal difference between a double layer and a single layer is expected as a function of the layer thickness. The data was extracted from graphs such as those shown in Figure 3c.

The grey levels from the experiments were processed analogous to the simulation data. From each image in Figure 4, mean grey values were determined for the single layer and the double layer. The difference between these signals was plotted as a function of the acceptance angle. Figure 6a shows the experimental results for both membranes. To determine the thickness, the position of the maximum needs to be compared to the simulations (see Figure 5). For visualization, the best-matching signal curve was plotted for each membrane. By this, the thickness of the thin and the thick membrane was determined to be 2 and 12 nm, respectively.

To estimate the error of the thickness determination, a CNM is imaged at two different kinetic ion energies (15 and 30 keV) and the results are compared to Monte Carlo simulations (see Figure 6b). The simulation of a 2.0 nm thick CNM (dashed lines) agrees well with the measurement at 30 keV energy for the thin membrane. This is reasonable as it is the same membrane as shown in Figure 6a. When evaluating the contrast at a nearby area at 15 keV ion energy, however, 2 nm is not the optimum thickness to reproduce the experimental contrast at 15 keV. At this lower incident ion energy, a thickness of 2.4 nm (dotted lines) matches best the measurement values. Still, the results suggest that the CNM thickness can be determined with sub-nanometer accuracy using dark-field STIM measurements. A mean CNM thickness value of 2.2 nm is a compromise between the two cases, and the error of this particular measurement is 9%.

To test the validity of the determined thickness and the approach described above, the results from the STIM dark-field imaging are compared to X-ray photoelectron spectroscopy (XPS) and energy-filtered transmission electron microscopy (EFTEM) data, both being established techniques for the thickness measurement of thin films. All three presented methods, STIM, XPS, and EFTEM, require an assumption about density

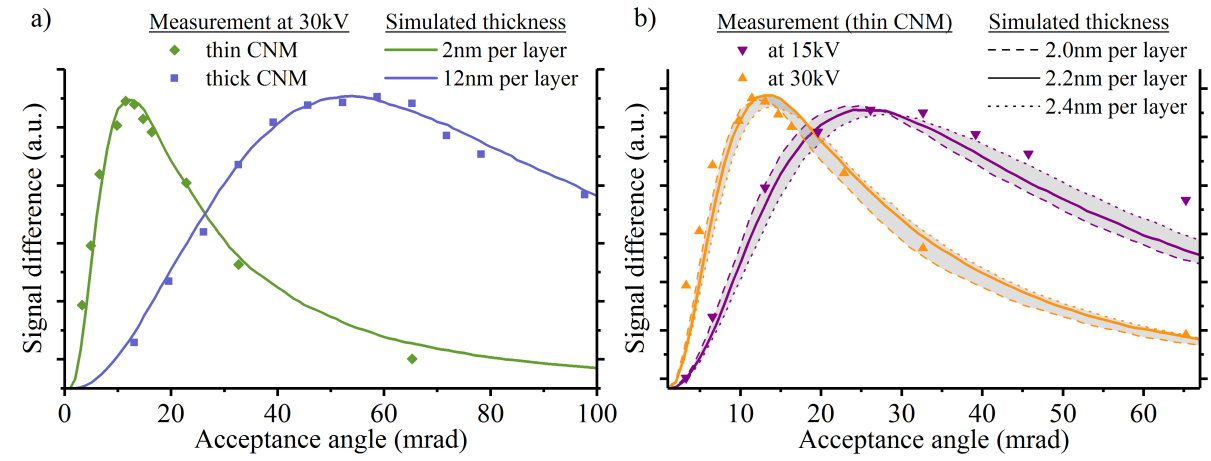

Figure 6: Thickness determination by dark-field STIM and Monte Carlo simulations. (a) The measured image grey values of single- and double-layer regions were extracted from both samples of Figure 4. According to the experimental data, the curve with the closest maximum was chosen based on Figure 5. Both curves are plotted for visualization. (b) Measurement of the same CNM (thin) at different energies to determine the variation of thickness results. The best-fitting curve at 15 keV yields a thickness of 2.4 nm per layer, at 30 keV it yields 2.0 nm per layer.

and composition of the material in order to calculate absolute thicknesses, so graphite was chosen as a well-characterized material.

XPS collects the signal from a measurement spot with a diameter of a few hundred micrometers. It has, therefore, a much lower lateral resolution than STIM. It requires the membrane to be placed on a solid bulk material. Therefore, from the same membrane batch used for STIM measurements, thin and thick CNMs were transferred onto a 300 nm Au film on a mica substrate for XPS analysis. The thickness was calculated from the attenuation of the Au $4f_{7/2}$ photoelectrons by the membrane on top. Details about the calculation can be found in the Supporting Information of the manuscript from Turchanin et al. [27]. In order to provide comparability of the results to STIM and EFTEM, the attenuation length was assumed to be 27 Å, the same as that of graphite [28]. The XPS results yield values of 2.1 nm for the thin CNM and 12.4 nm for the thick CNM. Both values are in good agreement with 2.2 nm and 12.0 nm measured by STIM (Table 1).

Table 1: Thickness values determined by STIM and other established methods.

	STIM	XPS	EFTEM 60 keV	EFTEM 80 keV
thin CNM	2.2 nm	2.1 nm	1.8 nm	1.7 nm
thick CNM	12.0 nm	12.4 nm	10.5 nm	11.0 nm

As a second method for comparison, EFTEM was performed on the samples after STIM measurements. EFTEM enables thickness mapping with a high lateral resolution. In EFTEM, elastically scattered electrons in a zero-loss energy-filtered image are compared to the total electron intensity of a non-filtered image [29]. It requires the estimation of an attenuation length λ, which was calculated by the Iakoubowskii model (Equation 9 in [30]), assuming here that the films exhibit the mass density of pure graphite. EFTEM measurements were done at kinetic energies of 60 and 80 keV to rule out possible deviations from the calculation of the attenuation length. Both energies are below the energy threshold for atom displacement in carbon membranes and should not lead to knock-on damage on the membrane [31]. The use of an energy filter reduces the beam energy at the sample by 3 keV, leading to electron mean free paths of 86.1 nm for 77 keV and 70.5 nm for 57 keV. The results for both thin and thick CNMs are listed in Table 1. The thicknesses are noticeably smaller than those obtained from STIM and XPS analyses. During EFTEM imaging it became clear that the membrane thickness decreased with increasing measurement time. In an extreme test scenario, the same area on the thick CNM was irradiated in TEM for 60 min while the thickness was monitored by EFTEM imaging (Figure 7a). The thickness decreases by 35% over 60 min. It should be noted, however, that one hour is very long compared to the usual measurement times of half a minute to a few minutes. Furthermore, the neglect of impurities in the CNM results in incorrect mean free paths λ and leads to a thickness deviation from the first image on.

To further investigate the observed phenomenon in the EFTEM measurement, HIM and Raman spectroscopy were performed on the samples after the EFTEM experiments. The SE image in Figure 7b shows that membrane turned brighter in the areas previously imaged with EFTEM, which is indicative of a higher

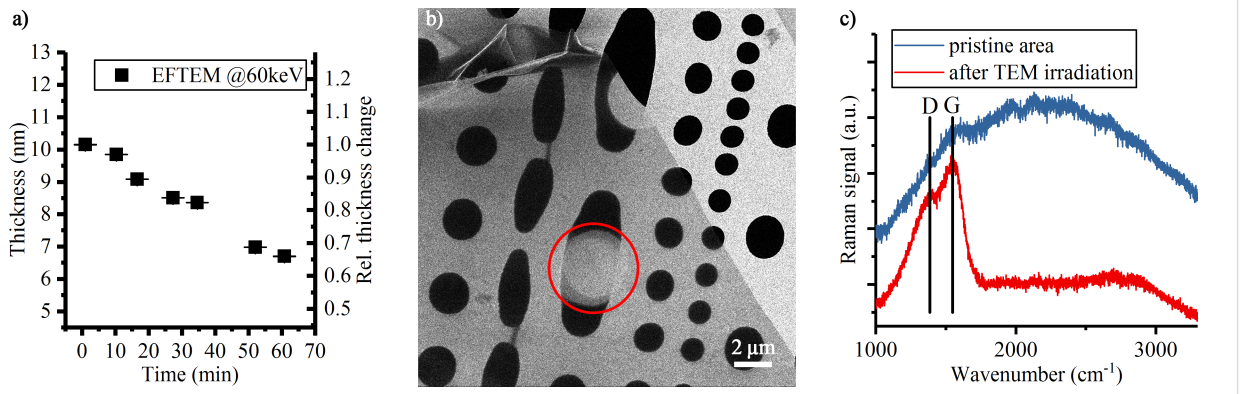

Figure 7: Alteration of a CNM by EFTEM at 60 keV beam energy. (a) The thickness decreases during EFTEM imaging, error bars refer to the standard error of the mean. The sample was exposed to the beam for 1 h and measured intermittently. (b) HIM SE image of an area on the CNM after taking two consecutive EFTEM images (red circle). After the area was exposed to the beam for 3 min, the area turned conductive as the bright signal in SE imaging indicates. (c) Raman measurement on the indicated area in (b) and a reference spectrum of a freestanding, non-irradiated area on the same sample. After irradiation the photoluminescence background drops and D and G peaks appear, showing a graphitization of the area exposed to EFTEM.

electric conductivity, as demonstrated in the following. In Figure 7c, a Raman measurement of this spot is compared to a non-exposed part of the membrane. The non-exposed membrane shows barely visible D and G bands on a strong photoluminescence background as it is reported for amorphous hydrogenated carbon films [32]. After exposure to TEM, the photoluminescence drops and the D and G bands become more pronounced, similar to a film of high-temperature annealed nanographite [33]. It was previously demonstrated in TEM that, at an energy of 80 keV, a graphitization of free-standing amorphous carbon can be induced [34]. It is also known that CNMs can turn from the amorphous state into nanocrystalline graphene upon heating [25]. It was observed that this comes with a loss of atoms, which is also apparent in this experiment by the decreasing membrane thickness (see Figure 7a).

The results from both methods, XPS and EFTEM, confirm the thickness measurement by STIM. While XPS and STIM are close regarding the absolute values, EFTEM shows a deviation. The approximation of the electron mean free path and the alteration of the CNM upon irradiation with high electron flux in EFTEM can explain this deviation.

Conclusion

This work demonstrates the capability of an easy-to-build dark-field STIM detector for ion microscopes. The dark-field STIM detector enables the imaging of very thin carbon nanomembranes with a high signal-to-noise ratio, which could not be achieved using the conventional ETD detector in the HIM. The evaluation of the contrast mechanism suggests that the detector is suitable for end-point detection, for example to drill small holes into thin foils. Thickness variations, caused by double layers or folds in membranes can be clearly visualized with the detector. In addition, thickness measurements with sub-nanometer precision are possible on thin foils or membranes when the contrast is evaluated and compared to Monte Carlo simulations. A comparison with established thickness measurements confirms the STIM results.

Experimental

A dark-field scanning transmission ion microscopy (STIM) holder was designed for a Zeiss Orion Plus helium ion microscope (HIM). All HIM and STIM experiments were conducted on the Zeiss Orion Plus using helium ions with kinetic energies of 30 and 15 keV. A 10 µm aperture was selected and the working distance was kept identical for all images at 9.8 mm. The beam current ranged from 0.3 to 0.5 pA between different sets of images but stayed constant within a set of images. The grid of the Everhart–Thornley detector was kept at 500 V while photomultiplier gain, brightness, and image intensity were adjusted for each set of images to keep the signal on all images within the dynamic range of the detector. Images were acquired at a dwell time of 0.5 µs with line integration of 64 lines. The field of view was set to 10 µm for the thin carbon membrane and to 15 µm for the thick membrane.

The carbon nanomembranes (CNMs) were formed by low-energy electron irradiation of aromatic self-assembled monolayers (thin CNMs) or spin coated layers of aromatic molecules (thick CNMs). The electron irradiation leads to a crosslinking of the aromatic molecules and results in an amorphous membrane whose thickness is defined by the initial aromatic layer. CNMs were transferred onto TEM grids (Quantifoil Multi A) using a sacrificial layer of poly(methyl methacrylate) [35]. Thin CNMs were prepared from terphenylthiol precursor molecules, thick CNMs were obtained from CNM Technologies GmbH (Bielefeld, Germany). The CNMs used for this experiment offer a low conductivity to give a negligible SE contribution.

Monte Carlo simulations of the ion trajectories were run using the software package TRIM in the program Stopping and Range of Ions in Matter (SRIM) [26]. The “Surface Sputtering/Monolayer Collision Steps” calculation was selected due to the limited thickness of the membranes to ensure that the collisions in each monolayer were considered. 50000 ions at 15 and 30 keV energy were simulated. The membranes were assumed to consist of pure carbon with the density of graphite of 2.253 g/cm^2. The annular deflection angles of the transmitted ions were obtained from the transmitted ions output file and their distribution was determined using a frequency count in steps of 1 mrad.

X-ray photoelectron spectroscopy was conducted on an Omicron Multiprobe instrument using a monochromatized Al Kα X-ray source (1486.7 eV, 225 W) and an Omicron Sphera hemispherical electron energy analyzer at a constant analyzer energy of 12.5 eV. The data was acquired under a photoelectron emission angle of 13° with respect to the surface normal.

Energy-filtered transmission electron microscopy was conducted at energies of 60 and 80 keV on a C_s-corrected JEOL JEM-ARM200F equipped with a cold field emission gun. A GATAN GIF-Quantum ER image filter and a 2k × 2k CCD camera (GATAN UltraScan) were used during EFTEM operation.

Acknowledgements

Annalena Wolff would like to thank Carl Zeiss and Bielefeld University for their support of the HIM Worldtour 2017. We thank the authors of the program SRIM for making the software freely available.

Funding

Annalena Wolff would like to thank AMAS/EMAS for the Early Career Scholarship and the QUT VC Performance Award fund, which all made the HIM World Tour 2017 and collaboration on this project possible.

ORCID® iDs

Jörg K. N. Lindner - https://orcid.org/0000-0003-2367-9610
André Beyer - https://orcid.org/0000-0002-9569-0344
Armin Gölzhäuser - https://orcid.org/0000-0002-0838-9028

References

1. Hlawacek, G.; Gölzhäuser, A., Eds. *Helium Ion Microscopy;* NanoScience and Technology; Springer International Publishing: Cham, Switzerland, 2016. doi:10.1007/978-3-319-41990-9
2. Leppänen, M.; Sundberg, L.-R.; Laanto, E.; de Freitas Almeida, G. M.; Papponen, P.; Maasilta, I. J. *Adv. Biosyst.* **2017,** *1,* 1700070. doi:10.1002/adbi.201700070
3. Schürmann, M.; Frese, N.; Beyer, A.; Heimann, P.; Widera, D.; Mönkemöller, V.; Huser, T.; Kaltschmidt, B.; Kaltschmidt, C.; Gölzhäuser, A. *Small* **2015,** *11,* 5781–5789. doi:10.1002/smll.201501540
4. Hlawacek, G.; Veligura, V.; van Gastel, R.; Poelsema, B. *J. Vac. Sci. Technol., B: Nanotechnol. Microelectron.: Mater., Process., Meas., Phenom.* **2014,** *32,* 20801. doi:10.1116/1.4863676
5. Ramachandra, R.; Griffin, B.; Joy, D. *Ultramicroscopy* **2009,** *109,* 748–757. doi:10.1016/j.ultramic.2009.01.013
6. Wirtz, T.; De Castro, O.; Audinot, J.-N.; Philipp, P. *Annu. Rev. Anal. Chem.* **2019,** *12,* 523–543. doi:10.1146/annurev-anchem-061318-115457
7. Kollmann, H.; Piao, X.; Esmann, M.; Becker, S. F.; Hou, D.; Huynh, C.; Kautschor, L.-O.; Bösker, G.; Vieker, H.; Beyer, A.; Gölzhäuser, A.; Park, N.; Vogelgesang, R.; Silies, M.; Lienau, C. *Nano Lett.* **2014,** *14,* 4778–4784. doi:10.1021/nl5019589
8. Kalhor, N.; Boden, S. A.; Mizuta, H. *Microelectron. Eng.* **2014,** *114,* 70–77. doi:10.1016/j.mee.2013.09.018
9. Emmrich, D.; Beyer, A.; Nadzeyka, A.; Bauerdick, S.; Meyer, J. C.; Kotakoski, J.; Gölzhäuser, A. *Appl. Phys. Lett.* **2016,** *108,* 163103. doi:10.1063/1.4947277
10. Röder, F.; Hlawacek, G.; Wintz, S.; Hübner, R.; Bischoff, L.; Lichte, H.; Potzger, K.; Lindner, J.; Fassbender, J.; Bali, R. *Sci. Rep.* **2015,** *5,* 16786. doi:10.1038/srep16786
11. Aramesh, M.; Mayamei, Y.; Wolff, A.; Ostrikov, K. K. *Nat. Commun.* **2018,** *9,* 835. doi:10.1038/s41467-018-03316-7
12. Winston, D.; Cord, B. M.; Ming, B.; Bell, D. C.; DiNatale, W. F.; Stern, L. A.; Vladar, A. E.; Postek, M. T.; Mondol, M. K.; Yang, J. K. W.; Berggren, K. K. *J. Vac. Sci. Technol., B: Microelectron. Nanometer Struct.–Process., Meas., Phenom.* **2009,** *27,* 2702. doi:10.1116/1.3250204
13. Flatabø, R.; Agarwal, A.; Hobbs, R.; Greve, M. M.; Holst, B.; Berggren, K. K. *Nanotechnology* **2018,** *29,* 275301. doi:10.1088/1361-6528/aabe22
14. Melli, M.; Polyakov, A.; Gargas, D.; Huynh, C.; Scipioni, L.; Bao, W.; Ogletree, D. F.; Schuck, P. J.; Cabrini, S.; Weber-Bargioni, A. *Nano Lett.* **2013,** *13,* 2687–2691. doi:10.1021/nl400844a
15. Bell, D. C.; Lemme, M. C.; Stern, L. A.; Williams, J. R.; Marcus, C. M. *Nanotechnology* **2009,** *20,* 455301. doi:10.1088/0957-4484/20/45/455301
16. Tan, S.; Klein, K.; Shima, D.; Livengood, R.; Mutunga, E.; Vladár, A. *J. Vac. Sci. Technol., B: Nanotechnol. Microelectron.: Mater., Process., Meas., Phenom.* **2014,** *32,* 6. doi:10.1116/1.4900728
17. Marshall, M. M.; Yang, J.; Hall, A. R. *Scanning* **2012,** *34,* 101–106. doi:10.1002/sca.21003
18. Notte, J., IV; Hill, R.; McVey, S. M.; Ramachandra, R.; Griffin, B.; Joy, D. *Microsc. Microanal.* **2010,** *16,* 599–603. doi:10.1017/s1431927610093682
19. Hall, A. R. *Microsc. Microanal.* **2013,** *19,* 740–744. doi:10.1017/s1431927613000500
20. Woehl, T. J.; White, R. M.; Keller, R. R. *Microsc. Microanal.* **2016,** *22,* 544–550. doi:10.1017/s1431927616000775
21. Kavanagh, K. L.; Herrmann, C.; Notte, J. A. *J. Vac. Sci. Technol., B: Nanotechnol. Microelectron.: Mater., Process., Meas., Phenom.* **2017,** *35,* 06G902. doi:10.1116/1.4991898
22. Turchanin, A.; Gölzhäuser, A. *Adv. Mater. (Weinheim, Ger.)* **2016,** *28,* 6075–6103. doi:10.1002/adma.201506058
23. Turchanin, A.; Gölzhäuser, A. *Prog. Surf. Sci.* **2012,** *87,* 108–162. doi:10.1016/j.progsurf.2012.05.001
24. Beyer, A.; Vieker, H.; Klett, R.; Meyer Zu Theenhausen, H.; Angelova, P.; Gölzhäuser, A. *Beilstein J. Nanotechnol.* **2015,** *6,* 1712–1720. doi:10.3762/bjnano.6.175
25. Turchanin, A.; Beyer, A.; Nottbohm, C. T.; Zhang, X.; Stosch, R.; Sologubenko, A.; Mayer, J.; Hinze, P.; Weimann, T.; Gölzhäuser, A. *Adv. Mater. (Weinheim, Ger.)* **2009,** *21,* 1233–1237. doi:10.1002/adma.200803078
26. Ziegler, J. F.; Ziegler, M. D.; Biersack, J. P. *Nucl. Instrum. Methods Phys. Res., Sect. B* **2010,** *268,* 1818–1823. doi:10.1016/j.nimb.2010.02.091
27. Turchanin, A.; Käfer, D.; El-Desawy, M.; Wöll, C.; Witte, G.; Gölzhäuser, A. *Langmuir* **2009,** *25,* 7342–7352. doi:10.1021/la803538z
28. Lesiak, B.; Jablonski, A.; Prussak, Z.; Mrozek, P. *Surf. Sci.* **1989,** *223,* 213–232. doi:10.1016/0039-6028(89)90735-8
29. Malis, T.; Cheng, S. C.; Egerton, R. F. *J. Electron Microsc. Tech.* **1988,** *8,* 193–200. doi:10.1002/jemt.1060080206
30. Iakoubovskii, K.; Mitsuishi, K.; Nakayama, Y.; Furuya, K. *Microsc. Res. Tech.* **2008,** *71,* 626–631. doi:10.1002/jemt.20597
31. Meyer, J. C.; Eder, F.; Kurasch, S.; Skakalova, V.; Kotakoski, J.; Park, H. J.; Roth, S.; Chuvilin, A.; Eyhusen, S.; Benner, G.; Krasheninnikov, A. V.; Kaiser, U. *Phys. Rev. Lett.* **2012,** *108,* 196102. doi:10.1103/physrevlett.108.196102
32. Marchon, B.; Gui, J.; Grannen, K.; Rauch, G. C.; Ager, J. W.; Silva, S. R. P.; Robertson, J. *IEEE Trans. Magn.* **1997,** *33,* 3148–3150. doi:10.1109/20.617873
33. Chu, P. K.; Li, L. *Mater. Chem. Phys.* **2006,** *96,* 253–277. doi:10.1016/j.matchemphys.2005.07.048
34. Börrnert, F.; Avdoshenko, S. M.; Bachmatiuk, A.; Ibrahim, I.; Büchner, B.; Cuniberti, G.; Rümmeli, M. H. *Adv. Mater. (Weinheim, Ger.)* **2012,** *24,* 5630–5635. doi:10.1002/adma.201202173
35. Nottbohm, C. T.; Turchanin, A.; Beyer, A.; Stosch, R.; Gölzhäuser, A. *Small* **2011,** *7,* 874–883. doi:10.1002/smll.201001993

License and Terms

BEILSTEIN JOURNAL OF NANOTECHNOLOGY

The patterning toolbox FIB-o-mat: Exploiting the full potential of focused helium ions for nanofabrication

Victor Deinhart[*1,2], Lisa-Marie Kern[3], Jan N. Kirchhof[4], Sabrina Juergensen[4], Joris Sturm[1,2], Enno Krauss[5], Thorsten Feichtner[6], Sviatoslav Kovalchuk[4], Michael Schneider[3], Dieter Engel[3], Bastian Pfau[3], Bert Hecht[5], Kirill I. Bolotin[4], Stephanie Reich[4] and Katja Höflich[2,§]

Full Research Paper

Open Access

Address:
[1]Ferdinand-Braun-Institut gGmbH, Leibniz-Institut für Höchstfrequenztechnik, Gustav-Kirchhoff-Str. 4, 12489 Berlin, Germany, [2]Corelab Correlative Microscopy and Spectroscopy, Helmholtz-Zentrum Berlin für Materialien und Energie, Hahn-Meitner-Platz 1, 14109 Berlin, Germany, [3]Max Born Institute for Nonlinear Optics and Short Pulse Spectroscopy, Max-Born-Straße 2A, 12489 Berlin, Germany, [4]Freie Universität Berlin, Arnimallee 14, 14195 Berlin, Germany, [5]Department of Experimental Physics 5, Röntgen Research Center for Complex Material Research (RCCM), Physics Institute, University of Würzburg, Am Hubland, D-97074 Würzburg, Germany and [6]Dipartimento di Fisica, Politecnico di Milano, Piazza Leonardo da Vinci, 32 20133 Milano, Italy

Email:
Victor Deinhart[*] - victor.deinhart@helmholtz-berlin.de

* Corresponding author
§ Present address: Ferdinand-Braun-Institut gGmbH, Leibniz-Institut für Höchstfrequenztechnik, Gustav-Kirchhoff-Str. 4, 12489 Berlin, Germany

Keywords:
automated patterning; focused He ion beam; graphene; magnetic multilayers; mechanical resonator; pattern generation; plasmonic antennas; two-dimensional materials

Beilstein J. Nanotechnol. **2021,** *12,* 304–318.
https://doi.org/10.3762/bjnano.12.25

Received: 17 November 2020
Accepted: 05 March 2021
Published: 06 April 2021

This article is part of the thematic issue "Ten years of the helium ion microscope".

Guest Editors: G. Hlawacek and A. Wolff

Abstract

Focused beams of helium ions are a powerful tool for high-fidelity machining with spatial precision below 5 nm. Achieving such a high patterning precision over large areas and for different materials in a reproducible manner, however, is not trivial. Here, we introduce the Python toolbox FIB-o-mat for automated pattern creation and optimization, providing full flexibility to accomplish demanding patterning tasks. FIB-o-mat offers high-level pattern creation, enabling high-fidelity large-area patterning and systematic variations in geometry and raster settings. It also offers low-level beam path creation, providing full control over the beam movement and including sophisticated optimization tools. Three applications showcasing the potential of He ion beam nanofabrication for two-dimensional material systems and devices using FIB-o-mat are presented.

Introduction

Future breakthroughs in nanotechnology will rely on the ability to fabricate materials and devices by design, that is, to tailor both material properties and device geometries according to a sophisticated blueprint. Thin layers and two-dimensional (2D) materials are especially interesting candidates for designer materials [1] as they are compatible with planar device geometries and may be combined in a straightforward manner, for example, by stacking. Applications of such materials may rely on (coupled) material excitations, such as plasmon polaritons in gold nanostructures [2], on physical properties, such as the exceptionally high mechanical stability of suspended graphene [3], or on asymmetric magnetic interactions as in Co/Pt films, enabling the formation of desired spin textures [4]. As the actual device geometry determines the response to external stimuli, the coupling strengths, and the corresponding figures of merit, ultimate control in nanopatterning down to the single-digit nanometer range is heavily sought after.

One promising candidate for ultraprecise nanofabrication is focused ion beam (FIB) machining. Focused ion beams locally remove material based on physical sputtering with a large degree of flexibility due to advanced beam control. FIB patterning is a direct single-step process without the need of potential contaminants, such as the resists used in lithographic approaches. For conventional gallium (Ga) ion beams the achievable minimum feature sizes are still limited to approx. 10 nm [2], and Ga implantation may cause unwanted modification of material properties. In contrast, the recently emerged helium ion microscopes (HIM) provide beam spot sizes below 1 nm [5]. The beam is formed by ionizing helium (He) atoms at an atomically sharp tip consisting of three tungsten atoms (trimer). The trimer is metastable and has to be reformed at irregular time intervals ranging from several days to one or two months. For imaging and nanofabrication, only one of the three atoms is selected. This nearly ideal point source allows not only for high-resolution imaging but also for the milling of smallest geometric features [5-7]. Furthermore, large-area machining is possible due to the extraordinary beam stability in combination with a large depth of focus. The first implies that the focus quality remains unchanged over long time intervals, for example, overnight, while the latter ensures that sample geometry and the slight unavoidable tilt of the sample does not reduce patterning quality. Hence, interim imaging and, thus, unintended ion beam modification can be avoided.

The FIB patterning process relies on the beam control that is well advanced and readily available in commercial ion microscopes. Ion microscopes of all manufacturers are equipped with patterning engines, that is, a digital-to-analog converter (DAC) patterning board, defining pixels that can be addressed by the beam, and a corresponding software that allows the user to set the beam parameters and to create geometries with specific raster styles. However, such vendor-specific software is adapted to standard use cases and lacks the flexibility to realize ultimate fidelity and robust large-area machining. So far, several patterning tools were developed, some of them only for specific photonic components, such as solid immersion lenses from diamond [8] or hole arrays and groove waveguides [9]. Others are more versatile but require proprietary software or are non-public. Hence, they are of restricted use for the community. Interesting approaches for the patterning of three-dimensional surface profiles rely on the creation of the respective three-dimensional objects in computer-aided design (CAD) software [10-14]. Here, the corresponding CAD file is converted to more general file types, such as stereo lithographic files (.stl) [10] and G-code [14], or directly into files that encode beam positions, so-called stream files [12]. In all these cases, it is beneficial to perform the material removal in thin slices of equal dose instead of relying on locally varying doses of a single slice [11]. This is a great benefit over the manufacturer-specific patterning options that allow for grey-scale patterning, where the grey values encode local doses. The results of the patterning can be improved through modeling of the relevant processes in FIB machining, especially angle-dependent physical sputtering [11] and redeposition [15], or geometric considerations [12]. In the same manner, locally varying doses in He ion-based resist patterning may be corrected based on heuristic modeling employing a point spread function that sums up all physical and chemical processes in resist activation [16]. All these methods have in common that the control over the actual beam path is limited. While there are attempts to reduce the amount of blanking operations [13] and to follow the geometry of the pattern, tools that allow one to create arbitrary patterns with a geometry-adapted beam path are not yet available. Since the beam path is of utmost importance for the patterning result, new tools are needed to achieve both ultimate resolution and shape fidelity [17].

Here, we introduce the modular patterning toolbox FIB-o-mat to create and optimize patterns for ion beam machining, including automation [18]. The idea of FIB-o-mat is to make use of the built-in functionality of the commercial patterning engine where appropriate, but to provide advanced options where required. FIB-o-mat provides an easily extendable modular toolbox to enable full control over the beam movement. The user can design patterns and subsequently specify optimized beam paths, which are translated into a file format appropriate for the respective patterning engine. Here, the capabilities and first implementations are demonstrated for He ion beam patterning in three different use cases. In general, FIB-o-mat is usable

for all sorts of ions and microscopes of multiple manufacturers. Only the output files have to be adapted to the specific patterning back end.

Ion Beam Machining with Light Ions

Focused Ga ion beams are ubiquitous in ion beam machining with well-established applications in material characterization, for example, TEM lamella fabrication, cross sections or tomographies [19,20], or in the fabrication of prototype nanostructures, such as plasmonic antennas [2]. In contrast, appropriate fields of application for focused beams of light ions are still under exploration. This is a consequence of the novelty of the technique and of several significant peculiarities in the behaviour of light ions upon interaction with a solid.

First, light ions exhibit a large interaction volume in the solid. The penetration depth of 30 keV He ions in silicon is more than five times larger than the penetration depth of Ga ions of the same energy [21]. The consequently large collision cascade may create a significant amount of heat. Even for small ion doses deformation of the manufactured structures can be observed when placed on a material of small heat capacity, such as glass (cf. subsection 3 of "Results and Discussion"). Here, it has to be mentioned that separating the influence of local heat creation from other beam-induced effects is not trivial (see Supporting Information File 1 for further details). Another consequence is the deep implantation of light ions. He and Ne are chemically inert and may therefore diffuse out of the substrate after a while. Diffusion in solids, however, is extremely inefficient, such that the majority of the primary ions will be implanted at their final trajectory position [22]. Hence, large ion doses lead to gas agglomeration and the formation of bubbles, manifesting as strong surface swelling [23]. Furthermore, the associated sputter rate of light ions is roughly an order of magnitude smaller than that of Ga ions [21,22].

In addition, the low ion mass has further implications. The local ion–solid interaction is a balance among several ion-induced, surface-related, and thermally triggered processes [24]. Physical sputtering is only one of the processes. Also, chemical reactions with adsorbed contaminants can occur and, under certain circumstances, may dominate over the atomic knock-out. Typically, ion beam machining is carried out under high-vacuum conditions, where the amount of contaminants in the chamber (mostly water, but also hydrocarbons) still can form a monolayer per second on average. Often, additional contaminants may be present on the sample surface, for example, residues from wet-chemical processing. The locally introduced energy can mobilize these contaminants such that they diffuse towards the beam center where they are polymerized [24]. In the worst case, this results in material build-up instead of sputtering. Already minor surface contamination can lead to unwanted side effects, such as carbonized edges that may change local material properties. Furthermore, locally varying sputter rates and increased minimum doses for sufficient material removal and increased heat damage may occur. All samples that are inert under oxidizing atmosphere should be cleaned in an oxygen plasma before ion beam machining. Generally, all samples should be introduced into the vacuum system one day in advance to allow possible contaminants to desorb from the samples and be pumped out. While these protocols can improve the technical conditions for the machining with light ions, other challenges such as small sputter rates and large interaction volumes persist.

Therefore, 2D materials are an ideal platform for ion beam machining with light ions. The lack (or non-relevance) of the interaction volume allows for a high spatial resolution, enabling the fabrication of structural features in the single-digit nanometer range where small sputter rates play a minor role. This holds true not only for monolayer 2D materials, such as graphene, but also for thin films forming quasi 2D geometries. The versatility of the corresponding materials opens a wide field of exciting applications including, but not limited to, the direct writing of defects to act as nuclei for epitaxial growth [25], the fabrication of two-dimensional phononic crystals [26], the magnetic patterning of suspended Co/Pt multilayers, the fabrication of two-dimensional mechanical resonators based on single-layer graphene, and the fabrication of coupled plasmonic nanoantennas from single-crystalline gold. The three latter examples are realized in this work by developing optimized patterning and automation routines [18].

Patterning and Beam Control

Patterning with an ion beam is a digital process where the beam spot dwells for a defined time at a fixed location and is then displaced by a defined distance ('pitch') to dwell again. To avoid unintended beam damage the ion beam may by blanked when it is displaced over larger distances. Figure 1a depicts a beam path, which is defined by the spot locations, their dwell times, and their pitches. The beam profile depends on the beam settings, given by acceleration voltage, extractor voltage (named 'best imaging voltage' (BIV) in the case of He ion microscopy), and the beam current, as well as on the quality of the focus. The beam profile is unknown a priori but can be typically described with a Gaussian profile in He ion microscopy [27]. It has to be mentioned that the beam parameters for a gas field ion source (GFIS) are strongly correlated and, thus, not independently adjustable. Due to the extremely small size of the source typical currents are only in the range of picoamperes. Varying the gas flux can finely adjust the beam current. However, too large gas fluxes lead to a reduced trimer lifetime. Other-

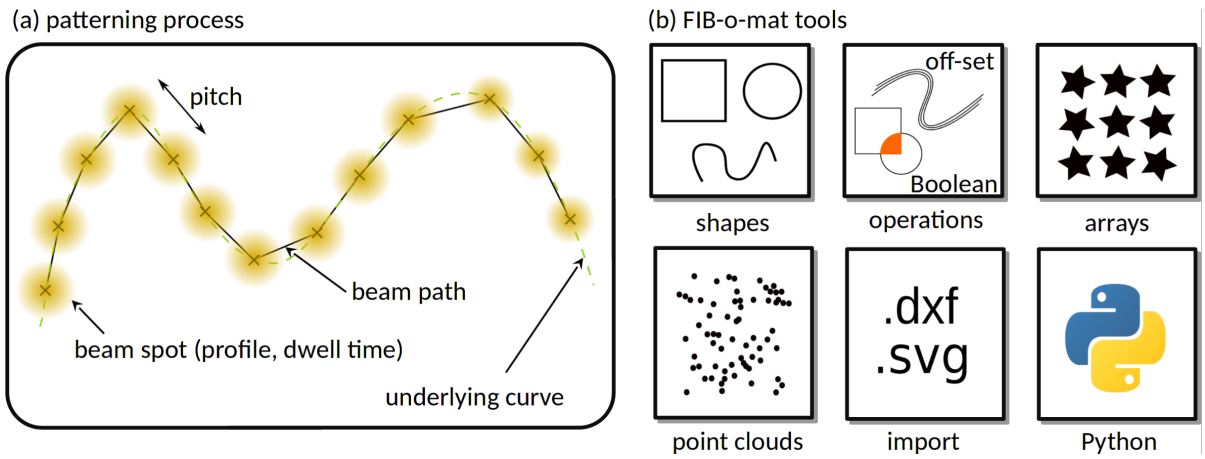

Figure 1: FIB-o-mat overview. (a) For patterning the beam spot follows a rasterized beam path with a defined pitch and dwell time per spot. The piece-wise continuous beam path could be generated from a curved shape (lime curve). Positions of the spots are given by the kinks of the beam path. (b) To create such beam paths FIB-o-mat provides geometric primitives that can be combined by Boolean operators, arranged in lattices and rasterized in different styles using the high-level beam path generation available from the microscope patterning software. Since high-fidelity patterning requires the adaption of the beam path to all edges of the geometry, the low-level beam path generation allows for the creation of point clouds in various ways, for example, by curve off-setting either of geometric primitives or imported graphics. Additionally, all Python functionality is available in FIB-o-mat.

wise, the current can be modified by the size of the selected aperture and by the location of the beam crossover relative to this aperture (named 'spot control' by the manufacturer). Placing the crossover into the aperture leads to the largest possible current but also to the most divergent beam. Placing the crossover above the aperture reduces not only the beam current but also all image errors by cutting off non-paraxial radiation. While the local sputter rate depends strongly on the primary ion flux and, therefore, the beam current, the fidelity of the structures requires an optimum beam profile. Hence, in patterning, typically, a compromise between the optimum beam properties and the largest possible sputter rate has to be found. Usually, the beam path is inferred from the priorly optimized beam settings and the specific target geometry. In the following, the combination of beam settings and patterning geometry is called 'pattern'.

Depending on the target geometries, the pattern creation process can become a complicated and potentially time-consuming task if done by hand. An automated and computer-aided patterning design process can simplify this task tremendously. In case of large arrays, even if the individual shapes are not complex themselves, the large number of them makes it unreasonable to create and layout everything manually. Also, if a pattern has to match desired geometric constraints, an automated pattern generation process can construct the complete pattern from few user-provided parameters by exploiting the defined constraints. This provides easy access to systematic variation of geometries and raster strategies. Finally, for complex pattern geometries, especially with curved edges, the available features of commercial patterning control software are not sufficient to even create the corresponding adapted beam paths. To address these issues, we developed the pattern generation toolbox FIB-o-mat with a Python interface. FIB-o-mat enables the creation of arbitrarily shaped pattern geometries in combination with geometry-adapted beam paths and optimization/automation tools. The code and Python package documentation can be found online at gitlab under the gpl3 license [18,28,29]. Pre-build packages are available on pypi [30].

The FIB-o-mat Toolbox

The overall design of FIB-o-mat relies on a two-step pattern definition: First, a pattern shape must be defined and, second, appropriate beam settings can be added to the pattern shape. By design, neither assumptions are made on certain settings (for example beam profile) nor are default values used. This may limit the convenience for standard tasks compared to vendor-specific patterning software but, in return, the design process is completely transparent to the user.

Figure 1b depitcs schematically the available tools to provide a maximum flexibility for pattern generation. To generate shapes, FIB-o-mat provides a range of geometric primitives, including points, polygons and lines, ellipses, arc splines, and parametric curves. These can be used as building blocks for custom shapes. Alternatively, .svg and .dxf files can be imported and their enclosed geometries will be automatically translated to geometric primitives defined in FIB-o-mat. All shapes can be

combined via Boolean operations and arranged in arbitrary two-dimensional lattices by defining a unit cell and displacement vectors. This is accomplished without explicit rasterization and, consequently, the process again results in analytic shape geometries. For rasterization of the obtained geometries, different line-by-line raster styles are available, such as serpentines or cross sections. Further, shapes can be off-set along their normal direction. If provided by the manufacturer, such curves may be loaded into the patterning engine and rasterized there. In most cases they are used to generate point clouds in which each point represents a beam location. This provides the possibility to adapt the beam path to arbitrary curved geometries, not only for the built-in primitive shapes and the Boolean derivatives but also for arbitrary imported shapes. Finally, full Python functionality is available with FIB-o-mat, for example to employ other geometric modeling libraries.

Pattern generation can be carried out at two different abstraction levels, depending on the needs of the user and the capabilities of the microscope software. High-level beam path generation is based on geometric primitives and raster routines available in the patterning generator of the microscope. Low-level beam path generation creates point clouds, which directly define the ion beam path.

1 High-level beam path generation and automation

For the high-level approach, the pattern is constructed from geometric primitives available in the patterning software of the microscope. In the same manner, the rasterization relies on the available parameters such as pitch, line distance, and line ordering in a rectangular pattern. The parameters have to be specified by the user within FIB-o-mat, which, in turn, generates a pattern file containing the shapes and the patterning parameters. The actual rasterizing of these geometric primitives is carried out by the patterning engine of the microscope. If, for example, a rectangle shall be rasterized line-by-line but with varying pitches for each line, FIB-o-mat would generate a list of lines with the corresponding raster parameters defined for each line.

The rasterization process for the high-level approach is schematically depicted in Figure 2. The simplest geometric entity is a spot. As shown in Figure 2a, spots with well-defined positions and corresponding dwell times and number of repeats can be created by FIB-o-mat. Typically, the only one-dimensional geometries available in commercial patterning software are straight lines and circle segments and the rasterization has to be carried out in a consecutive way, cf. Figure 2b. In the same manner, all two-dimensional geometric primitives have to make use of the pre-defined raster styles, such as line-by-line in one direction or alternating directions as well as cross-sectional rasterization (repeat each line until the full dose is applied before starting the next line) or serpentines (make the beam path continuous by turning the direction when starting the next line). In the case of circular primitives, rasterization in an azimuthal direction (raster lines follow the circular outline of the shape) is implemented by all major manufacturers.

There are several benefits of the high-level approach for patterning. As it relies on predefined geometric entities, the loading of generated patterning files can be faster than that of potentially huge point clouds. Especially a collection of many simple patterns with changing geometry or rasterization parameters will still result in relatively small file sizes. In addition, the patterning settings of the individual objects can be easily changed in the patterning software after loading the pattern file created with FIB-o-mat. While other microscopy parameters, such as the stage position, can be controlled via an application programming interface (API) or patterning options of the manufacturer, large-area patterning can be automated by FIB-o-mat. Another interesting approach for the automation of

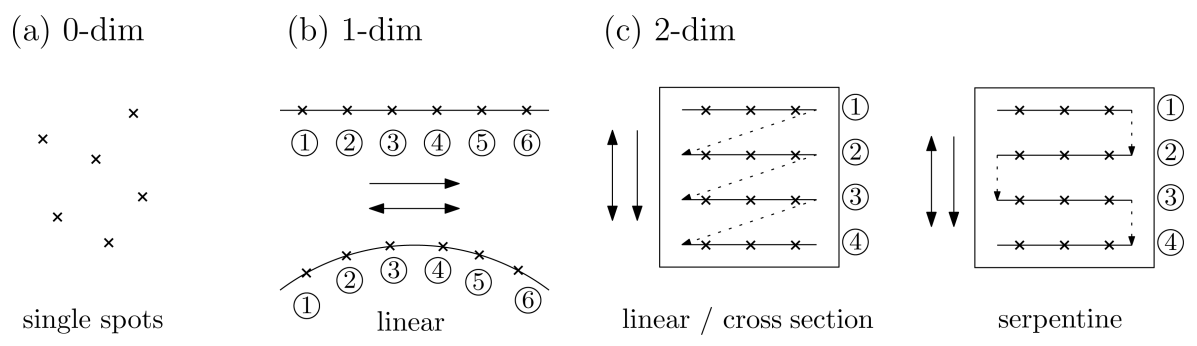

Figure 2: Geometric primitives and rasterization styles available for high-level pattern generation. (a) Single spots, (b) straight lines and circle outline segments, and (c) a rectangle as representative for available 2D primitives.

small and regularly arranged patterns makes use of the pitch in high-level patterns [31]. When setting the pitch of a 10 µm rectangle to 10 nm, an array of 1000 × 1000 holes with 10 nm spacing may be created. By placing such rectangles onto a rasterized curve, this curve will be replicated in the same manner. While this approach is fast and efficient for large arrays of patterns consisting of few points, it becomes unreasonable for arranging more complex subunits.

However, the flexibility of the high-level approach is low. Only geometric primitives pre-defined by the manufacturer along with few raster styles are available. For complex shapes, the available raster routines even reduce to a line-by-line rectangular raster once different geometric primitives are combined by Boolean operations. Therefore, in many application cases the beam path will not follow the geometry edges, leading to artifacts, especially when approaching the resolution limit of the machine.

Attention has to be paid when employing the geometric primitive 'spot' of the manufacturer software. The commercially implemented patterns contain not only the geometric shapes and raster styles but additional optimization strategies that are often not transparent to the user. One example is a beam stabilization position along with a certain waiting time after each repeat of the pattern. What may have a minor influence for two-dimensional patterns can become a major issue in the case of point clouds. An estimate for one of the established manufacturers gave a beam stabilization time of about 5 ms for each pattern summing up to almost 1.5 h when executing 1 million spots. Given the fact that typical dwell times are in the range of microseconds, the actual patterning time of this point cloud would be expected to take seconds.

2 Low-level beam path generation and optimization

Full control over the beam path is only provided by the low-level tools of FIB-o-mat. Here, the point cloud depicted in Figure 3a is not an assembly of pre-defined primitives. Instead, it represents a list of true beam positions. Such lists can be loaded into the microscope software as so-called deflection lists or stream files. FIB-o-mat creates the deflection lists by defining individual points as pre-rasterized geometry, as shown in Figure 3a, by rasterizing arbitrary parametrized curves, or by calculating off-set curves around arbitrary geometries as displayed in Figure 3b,c. In the latter two cases the rasterization of the curves can be defined in a custom manner. This includes all raster styles that are available in the high-level approach but also user-defined styles, such as the back-stitching depicted in Figure 3b,c. The provided tools allow for flexible pattern generation and mitigate typical problems in ion beam-based machining.

As the local material removal by ion beam impact is a complex interplay between different physical and chemical processes, many unwanted artifacts can (and typically will) occur during patterning [24]. The ion beam-induced physical sputtering does not cause a complete material removal. Instead, the material is locally redistributed [15]. The phenomenon is known as redeposition and can be minimized by varying the slow beam direction [17], that is, for line-by-line scanning, by starting from the first line in the first repeat and from the last line in the second repeat.

During ion beam machining of multi-crystalline materials the varying crystal orientations cause a variation in the local sputter rate due to ion channeling [24]. If one of the symmetry axes of

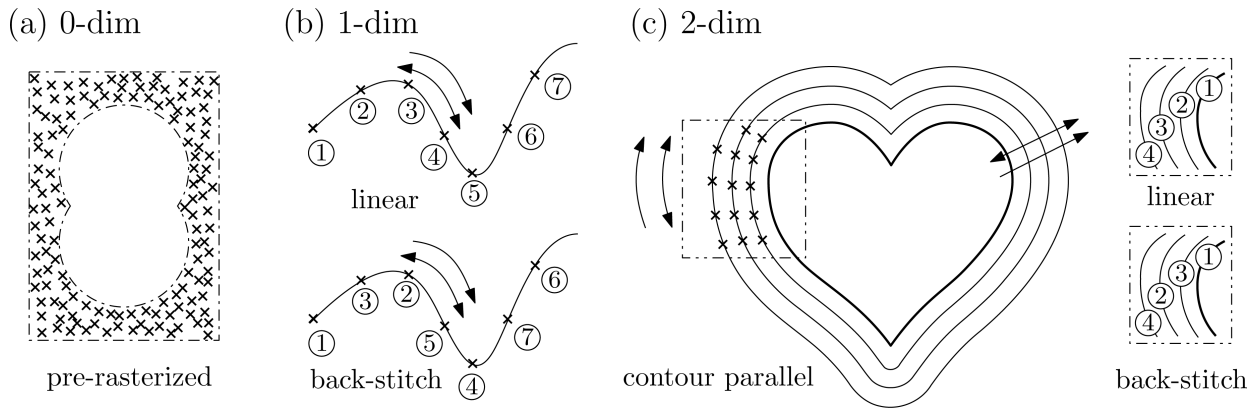

Figure 3: Geometric entities and rasterization styles available for low-level pattern generation. (a) Pre-rasterized point cloud, (b) arbitrary parametrized curves with custom rasterization, and (c) a heart as representative for arbitrary 2D geometries that can be either generated or loaded including custom raster styles.

the crystal lattice is oriented along the beam direction, the ion penetration depth is larger, which, in turn, reduces the sputter rate. The resulting surface roughness may be minimized by removing the material with only few cycles. For standard geometries, both of these optimization problems are already targeted with the high-level approach and the pre-defined raster strategies [17]. However, only the low-level approach enables these strategies for arbitrary shapes in combination with adapted beam paths.

Another typical artifact is a shape distortion via beam-induced modifications, possibly due to heat. This is a severe issue especially for ion beam machining with light ions (cf. section “Ion beam machining with light ions”). The ion beam locally introduces energy that needs time to dissipate before the beam reaches the same position and introduces energy again. In the low-level approach, the raster strategy can be customized such that the local dose per time is minimized (e.g., back-stitch or other custom point- or line-hopping approaches). If provided by the manufacturer, flags for beam blanking may be introduced as well. However, the number of beam blanking operations should be kept as low as possible, as it introduces ‘unused’ patterning time and may cause artifacts due to the limited blanking speed.

Once the point cloud of such an adapted beam path is created by rasterization with FIB-o-mat, regions of higher local point densities may appear. This occurs for large curvatures in the off-set curves as schematically depicted in Figure 4a. Here, the actual ion beam profile has an important influence as it defines how much the local dose deviates from the target dose. The local dose received at each spot location equals the sum of the dose applied there and the doses reaching that location from nearby points. By assuming a Gaussian profile of the beam, the local dose can be calculated by integrating over the profiles of all contributing spot locations. In the regions of higher point densities, this results in a local dose exceeding the target dose. For local dose correction, FIB-o-mat first rounds off regions of high curvature in the beam path by replacing them with circle segments. It is recommended to use radii of half the pitch for rounding to keep sufficient information about the geometry. In a second step, the dwell times of individual spot locations are reduced in an iterative manner such that the target dose can be achieved. Figure 4b shows the application of the local dose correction for a trimer geometry. Here, the local dose exceeded the target dose by about 50% before the optimization routine.

3 Programming and file formats

The FIB-o-mat toolbox is mainly written in Python and partly in C++. It can be compiled on any modern operating system. The modular layout of FIB-o-mat makes it easily extendable by any FIB user. Currently, only He ion beam patterning is supported, and all manufacturer-specific tools are not publicly available. In the future, it is planned to introduce and share back ends for microscopes of different manufacturers.

As the definitions of geometric primitives and raster styles change between different patterning tools, the corresponding high-level functions need to be implemented by the user if not yet present. All standard primitives and raster styles are available in FIB-o-mat. Alternatively, the low-level approach may be used for full flexibility of the beam path. During import of the graphics, due to the complexity of the .dxf file format, only a subset of features is supported in FIB-o-mat. Similar manufacturer-specific challenges occur during automation. Some manufacturers provide automation tools that can be accessed by the patterning software, others require the use of an API that may even have to be licensed. In the latter case, implementing automation using FIB-o-mat can be highly demanding, for example if the featured APIs are relatively restricted and based on a proprietary programming language.

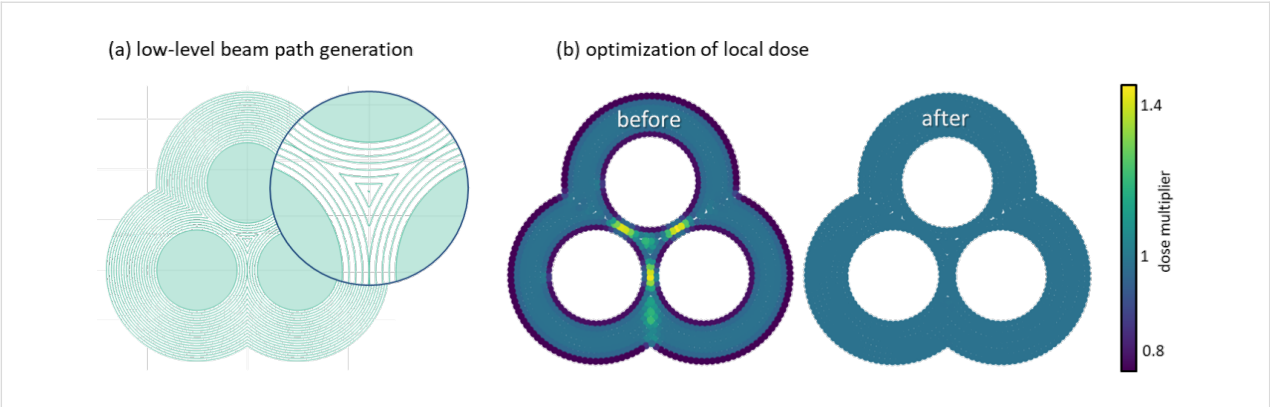

Figure 4: Geometry-optimized patterning. (a) Beam path generation by curve off-setting around arbitrary disconnected shapes. (b) Upon rasterizing curved beam paths, strongly curved regions can exhibit local doses larger than the target dose. This is corrected by a local dose optimization reducing the beam dwell time in these regions.

Another technical challenge concerns the obtained pattern sizes for the low-level approach in FIB-o-mat. Complex patterning tasks easily result in millions of points that may cause memory problems when loaded into the patterning engine of the microscope. Here, a binary file format is highly desirable instead of ascii files with plain text.

Results and Discussion

Three test cases were selected to demonstrate the different capabilities of FIB-o-mat. These include high-level patterning with automation of magnetic multilayers, low-level patterning with automation of suspended graphene and low-level patterning and beam path optimization for gold on glass. Patterns for all three test cases are available in the git repository of the FIB-o-mat package [18].

1 Magnetic patterning of Co/Pt multilayer films

Used FIB-o-mat features: high-level beam path generation with automation via stage control.

Magnetic thin films and multilayers are of great technological interest as platforms for spin-based devices encoding bits using nanoscale domain walls or skyrmions [4]. The magnetic properties of thin magnetic films and multilayers can directly be modified in a controlled manner by low-dose ion irradiation. Local variation of the dose using masks or focused ion beams leads to pure magnetic patterning without affecting the topography of the films [32]. The local modification of the magnetic properties, in particular anisotropy and exchange coupling (including the chiral Dzyaloshinskii–Moriya interaction), originates from structural modifications, such as interface structure, atomic ordering, atomic composition, and crystallographic phase [33,34].

Here, the impact of He irradiation on the ferromagnetic multilayer $[Co_{0.6}/Pt_{0.8}]_{15}$ is studied [35,36]. This multilayer shows perpendicular magnetic anisotropy arising from the Co/Pt interfaces and forms nanometer-scale, labyrinth-like domains with opposite out-of-plane magnetization in remanence. We are particularly interested in how ion irradiation changes the morphology of the magnetic domains and how it influences the nucleation and annihilation of domains in a typical adiabatic field cycle as well as after picosecond laser excitation [37,38].

The fabrication of the samples starts by depositing the magnetic multilayer onto 150 nm thick silicon nitride membranes via magnetron sputtering. The membranes are almost transparent for soft X-rays, which are later employed for imaging of the samples. Subsequently, the multilayer film is locally modified by He irradiation, employing different patterning layouts and varying the applied He ion dose. Typical patterns comprise checkerboard structures, lines, and dots with characteristic dimensions ranging from 50 nm to several micrometers. The applied He dose varies between 10 and 50 ions/nm^2. The the appropriate dose range was determined in prior automated dose tests (cf. Supporting Information File 1, section “Automation in FIB-o-mat”). The used ion beam current was 2.6 pA at an acceleration voltage of 30 kV and an extractor voltage of 32 kV. The dwell time was 1 µs and the pitch was 5 nm.

The magnetic nanometer-scale domain configurations were imaged via soft X-ray holography [39], exploiting X-ray magnetic circular dichroism [40] and giving rise to an absorption contrast of areas with different out-of-plane magnetization.

Areas irradiated with an ion dose of 50 ions/nm^2 no longer show an out-of-plane magnetization component. Based on previous experiments, we assume that the interfaces inside the multilayer are modified so severely that the magnetization switched to in-plane [32-35]. In contrast, an ion dose of 10 ions/nm^2 does not lead to a modification of the multilayer that is observable in the domain pattern or in the hysteresis of the sample. Similar ion dose ranges are reported elsewhere for Co/Pt multilayer systems on SiO_2 substrates [41]. Figure 5 shows images of the domain configuration in the multilayer irradiated with an ion dose of 30 ions/nm^2. The gray-scale images encode purely magnetic contrast with white and black colors indicating opposite out-of-plane magnetization. The sample was irradiated in a checkerboard-like pattern with a side length of each square of 500 nm and a total area irradiated of 20 × 20 µm. In this sample, the domain size in irradiated regions is significantly reduced as compared to domains in non-irradiated regions, as shown in Figure 5d (at 0 mT). Tailored modification of the magnetic film thus enables the coexistence of two magnetic structures in a checkerboard pattern, revealing different magnetic behavior side by side. The sample was imaged in a full applied-field sweep from saturation at positive field to saturation at negative field. During this measurement, images at particular applied fields were recorded (Figure 5). After saturating the magnetic film (at 390 mT, Figure 5a) and reducing the applied field, domains form (180 mT, Figure 5b) and grow (Figure 5c) first in irradiated regions, before domain formation in the non-irradiated regions starts from the edges of the checkerboard squares (0 mT, Figure 5d). Analogously, the non-irradiated regions saturate first at (−110 mT, Figure 5e), and the irradiated regions saturate later at less than (−320 mT, Figure 5f). Remarkably, the domains in the irradiated areas shrink to a dense array of small bubble domains close to the saturation point (Figure 5f). Hence, through He-assisted sample fabrication, the formation of magnetic domains can be enhanced in a controlled manner, probably due to the increased

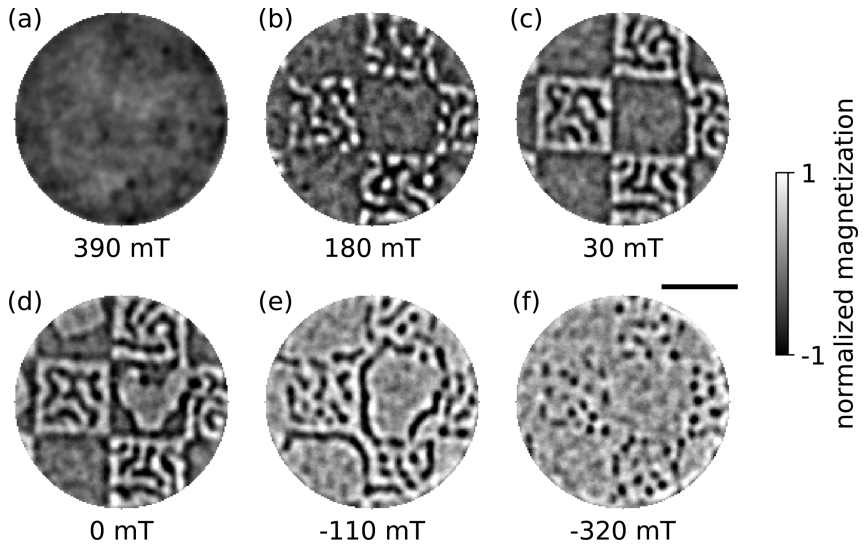

Figure 5: Magnetic nanopatterning of a Co/Pt multilayer. Fourier-transform holography (FTH) images (a–f) with a predefined field of view (FOV) of 1.5 µm illustrate a magnetic field cycle from positive saturation at 390 mT to negative saturation in an He ion irradiated sample, revealing a checkerboard pattern with 500 nm side length. The black–white contrast encodes domains with opposite out-of-plane magnetization. Starting from a saturated state (a), magnetic domains first form in ion-irradiated regions (b, c) before they appear in non-irradiated regions (d). The non-irradiated regions saturate earlier when the applied magnetic field is further decreased (e, f). The presented magnetic film, thus, supports the coexistence of regions with different magnetic properties. The scale bar is 500 nm.

density of pinning sites, that is, variations of the local anisotropy.

Since the influence of different ion doses and pattern shapes on the formation of magnetic domains is not known a priori for different magnetic material systems, a lot of different combinations of doses and shapes must be patterned initially (cf. Figure S2, Supporting Information File 1, where in total 42 different patterning sites are shown of which each site includes of a different shape/dose combination). Using the FIB-o-mat package, the creation of the patterns can be automated. The patterning is carried out with the automation tool of the NPVE software controlling the He ion microscope according to the FIB-o-mat patterns. No further manipulation of the patterns by the user is required. Hence, FIB-o-mat is technically not necessary for this task but constitutes a significant time-saver.

2 Mechanical resonators based on suspended single-layer graphene

Used FIB-o-mat features: low-level beam path generation and automation via stage control, patterns optimized for speed to generate a large number of trampolines with varying bridge widths.

Atomically thin graphene has extraordinary mechanical properties [3], and graphene nanomechanical resonators have been employed as various sensors [42-46]. Yet, the sensitivity at room temperature is limited by a rather low quality factor. Patterning of the devices into trampoline-shaped resonators yields a large increase in quality factor and, thus, device performance [47,48]. Furthermore, the material removal reduces the thermal coupling of the central device area to the supporting substrate. As graphene is a single-atomic layer, it exhibits the lowest possible heat capacity per unit area of the material [48]. Its broadband spectral absorbance [49], in combination with a thermal stability up to 2600 K [50], renders graphene an exciting candidate for room-temperature bolometry [51].

Single-layer graphene was grown by chemical vapor deposition onto a multicrystalline copper foil using methane as precursor gas at 1035 °C. For the transfer process, the graphene sheet was covered by a 500 nm thick PMMA layer. After etching the copper foil, the graphene sheet was transferred onto a SiN membrane with a regular grid of holes. The transfer process is described in detail elsewhere [52]. The SiN membrane was covered with a thin layer of gold, which allowed us to electrically contact the graphene sheet and actuate the resonators electrostatically. The motion of the devices is detected using a Michelson interferometer [48].

Figure 6a depicts a secondary electron HIM image of a patterned trampoline graphene resonator. A He ion current of 3 pA was employed at an acceleration voltage of 30 kV and a BIV of around 32.3 kV. The patterns were constructed from circle segments combined with linear segments to define length and width of the trampoline bridges. In the absence of contami-

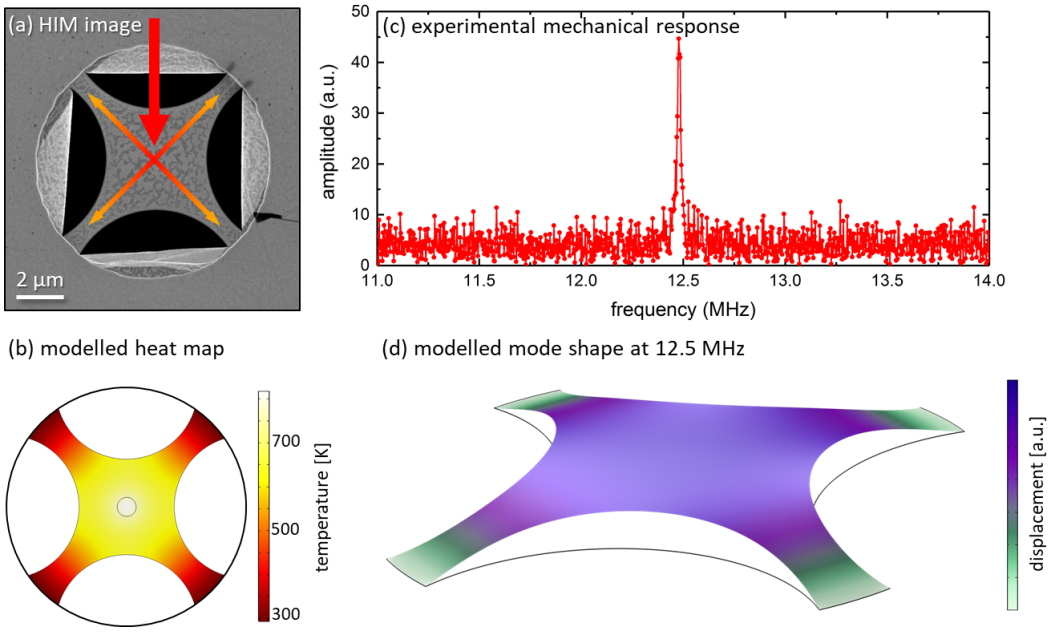

Figure 6: Single-layer graphene resonator. (a) Secondary electron He ion microscopy image of the graphene resonator patterned into a trampoline geometry. Laser excitation from the top is depicted schematically by the red arrow. (b) The corresponding heat distribution induced inside the trampoline due to the laser heating was obtained by finite element modelling. The resonator is excited by electrical gating and the displacement is detected in an interferometric read-out. (c) Experimentally determined frequency response of the fundamental mode of the trampoline resonator at 12.5 MHz with (d) the simulated mode shape of the fundamental resonance.

nants, a pitch of 50 pm in combination with a dwell time of 4 ms leads to well-defined single-repeat cuts. To avoid ion beam-induced modifications of the graphene sheet, the pattern location was adjusted at one of the SiN holes followed by automated stage moves and patterning. Thus, a large number of trampoline resonators could be fabricated without unintended beam impact due to imaging in a reasonable overall patterning time. The corresponding step-and-repeat list with the geometric primitives, path settings, and displacements was created in FIB-o-mat and could be directly loaded into the patterning engine of the microscope.

To probe the device, a laser spot with a width of around 1.3 µm at a wavelength of 632 nm was directed onto the central region of the resonator. A numerical description of the locally heated resonator was carried out by finite element modeling. The obtained heat map shows good thermal decoupling of the trampoline geometry with a large gradient. The central region exhibits temperatures around 800 K while the bridges stay close to room temperature. The resonance frequency of the fundamental mode is 12.5 MHz (cf. Figure 6b) and exhibits a quality factor of about 300 without laser heating. When suspended graphene is heated by a light source, the built-in tension in the device is reduced because graphene has a negative thermal expansion coefficient [53], and a down-shift in resonance frequency is observed. The mode frequency can be shifted up by 100 percent through increasing the laser power from 15 to 150 µW. The large bandwidth in combination with the increased responsiveness created by the trampoline pattern allows the system to operate as an ultra-sensitive and ultra-fast bolometer [48]. Finally, the increased quality factor and reduced thermal coupling to the substrate should allow for efficient side-band cooling experiments, which so far are hindered by very strong thermal coupling and low quality factors [54,55].

3 Plasmonic tetramer antennas based on single-crystalline gold flakes

Used FIB-o-mat features: low-level beam path generation with optimization concerning heat transport, patterning time, and local dose.

Thin flakes of single-crystalline gold constitute an ideal platform for plasmonic applications due to the lack of scattering losses at grain boundaries and surface roughness [56]. In nanostructured gold, collective excitations of the free electron gas may occur under the incidence of visible light [2]. These plasmon polaritons of individual nanoparticles are not only strongly resonant with the ability to concentrate light below the diffraction limit. They may also be efficiently coupled in closely packed ensembles of plasmonic particles. In the case of three-dimensional crystals from gold spheres even deep strong coupling of light and the plasmonic excitation at room tempera-

ture was achieved [57]. Here, we investigate the influence of the fabrication routine on the resonant response of small ensembles of coupled plasmonic scatterers, namely tetramers of spherical gold discs residing on a glass substrate. Such ensembles may feature dipole-forbidden eigenmodes [58] with low damping when being excited by the incidence of structured light [59]. First, we focus on comparable tetramer geometries to assess the influence on geometric fidelity and possible ion-beam induced material/substrate modifications on the plasmonic response by measuring the bright optical modes [59]. The target geometry for all fabrication techniques is a particle radius of 45 nm with a gap size of 35 nm. This is the geometry that can reliably fabricated by resist-based electron beam lithography on physically sputtered gold layers (cf. Figure 7a). Later, we will assess the ultimate resolution of He ion beam machining to minimize the gap sizes.

The gold flakes of approx. 30 nm thickness were wet-chemically synthesized on glass [60] and transferred to the target substrate via a PMMA-mediated method. On the target glass substrate, a thin layer of gold was sputtered with two empty square windows of 100 × 100 μm^2 in size, where the flakes were placed. The fabrication of the tetramer structures was carried out using Ga ion beam milling only, or a combination of He ion beam milling for the definition of the tetramer and Ga ion beam milling for the large-area removal of the surrounding gold. Figure 7b,c depicts the corresponding scanning electron beam micrographs. The limited image quality of the lithographically defined tetramer is caused by the fact that the isolated structures are located on a glass substrate, leading to severe charging effects. For Ga ion beam milling a current of 10 pA, a pitch of 3 nm and a dwell time of 1 μs were employed in a two-step patterning process. First, the surrounding gold was removed by rectangular scanning of a square of several micrometers from which a slightly larger tetramer shape was subtracted. Subsequently, the remaining tetramer was polished with ring shapes. During He ion beam patterning, first, the tetramer was patterned with a large outline of 40 nm thickness using an optimized low-level beam path defined in FIB-o-mat (cf. Supporting Information File 1, section “Challenges in the patterning of the plasmonic tetramers”). The beam path had a curve off-set of 0.25 nm. The pitch was 0.25 nm around the tetramer and 0.5 nm inside the tetramer. The dwell time was 5 μs, and the pattern was repeated 12 times. The employed beam current was around 2 pA at an acceleration voltage of 30 kV and a BIV of 32 kV. The second step was the removal of the surrounding gold with Ga using again a shape obtained by a Boolean operation.

Figure 7 shows that shape distortions mainly occur for the lithographically defined and the Ga FIB-fabricated tetramers. How-

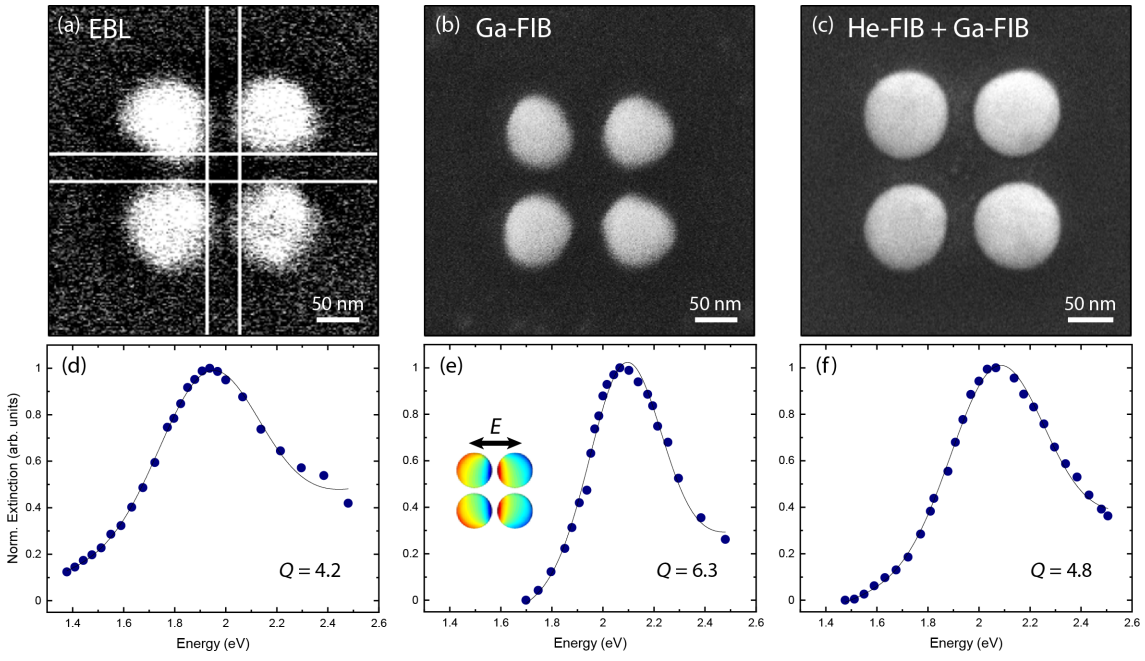

Figure 7: Coupled plasmonic antennas. (a–c) Scanning electron micrographs of gold tetramers on glass with a target geometry of 45 nm particle radius and 35 nm gap width, fabricated by different techniques: (a) by electron beam lithography, (b) Ga ion beam machining, and (c) He ion beam machining of the tetramer geometry and removal of surrounding gold by Ga FIB. The low image resolution in (a) is caused by the difficulties of imaging isolated tetramers on a non-conductive glass substrate. (d–f) Normalized extinction (sum of scattering and absorption) of the tetramers. The inset depicts the charge distribution of the excited plasmonic mode upon incidence of linearly polarized light.

ever, also in the case of the He ion beam-patterned tetramers the subsequent removal of gold using the Ga ion beam leads to slight distortions that were not present before. This is caused by the typical tails in the beam profile of a focused Ga ion beam [19]. Optical investigation was carried out using visible-light spectroscopy in a transmission spatial modulation setup. The spatial displacement of the focus modulates the signal [61] and the lock-in coupled detector provides an excellent signal-to-noise ratio for individual small scatterers.

Figure 7d–f shows the extinction (sum of scattering and absorption) spectra corresponding to the tetramers in Figure 7a–c, respectively. The extinction was measured for plane wave incident light of linear polarization. The polarization was chosen along the x axis as depicted in Figure 7e. This configuration and any other in-plane polarization excite the optically active E_u mode of the tetramer [59]. The plasmonic resonance is significantly broadened for the lithographically defined tetramer. Interestingly, the highest Q factor ($Q = \omega_{res}/\delta\omega$ with the resonance frequency $Q = \omega_{res}$ and the resonance width $\delta\omega$) was achieved for the tetramers obtained by pure Ga patterning, even though the monomer shape is not perfectly round. Each monomer acts as a small dipole in our measurement configuration and its response is not very sensitive to its actual shape as long as surface roughness does not increase the scattering losses. Finite-difference time-domain modeling taking into account the slightly varying geometries led to numerical Q factors of $Q_{num} = 3.3$ for tetramers fabricated by EBL, $Q_{num} = 5.4$ for Ga FIB, and $Q_{num} = 4.8$ for He FIB. This is in reasonable agreement with the experimental results.

The mutual coupling of the individual monomers, however, strongly depends on the interparticle distance due to the evanescent decay of the plasmonic near field. Hence, a nanopatterning approach that is able to realize sub-10 nm gaps in a reproducible manner is highly desired. He ion beam milling already demonstrated these capabilities in the fabrication of strongly coupled dimers with gap distances of less than 6 nm [62-64]. In all previous cases, the antenna shapes were pre-fabricated with Ga ion beam milling or lithographic approaches and only single-line cuts were performed with He ions to create dimer antennas. Here, we prove the ultimate resolution capabilities for the tetramer geometry with minimized gap sizes patterned in a gold flake of about 40 nm thickness using He beam milling for the complete antenna and not only for separating individual parts of a pre-fabricated antenna. Figure 8a depicts the secondary electron HIM image of a tetramer patterned using a similar low-level beam path as used for the tetramer in Figure 7c. As in the example above, the beam path was optimized regarding reduced heat damage and redeposition. However, the gap distance was defined by a single path between the monomers. Most importantly, this resulted reliably in gap sizes between 3 and 4 nm when the gold surface was free of contaminants and when optimum ion beam conditions were achieved. The mechanical He column adjustment was optimized such that almost no electronic beam tilt or shift corrections were necessary and a high spot control of 6 could be used for the 20 µm aperture at a standard gas flux of $2e^{-6}$ Torr. The thereby obtained beam current reached values between 1.2 and 1.8 pA, depending on the actually employed trimer.

However, this specific geometry results in large curvatures of the path when approaching the gaps. The red arrows in Figure 8a indicate regions of larger depth arising due to the locally increased dose. Local dose correction was performed as described in subsection 2 of “The FIB-o-mat toolbox” and

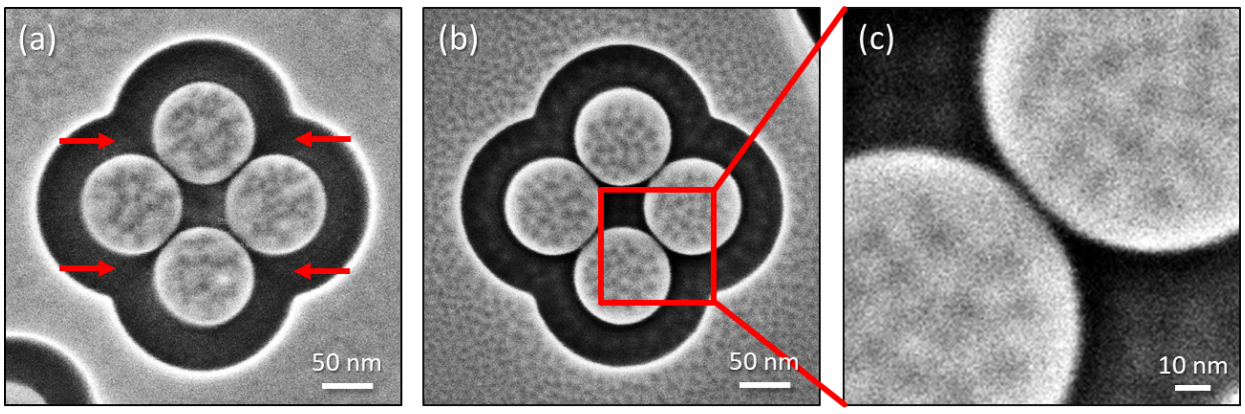

Figure 8: Optimized tetramer. Secondary electron He ion microscopy images of gold tetramers on glass with minimized gaps after certain steps of optimization. (a) The gap size was defined by a single line resulting in gap sizes of only 3 nm. The high-curvature regions cause an increased milling depth marked by red arrows. (b) After local dose correction, these trenches disappeared. (c) The close-up of (b) proves the remarkable high pattern fidelity with a gap size of about 3 nm.

enabled uniform milling down to the glass substrate. It has to be mentioned that the actual results of the patterning of thin gold flakes on glass varied strongly, depending on the cleanliness of substrate and gold flake (cf. Supporting Information File 1, section "Challenges in the patterning of the plasmonic tetramers"). Nevertheless, we show here, for the first time, high-fidelity patterning of plasmonic nanostructures with geometrical details as small as 3 nm. This is mainly achieved by defining a contour-parallel and dwell time-optimized beam path using FIB-o-mat. To the best of our knowledge, such geometry-adapted beam paths cannot be created by current patterning software provided by the instrument manufacturers. Furthermore, FIB-o-mat enables the rapid generation of different patterns with varying path geometries, local dwell times and pitches, as well as number of repetitions allowing for efficient patterning iteration and optimization.

Conclusions and Outlook

He ion beam machining offers exciting prospects for the fabrication of devices from two-dimensional and quasi two-dimensional materials. The extremely small spot size, large depth of field, and high stability render the He ion beam ideal for automated high-fidelity patterning in cases where low sputter rates are negligible. This holds especially true for two-dimensional materials where only small amounts of material have to be removed while guaranteeing highest patterning precision. Since He ion microscopy is a relatively new technique, its full potential still has to be exploited. Here, we contributed in developing the advanced pattern creation toolbox FIB-o-mat [18]. FIB-o-mat has a Python interface and a fully documented modular structure, such that it is easy to use and easy to extend. In its current version, it provides high-level pattern creation, low-level beam path generation, as well as optimization and automation tools for He ion beam machining. The aim is to extend FIB-o-mat such that the tools can be used with microscopes of any manufacturer, covering ion beam machining with a variety of ions.

For the efficient use of FIB-o-mat, the following workflow may be employed: (i) Define the geometry to be patterned. (ii) Define the beam path such that it follows the edges of the geometry, for example, by using the curve off-setting tool where required. (iii) Define a rasterization strategy in a way that artifacts, such as redeposition and other beam-induced effects, are minimized. (iv) When long patterning durations are necessary, vary the raster parameters (and/or increase the beam current). (v) In the case of curvatures in the beam path, use the local dose optimization to achieve a uniform target depth.

To demonstrate the capabilities of FIB-o-mat, three different 2D material systems were patterned. Multilayers of Co/Pt were modified regarding their local magnetic response without changing their topography. Suspended single-layer graphene was cut into trampoline-shaped mechanical resonators, and single-crystalline gold was patterned into coupled plasmonic antennas. In the former two cases, the ease to vary the geometry and patterning parameters in an automated way greatly facilitated both the systematic patterning optimization and a detailed analysis of the device properties. While these two cases pattern creation and automation can, in principle, be carried out using the software of the microscope manufacturer, it is impossible to create the adapted beam path for the tetramer geometry by any commercial patterning software. The realized minimum gap size of 3 nm for a gold thickness around 40 nm and the perfect spherical shapes of the monomer discs are not obtainable without beam path optimization, nor can they be obtained by any other fabrication technique. Hence, the low-level approach in FIB-o-mat provides the necessary functionalities to unlock the ultimate performance of He ion microscopy.

Supporting Information

Supporting Information File 1

Additional experimental data.
[https://www.beilstein-journals.org/bjnano/content/supplementary/2190-4286-12-25-S1.pdf]

Acknowledgements

The ion beam patterning was performed in the Corelab Correlative Microscopy and Spectroscopy at Helmholtz-Zentrum Berlin.

Funding

Victor Deinhart and Katja Höflich acknowledge financial support from German Research Foundation (DFG) within the project 'chiralFEBID' under grant no. HO 5461/3-1 and of the Federal Ministry of Education and Research within the project 'EPRoC' under grant no. 03SF0565. Furthermore, we would like to highlight the support from the EU Cost Action CA 19140 'FIT4NANO', https://www.fit4nano.eu. Authors from the Max Born Institute acknowledge financial support from the Leibniz Association via grant no. K162/2018 (OptiSPIN). Jan Kirchhof and Kirill I. Bolotin were supported by the European Research Council (ERC) under grant no. 639739 and DFG Collaborative Research Centre TRR 227. Sabrina Jürgensen and Stephanie Reich were supported by the ERC within the project DarkSERS (772108) and the Focus Area NanoScale of the Freie Universität Berlin. Thorsten Feichtner and Bert Hecht acknowledge financial support from the DFG through the Würzburg-Dresden Cluster of Excellence on Complexity and Topology in

Quantum Matter – *ct.qmat* (EXC 2147, project-id 39085490). Thorsten Feichtner additionally acknowledges financial support from the European Commission through the Marie Skłodowska-Curie Actions (MSCA) individual fellowship project *PoSH-GOAT* (project-id 837928).

ORCID® iDs

Lisa-Marie Kern - https://orcid.org/0000-0001-9781-9132
Jan N. Kirchhof - https://orcid.org/0000-0001-8576-4787
Sabrina Juergensen - https://orcid.org/0000-0001-6528-4954
Enno Krauss - https://orcid.org/0000-0001-5241-5003
Thorsten Feichtner - https://orcid.org/0000-0002-0605-6481
Sviatoslav Kovalchuk - https://orcid.org/0000-0002-4817-1939
Michael Schneider - https://orcid.org/0000-0001-9262-4838
Dieter Engel - https://orcid.org/0000-0001-9255-9554
Bastian Pfau - https://orcid.org/0000-0001-9057-0346
Katja Höflich - https://orcid.org/0000-0003-4088-2928

References

1. Novoselov, K. S.; Mishchenko, A.; Carvalho, A.; Castro Neto, A. H. *Science* **2016,** *353,* aac9439. doi:10.1126/science.aac9439
2. Biagioni, P.; Huang, J.-S.; Hecht, B. *Rep. Prog. Phys.* **2012,** *75,* 024402. doi:10.1088/0034-4885/75/2/024402
3. Lee, C.; Wei, X.; Kysar, J. W.; Hone, J. *Science* **2008,** *321,* 385–388. doi:10.1126/science.1157996
4. Fert, A.; Cros, V.; Sampaio, J. *Nat. Nanotechnol.* **2013,** *8,* 152–156. doi:10.1038/nnano.2013.29
5. Hlawacek, G.; Veligura, V.; van Gastel, R.; Poelsema, B. *J. Vac. Sci. Technol., B: Nanotechnol. Microelectron.: Mater., Process., Meas., Phenom.* **2014,** *32,* 020801. doi:10.1116/1.4863676
6. Kalhor, N.; Boden, S. A.; Mizuta, H. *Microelectron. Eng.* **2013,** *114,* 70–77. doi:10.1016/j.mee.2013.09.018
7. Stanford, M. G.; Lewis, B. B.; Mahady, K.; Fowlkes, J. D.; Rack, P. D. *J. Vac. Sci. Technol., B: Nanotechnol. Microelectron.: Mater., Process., Meas., Phenom.* **2017,** *35,* 030802. doi:10.1116/1.4981016
8. Jamali, M.; Gerhardt, I.; Rezai, M.; Frenner, K.; Fedder, H.; Wrachtrup, J. *Rev. Sci. Instrum.* **2014,** *85,* 123703. doi:10.1063/1.4902818
9. NanoCraft-FIBstream: Focused Ion Beam Stream File Generator. https://nanohub.org/resources/24027?rev=24 (accessed March 1, 2021). doi:10.4231/d3dn3zx26
10. Lalev, G.; Dimov, S.; Kettle, J.; van Delft, F.; Minev, R. *Proc. Inst. Mech. Eng., Part B* **2008,** *222,* 67–76. doi:10.1243/09544054jem864
11. Svintsov, A.; Zaitsev, S.; Lalev, G.; Dimov, S.; Velkova, V.; Hirshy, H. *Microelectron. Eng.* **2009,** *86,* 544–547. doi:10.1016/j.mee.2009.01.073
12. Kim, H.-B. *Microelectron. Eng.* **2012,** *91,* 14–18. doi:10.1016/j.mee.2011.11.015
13. De Felicis, D.; Mughal, M. Z.; Bemporad, E. *Micron* **2017,** *101,* 8–15. doi:10.1016/j.micron.2017.05.005
14. Niessen, F.; Nancarrow, M. J. B. *Nanotechnology* **2019,** *30,* 435301. doi:10.1088/1361-6528/ab329d
15. Lindsey, S.; Waid, S.; Hobler, G.; Wanzenböck, H. D.; Bertagnolli, E. *Nucl. Instrum. Methods Phys. Res., Sect. B* **2014,** *341,* 77–83. doi:10.1016/j.nimb.2014.09.006
16. Kalhor, N.; Mulckhuyse, W.; Alkemade, P.; Maas, D. *Proc. SPIE* **2015,** *9425,* 305–313. doi:10.1117/12.2085791
17. Yoon, H.-S.; Kim, C.-S.; Lee, H.-T.; Ahn, S.-H. *Vacuum* **2017,** *143,* 40–49. doi:10.1016/j.vacuum.2017.05.023
18. FIB-o-mat gitlab repository. https://gitlab.com/viggge/fib-o-mat/ (accessed Nov 9, 2020).
19. Gianuzzi, L.; Stevie, F. *Introduction to focused ion beams;* Springer Science & Business Media, 2005. doi:10.1007/b101190
20. Utke, I.; Moshkalev, S.; Russell, P., Eds. *Nanofabrication Using Focused Ion and Electron Beams: Principles and Applications;* Oxford University Press, 2012.
21. Tan, S.; Livengood, R. H.; Shima, D.; Notte, J. A.; McVey, S. *J. Vac. Sci. Technol., B: Microelectron. Nanometer Struct.–Process., Meas., Phenom.* **2010,** *28,* C6F15. doi:10.1116/1.3511509
22. Shorubalko, I.; Pillatsch, L.; Utke, I. Direct–Write Milling and Deposition with Noble Gases. In *Helium Ion Microscopy;* Hlawacek, G.; Gölzhäuser, A., Eds.; Springer International Publishing: Cham, Switzerland, 2016; pp 355–393. doi:10.1007/978-3-319-41990-9_15
23. Xia, D.; McVey, S.; Huynh, C.; Kuehn, W. *ACS Appl. Mater. Interfaces* **2019,** *11,* 5509–5516. doi:10.1021/acsami.8b18083
24. Utke, I.; Hoffmann, P.; Melngailis, J. *J. Vac. Sci. Technol., B: Microelectron. Nanometer Struct.–Process., Meas., Phenom.* **2008,** *26,* 1197–1276. doi:10.1116/1.2955728
25. Heilmann, M.; Deinhart, V.; Tahraoui, A.; Höflich, K.; Lopes, J. M. J. *arXiv* **2020,** No. 2009.13910.
26. Kirchhof, J. N.; Weinel, K.; Heeg, S.; Deinhart, V.; Kovalchuk, S.; Höflich, K.; Bolotin, K. I. *Nano Lett.* **2021,** *21,* 2174–2182. doi:10.1021/acs.nanolett.0c04986
27. Urban, R.; Wolkow, R. A.; Pitters, J. L. Single Atom Gas Field Ion Sources for Scanning Ion Microscopy. In *Helium Ion Microscopy;* Hlawacek, G.; Gölzhäuser, A., Eds.; NanoScience and Technology; Springer International Publishing, 2016; pp 31–61. doi:10.1007/978-3-319-41990-9_2
28. FIB-o-mat documentation. https://fib-o-mat.readthedocs.io/en/latest/ (accessed Nov 9, 2020).
29. GPLv3 license. https://www.gnu.org/licenses/gpl-3.0.en.html (accessed Nov 9, 2020).
30. FIB-o-mat pypi package. https://pypi.org/project/fibomat/ (accessed Nov 9, 2020).
31. Fleger, Y.; Gotlib-Vainshtein, K.; Talyosef, Y. *J. Microsc. (Oxford, U. K.)* **2017,** *265,* 307–312. doi:10.1111/jmi.12500
32. Chappert, C. *Science* **1998,** *280,* 1919–1922. doi:10.1126/science.280.5371.1919
33. Fassbender, J.; Ravelosona, D.; Samson, Y. *J. Phys. D: Appl. Phys.* **2004,** *37,* R179–R196. doi:10.1088/0022-3727/37/16/r01
34. Fassbender, J.; McCord, J. *J. Magn. Magn. Mater.* **2008,** *320,* 579–596. doi:10.1016/j.jmmm.2007.07.032
35. Devolder, T.; Ferré, J.; Chappert, C.; Bernas, H.; Jamet, J.-P.; Mathet, V. *Phys. Rev. B* **2001,** *64,* 064415. doi:10.1103/physrevb.64.064415
36. Ferré, J.; Devolder, T.; Bernas, H.; Jamet, J. P.; Repain, V.; Bauer, M.; Vernier, N.; Chappert, C. *J. Phys. D: Appl. Phys.* **2003,** *36,* 3103–3108. doi:10.1088/0022-3727/36/24/002
37. Je, S.-G.; Vallobra, P.; Srivastava, T.; Rojas-Sánchez, J.-C.; Pham, T. H.; Hehn, M.; Malinowski, G.; Baraduc, C.; Auffret, S.; Gaudin, G.; Mangin, S.; Béa, H.; Boulle, O. *Nano Lett.* **2018,** *18,* 7362–7371. doi:10.1021/acs.nanolett.8b03653
38. Berruto, G.; Madan, I.; Murooka, Y.; Vanacore, G. M.; Pomarico, E.; Rajeswari, J.; Lamb, R.; Huang, P.; Kruchkov, A. J.; Togawa, Y.; LaGrange, T.; McGrouther, D.; Rønnow, H. M.; Carbone, F. *Phys. Rev. Lett.* **2018,** *120,* 117201. doi:10.1103/physrevlett.120.117201

39. Eisebitt, S.; Lüning, J.; Schlotter, W. F.; Lörgen, M.; Hellwig, O.; Eberhardt, W.; Stöhr, J. *Nature* **2004,** *432,* 885–888. doi:10.1038/nature03139
40. StÄhr, J. *J. Electron Spectrosc. Relat. Phenom.* **1995,** *75,* 253–272. doi:10.1016/0368-2048(95)02537-5
41. Sapozhnikov, M. V.; Vdovichev, S. N.; Ermolaeva, O. L.; Gusev, N. S.; Fraerman, A. A.; Gusev, S. A.; Petrov, Y. V. *Appl. Phys. Lett.* **2016,** *109,* 042406. doi:10.1063/1.4958300
42. Verbiest, G. J.; Kirchhof, J. N.; Sonntag, J.; Goldsche, M.; Khodkov, T.; Stampfer, C. *Nano Lett.* **2018,** *18,* 5132–5137. doi:10.1021/acs.nanolett.8b02036
43. Chaste, J.; Eichler, A.; Moser, J.; Ceballos, G.; Rurali, R.; Bachtold, A. *Nat. Nanotechnol.* **2012,** *7,* 301–304. doi:10.1038/nnano.2012.42
44. Steele, G. A.; Hüttel, A. K.; Witkamp, B.; Poot, M.; Meerwaldt, H. B.; Kouwenhoven, L. P.; van der Zant, H. S. J. *Science* **2009,** *325,* 1103–1107. doi:10.1126/science.1176076
45. Weber, P.; Güttinger, J.; Noury, A.; Vergara-Cruz, J.; Bachtold, A. *Nat. Commun.* **2016,** *7,* 12496. doi:10.1038/ncomms12496
46. Annamalai, M.; Mathew, S.; Viswanathan, V.; Fang, C.; Pickard, D. S.; Palaniapan, M. Design, fabrication and Helium Ion Microscope patterning of suspended nanomechanical graphene structures for NEMS applications. In *2011 16th International Solid-State Sensors, Actuators and Microsystems Conference,* IEEE, 2011; pp 2578–2581.
47. Reinhardt, C.; Müller, T.; Bourassa, A.; Sankey, J. C. *Phys. Rev. X* **2016,** *6,* 021001. doi:10.1103/physrevx.6.021001
48. Blaikie, A.; Miller, D.; Alemán, B. J. *Nat. Commun.* **2019,** *10,* 4726. doi:10.1038/s41467-019-12562-2
49. Nair, R. R.; Blake, P.; Grigorenko, A. N.; Novoselov, K. S.; Booth, T. J.; Stauber, T.; Peres, N. M. R.; Geim, A. K. *Science* **2008,** *320,* 1308. doi:10.1126/science.1156965
50. Kim, K.; Regan, W.; Geng, B.; Alemán, B.; Kessler, B. M.; Wang, F.; Crommie, M. F.; Zettl, A. *Phys. Status Solidi RRL* **2010,** *4,* 302–304. doi:10.1002/pssr.201000244
51. Koppens, F. H. L.; Mueller, T.; Avouris, P.; Ferrari, A. C.; Vitiello, M. S.; Polini, M. *Nat. Nanotechnol.* **2014,** *9,* 780–793. doi:10.1038/nnano.2014.215
52. Nicholl, R. J. T.; Conley, H. J.; Lavrik, N. V.; Vlassiouk, I.; Puzyrev, Y. S.; Sreenivas, V. P.; Pantelides, S. T.; Bolotin, K. I. *Nat. Commun.* **2015,** *6,* 8789. doi:10.1038/ncomms9789
53. Yoon, D.; Son, Y.-W.; Cheong, H. *Nano Lett.* **2011,** *11,* 3227–3231. doi:10.1021/nl201488g
54. Martin, C. *Nat. Nanotechnol.* **2016,** *11,* 112. doi:10.1038/nnano.2016.8
55. Barton, R. A.; Storch, I. R.; Adiga, V. P.; Sakakibara, R.; Cipriany, B. R.; Ilic, B.; Wang, S. P.; Ong, P.; McEuen, P. L.; Parpia, J. M.; Craighead, H. G. *Nano Lett.* **2012,** *12,* 4681–4686. doi:10.1021/nl302036x
56. Huang, J.-S.; Callegari, V.; Geisler, P.; Brüning, C.; Kern, J.; Prangsma, J. C.; Wu, X.; Feichtner, T.; Ziegler, J.; Weinmann, P.; Kamp, M.; Forchel, A.; Biagioni, P.; Sennhauser, U.; Hecht, B. *Nat. Commun.* **2010,** *1,* 150. doi:10.1038/ncomms1143
57. Mueller, N. S.; Okamura, Y.; Vieira, B. G. M.; Juergensen, S.; Lange, H.; Barros, E. B.; Schulz, F.; Reich, S. *Nature* **2020,** *583,* 780–784. doi:10.1038/s41586-020-2508-1
58. Mueller, N. S.; Vieira, B. G. M.; Schulz, F.; Kusch, P.; Oddone, V.; Barros, E. B.; Lange, H.; Reich, S. *ACS Photonics* **2018,** *5,* 3962–3969. doi:10.1021/acsphotonics.8b00898
59. Reich, S.; Mueller, N. S.; Bubula, M. *ACS Photonics* **2020,** *7,* 1537–1550. doi:10.1021/acsphotonics.0c00359
60. Krauss, E.; Kullock, R.; Wu, X.; Geisler, P.; Lundt, N.; Kamp, M.; Hecht, B. *Cryst. Growth Des.* **2018,** *18,* 1297–1302. doi:10.1021/acs.cgd.7b00849
61. Alam, M. Z.; Schulz, S. A.; Upham, J.; De Leon, I.; Boyd, R. W. *Nat. Photonics* **2018,** *12,* 79–83. doi:10.1038/s41566-017-0089-9
62. Gittinger, M.; Höflich, K.; Smirnov, V.; Kollmann, H.; Lienau, C.; Silies, M. *Nanophotonics* **2020,** *9,* 401–412. doi:10.1515/nanoph-2019-0379
63. Scholder, O.; Jefimovs, K.; Shorubalko, I.; Hafner, C.; Sennhauser, U.; Bona, G.-L. *Nanotechnology* **2013,** *24,* 395301. doi:10.1088/0957-4484/24/39/395301
64. Kollmann, H.; Piao, X.; Esmann, M.; Becker, S. F.; Hou, D.; Huynh, C.; Kautschor, L.-O.; Bösker, G.; Vieker, H.; Beyer, A.; Gölzhäuser, A.; Park, N.; Vogelgesang, R.; Silies, M.; Lienau, C. *Nano Lett.* **2014,** *14,* 4778–4784. doi:10.1021/nl5019589

License and Terms

BEILSTEIN JOURNAL OF NANOTECHNOLOGY

A review of defect engineering, ion implantation, and nanofabrication using the helium ion microscope

Frances I. Allen[1,2]

Review

Open Access

Address:
[1]Department of Materials Science and Engineering, University of California, Berkeley, CA 94720, USA and [2]California Institute for Quantitative Biosciences, University of California, Berkeley, CA 94720, USA

Email:
Frances I. Allen - francesallen@berkeley.edu

Keywords:
defect engineering; focused helium ion beam-induced deposition; focused helium ion beam milling; helium ion beam lithography; helium ion implantation

Beilstein J. Nanotechnol. **2021,** *12,* 633–664.
https://doi.org/10.3762/bjnano.12.52

Received: 19 October 2020
Accepted: 30 April 2021
Published: 02 July 2021

This article is part of the thematic issue "Ten years of the helium ion microscope".

Guest Editors: G. Hlawacek and A. Wolff

Abstract

The helium ion microscope has emerged as a multifaceted instrument enabling a broad range of applications beyond imaging in which the finely focused helium ion beam is used for a variety of defect engineering, ion implantation, and nanofabrication tasks. Operation of the ion source with neon has extended the reach of this technology even further. This paper reviews the materials modification research that has been enabled by the helium ion microscope since its commercialization in 2007, ranging from fundamental studies of beam–sample effects, to the prototyping of new devices with features in the sub-10 nm domain.

Introduction

Since the helium ion microscope (HIM) was introduced 15 years ago [1-3], over one hundred HIMs have been installed worldwide and over one thousand research papers enabled by the HIM have been published. True to its classification as a microscope, and indeed its originally intended purpose, the HIM is widely used for microscopy. The microscopy functionality is primarily based on the detection of the secondary electrons that are generated by the finely focused ion beam as it is scanned across the sample. Compared with the scanning electron microscope (SEM), the HIM offers enhanced surface sensitivity, greater topographic contrast, and a larger depth of field [4,5]. A charge-neutralization system based on flooding the scanned region with low-energy electrons also permits high-quality imaging of electrically insulating materials, such as biological samples, thus avoiding the need for conductive coatings that can introduce artifacts and obscure nanoscale surface features [6,7]. Through extension of the technology to enable operation of the ion source with neon, sputtering at higher rates is made possible while retaining a small probe size. This has also opened the door to in situ materials analysis in the HIM using secondary ion mass spectrometry [8]. Further forms of materials analysis using the HIM include techniques based on the collection of backscattered helium ions and ionoluminescence [5].

Beyond microscopy and microanalysis, the HIM is also widely employed for materials processing, using the focused ion beam to intentionally modify the sample in some way. These operations essentially fall into two categories: At lower ion doses, various irradiation effects, such as defect formation and ion implantation, are used to locally change the properties of the material, and at higher doses, nanofabrication is performed using localized material removal (by sputtering) or addition (by gas-assisted deposition). Sometimes, lower-dose irradiation effects also lead to a nanofabrication outcome. For example, localized swelling by ion implantation can be used to pattern nanoscale surface topographies, ion-induced collisional mixing can restructure buried interfaces, and ion-induced chemical changes can be used for resist-based lithography. In the following, the field of materials modification research using the HIM is reviewed, subdivided into the following areas: 1. defect engineering, 2. ion implantation, 3. irradiation-induced restructuring, 4. resist-based lithography, 5. direct-write lithography/milling (including gas-assisted milling), and 6. gas-assisted deposition. Each topic is illustrated using a series of research highlights from the literature. In many cases, a particular application draws on the effects of more than one of the above areas, which is also discussed. At the root of all of these applications are the unique characteristics of the beam and its interaction with the sample. A quick recap of these details will be given first.

The intention of this review is to present the foundations and to summarize the state of the art. The list of referenced works is certainly not exhaustive in this extensive and rapidly evolving field. For previous reviews, the reader is referred to [9-13].

Key features of the beam and the beam–sample interaction

The enabling foundation of all HIM applications, from imaging to nanofabrication, comes down to the unique characteristics of the beam and its interaction with the sample. The HIM ion beam is generated by a highly specialized gas field-ionization source (GFIS), comprising a tungsten needle with a three-sided pyramidal tip that is atomically sharp. The tip is held at high voltage and helium (or neon) gas is supplied to the source chamber. Ionization in the high-field region of the tip apex forms the positively charged ions that are extracted and delivered to the sample via the ion optical column (Figure 1a). Generally, the source is configured to run in the stable configuration of just three atoms at the tip apex (named the trimer), generating three beamlets. Via appropriate beam alignment and aperture selection, the emission from a single atom is selected. Since the source is atomically sharp, the virtual source size is exceptionally small and the source brightness is exceptionally high. With a small intrinsic energy spread of the helium ions of less than 1 eV, chromatic aberration effects are minimized, and with a de Broglie wavelength of just 0.08 pm, diffraction effects do not appreciably limit the ultimate beam size. Beam spot sizes on the sample down to 0.5 nm in diameter in the case of helium, and 2 nm for neon, are routinely obtained. For detailed discussions of the unique source characteristics of the HIM and its beam optics the reader is referred to [5,14].

In addition to the small probe size, the interaction volume of the helium ions (beam energy of typically 10–30 keV) is also characteristically narrow, especially over the first 100 nm or so in depth in the material (see Figure 1b). This means that defect creation, implantation, sputtering, and deposition can all be very localized. Correspondingly, the secondary electrons that are generated (escape depth of a few nanometers) emanate from an area not that much larger than the original impact area of the beam. These characteristics, together with a low yield of backscattered ions and therefore a very small amount of second-generation secondary electrons, enable high-resolution resist-based lithography and high-resolution ion beam-induced deposition with dramatically reduced proximity effects. In the case of neon (also shown in Figure 1b), there is more scattering close to the surface, but the advantage for milling is a sputter yield that is about two orders of magnitude higher than that of helium at the same beam energy [17].

Early HIM work by Livengood et al. investigated the interaction volume and resulting modification of the sample for helium ions impinging on bulk silicon and copper targets providing key insights into the beam–sample interaction [16]. Dose series were conducted and the interaction volumes directly visualized by preparing cross sections by gallium focused ion beam milling that were inspected by transmission electron microscopy (TEM). In this way, the microstructural effect of increasing the helium ion-induced defect density was probed, and threshold doses for a series of structural changes, such as amorphization and subsurface swelling, were established (Figure 1c). The motivation for this study at the time was to investigate the invasiveness of the helium ion beam with respect to nanofabrication tasks in the semiconductor industry. Yet, the impact of this work has been far-reaching, providing a valuable benchmark for a range of applications focused on either purposefully creating, or avoiding, varying degrees of disorder in a material. In the following, a range of applications based on these irradiation effects is described, starting with defect engineering studies at the lowest doses and then moving through higher-dose applications. The final applications using the highest doses (many orders of magnitude higher than the largest dose shown in Figure 1c) are milling and gas-assisted ion beam-induced deposition.

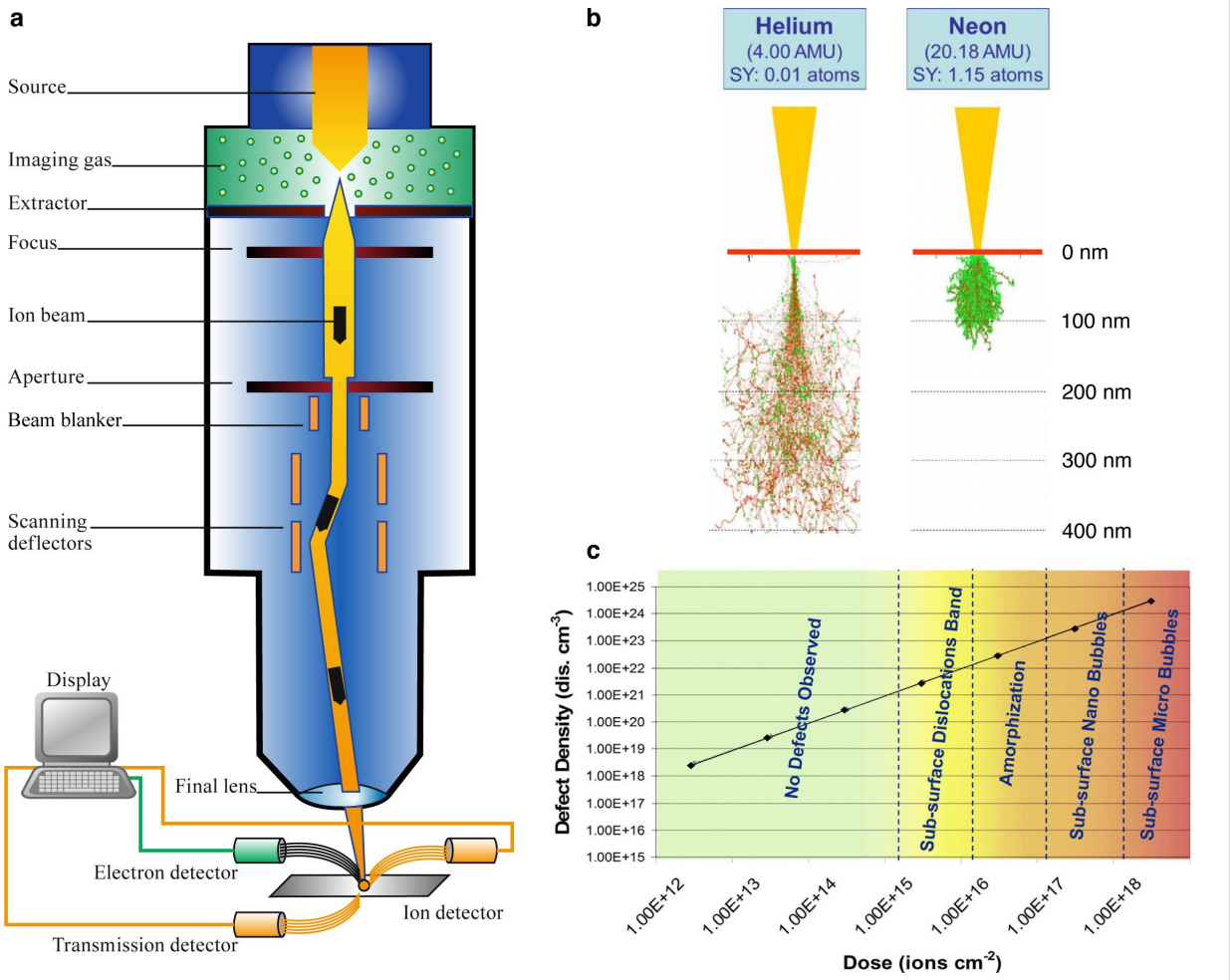

Figure 1: (a) Schematic diagram of the helium ion microscope. Adapted with permission from Cambridge University Press, [2], Morgan et al., An Introduction to the Helium Ion Microscope, Microscopy Today, 14(4), 24-31. Copyright 2006 Microscopy Society of America. **(b)** Simulated interaction volumes for 30 keV helium and neon ions incident on a silicon sample with sputter yield (SY) given for each case. Adapted with permission from [15]. Copyright 2010 American Vacuum Society. **(c)** Defect density versus dose for helium ions incident on bulk silicon and copper highlighting the threshold doses for various types of subsurface effects. Adapted with permission from [16]. Copyright 2009 American Vacuum Society. This content is not subject to CC BY 4.0.

Review

1 Defect engineering

The use of the HIM as a source of localized helium ion irradiation with which to tune material properties through the introduction of lattice defects has been demonstrated in a variety of nanoengineering applications. The generation of vacancies, preferential sputtering of one atomic species over another, and the introduction of increasing amounts of disorder leading to eventual amorphization of a crystalline material are all dials to turn. The properties engineered span electronic, magnetic, optical, chemical, and thermal properties. In the case of 2D and thin-film materials supported on a substrate, defects induced by backscattered ions and sputtered atoms also need to be considered. A recent computational analysis of these substrate effects can be found in [18].

Electrical and electronic properties

The majority of defect engineering studies using the HIM have focused on tuning electrical conductivity. First work in this area concentrated on graphene, seeking to locally modulate its 2D electronic structure through site-selective irradiation, rather than through chemical functionalization of its surface. Nakaharai et al. irradiated supported single-layer graphene with 30 keV helium ions increasing the dose from ca. 2×10^{15} to 1×10^{16} ions/cm^2 (corresponding to an estimated vacancy defect concentration of 0.2–1.3%) and, within this dose range, measured a metal–insulator transition [19]. Raman analysis showed that even at the highest dose (i.e., for strongly insulating graphene), the crystal lattice structure of the graphene sheet was essentially preserved. A subsequent study by Moktadir et al. investigated the nature of the ion-induced defects further, and deter-

mined that after irradiation, the ion-induced vacancies become saturated with oxygen [20]. The authors of the latter thus proposed that the mechanism behind the irradiation-induced insulating behavior involved oxygen groups acting as charge traps that pin the Fermi level at the Dirac point.

Later conductivity tuning of graphene went on to combine this irradiation-induced effect with the fine patterning capabilities of the HIM performing line irradiations across graphene with varying step sizes between dwell points [21]. This produced continuously irradiated lines in the one extreme, and lines comprising a chain of separated points in the other. Conductivity analysis of these samples showed that in addition to the total dose, the scan strategy (which controls the uniformity of the dose and hence the uniformity of the resulting defects) can also be used to tune the local conductivity. A further study demonstrating the importance of factors other than the total dose investigated the effect of the size of the irradiated area [22]. Regions of monolayer graphene (again, supported) were irradiated using pattern shapes of different sizes, exploring lateral dimensions down to 10 nm, but all for the same total dose. It was found that the conductivities of the irradiated areas depended strongly on their geometrical size; for smaller areas, the same degree of insulating behavior as for the larger areas could not be achieved, even though the defect density was the same. The authors described a hopping carrier transport model to explain the effect and pointed out that the observed behavior essentially places a limit on the spatial resolution attainable when using the helium ion beam to selectively dose and thus change the conductivity of nanoscale regions. Several other studies of selective helium ion-induced conductivity changes in graphene have also been conducted [23] and a theoretical treatment of defect-induced conductivity changes upon helium ion irradiation of free-standing compared to supported monolayer graphene can be found in [24].

Various 2D transition metal dichalcogenides have also been the subject of conductivity-tuning studies in the HIM. For example, Fox et al. showed that site-selective helium ion irradiation, introducing point defects and local disorder, transformed targeted regions of a supported pristine few-layer MoS_2 flake from semiconducting to insulating at a dose of ca. 1×10^{15} ions/cm^2 [25]. The dose-versus-resistivity plot from this work is shown in Figure 2a. Upon increasing the dose to ca. 1×10^{17} ions/cm^2, the material became amorphous, and the conductivity behavior changed to metallic. This was attributed to preferential sputtering of sulfur, increasing the relative amount of molybdenum in the material. Finally, at even higher doses, insulating behavior re-emerged, presumed to be due to excessive material removal by sputtering. In related work, a nearest-neighbor hopping mechanism mediated by the formation of extended metallic edge states in the defective lattice was proposed for the pseudometallic regime [26]. Line irradiation with helium ions bisecting a monolayer MoS_2 flake has been shown to create a defective channel that can be used to fabricate a 2D memristive device [27]. And in a subsequent study, field-effect transistors based on monolayer MoS_2 were irradiated with helium ions over the transistor channel and the effect of varying the size and position of the irradiated area on the electrical performance of the device was characterized [28].

Complimentary work on few-layer WSe_2 by Stanford et al. also observed semiconductor–insulator–metal transitions for increasing dose, noting preferential sputtering of selenium [29]. Here it was found that for a given dose, hole transport was degraded more than electron transport. The authors went on to demonstrate a lateral p–n-like homojunction by irradiating just one side of a portion of WSe_2 bridging two metal contacts to create semiconducting (pristine) and insulating (irradiated) halves contacted by the source and drain electrodes (Figure 2b). Direct-write of further logic circuits into single flakes of WSe_2 and WS_2 has also been demonstrated [26]. In addition, density functional theory has been used to model the effect of ion-induced defects on the electronic band structure of various 2D transition metal dichalcogenides [26,30,36], and band-excitation Kelvin probe microscopy has been used to probe the resulting changes in the local work function [30]. In several of these works, high-resolution scanning TEM (STEM) imaging has been performed to enable the analysis of the defects created on the atomic scale [26,29,30] (see, e.g., Figure 2c).

Apart from 2D materials, thin-film samples have also been the subject of electronic property tuning by localized helium ion irradiation. For example, using a helium ion dose of 5×10^{14} ions/cm^2, permanent local tuning of the charge density in an amorphous thin film of the semiconductor indium gallium zinc oxide (film thickness 50 nm) has been demonstrated, thereby enabling activation of the electronic conduction properties of the material without needing to rely on thermal activation [37].

And finally in the category of electronic applications, a number of studies have used the HIM to direct-write Josephson tunnel junctions into thin films of high-transition-temperature superconductors. This was first demonstrated by Cybart et al. for the cuprate superconductor $YBa_2Cu_3O_{7-\delta}$ (YBCO), by scanning the helium ion beam in line mode across 4 μm wide strips of YBCO that had been locally pre-thinned to a thickness of 30 nm using argon ion milling [31]. Due to the high-resolution writing capability of the HIM, junction barriers of width 1–2 nm were created, that is, narrow enough for the tunneling current to propagate. An overview of the sample and a schematic outlining the

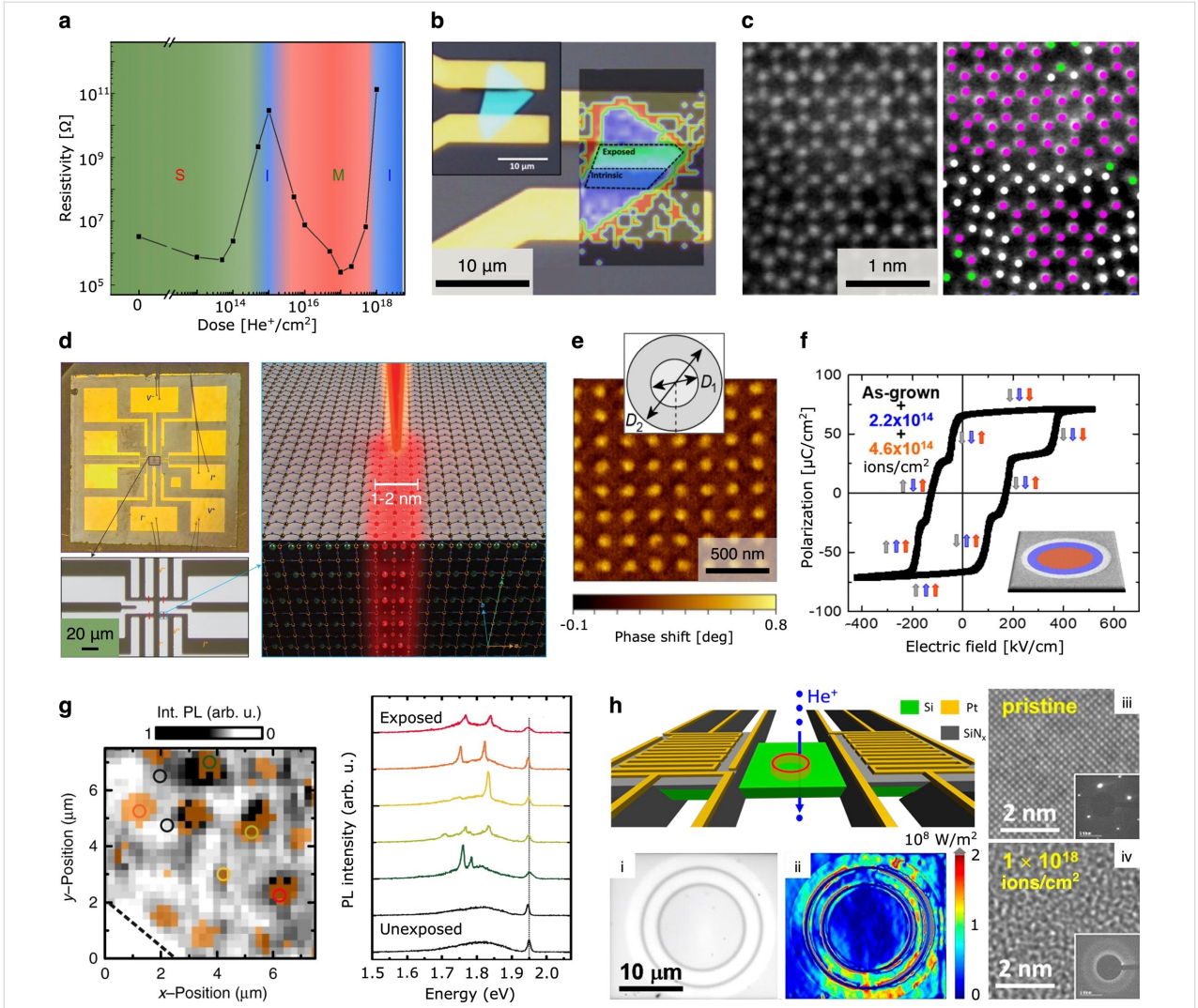

Figure 2: Defect engineering using the HIM. **(a)** Plot of resistivity versus dose for helium ion-irradiated MoS_2 (few-layer) showing multiple phase transitions: semiconducting (S), insulating (I), metallic (M). Reprinted with permission from [25]. Copyright 2015 American Chemical Society. **(b)** Electronic homojunction in few-layer WSe_2 created by site-selective helium ion irradiation: colorized Raman map on the right with optical micrograph of the device shown top left. Adapted from [29]. Copyright 2016 Stanford et al., licensed under a Creative Commons Attribution 4.0 International License, http://creativecommons.org/licenses/by/4.0/. **(c)** STEM-based analysis of atomic defects in single-layer $MoSe_2$ created by helium ion irradiation. Adapted from [30]. Copyright 2016 Iberi et al., licensed under a Creative Commons Attribution 4.0 International License, http://creativecommons.org/licenses/by/4.0/. **(d)** Fabrication of Josephson junctions in a thin-film high-temperature superconductor by helium line irradiation: YBCO-based device with gold contacts (left) and schematic showing the irradiation approach (right). Adapted by permission from Springer Nature, [31], Nature Nanotechnology, Nano Josephson superconducting tunnel junctions in $YBa_2Cu_3O_{7-\delta}$ directly patterned with a focused helium ion beam, Cybart et al. Copyright 2015 Nature Publishing Group. **(e)** Magnetic force microscopy of a nanoscale array of discs with reduced magnetic anisotropy patterned into a Co/Pt multilayer: concentric helium ion irradiation scheme for each disc shown inset. Adapted from [32]. Copyright 2019 Sapozhnikov et al., licensed under a Creative Commons Attribution 4.0 International License, https://creativecommons.org/licenses/by/4.0/. **(f)** Multilevel ferroelectric switching of nanostructures fabricated by helium ion irradiation of a $PbZr_{0.2}Ti_{0.8}O_3$ thin film using concentric patterns with variable dose. Adapted with permission from [33]. Copyright 2018 by the American Physical Society. **(g)** Site-selective formation of optically active defects in MoS_2: photoluminescence (PL) map of an array created by localized helium ion irradiation (100 × 100 nm fields, pitch 2 µm) and corresponding PL spectra for regions marked with the colored circles. Adapted from [34]. Copyright 2019 Klein et al., licensed under a Creative Commons Attribution 4.0 International License, http://creativecommons.org/licenses/by/4.0/. **(h)** Demonstration of a microscale thermal cloak using helium ion irradiation to site-selectively tune the thermal conductivity of a suspended silicon membrane: schematic of device (top left), (i) optical image showing irradiated regions (darker contrast), (ii) corresponding heat flux map, (iii) TEM analysis of pristine silicon, (iv) TEM analysis of an irradiated region. Adapted with permission from [35]. Copyright 2019 American Chemical Society. The content of (a), (d), (f) and (h) is not subject to CC BY 4.0.

irradiation approach are shown in Figure 2d. The electronic properties of the junction barrier can be continuously tuned by varying the irradiation dose, and the authors showed that by using irradiation doses of 2×10^{16} and 6×10^{16} ions/cm^2, tunnel junctions with barriers exhibiting normal-metal and insulator behavior, respectively, were obtained. Similarly, the fabrication of superconducting quantum interference devices (SQUIDs) was demonstrated, using the helium line irradiation

method to direct-write metallic and insulating Josephson junctions into pre-fabricated YBCO circuits [38].

By increasing the helium ion dose further, to the order of 10^{17} ions/cm^2, highly resistive (amorphous) regions can be patterned into the YBCO thin film and thus be used to define precise sample geometries, without material removal. For example, high-dose irradiation over larger areas leaving a narrow gap in between has been used to define YBCO nanowires, which were then line-irradiated at lower dose to form nanowire-based Josephson junctions [39]. Similar multi-step irradiation routines have been used to fabricate SQUID micromagnetometers entirely using helium ion irradiation [40-43], nano-SQUID-based transimpedance amplifiers [44], and Josephson junctions in the superconducting bridge of spiral terahertz antenna structures [45]. The performance of Josephson junctions in YBCO thin films fabricated using the HIM has been further evaluated in [46].

Cross-sectional STEM analysis of helium line irradiations of YBCO has shown that the crystallinity of the Josephson junction barriers is essentially preserved, highlighting the high sensitivity of the electronic transport properties of YBCO to point defects introduced into the lattice [43]. The same study also confirmed that minimal lateral scatter of the ions in the YBCO thin film occurs; even at the higher doses used to induce amorphisity, the irradiated channels remain narrow and confined. In contrast, in a study based on another cuprate-based superconductor, $La_{1.84}Sr_{0.16}CuO_4$ (LSCO), it was found that significantly higher doses (10^{18} ions/cm^2) were necessary to induce resistive behavior [47], that is, an order of magnitude higher than the respective dose for YBCO. Moreover, significant lateral scatter of the helium ions in the LSCO thin film was observed, even for the lower doses, exacerbated by ion backscatter from the substrate interface. However, in the case of another high-temperature superconductor, MgB_2, the creation of high-quality Josephson junctions by the HIM method has again been demonstrated [48].

Ferromagnetic properties

The first demonstration of defect engineering using the HIM was actually for a magnetic device by Franken and co-authors [49]. In this work, ferromagnetic microstrips comprising Pt(4 nm)/Co(0.6 nm)/Pt(2 nm) layers on an SiO_2/Si substrate were irradiated on one half with 25 keV helium ions. It was found that at a dose of 2×10^{15} ions/cm^2 a domain wall could be injected into the structure due to the introduction of lattice defects that locally reduced the perpendicular magnetic anisotropy. By raising the dose slightly to 3×10^{15} ions/cm^2, the domain walls could then be pinned in a highly reproducible manner. The same publication compared these results with those obtained using gallium ion irradiation and found that domain wall pinning was more pronounced in the helium ion case. This was attributed to the higher resolution capability of the helium ion beam enabling the creation of a sharper energy barrier at the domain wall.

Later work in this area employed similar helium ion doses ($1–4 \times 10^{15}$ ions/cm^2) to locally reduce the perpendicular magnetic anisotropy in a Co/Pt multilayered thin film [50]. Here, patterns comprising an arrangement of discs of 100 nm diameter with a pitch of 200 nm were irradiated, demonstrating the capability of the focused helium ion beam method to achieve magnetic property engineering in the form of a nanoscale periodic array. In follow-up work, consistent magnetization reversal for all disks was achieved by inhomogeneous irradiation using a concentric pattern with a higher dose on the outside, rather than using homogeneous irradiation [32] (Figure 2e). Nanoscale magnetic patterning of Co/Pt multilayers using a checkerboard helium ion irradiation pattern has also recently been demonstrated [51]. Furthermore, tuning of the metamagnetic transition temperature of an FeRh thin film (from antiferromagnetic to ferromagnetic behavior) has been achieved by varying the helium ion dose from 1×10^{14} to 5×10^{15} ions/cm^2, with the patterning of features down to 25 nm in size [52].

In a study implementing doses up to 1×10^{17} ions/cm^2, stripe patterns were irradiated onto a magnetic thin film structure (this time comprising a ferro- and an antiferromagnetic layer) [53]. The reason for using the higher doses was to investigate the effect of helium implantation and subsequent swelling of the layers and the underlying substrate on the magnetic modification obtained. It was found that helium ion bombardment influenced the magnetic anisotropy in both layers of the structure, strongly reducing the saturation magnetization of the layer system. Moreover, the behavior observed correlated with both the introduction of lattice vacancy defects, and with an increase in the average interatomic distances due to swelling, that is, a magnetovolume effect. And in a recent report implementing in situ current–voltage characterization, site-selective helium ion irradiation of cobalt-based magnetic multilayer structures has been used to modulate the local magnetic anisotropy, with multilevel switching achieved [54].

The neon ion beam of the HIM has also been used to tailor magnetic properties. The heavier ions were used to introduce chemical disorder into the target lattice through the local displacement of atoms in the collision cascade to create individual ferromagnetic domains in a previously non-ferromagnetic material [55]. In the cited work, Röder et al. used this phenomenon of disorder-induced ferromagnetism, together with the small

probe size of the neon ion beam, to directly write nanomagnets into a chemically ordered non-ferromagnetic $Fe_{60}Al_{40}$ precursor film.

Ferroelectric properties

Similar to the magnetic anisotropy experiments described above, helium ion irradiation using the HIM has also been used to locally modify ferroelectric properties. For example, pinning of ferroelectric domains in $PbZr_{0.2}Ti_{0.8}O_3$ thin films at doses of 0.22×10^{15} to 1×10^{15} ions/cm^2 has been demonstrated, and through site-selective direct-write patterning with variable dose, various nanostructures with novel ferroelectric-switching functionalities have been fabricated [33] (Figure 2f). Using similar doses, out-of-plane piezoelectricity has been patterned into multilayered $MoTe_2$ [56]. In the case of helium ion irradiation of a bulk van der Waals layered ferroelectric semiconductor crystal ($CuInP_2S_6$), local volume expansion due to helium ion implantation was observed, forming a conical surface topography within which for increasing dose the ferroelectric domains were gradually destroyed [57].

Optical properties

In early work concerned with tuning optical properties with the HIM, arrays of nitrogen-vacancy centers were fabricated in diamond [58,59]. Starting with a diamond sample that already contained substitutional nitrogen, the focused helium ion beam was used to create lattice vacancies at predefined locations (in a similar manner to the related electron beam-based methods). After annealing to allow for diffusion of the vacancies, the presence of nitrogen-vacancy centers was confirmed by photoluminescence. Conversely, helium ion irradiation of another material, silicon nitride, in the HIM was found to reduce its fluorescence [60]. This was attributed to ion beam-induced disruption of the optically active defects present in the material. In the cited work, the effect was used to locally reduce the fluorescence of patches of a silicon nitride membrane that were subsequently perforated by helium ion beam milling to create solid-state nanopores for biomolecule detection. Following this approach, a low fluorescence background was achieved, facilitating the translocation detection of fluorescently labeled biomolecules by optical means, as opposed to having to rely on the conventional ionic current method. Nanopore fabrication using the HIM is discussed in more detail in Section 5.

The HIM has also been used to tune the optical properties of quantum well structures [61]. In this work, epitaxially grown InGaAs/GaAs single quantum well structures were patterned with sets of stripes to emulate a grating structure, using doses of less than 10^{12} ions/cm^2. The result was a periodic spatial modulation of the excitonic resonance of the quantum well perpendicular to the buried quantum well layer. Since the doses were so low, the change in optical properties was attributed to the local accumulation of defects (as opposed to collisional phase mixing). In a plasmonic application, resonant triangular nanostructures were created in a graphene sheet supported on SiO_2/Si by selectively irradiating the graphene in the regions around the intended structures (note, the graphene was not milled away) [62]. Tuning of the resonant behavior of the nanostructures was demonstrated by adjusting the irradiation dose.

Closely related to the electronic property tuning of 2D transition metal dichalcogenides described earlier, irradiation-induced changes in the optical response of this class of materials has also been investigated using the HIM. This was first performed for few-layer WSe_2 [29] and monolayer $MoSe_2$ [30] (for the latter, changes in nanomechanical properties were also probed). In subsequent work on monolayer MoS_2 by Klein et al., the effects of ion dose on the optical and valleytronic properties of the material were investigated [36]. In this study, Raman spectroscopy was used to systematically probe the effect of increasing disorder for increasing irradiation dose, and the corresponding distance between the ion-induced defects for each dose level was inferred. At lower doses, a redshift in disorder-related photoluminesce peaks was observed, attributed to chemisorption at monosulfur vacancies, whereas for doses higher than 10^{14} ions/cm^2, a strong reduction in all photoluminescence peaks occurred, corresponding to high levels of disorder in the crystal. Up to this critical dose, it was shown that the valley polarization properties of the material were preserved (indicating that the electronic band structure of the semiconductor was largely unaffected). Only for high levels of disorder introduced into the system was the band structure degraded. Based on these results, the authors determined a critical dose for nanostructuring MoS_2 below which the optical and valleytronic properties of the material are conserved. In subsequent work, the formation of arrays of optically active defects in monolayer MoS_2 was demonstrated, using localized helium ion irradiation followed by encapsulation in hBN in order to enhance the optical quality of the defect states [34]. Results from this study are shown in Figure 2g. A recent study of the effect of helium ion-induced disorder on the Raman modes and photoluminscence behavior of bilayer MoS_2 can be found in [63].

Chemical properties

Local helium ion irradiation has also been shown to modify the chemical properties of a material, for example, chemical etch rates. In HIM studies by Petrov et al. irradiating silicon nitride [64,65] and silicon dioxide [66,67] with 10^{15}–10^{16} ions/cm^2, the rate of subsequent wet-etching of the irradiated regions with hydrofluoric acid was found to increase by up to a factor of three (for Si_3N_4) and five (for SiO_2). The change was attributed to ion-induced defects and demonstrates another potential form

of HIM-enabled nanofabrication, namely site-specific ion-enhanced etching with high spatial resolution. Similarly, site-selective etching of MoS_2 has been demonstrated using helium ion irradiation to create defective regions that become activated for oxygen adsorption and subsequent oxidative etching when heated in air [68].

Helium ion irradiation in the HIM, this time using a defocused beam to irradiate larger areas, has also been used to generate defects in exfoliated flakes of molybdenum dichalcogenides (MoS_2 and $MoSe_2$) to activate the catalytic activity of the basal planes of the crystal for hydrogen evolution reactions [69].

Thermal properties

Further defect engineering studies using the HIM have been concerned with tuning the thermal properties of materials. The first example of this demonstrated site-selective engineering of thermal conductivity along the length of individual nanowires [70]. Here, Zhao et al. irradiated discrete sections of free-standing crystalline silicon nanowires of 160 nm diameter to a series of target doses. It was found that a dramatic decrease in thermal conductivity occurred already at relatively low doses, corresponding to point defect concentrations of only a few percent. This result indicated a strong phonon scattering effect from the few point defects introduced. For higher doses above ca. 2×10^{16} ions/cm^2, complete amorphization of the material occurred, although it was noted that the overall morphology of the structure was unaffected. This ability to locally tune the thermal conductivity by selective helium ion irradiation has since been used to manipulate heat flow in suspended crystalline silicon membranes, patterning concentric circles at variable dose to demonstrate a microscale thermal cloak [35] (Figure 2h).

In a subsequent study by Jin et al., dose-controlled localized helium ion irradiation has been used to introduce lattice defects into VO_2 nanowires with which to control the conduction mechanisms of thermal and electrical transport in this material [71]. By performing a dose series and measuring the thermal and electrical conductivities of helium ion-irradiated VO_2 around its insulator–metal transition temperature, a fundamental study of the contradictorily low electronic thermal conductivity of VO_2 in the metallic regime was enabled. Similarly, Bi_2Te_3 nanoribbons have been irradiated with helium ions in order to defect-tune conduction mechanisms and study the anomalously high electronic thermal conductivity of this material [72].

Additional defect engineering studies

Defect formation in supported and free-standing multiwalled carbon nanotubes upon irradiation with both 25 keV helium and neon ions has also been investigated, since ion (and electron) irradiation can be used to modify the mechanical, electronic, and magnetic properties of these materials [73]. In this work, the focus was on characterizing the accumulation of defects and structural changes for increasing dose, using correlative Raman spectroscopy and TEM. The effect of sample thinning due to sputtering on the overall damage evolution process was also noted.

2 Ion implantation

Helium ion implantation and the associated structural changes to a material are often unwanted, with measures taken to avoid these effects. However, the HIM also offers a unique opportunity for fundamental studies of helium ion implantation phenomena (such as the formation of helium nanobubbles and blisters), as well as the opportunity to leverage these phenomena for practical applications. Using the HIM, individual grains/interfaces/regions of interest can be irradiated with a known dose of ions for systematic studies on the nanoscale. This brings certain advantages compared with the traditionally used large-scale experiments. For example, although experiments using ion accelerators and plasma ion sources enable investigations over a wide range of beam energies and give the experimenter much freedom in terms of sample environment, the beam spot sizes are large (typically hundreds of micrometers), preventing study of the irradiation response of individual micro- and nanoscale features. In addition, the large-scale experiments are much less controlled in terms of dose, whereas with the HIM, systematic repeatable studies over many samples can be performed. In fact, at doses below the threshold for nanobubble formation, the introduction of helium atoms into interstitial sites can be used to delicately induce strain into a crystal lattice, which can be leveraged for strain engineering. And at higher doses, localized and controlled surface swelling can be used to create 3D structures from an initially flat substrate, that is, ion implantation using the HIM can also be used for nanofabrication.

Strain engineering

When helium ions are implanted into a crystal lattice they insert as atoms into interstitial sites, and due to their chemical inertness, do not react with the material. This interstitial placement induces strain into the lattice and hence offers a method for so-called strain engineering of a range of physical properties. Very recently, ion implantation using the HIM has been investigated for this purpose, demonstrating the patterning of out-of-plane strain into epitaxial thin films of bismuth ferrite [74]. In this work, Toulouse et al. showed that by continuously varying the dose, continuous elongation of the unit cell in the out-of-plane direction could be achieved, thus enabling fine control over the strain induced. Future work in this direction using the high-resolution patterning capabilities of the HIM for highly tunable strain engineering on the nanoscale is to be expected.

Related to this are the ion implantation-induced membrane folding studies discussed at the end of Section 3.

Helium nanobubbles and blisters

At higher doses, the vacancies and interstitials that form in a crystalline material upon helium ion irradiation can diffuse and combine to form helium nanobubbles. And upon increasing the irradiation dose further, nanobubbles can coalesce to form larger cavities. Eventual rupture of cavities formed in near-surface regions can then lead to surface blistering. These phenomenona have been known and investigated for several decades. In early HIM studies on the subsurface effects of helium ions on bulk silicon and copper targets by Livengood et al., the formation of nanobubbles and larger subsurface voids was indeed also observed [16]. Threshold doses for the formation of a subsurface dislocation band, for the onset of amorphization, and for the formation of nanobubbles and larger voids, were established (as shown earlier in Figure 1c). Tan et al. performed detailed TEM cross-sectional analysis of the implantation profiles from line exposures [75] (Figure 3a). A recent extension of this work has been reported by Li et al. [76], which includes strain field analysis (Figure 3b) and a survey of bubble size distributions. In work using a gold target, Veligura et al. investigated the effect of varying the beam energy on the subsurface damage process [77]. For high-dose implantation at high beam energies (35 keV), blister formation was observed, as in [16]. This is explained by the formation and accumulation of helium nanobubbles beneath the surface that cannot escape, and which coalesce to form a subsurface cavity (blister). However, at lower beam energies (15 keV), the authors observed that the helium nanobubbles formed closer to the surface, creating a porous structure via which helium can then escape and blister formation is avoided [77].

A further interesting effect of helium ion irradiation of crystalline materials under certain conditions is the formation of a

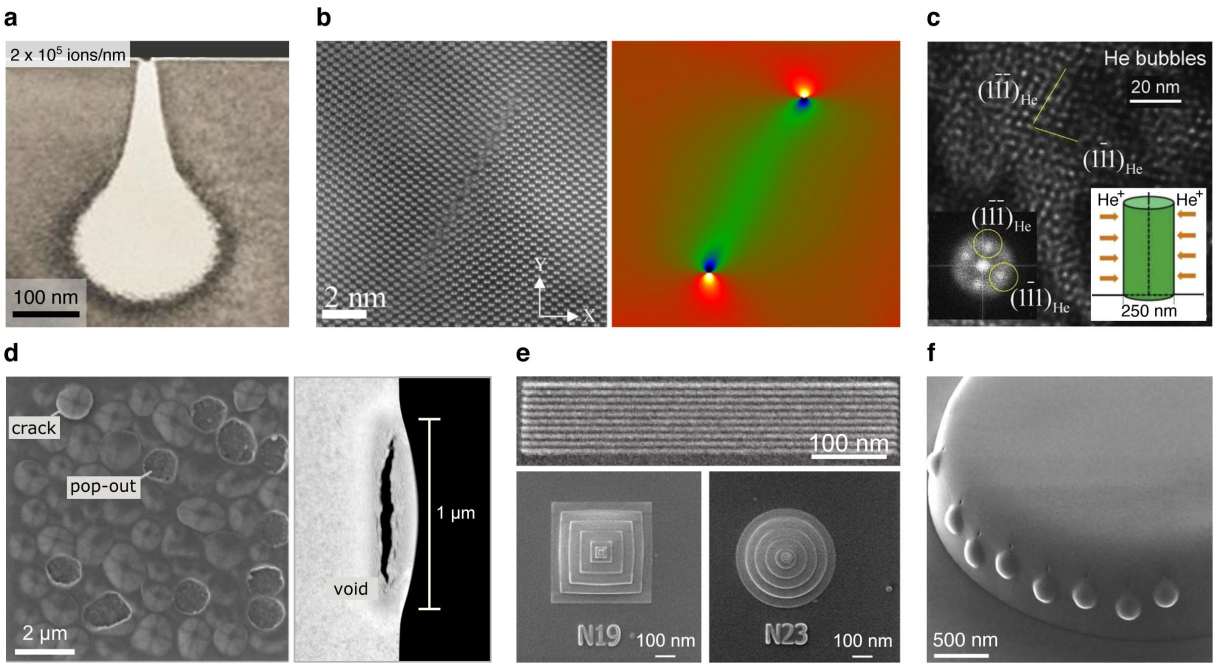

Figure 3: Effects of helium ion implantation studied with the HIM. **(a)** TEM cross-section analysis of the implant profile of 35 keV helium ions (line scan) in silicon for a dose above the amorphization threshold (the bright teardrop-shaped volume is the amorphized region). Adapted with permission from [75]. Copyright 2014 American Vacuum Society. **(b)** STEM image of a silicon crystal irradiated with helium ions in line-scan mode (left) with corresponding strain field analysis (right). Adapted with permission from [76]. Copyright 2019 American Vacuum Society. **(c)** Helium gas-bubble superlattice formed in copper: TEM image showing helium nanobubbles (bright contrast) with corresponding fast Fourier transform; schematic outlining the implantation principle from opposite sides of a flipped nanopillar shown inset. Adapted from [78]. Copyright © 2016 Acta Materialia Inc. Published by Elsevier Ltd. [78] is an open access article under a Creative Commons Attribution 4.0 International License (http://creativecommons.org/licenses/by/4.0/). **(d)** HIM image of helium blisters formed on tungsten (left) and STEM cross-section analysis of a single blister (right). Adapted from [84], Scripta Materialia, 178, Allen et al., Key mechanistic features of swelling and blistering of helium-ion-irradiated tungsten, 256-260, Copyright (2019) Acta Materialia Inc., with permission from Elsevier. **(e)** Helium nanoscale tumefaction to create raised lines and pyramid/cone structures in silicon. Adapted from [94], Zhang et al., Direct-write three-dimensional nanofabrication of nanopyramids and nanocones on Si by nanotumefaction using a helium ion microscope, Nanotechnology, Vol. 26(25), 255303, first published 4 June 2015. Copyright © 2015 IOP Publishing Ltd. Reproduced with permission. All rights reserved. **(f)** Helium point irradiations into the side of a diamond microscale disk creating precise surface protrusions. Adapted from [95], Kim et al., Focused-helium-ion-beam blow forming of nanostructures: radiation damage and nanofabrication, Nanotechnology, Vol. 31(4), 045302, first published 24 October 2019. Copyright © 2019 IOP Publishing Ltd. Reproduced with permission. All rights reserved. The content of (a), (b), (d), (e) and (f) is not subject to CC BY 4.0. For (c), please see the copyright notice in the caption.

so-called gas bubble superlattice, comprising a periodic 3D array of nanobubbles imposed onto the host lattice. This can result in so-called radiation hardening of the material, which is of particular significance in the development of radiation-tolerant structural materials for deployment in nuclear fission and future nuclear fusion reactors. It has been shown that the gas bubble superlattice can be created by both broad beam or plasma exposure, as well as by repeated scanning of a selected area with the focused helium ion beam of the HIM. Wang et al. used the HIM to conduct a systematic study of the effect of such a helium gas bubble superlattice on the mechanical properties of copper, which is representative of a range of fcc alloys that are known to exhibit radiation tolerance [78]. Copper nanopillar specimens were irradiated at room temperature with known doses of helium ions to generate the gas bubble superlattice (Figure 3c) and subsequently nanomechanical compression testing of the implanted structures was performed by in situ TEM to enable direct and quantitative observation of the superlattice during deformation.

Other materials of interest for nuclear reactor design that have been the subject of HIM irradiation studies include silicon carbide grains in a pyrolytic carbon matrix [79], α-$LiAlO_2$ pellets [80], tristructural-isotropic fuel particles [81], oxide dispersion-strengthened steels [82], tungsten [83-85], an Fe–Zr alloy [86], a Y_2O_3/Fe bilayer [87], and nanocluster films of magnetite and core–shell iron–magnetite nanoparticles [88]. In these studies, various implantation effects have been investigated, including the tendency for grain boundaries and interfaces to act as sinks for irradiation-induced defects and implanted ions [79,80,82,83,86,87], and at higher doses, the subsurface swelling that results in blistering and delamination [84] (Figure 3d), which for deployment of a material in a reactor needs to be avoided [80,82-85].

Returning to silicon, the nanomechanical properties of helium ion-irradiated silicon nanopillars have since been investigated as well, observing a softening behavior upon amorphization and swelling [89]. Helium ion irradiation of single-crystal diamond nanopillars has revealed an orientation dependence of the irradiation damage and associated mechanical response, with the typical swelling also observed [90]. In contrast, studies of both helium and neon ion-irradiated polymers have shown that swelling does not occur at the threshold doses observed for crystalline targets, attributed to the significantly higher diffusion coefficients of the noble gas atoms in the polymer, allowing the gas to diffuse out rather than accumulate [91]. In fact, a study has used localized helium ion irradiation to locally shrink a polymer and thereby modify the height of metallic thin films supported on a polymer substrate [92]. This effect was attributed to ion-induced scission of the polymer chains and subsequent cross-linking and compaction, which can be understood in terms of the dominance of energy losses by electronic scattering in the case of light ions such as helium, compared with the nuclear scattering that dominates energy loss for heavier ions. Yet, even in polymeric materials, swelling under implantation with high doses can still occur, and in general, the above studies underscore the advantage for many nanofabrication applications of a sample that is thinner than the ion stopping distance such that implantation effects can be avoided [93]. Although in some cases subsurface swelling is specifically desired, as described further below.

Nanofabrication using subsurface swelling

The localized volume expansion observed for a range of crystalline materials upon helium ion irradiation at high dose has also been put to use for several nanofabrication tasks. For example, irradiation of silicon substrates has been used to pattern raised lines, achieving a half-pitch down to 3.5 nm [94] (Figure 3e, top). In the same study, 3D nanopyramids and nanocones rising from the silicon surface were also created, achieved by dosing a series of concentric square frame and annulus patterns, respectively, with increasing dose from the perimeter to the center (Figure 3e, bottom). This tumefaction technique has the potential to be used to fabricate molds for nanoimprint lithography. In a recent study, localized helium ion implantation into diamond nanostructures using point or line-scan exposures has been employed for nanoscale "blow-forming", producing precise surface protrusions in the regions targeted [95] (Figure 3f).

Finally, helium ion-induced swelling of a substrate can also be used to intentionally deform a supported structure. For example, a silicon substrate supporting an amorphous nanoporous aluminum oxide structure was irradiated with helium ions causing dome-shaped swelling of the substrate and thereby 3D deformation of the supported material, accompanied by enlargement of the nanopores to accommodate the new topography [96].

3 Irradiation-induced restructuring

The following applications have used localized helium ion irradiation in the HIM to change the morphology and/or internal structure of a material by ion-induced mass transport along surfaces, ion-induced collisional atomic mixing, and through stress gradients induced in membrane targets by ion implantation.

Ion-induced mass transport

In one example of a morphological change attributed to ion-induced mass transport, segments of a free-standing GaAs nanowire of 100 nm diameter were irradiated locally with 30 keV helium ions at relatively low dose resulting in local thinning of the wire [97] (Figure 4a). Given the low dose applied, sput-

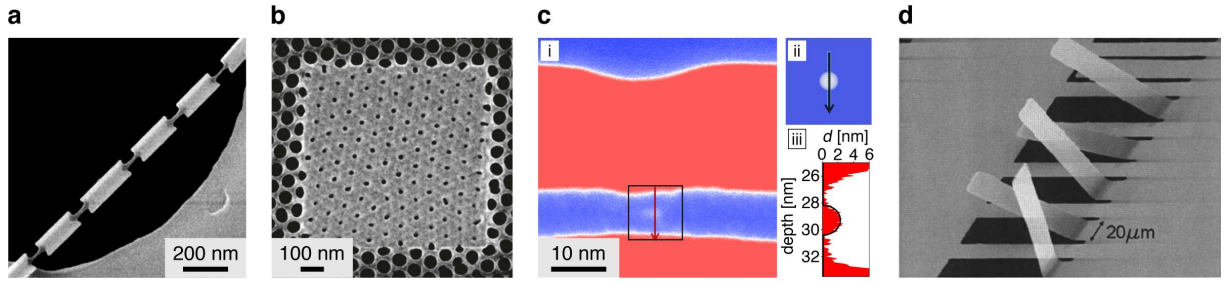

Figure 4: Examples of restructuring using localized helium and neon ion irradiation. **(a)** Localized thinning of a GaAs nanowire by site-selective helium ion irradiation at low dose: The proposed mechanism is mass transport by surface diffusion. Adapted from [97]. Copyright © 2017 WILEY-VCH Verlag GmbH & Co. KGaA, Weinheim. Used with permission from Aramesh, M., Ion-Beam Sculpting of Nanowires, physica status solidi (RRL)-Rapid Research Letters, John Wiley and Sons. **(b)** Related pore shrinking of nanoporous amorphous aluminum oxide by helium ion irradiation. Adapted from [96]. Copyright 2018 Aramesh et al., licensed under a Creative Commons Attribution 4.0 International License, http://creativecommons.org/licenses/by/4.0/. **(c)** Collisional mixing creating a silicon nanoparticle in a buried SiO_2 layer by localized neon ion irradiation: (i) energy-filtered TEM map, (ii) simulated projection thickness of the silicon nanoparticle, (iii) measured projection thickness (red) and simulated (black). Adapted from [98]. Copyright 2018 Xu et al., licensed under a Creative Commons Attribution 4.0 International License, http://creativecommons.org/licenses/by/4.0/. **(d)** Membrane folding by localized helium ion irradiation using different beam energies at the base of free-standing silicon nitride cantilevers. Reprinted with permission from [99]. Copyright 2007 American Vacuum Society. The content of (a) and (d) is not subject to CC BY 4.0.

tering alone could not account for the dimension reduction observed. In fact, thickening of the adjacent unexposed regions was noted, thus adding weight to the hypothesis that ion-induced mass transport by surface diffusion was primarily responsible for the thinning effect encountered. In a related study, helium ion irradiation of an amorphous nanoporous aluminum oxide sample caused pores to markedly shrink in size, also attributed to ion-induced mass transport [96] (Figure 4b).

Further related to mass transport, local helium ion irradiation has been used to induce the growth of semiconductor nanowires [97]. In this study by Aramesh, gold catalyst nanoparticles were distributed onto GaAs and InAs substrates and upon irradiating selected regions with helium ions, semiconductor nanowires grew from the gold nucleation sites. By increasing the beam energy and current, the growth of single-crystal nanowires was also shown. This is reminiscent of nanowire growth by the vapor–solid–liquid mechanism, except here the process was performed at room temperature and without the flow of a gaseous precursor. In the HIM case it was proposed that the nanowire growth process was catalyzed by a combination of irradiation-induced diffusion and local ionization.

Ion-induced collisional mixing

Another form of restructuring, this time using the neon ion beam, was demonstrated by Xu et al. using a collisional ion beam-induced mixing technique [98]. Here, neon line irradiation of an Si(25 nm)/SiO_2(6.5 nm)/Si(bulk) stack was used to induce collisional mixing of silicon atoms into the buried SiO_2 layer. Upon subsequent thermal annealing, 1D chains of silicon nanocrystals of 2.2 nm diameter self-assembled in the center of the SiO_2 layer. A TEM-based analysis of an isolated silicon nanocrystal from this work is shown in Figure 4c. The authors highlighted that the demonstration presents a promising new technique for the fabrication of single-electron transistor devices. This work is also closely related to the magnetic property tuning by Röder et al. described in Section 1, where localized neon ion irradiation was used to create ferromagnetic domains by introducing chemical disorder as a result of the ion-induced nuclear collision cascade [55].

In a further study, ion beam-induced mixing using both helium and neon ions in an Mo/Si multilayer beneath a 50 nm nickel layer was reported [100]. This was in fact a milling study for mask repair for extreme-ultraviolet (EUV) lithography applications (nickel being a candidate EUV mask absorber material, and Mo/Si being the EUV mirror). In this particular case, the observed mixing effect of atoms between the layers was undesired.

Membrane folding

Recently, several papers on FIB-enabled nanoscale kirigami have been published using the gallium FIB to mill line patterns in free-standing membranes (equivalent to traditional macroscale paper cuts) followed by localized gallium ion implantation to induce stress gradients across the membrane that lead to deformation by buckling [101]. Various intricate 3D structures have been created following this approach. Interestingly, right at the beginning of HIM-based research, membrane folding using localized helium ion irradiation was also demonstrated [99] (Figure 4d). In this work by Arora et al., free-standing cantilevers in silicon nitride membranes that had been prepared by photolithography were irradiated near the base with helium ions at different energies. Upwards versus downwards bending was observed, depending on the implantation depth profiles. It is conceivable that by using the HIM to both mill the

cuts and induce the buckling, the size of FIB-based nanoscale kirigami structures can be further reduced compared to what is currently possible using the gallium FIB technique. First steps in this direction have recently been taken [102].

4 Resist-based lithography

The patterning of mask structures for resist-based lithography also relies on irradiation effects. Here, the goal is to create a 2D or 3D structure through a templating approach, whereby a chemical change is induced in the resist layer causing it to become either insoluble (negative tone resist) or soluble (positive tone resist) in the subsequent development step. The drive to fabricate devices with ever reducing dimensions has meant that alternatives to diffraction-limited photon-based lithography have evolved, using charged particle beams [103]. Electron beam lithography (EBL) can achieve minimum features sizes approaching 5 nm, but key drawbacks of using electrons (beam energies typically up to 100 keV) are the low sensitivity of the resists to these particles and also proximity effects (i.e., unintentional exposure of resist surrounding the targeted pixel) due to backscattered electrons from the substrate and the secondary electrons they generate. In contrast, for ion beam lithography, the sensitivity gain can be orders of magnitude higher and the proximity effect is dramatically reduced, due to the much lower propensity of the ions to backscatter. However, before the introduction of the HIM, ion beam-based lithography mainly relied on the gallium FIB, for which major drawbacks were ion beam sputtering of the resist and the relatively large beam spot size (several nanometers) with its significant beam tails. Helium ion beam lithography (HIBL) using the HIM is therefore a lucrative alternative, combining the benefits of the tightly focused probe and low sputter yield of the light ions with the high resist sensitivity and greatly reduced proximity effect afforded by the ion beam-based method. Reviews of HIBL can be found in [104,105].

Sub-10 nm patterning

Resist-based HIBL was already investigated in the early years of the HIM and the fabrication of sub-10 nm structures was soon demonstrated [106,107]. Moreover, remarkably dense patterning of sub-10 nm features was achieved. For example, Sidorkin et al. demonstrated patterning of 6 nm dots with a half-pitch of 7 nm in HSQ resist [106] (Figure 5a). These results showcased both (1) the high patterning resolution of individual features, made possible by the subnanometer probe, minimal lateral scatter of ions in the resist, and associated narrow spatial distribution of secondary electrons, as well as (2) the greatly reduced proximity effect, due to negligible backscatter of the helium ions and thus negligible presence of second-generation secondary electrons, that together would otherwise cause feature blurring. The beam–sample interactions involved in the exposure of the resist are summarized schematically by Winston et al. in Figure 5b [107]. Modeling and experimental measurements of the 2D point-spread function for HIBL (i.e., the spatial distribution of energy deposition, which determines the proximity effect) can be found in the same reference. Cai et al. extended this work to a 3D visualization of the point-spread function by performing point exposures on HSQ through a thin layer of silicon nitride and then developing the resist to remove non-exposed regions, leaving drop-shaped cross-linked structures that define the 3D exposed volumes [108] (Figure 5c). The authors also directly exposed substrate-supported resists from the front side and fabricated hollow and suspended nanostructures (see Figure 5d) by appropriate choice of beam energy and dose during the patterning process. A further study has investigated the HIBL proximity effect for large-area exposures, as well as the potential to use HIBL to pattern tilted samples, making use of the large depth of field of the HIM [109]. A model-based method for HIBL proximity-effect correction has also been developed [110]. And a recent study has investigated the resist sensitivities and ion scattering profiles for 30 keV helium ions compared with a few heavier ions of similar energies [111].

A number of measurements have been made of the dose required to achieve HIBL full exposure of EBL-standard HSQ and PMMA resists, consistently finding that compared with electrons, one to two orders of magnitude lower doses of helium ions are required [114-116]. The high sensitivity to helium ions of the inorganic HafSOx resist (designed for EUV lithography) has been explored [117] and the unique potential to use HIBL to pre-screen EUV resists has been evaluated [118-120]. The advantages of HIBL have also been highlighted using a number of other novel resists, including a fullerene-based molecular resist [121], a tetracene molecular resist [122], and various organic–inorganic resists [123-129]. The enhanced sensitivity of resists to helium ions has been attributed to the higher secondary electron emission yield and the fact that the helium ions deposit their energy over much shorter distances in the resist, thus increasing the local energy density.

HIBL has also been combined with nanoimprint lithography, achieving lines down to a half-pitch of 4 nm [130]. In this technique, the helium ion beam is first used to pattern a resist to make a master template. The template is then pressed into a second resist, which is cured by UV exposure before the master template is retracted and re-used. Hereby, the high resolution and the low proximity effect of HIBL are combined with the high-throughput and low-cost benefits of nanoimprint. In another HIBL-related study, helium ion irradiation was used to induce varying degrees of cross-linking of aromatic self-assembled monolayers supported on a gold substrate, followed by

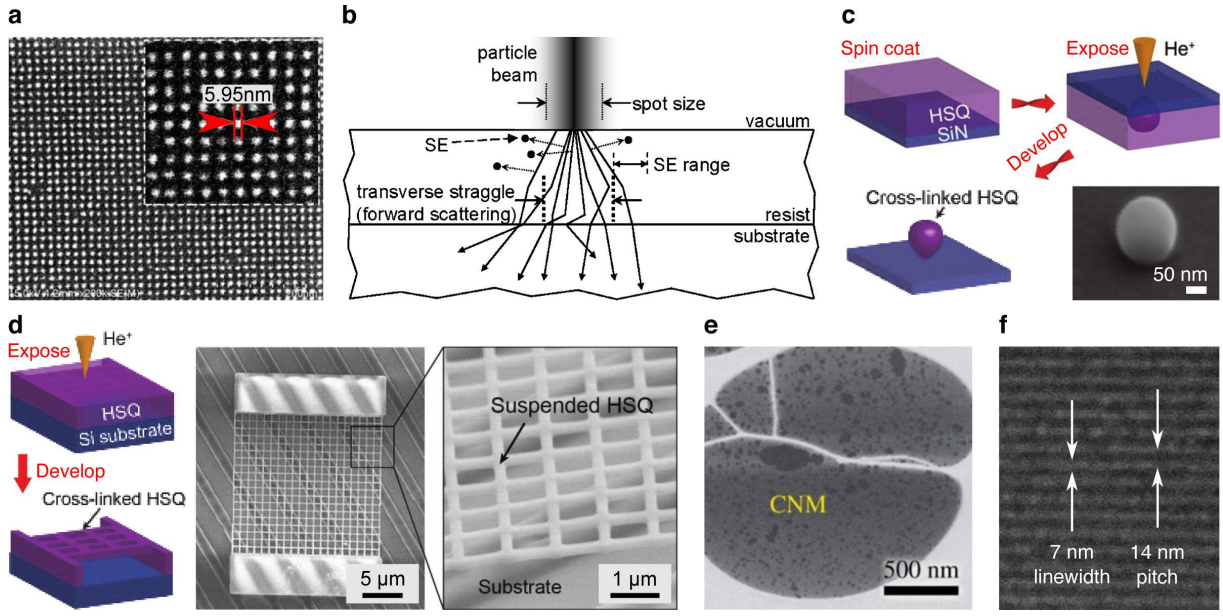

Figure 5: Resist-based lithography using helium and neon ions. **(a)** 6 nm dots on a half-pitch of 7 nm fabricated in HSQ by HIBL. Adapted with permission from [106]. Copyright 2009 American Vacuum Society. **(b)** Schematic summarizing the beam–sample interactions involved in resist exposure (ion backscatter from the resist–substrate interface is negligible). Reprinted with permission from [107]. Copyright 2009 American Vacuum Society. **(c)** Procedure for the 3D measurement of the point-spread function for HIBL using a through-membrane exposure technique: The SEM image shows a cross-linked volume of HSQ upon development of the resist following the point exposure. Adapted from [108]. Copyright © 2018 WILEY-VCH Verlag GmbH & Co. KGaA, Weinheim. Used with permission from Cai et al., 3D Volumetric Energy Deposition of Focused Helium Ion Beam Lithography: Visualization, Modeling, and Applications in Nanofabrication, Advanced Materials Interfaces, John Wiley and Sons. **(d)** Fabrication of a suspended mesh structure by direct exposure of the resist from the front side. Adapted from [108]. Copyright © 2018 WILEY-VCH Verlag GmbH & Co. KGaA, Weinheim. Used with permission from Cai et al., 3D Volumetric Energy Deposition of Focused Helium Ion Beam Lithography: Visualization, Modeling, and Applications in Nanofabrication, Advanced Materials Interfaces, John Wiley and Sons. **(e)** Carbon nanomembrane (CNM) fabricated by HIBL of aromatic self-assembled monolayers. Reprinted from [112]. Copyright 2014 Zhang et al., licensed under a Creative Commons Attribution 4.0 International License, http://creativecommons.org/licenses/by/4.0/. **(f)** 7 nm lines on a half-pitch of 7 nm fabricated in HSQ by NIBL. Adapted with permission from [113]. Copyright 2011 American Chemical Society. The content of (a), (b), (c), (d) and (f) is not subject to CC BY 4.0.

removal of the non-cross-linked regions by adhesion to a PMMA film [112]. This leaves the exposed (cross-linked) regions behind, presenting an alternative to the conventional methods for carbon nanomembrane production in which cross-linking is induced by electron or UV exposure. Figure 5e shows a carbon nanomembrane from the above reference, fabricated by the HIBL method.

Finally, the neon ion beam of the HIM has been employed for resist-based lithography as well [113]. In fact, this happened only a couple of years after the first HIM HIBL work. Winston et al. showed that using neon ion beam lithography (NIBL), 7 nm diameter lines with a half-pitch also of 7 nm could be fabricated in HSQ (Figure 5f), which is comparable with both high-end EBL and HIBL. For similar beam energies, an exposure efficiency in the NIBL case of approximately one thousand times greater than EBL, and ten times greater than HIBL, was determined.

5 Direct-write lithography/milling

Direct-write ion beam lithography is a resistless technique in which patterning is achieved by direct milling with the focused ion beam (FIB). Due to helium ion implantation effects, the optimum sample geometry for direct-write helium FIB lithography is a free-standing film of thickness less than the penetration depth of the ions in the material. For such thin samples, helium implantation is largely avoided, because most of the ions pass right through. Furthermore, since there is minimal lateral scatter over such short distances and no backscatter from an underlying substrate, the sample can be milled with minimal beam-broadening effects and thus the narrowest cuts can be obtained. However, various strategies have also been developed to enable helium FIB milling of bulk samples that mitigate ion implantation effects, either by increasing the milling rate and thus decreasing the total dose, for example, by gas-assisted milling, or by using substrates that allow out-diffusion of the implanted ions.

Another strategy involves the pre-milling of coarser features with the gallium FIB and/or neon FIB allowing the final precision cuts to be performed with the helium FIB at lower total dose, since by that stage less material has to be removed. For certain applications requiring precise efficient mills without gallium contamination, neon FIB for the final (or only) milling step is employed.

2D and 1D materials

In early helium FIB milling experiments, precise patterning of nanoribbons in a suspended graphene sheet was demonstrated, with nanoribbon widths down 5 nm achieved [131]. Graphene nanoribbons are of great interest, since they allow researchers to engineer a bandgap into the material due to quantum confinement effects. Furthermore, by creating the nanoribbons by direct milling as opposed to using a resist, resist residues and the resulting graphene ripples can be avoided. In work by Abbas et al., helium FIB milling of graphene on an SiO_2/Si substrate was able to produce graphene nanoribbon arrays that indeed demonstrated semiconducting behavior [132]. An array from this work comprising 5 nm wide high-aspect-ratio nanoribbons closely packed with a half-pitch of 5 nm is shown in Figure 6a. The authors also investigated the potential use of these graphene nanoribbon arrays for chemical sensing, demonstrating exceptional sensitivity to NO_2. In another study, helium FIB milling of graphene on SiO_2/Si was used in combination with EBL to fabricate graphene-based quantum dot devices [133].

Returning our attention to free-standing graphene, helium FIB milling of such samples has also been used to fabricate nanomechanical diaphragm structures [51,134]. An example is shown in Figure 6b, where a set of curved and straight lines (with sub-10 nm linewidths) were helium FIB-milled into the graphene to form a radial arrangement of flexure beams. For further reading, an experimental and theoretical study of helium (and gallium) ion bombardment of free-standing graphene predicting the sputter yields for atomically thin targets can be found in [145]. And a further study of the dynamics of milling free-standing graphene with the helium FIB can be found in [146].

Samples typically need to be imaged with the HIM before milling commences (unless working "blind" with the aid of alignment markers). Therefore, it is important to establish safe imaging doses that will avoid the generation of unwanted defects in the material. Early studies by Fox et al. used Raman spectroscopy to investigate helium ion-induced defect densities in graphene and suggested a safe imaging dose of 10^{13} ions/cm^2 for this material [147]. This equates to either an image recorded at low magnification, or a high magnification image acquired with a low signal-to-noise ratio. The authors also noted enhanced damage for supported graphene compared to free-standing, attributed to the interactions of backscattered ions and sputtered atoms from the substrate. However, damage is relative and the threshold doses to be applied depend on the particular experiment proposed. For example, elsewhere, irradiation of narrow stripe patterns into supported graphene using doses of 10^{13} ions/cm^2 was shown to create enough disorder to induce a transition from metallic to insulator behavior [148]. A possible strategy to mitigate the beam damage of graphene in helium FIB milling applications involves encapsulating the graphene between flakes of hBN [149]. Here, Nanda et al. showed that defects induced by the helium ions in the sandwiched graphene sheet can heal by self-annealing and nitrogen doping. The efficacy of the technique was further investigated by the same group in an experiment in which encapsulated graphene sheets on an SiO_2/Si substrate were milled with the helium FIB to create nanoribbons [150]. While defects and disorder in the nanoribbons beyond the patterned areas were still detected, the authors noted that the encapsulation method did prevent the surface contamination effects that readily manifest when milling unprotected graphene samples.

In further studies of helium (and neon) FIB milling of graphene on SiO_2 substrates by Iberi et al., isolated graphene pad structures were created using perimeter line mills to define the pad structures and thus separate them from the surrounding graphene [135,151]. Here it was found that the secondary electron contrast upon imaging the pad structures with the ion beam enabled the in situ determination of whether or not an electrically isolated graphene pad had been obtained. As soon as the pad is isolated, dark contrast from the pad is observed, indicative of charging of the now non-grounded graphene on the insulating substrate. The authors demonstrated how the technique can be used to create narrow conducting graphene strips on the insulating substrate, gauging the preservation of the conductive behavior of the strips based on the contrast mechanism described above (see also Figure 6c). Effects limiting the minimum feature sizes achievable, including the ion beam profile and ion backscatter from the substrate, were discussed.

While most helium FIB milling of 2D materials has focused on graphene, a few studies have also focused on other 2D materials. For example, Fox et al. fabricated nanoribbons with diameters down to 7 nm in free-standing few-layer MoS_2 [25]. High-resolution analysis of the nanoribbons by TEM revealed that sharp cuts with amorphous edges of thickness less than 1 nm could be achieved (Figure 6d). This damage layer correlated closely with the probe size of the helium ion beam used in the experiments (marked with the red circle in the figure) and is a good demonstration of what is possible when substrate backscatter effects are excluded through the use of a free-

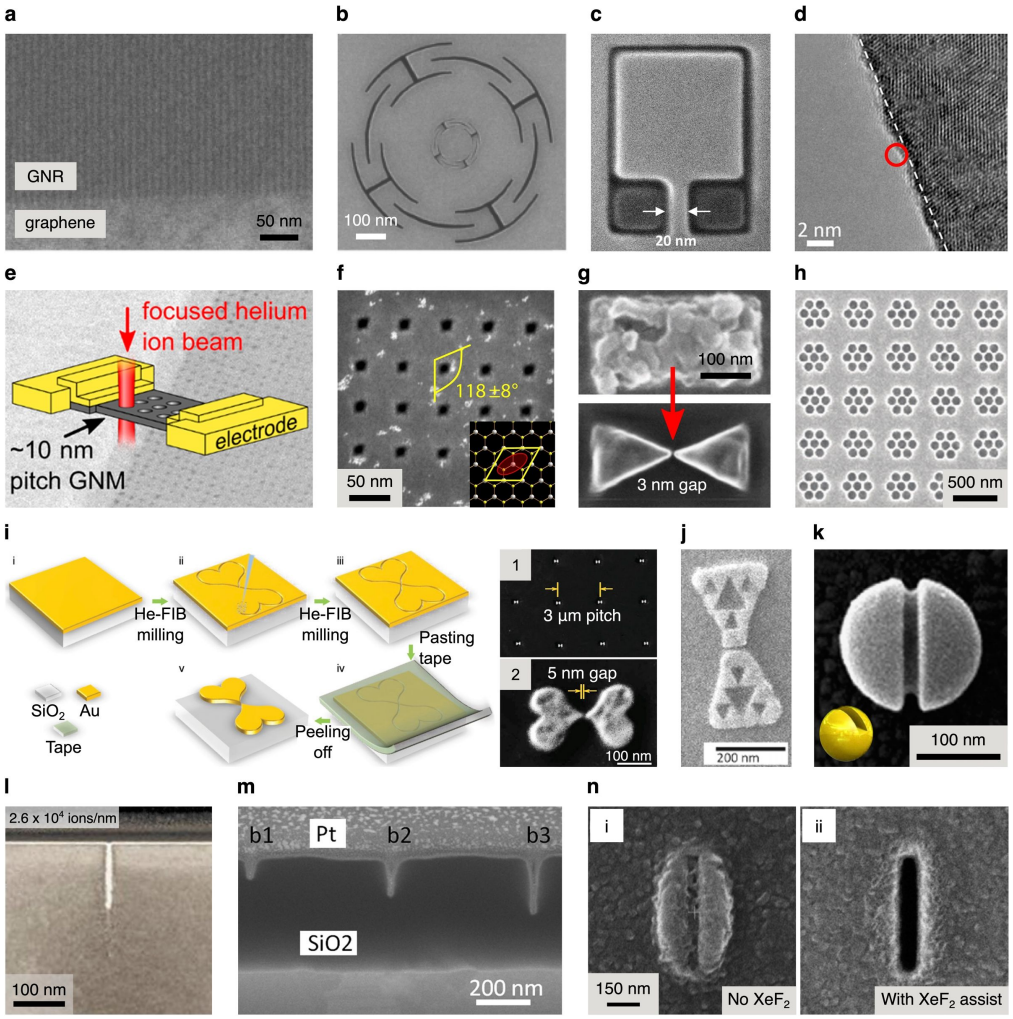

Figure 6: Examples of helium and neon FIB milling. **(a)** Graphene nanoribbons (GNR) fabricated by helium FIB milling of graphene on SiO_2/Si. Adapted with permission from [132]. Copyright 2014 American Chemical Society. **(b)** Nanomechanical diaphragm structure (nested) fabricated by helium FIB milling of a free-standing graphene flake. Adapted with permission from [134]. Copyright 2011 IEEE. **(c)** Graphene pad structures fabricated by helium FIB milling of graphene on SiO_2, imaged using the HIM: Dark contrast indicates pads that are electrically isolated; a 20 nm wide conductive strip connects the large pad at the top. Adapted from [135]. Copyright 2015 Iberi et al., licensed under a Creative Commons Attribution 4.0 International License, http://creativecommons.org/licenses/by/4.0/. **(d)** TEM image of a helium FIB-milled edge of a free-standing MoS_2 flake: The dashed line indicates the extent of amorphization; the red circle represents the size of the helium ion beam used. Adapted with permission from [25]. Copyright 2015 American Chemical Society. **(e)** Free-standing graphene nanomesh (GNM) fabricated by helium FIB milling to demonstrate quantum confinement. Adapted with permission from [136]. Copyright 2018 American Chemical Society. **(f)** Rhombus-shaped nanopores in free-standing MoS_2 fabricated using helium FIB milling implementing an elliptical beam shape. Adapted from [137], Deng et al., Nano-patterning of a monolayer molybdenum disulfide with sub-nanometer helium ion beam: considering its shape, size and damage, Nanotechnology, Vol. 31(34), 345302, first published 12 June 2020, Copyright © 2020 IOP Publishing Ltd. Reproduced with permission. All rights reserved. **(g)** Aluminum bow-tie plasmonic antenna on glass fabricated by helium FIB milling. Adapted with permission from [138]. Copyright 2018 American Chemical Society. **(h)** Plasmonic heptamer nanohole arrays in a gold film on SiO_2 fabricated by helium FIB milling. Adapted from [139]. Copyright 2019 Hahn et al., licensed under a Creative Commons Attribution 4.0 International License, https://creativecommons.org/licenses/by/4.0/. **(i)** Schematic of the sketch-and-peel method using helium FIB milling to outline the desired shapes in a gold film on SiO_2: (1) SEM image of an array of heart-shaped plasmonic dimer structures, (2) individual dimer. Adapted from [140]. Copyright © 2020 WILEY-VCH Verlag GmbH & Co. KGaA, Weinheim. Used with permission from Chen et al., Topology Optimization-Based Inverse Design of Plasmonic Nanodimer with Maximum Near-Field Enhancement, Advanced Functional Materials, John Wiley and Sons. **(j)** Gold bow-tie plasmonic antenna with internal fractal structure on glass fabricated by helium FIB milling of an EBL bow-tie prestructure. Adapted from [141], Seitl et al., Miniaturized fractal optical nanoantennas defined by focused helium ion beam milling, Nanotechnology, Vol. 31(7), 075301, first published 14 November 2019, Copyright © 2019 IOP Publishing Ltd. Reproduced with permission. All rights reserved. **(k)** 3D plasmonic split-ball resonator fabricated by helium FIB milling of a silver nanosphere. Adapted by permission from Springer Nature, [142], Nature Communications, Split-ball resonator as a three-dimensional analogue of planar split-rings, Kuznetsov et al. Copyright 2014, Nature Publishing Group, a division of Macmillan Publishers Limited. All Rights Reserved. **(l)** Cross-sectional TEM analysis of a helium FIB-milled via in bulk silicon. Adapted with permission from [75]. Copyright 2014 American Vacuum Society. **(m)** Cross-sectional TEM analysis of neon FIB vias milled into SiO_2. Adapted with permission from [143]. Copyright 2011 American Vacuum Society. **(n)** Helium FIB-milled slots in a titanium film (top views): (i) without, and (ii) with XeF_2 gas assist. Adapted with permission from [144]. Copyright 2016 American Chemical Society. The content of (a), (b), (d), (e), (f), (g), (i), (j), (k), (l), (m) and (n) is not subject to CC BY 4.0.

standing geometry. Helium FIB milling of nanoribbons into free-standing hBN has also been demonstrated [152], as well as the milling of high-quality grating structures into supported hBN flakes [153]. In the latter case for the supported material, neon FIB milling was shown to be advantageous due to the higher sputter yield while retaining a high-precision milling capability.

Helium FIB milling has also been applied to materials that could be classified as being 1D. For example, helium FIB milling has been used to create 3 nm nanogaps in metallic single-walled carbon nanotubes [154]. The nanotubes were supported on an SiO_2/Si substrate and the nanogaps that were milled divided individual carbon nanotubes to form two closely spaced electrodes, which were used to probe individual organic molecules. In addition, linear arrays of holes have been helium FIB-milled along the lengths of free-standing amorphous SiCN nanobeams [155]. This work demonstrated the ability to tune the resonant behavior of nanomechanical resonators using a simple FIB-based post-fabrication method.

Nanopores

The fabrication of nanopores in thin membranes (free-standing, typically silicon nitride) is a further area that has benefited from the high milling precision of the helium FIB. Solid-state nanopores are central to pore-based biosensing applications, including DNA sequencing, in which the flow of ion current is monitored as the biomolecule passes through the pore. The size of the pore must be commensurate with the size of the biomolecule to be detected; double-stranded DNA has a width of ca. 2 nm. To be commercially viable, high-throughput methods for the fabrication of nanopores with precisely tuned diameters is key, and neither the gallium FIB nor electron beam-based "sculpting" techniques meet this need, since they are multi-step processes involving a final pore-closing routine to obtain the final diameters desired. In contrast, the helium FIB is able to routinely fabricate arrays of precise nanopores with diameters down to 4 nm in a one-step process [156], which has garnered significant interest in the field. Hall et al. have also reported the fabrication of individual nanopores in ca. 40 nm thick silicon nitride membranes with diameters down to 2.5 nm [157]. The pores are milled in spot mode (constant dwell on a single point) and the size of the pore is controlled by the irradiation dose. Through the implementation of automated stage movement and milling routines, patterning over large areas with high accuracy can be achieved [158]. A review of solid-state nanopore fabrication by helium FIB milling for the detection and analysis of biomolecules can be found in [159]. In closely related work, the translocation of virus particles (rod-shaped tobacco mosaic virus) through solid-state helium FIB nanopores has also been reported [160].

In order to monitor the thinning of the silicon nitride membrane in situ, and allow for sensitive endpoint detection, the transmitted ion current can be measured [161]. Tracking of the transmitted ion current has also been used for controlled thinning of larger areas of the silicon nitride membrane, followed by pore drilling with the helium FIB in spot mode in the normal fashion [162], or pore fabrication via electric field-driven controlled breakdown in the thinned regions [163]. The advantage of pre-thinning is the enhanced signal-to-noise ratio that is observed for translocation through nanopores in thinner membranes. Following the selective pre-thinning method described, this enhanced performance can be achieved while at the same time retaining the robustness of the device afforded by the overall thicker membrane. Measurement of the transmitted ion current during pore milling has also been used to track the growth behavior of larger pores, providing a convenient means to measure the point-spread function of the helium ion beam [164,165].

An important factor to take into account when performing any helium FIB nanofabrication (or even imaging, for that matter), is the potential detrimental effect of hydrocarbon contamination. For example, in work by Emmrich et al. using silicon nitride membranes exposed to differing degrees of plasma treatment prior to milling, it was found that the degree of hydrocarbon contamination remaining on the surface affected the subsequent milling of circle patterns when using different concentric scan strategies [164]. When milling a concentric circular pattern starting from the outside and moving in, hydrocarbon contamination was found to follow the path of the beam, limiting the size of the final milled pattern, whereas when the milling started from the center, hydrocarbons were prevented from diffusing inwards enabling the mill process to proceed largely unaffected. For the fully cleaned membranes, the scan strategy had no effect on the final pore size, since the hydrocarbon effect was no longer at play.

Apart from silicon nitride, helium FIB milling has also been used to create nanopores in other free-standing membranes, with minimum pore diameter records as follows: 1.3 nm diameter in a 1 nm thick carbon nanomembrane [164], 2.6 nm diameter in single-layer graphene [145], 4 nm diameter in few-layer and monolayer hBN [152,166], and 1.3 nm diameter in monolayer MoS_2 [137]. Ion conductance and DNA translocation through helium FIB-milled graphene nanopores has been reported [167], as has the fabrication of suspended graphene nanomesh structures (3–4 nm pores on a pitch of ≤10 nm, Figure 6e) that demonstrated bandgap opening by quantum confinement [136]. In follow-up work to the latter, the size of the bandgap was tuned by varying the porosity of the nanomesh through adjusting the pitch of the periodic nanopore array [168].

In recent work on free-standing MoS_2, another interesting phenomenon was observed, namely that by milling with a slightly stigmated beam (again, in spot mode), rhombus-shaped nanopores could be obtained with a geometry following that of the hexagonal MoS_2 lattice [137] (Figure 6f). By helium FIB milling sub-10 nm pores into hBN and growing graphene into the voids, stable graphene quantum dot arrays have also been produced [166]. And when milling larger pores of 250 nm diameter into a 100 nm gold film on a glass substrate, the formation of "volcano-shaped" nanopores has been observed [169]. The raised perimeters around the pores may result from swelling of the gold, since helium ions have a relatively short stopping distance in this material, with possible contributions from the redeposition of sputtered atoms, or irradiation-induced mass transport.

The technically most challenging nanopores to fabricate are atomically precise ones consisting of just a few ejected atoms from a 2D material. Exploratory studies using both helium and neon ion irradiation in the HIM have been conducted in this area. For example, in work by Yoon et al., 500 nm square fields of free-standing graphene were irradiated with helium/neon ions by rastering the beam to achieve a uniform areal dose and subsequently the samples were annealed to stabilize the defects before inspection by high-resolution STEM [170]. Coupled with analysis based on atomistic simulations it was found that in the case of helium ion irradiation, vacancy defects involving local bond rearrangements were favored, whereas for neon ion irradiation, monovacancy defects were preferred. It was thus concluded that in order to transfer sufficient energy to efficiently displace carbon atoms from the lattice, irradiation with the higher mass ion (neon) is required. This work is directly related to the defect engineering studies described in Section 1, where helium ion irradiation of 2D materials was also used to create vacancies that were similarly investigated by high-resolution STEM [26,29,30]. Further work in this area has used Raman spectroscopy in combination with a model for defect activation to investigate the size and distribution of vacancy defects formed by broad-area illumination, using helium/neon ions and free-standing/supported monolayer graphene/MoS_2 [171]. Very recently, the fabrication of atomic-scale nanopores in bilayer graphene for selective gas permeation was reported using a combined approach of helium ion bombardment to nucleate the defects followed by treatment in hydrogen plasma to expand the pores to the desired size [172].

A further interesting application involving helium FIB nanopores is the milling of holes into a thin layer of SiO_2 on a silicon substrate to create dot arrays of exposed silicon that act as nucleation sites for semiconductor nanowire growth by molecular beam epitaxy [173].

Plasmonic structures

The precise milling capability of the helium FIB has also been used for the fabrication of various plasmonic structures, for which smaller gap sizes are critical in order to maximize the local field enhancement. For example, plasmonic dipole antenna structures have been fabricated whereby 20 nm thick gold islands (fabricated by EBL) on borosilicate glass were divided using a helium FIB cut, achieving gap sizes down to 3.5 nm [174]. Similarly, precise helium FIB thinning of a narrow band across the center of individual gold islands, followed by completely milling away the thinned material from the sides to leave a constriction in the middle, has been used to fabricate thin and narrow conducting bridges (bridge heights of a few nanometers and widths down to 5 nm) that can be used to modulate the plasmonic behavior of the antenna [175]. In a further study, helium FIB milling was used to create a ca. 5 nm gap in the elbow of L-shaped gold nanoantennae [176].

The fabrication of high-quality bow-tie antennae using the helium FIB has also been demonstrated. For example, in work by Kollmann et al., 30 nm gold on borosilicate was first milled using the gallium FIB to create a fused antenna structure of opposing triangular shapes, after which the helium FIB was used to create a sharp cut in the center giving a gap size of 6 nm [177]. The bow-tie structures fabricated in this manner had vastly improved non-linear performance due to the small gap with sharp sidewalls achieved by the helium FIB. The use of the helium FIB instead of the gallium FIB to fabricate the nanogap also means that implanted metallic residue at the milled interface is avoided, which would otherwise change the dielectric function of the material and degrade the plasmonic performance of the antenna. A similar fabrication of bow-tie structures in aluminum thin films has been demonstrated by Simeone et al., in this case achieving gap sizes down to 3 nm using the helium FIB to mill the entire structure into aluminum pads prepared by EBL [138] (Figure 6g). Here, a favorable smoothing of the surface of the evaporated aluminum during the helium FIB fabrication process was also observed, the underlying mechanism of which warrants further study.

Moving to other types of plasmonic structures, helium FIB milling of high-quality coaxial plasmonic resonators has been demonstrated [178]. In this work, Melli et al. used the helium FIB to mill 100 nm thick gold on fused silica to fabricate a plasmonic ring structure comprising a circular gap of diameter 200 nm and width 8 nm, which demonstrated an optical performance that matched theoretical predictions. The authors credited the high performance to the small gap size, vertical side walls, minimal edge rounding, and flat central mesa enabled by the helium FIB approach. In comparison, gallium FIB milling produced gap widths larger than 20 nm, V-shaped side walls,

rounded edges and a perturbed top surface. By optimizing the gold film itself to enable more uniform milling rates, for example, by increasing the grain sizes in polycrystalline films by annealing [179,180], or by using single-crystal gold [181], further improvements in both gap size and reproducibility can be achieved. Additional plasmonic structures that have been fabricated by helium FIB milling include trimeric assemblies of resonant nanoapertures [182], arrays of nanostructured radial resonant apertures [183], and plasmonic heptamer nanohole arrays [139] (Figure 6h), all in gold films, as well as multiresonant plasmonic nanoslit cavities [184] and plasmonic tetramer nanoantennae [51] in crystalline gold platelets. In the latter study, an advanced beam patterning toolbox with beam path optimization was recently introduced [51].

A novel strategy for the fabrication of large assemblies of plasmonic structures is the so-called "sketch and peel" method [185,186]. First developed by Chen et al. for EBL, it was then extended to FIB milling, thus circumventing the need for a resist and enabling more flexibility in terms of the substrate. In the FIB method, ion milling is used to outline, or "sketch" shapes into a supported gold film, after which the unwanted portions of the film are removed by selective peeling. The explanation for the selective peel is proposed to be redeposition of sputtered material onto the sidewalls of the cuts, which protects the outlined shapes from being removed with the rest of the film during the peeling process. The significant advantage of this technique is that large assemblies can be fabricated rapidly, since only the outlines need to be milled, rather that having to mill away all of the gold film around each desired structure. For helium FIB milling, the high speed of the sketch-and-peel approach is particularly compelling, due to the inherently low sputter yield of the light ions. Furthermore, for all the areas that are not patterned by the beam, beam damage to the underlying substrate is avoided. Compared with the gallium FIB, sketch-and-peel using the helium FIB enables finer cuts and, in the first demonstrations, the fabrication of arrays of plasmonic dimer structures with a gap size of 15 nm was achieved [186]. Subsequent iterations of the method routinely report gap sizes of 5 nm [180,181], including the fabrication of heart-shaped nanodimers defined using a shared boundary in the center to create the nanogap as opposed to milling the dimer outline and gap separately [140] (Figure 6i). To further increase the efficiency of the process, a combination of gallium and helium FIB milling can be applied, the former for the coarser outlines and the latter for the fine cuts forming the nanogaps [180,187]. The advantage of using single-crystal gold to ensure uniform sputter rates, and thus ultimately enable milling of narrower cuts with enhanced reproducibility, has also been demonstrated for the sketch-and-peel method [181]. In the latter, Laible et al. also investigated the fabrication of gold pre-stuctures by EBL and argon ion milling (rectangles or connected bow-tie shapes) as another means to reduce the milling time for large assemblies, whereby the final nanostructures themselves were defined using optimized helium FIB milling strategies based on multidirectional scans. In follow-up work by the same group, bow-tie nanoantennae with fractal internal geometries were fabricated, using bow-tie pre-structures prepared by EBL that were then milled with the helium FIB to accurately define the nanogaps and the internal fractal patterns [141] (Figure 6j).

3D plasmonic structures with tunable magnetic response at optical frequencies have also been fabricated by helium FIB milling [142]. In this work, spherical nanoparticles of gold/silver were fashioned with a precise nanoscale cut using the helium FIB, creating "split-ball" resonators with nanometer control over the width and depth of the cut (Figure 6k). In another 3D example, the helium FIB has been used to mill nanoscale apertures into the center of hollow pyramidal [188] and hemispherical [189] gold microstructures for sensing applications via local electric field enhancement. 3D plasmonic gold tips that were pre-milled with the gallium FIB and then finely shaped with the helium FIB have also been produced [190].

Bulk samples: semiconductor industry applications and further next-generation devices

As mentioned previously, the ideal sample for helium FIB milling is a free-standing material that is thinner than the stopping distance of the helium ions, such that most pass through and thus cannot accumulate. However, suspended membranes are not always the desired geometry for devices, and indeed a number of the examples already given were for thin materials supported on bulk substrates. For FIB applications in the semiconductor industry (circuit edit, failure analysis, mask repair, and device prototyping), the samples of prime concern are bulk materials, and thus bulk effects must be considered and mitigated. In fact, for semiconductor applications and for the fabrication of next-generation devices on bulk substrates, the neon FIB is of particular interest, due to the higher sputter yield and reduced penetration depth of the heavier ions.

Certain substrates are less susceptible to the swelling that can occur under helium ion irradiation, since they allow the helium to diffuse out. These favorable substrates are non-crystalline and a key one is amorphous SiO_2, for example, in the form of several hundred nanometers of amorphous SiO_2 on a silicon wafer, or as a bulk glass substrate. If such a substrate can be selected, the full advantages of helium FIB milling to create narrow cuts with high aspect ratio can be realized. For example, in early work, 10 nm wide vias with an aspect ratio of up to 1:12.5 in a supported gold layer were reported [191]. Using

gallium FIB milling, such high aspect ratios are unobtainable, due to the significant taper angle of the sidewalls that give gallium FIB vias their characteristic V-shape, with aspect ratios rarely above 1:5. The strongly tapered side walls of gallium FIB vias largely result from redeposition, and while there is also redeposition in helium FIB vias, the sputter yield under glancing incidence for helium ions is much more strongly peaked compared to gallium ions, thus significantly reducing the taper effect [192]. Further demonstrating the small taper angle for helium FIB milling, through-holes in a (free-standing) 100 nm thick gold film with diameters of 5 nm and, thus, aspect ratios of 1:20 have also been reported [193].

Significant differences between the beam–sample interaction profiles for thin-film compared to bulk sample geometries have been revealed by Tan et al. through cross-sectional TEM analysis of helium FIB line mills of varying dose in suspended silicon membranes compared to bulk single-crystal silicon [75]. For the bulk sample, a via starts to form, but at high dose closes again as a result of damage accumulation and volume expansion due to the implanted helium. Eventually, significant amorphization occurs within a characteristic teardrop-shaped volume. In contrast, in the membrane case, forward-sputtering from the back of the membrane dominates and the overall sputter yield is much higher, with minimal helium implantation, thus enabling the milling of narrow high-aspect-ratio vias. As the milling progresses and the membrane thins, the ratio of back- to forward sputtering changes, eventually giving rise to an upturned V-shaped profile.

However, as mentioned, it is the bulk sample that is of concern in the semiconductor industry. Although sharp vias can be obtained in bulk silicon using the helium FIB when selecting the appropriate dose, as shown in Figure 6l [75], helium ions are still implanted at the base. For applications such as circuit edit and mask repair, the deep penetration depth of helium ions and associated damage effects (amorphization, nanobubble formation, and swelling) cannot be tolerated. Moreover, a higher sputter efficiency is needed so that larger volumes of material can be removed. Here, the neon FIB is a favorable alternative, since it has a shallower implant depth than helium and a higher sputter yield, as first shown by Tan, Livengood, and co-authors, and later by others [15,17,100,143,194]. In fact, the sputter yield for neon increases for decreasing beam energy (which is the reverse of what happens for gallium). Thus, it is actually more favorable to operate at lower neon beam energies (e.g., 10 keV), which also reduces the penetration depth and amount of subsurface damage [15,195]. This is important, because as with helium ion irradiation, neon nanobubbles can still form and the associated swelling can still occur [15,17,100,195-198].

By using the neon FIB in place of gallium FIB, the detrimental contamination of semiconductor materials with gallium is avoided. Further, as recently demonstrated for 10 keV neon FIB milling of the group-III–V semiconductor GaAs, trenches with a smooth surface at the base can be produced (i.e., no porosity due to neon nanobubbles), which also do not exhibit the gallium-rich droplets that occur for gallium FIB milling as a result of preferential sputtering of the group-V element [195]. It should be noted, however, that the milling behavior of the group-III–V semiconductors varies, with different morphological changes observed depending on the particular material in question. For example, in experiments on GaSb milled using neon ions of the same energy and at the same dose as in the previous study, surface porosity was induced, whereas at slightly lower doses, the formation of gallium-rich nanodots on the GaSb surface occurred [198]. Thus, in addition to creating smooth surfaces, neon FIB milling can also be used for selective surface nanostructuring.

Neon FIB vias with relatively high aspect ratios (up to ca. 8:1), compared with their gallium FIB counterparts, have been demonstrated, although they are similarly limited by a V-shaped profile [17,143,199] (Figure 6m). 3D Monte Carlo simulations of the evolution of the neon FIB via profiles have been performed and find close agreement with the profiles determined experimentally, explaining the sidewall tapering as resulting from an increase in redeposition rate and a decrease in effective sputter rate with depth, correlating with the decreasing open angle of the via [196,200,201]. Recent refinements to the Monte Carlo code by Mahady et al. have revealed that in order to accurately predict the width of the neon FIB vias, an effective beam profile needs to be used as the input, rather than the measured one. This is because artifacts such as platform vibrations seem to be broadening the mills, resulting in simulated via widths that are narrower than the real ones [202].

The favorable sputter yield of neon and the fact that the implanted ions are not metallic has also been put to use for the fabrication of superconducting nanowires on bulk substrates, where selected regions of Nb and NbN films were milled away to form constrictions of the desired dimensions [203-205]. Furthermore, neon FIB milling has been used to investigate the effect of miniaturization on the switching currents of magnetic tunnel junction devices by successively reducing the device size using neon FIB cuts into the sub-10 nm range [206].

Minimizing subsurface damage

Apart from working with thin free-standing samples or selecting substrates that are less susceptible to swelling, one approach to reduce substrate swelling is to heat the sample during the milling. This encourages out-diffusion of the implanted helium

before it can accumulate and also promotes annealing of ion-induced defects. Techniques using an in situ MEMS-based heater [207] and localized in situ pulsed laser-based heating [208] have been developed. In the latter, Stanford et al. showed that around 90% of the implanted helium can be driven out using the laser-assist process, and that peripheral damage when milling graphene on an SiO_2 substrate can also be mitigated. Pulsed laser assist during helium FIB milling has also been shown to be an effective strategy to mitigate the ion beam-induced deposition of carbon from residual hydrocarbon species that can otherwise compete with the milling process [102].

Another approach to minimize subsurface damage is to increase the milling rate, so that the total ion dose (and hence total amount of implanted helium) required to mill a given feature is significantly reduced. To achieve this, gas-assisted etching can be employed. This involves delivering a gaseous precursor to the region of the sample being milled, just as one does in FIB-induced deposition (see Section 6), except here, a gas is chosen that will generate radicals upon dissociation of its molecules that then form volatile reaction products with atoms from the substrate material, thus enhancing the rate of their removal. Using this method, XeF_2-assisted helium FIB milling of a 200 nm thick titanium film on a 30 nm silicon nitride membrane was demonstrated [144]. The authors showed that by increasing the milling rate, the amount of subsurface damage could be minimized to such an extent that swelling was essentially eliminated (Figure 6n). Gas-assisted helium FIB milling using XeF_2 has also been demonstrated for the fabrication of WSe_2 nanoribbons on SiO_2 substrates, with a fivefold enhancement of the mill rate reported [209]. Yet, it was noted that defects were still generated up to 120 nm from the milled edges due to backscattered ions and recoiled atoms from the substrate. As for the neon FIB, Monte Carlo simulations together with experiments have been used to investigate XeF_2-assisted neon FIB milling of vias in SiO_2 [210]. Prior to this work, experimental studies of the assist process for neon FIB milling of larger areas of an SiO_2 target had also been performed [199], and more recently, XeF_2-assisted helium and neon FIB milling of TiN thin films [211] and resist patterns [194] has been investigated.

Laser-assisted milling can also be combined with gas-assisted milling to increase milling rates even further. This is because thermal effects increase the diffusion rates of the XeF_2 precursor molecules and of the reaction by-products. Using this combined approach, Stanford et al. showed that approximately a ninefold enhancement in helium FIB milling rates compared to non-assisted milling can be achieved [144].

Finally, using a method without any beam assist, it has been shown that the sample can be tilted relative to the beam normal in order to favorably shift and foreshorten the volume of the beam–sample interaction [212]. In this work by Hang et al., 30 keV helium ions were used to mill lines into graphene supported on a substrate comprising SiO_2(300 nm)/Si. Under normal incidence, significant substrate swelling occurred, which can be attributed to a significant proportion of the helium ions accumulating in the silicon. In contrast, by tilting the specimen from the horizontal position by 43°, swelling was avoided, since then most of the ions accumulated in the amorphous SiO_2 layer, allowing the helium to diffuse away. However, through analysis by Raman spectroscopy, defects in the graphene lattice extending up to 300 nm away from the milled lines were detected, indicating damage caused by backscatter helium ions and possibly also recoiled substrate atoms.

Specimens for materials analysis

Another important application of FIB milling in general is the fabrication of electron-transparent specimens for materials analysis by TEM. The gallium FIB has been the workhorse instrument in this area. Yet, there are certain samples that are susceptible to artifacts from gallium ions. Hence, alternative ion species for FIB-based preparation are of interest. For example, aluminum and its alloys tend to become contaminated and embrittled as a result of the segregation of gallium along grain boundaries and interfaces. Also, semiconductor materials have been shown to develop gallium precipitates and droplets [213,214].

The use of the helium FIB [215] and neon FIB [197] to thin TEM lamellae has been investigated. In these studies, the lamellae were first pre-thinned using the gallium FIB and then the final thinning step was performed using helium/neon. Under glancing incidence, helium FIB milling was shown to reduce surface roughness, remove surface contamination, and produce thinner specimens with crystallinity preserved [215]. However, helium FIB milling is inherently slow due to the low sputter yield of the light ion. Therefore the neon FIB, with a higher sputter yield, while retaining the precision characteristics of the GFIS beam, is a lucrative alternative. By switching from gallium to neon milling at a judicious time point (i.e., while the central region of the lamella is still gallium-free), it has been shown that final TEM specimens that do not contain gallium can be obtained [197]. Another advantage of the neon FIB method is that during the final milling stage, the thickness of the lamella can be monitored accurately by end-on imaging using the neon ion beam. Compared with imaging with low-energy gallium ions (low-energy gallium is conventionally used for the final mill step), the thickness of the lamella can be visualized very clearly using the neon ion beam. However, although the neon FIB allows for more precise milling, it should be noted that beam-induced damage such as dislocations are still compa-

rable to those resulting from the conventional gallium FIB method [197]. The application of neon FIB milling for the fabrication of tips for atom probe tomography, similarly limited by gallium-only milling for certain materials, is also underway [216].

FIB milling is also widely used to fabricate specimens for micro- and nanomechanical tests. Again, gallium contamination can be a concern, this time due to potential changes in the mechanical properties of the material. Thus here too, FIB species other than gallium are being explored. In this regard, helium FIB milling has been tested to create sharp notches for small-scale fracture toughness measurements [217]. Although sharp notches could be produced, a significant limitation is helium implantation into the material beneath the notch forming nanobubbles, which also affects the nanomechanical behavior of the material. Similarly, when using the helium FIB to prepare silicon nanopillars for in situ TEM nanomechanical compression testing, nanobubbles formed inside the pillars resulting in a decrease in the yield stress of the material [89]. In future work, gas-assisted etching might be used to increase sputter rates and thus decrease the total amount of ion implantation, as described earlier. Alternatively, sample geometries that in the milling direction are thinner than the helium ion stopping distance could be considered. Neon FIB milling is also a possibility. Indeed, in a study in which the neon ion beam was used to irradiate silicon nanopillars, it was found that by irradiating at elevated temperature, the material remained crystalline and controlled thinning by sputtering could be achieved [218]. In contrast, at room temperature, amorphization occurred and the nanopillars evolved into conical shapes due to viscous flow.

6 Gas-assisted deposition

FIB-induced deposition (FIBID) is a further area of direct-write nanofabrication benefiting from the high-resolution characteristics of the HIM, enabling the fabrication of structures with dimensions smaller than are possible using conventional gallium-based FIBID. Moreover, the deposition rates of helium FIBID have been found to approach those of focused electron-beam-induced deposition (FEBID), thus realizing a form of FIBID that delivers both high resolution and high rate. Similarly to resist-based HIBL, proximity effects are also minimized in helium FIBID. For a detailed review of early helium FIBID work, the reader is referred to [219].

Deposition rates, deposit dimensions, compositions and resistivities

In FIBID, a chemical precursor is introduced into the vacuum chamber, typically in the form of a gas injected via a needle placed close to the specimen. The precursor molecules are then dissociated into volatile and non-volatile fragments as a result of interactions with the primary ion beam, secondary electrons, and backscattered ions, with potential contributions also from excited atoms and thermal effects [220]. The non-volatile fragments are deposited at the locations scanned by the beam and the volatile fragments are pumped away.

The first studies of helium FIBID were reported by Sanford et al. and used a standard FIBID/FEBID platinum-based organometallic gaseous precursor to grow broad deposits in the micrometer size range [221]. Deposition rates of 0.2–0.6 μm^3/nC were reported, comparable to those achieved by gallium FIBID (i.e., relatively fast). In terms of purity, percentage compositions of platinum of up to 20% were measured, comparable to those typically obtained by FEBID (i.e., fairly low). Yet later, Drezner et al. experimented with ca. 200 nm wide pillar deposits and demonstrated that by varying the beam current, higher purity deposits containing up to 40% platinum could be achieved, thus approaching the purity levels of gallium FIBID [222], without co-implanting gallium. In this particular work, it was found that decreasing the beam current decreased the deposition rate, resulting in shorter pillars with a higher platinum content. This was attributed to a higher availability of precursor when the growth rate was slower. A similar trend for the growth rate as a function of ion current was reported by others [223]. However, in Sanford's earlier study [221], and in later work investigating the growth of much narrower pillars (described further below), the opposite was found, with decreasing current resulting in faster vertical growth rates [224]. This highlights the complex interplay of processes involved in FIBID and the important difference between operating in a reaction-limited versus a mass-limited regime. Interestingly, Drezner and co-authors also found that the platinum content varied along the length of their pillars, and was greatest near the top [222]. Amorphization and swelling of the substrate immediately beneath the deposit were also noted.

Soon after the first demonstration of helium FIBID for relatively large deposits, Chen et al. demonstrated the growth of platinum-based nanopillars by continuous illumination in spot mode, achieving diameters down to 36 nm, that is, approximately four times narrower than nanopillars grown by gallium FIBID and comparable to the minimum widths achieved by FEBID [224]. In early work, very tall nanopillars with aspect ratios up to 1:130 were also demonstrated [225], and more recently, aspect ratios of 1:200 have been reported [226]. An analytical model [227] and Monte Carlo simulations [224,228] were developed to investigate the deposition mechanism, concluding that pillar growth in the vertical direction (height) is due to the precursor dissociation reactions induced by the incident ions and the secondary electrons they generate, whereas lateral pillar growth (width), is predominantly caused by the interactions of scat-

tered ions and their associated secondary electrons as they exit the sides of the pillar. Since the density of primary ions and their secondary electrons at the apex is much higher than that of the scattered ions and associated secondaries at the sides, the growth rate in the vertical direction is much faster and pillars with high aspect ratio can be obtained. Furthermore, since there is limited backscatter of ions from the substrate, proximity effects are minimized. For example, the halos that form around nanopillars grown by FEBID are not observed in the helium FIBID case. For constant ion dose it was found that decreasing the ion current resulted in the tallest and narrowest pillars, indicating a growth rate regime limited by the availability of precursor at the apex [224,227,228]. Subsequent work by Alkemade et al. investigated pulsed deposition, achieved by scanning an array of points in a cyclic fashion to grow a set of nanopillars in parallel (rather than growing individual nanopillars one by one, by continuous illumination of the same spot) [229]. It was found that a pulsed beam approach can alleviate depletion of the precursor at the apex, since the precursor supply is constantly refreshed. Following this approach, the authors demonstrated enhanced vertical growth rates for pulsed deposition, with the fastest rates achieved for the shortest dwell times.

Since the width of the nanopillar is determined by lateral scattering, as described above, the nanopillar widths are greater than the beam diameter (pillar widths are typically 30–40 nm). And since the beam spreads in a conical fashion to a depth of around 300 nm, the tips of helium FIBID nanopillars are markedly cone-shaped [224,227,230]. This feature can be used to create smaller-diameter (ca. 10 nm) dot deposits using short dwell times, so that only the first part of the conical shape is formed [231]. Alternatively, the beam can be scanned horizontally across the surface to deposit lines. For example, pairs of lines with line widths down to 13 nm on a half-pitch down to 8 nm have been demonstrated, as shown in Figure 7a [232]. Individual lines with diameters down 10 nm have also been achieved [233,234], including in the free-form patterning of a miniaturized reproduction of a 13th century painting [235] (Figure 7b). With respect to the nanopillars, an effective method to reduce their diameter is to gradually move the beam laterally during the deposition, rather than hovering over the same point in spot mode. In this way, a nanopillar is grown horizontally rather than vertically, and since the sample volume beneath the beam interaction point is thus significantly reduced, there is much less broadening and narrower structures can be grown [236]. Following this approach, nanopillars with diameters down to 14 nm have been demonstrated (Figure 7c). In further regard to pillar widths, 3D Monte Carlo simulations have in fact predicted that neon FIBID nanopillars could have even smaller diameters than their helium FIBID counterparts, due to the smaller overall interaction volume for neon causing less broadening further down the pillar, and also due to the lower secondary electron emission yield [237]. Experimental investigations of this proposed effect for neon FIBID are still pending.

A unique feature of helium FIBID nanopillars is that they can have hollow cores. This is a direct consequence of the highly localized interaction of the helium ions, as illustrated by Monte Carlo simulations of helium FIBID nanopillar growth, see Figure 7d [224]. In the referenced figure we see a cross-section through a simulated helium FIBID nanopillar, color-coded according to the species that induced the deposition in a particular area. The central column, shown in red and just a nanometer or so wide, indicates the region where deposition is induced by the primary helium ions. However, deposition always competes with sputtering, and if the sputtering rate is high enough, then the central region of the pillar can be milled out as the nanopillar grows, creating a columnar void. Hollow helium FIBID nanopillars were first observed by Kohama et al., with the hollow cores visualized by STEM [238] (Figure 7e). In the case of hollow nanopillars grown on silicon substrates, the authors also noted subsurface damage in the form of swelling. They showed that this swelling can be minimized by increasing the growth rate of the nanopillar, since then the pillar can more quickly shield the material below. Interestingly, in the case of thin amorphous carbon substrates (about 300 nm thick), which did not exhibit such pronounced swelling, the growth of a smaller nanopillar "twin" on the back surface was observed in addition to the one on the top, with a columnar void in each [246].

The electrical resistivities of helium and neon FIBID deposits have also been investigated. For metallic deposits where high conductivity is desired, gallium FIBID is advantageous, since co-implanted gallium increases the metal content thus improving the conductivity. In contrast, FEBID generally results in lower metal contents, both due to the nature of the electron beam-based deposition reaction as well as due to the absence of a co-implanted metal species. In helium and neon FIBID experiments by Wu et al. using the standard platinum-based precursor, a number of nanowires were deposited and their resistivities were measured [239]. It was found that the helium FIBID nanowires had rather high room-temperature resistivities (i.e., low conductivity), similar to those obtained using FEBID. In contrast, the resistivities of the neon FIBID nanowires were found to be significantly lower. TEM elemental analysis showed that the platinum content of the nanowires was actually about the same in each case (15–16%); the observed difference was the microstructure. For the helium FIBID nanowires, small platinum nanocrystals (about 3 nm in diameter) in a carbon matrix were observed, whereas for the neon FIBID nanowires slightly coarser nanoparticles in the carbon matrix (about

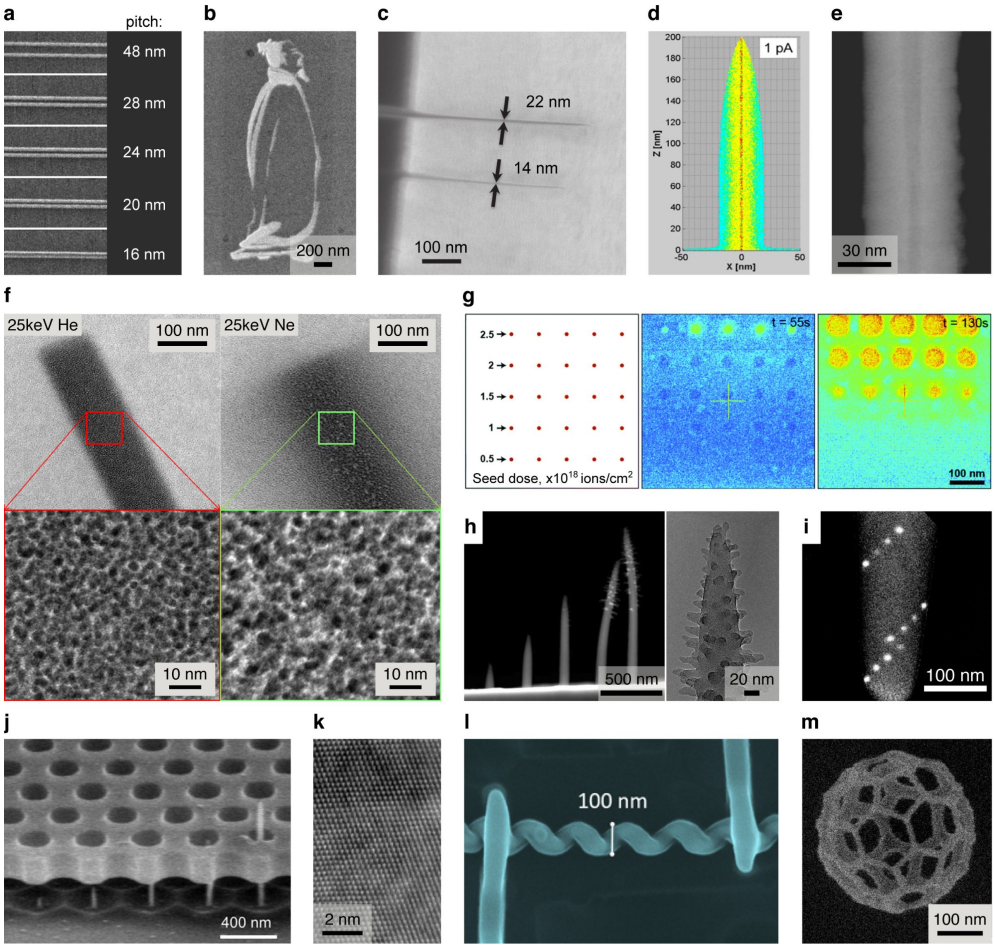

Figure 7: Examples of helium and neon FIBID. **(a)** Platinum-based line deposits fabricated using helium FIBID demonstrating a half-pitch down to 8 nm. Adapted with permission from Cambridge University Press, [232], Scipioni et al., A Design-of-Experiments Approach to Characterizing Beam-Induced Deposition in the Helium Ion Microscope, Microscopy Today, 19(3), 22-26. Copyright 2011 Microscopy Society of America. **(b)** Reproduction of a 13th century painting of a Chinese poet using helium FIBID with line widths down to 10 nm. Adapted from [235]. Copyright © 2012 Wiley Periodicals, Inc. Used with permission from Alkemade et al., Imaging and Nanofabrication With the Helium Ion Microscope of the Van Leeuwenhoek Laboratory in Delft, Scanning, John Wiley and Sons. **(c)** Horizontally grown platinum-based nanopillars using helium FIBID. Adapted with permission from [236]. Copyright 2015 American Vacuum Society. **(d)** Cross-section through a 3D Monte Carlo simulation of a helium FIBID nanopillar colorized according to the particles inducing the deposition: red (primary ions), yellow (secondary electrons - first generation), green (forward-scattered ions), cyan (secondary electrons - second generation). Adapted from [224], Chen et al., Nanopillar growth by focused helium ion-beam-induced deposition, Nanotechnology, Vol. 21(45), 455302, first published 14 October 2010. Copyright © 2010 IOP Publishing Ltd. Reproduced with permission. All rights reserved. **(e)** Hollow tungsten-based nanopillar fabricated using helium FIBID, imaged by STEM. Adapted with permission from [238]. Copyright 2013 American Vacuum Society. **(f)** TEM analysis of platinum-based in-plane nanowire deposits fabricated using helium FIBID (left) and neon FIBID (right). Adapted from [239], Wu et al., Synthesis of nanowires via helium and neon focused ion beam induced deposition with the gas field ion microscope, Nanotechnology, Vol. 24(17), 175302, first published 2 April 2013, Copyright © 2013 IOP Publishing Ltd. Reproduced with permission. All rights reserved. **(g)** Helium FIBID using a liquid precursor capped by a silicon nitride membrane: Nanoparticles are first seeded at pre-defined locations using point exposures, then the beam is rastered over the full area for controlled growth/imaging (colorized HIM images for two successive time points are shown). Adapted with permission of Royal Society of Chemistry, from [240], Building with ions: towards direct write of platinum nanostructures using in situ liquid cell helium ion microscopy, levlev et al., 9(35), Copyright 2017; permission conveyed through Copyright Clearance Center, Inc. **(h)** Branched nanopillars obtained by helium FIBID of an insulator precursor, imaged by (S)TEM. Adapted from [241]. Copyright 2021 Allen, licensed under a Creative Commons Attribution 4.0 International License, https://creativecommons.org/licenses/by/4.0/. **(i)** Tungsten-based nanodots fabricated using helium FIBID serving as alignment markers for electron tomography. Adapted from [242], Micron, 50, Hayashida et al., High-precision alignment of electron tomography tilt series using markers formed in helium-ion microscope, 29-34, Copyright (2013), with permission from Elsevier. **(j)** Local modulation of the dielectric properties of a photonic crystal with platinum-based nanopillars fabricated using helium FIBID. Adapted from [219] by permission from Springer Nature and with kind permission from the author P.F.A. Alkemade, Applied Physics A, Focused helium-ion-beam-induced deposition, Alkemade, P.F.A., and Miro, H. Copyright 2014 Springer-Verlag Berlin Heidelberg, Copyright P.F.A. Alkemade. **(k)** High-resolution STEM analysis of a portion of a tungsten-based nanopillar grown vertically by helium FIBID. Adapted from [243]. Copyright 2020 Córdoba et al., licensed under a Creative Commons Attribution 4.0 International License, https://creativecommons.org/licenses/by/4.0/. **(l)** Tungsten-based nanohelix fabricated using helium FIBID (with platinum contacts). Adapted with permission from [244]. Copyright 2019 American Chemical Society. Further permissions related to the material excerpted should be directed to the ACS. **(m)** Platinum-based deltahedron fabricated using helium FIBID. Adapted from [245]. Copyright 2020 Belianinov et al., licensed under a Creative Commons Attribution 4.0 International License, https://creativecommons.org/licenses/by/4.0/. The content of (a), (b), (c), (d), (e), (f), (g), (i), (j) and (l) is not subject to CC BY 4.0.

4.5 nm in diameter) were present (Figure 7f). Thus, the difference in conductivities was attributed to the difference in platinum particle size, with the larger particle size in the neon case proposed to be due to the reduced range of those ions and thus higher density of energy deposition (neon ion stopping being dominated by nuclear scattering, as opposed to electronic scattering for helium).

Precursor choice also has a significant effect on the resistivity. For example, in work using a cobalt-based precursor, helium FIBID achieving high-purity low-resistivity metallic nanowires was demonstrated, with TEM analysis revealing cobalt nanocrystallites of ca. 6 nm diameter and negligible carbon content [233]. Crucially, this work showed that by appropriate choice of the precursor, both high-resolution and high-purity deposits can be obtained using the helium FIBID method. Very recently, differences in composition and resistivity for tungsten-based nanowires depending on whether the deposition was performed in-plane onto the substrate or vertically in a nanopillar geometry were highlighted, pointing to differences in the relative contributions of the various beam–sample interactions in each case [234].

The precursor also needs not be a gas. In work by Ievlev et al., helium FIBID using a liquid precursor has been demonstrated [240]. In this setup, an in situ liquid cell is filled with a liquid precursor and capped with a 50 nm thick silicon nitride window. The helium ion beam is focused onto the window at pre-defined locations to seed nanoparticles on the back side (i.e., in the liquid) and the ion beam is then rastered over the window for controlled growth of the deposits and imaging (Figure 7g). An advantage of this approach over the usual gaseous precursor method is that the purity of the deposits can be greatly enhanced. For example, using a K_2PtCl_6 liquid precursor, the researchers demonstrated platinum deposit purities of 95%.

As for the deposition of insulating materials, FIBID using noble gas beams has the natural advantage of being able to create insulating deposits without any trace of implanted metallic species. Indeed, helium and neon FIBID of pad structures using the precursor pentamethylcyclopentasiloxane has been shown to yield resistivities two to three orders of magnitude higher than those achieved by gallium FIBID [199]. Helium FIBID of nanopillars using an insulator precursor has also been shown to result in the formation of side branches on the main body of the pillar, attributed to a charging effect [192,241] (Figure 7h).

Applications of helium FIBID

Early on, the fabrication of nanodots by helium FIBID was demonstrated as a technique to obtain fiducial markers at pre-defined locations to be used to align image series for TEM tomography [231,242] (Figure 7i). The use of helium FIBID to pattern seed layers for subsequent growth by atomic layer deposition has also been explored [235,247]. However, the most active area of research using helium FIBID has been based on the fabrication of nanopillars. For example, platinum-based nanopillars have been used to modulate the dielectric constant of individual holes in a photonic crystal [219]. This was achieved by suspending the photonic crystal above a substrate and growing the nanopillars onto that substrate such that they protruded into the holes of the photonic material (Figure 7j). Helium FIBID nanopillars have also been grown onto atomic force microscopy (AFM) cantilevers to create sharp tips with high aspect ratios [248]. And the horizontal nanopillar growth method mentioned previously has been used to grow even narrower tips with a perpendicular bar shape at the end to create hammerhead probes for AFM [236].

The phenomenon of hollow helium FIBID nanopillars has been used by Córdoba et al. for the fabrication of superconducting hollow tungsten-based crystalline nanowires (tungsten contents of up to 70 atom %) [226]. The structures were grown vertically and then laid down onto substrates for four-point-probe magnetotransport measurements. The particular superconducting behavior of these hollow nanostructures, observed upon cooling to 6.4 K, has been attributed to the pinning of superconducting vortices along a single line in the core, creating a quasi-1D superconductor. A study of the effect of current and dose on the lateral dimensions of the hollow nanopillars, together with further microstructural analysis, can be found in [243]. From this work, the high degree of crystallinity of the vertically grown tungsten-based nanowires can be seen in the high-resolution STEM image of Figure 7k. The fabrication of elegant 3D superconducting tungsten-based nanohelices has also been demonstrated, achieving ultrasmall helix diameters and pitch [244] (Figure 7l). In another helium FIBID superconductivity application, this time using in-plane deposition, tungsten-based nanowires up to 390 μm in length were deposited in order to connect to niobium thin-film islands, to fabricate hybrid microwave resonators [249]. The superconducting properties of tungsten-based in-plane helium-FIBID nanowires have been further investigated in [234].

Finally, experimental investigations supported by Monte Carlo simulations are underway to enable helium FIBID of complex nanopillar-based 3D mesh objects with sizes in the submicrometer domain [245] (Figure 7m).

Conclusion and Outlook

The impact of the helium ion microscope, since it was introduced in 2007, has been far-reaching. In addition to its unique

properties as an imaging instrument, it has enabled fundamental study of a variety of physical processes and the fabrication of nanoscale structures and devices not possible by other means. As this review article has described, these applications make use of localized irradiation over a wide range of ion doses, generating point defects for various forms of defect engineering, implanting ions to form nanobubbles for basic research into the irradiation response of materials, inducing subsurface swelling for patterning by nanoscale tumefaction, re-structuring materials externally by ion-induced mass transport and internally by collisional mixing, inducing stress gradients for controlled deformation of membranes, patterning resists for advanced ion beam lithography, and at the highest doses, selectively removing material by ion milling and adding material by gas-assisted deposition to fabricate a range of nanostructures for device prototyping that is truly at the cutting edge.

Future exciting avenues to pursue include continued development of in situ platforms for additional control over the sample environment and for real-time characterization of property effects, novel applications of irradiation-induced phenomena and FIB-based nanofabrication aided by extension of the available energy range of the ions to both higher and lower values, and further development of 3D nanofabrication techniques to propel breakthroughs in the 3D nano realm.

Acknowledgements

The author gratefully acknowledges support from the Biomolecular Nanotechnology Center, QB3, UC Berkeley and from the Department of Materials Science and Engineering, UC Berkeley. Many thanks to the helium ion microscopy community for countless insightful discussions over the years. Special thanks to John Notte of Carl Zeiss for his invaluable database of HIM publications.

ORCID® iDs

Frances I. Allen - https://orcid.org/0000-0002-0311-8624

References

1. Ward, B. W.; Notte, J. A.; Economou, N. P. *J. Vac. Sci. Technol., B: Microelectron. Nanometer Struct.–Process., Meas., Phenom.* **2006,** *24,* 2871–2874. doi:10.1116/1.2357967
2. Morgan, J.; Notte, J.; Hill, R.; Ward, B. *Microsc. Today* **2006,** *14* (4), 24–31. doi:10.1017/s1551929500050240
3. Notte, J.; Ward, B.; Economou, N.; Hill, R.; Percival, R.; Farkas, L.; McVey, S. *AIP Conf. Proc.* **2007,** *931,* 489–496. doi:10.1063/1.2799423
4. Bell, D. C. *Microsc. Microanal.* **2009,** *15,* 147–153. doi:10.1017/s1431927609090138
5. Hlawacek, G. Ion Microscopy. In *Springer Handbook of Microscopy;* Hawkes, P. W.; Spence, J. C. H., Eds.; Springer International Publishing: Cham, Switzerland, 2019; pp 677–714. doi:10.1007/978-3-030-00069-1_14
6. Joens, M. S.; Huynh, C.; Kasuboski, J. M.; Ferranti, D.; Sigal, Y. J.; Zeitvogel, F.; Obst, M.; Burkhardt, C. J.; Curran, K. P.; Chalasani, S. H.; Stern, L. A.; Goetze, B.; Fitzpatrick, J. A. J. *Sci. Rep.* **2013,** *3,* 3514. doi:10.1038/srep03514
7. Schmidt, M.; Byrne, J. M.; Maasilta, I. J. *Beilstein J. Nanotechnol.* **2021,** *12,* 1–23. doi:10.3762/bjnano.12.1
8. Wirtz, T.; De Castro, O.; Audinot, J.-N.; Philipp, P. *Annu. Rev. Anal. Chem.* **2019,** *12,* 523–543. doi:10.1146/annurev-anchem-061318-115457
9. He, S.; Tian, R.; Wu, W.; Li, W.-D.; Wang, D. *Int. J. Extreme Manuf.* **2021,** *3,* 012001. doi:10.1088/2631-7990/abc673
10. Hlawacek, G.; Gölzhäuser, A., Eds. *Helium Ion Microscopy;* NanoScience and Technology; Springer International Publishing: Cham, Switzerland, 2016. doi:10.1007/978-3-319-41990-9
11. Stanford, M. G.; Lewis, B. B.; Mahady, K.; Fowlkes, J. D.; Rack, P. D. *J. Vac. Sci. Technol., B: Nanotechnol. Microelectron.: Mater., Process., Meas., Phenom.* **2017,** *35,* 030802. doi:10.1116/1.4981016
12. Belianinov, A.; Burch, M. J.; Kim, S.; Tan, S.; Hlawacek, G.; Ovchinnikova, O. S. *MRS Bull.* **2017,** *42,* 660–666. doi:10.1557/mrs.2017.185
13. Joy, D. C. *Helium Ion Microscopy: Principles and Applications;* Springer: New York, NY, USA, 2013. doi:10.1007/978-1-4614-8660-2
14. Notte, J.; Huang, J. The Helium Ion Microscope. In *Helium Ion Microscopy;* Hlawacek, G.; Gölzhäuser, A., Eds.; Springer International Publishing: Cham, 2016; pp 3–30. doi:10.1007/978-3-319-41990-9_1
15. Tan, S.; Livengood, R.; Shima, D.; Notte, J.; McVey, S. *J. Vac. Sci. Technol., B: Nanotechnol. Microelectron.: Mater., Process., Meas., Phenom.* **2010,** *28,* C6F15. doi:10.1116/1.3511509
16. Livengood, R.; Tan, S.; Greenzweig, Y.; Notte, J.; McVey, S. *J. Vac. Sci. Technol., B: Microelectron. Nanometer Struct.–Process., Meas., Phenom.* **2009,** *27,* 3244–3249. doi:10.1116/1.3237101
17. Livengood, R. H.; Tan, S.; Hallstein, R.; Notte, J.; McVey, S.; Faridur Rahman, F. H. M. *Nucl. Instrum. Methods Phys. Res., Sect. A* **2011,** *645,* 136–140. doi:10.1016/j.nima.2010.12.220
18. Kretschmer, S.; Maslov, M.; Ghaderzadeh, S.; Ghorbani-Asl, M.; Hlawacek, G.; Krasheninnikov, A. V. *ACS Appl. Mater. Interfaces* **2018,** *10,* 30827–30836. doi:10.1021/acsami.8b08471
19. Nakaharai, S.; Iijima, T.; Ogawa, S.; Suzuki, S.; Li, S.-L.; Tsukagoshi, K.; Sato, S.; Yokoyama, N. *ACS Nano* **2013,** *7,* 5694–5700. doi:10.1021/nn401992q
20. Moktadir, Z.; Hang, S.; Mizuta, H. *Carbon* **2015,** *93,* 325–334. doi:10.1016/j.carbon.2015.05.049
21. Zhou, Y.; Maguire, P.; Jadwiszczak, J.; Muruganathan, M.; Mizuta, H.; Zhang, H. *Nanotechnology* **2016,** *27,* 325302. doi:10.1088/0957-4484/27/32/325302
22. Naitou, Y.; Ogawa, S. *AIP Adv.* **2017,** *7,* 045203. doi:10.1063/1.4979983
23. Araujo, E. N. D.; Brant, J. C.; Archanjo, B. S.; Medeiros-Ribeiro, G.; Alves, E. S. *Phys. E (Amsterdam, Neth.)* **2018,** *100,* 40–44. doi:10.1016/j.physe.2018.02.025
24. Srivastava, S.; Kino, H.; Nakaharai, S.; Verveniotis, E.; Okawa, Y.; Ogawa, S.; Joachim, C.; Aono, M. *Nanotechnology* **2017,** *28,* 035703. doi:10.1088/1361-6528/28/3/035703
25. Fox, D. S.; Zhou, Y.; Maguire, P.; O'Neill, A.; Ó'Coileáin, C.; Gatensby, R.; Glushenkov, A. M.; Tao, T.; Duesberg, G. S.; Shvets, I. V.; Abid, M.; Abid, M.; Wu, H.-C.; Chen, Y.; Coleman, J. N.; Donegan, J. F.; Zhang, H. *Nano Lett.* **2015,** *15,* 5307–5313. doi:10.1021/acs.nanolett.5b01673

26. Stanford, M. G.; Pudasaini, P. R.; Gallmeier, E. T.; Cross, N.; Liang, L.; Oyedele, A.; Duscher, G.; MahjouriâSamani, M.; Wang, K.; Xiao, K.; Geohegan, D. B.; Belianinov, A.; Sumpter, B. G.; Rack, P. D. *Adv. Funct. Mater.* **2017,** *27,* 1702829. doi:10.1002/adfm.201702829
27. Jadwiszczak, J.; Keane, D.; Maguire, P.; Cullen, C. P.; Zhou, Y.; Song, H.; Downing, C.; Fox, D.; McEvoy, N.; Zhu, R.; Xu, J.; Duesberg, G. S.; Liao, Z.-M.; Boland, J. J.; Zhang, H. *ACS Nano* **2019,** *13,* 14262–14273. doi:10.1021/acsnano.9b07421
28. Jadwiszczak, J.; Maguire, P.; Cullen, C. P.; Duesberg, G. S.; Zhang, H. *Beilstein J. Nanotechnol.* **2020,** *11,* 1329–1335. doi:10.3762/bjnano.11.117
29. Stanford, M. G.; Pudasaini, P. R.; Belianinov, A.; Cross, N.; Noh, J. H.; Koehler, M. R.; Mandrus, D. G.; Duscher, G.; Rondinone, A. J.; Ivanov, I. N.; Ward, T. Z.; Rack, P. D. *Sci. Rep.* **2016,** *6,* 27276. doi:10.1038/srep27276
30. Iberi, V.; Liang, L.; Ievlev, A. V.; Stanford, M. G.; Lin, M.-W.; Li, X.; Mahjouri-Samani, M.; Jesse, S.; Sumpter, B. G.; Kalinin, S. V.; Joy, D. C.; Xiao, K.; Belianinov, A.; Ovchinnikova, O. S. *Sci. Rep.* **2016,** *6,* 30481. doi:10.1038/srep30481
31. Cybart, S. A.; Cho, E. Y.; Wong, T. J.; Wehlin, B. H.; Ma, M. K.; Huynh, C.; Dynes, R. C. *Nat. Nanotechnol.* **2015,** *10,* 598–602. doi:10.1038/nnano.2015.76
32. Sapozhnikov, M. V.; Petrov, Y. V.; Gusev, N. S.; Temiryazev, A. G.; Ermolaeva, O. L.; Mironov, V. L.; Udalov, O. G. *Materials* **2019,** *13,* 99. doi:10.3390/ma13010099
33. Saremi, S.; Xu, R.; Allen, F. I.; Maher, J.; Agar, J. C.; Gao, R.; Hosemann, P.; Martin, L. W. *Phys. Rev. Mater.* **2018,** *2,* 084414. doi:10.1103/physrevmaterials.2.084414
34. Klein, J.; Lorke, M.; Florian, M.; Sigger, F.; Sigl, L.; Rey, S.; Wierzbowski, J.; Cerne, J.; Müller, K.; Mitterreiter, E.; Zimmermann, P.; Taniguchi, T.; Watanabe, K.; Wurstbauer, U.; Kaniber, M.; Knap, M.; Schmidt, R.; Finley, J. J.; Holleitner, A. W. *Nat. Commun.* **2019,** *10,* 2755. doi:10.1038/s41467-019-10632-z
35. Choe, H. S.; Prabhakar, R.; Wehmeyer, G.; Allen, F. I.; Lee, W.; Jin, L.; Li, Y.; Yang, P.; Qiu, C.-W.; Dames, C.; Scott, M.; Minor, A.; Bahk, J.-H.; Wu, J. *Nano Lett.* **2019,** *19,* 3830–3837. doi:10.1021/acs.nanolett.9b00984
36. Klein, J.; Kuc, A.; Nolinder, A.; Altzschner, M.; Wierzbowski, J.; Sigger, F.; Kreupl, F.; Finley, J. J.; Wurstbauer, U.; Holleitner, A. W.; Kaniber, M. *2D Mater.* **2017,** *5,* 011007. doi:10.1088/2053-1583/aa9642
37. Stanford, M. G.; Noh, J. H.; Mahady, K.; Ievlev, A. V.; Maksymovych, P.; Ovchinnikova, O. S.; Rack, P. D. *ACS Appl. Mater. Interfaces* **2017,** *9,* 35125–35132. doi:10.1021/acsami.7b10449
38. Cho, E. Y.; Ma, M. K.; Huynh, C.; Pratt, K.; Paulson, D. N.; Glyantsev, V. N.; Dynes, R. C.; Cybart, S. A. *Appl. Phys. Lett.* **2015,** *106,* 252601. doi:10.1063/1.4922640
39. Cho, E. Y.; Zhou, Y. W.; Cho, J. Y.; Cybart, S. A. *Appl. Phys. Lett.* **2018,** *113,* 022604. doi:10.1063/1.5042105
40. Cho, E. Y.; Li, H.; LeFebvre, J. C.; Zhou, Y. W.; Dynes, R. C.; Cybart, S. A. *Appl. Phys. Lett.* **2018,** *113,* 162602. doi:10.1063/1.5048776
41. Wang, J.; Li, H.; Cho, E. Y.; LeFebvere, J. C.; Cybart, S. A. *IEEE Trans. Appl. Supercond.* **2019,** *29,* 1–4. doi:10.1109/tasc.2019.2904479
42. Li, H.; Cho, E. Y.; Cai, H.; Wang, Y.-T.; McCoy, S. J.; Cybart, S. A. *IEEE Trans. Appl. Supercond.* **2019,** *29,* 1–4. doi:10.1109/tasc.2019.2898692
43. Müller, B.; Karrer, M.; Limberger, F.; Becker, M.; Schröppel, B.; Burkhardt, C. J.; Kleiner, R.; Goldobin, E.; Koelle, D. *Phys. Rev. Appl.* **2019,** *11,* 044082. doi:10.1103/physrevapplied.11.044082
44. Li, H.; Cai, H.; Cho, E. Y.; McCoy, S. J.; Wang, Y.-T.; LeFebvre, J. C.; Zhou, Y. W.; Cybart, S. A. *Appl. Phys. Lett.* **2020,** *116,* 070601. doi:10.1063/1.5143026
45. Cortez, A. T.; Cho, E. Y.; Li, H.; Cunnane, D.; Karasik, B.; Cybart, S. A. *IEEE Trans. Appl. Supercond.* **2019,** *29,* 1–5. doi:10.1109/tasc.2019.2905166
46. Couëdo, F.; Amari, P.; Feuillet-Palma, C.; Ulysse, C.; Srivastava, Y. K.; Singh, R.; Bergeal, N.; Lesueur, J. *Sci. Rep.* **2020,** *10,* 10256. doi:10.1038/s41598-020-66882-1
47. Gozar, A.; Litombe, N. E.; Hoffman, J. E.; Božović, I. *Nano Lett.* **2017,** *17,* 1582–1586. doi:10.1021/acs.nanolett.6b04729
48. Kasaei, L.; Melbourne, T.; Manichev, V.; Feldman, L. C.; Gustafsson, T.; Chen, K.; Xi, X. X.; Davidson, B. A. *AIP Adv.* **2018,** *8,* 075020. doi:10.1063/1.5030751
49. Franken, J. H.; Hoeijmakers, M.; Lavrijsen, R.; Kohlhepp, J. T.; Swagten, H. J. M.; Koopmans, B.; van Veldhoven, E.; Maas, D. J. *J. Appl. Phys.* **2011,** *109,* 07D504. doi:10.1063/1.3549589
50. Sapozhnikov, M. V.; Vdovichev, S. N.; Ermolaeva, O. L.; Gusev, N. S.; Fraerman, A. A.; Gusev, S. A.; Petrov, Y. V. *Appl. Phys. Lett.* **2016,** *109,* 042406. doi:10.1063/1.4958300
51. Deinhart, V.; Kern, L.-M.; Kirchhof, J. N.; Juergensen, S.; Sturm, J.; Krauss, E.; Feichtner, T.; Kovalchuk, S.; Schneider, M.; Engel, D.; Pfau, B.; Hecht, B.; Bolotin, K. I.; Reich, S.; Höflich, K. *Beilstein J. Nanotechnol.* **2021,** *12,* 304–318. doi:10.3762/bjnano.12.25
52. Cress, C. D.; Wickramaratne, D.; Rosenberger, M. R.; Hennighausen, Z.; Callahan, P. G.; LaGasse, S. W.; Bernstein, N.; van 't Erve, O. M.; Jonker, B. T.; Qadri, S. B.; Prestigiacomo, J. C.; Currie, M.; Mazin, I. I.; Bennett, S. P. *ACS Appl. Mater. Interfaces* **2021,** *13,* 836–847. doi:10.1021/acsami.0c13565
53. Huckfeldt, H.; Gaul, A.; David Müglich, N.; Holzinger, D.; Nissen, D.; Albrecht, M.; Emmrich, D.; Beyer, A.; Gölzhäuser, A.; Ehresmann, A. *J. Phys.: Condens. Matter* **2017,** *29,* 125801. doi:10.1088/1361-648x/aa5ad5
54. Dunne, P.; Fowley, C.; Hlawacek, G.; Kurian, J.; Atcheson, G.; Colis, S.; Teichert, N.; Kundys, B.; Venkatesan, M.; Lindner, J.; Deac, A. M.; Hermans, T. M.; Coey, J. M. D.; Doudin, B. *Nano Lett.* **2020,** *20,* 7036–7042. doi:10.1021/acs.nanolett.0c02060
55. Röder, F.; Hlawacek, G.; Wintz, S.; Hübner, R.; Bischoff, L.; Lichte, H.; Potzger, K.; Lindner, J.; Fassbender, J.; Bali, R. *Sci. Rep.* **2015,** *5,* 16786. doi:10.1038/srep16786
56. Seol, D.; Kim, S.; Jang, W.-S.; Jin, Y.; Kang, S.; Kim, S.; Won, D.; Lee, C.; Kim, Y.-M.; Lee, J.; Yang, H.; Jeong, M. S.; Belianinov, A.; Tselev, A.; Somnath, S.; Smith, C. R.; Ovchinnikova, O. S.; Balke, N.; Kim, Y. *Nano Energy* **2021,** *79,* 105451. doi:10.1016/j.nanoen.2020.105451
57. Belianinov, A.; Iberi, V.; Tselev, A.; Susner, M. A.; McGuire, M. A.; Joy, D.; Jesse, S.; Rondinone, A. J.; Kalinin, S. V.; Ovchinnikova, O. S. *ACS Appl. Mater. Interfaces* **2016,** *8,* 7349–7355. doi:10.1021/acsami.5b12056
58. Huang, Z.; Li, W.-D.; Santori, C.; Acosta, V. M.; Faraon, A.; Ishikawa, T.; Wu, W.; Winston, D.; Williams, R. S.; Beausoleil, R. G. *Appl. Phys. Lett.* **2013,** *103,* 081906. doi:10.1063/1.4819339
59. McCloskey, D.; Fox, D.; O'Hara, N.; Usov, V.; Scanlan, D.; McEvoy, N.; Duesberg, G. S.; Cross, G. L. W.; Zhang, H. Z.; Donegan, J. F. *Appl. Phys. Lett.* **2014,** *104,* 031109. doi:10.1063/1.4862331

60. Sawafta, F.; Clancy, B.; Carlsen, A. T.; Huber, M.; Hall, A. R. *Nanoscale* **2014,** *6,* 6991–6996. doi:10.1039/c4nr00305e
61. Kapitonov, Y. V.; Shapochkin, P. Y.; Beliaev, L. Y.; Petrov, Y. V.; Efimov, Y. P.; Eliseev, S. A.; Lovtcius, V. A.; Petrov, V. V.; Ovsyankin, V. V. *Opt. Lett.* **2016,** *41,* 104–106. doi:10.1364/ol.41.000104
62. Jiang, X.; Cai, W.; Luo, W.; Xiang, Y.; Zhang, N.; Ren, M.; Zhang, X.; Xu, J. *Nanotechnology* **2018,** *29,* 385205. doi:10.1088/1361-6528/aad0b4
63. Maguire, P.; Downing, C.; Jadwiszczak, J.; O'Brien, M.; Keane, D.; McManus, J. B.; Duesberg, G. S.; Nicolosi, V.; McEvoy, N.; Zhang, H. *J. Appl. Phys.* **2019,** *125,* 064305. doi:10.1063/1.5086366
64. Petrov, Y. V.; Sharov, T. V.; Baraban, A. P.; Vyvenko, O. F. *Nucl. Instrum. Methods Phys. Res., Sect. B* **2015,** *349,* 90–95. doi:10.1016/j.nimb.2015.02.054
65. Petrov, Y. V.; Ubyivovk, E. V.; Baraban, A. P. *AIP Conf. Proc.* **2019,** *2064,* 030012. doi:10.1063/1.5087674
66. Petrov, Y. V.; Grigoryev, E. A.; Sharov, T. V.; Baraban, A. P. *Nucl. Instrum. Methods Phys. Res., Sect. B* **2018,** *418,* 94–100. doi:10.1016/j.nimb.2018.01.011
67. Petrov, Y. V.; Grigoryev, E. A.; Baraban, A. P. *Nanotechnology* **2020,** *31,* 215301. doi:10.1088/1361-6528/ab6fe3
68. Maguire, P.; Jadwiszczak, J.; O'Brien, M.; Keane, D.; Duesberg, G. S.; McEvoy, N.; Zhang, H. *J. Appl. Phys.* **2019,** *126,* 164301. doi:10.1063/1.5115036
69. Mitterreiter, E.; Liang, Y.; Golibrzuch, M.; McLaughlin, D.; Csoklich, C.; Bartl, J. D.; Holleitner, A.; Wurstbauer, U.; Bandarenka, A. S. *npj 2D Mater. Appl.* **2019,** *3,* 25. doi:10.1038/s41699-019-0107-5
70. Zhao, Y.; Liu, D.; Chen, J.; Zhu, L.; Belianinov, A.; Ovchinnikova, O. S.; Unocic, R. R.; Burch, M. J.; Kim, S.; Hao, H.; Pickard, D. S.; Li, B.; Thong, J. T. L. *Nat. Commun.* **2017,** *8,* 15919. doi:10.1038/ncomms15919
71. Jin, L.; Zeltmann, S. E.; Choe, H. S.; Liu, H.; Allen, F. I.; Minor, A. M.; Wu, J. *Phys. Rev. B* **2020,** *102,* 041120. doi:10.1103/physrevb.102.041120
72. Choe, H. S.; Li, J.; Zheng, W.; Lee, J.; Suh, J.; Allen, F. I.; Liu, H.; Choi, H.-J.; Walukiewicz, W.; Zheng, H.; Wu, J. *Appl. Phys. Lett.* **2019,** *114,* 152101. doi:10.1063/1.5092221
73. Eswara, S.; Audinot, J.-N.; El Adib, B.; Guennou, M.; Wirtz, T.; Philipp, P. *Beilstein J. Nanotechnol.* **2018,** *9,* 1951–1963. doi:10.3762/bjnano.9.186
74. Toulouse, C.; Fischer, J.; Farokhipoor, S.; Yedra, L.; Carlà, F.; Jarnac, A.; Elkaim, E.; Fertey, P.; Audinot, J.-N.; Wirtz, T.; Noheda, B.; Garcia, V.; Fusil, S.; Alonso, I. P.; Guennou, M.; Kreisel, J. *Phys. Rev. Mater.* **2021,** *5,* 024404. doi:10.1103/physrevmaterials.5.024404
75. Tan, S.; Klein, K.; Shima, D.; Livengood, R.; Mutunga, E.; Vladár, A. *J. Vac. Sci. Technol., B: Nanotechnol. Microelectron.: Mater., Process., Meas., Phenom.* **2014,** *32,* 06FA01. doi:10.1116/1.4900728
76. Li, R.; Zhu, R.; Chen, S.; He, C.; Li, M.; Zhang, J.; Gao, P.; Liao, Z.; Xu, J. *J. Vac. Sci. Technol., B: Nanotechnol. Microelectron.: Mater., Process., Meas., Phenom.* **2019,** *37,* 031804. doi:10.1116/1.5096908
77. Veligura, V.; Hlawacek, G.; Berkelaar, R. P.; van Gastel, R.; Zandvliet, H. J. W.; Poelsema, B. *Beilstein J. Nanotechnol.* **2013,** *4,* 453–460. doi:10.3762/bjnano.4.53
78. Wang, Z.-J.; Allen, F. I.; Shan, Z.-W.; Hosemann, P. *Acta Mater.* **2016,** *121,* 78–84. doi:10.1016/j.actamat.2016.08.085
79. Liu, W.; Cheng, L.; Li, X.; Wang, Y. *Nanoscale* **2016,** *8,* 762–765. doi:10.1039/c5nr06659j
80. Jiang, W.; Zhang, J.; Edwards, D. J.; Overman, N. R.; Zhu, Z.; Price, L.; Gigax, J.; Castanon, E.; Shao, L.; Senor, D. J. *J. Nucl. Mater.* **2017,** *494,* 411–421. doi:10.1016/j.jnucmat.2017.07.048
81. Frazer, D.; Szornel, J.; Krumwiede, D. L.; Terrani, K. A.; Hosemann, P. *Exp. Mech.* **2017,** *57,* 1081–1090. doi:10.1007/s11340-017-0277-z
82. Bergner, F.; Hlawacek, G.; Heintze, C. *J. Nucl. Mater.* **2018,** *505,* 267–275. doi:10.1016/j.jnucmat.2017.07.054
83. Chen, Z.; Niu, L.-L.; Wang, Z.; Tian, L.; Kecskes, L.; Zhu, K.; Wei, Q. *Acta Mater.* **2018,** *147,* 100–112. doi:10.1016/j.actamat.2018.01.015
84. Allen, F. I.; Hosemann, P.; Balooch, M. *Scr. Mater.* **2020,** *178,* 256–260. doi:10.1016/j.scriptamat.2019.11.039
85. Xiao, S.; Ma, Y.; Tian, L.; Li, M.; Qi, C.; Wang, B. *Nucl. Mater. Energy* **2020,** *23,* 100746. doi:10.1016/j.nme.2020.100746
86. Shan, G. B.; Chen, Y. Z.; Liang, N. N.; Dong, H.; Zhang, W. X.; Suo, T.; Liu, F. *Mater. Lett.* **2019,** *238,* 261–263. doi:10.1016/j.matlet.2018.12.018
87. Mairov, A.; Frazer, D.; Hosemann, P.; Sridharan, K. *Scr. Mater.* **2019,** *162,* 156–160. doi:10.1016/j.scriptamat.2018.11.006
88. Jiang, W.; Sundararajan, J. A.; Varga, T.; Bowden, M. E.; Qiang, Y.; McCloy, J. S.; Henager, C. H., Jr.; Montgomery, R. O. *Adv. Funct. Mater.* **2014,** *24,* 6210–6218. doi:10.1002/adfm.201400553
89. Wang, Y.-C.; Tian, L.; Liu, F.; Qin, Y.-B.; Zheng, G.; Wang, J.-T.; Ma, E.; Shan, Z.-W. *Small* **2017,** *13,* 1601753. doi:10.1002/smll.201601753
90. Chen, M.; Best, J. P.; Shorubalko, I.; Michler, J.; Spolenak, R.; Wheeler, J. M. *Carbon* **2020,** *158,* 337–345. doi:10.1016/j.carbon.2019.10.078
91. Rzeznik, L.; Fleming, Y.; Wirtz, T.; Philipp, P. *Beilstein J. Nanotechnol.* **2016,** *7,* 1113–1128. doi:10.3762/bjnano.7.104
92. Tavares, L.; Chiriaev, S.; Adashkevich, V.; Taboryski, R.; Rubahn, H.-G. *Nanotechnology* **2020,** *31,* 145303. doi:10.1088/1361-6528/ab6679
93. Allen, F. I.; Velez, N. R.; Thayer, R. C.; Patel, N. H.; Jones, M. A.; Meyers, G. F.; Minor, A. M. *Nanoscale* **2019,** *11,* 1403–1409. doi:10.1039/c8nr08224c
94. Zhang, L.; Heinig, N. F.; Bazargan, S.; Abd-Ellah, M.; Moghimi, N.; Leung, K. T. *Nanotechnology* **2015,** *26,* 255303. doi:10.1088/0957-4484/26/25/255303
95. Kim, C.-S.; Hobbs, R. G.; Agarwal, A.; Yang, Y.; Manfrinato, V. R.; Short, M. P.; Li, J.; Berggren, K. K. *Nanotechnology* **2020,** *31,* 045302. doi:10.1088/1361-6528/ab4a65
96. Aramesh, M.; Mayamei, Y.; Wolff, A.; Ostrikov, K. K. *Nat. Commun.* **2018,** *9,* 835. doi:10.1038/s41467-018-03316-7
97. Aramesh, M. *Phys. Status Solidi RRL* **2018,** *12,* 1700333. doi:10.1002/pssr.201700333
98. Xu, X.; Prüfer, T.; Wolf, D.; Engelmann, H.-J.; Bischoff, L.; Hübner, R.; Heinig, K.-H.; Möller, W.; Facsko, S.; von Borany, J.; Hlawacek, G. *Beilstein J. Nanotechnol.* **2018,** *9,* 2883–2892. doi:10.3762/bjnano.9.267
99. Arora, W. J.; Sijbrandij, S.; Stern, L.; Notte, J.; Smith, H. I.; Barbastathis, G. *J. Vac. Sci. Technol., B: Microelectron. Nanometer Struct.–Process., Meas., Phenom.* **2007,** *25,* 2184–2187. doi:10.1116/1.2779049

100. Gonzalez, C. M.; Timilsina, R.; Li, G.; Duscher, G.; Rack, P. D.; Slingenbergh, W.; van Dorp, W. F.; De Hosson, J. T. M.; Klein, K. L.; Wu, H. M.; Stern, L. A. *J. Vac. Sci. Technol., B: Nanotechnol. Microelectron.: Mater., Process ., Meas., Phenom.* **2014,** *32,* 021602. doi:10.1116/1.4868027
101. Liu, Z.; Du, H.; Li, J.; Lu, L.; Li, Z.-Y.; Fang, N. X. *Sci. Adv.* **2018,** *4,* eaat4436. doi:10.1126/sciadv.aat4436
102. Zhang, C.; Dyck, O.; Garfinkel, D. A.; Stanford, M. G.; Belianinov, A. A.; Fowlkes, J. D.; Jesse, S.; Rack, P. D. *Nanomaterials* **2019,** *9,* 1394. doi:10.3390/nano9101394
103. Prewett, P. D.; Hagen, C. W.; Lenk, C.; Lenk, S.; Kaestner, M.; Ivanov, T.; Ahmad, A.; Rangelow, I. W.; Shi, X.; Boden, S. A.; Robinson, A. P. G.; Yang, D.; Hari, S.; Scotuzzi, M.; Huq, E. *Beilstein J. Nanotechnol.* **2018,** *9,* 2855–2882. doi:10.3762/bjnano.9.266
104. Shi, X.; Boden, S. A. Chapter 17 - Scanning helium ion beam lithography. In *Frontiers of Nanoscience;* Robinson, A.; Lawson, R., Eds.; Elsevier, 2016; Vol. 11, pp 563–594. doi:10.1016/b978-0-08-100354-1.00017-x
105. Kalhor, N.; Alkemade, P. F. A. Resist Assisted Patterning. In *Helium Ion Microscopy;* Hlawacek, G.; Gölzhäuser, A., Eds.; Springer International Publishing: Cham, 2016; pp 395–414. doi:10.1007/978-3-319-41990-9_16
106. Sidorkin, V.; van Veldhoven, E.; van der Drift, E.; Alkemade, P.; Salemink, H.; Maas, D. *J. Vac. Sci. Technol., B: Microelectron. Nanometer Struct.–Process., Meas., Phenom.* **2009,** *27,* L18–L20. doi:10.1116/1.3182742
107. Winston, D.; Cord, B. M.; Ming, B.; Bell, D. C.; DiNatale, W. F.; Stern, L. A.; Vladar, A. E.; Postek, M. T.; Mondol, M. K.; Yang, J. K. W.; Berggren, K. K. *J. Vac. Sci. Technol., B: Microelectron. Nanometer Struct.–Process., Meas., Phenom.* **2009,** *27,* 2702–2706. doi:10.1116/1.3250204
108. Cai, J.; Zhu, Z.; Alkemade, P. F. A.; van Veldhoven, E.; Wang, Q.; Ge, H.; Rodrigues, S. P.; Cai, W.; Li, W.-D. *Adv. Mater. (Weinheim, Ger.)* **2018,** *5,* 1800203. doi:10.1002/admi.201800203
109. Flatabø, R.; Agarwal, A.; Hobbs, R.; Greve, M. M.; Holst, B.; Berggren, K. K. *Nanotechnology* **2018,** *29,* 275301. doi:10.1088/1361-6528/aabe22
110. Lee, C.-L.; Chien, S.-W.; Tsai, K.-Y. *Proc. SPIE* **2018,** *10584,* 105841C. doi:10.1117/12.2297691
111. Zhang, L.; Thomas, J. P.; Guan, X.; Heinig, N. F.; Leung, K. T. *Nanotechnology* **2020,** *31,* 325301. doi:10.1088/1361-6528/ab8d69
112. Zhang, X.; Vieker, H.; Beyer, A.; Gölzhäuser, A. *Beilstein J. Nanotechnol.* **2014,** *5,* 188–194. doi:10.3762/bjnano.5.20
113. Winston, D.; Manfrinato, V. R.; Nicaise, S. M.; Cheong, L. L.; Duan, H.; Ferranti, D.; Marshman, J.; McVey, S.; Stern, L.; Notte, J.; Berggren, K. K. *Nano Lett.* **2011,** *11,* 4343–4347. doi:10.1021/nl202447n
114. Alkemade, P.; Sidorkin, V.; Chen, P.; van der Drift, E.; van Langen, A.; Maas, D.; van Velhoven, E.; Scipioni, L. *Microsc. Anal.* **2010,** *24,* 5–8.
115. van der Drift, E.; Maas, D. J. Helium Ion Lithography. In *Nanofabrication: Techniques and Principles;* Stepanova, M.; Dew, S., Eds.; Springer Vienna: Vienna, 2012; pp 93–116. doi:10.1007/978-3-7091-0424-8_4
116. Fallica, R.; Kirchner, R.; Ekinci, Y.; Mailly, D. *J. Vac. Sci. Technol., B: Nanotechnol. Microelectron.: Mater., Process ., Meas., Phenom.* **2016,** *34,* 06K702. doi:10.1116/1.4967183
117. Luo, F.; Manichev, V.; Li, M.; Mitchson, G.; Yakshinskiy, B.; Gustafsson, T.; Johnson, D.; Garfunkel, E. Helium ion beam lithography (HIBL) using HafSOx as the resist. In *Advances in Patterning Materials and Processes XXXIII,* International Society for Optics and Photonics, 2016; p 977928. doi:10.1117/12.2219239
118. Maas, D.; van Veldhoven, E.; van Langen-Suurling, A.; Alkemade, P. F. A.; Wuister, S.; Hoefnagels, R.; Verspaget, C.; Meessen, J.; Fliervoet, T. Evaluation of EUV resist performance below 20nm CD using helium ion lithography. In *Extreme Ultraviolet (EUV) Lithography V,* International Society for Optics and Photonics, 2014; 90482Z. doi:10.1117/12.2046917
119. Kalhor, N.; Mulckhuyse, W.; Alkemade, P.; Maas, D. Impact of pixel-dose optimization on pattern fidelity for helium ion beam lithography on EUV resist. In *Advances in Patterning Materials and Processes XXXII,* Wallow, T. I.; Hohle, C. K., Eds.; International Society for Optics and Photonics, 2015; p 942513. doi:10.1117/12.2085791
120. Li, M.; Manichev, V.; Yu, F.; Hutchison, D.; Nyman, M.; Gustafsson, T.; Feldman, L. C.; Garfunkel, E. L. Novel Sn-based photoresist for high aspect ratio patterning. In *Advances in Patterning Materials and Processes XXXV,* International Society for Optics and Photonics, 2018; 105860K. doi:10.1117/12.2297440
121. Shi, X.; Prewett, P.; Huq, E.; Bagnall, D. M.; Robinson, A. P. G.; Boden, S. A. *Microelectron. Eng.* **2016,** *155,* 74–78. doi:10.1016/j.mee.2016.02.045
122. Hartl, H.; East, C.; Xu, Y.; Yambem, S. D.; Fairfull-Smith, K. E.; MacLeod, J. *Nanotechnology* **2019,** *30,* 335301. doi:10.1088/1361-6528/ab1b86
123. Reddy, P. G.; Thakur, N.; Lee, C.-L.; Chien, S.-W.; Pradeep, C. P.; Ghosh, S.; Tsai, K.-Y.; Gonsalves, K. E. *AIP Adv.* **2017,** *7,* 085314. doi:10.1063/1.4989981
124. Sharma, S. K.; Reddy, P. G.; Moinuddin, M. G.; Ghosh, S.; Pradeep, C. P.; Gonsalves, K. E. Helium ion active hybrid non-chemically amplified resist (n-CAR) for sub-10 nm patterning applications. In *Novel Patterning Technologies 2018,* International Society for Optics and Photonics, 2018; p 1058409. doi:10.1117/12.2297537
125. Cattoni, A.; Mailly, D.; Dalstein, O.; Faustini, M.; Seniutinas, G.; Rösner, B.; David, C. *Microelectron. Eng.* **2018,** *193,* 18–22. doi:10.1016/j.mee.2018.02.015
126. Lewis, S. M.; Hunt, M. S.; DeRose, G. A.; Alty, H. R.; Li, J.; Wertheim, A.; De Rose, L.; Timco, G. A.; Scherer, A.; Yeates, S. G.; Winpenny, R. E. P. *Nano Lett.* **2019,** *19,* 6043–6048. doi:10.1021/acs.nanolett.9b01911
127. Kumar, R.; Chauhan, M.; Moinuddin, M. G.; Sharma, S. K.; Gonsalves, K. E. *ACS Appl. Mater. Interfaces* **2020,** *12,* 19616–19624. doi:10.1021/acsami.9b21414
128. Sharma, S. K.; Kumar, R.; Chauhan, M.; Moinuddin, M. G.; Peter, J.; Ghosh, S.; Pradeep, C. P.; Gonsalves, K. E. All-new nickel-based Metal Core Organic Cluster (MCOC) resist for N7+ node patterning. In *Advances in Patterning Materials and Processes XXXVII,* International Society for Optics and Photonics, 2020; p 1132604. doi:10.1117/12.2552189
129. Sharma, S. K.; Moinuddin, M. G.; Yogesh, M.; Sharma, S.; Sahani, M.; Ghosh, S.; Gonsalves, K. E. Focusing on nanoparticles-based photomultiplier in n-CARs. In *Advances in Patterning Materials and Processes XXXVII,* International Society for Optics and Photonics, 2020; 113261C. doi:10.1117/12.2552190

130. Li, W.-D.; Wu, W.; Stanley Williams, R. *J. Vac. Sci. Technol., B: Nanotechnol. Microelectron.: Mater., Process ., Meas., Phenom.* **2012,** *30,* 06F304. doi:10.1116/1.4758768
131. Pickard, D.; Scipioni, L. Graphene Nano-Ribbon Patterning in the ORION® PLUS. In *Carl Zeiss Application Note*. Carl Zeiss, 2009; https://www.tcd.ie/Physics/research/groups/pan/teaching/PY5019/HIM/AN_ORION_PLUS_Graphene.pdf.
132. Abbas, A. N.; Liu, G.; Liu, B.; Zhang, L.; Liu, H.; Ohlberg, D.; Wu, W.; Zhou, C. *ACS Nano* **2014,** *8,* 1538–1546. doi:10.1021/nn405759v
133. Kalhor, N.; Boden, S. A.; Mizuta, H. *Microelectron. Eng.* **2014,** *114,* 70–77. doi:10.1016/j.mee.2013.09.018
134. Annamalai, M.; Mathew, S.; Viswanathan, V.; Fang, C.; Pickard, D. S.; Palaniapan, M. Design, fabrication and Helium Ion Microscope patterning of suspended nanomechanical graphene structures for NEMS applications. In *2011 16th International Solid-State Sensors, Actuators and Microsystems Conference,* IEEE, 2011; pp 2578–2581. doi:10.1109/transducers.2011.5969824
135. Iberi, V.; Vlassiouk, I.; Zhang, X.-G.; Matola, B.; Linn, A.; Joy, D. C.; Rondinone, A. J. *Sci. Rep.* **2015,** *5,* 11952. doi:10.1038/srep11952
136. Schmidt, M. E.; Iwasaki, T.; Muruganathan, M.; Haque, M.; Van Ngoc, H.; Ogawa, S.; Mizuta, H. *ACS Appl. Mater. Interfaces* **2018,** *10,* 10362–10368. doi:10.1021/acsami.8b00427
137. Deng, Y.; Wang, G.; Qiu, Y.; He, D.; Lin, J.; He, J. *Nanotechnology* **2020,** *31,* 345302. doi:10.1088/1361-6528/ab90b5
138. Simeone, D.; Esposito, M.; Scuderi, M.; Calafiore, G.; Palermo, G.; De Luca, A.; Todisco, F.; Sanvitto, D.; Nicotra, G.; Cabrini, S.; Tasco, V.; Passaseo, A.; Cuscunà, M. *ACS Photonics* **2018,** *5,* 3399–3407. doi:10.1021/acsphotonics.8b00665
139. Hahn, C.; Hajebifard, A.; Berini, P. *Nanophotonics* **2020,** *9,* 393–399. doi:10.1515/nanoph-2019-0385
140. Chen, Y.; Hu, Y.; Zhao, J.; Deng, Y.; Wang, Z.; Cheng, X.; Lei, D.; Deng, Y.; Duan, H. *Adv. Funct. Mater.* **2020,** *30,* 2000642. doi:10.1002/adfm.202000642
141. Seitl, L.; Laible, F.; Dickreuter, S.; Gollmer, D. A.; Kern, D. P.; Fleischer, M. *Nanotechnology* **2020,** *31,* 075301. doi:10.1088/1361-6528/ab5120
142. Kuznetsov, A. I.; Miroshnichenko, A. E.; Hsing Fu, Y.; Viswanathan, V.; Rahmani, M.; Valuckas, V.; Ying Pan, Z.; Kivshar, Y.; Pickard, D. S.; Luk'yanchuk, B. *Nat. Commun.* **2014,** *5,* 3104. doi:10.1038/ncomms4104
143. Tan, S.; Livengood, R.; Hack, P.; Hallstein, R.; Shima, D.; Notte, J.; McVey, S. *J. Vac. Sci. Technol., B: Nanotechnol. Microelectron.: Mater., Process ., Meas., Phenom.* **2011,** *29,* 06F604. doi:10.1116/1.3660797
144. Stanford, M. G.; Mahady, K.; Lewis, B. B.; Fowlkes, J. D.; Tan, S.; Livengood, R.; Magel, G. A.; Moore, T. M.; Rack, P. D. *ACS Appl. Mater. Interfaces* **2016,** *8,* 29155–29162. doi:10.1021/acsami.6b09758
145. Buchheim, J.; Wyss, R. M.; Shorubalko, I.; Park, H. G. *Nanoscale* **2016,** *8,* 8345–8354. doi:10.1039/c6nr00154h
146. Kim, S.; Dyck, O.; Ievlev, A. V.; Vlassiouk, I. V.; Kalinin, S. V.; Belianinov, A.; Jesse, S.; Ovchinnikova, O. S. *Carbon* **2018,** *138,* 277–282. doi:10.1016/j.carbon.2018.06.017
147. Fox, D.; Zhou, Y. B.; O'Neill, A.; Kumar, S.; Wang, J. J.; Coleman, J. N.; Duesberg, G. S.; Donegan, J. F.; Zhang, H. Z. *Nanotechnology* **2013,** *24,* 335702. doi:10.1088/0957-4484/24/33/335702
148. Araujo, E. N. D.; Brant, J. C.; Archanjo, B. S.; Medeiros-Ribeiro, G.; Plentz, F.; Alves, E. S. *Phys. Rev. B* **2015,** *91,* 245414. doi:10.1103/physrevb.91.245414
149. Nanda, G.; Goswami, S.; Watanabe, K.; Taniguchi, T.; Alkemade, P. F. A. *Nano Lett.* **2015,** *15,* 4006–4012. doi:10.1021/acs.nanolett.5b00939
150. Nanda, G.; Hlawacek, G.; Goswami, S.; Watanabe, K.; Taniguchi, T.; Alkemade, P. F. A. *Carbon* **2017,** *119,* 419–425. doi:10.1016/j.carbon.2017.04.062
151. Iberi, V.; Ievlev, A. V.; Vlassiouk, I.; Jesse, S.; Kalinin, S. V.; Joy, D. C.; Rondinone, A. J.; Belianinov, A.; Ovchinnikova, O. S. *Nanotechnology* **2016,** *27,* 125302. doi:10.1088/0957-4484/27/12/125302
152. Gilbert, S. M.; Liu, S.; Schumm, G.; Zettl, A. *MRS Adv.* **2018,** *3,* 327–331. doi:10.1557/adv.2018.117
153. López, J. J.; Ambrosio, A.; Dai, S.; Huynh, C.; Bell, D. C.; Lin, X.; Rivera, N.; Huang, S.; Ma, Q.; Eyhusen, S.; Kaminer, I. E.; Watanabe, K.; Taniguchi, T.; Kong, J.; Basov, D. N.; Jarillo-Herrero, P.; Soljačić, M. *Small* **2018,** *14,* 1800072. doi:10.1002/smll.201800072
154. Thiele, C.; Vieker, H.; Beyer, A.; Flavel, B. S.; Hennrich, F.; Muñoz Torres, D.; Eaton, T. R.; Mayor, M.; Kappes, M. M.; Gölzhäuser, A.; v. Löhneysen, H.; Krupke, R. *Appl. Phys. Lett.* **2014,** *104,* 103102. doi:10.1063/1.4868097
155. Zheng, W.; Li, P.; van den Hurk, R.; Evoy, S. *Sensors* **2016,** *16,* 1080. doi:10.3390/s16071080
156. Yang, J.; Ferranti, D. C.; Stern, L. A.; Sanford, C. A.; Huang, J.; Ren, Z.; Qin, L.-C.; Hall, A. R. *Nanotechnology* **2011,** *22,* 285310. doi:10.1088/0957-4484/22/28/285310
157. Hall, A. R. *Microsc. Today* **2012,** *20* (5), 24–29. doi:10.1017/s1551929512000703
158. Xia, D.; Huynh, C.; McVey, S.; Kobler, A.; Stern, L.; Yuan, Z.; Ling, X. S. *Nanoscale* **2018,** *10,* 5198–5204. doi:10.1039/c7nr08406d
159. Zahid, O. K.; Hall, A. R. Helium Ion Microscope Fabrication of Solid-State Nanopore Devices for Biomolecule Analysis. In *Helium Ion Microscopy;* Hlawacek, G.; Gölzhäuser, A., Eds.; Springer International Publishing: Cham, Switzerland, 2016; pp 447–470. doi:10.1007/978-3-319-41990-9_18
160. Wu, H.; Chen, Y.; Zhou, Q.; Wang, R.; Xia, B.; Ma, D.; Luo, K.; Liu, Q. *Anal. Chem. (Washington, DC, U. S.)* **2016,** *88,* 2502–2510. doi:10.1021/acs.analchem.5b04905
161. Hall, A. R. *Microsc. Microanal.* **2013,** *19,* 740–744. doi:10.1017/s1431927613000500
162. Sawafta, F.; Carlsen, A. T.; Hall, A. R. *Sensors* **2014,** *14,* 8150–8161. doi:10.3390/s140508150
163. Carlsen, A. T.; Briggs, K.; Hall, A. R.; Tabard-Cossa, V. *Nanotechnology* **2017,** *28,* 085304. doi:10.1088/1361-6528/aa564d
164. Emmrich, D.; Beyer, A.; Nadzeyka, A.; Bauerdick, S.; Meyer, J. C.; Kotakoski, J.; Gölzhäuser, A. *Appl. Phys. Lett.* **2016,** *108,* 163103. doi:10.1063/1.4947277
165. Shorubalko, I.; Choi, K.; Stiefel, M.; Park, H. G. *Beilstein J. Nanotechnol.* **2017,** *8,* 682–687. doi:10.3762/bjnano.8.73
166. Chen, D.; Qiao, R.; Xu, X.; Dong, W.; Wang, L.; Ma, R.; Liu, C.; Zhang, Z.; Wu, M.; Liu, L.; Bao, L.; Wang, H.-T.; Gao, P.; Liu, K.; Yu, D. *Nanoscale* **2019,** *11,* 4226–4230. doi:10.1039/c9nr00412b
167. Deng, Y.; Huang, Q.; Zhao, Y.; Zhou, D.; Ying, C.; Wang, D. *Nanotechnology* **2017,** *28,* 045302. doi:10.1088/1361-6528/28/4/045302
168. Liu, F.; Wang, Z.; Nakanao, S.; Ogawa, S.; Morita, Y.; Schmidt, M.; Haque, M.; Muruganathan, M.; Mizuta, H. *Micromachines* **2020,** *11,* 387. doi:10.3390/mi11040387

169. Wang, H.; Xie, W.; Wang, Y.; Zhu, J.; Liu, M.; Lu, W.; Deng, Y.; Wang, G.; Wang, D. *J. Vac. Sci. Technol., B: Nanotechnol. Microelectron.: Mater., Process ., Meas., Phenom.* **2018,** *36,* 011603. doi:10.1116/1.5001927
170. Yoon, K.; Rahnamoun, A.; Swett, J. L.; Iberi, V.; Cullen, D. A.; Vlassiouk, I. V.; Belianinov, A.; Jesse, S.; Sang, X.; Ovchinnikova, O. S.; Rondinone, A. J.; Unocic, R. R.; van Duin, A. C. T. *ACS Nano* **2016,** *10,* 8376–8384. doi:10.1021/acsnano.6b03036
171. Maguire, P.; Fox, D. S.; Zhou, Y.; Wang, Q.; O'Brien, M.; Jadwiszczak, J.; Cullen, C. P.; McManus, J.; Bateman, S.; McEvoy, N.; Duesberg, G. S.; Zhang, H. *Phys. Rev. B* **2018,** *98,* 134109. doi:10.1103/physrevb.98.134109
172. Liu, J.; Jin, L.; Allen, F. I.; Gao, Y.; Ci, P.; Kang, F.; Wu, J. *Nano Lett.* **2021,** *21,* 2183–2190. doi:10.1021/acs.nanolett.0c04989
173. Yang, C.-W.; Chen, W.-C.; Chou, C.; Lin, H.-H. *J. Cryst. Growth* **2017,** *484,* 56–63. doi:10.1016/j.jcrysgro.2017.12.029
174. Scholder, O.; Jefimovs, K.; Shorubalko, I.; Hafner, C.; Sennhauser, U.; Bona, G.-L. *Nanotechnology* **2013,** *24,* 395301. doi:10.1088/0957-4484/24/39/395301
175. Wang, Y.; Abb, M.; Boden, S. A.; Aizpurua, J.; de Groot, C. H.; Muskens, O. L. *Nano Lett.* **2013,** *13,* 5647–5653. doi:10.1021/nl403316z
176. Black, L.-J.; Wang, Y.; Abb, M.; Boden, S. A.; de Groot, C. H.; Arbouet, A.; Muskens, O. L. New plasmonic materials and fabrication tools for near- and mid-infrared sensing and spectroscopy. In *Chemical, Biological, Radiological, Nuclear, and Explosives (CBRNE) Sensing XVI,* International Society for Optics and Photonics, 2015; 94550K. doi:10.1117/12.2181668
177. Kollmann, H.; Piao, X.; Esmann, M.; Becker, S. F.; Hou, D.; Huynh, C.; Kautschor, L.-O.; Bösker, G.; Vieker, H.; Beyer, A.; Gölzhäuser, A.; Park, N.; Vogelgesang, R.; Silies, M.; Lienau, C. *Nano Lett.* **2014,** *14,* 4778–4784. doi:10.1021/nl5019589
178. Melli, M.; Polyakov, A.; Gargas, D.; Huynh, C.; Scipioni, L.; Bao, W.; Ogletree, D. F.; Schuck, P. J.; Cabrini, S.; Weber-Bargioni, A. *Nano Lett.* **2013,** *13,* 2687–2691. doi:10.1021/nl400844a
179. Zhang, C.; Li, J.; Belianinov, A.; Ma, Z.; Renshaw, C. K.; Gelfand, R. M. *Nanotechnology* **2020,** *31,* 465302. doi:10.1088/1361-6528/abae99
180. Gittinger, M.; Höflich, K.; Smirnov, V.; Kollmann, H.; Lienau, C.; Silies, M. *Nanophotonics* **2020,** *9,* 401–412. doi:10.1515/nanoph-2019-0379
181. Laible, F.; Dreser, C.; Kern, D. P.; Fleischer, M. *Nanotechnology* **2019,** *30,* 235302. doi:10.1088/1361-6528/ab0506
182. Singh, K.; Panchenko, E.; Nasr, B.; Liu, A.; Wesemann, L.; Davis, T. J.; Roberts, A. *Beilstein J. Nanotechnol.* **2018,** *9,* 1491–1500. doi:10.3762/bjnano.9.140
183. Semple, M.; Baladi, E.; Iyer, A. K. *IEEE J. Sel. Top. Quantum Electron.* **2019,** *25,* 1–8. doi:10.1109/jstqe.2019.2896277
184. Chen, K.; Razinskas, G.; Vieker, H.; Gross, H.; Wu, X.; Beyer, A.; Gölzhäuser, A.; Hecht, B. *Nanoscale* **2018,** *10,* 17148–17155. doi:10.1039/c8nr02160k
185. Chen, Y.; Xiang, Q.; Li, Z.; Wang, Y.; Meng, Y.; Duan, H. *Nano Lett.* **2016,** *16,* 3253–3259. doi:10.1021/acs.nanolett.6b00788
186. Chen, Y.; Bi, K.; Wang, Q.; Zheng, M.; Liu, Q.; Han, Y.; Yang, J.; Chang, S.; Zhang, G.; Duan, H. *ACS Nano* **2016,** *10,* 11228–11236. doi:10.1021/acsnano.6b06290
187. Smirnov, V.; Stephan, S.; Westphal, M.; Emmrich, D.; Beyer, A.; Gölzhäuser, A.; Lienau, C.; Silies, M. *ACS Photonics* **2021,** *8,* 832–840. doi:10.1021/acsphotonics.0c01797
188. Grant-Jacob, J. A.; Zin Oo, S.; Carpignano, F.; Boden, S. A.; Brocklesby, W. S.; Charlton, M. D. B.; Melvin, T. *Nanotechnology* **2016,** *27,* 065302. doi:10.1088/0957-4484/27/6/065302
189. Oo, S. Z.; Silva, G.; Carpignano, F.; Noual, A.; Pechstedt, K.; Mateos, L.; Grant-Jacob, J. A.; Brocklesby, B.; Horak, P.; Charlton, M.; Boden, S. A.; Melvin, T. *Sens. Bio-Sens. Res.* **2016,** *7,* 133–140. doi:10.1016/j.sbsr.2016.01.001
190. Archanjo, B. S.; Vasconcelos, T. L.; Oliveira, B. S.; Song, C.; Allen, F. I.; Achete, C. A.; Ercius, P. *ACS Photonics* **2018,** *5,* 2834–2842. doi:10.1021/acsphotonics.8b00125
191. Scipioni, L.; Ferranti, D. C.; Smentkowski, V. S.; Potyrailo, R. A. *J. Vac. Sci. Technol., B: Nanotechnol. Microelectron.: Mater., Process ., Meas., Phenom.* **2010,** *28,* C6P18. doi:10.1116/1.3517514
192. Alkemade, P. F. A.; van Veldhoven, E. Deposition, Milling, and Etching with a Focused Helium Ion Beam. In *Nanofabrication: Techniques and Principles;* Stepanova, M.; Dew, S., Eds.; Springer Vienna: Vienna, Austria, 2012; pp 275–300. doi:10.1007/978-3-7091-0424-8_11
193. Ananth, M.; Stern, L.; Ferranti, D.; Huynh, C.; Notte, J.; Scipioni, L.; Sanford, C.; Thompson, B. Creating nanohole arrays with the helium ion microscope. In *Scanning Microscopies 2011: Advanced Microscopy Technologies for Defense, Homeland Security, Forensic, Life, Environmental, and Industrial Sciences,* International Society for Optics and Photonics, 2011; 80360M. doi:10.1117/12.887497
194. Xia, D.; Zhu, X.; Khanom, F.; Runt, D. *Nanotechnology* **2020,** *31,* 475301. doi:10.1088/1361-6528/abafd6
195. Xia, D.; Jiang, Y.-B.; Notte, J.; Runt, D. *Appl. Surf. Sci.* **2021,** *538,* 147922. doi:10.1016/j.apsusc.2020.147922
196. Timilsina, R.; Tan, S.; Livengood, R.; Rack, P. D. *Nanotechnology* **2014,** *25,* 485704. doi:10.1088/0957-4484/25/48/485704
197. Pekin, T. C.; Allen, F. I.; Minor, A. M. J. *J. Microsc. (Oxford, U. K.)* **2016,** *264,* 59–63. doi:10.1111/jmi.12416
198. El-Atwani, O.; Huynh, C.; Norris, S. *Appl. Surf. Sci.* **2016,** *370,* 557–564. doi:10.1016/j.apsusc.2016.02.109
199. Wu, H.; Ferranti, D.; Stern, L. *Microelectron. Reliab.* **2014,** *54,* 1779–1784. doi:10.1016/j.microrel.2014.08.003
200. Timilsina, R.; Rack, P. D. *Nanotechnology* **2013,** *24,* 495303. doi:10.1088/0957-4484/24/49/495303
201. Mahady, K.; Tan, S.; Greenzweig, Y.; Livengood, R.; Raveh, A.; Rack, P. *Nanotechnology* **2017,** *28,* 045305. doi:10.1088/1361-6528/28/4/045305
202. Mahady, K. T.; Tan, S.; Greenzweig, Y.; Raveh, A.; Rack, P. D. *Nanotechnology* **2018,** *29,* 495301. doi:10.1088/1361-6528/aae183
203. Burnett, J.; Sagar, J.; Kennedy, O. W.; Warburton, P. A.; Fenton, J. C. *Phys. Rev. Appl.* **2017,** *8,* 014039. doi:10.1103/physrevapplied.8.014039
204. Kennedy, O. W.; Burnett, J.; Fenton, J. C.; Constantino, N. G. N.; Warburton, P. A.; Morton, J. J. L.; Dupont-Ferrier, E. *Phys. Rev. Appl.* **2019,** *11,* 014006. doi:10.1103/physrevapplied.11.014006
205. Potter, J. A.; Kennedy, O. W.; Fenton, J. C.; Warburton, P. A. *IEEE Trans. Appl. Supercond.* **2020,** *30,* 1100704. doi:10.1109/tasc.2020.3018545
206. Hong, J.; Hadjikhani, A.; Stone, M.; Allen, F. I.; Safonov, V.; Liang, P.; Bokor, J.; Khizroev, S. *IEEE Trans. Magn.* **2016,** *52,* 1–4. doi:10.1109/tmag.2016.2530622

207. Rudneva, M.; van Veldhoven, E.; Malladi, S. K.; Maas, D.; Zandbergen, H. W. *J. Mater. Res.* **2013,** *28,* 1013–1020. doi:10.1557/jmr.2013.30
208. Stanford, M. G.; Lewis, B. B.; Iberi, V.; Fowlkes, J. D.; Tan, S.; Livengood, R.; Rack, P. D. *Small* **2016,** *12,* 1779–1787. doi:10.1002/smll.201503680
209. Stanford, M. G.; Pudasaini, P. R.; Cross, N.; Mahady, K.; Hoffman, A. N.; Mandrus, D. G.; Duscher, G.; Chisholm, M. F.; Rack, P. D. *Small Methods* **2017,** *1,* 1600060. doi:10.1002/smtd.201600060
210. Mahady, K. T.; Tan, S.; Greenzweig, Y.; Raveh, A.; Rack, P. D. *Nanoscale Adv.* **2019,** *1,* 3584–3596. doi:10.1039/c9na00390h
211. Xia, D.; McVey, S.; Huynh, C.; Kuehn, W. *ACS Appl. Mater. Interfaces* **2019,** *11,* 5509–5516. doi:10.1021/acsami.8b18083
212. Hang, S.; Moktadir, Z.; Mizuta, H. *Carbon* **2014,** *72,* 233–241. doi:10.1016/j.carbon.2014.01.071
213. Unocic, K. A.; Mills, M. J.; Daehn, G. S. *J. Microsc. (Oxford, U. K.)* **2010,** *240,* 227–238. doi:10.1111/j.1365-2818.2010.03401.x
214. Reiner, J. C.; Nellen, P.; Sennhauser, U. *Microelectron. Reliab.* **2004,** *44,* 1583–1588. doi:10.1016/j.microrel.2004.07.073
215. Fox, D.; Chen, Y.; Faulkner, C. C.; Zhang, H. *Beilstein J. Nanotechnol.* **2012,** *3,* 579–585. doi:10.3762/bjnano.3.67
216. Allen, F.; Notte, J.; Xia, D.; Blanchard, P.; Zhang, R.; Minor, A.; Sanford, N. *Microsc. Microanal.* **2020,** *26,* 184. doi:10.1017/s1431927620013719
217. Best, J. P.; Zechner, J.; Shorubalko, I.; Oboňa, J. V.; Wehrs, J.; Morstein, M.; Michler, J. *Scr. Mater.* **2016,** *112,* 71–74. doi:10.1016/j.scriptamat.2015.09.014
218. Xu, X.; Heinig, K.-H.; Möller, W.; Engelmann, H.-J.; Klingner, N.; Gharbi, A.; Tiron, R.; von Borany, J.; Hlawacek, G. *Semicond. Sci. Technol.* **2019,** *35,* 015021. doi:10.1088/1361-6641/ab57ba
219. Alkemade, P. F. A.; Miro, H. *Appl. Phys. A: Mater. Sci. Process.* **2014,** *117,* 1727–1747. doi:10.1007/s00339-014-8763-y
220. Utke, I.; Hoffmann, P.; Melngailis, J. *J. Vac. Sci. Technol., B: Microelectron. Nanometer Struct.–Process., Meas., Phenom.* **2008,** *26,* 1197–1276. doi:10.1116/1.2955728
221. Sanford, C. A.; Stern, L.; Barriss, L.; Farkas, L.; DiManna, M.; Mello, R.; Maas, D. J.; Alkemade, P. F. A. *J. Vac. Sci. Technol., B: Microelectron. Nanometer Struct.–Process., Meas., Phenom.* **2009,** *27,* 2660–2667. doi:10.1116/1.3237095
222. Drezner, Y.; Greenzweig, Y.; Fishman, D.; van Veldhoven, E.; Maas, D. J.; Raveh, A.; Livengood, R. H. *J. Vac. Sci. Technol., B: Nanotechnol. Microelectron.: Mater., Process., Meas., Phenom.* **2012,** *30,* 041210. doi:10.1116/1.4732074
223. Boden, S. A.; Moktadir, Z.; Bagnall, D. M.; Mizuta, H.; Rutt, H. N. *Microelectron. Eng.* **2011,** *88,* 2452–2455. doi:10.1016/j.mee.2010.11.041
224. Chen, P.; van Veldhoven, E.; Sanford, C. A.; Salemink, H. W. M.; Maas, D. J.; Smith, D. A.; Rack, P. D.; Alkemade, P. F. A. *Nanotechnology* **2010,** *21,* 455302. doi:10.1088/0957-4484/21/45/455302
225. Hill, R.; Faridur Rahman, F. H. M. *Nucl. Instrum. Methods Phys. Res., Sect. A* **2011,** *645,* 96–101. doi:10.1016/j.nima.2010.12.123
226. Córdoba, R.; Ibarra, A.; Mailly, D.; De Teresa, J. M. *Nano Lett.* **2018,** *18,* 1379–1386. doi:10.1021/acs.nanolett.7b05103
227. Alkemade, P. F. A.; Chen, P.; van Veldhoven, E.; Maas, D. *J. Vac. Sci. Technol., B: Nanotechnol. Microelectron.: Mater., Process., Meas., Phenom.* **2010,** *28,* C6F22. doi:10.1116/1.3517536
228. Smith, D. A.; Joy, D. C.; Rack, P. D. *Nanotechnology* **2010,** *21,* 175302. doi:10.1088/0957-4484/21/17/175302
229. Alkemade, P. F. A.; Miro, H.; van Veldhoven, E.; Maas, D. J.; Smith, D. A.; Rack, P. D. *J. Vac. Sci. Technol., B: Nanotechnol. Microelectron.: Mater., Process., Meas., Phenom.* **2011,** *29,* 06FG05. doi:10.1116/1.3656347
230. Maas, D.; van Veldhoven, E.; Chen, P.; Sidorkin, V.; Salemink, H.; van der Drift, E.; Alkemade, P. Nanofabrication with a helium ion microscope. In *Metrology, Inspection, and Process Control for Microlithography XXIV,* International Society for Optics and Photonics, 2010; p 763814. doi:10.1117/12.862438
231. Hayashida, M.; Iijima, T.; Fujimoto, T.; Ogawa, S. *Micron* **2012,** *43,* 992–995. doi:10.1016/j.micron.2012.03.012
232. Scipioni, L.; Sanford, C.; van Veldhoven, E.; Maas, D. *Microsc. Today* **2011,** *19* (3), 22–26. doi:10.1017/s1551929511000307
233. Wu, H.; Stern, L. A.; Xia, D.; Ferranti, D.; Thompson, B.; Klein, K. L.; Gonzalez, C. M.; Rack, P. D. *J. Mater. Sci.: Mater. Electron.* **2014,** *25,* 587–595. doi:10.1007/s10854-013-1522-6
234. Orús, P.; Córdoba, R.; Hlawacek, G.; De Teresa, J. M. *Nanotechnology* **2021,** *32,* 085301. doi:10.1088/1361-6528/abc91c
235. Alkemade, P. F. A.; Koster, E. M.; van Veldhoven, E.; Maas, D. J. *Scanning* **2012,** *34,* 90–100. doi:10.1002/sca.21009
236. Nanda, G.; van Veldhoven, E.; Maas, D.; Sadeghian, H.; Alkemade, P. F. A. *J. Vac. Sci. Technol., B: Nanotechnol. Microelectron.: Mater., Process., Meas., Phenom.* **2015,** *33,* 06F503. doi:10.1116/1.4936068
237. Timilsina, R.; Smith, D. A.; Rack, P. D. *Nanotechnology* **2013,** *24,* 115302. doi:10.1088/0957-4484/24/11/115302
238. Kohama, K.; Iijima, T.; Hayashida, M.; Ogawa, S. *J. Vac. Sci. Technol., B: Nanotechnol. Microelectron.: Mater., Process., Meas., Phenom.* **2013,** *31,* 031802. doi:10.1116/1.4800983
239. Wu, H. M.; Stern, L. A.; Chen, J. H.; Huth, M.; Schwalb, C. H.; Winhold, M.; Porrati, F.; Gonzalez, C. M.; Timilsina, R.; Rack, P. D. *Nanotechnology* **2013,** *24,* 175302. doi:10.1088/0957-4484/24/17/175302
240. Ievlev, A. V.; Jakowski, J.; Burch, M. J.; Iberi, V.; Hysmith, H.; Joy, D. C.; Sumpter, B. G.; Belianinov, A.; Unocic, R. R.; Ovchinnikova, O. S. *Nanoscale* **2017,** *9,* 12949–12956. doi:10.1039/c7nr04417h
241. Allen, F. I. *Micromachines* **2021,** *12,* 232. doi:10.3390/mi12030232
242. Hayashida, M.; Iijima, T.; Tsukahara, M.; Ogawa, S. *Micron* **2013,** *50,* 29–34. doi:10.1016/j.micron.2013.04.002
243. Córdoba, R.; Ibarra, A.; Mailly, D.; Guillamón, I.; Suderow, H.; De Teresa, J. M. *Beilstein J. Nanotechnol.* **2020,** *11,* 1198–1206. doi:10.3762/bjnano.11.104
244. Córdoba, R.; Mailly, D.; Rezaev, R. O.; Smirnova, E. I.; Schmidt, O. G.; Fomin, V. M.; Zeitler, U.; Guillamón, I.; Suderow, H.; De Teresa, J. M. *Nano Lett.* **2019,** *19,* 8597–8604. doi:10.1021/acs.nanolett.9b03153
245. Belianinov, A.; Burch, M. J.; Ievlev, A.; Kim, S.; Stanford, M. G.; Mahady, K.; Lewis, B. B.; Fowlkes, J. D.; Rack, P. D.; Ovchinnikova, O. S. *Micromachines* **2020,** *11,* 527. doi:10.3390/mi11050527
246. Kohama, K.; Iijima, T.; Hayashida, M.; Ogawa, S. Beam-substrate interaction during tungsten deposition by helium ion microscope. In *2013 IEEE International Interconnect Technology Conference - IITC,* IEEE, 2013; pp 1–3. doi:10.1109/iitc.2013.6615576
247. Yang, P.-S.; Huang, Z.-d.; Huang, K.-W.; Chen, M.-J. *Ultramicroscopy* **2020,** *211,* 112952. doi:10.1016/j.ultramic.2020.112952

248. Onishi, K.; Guo, H.; Nagano, S.; Fujita, D. *Microscopy (Oxford, U. K.)* **2014,** *63* (Suppl. 1), i30. doi:10.1093/jmicro/dfu075
249. Basset, J.; Watfa, D.; Aiello, G.; Féchant, M.; Morvan, A.; Estève, J.; Gabelli, J.; Aprili, M.; Weil, R.; Kasumov, A.; Bouchiat, H.; Deblock, R. *Appl. Phys. Lett.* **2019,** *114,* 102601. doi:10.1063/1.5080925

License and Terms

BEILSTEIN JOURNAL OF NANOTECHNOLOGY

Is the Ne operation of the helium ion microscope suitable for electron backscatter diffraction sample preparation?

Annalena Wolff

Full Research Paper

Open Access

Address:
Central Analytical Research Facility, Institute for Future Environments, Queensland University of Technology, 2 George St, Brisbane 4000, QLD, Australia

Email:
Annalena Wolff - Annalena.wolff@qut.edu.au

Keywords:
electron backscatter diffraction (EBSD); Ga; helium ion microscope (HIM); ion polishing; Ne

Beilstein J. Nanotechnol. **2021,** *12,* 965–983.
https://doi.org/10.3762/bjnano.12.73

Received: 04 January 2021
Accepted: 21 June 2021
Published: 31 August 2021

This article is part of the thematic issue "Ten years of the helium ion microscope".

Associate Editor: A. Gölzhäuser

Abstract

Electron backscatter diffraction (EBSD) is a powerful characterization technique which allows the study of microstructure, grain size, and orientation as well as strain of a crystallographic sample. In addition, the technique can be used for phase analysis. A mirror-flat sample surface is required for this analysis technique and different polishing approaches have been used over the years. A commonly used approach is the focused ion beam (FIB) polishing. Unfortunately, artefacts that can be easily induced by Ga FIB polishing approaches are seldom published. This work aims to provide a better understanding of the underlying causes for artefact formation and to assess if the helium ion microscope is better suited to achieve the required mirror-flat sample surface when operating the ion source with Ne instead of He. Copper was chosen as a test material and polished using Ga and Ne ions with different ion energies as well as incident angles. The results show that crystal structure alterations and, in some instances, phase transformation of Cu to Cu_3Ga occurred when polishing with Ga ions. Polishing with high-energy Ne ions at a glancing angle maintains the crystal structure and significantly improves indexing in EBSD measurements. By milling down to a depth equaling the depth of the interaction volume, a steady-state condition of ion impurity concentration and number of induced defects is reached. The EBSD measurements and Monte Carlo simulations indicate that when this steady-state condition is reached more quickly, which can be achieved using high-energy Ne ions at a glancing incidence, then the overall damage to the specimen is reduced.

Introduction

The helium ion microscope (HIM) has sparked interest in many disciplines since its commercial release in the first decade of the 21st century [1]. From its beginnings as primarily an imaging tool [2-9] it was established as a key tool in nanofabrication [10-15], defect engineering [16,17], and recently for material analysis [18,19]. The extended range of applications in which the second-generation HIM (Orion Nanofab) is used for nowadays is supported by using up to three different ion species (He,

Ne, and Ga). The versatility in its application can be understood when considering ion–solid interactions which occur when an energetic ion interacts with a specimen. An overview of the different interaction types is illustrated in Figure 1. The ions, irrespective of the ion species, interact with the sample atoms via nuclear and electronic interactions. The electronic interactions lead to secondary electron emission and polymerization while the nuclear interactions lead to sputtering, sample atom displacements, replacement collisions, vacancy formation, and a collision cascade as well as backscattered ions, secondary ion emission, and ion implantation. A more detailed description of ion–solid interactions can be found in [20,21]. The difference between different ion species, energies, and incident angles lies in the statistics of the ion–solid interactions and determines the application space for ion species. Higher energy (25–30 keV) He ions predominantly interact via electronic interactions while Ga ions of the same energy predominantly interact via nuclear interactions, making the latter an ideal candidate for sputtering applications. Neon interacts almost equally via electronic and nuclear interactions at those energies and allows for fast material removal per incident ion. As an inert ion species, neon has been proven advantageous for processing semiconducting materials in which Ga induces sample alterations and material behavior changes due to doping [22]. Not all nuclear interactions lead to sputtering. If the sample atom cannot be removed from the sample because of insufficient energy transfer or because the sample atom cannot exit the sample due to its sub-surface position, defects such as interstitials or vacancies can be created [23]. This can induce a significant amount of crystal structure alterations in a sample and thus artefacts. While these artefacts are well recognized for transmission electron microscopy (TEM) lamella preparation, in which the lamella preparation steps are designed to reduce the thickness of the amorphous layer on each side of the TEM lamella and to minimize artefacts [24], procedures and induced artefacts for other techniques such as electron backscatter diffraction (EBSD) polishing are not well documented in the literature.

The work presented here looks at the ion-beam-induced artefacts when polishing copper for EBSD measurements for different ion species (Ga, Ne) as well as polishing protocols. EBSD is a characterization technique in scanning electron microscopes (SEMs) that allows for the study of microstructure, local texture, grain size and orientations, as well as the strain of crystalline samples [25]. A detailed overview of this technique can be found in [26]. EBSD can be used for phase identification, which makes it a powerful complementary technique to energy-dispersive X-ray spectroscopy (EDS) and wavelength dispersive spectroscopy (WDS). The sample surface is conventionally tilted to 70° for the measurement and the backscatter diffraction of the SEM beam electrons leads to the formation of

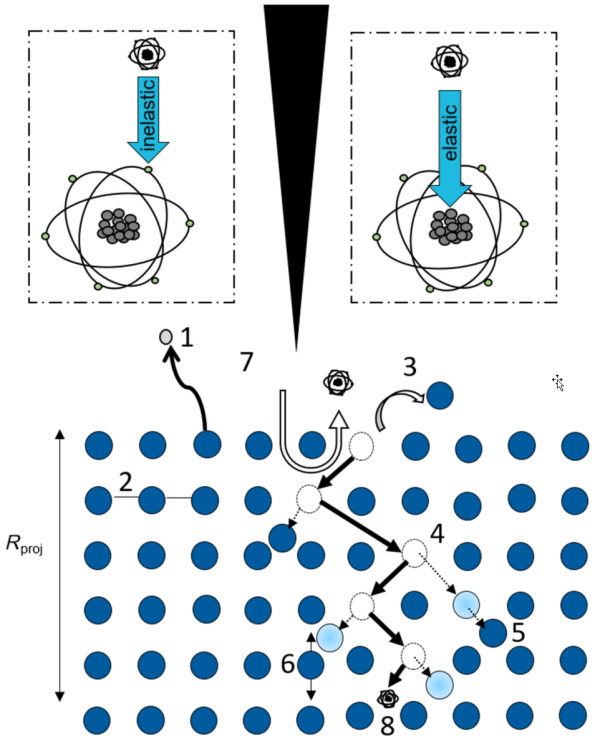

Figure 1: Illustration of the underlying ion–solid interactions that occur when irradiating a sample with different ion species. The incident ions (black) can interact via inelastic (top left inset) or elastic collisions (top right inset) with the sample atoms (blue). As a result of the inelastic interactions, secondary electrons (1) can be generated or polymerization (2) can occur. The elastic interactions can lead to sputtering (3), vacancy formation (4), displacements (5), phonons (6), backscattered ions (7), and ion implantation (8). The number of the different interactions created are given for different ion species when considering 10,000 incident ions impacting on a silicon sample. These numbers were obtained from SRIM simulations.

Kikuchi patterns on the EBSD phosphor screen which are characteristic of the crystal structure and orientation of the sample at the scan point. EBSD is a surface-sensitive technique and the signal comes from approximately the first 20 nm of the sample [27]. A thorough sample preparation and mirror-finished polish without inducing a significant number of artefacts in the sample top layer is, therefore, required for this technique.

Numerous sample preparation procedures exist to achieve the required mirror finish of the sample surface. Depending on the material, mechanical polishing [28], electropolishing [29], or ion polishing [30] are the key techniques. A thorough overview of the different EBSD preparation techniques can be found elsewhere [31]. Throughout the past years, Ga-focused ion beam/scanning electron microscopes (Ga FIB/SEMs) have been used to polish samples [32,33]. Although it is recognized within the FIB community that Ga can induce artefacts in the sample [34-37], many of the encountered artefacts, which can potentially lead to misinterpretation of the results, are unfortunately never

published. Besides the initial study by Michael [34], which showed that Ga ion polishing can phase transform Cu to Cu_3Ga as well as a follow up study investigating microtextural modifications in samples when using a Ga FIB [35], a recent study reported transformations of a crystal structure from hcp to fcc when polishing Ti with a FIB [38]. The work presented here looks at ion–solid interactions and aims to provide a better understanding of FIB polishing-induced artefacts. The work aims to assess if Ne is a more suitable ion species than Ga for EBSD sample preparation. Cu has been previously reported to phase transform under Ga FIB polishing and conventional Cu TEM grids are, therefore, used here as a test material and are polished using Ga and Ne ions of different energies, incident angles, and ion doses. Both normal and glancing angles are investigated, the former for completeness and to allow comparison to literature and the later since it is the conventionally used geometry for polishing. Changes in the crystal structure, which would lead to altered EBSD results, are assessed by EBSD measurements as well as by scanning transmission electron microscopy (STEM), TEM, TEM selected area electron diffraction (SAED), and TEM dark-field (DF) measurements. The results for each experiment are compared to those of a non-irradiated area of the Cu TEM grid. Monte Carlo simulations of the occurring ion–solid interactions are evaluated to determine the resulting interaction volume of the ions for the various conditions as well as vacancy formation and implanted impurity concentration. In addition, the achieved results are compared to those achieved by the conventionally used argon ion polishing (PIPS) and electropolishing approaches.

Results and Discussion

To assess the impact of polishing samples for EBSD with a focused ion beam, Cu TEM grids were polished using different ion species (Ga, Ne) at different energies and incidence angles. A schematic overview of the experiments is given in Figure 2. STEM, TEM, SAED, as well as EBSD measurements were performed to assess if and how the crystal structure of the sample was altered during different polishing procedures. For each sample, EBSD measurements were performed on the bulk specimen, thus the native Cu TEM grid serves as a true control sample. Thin foils of each specimen were then prepared using FIB for the TEM measurements. For each sample, the results were evaluated and compared to an unpolished area on the Cu TEM grids (control experiments). To ensure that the FIB TEM lamella preparation does not affect the TEM measurements of the crystal structure, TEM foils were additionally prepared using PIPS and electropolishing. The measurements and comparison of the FIB-prepared TEM lamella as well as the electropolished and PIPS-prepared thin foils are given in the Supporting Information File 6 and show that the FIB preparation of the thin foils for the TEM and STEM analysis did not produce artefacts that would compromise the TEM analysis. Monte Carlo simulations were performed using the program Stopping and Range of Ions in Matter (SRIM) to better understand the underpinning ion–solid interactions for the different settings [22]. The extent of created dislocations, vacancies as well as ion impurity concentration within the smaller of either the EBSD information depth (20 nm) or interaction volume depth are evaluated and correlated to the experiments.

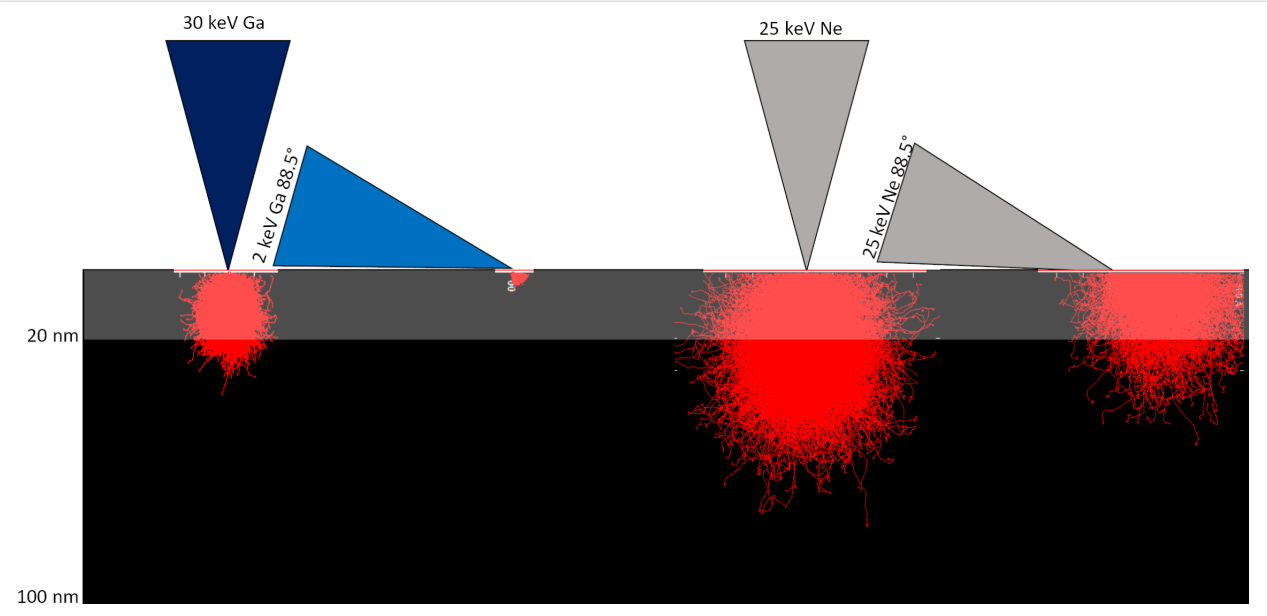

Figure 2: Illustration of the experimental polishing setup for the different ion species, ion energies, and incident angles. The experiments with Ga ions are displayed in blue on the left. The experiments using Ne ions are displayed in grey on the right. The EBSD signal depth is highlighted by the transparent rectangle. The SRIM-simulated ion trajectories for the different ion species, ion energies, and incident angles are shown in red.

Non-irradiated copper

To verify the original specimen structure, TEM electron diffraction on thin foils as well as EBSD measurements on the bulk Cu TEM grid sample were performed and the results analyzed. While the EBSD measurement of the non-irradiated copper shows the original sample crystal structure, and can be considered as a true control sample, the TEM thin foils were prepared using FIB.

The STEM (Figure 3a) measurements were taken in the Ga FIB/SEM and the TEM measurements (Figure 3b) were performed on the FIB-prepared thin TEM lamella to visualize the original grain structure on the sample surface. The corresponding SAED pattern is shown in Figure 3c. The SAED pattern was inverted for better visibility here. The angles α and β between the reflections were both measured to be 45° and the distance ratio of the reflections determined to be 1.4, suggesting a fcc crystal structure with [100] zone axis (ZA). The measured d-spacing for $d_{022,A}$ = 0.133 nm is in agreement with the reported d-spacing for Cu with d_{022} = 0.1278 nm according to the International Centre for Diffraction Data (ICDD, PDF number 00-004-0836). The measured d-spacing for $d_{002,B}$ = 0.192 nm is slightly larger than the reported value of $d_{002,Cu}$ = 0.181 nm for Cu; however, within an acceptable discrepancy. It is likely that the stamping process used to create TEM grids has induced this strain and the result is not unexpected.

An EBSD orientation map of the non-irradiated copper sample was recorded over a 39 µm field of view using a 39 nm step size on a sufficiently flat sample area for 14.5 h. 20% zero solutions we returned for that specific area. Most areas on the sample returned up to 80% zero solutions under the same conditions due to the roughness of the surface sample (see below Figure 7). The inverse pole figure (IPF X) is shown in Figure 3d. The band contrast and grain boundary map overlay is shown in Figure 3e. A statistical evaluation of the grain boundaries shows that ≈8% of the grain boundaries are low-angle grain boundaries (LAGB). These are displayed in yellow in Figure 3e. High-angle grain boundaries (HAGB) which are displayed in red in Figure 3e correspond to 92% of the grain boundaries. These values serve as reference values throughout the work against which the ion-irradiation-induced effects are evaluated. All values can be found in Table 1.

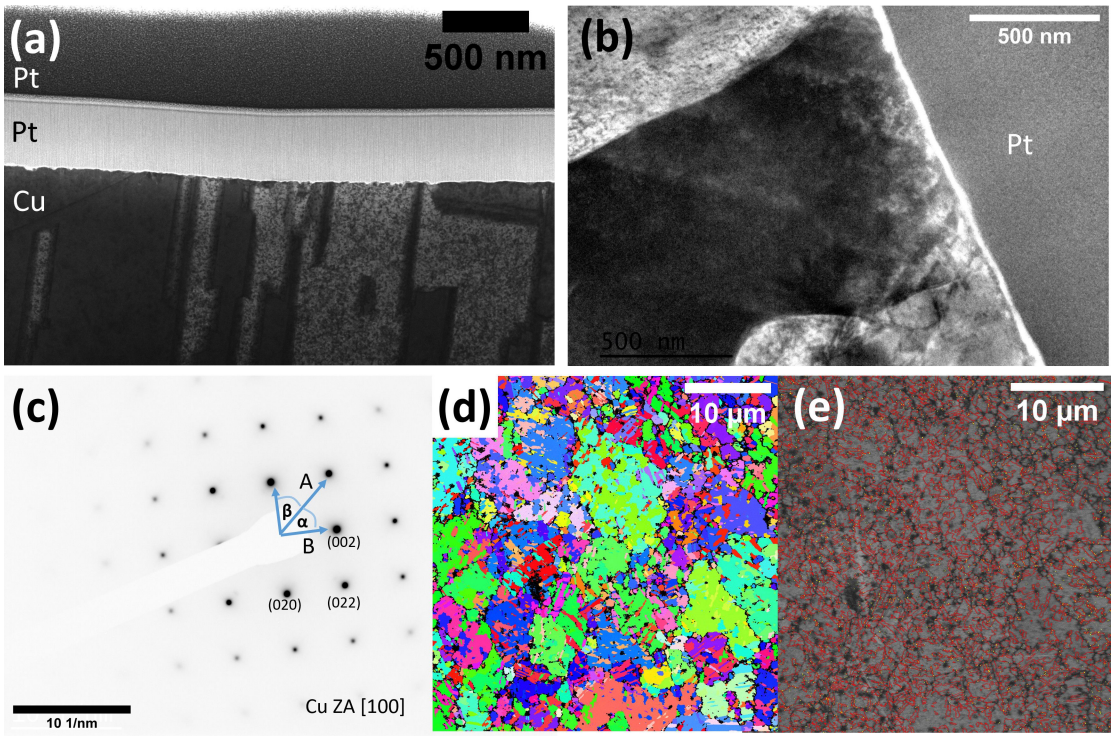

Figure 3: STEM, TEM, and EBSD measurements of an unpolished Cu control sample. (a) 30 kV STEM image showing a cross-sectional sample view of the Cu sample and the protective Pt-rich layers deposited with the ion beam and electron beam during TEM lamella preparation. (b) TEM image showing a cross-sectional sample view. (c) An inverted SAED pattern recorded underneath the sample surface. (d) IPF X EBSD orientation map. (e) Overlay of the band contrast and grain boundary map. HAGB are displayed in red, LAGB are displayed in yellow. The EBSD measurements were recorded on a sufficiently flat area.

Table 1: Summary of the results for different polishing experiments. The impurity concentration, sputtering yield (SY), Cu atom displacements, phase, high-angle grain boundaries and low-angle grain boundaries as well as the defect percentage determined from SRIM simulations, TEM, and EBSD measurements are given for different polishing experiments.

Polishing experiment	Impurity concentration	SY	Cu atom displacements	Phase	HAGB %	LAGB %
30 keV Ga 2247 and 3371 ions/nm^2	12–36%	10	138	Cu_3Ga	56	44
2 keV Ga 2247 ions/nm^2, glancing angle	100%	5	22	Cu_3Ga	83	17
25 keV Ne 2247 and 3371 ions/nm^2	100%	4	180–266	Cu	33	64
25 keV Ne 2247 ions/nm^2 glancing angle	12%	12	17	Cu	92	8
control experiment bulk non-irradiated	NA	NA	NA	Cu	92	8
10 s electropolished Cu	NA	NA	NA	Cu	61	39
PIPS	NA	—	NA	Cu	87	13

Non-irradiated copper: electropolishing and Ar ion polishing

To evaluate the effect of electropolishing and argon ion polishing on EBSD measurements, the Cu sample was polished using these conventional techniques. The measurements as well as the corresponding measurements for the unpolished control sample are given in Figure 4 to enable a direct comparison. While a significant reduction in zero solutions (4%) and thus a well-indexed EBSD map (Figure 4g) could be achieved by electropolishing the sample for 10 s, a higher number of LAGB (67%) were found in comparison to the control sample (Figure 4f). In addition, the kernel average misorientation (KAM) map,

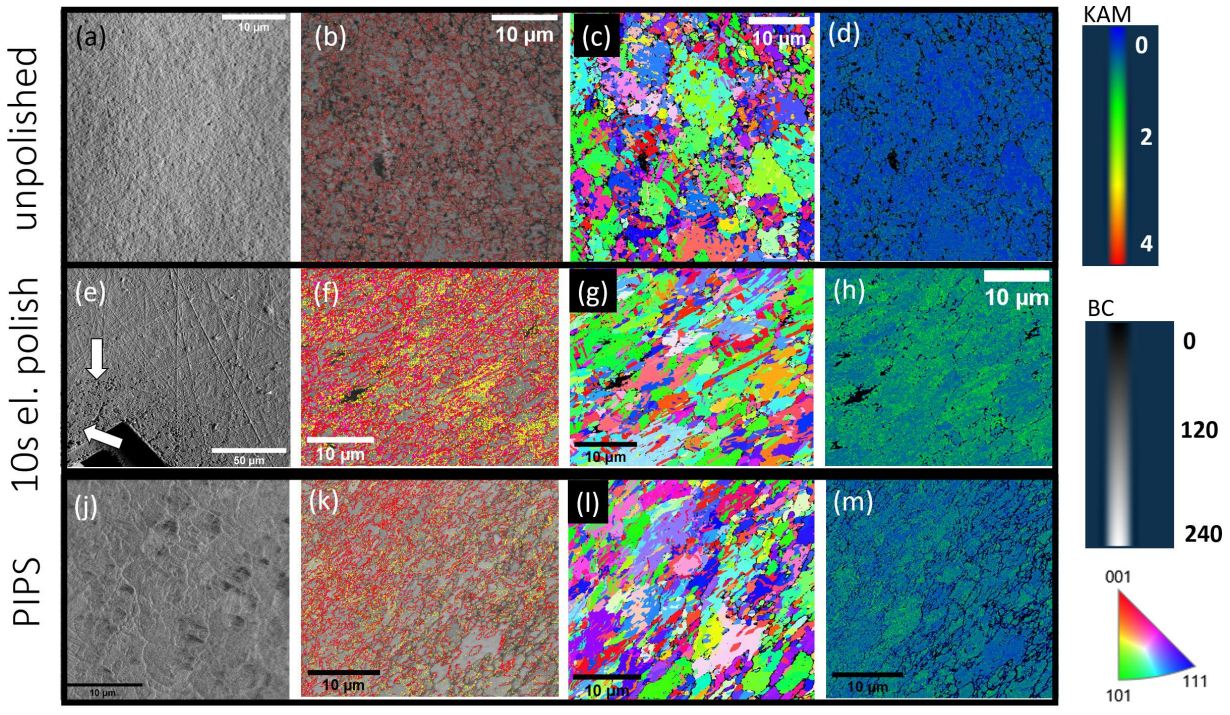

Figure 4: EBSD measurements of unpolished, electropolished, and low-energy Ar ion-polished Cu sample. Top row: sufficiently smooth area on an unpolished Cu sample. (a) FSD image showing the sample surface. (b) Overlay of the band contrast and grain boundary map. HAGB are displayed in red, LAGB are displayed in yellow. (c) IPF X EBSD orientation map. (d) KAM map. Blue indicates a lower kernel average misorientation, green corresponds to a higher kernel average misorientation. Middle row: 10 s electropolished Cu sample. (e) FSD image showing the sample surface. Surface alterations such as voids are highlighted by white arrows. (f) Overlay of the band contrast and grain boundary map. HAGB are displayed in red, LAGB are displayed in yellow. (g) IPF X EBSD orientation map. (h) KAM map. Blue indicates a lower kernel average misorientation, green corresponds to a higher kernel average misorientation. Bottom row: PIPS polished Cu sample. (j) FSD image showing the sample surface. (k) Overlay of the band contrast and grain boundary map. HAGB are displayed in red, LAGB are displayed in yellow. (l) IPF X EBSD orientation map. (m) KAM map. Blue indicates a lower kernel average misorientation, green corresponds to higher kernel average misorientation.

(shown in Figure 4h) shows a higher level of misorientation compared to the control sample. This suggests that the used electropolishing protocol induced some artefacts in this sample which could lead to misinterpretation for stress/strain analysis of the sample. The forward scatter diffraction (FSD) image (Figure 4e) shows void formation on the sample surface and significant sample surface alterations close to the area that was polished. These surface alterations become less severe at larger distances from the central polished area as evidenced in the top right corner of the FSD image. The results suggest that electropolishing yields well-indexed EBSD maps. However, the induced changes in the crystal structure make the used electropolishing protocol not feasible for stress and strain analysis of the Cu sample.

Argon ion polishing of the Cu sample produced better results than electropolishing. The FSD image (Figure 4j) reveals grains and does not show obvious sample surface alterations in comparison to the electropolishing approaches. While the number of LAGB with 17% in the grain boundary map (Figure 4k) is still slightly larger than that for the control experiment, it is lower than the observed number for electropolishing. The level of misorientation in the KAM maps (Figure 4m) is significantly reduced in comparison to the electropolishing KAM maps. However, it is still larger than that for the original control experiment suggesting that some changes to the crystal structure were induced by this polishing approach. While a well-indexed EBSD map (Figure 4l) could be recorded, the induced crystallographic artefacts could mean a challenging stress/strain analysis.

Irradiation of copper at 0° incidence angle

To assess the effect of ion irradiation, the copper TEM lamella grids were irradiated with Ga ions using a Ga FIB/SEM or Ne ions using HIM. An ion dose of 3371 ions/nm^2 was chosen to allow a comparison with a previously reported study on Ga-induced phase transformations in copper [34]. A lower ion dose (2247 ions/nm^2) was also evaluated as it corresponds to the dose that is achieved for commonly reported EBSD polishing time values over larger areas [39].

30 keV Ga ion irradiation at 0° incidence angle

The ion trajectory plot (Figure 2) obtained using SRIM shows that the interaction volume depth of the 30 keV Ga ions in Cu is ≈25 nm and is in the same range as the EBSD signal information depth of 20 nm. Throughout the interaction depth, 786 vacancies are created per incident ion while ten atoms are sputtered. The total number of induced defects and number of implanted ions is limited in FIBs that are optimized for patterning applications (such as Ga FIB/SEM or HIM when operated with Ne). The highest concentration of ion implantation and defects is reached once the sample has been milled down to a depth which corresponds to the interaction volume depth. This is referred to as the steady-state condition. The time it takes to mill the sample to that depth and until the steady-state condition is reached determines the maximal area of specific ion implantation concentration. The calculations presented here determine the upper limit since sputtered and backscattered ions are not considered here. To determine the time until this steady-state condition is reached when using 30 keV Ga ions at a frontal irradiation, the copper sample was milled for 3 min using a 0.3 nA beam current (1872 ions per 1 µs) and the milled depth was measured by TEM for different grains (see Supporting Information File 1). Both the TEM image and the FSD image, the latter is recorded with the EBSD detector and highlights the surface topography, show the different milling depths for different grains. Faster milling grains were milled to a 226 nm depth. The steady-state condition is reached after 20 s for those grains. A total of 3.8×10^{10} Ga ions will interact with the sample in that area during this time when irradiating a 100 µm^2 area. This is a significantly high number of implanted Ga atoms when considering that only 2.1×10^{11} Cu atoms are present within a volume determined by the interaction volume depth (≈25 nm) and the 100 µm^2 size of the irradiated area, corresponding to ≈18% of impurity concentration. The number of copper atoms within the volume was calculated using the copper mass density of 8.93×10^3 kg/m^3 and its atomic mass of 63.55 g/mol. For the slower milling grain, which only milled to a depth of 110 nm during the irradiation, the steady-state condition is reached significantly later within ≈40 s, allowing for up to 7.6×10^{10} Ga ions to be implanted in these grains. This corresponds to a 36% of impurity concentration and would be sufficiently high to form a Cu_3Ga phase. This value represents an average and does not take random elements of the Ga distribution into account. The simulation results suggest that phase transformations are not likely to occur homogeneously throughout the sample but rather are confined to grains with a lower sputtering rate. Both estimated concentration values are well within the published range of 1 to 50 atom % [40].

To experimentally assess the impact, the copper TEM grid was irradiated with 30 keV Ga ions at a 0° incident angle. Throughout the irradiation process changes in the ion image contrast occur with darker patches forming in the irradiated area in the ion channeling images. A detailed discussion on channeling contrast and the effect of grain orientation on milling speed can be found in [35]. The different stages of dark patch formation are shown in Figure 5a–c and a video of the occurring sample change is given in Supporting Information File 2. The patches appear to nucleate around the grain boundaries at the darker grains within the sample and then gradually increase in size and merge. The patches are highlighted with blue arrows in

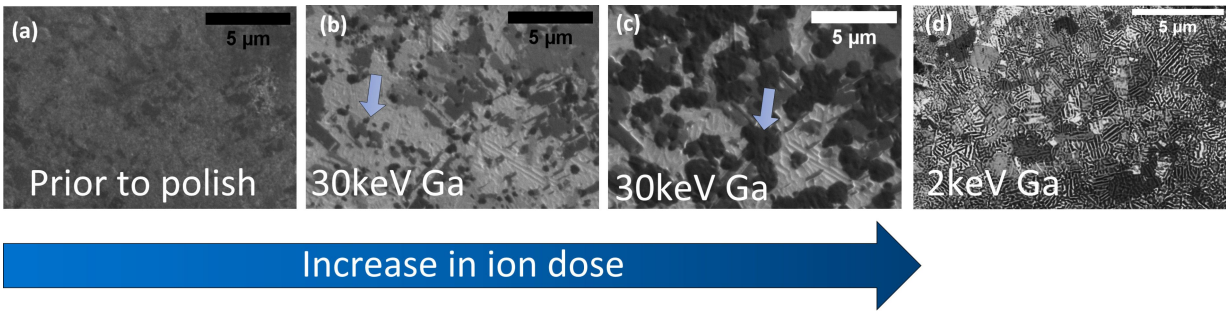

Figure 5: Ion channeling images showing the changes in ion channel contrast upon Ga irradiation. 30 keV Ga 0° incidence irradiation (a–c) as well as 2 keV Ga 88.5° incidence irradiation (d) are shown. (a) Start of the 30 keV Ga 0° incidence irradiation, (b) intermediate ion dose delivered, (c) irradiation dose of 3371 ions/nm^2 delivered. (d) 2 keV Ga 88.5° incidence irradiation with a delivered irradiation dose of 2247 ions/nm^2.

Figure 5b and Figure 5c. The darker grains are the slower milling grains [11] which can accumulate a higher Ga impurity concentration according to the calculations above. To verify this, EDS measurements (see Supporting Information File 3) were performed on a Ga irradiated area on slower and faster milling grains. These grains can easily be distinguished in SEM images due to their significant height differences. The Ga peak can be clearly identified in the measurements on the slower milling grain suggesting a significantly higher amount of incorporated Ga in those grains. A careful assessment of the ion channeling images and corresponding dose (see video Supporting Information File 2) suggests that significantly large dark patches are already present at an ion dose of 2247 ions/nm^2 which is below the previously reported ion dose of 3371 ions/nm^2 [24] (see Figure 5c). The impurity concentration for the slow milling grains is 25% when using this lower ion dose and would be sufficiently large to allow the formation of the Cu_3Ga phase.

To evaluate if a significant phase transformation and sample alteration occur at a lower ion dose than previously reported, the two different ion doses (2247 ions/nm^2 and 3371 ions/nm^2) were assessed individually and the results compared. TEM lamellae were prepared for irradiated areas and STEM, dark-field and bright-field measurements as well as TEM SAED measurements were performed to evaluate the crystal structure underneath the irradiated area. The corresponding measurements are shown in Figure 6a–h. The SAED patters are inverted for better visibility in both cases. For the lowest ion dose of 2247 ions/nm^2 (Figure 6e–h) the STEM measurements (Figure 6e) show a distinct layer of grains directly on the sample surface. This layer (highlighted by the blue arrows) is several hundreds of nanometers thick and significantly larger than the interaction volume. The TEM image (Figure 6f) shows a different behavior in comparison to the control sample, with more dislocations, defects, and precipitates (indicated by arrows) visible. The SAED pattern (Figure 6g) shows that the sample is crystalline. The angles between the reflections were determined to be $\alpha = 32°$ and $\beta = 58°$. The distance ratios between the reflections were determined to be $C/A = 1.6$ and $C/B = 1.89$ suggesting a hcp structure with [210] ZA (see Figure 6h for the simulated SAED pattern) or potentially a distorted fcc structure with $[\bar{1}12]$ ZA. The measured d-spacing values of $d_{hkl,A} = 0.135$ nm, $d_{hkl,B} = 0.114$ nm, $d_{hkl,C} = 0.215$ nm match the reported distances $d_{1\bar{2}0} = 0.130$ nm, $d_{1\bar{2}2} = 0.111$ nm, $d_{002} = 0.211$ nm for the Cu_3Ga phase (PDF number 04-020-0557) more closely than those reported for Cu ($d_{hkl} = 0.128$ nm, $d_{hkl} = 0.109$ nm, $d_{hkl} = 0.209$ nm). For a higher ion dose of 3371 ions/nm^2, the STEM measurements (Figure 6a) also show a layer of small grains directly underneath the irradiated surface which is distinctly different from the non-irradiated copper sample. TEM analysis (Figure 6b) of the irradiated sample shows many defects and precipitates. The defects and precipitates appear more pronounced for this higher ion dose experiment. The corresponding electron diffraction pattern is shown in Figure 6c. The angles between the reflections were determined to be $\alpha = 60°$. The distance ratios between the reflections were determined to be $A/B = 1$ suggesting a hcp structure with [001] ZA or a fcc structure with [111] ZA. The measured d-spacing of $d_{hkl,A} = 0.225$ nm, matches the reported d-spacing values of $d_{100} = 0.226$ nm for the Cu_3Ga phase. The simulated SAED pattern is shown in Figure 6d. It is distinctly different from those reported for Cu ($d_{2\bar{2}0} = 0.1278$ nm). This is in good agreement with previous reports [34].

To evaluate the effect on the EBSD measurements and to verify the Cu_3Ga phase with an additional independent technique, different areas were irradiated with the lowest and the highest ion dose and the EBSD orientation and phase maps were recorded and evaluated. The measurements and evaluations are shown in Figure 7a–c. The figure insets show the experiments with the

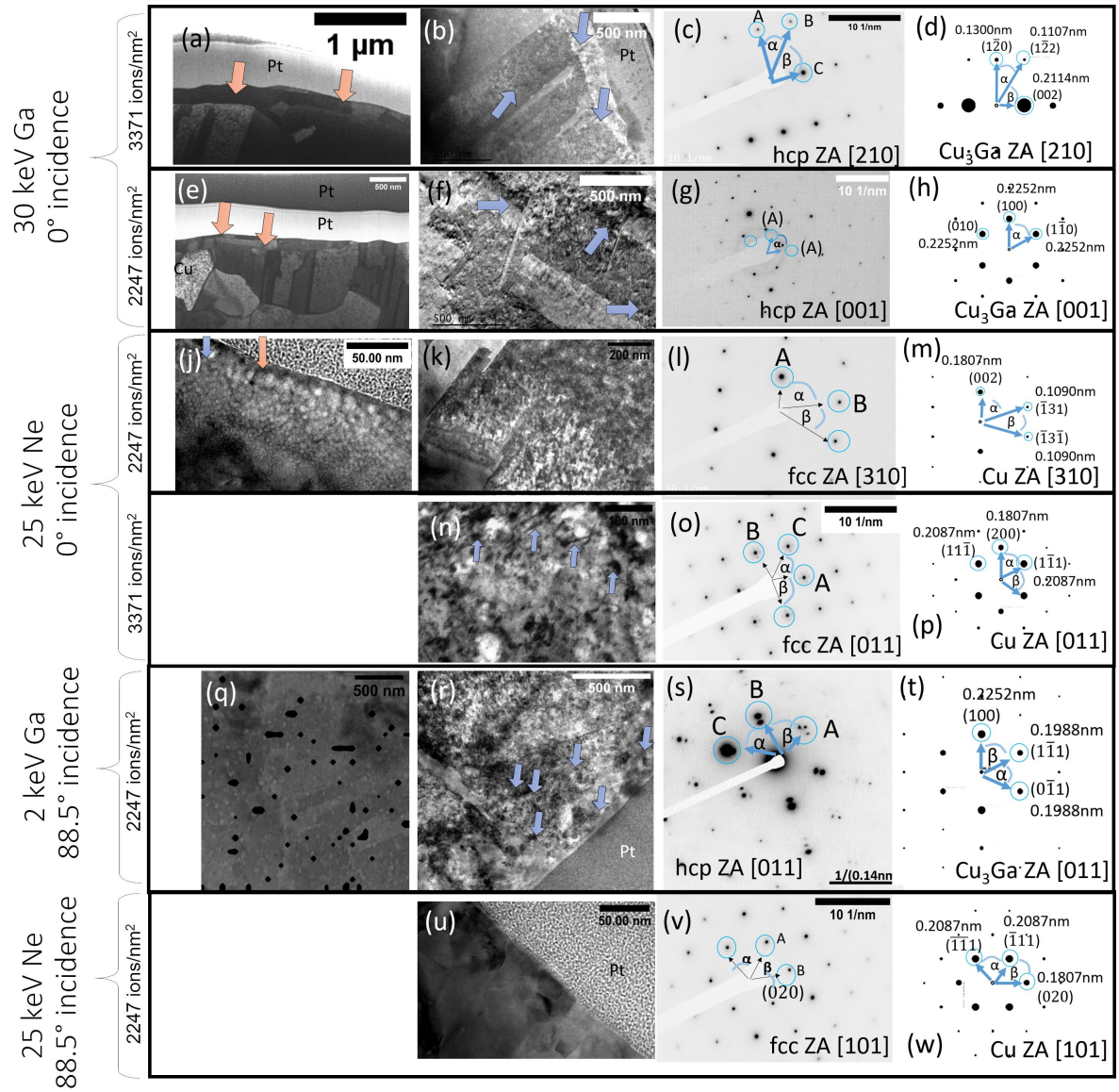

Figure 6: STEM, TEM, SAED, and simulated SAED patterns for the different ion irradiation approaches. (a–d) 30 keV Ga, 0° incidence irradiation, 3371 ions/nm^2 delivered. (a) STEM showing the cross-sectional view of the irradiated sample. The orange arrows indicate the presence of a thin grain layer present on the sample surface. (b) The blue arrows in the TEM image highlight defects and precipitates. (c) A SAED pattern. (d)The corresponding SAED pattern simulation. (e–h) 30 keV Ga, 0° incidence irradiation, 2247 ions/nm^2 delivered. (e) STEM showing the cross-sectional view of the irradiated sample. The orange arrows indicate the presence of a thin grain layer present on the sample surface. (f) The blue arrows in the TEM image highlight defects and precipitates. (g) A SAED pattern. (h) The corresponding SAED pattern simulation. (j–m) 25 keV Ne, 0° incidence irradiation, 2247 ions/nm^2 delivered. (j) A TEM image showing Ne bubble formation underneath the sample surface within the interaction volume. (k) A TEM image showing a cross-sectional sample view. Defects and precipitates are highlighted by blue arrows. (l) A SAED pattern of the irradiated area. (m) The corresponding SAED pattern simulation. (n–p) 25 keV Ne, 0° incidence irradiation with 3371 ions/nm^2 and 2247 ions/nm^2 doses. (n) A TEM image showing Ne bubble formation underneath the sample surface within the interaction volume. (o) A SAED pattern of the irradiated area. (p) The corresponding SAED pattern simulation. (q–t) 2 keV Ga, 88.5° incidence irradiation, 2247 ions/nm^2 delivered. (q) STEM DF measurement overlaid with 1σ thresholded Ga TruMap (black regions) showing the cross-sectional view. (r) TEM measurement of the irradiated area in a cross-sectional view. Defects and precipitates are highlighted by blue arrows. (s) A SAED pattern of the irradiated area. (t) The corresponding SAED pattern simulation. (u–w) 25 keV Ne, 88.5° incidence irradiation, 2247 ions/nm^2 delivered. (u) A TEM measurement showing the cross-section of the irradiated area. (v) A SAED pattern of the irradiated area. (w) The corresponding SAED pattern simulation.

lowest ion dose. The 0° incidence angle milling creates a strong surface topography in both cases, as evidenced in the forward scatter diffraction image (Figure 7a). Figure 7a shows an overlay of the FSD image with the phase map. A strong surface topography was expected as different grain orientations mill at different rates. As a result of the induced strong topography, a

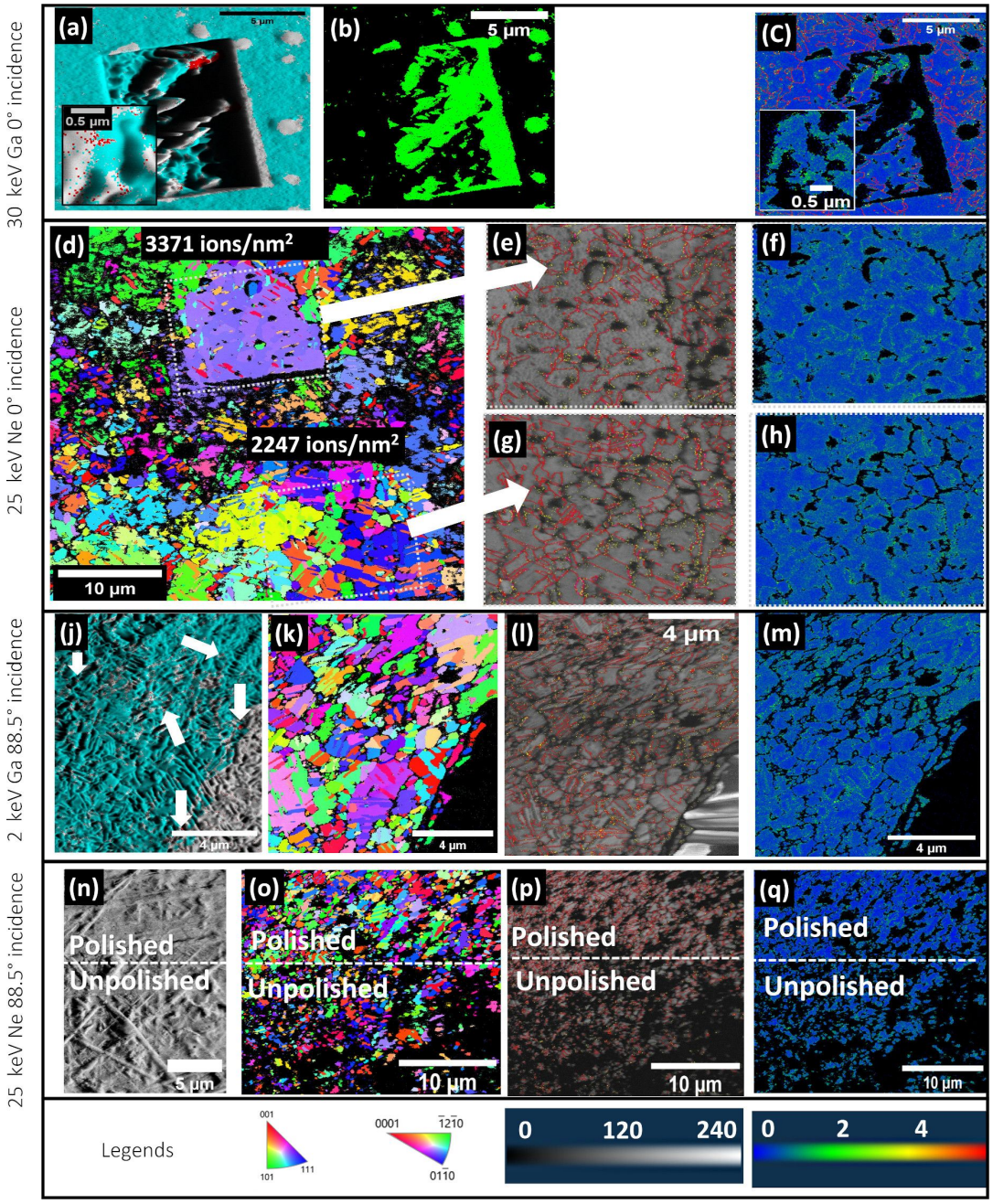

Figure 7: EBSD measurements and evaluation for different ion irradiation approaches. (a–c) 30 keV Ga, 0° incidence irradiation: The main images correspond to the highest ion dose of 3371 ions/nm^2. The insets correspond to the lowest ion dose of 2247 ions/nm^2. (a) Forward scatter diffraction image overlaid with the phase map. Blue corresponds to Cu, red corresponds to the Cu_3Ga phase. (b) Zero solution map. The zero solutions are indicated by green points. (c) KAM map overlaid with the grain boundary map. Blue indicates a lower kernel average misorientation, green corresponds to a higher kernel average misorientation. HAGB are shown in red. LAGB are shown in yellow. (d–h) 25 keV Ne, 0° incidence irradiation with 3371 ions/nm^2 and 2247 ions/nm^2 doses. (d) IPF X orientation map showing two irradiated areas as well as the unpolished Cu sample surrounding the areas. (e,g) Band contrast and grain boundary maps. HAGB are displayed in red, LAGB are displayed in yellow for 3371 ions/nm^2 (e) and 2247 ions/nm^2 (g). (f,h) KAM maps for 3371 ions/nm^2 (f) and 2247 ions/nm^2 (h). A higher misorientation in both KAM maps is shown in green. (j–m) 2 keV Ga, 88.5° incidence irradiation with 2247 ions/nm^2: EBSD and ion channeling measurements of 2 keV Ga glancing angle irradiated area with 3371 ions/nm^2. (j) Overlay of an FSD image with a phase map. Blue corresponds to the Cu phase, red corresponds to the Cu_3Ga phase. (k) IPF X orientation map. (l) Band contrast and grain boundary map. HAGB are displayed in red, LAGB are displayed in yellow. (m) KAM map, green shows higher misorientation. (n–q) 25 keV Ne, 88.5° incidence irradiation with 2247 ions/nm^2. (n) FSD image showing the polished and unpolished sample surface. (o) IPF X orientation map showing a polished and unpolished area on the sample. (p) Band contrast and grain boundary map of a polished as well as unpolished region on the sample. HAGB are displayed in red, LAGB are displayed in yellow. (q) KAM map of a polished as well as unpolished region on the sample. A higher kernel average misorientation is shown in green.

lot of the regions cannot be indexed, returning twice the amount of zero solutions for the pattern indexing when compared to an unpolished area close by on the sample. The extent of the zero solutions can be seen in Figure 7b where the areas of zero solutions are displayed in green. This effect is not surprising and the samples are rarely polished with a 0° incidence angle for this reason. The phase map (Figure 7a) clearly shows that both the copper (blue) as well as Cu_3Ga (red) phase are present within the irradiated area in both cases. The Cu_3Ga phase is located at topographically higher regions as evidenced in the overlay with the FSD. These regions mill at a reduced rate and the steady-state condition is reached later, allowing for a higher Ga impurity implantation concentration. The experimental result is in good agreement with the theoretical prediction from the Monte Carlo simulation and subsequent calculations. The Cu_3Ga phase-transformed regions are larger for the highest ion dose when compared to the lowest ion dose. This is expected as more ions were implanted in the overall sample during the polishing process for the highest ion dose when considering not a single grain but rather a multitude of grains, in which each one reaches the steady-state condition at different times. This result is in good agreement with the observed dark patch growth in the ion channeling images. The kernel average misorientation map and grain boundary map overlay (Figure 7c) shows a higher local misorientation and low-angle grain boundaries within the topographically higher regions, suggesting a higher number of defects and strain in those regions. A higher misorientation is represented by green areas in the KAM map. This result is in good agreement with the TEM measurements which also showed an increased defect density. The faster milling grains are indexed as the Cu phase. This was expected from the calculations as the maximal Ga implantation concentration is below the critical threshold required to phase transform to Cu_3Ga. The KAM and grain boundary evaluation do not show significant strain in these regions. The maximal number of defects and implantation concentration is lower for these faster milling grains as the steady-state condition is reached earlier and less defects are created.

The experiment shows that phase transformations of Cu to Cu_3Ga can occur within 2 to 3 min when polishing samples using a Ga FIB. The phase transformations occur in slower milling grains. The calculations suggest that a concentration of ≈36% of Ga can be found within these topographically higher regions which exceeds the required concentration threshold to form the Cu_3Ga phase. In addition, a higher strain and defect density can be observed here suggesting significant crystal structure alterations. Faster milling grains, however, do not reach this critical concentration and phase transformations. In addition, significant crystal structure changes could not be observed in the EBSD measurements for those grains. The measurements suggest that the damage and occurring phase transformation are linked to the speed at which the steady-state condition can be reached. For a steady-state condition that is reached sufficiently quickly (fast milling grains), sample alterations can be avoided.

25 keV Ne ion irradiation at 0° incidence angle

Ga as an ion species causes problems with phase transformations from copper to Cu_3Ga. Using a different ion species holds the potential to avoid this problem and Ne, as an inert ion species, appears as a suitable candidate. To test if Ne is suitable to polish the copper sample for EBSD measurements, the copper TEM grid was irradiated using two different ion doses 3371 ions/nm^2 and 2247 ions/nm^2 at a 0° incidence angle. An acceleration voltage of 25 kV is a commonly used operating parameter for patterning with neon and was chosen for that reason in these experiments. To achieve 30 keV Ne ions, the extractor would have to be raised to >37.5 kV which can lead to source blunting of a newly installed source. The value of 25 keV is sufficiently close to enable a comparison with the 30 keV Ga and allows for an easy and safe operation.

The Monte Carlo simulations show that the interaction volume of 25 keV Ne ions extends beyond the EBSD signal depth (see Figure 2). A total of 532 vacancies are produced per incident Ne ion. However, a significant portion of the vacancies are created below the EBSD signal depth (Supporting Information File 4), in contrast to Ga ions. The combination of these two effects suggests that only 1/3 of the vacancies (266 vacancies per incident ion) are created within the EBSD signal depth in comparison to the 30 keV Ga ion irradiation. Only four atoms are statistically sputtered per incident 25 keV Ne ion. This is significantly less than that for Ga (ten Cu atoms are sputtered per incident ion). The combination of a lower sputtering rate and a larger interaction volume depth for Ne is expected to result in an overall higher ion implantation concentration for Ne as the steady-state condition is reached later. To determine the dose required to reach the steady-state condition, the sample was irradiated with 3371 ions/nm^2 and a TEM lamella was prepared. The depth for a slow milling grain was measured to be 144 nm in the cross-sectional view. Considering that the interaction volume depth is 70 nm, the steady-state condition is reached at a dose of 1638 ions/nm^2. Throughout this time, 1.64×10^{11} Ne ions interact with the sample and implant in the sample. This is approximately the number of Cu atoms in the EBSD depth (2.1×10^{11} Cu atoms).

The TEM lamellae were prepared from both the lowest ion dose irradiated area (2247 ions/nm^2) as well as the highest ion dose irradiated area (3371 ions/nm^2). The TEM measurements and diffraction patterns are shown in Figure 6. The TEM measure-

ments of the lowest dose (2247 ions/nm^2) irradiated area, see Figure 6k, show a higher defect concentration in comparison to the control sample. A significant amount of twinning can be observed at the grain boundaries. The corresponding SAED pattern for the lowest ion dose irradiated area (2247 ions/nm^2) is given in Figure 6l. The angles between the reflections were determined to be $\alpha = 34°$ and $\beta = 71°$ and the distance ratio to $A/B = 1.67$ suggesting an fcc phase with [310] ZA. The corresponding SAED simulated pattern is shown in Figure 6m. The measured reflexes were $d_{hkl,A} = 0.187$ nm and $d_{hkl,B} = 0.112$ nm which correspond to those reported for Cu ($d_{002,Cu} = 0.181$ nm and $d_{\bar{1}31,Cu} = 0.109$ nm). The deviation of the d-spacing for the (002) reflection was also observed for the non-irradiated control experiment. The TEM measurements of the highest dose (3371 ions/nm^2) irradiated area (see Figure 6n) show a significantly higher number of defects and line defects in comparison to the control sample. The corresponding SAED pattern is given in Figure 6o. The angles between the reflections were determined to be $\alpha = 52°$ and $\beta = 70°$ and the distance ratio to $A/B = 1.15$ suggesting an fcc phase with [011] ZA. The corresponding simulated SAED pattern is given in Figure 6p. The measured reflections were $d_{hkl,A} = 0.217$ nm and $d_{hkl,B} = 0.189$ nm which correspond to those reported for Cu ($d_{1\bar{1}1,Cu} = 0.209$ nm and $d_{200,Cu} = 0.181$ nm). The distances as well as the angles between the reflections show deviations from the expected literature values. For example, the (200) and the $(1\bar{1}1)$ reflections show deviations of ≈0.01 nm. This behavior was previously observed for the (200) reflection only in the control sample. The enlarged d-spacing values for the $(1\bar{1}1)$ reflection suggest additional strain within the lattice. Furthermore, satellite peaks can be seen around the major reflections for this higher ion dose. To further assess the additional reflections, dark-field images were recorded for a satellite peak (see Figure 8a and Figure 8b). The bright areas in the dark-field image, which correspond to the satellite peak, are located around the grain boundaries and extend several hundreds of nanometers into the sample. A total of 4.36×10^{13} vacancies are created within the EBSD signal depth until the steady-state condition is reached. This suggests that every Cu atom would statistically be displaced 266 times during the irradiation process. These extremely high numbers of implanted Ne and created defects are likely the cause of the significant crystal alterations observed in the TEM measurements here. The calculations presented above concern a specific grain which was milled more slowly than other grains. According to this calculation, the steady-state condition is reached before the lowest ion dose is delivered. It would, therefore, be expected that the lowest and highest ion doses would yield the same result. The calculation, though, represents only a single measured grain and does not consider faster milling grains or grains which were milled slower. These grains would reach the steady-state condition at different stages and the delivered ion dose may make a big difference for those grains and would explain the observed results. Overall, the highest ion dose would produce more defects and a higher impurity concentration when averaged over many different grains which agrees with the TEM results. A 0° incidence irradiation with Ne produces bubbles directly underneath the sample surface (Figure 6j). The depth of the bubble layer directly corresponds to the interaction volume depth and the size of the bubbles corresponds to the distribution of ion ranges. Bubble formation is a well-documented artefact for He [41]. It is not surprising to find this for Ne considering the excessive number of implanted Ne ions resulting in oversaturation and hence bubble formation for this polishing procedure.

To evaluate the effect on the EBSD patterns, EBSD orientation maps for both the highest (3371 ion/nm^2) and lowest (2247 ions/nm^2) ion dose irradiated areas were recorded and evaluated. In both cases, the amount of zero solutions could be reduced by 1/3 and the patterns indexed within the polished area. The IPF X orientation map of the irradiated areas and the surrounding unpolished Cu is given in Figure 7d. A careful evaluation of the grain boundaries in both cases shows a significantly higher percentage of LAGB (see Table 1) with 66% when compared to the control sample with 8%. The evaluation was performed on EBSD measurements of individual areas to avoid contributions from the non-irradiated areas of the sample shown in Figure 7d. The band contrast and grain boundary maps for the irradiated areas are shown in Figure 7e and Figure 7g. The LAGB are displayed in yellow and the HAGB are displayed in red. The KAM maps (Figure 7f and Figure 7h) show a significantly higher level of misorientation in the irradiated sample (shown in green in the map). The measurements suggest changes in the microstructure and this is in good agreement with the TEM measurements which suggested a higher defect density and presented satellite peaks in the SAED pattern for the highest ion dose irradiation. Even though phase transformations could not be observed, significant crystal structure alterations as well as Ne bubble formation throughout the EBSD signal depth occurred when processing the sample at a 0° incidence angle, suggesting that this setting is unsuitable and can lead to EBSD result misinterpretation, especially for strain and deformation analysis.

Glancing angle irradiation of copper

Polishing samples at glancing angles with Ga FIBs using low energies, often for prolonged periods of time, is commonly reported [42,43]. The polishing performance of Ga FIB as well as of HIM operated with Ne was tested for glancing angle irradiation. The different irradiation measurements are illustrated in Figure 2.

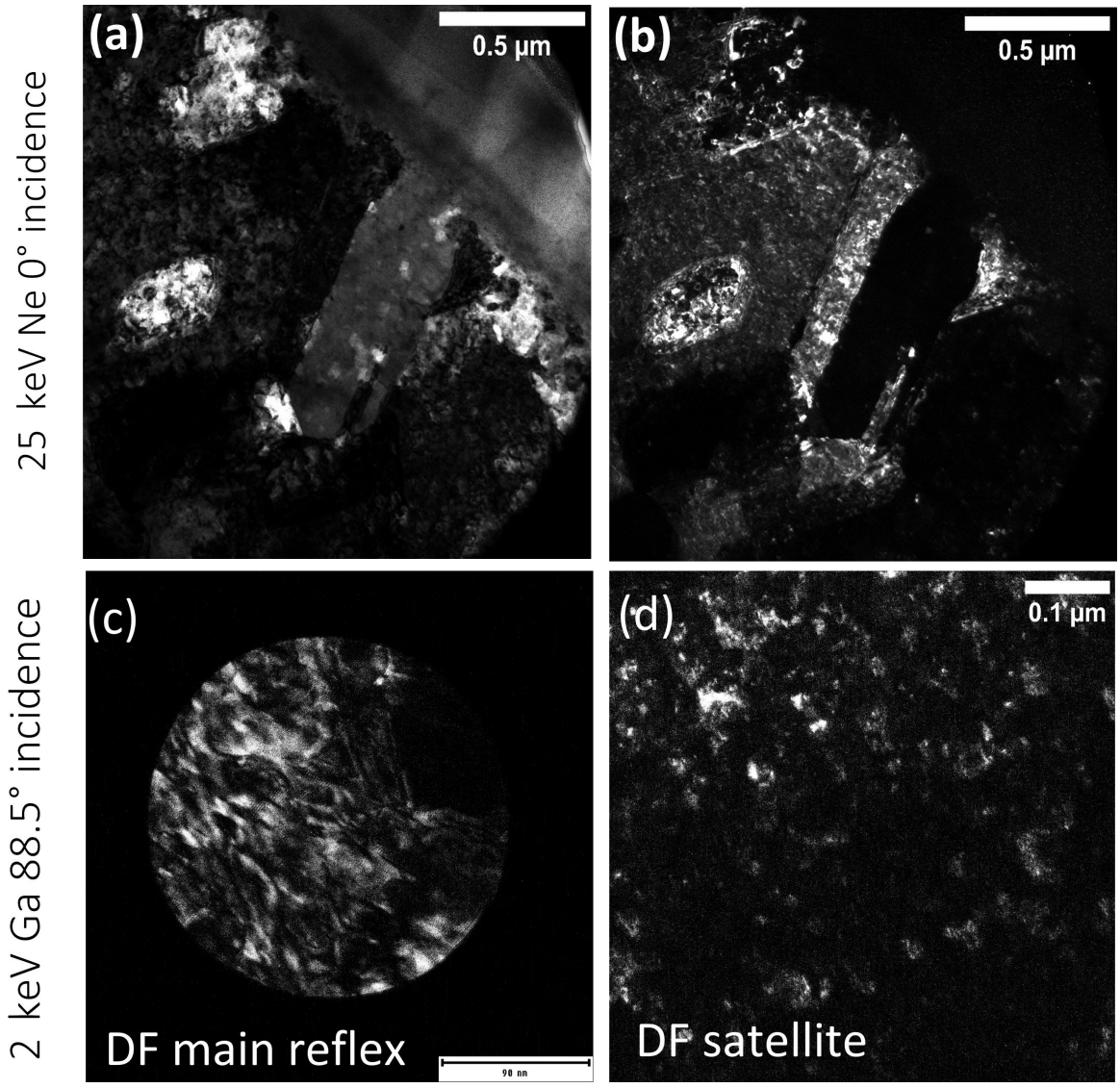

Figure 8: TEM measurements of a 25 keV Ne 0° incidence (top row) as well as 2 keV Ga 88.5° incidence (bottom row) irradiated Cu sample in a cross-sectional view. (a) Bright-field image of a satellite peak for the Ne-irradiated sample. (b) DF image of the satellite bright-field peak for the Ne-irradiated sample. (c) DF image of the main reflection. (d) DF image of the satellite reflection.

2 keV Ga ion irradiation at a glancing angle

The Monte Carlo simulations (Figure 2) show that the interaction volume of the 2 keV Ga ions is reduced to the top of the EBSD signal information depth with ≈3 nm when using glancing angles. This suggests that a significant portion of the sample should be unaltered in the EBSD signal volume.

As phase transformations started to occur for the lowest ion dose, the lowest dose of 2247 ions/nm^2 was used here. To irradiate a 100 µm^2 area with 2247 ions/nm^2, a longer irradiation time is required for the glancing angles in comparison to a 0° incidence angle irradiation. This can be understood when considering the projection of the irradiation area on the actual sample area. The area on the sample itself is larger as a result of the glancing angle which is illustrated in Figure 9. The total irradiation time of 33 min was used and was determined in a pre-experiment in which the polished area on the sample was measured. This approach was chosen, rather than determining the required time via calculation, since small deviations in the glancing angle have a large effect on the actual irradiated area and, therefore, on the required dose. For example, a glancing angle of 86.5° would result in a 1650 µm^2 area while an 88.5°

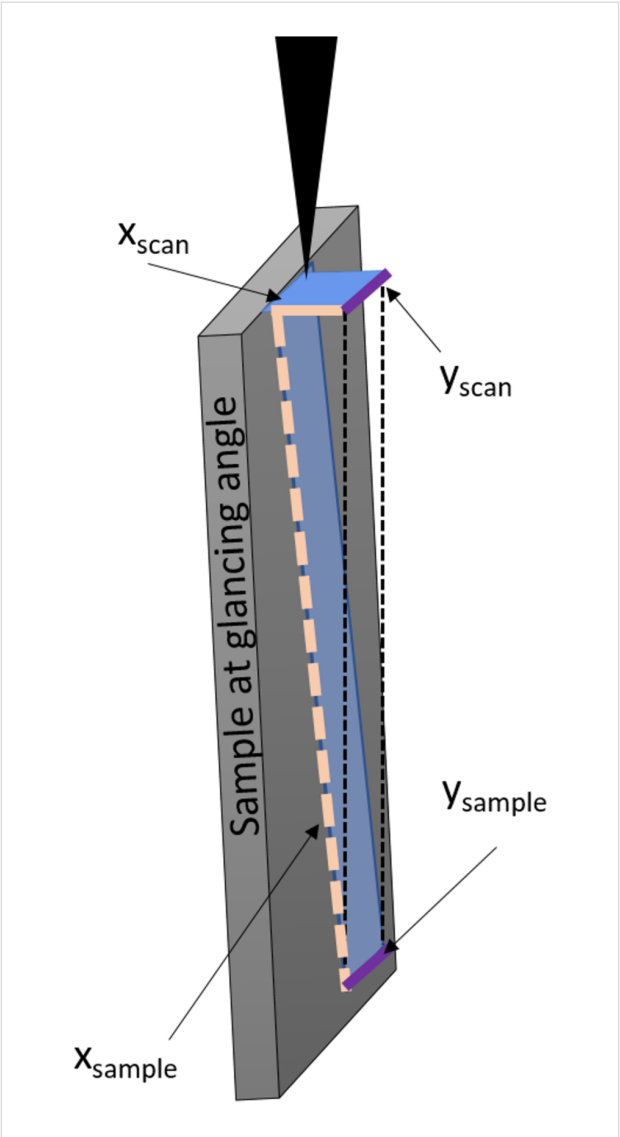

Figure 9: Illustration showing the enlarged irradiation area resulting from polishing at glancing angles. The scan size remains unchanged in the *y*-direction which is indicated by purple lines. The irradiated area is increased in size in the *x*-direction as a result of the projection of the setup irradiation area onto the tilted sample surface (light orange lines).

angle would result in a 3820 µm^2 area. The TEM copper grids can be slightly tilted in a holder and since such small angular changes have significant effects, a more accurate pre-experimental verification was used to determine the time required for delivering 2247 ions/nm^2. Polishing times on the order of 30 min at glancing angles are often reported in the literature and, therefore, represent a meaningful parameter. The height difference was measured to be 26 nm in TEM images for slower milling grains which means that the steady-state condition is reached after 228 s. Throughout this time, 4.27×10^{11} Ga ions interact with the sample and this represents the upper limit for Ga impurity concentration in the sample. There are only 4.19×10^{11} Cu atoms within the volume defined by the irradiated area (1650 µm^2) and the interaction volume depth is 3 nm. While the majority of the sample should remain unaltered, there is, in theory, an excessively high Ga impurity concentration in the top layer which is above the Ga concentration threshold required to form a Cu_3Ga phase. The Monte Carlo simulations suggest that 22 vacancies are created per incident ion. As a result, 9.4×10^{12} vacancies are created within the first 3 nm until the steady-state condition is reached. This number is larger than the actual number of Cu atoms, suggesting that every Cu atom is dislocated approximately 22 times from a lattice position. The calculation suggests that the Cu atoms are drastically moving throughout the irradiation process but are less often displaced in comparison to 30 keV Ga (see Table 1). The sputtering rate is significantly reduced with five Cu atoms per incident ion in comparison to the frontal irradiation with 30 keV Ga ions (see Table 1). The resulting slower milling leads to an increased time until the steady-state condition is reached and, therefore, higher defect density and impurity concentration are expected.

Throughout the experimental ion irradiation process, changes in the ion image contrast occur with darker stripes forming within the grains in the irradiated area (see Figure 5d). They cover 24% of the irradiated area. This value was determined using a threshold analysis in the image analysis program FIJI. The measured width of the stripes ranges from 70 to 150 nm. The corresponding FSD measurement (Figure 7j) shows that these stripes are closely related to differences in the sample topography.

A TEM lamella was prepared from the top part of the irradiated area and diffraction patterns underneath the evaluated sample surface. The TEM image (see Figure 6r), recorded directly underneath the sample surface shows a significant number of defects and precipitates. The SAED pattern (Figure 6s) shows a distinctly different behavior of both the control experiment and the 30 keV Ga 0° incidence angle irradiation experiment, with satellite reflections surrounding the main reflection. A similar diffraction pattern was previously observed for the periodic antiphase structure of CuAuII [42]. It is unlikely that the reflections are caused by oxide growth on the free Cu surface. If the satellite reflexes were caused by double diffraction (first from the Cu layer and then from the oxide layer) the satellite peaks would be observed for all lamellae as they were all prepared equal. The satellite peaks would also be present on both the irradiated as well as the non-irradiated area of the TEM lamella. For TEM lamella preparation, the irradiated area was immediately covered with a protective layer in situ, making oxidation unlikely. The angles between the reflections were measured to be $\alpha = 55°$ and $\beta = 62°$ and the ratio of distances determined to

be A/B = 1.05 for the main reflection. The pattern matches best a hcp structure with [011] ZA. The corresponding simulated SAED pattern is given in Figure 6t. The next best possible candidate would be a drastically distorted fcc structure with $[\bar{1}14]$ ZA. The angles of $\alpha = 65°$ and $\beta = 50°$ as well as the ratio of A/B = 1.17 for the fcc structure are significantly different, making this an unlikely candidate. A comparison between the reported d-spacing values for Cu ($d_{hkl,A}$ = 0.128 nm and $d_{hkl,A}$ = 0.109 nm) and the measured d-spacing values $d_{hkl,A}$ = 0.220 nm and $d_{hkl,B}$ = 0.201 nm shows a significant mismatch, suggesting that the SAED pattern does not correspond to a Cu fcc structure with a $[\bar{1}14]$ ZA. Instead, the pattern matches the diffraction pattern for the Cu_3Ga phase with a [011] ZA. The measured d-spacing values match the reported d-spacing values d_{100} = 0.225 nm and $d_{01\bar{1}}$ = 0.200 nm for the Cu_3Ga hcp structure. To further evaluate the satellite peaks, dark-field images were recorded for the main reflection peak and the satellite peak. The corresponding measurements are shown in Figure 8c and Figure 8d. The image shows that small clusters light up in the dark-field image of the satellite peak which have similar sizes as the observed stripes in the ion channeling image in Figure 6r. Anti-phase domains, which have been reported to produce such satellite spots in intermetallics such as CuAuII [44] can be understood as planar crystallographic defects. In anti-phase domain regions, every atom sits on its anti-site which can be imagined as a region consisting of anti-site defects. These regions could have been formed as a result of the high Ga implantation concentration and induced dislocations/vacancies within this area. The same behavior was observed for the 25 keV Ne 0° incidence angle irradiation for which an equally high number of implanted ions and defect formation was observed.

The TEM measurements show that defects and precipitates occur predominantly around grain boundaries and that these features can be found at a significant distance below the sample surface. The evaluation of the SRIM simulation suggested that each copper atom is displaced around 22 times during the polishing process. A high enough Cu atom as well as Ga ion mobility is likely to move ions as well as displaced Cu atoms into grain boundaries. Grain boundaries can facilitate transport deeper into the material and this could significantly alter the sample below the initially expected 3 nm alteration layer and would explain the position of defects/inclusions in the TEM images and bright clusters in the dark-field image. To assess this theory, EDS measurements were performed on the TEM lamella using 30 keV electrons. An overlay of a dark-field STEM image and the background-subtracted, peak-deconvoluted, 1σ-thresholded EDS Ga map (Tru map) is shown in Figure 6q. The different grains are clearly visible in the DF STEM image. The overlay shows that the Ga (black spheres) can end up several hundreds of nanometers below the sample surface along the grain boundaries. A sufficiently high Ga concentration can be reached in some areas and a phase transformation can occur much deeper within the sample than initially anticipated with 3 nm. The measurement shows that the initial assumption of a limited damage layer of 3 nm is incorrect. However, those sample alterations can occur throughout the entire EBSD signal depth (and beyond) once the Ga migrates along the grain boundaries.

To evaluate the effect on the EBSD pattern, an orientation and phase map of an irradiated area was recorded. Less surface topography was induced in comparison to a 0° incidence irradiation which allows better indexing and a significantly lower zero solution return (zero solution by ≈66% in comparison to the surrounding area). The overlay of the FSD image with the phase map (Figure 7j) shows that the Cu_3Ga phase can be found within the topographically higher regions. The same behavior was also observed for the frontal irradiation with 30 keV ions suggesting that 30 min polishing with Ga ions at glancing angles can induce phase transformations on copper in slower milling grains. This is in good agreement with the initial calculations suggesting that a sufficiently high Ga impurity concentration is reached within the top layer of the EBSD signal depth during the irradiation process for those grains. The phase-transformed areas are significantly smaller in comparison to the 30 keV Ga frontal polishing. A reason as to why this is could be the differences in the final sample topography after polishing. The resulting topographically higher regions are significantly smaller in area when polishing at glancing angles with 2 keV Ga, as evidenced in the FSD image (Figure 7j). This limits the area size in which a phase transformation to Cu_3Ga can occur. This effect would explain why the overall phase-transformed area is significantly smaller here despite a resulting higher Ga impurity concentration in comparison to the 30 keV Ga frontal polishing. It is plausible that the excess of Ga ions are incorporated into the lattice once the required impurity concentration for a phase transformation to Cu_3Ga is locally reached. The evaluation of the grain boundaries shows distinct deviations from the control sample. A significantly higher amount of LAGB is now present in the sample (see Figure 7l), with 17% in comparison to 8% observed for the control sample. The percentage of the different grain boundaries can be found in Table 1. LAGB can be indicators of recrystallization processes and can be observed for materials with higher defect densities. The KAM map (Figure 7m) shows a higher level of misorientation in the irradiated sample (shown in green in the map). This is in good agreement with the TEM measurements. It is not surprising to see alterations to the crystal structure as a result of the ion–solid interactions, especially considering the resulting impurity concentration and number of created defects. While a

well-indexed EBSD map can be obtained using this polishing technique, significant crystal structure alterations as well as localized phase transformations occur making this approach unsuitable for polishing Cu samples without inducing significant sample alterations.

25 keV Ne ion irradiation at 88.5° glancing angle

Since EBSD polishing is conventionally done at glancing angles, the Cu sample was irradiated with Ne at a glancing angle. Ne ions at 25 keV were used for these experiments. This setting was chosen over a lower ion energy as the interaction volume depth for both 25 keV Ne ions as well as 10 keV Ne ions (lowest possible ion landing energy) extends beyond the EBSD signal depth. Furthermore, the extractor voltage would need to be lowered to achieve sub-10 keV ion energies which significantly compromises Ne stability during the time-consuming polishing process and which should be avoided to ensure an even polishing. Furthermore, the sputtering yield for 10 keV Ne ions at an 88.5° glancing angle incidence is eight and thus smaller than that for 25 keV Ne ions. This would lead to a higher required dose to reach the steady-state condition and thus has the potential to create more defects.

The Monte Carlo simulations (Figure 2) show that the interaction volume of 25 keV Ne ions extends only marginally beyond the EBSD signal depth with 30 nm. The number of vacancies that are induced within the EBSD signal length is significantly reduced with ≈170 vacancies per ion while the number of sputtered atoms (12 atoms per incident ion) is the highest for the different polishing setups. The sputtering rate limits the overall number of created vacancies as well as the ion implantation concentration. A milling depth of 220 nm was achieved during the irradiation and significant topographic differences between grains were not observed. The steady-state condition is reached after 3.0×10^{10} Ne ions have interacted with the sample. This corresponds to a maximal impurity concentration of 12% which is significantly lower than that for a 0° incidence irradiation. Throughout this time, each Cu atom is displaced from its lattice site 17 times. Both the resulting impurity concentration as well as the number of created Cu displacements/vacancies are the lowest for this polishing experiment in comparison to the frontal Ne polishing and all Ga polishing experiments (see Table 1).

The cross-sectional view of the TEM measurement of the irradiated area is shown in Figure 6u. A significant number of defects and interstitials cannot be observed here and indeed the sample has a similar appearance of the control experiment. The SAED pattern (Figure 6v) was recorded in a position underneath the sample surface on the prepared TEM lamella. The angles were determined to be $\alpha = 52°$ and $\beta = 70°$ and the distance ratio $A/B = 1.15$ suggesting an fcc phase with [101] ZA. The corresponding simulated SAED pattern is given in Figure 6w. The d-spacing values were measured to be $d_{hkl} = 0.215$ nm and $d_{hkl} = 0.189$ nm which are in agreement with those reported for Cu ($d_{1\bar{1}1,Cu} = 0.209$ nm and $d_{200,Cu} = 0.181$ nm). The diffraction pattern corresponds to that of the copper phase with a [101] ZA. The deviation for the (200) reflection was also observed for the control sample and the results are overall in good agreement with the control experiment, suggesting that no significant crystal structure alteration occurred using this polishing protocol. Bubble formation could not be observed in the TEM images. The impurity concentration is likely not high enough for the required supersaturation and subsequent bubble formation. Furthermore, the reduced range of Ne ions at glancing angles would produce bubbles directly underneath the sample surface rather than at a significant distance underneath the sample surface. The closest distance to the sample surface, from which gas bubbles could escape, as well as the highest removal rate of atoms at the sample surface (due to the highest sputtering yield, see Table 1) are both likely to contribute to a lower overall amount of Ne accumulation in the sample, making bubble formation as well as interstitials less likely.

The FSD image of the sample (Figure 7n) shows the difference between the polished and unpolished sample area. The EBSD IPF X orientation map (Figure 7o) of non-polished sample areas as well as a 10 µm wide polished stripe show that a significant improvement in indexing can be achieved when polishing the sample with 25 keV Ne ions at a glancing angle. Overall, zero solutions could be halved. An evaluation of the grain boundaries (see Figure 7p) shows that 92% of the grain boundaries are high-angle grain boundaries and 8% are low-angle grain boundaries which is in good agreement with the control experiment. The KAM map (Figure 7q) shows no difference in misorientation between the sample and the polished area, suggesting that significant changes to the crystal structure were avoided.

The results suggest that Ne ions are a suitable ion species to polish copper for EBSD measurements. Phase transformations to Cu_3Ga could be avoided by using the inert ion species. Crystal structure alterations could be avoided when polishing at high energy at glancing angles. The measurements and Monte Carlo simulations suggest that significant crystal structure alterations occur for a sufficiently high ion implantation concentration as well as defect formation within the sample. Minimizing these is essential to avoid ion-beam-induced artefacts for EBSD measurements and polishing with higher energy Ne ions (25 keV) at glancing angles achieves exactly this.

To verify if Ga milling would lead to similar significant artefacts in 3D EBSD applications when using a Ga FIB/SEM, the

intersection of the irradiated Cu and the non-irradiated Cu was analyzed. TEM lamellae were prepared containing regions of both polished and unpolished sections of the sample. The altered area could only be found directly underneath the polished area and did not appear to significantly extend sideways for this material (see Supporting Information File 5) when using high-energy (30 keV) Ga ions. The ion-beam-exposed area was milled away and was not considered in EBSD measurements for 3D reconstructions. This concept is illustrated in Supporting Information File 6. This would explain why problems have not yet been reported with 3D EBSD. Considering the migration of ions along the grain boundaries, a more thorough assessment of potential sample alterations depending on the ion species should be carried out in future.

Conclusion

The presented results show that ion beam polishing can induce artefacts which can easily lead to misinterpretation of EBSD measurements. The often-used Ga FIB polishing can induce phase transformation as well as significant changes in the crystal structure, even for polishing with lower ion energies at glancing angles as shown in this work for simple samples, such as Cu. While well-indexed EBSD maps could be achieved using electropolishing and PIPS, both methods introduced crystallographic artefacts in the sample, leading to a higher number of LAGB and a higher KAM. The results suggest that polishing with high-energy Ne ions (25 keV) at glancing angles significantly improves indexing without changing the crystal structure of the sample. A detailed study on microtextural modifications and texture development with respect to easy channeling direction as well as a function of grain size should be carried out in different materials in the future. The evaluation of the experimental results and the Monte Carlo simulations suggest that impurity concentration as well as atom displacements within the sample are the key drivers for phase change and significant crystal structure changes. Minimizing the resulting ion implantation concentration as well as the number of displacements per individual sample atom within the EBSD signal depth is essential to avoid artefacts. This is achieved by quickly reaching the steady-state condition. The results show that the high sputtering yield of the 25 keV Ne when polishing at glancing angles leads to a quickly achieved steady-state condition which limits impurity concentration as well as atom displacements within the sample. This work shows that the HIM operated with Ne is a suitable instrument for EBSD sample preparation and it is able to prepare perfect samples for EBSD investigations of Cu.

Experimental

Control experiment

To study the native crystal structure of the sample, EBSD measurements were performed on a conventional bulk copper TEM grid (Omniprobe Cu TEM grids) which had not been irradiated by ions.

Irradiation of copper

Conventional copper TEM grids (Omniprobe Cu TEM grids) were irradiated using different ion species (Ga and Ne), different incident ion energies (30, 25, and 2 keV), different doses (3371 and 2247 ions/nm^2), as well as different incidence angles (0° incidence and glancing angle irradiation). The irradiation experiments were performed using the Zeiss Orion Nanofab Helium Ion Microscope (Ne) as well as the Thermo Fisher, Scios (Ga) FIB/SEM.

Lamella preparation using FIB and TEM

The TEM lamellae were prepared using the Thermo Fischer Scios Ga FIB/SEM. The irradiated area was identified by using SEM (30 kV acceleration voltage, 25 pA) and a lamella was prepared such that half of the TEM lamella had an irradiated area while the other half of the lamella had a non-irradiated area for the control measurement. This approach was chosen to ensure that the TEM lamella preparation did not alter the irradiation area in any way and that all regions surrounding the irradiated area were equivalent on the sample. A >500 nm thick platinum layer was deposited using the electron beam (2 keV, 2.3 nA) to protect the sample surface from any potential ion beam alteration throughout the subsequent processes, including the ion–solid interactions which occur with the sample during the first few moments of the ion beam deposition that could alter the sample surface. A further 1 µm thick platinum layer (16 µm long, 2 µm wide) was then deposited using the ion beam (30 kV acceleration voltage, 0.3 nA beam current). The cross-sections were cut using a 30 kV acceleration voltage and 7 nA beam current. The region of interest was then cut out and lifted onto a TEM grid where it was subsequently thinned using 0.5 nA and 0.1 nA beam current at a stage tilt of ±1.8° from the perpendicular ion beam incidence until the electron transparency was reached for 5 keV electrons (SEM). The lamella was then polished with the ion beam using a 5 kV acceleration voltage and 16 pA beam current and subsequently with 2 kV acceleration voltage and 27 pA beam current at a stage tilt of ±6° from the perpendicular ion beam incidence. The 2 kV polish was performed to reduce the damage layer on each side of the TEM lamella.

Alternative TEM lamella preparation: argon ion milling

To ensure that the FIB TEM lamella preparation did not alter the crystal structure for the TEM measurements, additional thin foils were prepared using argon ion mill, which is considered a conventional TEM sample preparation technique. For the

argon ion milling, a Gatan PIPS was used. The conventional copper TEM grids (Omniprobe Cu TEM grids) were thinned down using the following steps: 4 keV, 5° top, 3° bottom, 3 rpm for 30 min followed by 2.5 keV, 4° top, 2° bottom, 3 rpm for 5 min and subsequently 0.5 keV, 5° top, 3° bottom, 3 rpm for 3 min.

Electropolishing

Conventional copper TEM grids (Omniprobe Cu TEM grids) were electropolished using a Fishione Instruments Model 120 twin-jet polisher. An 82 wt % of phosphoric acid bath was used for the experiments. The samples were polished using 1–8 V DC using the speed 4 polish 1 settings. The recipe for copper samples was provided in the user manual of the system. The sample was polished for 10 s for EBSD measurements. An additional sample was electropolished for 15 s to electron transparency to create a control sample for the TEM measurement.

Transmission electron microscopy

All TEM measurements were performed using a JEOL 2100 TEM. Electron diffraction measurements were performed using alpha 2, spot 4, condenser aperture 4, and no objective aperture. The TEM imaging was performed using alpha 2 spot 1, condenser aperture 4, and objective aperture 1. Centered dark-field imaging was performed using alpha 2 spot 1, condenser aperture 4, and a sufficiently small objective aperture which allowed to select the satellite peaks.

Scanning transmission electron microscopy

All STEM measurements were performed inside the Thermo Fischer Scios Ga FIB/SEM using the STEM detector with exception of the STEM/EDS combined measurement which was performed using the Tescan S8000X Xe plasma FIB/SEM. In both cases a 30 kV acceleration voltage was used.

Electron backscatter diffraction

All EBSD measurements were performed on a bulk Cu TEM grid specimen to ensure that the sample was not altered or processed in any way other than by the ion irradiation itself. The EBSD measurements were performed using an Oxford Symmetry EBSD detector on a Tescan S8000X Xe plasma FIB/SEM. The EBSD maps were recorded using the following SEM parameters: 20 kV, 300 pA, 6 mm WD, and 70° pre-tilted sample holder.

The following EBSD detector parameters were used for all EBSD experiments: resolution mode, 50 ms exposure time, solver settings: optimized TKD solver and 10 Hough bands. For larger area maps (non-polished sample, all Ne-irradiated samples) with a 39 µm field of view, a 39 nm step size was used. In addition, maps with a field of view of ≈15 µm were recorded for the statistical evaluation of all irradiated areas. A 15 nm step size was used for these measurements.

Energy-dispersive X-ray spectroscopy

The EDS point spectra were recorded using an Oxford Ultim Max 100 EDS detector on the Tescan S8000X Xe plasma FIB/SEM. The EDS maps were background subtracted and peak deconvoluted (TruMap). In addition, a 1σ threshold was applied to ensure that only statistically significant data was included in the maps. The SEM parameters (30 kV acceleration voltage and 1 nA beam current) were chosen in the analytical mode.

Supporting Information

Supporting Information File 1

STEM image showing a cross-sectional view of an ion-polished Cu sample (30 keV Ga, 3371 ions/nm^2). Differences in the milling depth for different grains are visible.
[https://www.beilstein-journals.org/bjnano/content/supplementary/2190-4286-12-73-S1.tif]

Supporting Information File 2

Ion channeling video showing a Cu sample changing during Ga ion polishing.
[https://www.beilstein-journals.org/bjnano/content/supplementary/2190-4286-12-73-S2.mp4]

Supporting Information File 3

Energy-dispersive X-ray point spectra recorded on a slower milling grain and on a faster milling grain of a 30 keV Ga ion-polished Cu sample. A dose of 3371 ions/nm^2 was used for the polishing experiment.
[https://www.beilstein-journals.org/bjnano/content/supplementary/2190-4286-12-73-S3.png]

Supporting Information File 4

SRIM simulation showing vacancies for 25 keV Ne ion irradiation of Cu at a 0° incidence angle.
[https://www.beilstein-journals.org/bjnano/content/supplementary/2190-4286-12-73-S4.bmp]

Supporting Information File 5

STEM image showing the interface of a non-irradiated area and a 30 kV Ga 0° incidence irradiated area.
[https://www.beilstein-journals.org/bjnano/content/supplementary/2190-4286-12-73-S5.tif]

Supporting Information File 6

SAED patterns of a non-irradiated Cu sample prepared by electropolishing, PIPS, and FIB. In all cases, the SAED pattern matches that of Cu. (a) Electropolishing, the SAED pattern matches the [110] ZA for Cu. The measured d-spacing for $d_{200,A}$ = 0.177 nm is slightly smaller than the reported value of $d_{002,Cu}$ = 0.181 nm for Cu (PDF number 00-004-0836); however, within an acceptable discrepancy for this d-spacing. The measured d-spacing for $d_{11-1,B}$ = 0.209 nm matches the reported value of $d_{111,Cu}$ = 0.209 nm. (b) PIPS, the SAED pattern matches the [310] ZA for Cu. The measured d-spacing for $d_{131,A}$ = 0.209 nm matches the reported value of $d_{111,Cu}$ = 0.209 nm. The measured d-spacing for $d_{200,B}$ = 0.189 nm is slightly larger than the reported value of $d_{002,Cu}$ = 0.181 nm for Cu (PDF number 00-004-0836); however, within an acceptable discrepancy for this d-spacing. (c) FIB-prepared TEM lamella, the SAED pattern matches the [100] ZA for Cu. The measured d-spacing for $d_{022,A}$ = 0.133 nm is in good agreement with the reported value of $d_{022,Cu}$ = 0.128 nm for Cu (PDF number 00-004-0836). The measured d-spacing for $d_{002,B}$ = 0.192 nm is slightly larger than the reported value of $d_{002,Cu}$ = 0.181 nm for Cu (PDF number 00-004-0836), however; within an acceptable discrepancy for this d-spacing. The SAED measurements recorded on all the TEM lamellae which were prepared using different methods are in good agreement, suggesting that the FIB TEM lamella preparation did not significantly alter the TEM measurement results.
[https://www.beilstein-journals.org/bjnano/content/supplementary/2190-4286-12-73-S6.tif]

Acknowledgements

The author would like to thank the authors of the programs SRIM and FIJI for making the software freely available. The author would like to acknowledge the Central Analytical Research Facility CARF (Tescan S8000X PFIB/SEM, Zeiss Orion Nanofab Helium Ion Microscope), operated by the Queensland University of Technology (QUT). The author would also like to acknowledge the Centre for Microscopy and Microanalysis operated by the University of Queensland for the access to the Thermo Fischer Scios Ga FIB/SEM.

The author would like to sincerely thank Dr Peter Hines, Dr Jamie Riches, and Dr Graeme Auchterlonie for the discussions about the TEM results and crystallography. The author would like to thank Dr Jamie Riches for the support on the TEM and for preparing the sample using PIPS. The author would like to thank Prof. Nikki Stanford and Dr Vijay Bhatia for the discussions about EBSD. The author would like to thank Rebecca Fieth for preparing the electropolishing samples.

The author would like to thank the staff at Zeiss (Peabody), especially John Notte, David Ferranti, and Fouzia Khanom for organizing the instrument time in the factory to learn and optimize Ne operations. The learnt tips and tricks were essential to ensure stable Ne operation for hours on the HIM.

ORCID® iDs

Annalena Wolff - https://orcid.org/0000-0003-3118-372X

References

1. Hlawacek, G.; Gölzhäuser, A., Eds. *Helium Ion Microscopy;* NanoScience and Technology; Springer International Publishing: Cham, Switzerland, 2016. doi:10.1007/978-3-319-41990-9
2. Pöpsel, C.; Becker, J.; Jeon, N.; Döblinger, M.; Stettner, T.; Gottschalk, Y. T.; Loitsch, B.; Matich, S.; Altzschner, M.; Holleitner, A. W.; Finley, J. J.; Lauhon, L. J.; Koblmüller, G. *Nano Lett.* **2018,** *18,* 3911–3919. doi:10.1021/acs.nanolett.8b01282
3. Turchanin, A.; Gölzhäuser, A. *Adv. Mater. (Weinheim, Ger.)* **2016,** *28,* 6075–6103. doi:10.1002/adma.201506058
4. Leppänen, M.; Sundberg, L.-R.; Laanto, E.; de Freitas Almeida, G. M.; Papponen, P.; Maasilta, I. J. *Adv. Biosyst.* **2017,** *1,* 1700070. doi:10.1002/adbi.201700070
5. Said, N.; Chatzinotas, A.; Schmidt, M. *Adv. Biosyst.* **2019,** *3,* 1800250. doi:10.1002/adbi.201800250
6. Zhang, K.; Song, Y.; Jiang, S.; Jiang, Z.; Jia, C.; Huang, Y.; Wen, M.; Liu, W.; Wang, P.; Li, X.; Liu, T.; Xie, X.; Shan, C.; Liu, X.; Wang, X. *Geofluids* **2019,** *2019,* 5274327. doi:10.1155/2019/5274327
7. Mattei, C.; Lim, R.; Drury, H.; Nasr, B.; Li, Z.; Tadros, M. A.; D'Abaco, G. M.; Stok, K. S.; Nayagam, B. A.; Dottori, M. *Front. Cell Dev. Biol.* **2019,** *7,* 25. doi:10.3389/fcell.2019.00025
8. Xia, D.; McVey, S.; Huynh, C.; Kuehn, W. *ACS Appl. Mater. Interfaces* **2019,** *11,* 5509–5516. doi:10.1021/acsami.8b18083
9. Alkemade, P. F. A.; van Veldhoven, E. *Deposition, Milling, and Etching with a Focused Helium Ion Beam;* Nanofabrication; Springer Vienna: Vienna, Austria, 2012; pp 275–300. doi:10.1007/978-3-7091-0424-8_11
10. Cordoba, R.; Ibarra, A.; Mailly, D.; De Teresa, J. M. *Nano Lett.* **2018,** *18,* 1379–1386. doi:10.1021/acs.nanolett.7b05103
11. Calafiore, G.; Koshelev, A.; Darlington, T. P.; Borys, N. J.; Melli, M.; Polyakov, A.; Cantarella, G.; Allen, F. I.; Lum, P.; Wong, E.; Sassolini, S.; Weber-Bargioni, A.; Schuck, P. J.; Cabrini, S.; Munechika, K. *Sci. Rep.* **2017,** *7,* 1651. doi:10.1038/s41598-017-01871-5
12. Semple, M.; Baladi, E.; Iyer, A. K. *IEEE J. Sel. Top. Quantum Electron.* **2019,** *25,* 1–8. doi:10.1109/jstqe.2019.2896277
13. Takashima, H.; Fukuda, A.; Maruya, H.; Tashima, T.; Schell, A. W.; Takeuchi, S. *Opt. Express* **2019,** *27,* 6792. doi:10.1364/oe.27.006792
14. Chen, K.; Razinskas, G.; Vieker, H.; Gross, H.; Wu, X.; Beyer, A.; Gölzhäuser, A.; Hecht, B. *Nanoscale* **2018,** *10,* 17148–17155. doi:10.1039/c8nr02160k
15. Cho, E. Y.; Li, H.; LeFebvre, J. C.; Zhou, Y. W.; Dynes, R. C.; Cybart, S. A. *Appl. Phys. Lett.* **2018,** *113,* 162602. doi:10.1063/1.5048776

16. Aramesh, M.; Mayamei, Y.; Wolff, A.; Ostrikov, K. *Nat. Commun.* **2018,** *9,* 835. doi:10.1038/s41467-018-03316-7
17. Hlawacek, G.; Bali, R.; Röder, F.; Aleksandrov, Y.; Semisalova, A.; Wintz, S.; Wagner, K.; Schultheiss, H.; Facsko, S.; Fassbender, J. *Microsc. Microanal.* **2016,** *22,* 1716–1717. doi:10.1017/s1431927616009429
18. Dowsett, D.; Wirtz, T. *Anal. Chem. (Washington, DC, U. S.)* **2017,** *89,* 8957–8965. doi:10.1021/acs.analchem.7b01481
19. Wirtz, T.; De Castro, O.; Audinot, J.-N.; Philipp, P. *Annu. Rev. Anal. Chem.* **2019,** *12,* 523–543. doi:10.1146/annurev-anchem-061318-115457
20. Giannuzzi, L. A.; Stevie, F. A., Eds. *Introduction to Focused Ion Beams;* Springer US: Boston, MA, U.S.A., 2005. doi:10.1007/b101190
21. Wolff, A.; Klingner, N.; Thompson, W.; Zhou, Y.; Lin, J.; Peng, Y. Y.; Ramshaw, J. A. M.; Xiao, Y. *J. Microsc. (Oxford, U. K.)* **2018,** *272,* 47–59. doi:10.1111/jmi.12731
22. Einsle, J. F.; Bouillard, J.-S.; Dickson, W.; Zayats, A. V. *Nanoscale Res. Lett.* **2011,** *6,* 572. doi:10.1186/1556-276x-6-572
23. Ziegler, J. F.; Ziegler, M. D.; Biersack, J. P. *SRIM – The stopping and range of ions in matter (2010);* Nuclear Instruments and Methods in Physics Research Section B: Beam Interactions with Materials and Atoms, Vol. 268; Elsevier: Amsterdam, Netherlands, 2010; pp 1818–1823. doi:10.1016/j.nimb.2010.02.091
24. Mayer, J.; Giannuzzi, L. A.; Kamino, T.; Michael, J. *MRS Bull.* **2007,** *32,* 400–407. doi:10.1557/mrs2007.63
25. Wilkinson, A. J.; Britton, T. B. *Mater. Today* **2012,** *15,* 366–376. doi:10.1016/s1369-7021(12)70163-3
26. Schwartz, A. J.; Kumar, M.; Adams, B. L., Eds. *Electron Backscatter Diffraction in Materials Science;* Springer US: Boston, MA, U.S.A., 2000. doi:10.1007/978-1-4757-3205-4
27. Nowakowski, P.; Schlenker, J.; Ray, M.; Fischione, P. *Microsc. Microanal.* **2016,** *22,* 12–13. doi:10.1017/s143192761600091x
28. Nowell, M. M.; Witt, R. A.; True, B. *Microsc. Microanal.* **2005,** *11,* 504–505. doi:10.1017/s143192760550672x
29. Wynick, G. L.; Boehlert, C. J. *Mater. Charact.* **2005,** *55,* 190–202. doi:10.1016/j.matchar.2005.04.008
30. Zaefferer, S.; Romano, P.; Friedel, F. J. *J. Microsc. (Oxford, U. K.)* **2008,** *230,* 499–508. doi:10.1111/j.1365-2818.2008.02010.x
31. Kim, D.-I.; Kim, B.-K.; Kim, J.-H. *Appl. Microsc.* **2015,** *45,* 218–224. doi:10.9729/am.2015.45.4.218
32. Saowadee, N.; Agersted, K.; Ubhi, H. S.; Bowen, J. R. *J. Microsc. (Oxford, U. K.)* **2013,** *249,* 36–40. doi:10.1111/j.1365-2818.2012.03677.x
33. Michael, J.; Giannuzzi, L. *Microsc. Microanal.* **2007,** *13,* 926–927. doi:10.1017/s1431927607071796
34. Michael, J. R. *Microsc. Microanal.* **2006,** *12,* 1248–1249. doi:10.1017/s1431927606062015
35. Michael, J. R. *Microsc. Microanal.* **2011,** *17,* 386–397. doi:10.1017/s1431927611000171
36. Xiao, Y.; Maier-Kiener, V.; Michler, J.; Spolenak, R.; Wheeler, J. M. *Mater. Des.* **2019,** *181,* 107914. doi:10.1016/j.matdes.2019.107914
37. Kiener, D.; Motz, C.; Rester, M.; Jenko, M.; Dehm, G. *Mater. Sci. Eng., A* **2007,** *459,* 262–272. doi:10.1016/j.msea.2007.01.046
38. Traylor, R.; Zhang, R.; Kacher, J.; Douglas, J. O.; Bagot, P. A. J.; Minor, A. M. *Acta Mater.* **2020,** *184,* 199–210. doi:10.1016/j.actamat.2019.11.047
39. Radi, Z.; Havancsák, K.; Kalácska, S.; Baris, A. Surface polishing and slope cut by parallel ar ion beams for high resolution electron backscatter diffraction measurements. In *2014 International Conference on Nanoscience and Nanotechnology,* Feb 2–6, 2014; IEEE: Piscataway, NJ, U.S.A., 2014. doi:10.1109/iconn.2014.6965245
40. Volkert, C. A.; Minor, A. M. *MRS Bull.* **2007,** *32,* 389–399. doi:10.1557/mrs2007.62
41. Wang, Y.-C.; Tian, L.; Liu, F.; Qin, Y.-B.; Zheng, G.; Wang, J.-T.; Ma, E.; Shan, Z.-W. *Small* **2017,** *13,* 1601753. doi:10.1002/smll.201601753
42. Guo, J.; Amira, S.; Gougeon, P.; Chen, X.-G. *Mater. Charact.* **2011,** *62,* 865–877. doi:10.1016/j.matchar.2011.06.007
43. Michael, J.; Kotula, P. *Microsc. Microanal.* **2008,** *14,* 976–977. doi:10.1017/s1431927608081294
44. Edington, J. W. *Practical Electron Microscopy in Materials Science, Monograph 2 Electron Diffraction in the Electron Microscope;* The Macmillan Press LTD, 1975; pp 66 ff. doi:10.1007/978-1-349-02595-4

License and Terms